Centre Eau Terre Environnement

ASSESSMENT OF THE DEEP GEOTHERMAL ENERGY SOURCE POTENTIAL IN REMOTE NORTHERN REGIONS: A STUDY UNDERTAKEN IN THE SUBARCTIC OFF-GRID COMMUNITY OF KUUJJUAQ, NUNAVIK, CANADA

Par

Mafalda Alexandra Marques Miranda

Thèse présentée pour l'obtention du grade de

Philosophiae Doctor (Ph.D.)

en sciences de la terre

Jury d'évaluation

Président du jury et examinateur interne	Erwan Gloaguen INRS
Examinateur externe	Biao Li Department of Building, Civil and Environmental Engineering Concordia University
Examinateur interne	Matthew Minnick Respec
Directeur de recherche	Jasmin Raymond INRS
Codirecteur de recherche	Chrystel Dezayes BRGM

ACKNOWLEDGMENTS

To Jasmin Raymond. Thank you for the opportunity to pursue my PhD in a topic that I am passionate about. Although I am terrible at job interviews, you did choose me for the position and for that I am truly grateful. I hope to have been up to the challenge. Working with you has helped me to push myself beyond what I thought I was capable of. You are a great mentor, and it has been a pleasure being part of your team.

To Chrystel Dezayes. Thank you for accepting to co-supervise this work and for all the discussions, comments and corrections.

To Erwan Gloaguen, Biao Li and Matthew Minnick. Thank you for accepting to take a critical look at my work and for judging this thesis constructively.

To Nelson Rodrigues and Alcides Pereira. If I am here today, I owe it in part to you both. Thank you for 7 years ago accepting to be my supervisors and for the posterior opportunity to keep working with you until the day I came to Canada. If you had not given me a shot back then, I would most likely not be here today.

To Jonathan Willis-Richards. Thank you for introducing me to the EGS and rock mechanics world and for all the exchanges, discussions, comments, and suggestions. Your advice has been greatly appreciated.

To Nicolò and Félix-Antoine. Thank you for all the discussions and brainstorming.

To Jean-François Dutil, Sérgio Seco and Stefane Premont. Thank you for the support with the analyzes of the radiogenic and chemical elements.

To Cynthia Brind’Amour-Cote. Thank you for the support during the field campaign.

To my old and current teammates and colleagues. Thank you for your support and companionship.

To Jorge, Cecilia, Shiva, Félix, Ali and Ouassim. Thank you for your friendship, you made these years more pleasant.

To my family. Thank you for helping me to spread my wings and fly.

Funding

This thesis was funded by the *Institut nordique du Quebec* (INQ) through the *Chaire de recherche INQ sur le potentiel géothermique du Nord* awarded to Jasmin Raymond. The *Centre d'études nordiques* (CEN), supported by the *Fonds de recherche du Quebec – nature et technologies* (FRQNT), and the *Observatoire Homme Milieu Nunavik* (OHMI) are further acknowledged for helping with field campaigns cost and logistics.

RÉSUMÉ

Les systèmes géothermiques ouvragés peuvent être une solution pour diminuer la dépendance aux combustibles fossiles des communautés nordiques éloignées du Canada. Toutefois, l'inexistence de forages d'exploration profonds, et plus généralement de donnés sur le sous-sol, à proximité des communautés visées induit de nombreuses incertitudes qui ont été abordées dans cette thèse. Les travaux entrepris dans la communauté de Kuujjuaq (Nunavik, Canada) ont permis de définir des lignes directrices et d'adapter les méthodes existantes qui peuvent maintenant être étendues à d'autres communautés éloignées faisant face à des défis similaires d'exploration géothermique.

Le flux de chaleur a été déduit numériquement par résolution d'un problème inverse de conduction de chaleur en 1D. L'algorithme de Nelder-Mead a été utilisé pour minimiser la somme des moindres carrés et trouver le flux de chaleur optimal qui permet de reproduire un profil de température d'une profondeur de 80 m mesuré dans un puits d'observation hydrogéologique. Le flux de chaleur simulé s'est révélé sensible à l'histoire paléoclimatique et aux propriétés thermophysiques. Par conséquent, ces différentes sources d'incertitude affectent les prédictions de la température en profondeur et l'évaluation de l'énergie thermique en place. Des simulations de Monte Carlo ont révélé que la température du réservoir et le facteur de récupération sont les paramètres les plus influents qui affectent les ressources géothermiques et la production potentielle de chaleur et d'électricité. Les analyses de risque suggèrent que la production de chaleur géothermique à Kuujjuaq implique un risque moyen à faible, alors que la production d'électricité et la cogénération présentent un risque élevé à moyen. De plus, un modèle de contrainte *a priori* a été proposé pour Kuujjuaq considérant des corrélations empiriques, la modélisation analytique et des simulations de Monte Carlo, lesquelles ont été calibrées avec des données régionales. Ce modèle fournit une première évaluation du régime de contrainte dans la région, essentiel à la simulation du développement de systèmes géothermiques ouvragés à Kuujjuaq. Les simulations couplées des processus mécanique, hydraulique et thermique ont révélé qu'un sous-sol mécaniquement faible et hydrauliquement conducteur favoriserait le développement de réservoirs d'un potentiel intérêt commercial.

L'approche décrite dans cette thèse représentent une contribution significative pour une première évaluation des ressources géothermiques profondes avec des moyens abordables pour les communautés nordiques et éloignées. Ces ressources ont le potentiel de répondre à la

demande annuelle moyenne de chauffage à Kuujjuaq et l'exploration géothermique vaut la peine de se poursuivre afin d'affiner ce potentiel et d'envisager son exploitation future.

Mots-clés : Propriétés thermophysiques; modélisation inverse; conduction de chaleur; flux de chaleur; température en profondeur; régime de contraintes; méthode de Monte Carlo; modélisation thermo-hydro-mécanique; modèle de cisaillement-dilatation; coût actualisé de l'énergie

ABSTRACT

Renewable off-grid technologies, such as engineered geothermal energy systems, can be a solution to offset the fossil fuel dependency of Canadian remote northern communities. However, the lack of deep exploratory boreholes, and subsurface data in general, nearby target communities induces sources of uncertainty that were addressed in this thesis. The work undertaken in the community of Kuujjuaq (Nunavik, Canada) allowed defining guidelines and adapt existing methodologies. Such methods can now be extended to other remote settlements facing similar geothermal exploration challenges.

The terrestrial heat flux was inferred numerically by function comparison solving a 1D inverse heat conduction problem. The Nelder-Mead algorithm was used to minimize the sum of least squares to find the optimal heat flux that best matched a 80-m-temperature profile measured in a groundwater monitoring well. The simulated heat flux revealed to be sensitive to the paleoclimate history and thermophysical properties conditions. Consequently, these uncertainty sources affect prediction of the subsurface temperature and evaluation of the thermal energy in place. Monte Carlo-based global sensitivity analysis revealed that the reservoir temperature and recovery factor are the most influential parameters affecting the geothermal energy source and the potential heat and power output. Risk analyzes suggest that geothermal heat production in Kuujjuaq is a medium to low-risk application while electricity generation and combined heat and power are high to medium risk. Furthermore, an a priori stress model was proposed for Kuujjuaq based on empirical correlations, analytical modeling and Monte Carlo simulations, which were calibrated with regional literature data. This model provides a first-order assessment of the stress regime in the region, required to simulate the development of engineered geothermal energy systems in Kuujjuaq. Coupled simulations of mechanical, hydraulic and thermal processes revealed that a mechanically weak and hydraulically conductive subsurface could favor the development of reservoirs of potential commercial interest.

The approach outlined in this thesis represent a significant contribution for a first-order evaluation of the deep geothermal energy source with means affordable to the northern and remote communities. The deep geothermal energy source has potential to fulfill Kuujjuaq average annual heating demand and, thus, further geothermal exploration is worthwhile to refine this potential and consider its exploration in the future.

Keywords : Thermophysical properties; inverse modeling; heat conduction; heat flux; subsurface temperature; stress regime; Monte Carlo method; thermo-hydro-mechanical modeling; shear-dilation model; levelized cost of energy

SOMMAIRE RÉCAPITULATIF

Introduction

Le Canada a un énorme potentiel pour le développement des énergies renouvelables. Toutefois, il y a encore 239 communautés qui dépendent uniquement du diesel pour la production d'électricité et du chauffage (p.ex., Arriaga et al., 2017). Cela représente environ 200 000 habitants sans approvisionnement en énergie propre qui dépendent de manière critique des produits pétroliers pour leur sécurité et leur croissance économique. En fait, le cadre énergétique actuel de ces communautés retarde leur progrès socio-économique et est une barrière à l'amélioration de leur niveau de vie. Au Nunavik, par exemple, les coûts des aliments sont environ 57 % plus élevés qu'ailleurs au Québec (KRG et al., 2010). L'accès à une source d'énergie propre, fiable et abordable est donc une priorité pour le développement socio-économique des communautés canadiennes éloignées et des solutions renouvelables hors réseau, telles que l'énergie géothermique, pourraient contribuer à changer ce cycle de pauvreté intimement liée à l'énergie. En fait, les plans d'action et les engagements du Canada sur le climat visent à faire en sorte que les communautés rurales, éloignées et autochtones aient la possibilité d'être alimentées par une énergie propre et fiable d'ici 2030 (GCan, 2016 ; ECCC, 2020). Toutefois, pour être une alternative viable à la dépendance au diesel, une source d'énergie renouvelable doit être produite localement, être fiable, être suffisamment abondante pour répondre à un pourcentage important de la demande du marché et être obtenue à un coût compétitif par rapport au diesel. De plus, la solution optimale d'énergie renouvelable hors réseau devrait répondre non seulement aux besoins en électricité, mais également aux besoins de chauffage.

Parmi les options disponibles, l'énergie géothermique profonde a l'avantage d'être produite 24 heures sur 24, 7 jours sur 7, quelles que soient les conditions météorologiques. L'énergie géothermique a aussi l'avantage d'être omniprésente sur toute la surface du globe et, en fonction de la température de la ressource, peut être utilisée pour différentes applications (Lindal, 1973 ; Kagel et al., 2005 ; Glassley, 2010). En fait, les ressources géothermiques profondes reçoivent actuellement une attention accrue en tant que source d'énergie alternative renouvelable et locale capable de fournir de la chaleur et de l'électricité de base aux communautés hors réseau (p.ex., Majorowicz et al., 2010a ; Majorowicz et al., 2010b ; Kunkel et al., 2012 ; Grasby et al., 2013 ; Walsh, 2013 ; Majorowicz et al., 2014b ; Majorowicz et al., 2015a ; Majorowicz et al., 2020 ; Majorowicz et al., 2021). La production d'énergie pendant les conditions de pointe peut être couplée à des systèmes auxiliaires renouvelables ou non renouvelables associés à une centrale géothermique pour être plus économique et répondre aux charges de chauffage dans les climats froids (Mahbaz et al., 2020).

Une évaluation des ressources géothermiques à l'échelle canadienne a été réalisée par Grasby et al. (2012). Cette étude suggère que le Bouclier canadien serait une zone prometteuse pour la production d'énergie géothermique avec des concepts alternatifs et non conventionnels, tels que les systèmes géothermiques ouvragés (Figure 1.12). En plus, une étude de faisabilité réalisée récemment au Nunavut suggère également que ces systèmes pourraient être une solution afin d'extraire les ressources géothermiques profondes dans le Bouclier canadien (Minnick et al., 2018). Il est donc important, et c'est le but principal de cette thèse, d'évaluer la faisabilité technique et économique des systèmes géothermiques ouvragés dans les communautés hors réseau installées dans le Bouclier canadien.

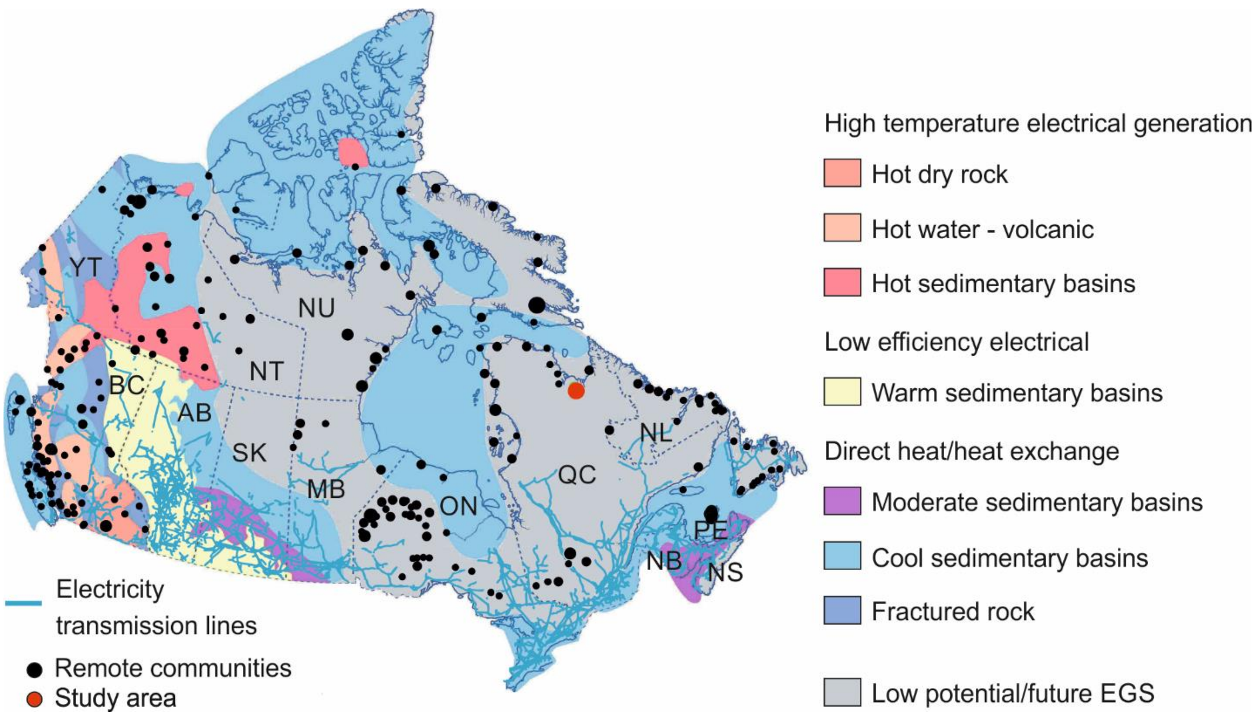

Figure 1.12 Répartition du potentiel géothermique au Canada en fonction de l'utilisation finale et l'emplacement du réseau électrique et des communautés éloignées. Provinces : BC – Colombie-Britannique, AB – Alberta, SK – Saskatchewan, MB – Manitoba, ON – Ontario, QC – Québec, NL – Terre-Neuve-et-Labrador, NB – Nouveau-Brunswick, NS – Nouvelle-Écosse, PE – Prince Edward. Territoires : YT – Yukon, NT – Territoires du Nord-Ouest, NU – Nunavut. Le lecteur est renvoyé à la source originale pour plus de détails, redessiné selon Grasby et al. (2012) et Arriaga et al. (2017).

La caractérisation géologique d'un site est une étape clé pour arriver au développement de systèmes géothermiques ouvragés (Nakatsuka, 1999). Des paramètres associés à la géologie régionale et locale ont un rôle sur les régimes thermiques, hydrauliques et mécaniques des roches, qui, à leur tour, ont une influence importante sur la conception de systèmes géothermiques ouvragés (Figure 1.30). De plus, les manières de développer ces systèmes sont spécifiques à chaque site (Evans et al., 1999) et, donc, une caractérisation géologique précise est indispensable pour la conception de ces systèmes.

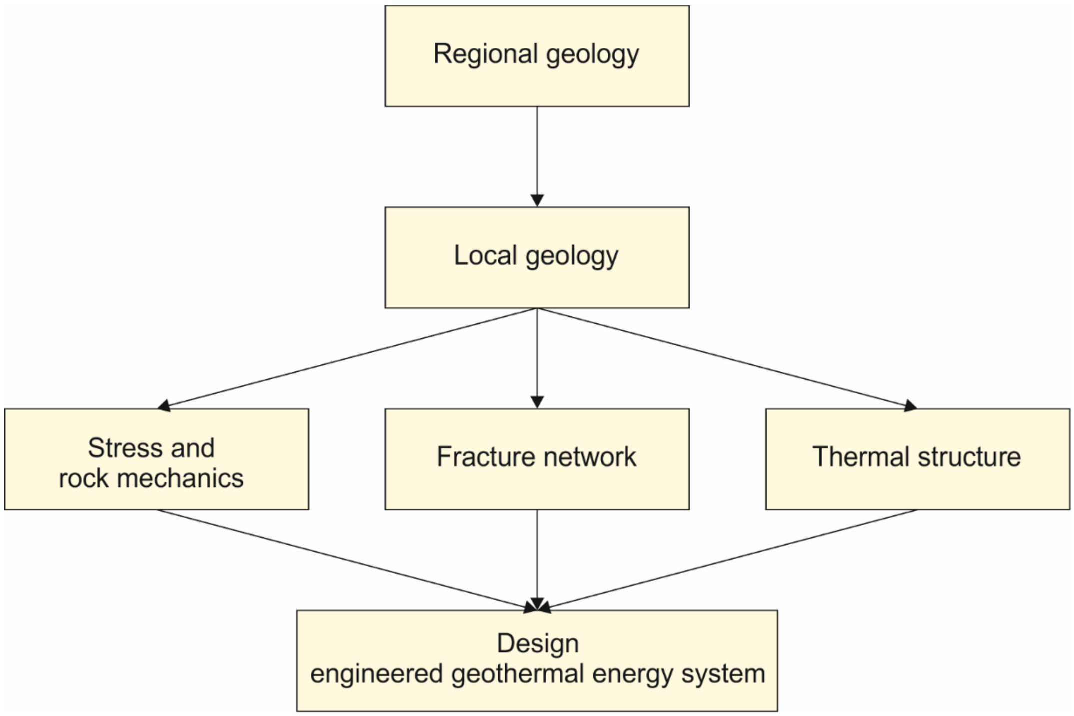

Figure 1.30 Caractérisation géologique à réaliser pour le développement des systèmes géothermiques ouvragés, adapté de Nakatsuka (1999).

Des travaux antérieurs pour évaluer le potentiel géothermique du nord du Québec ont été réalisés par Majorowicz et al. (2015a) et Comeau et al. (2017). Ce dernier a réalisé une compilation des évaluations du flux de chaleur terrestre selon les données disponibles pour le nord du Québec (Figure 1.24a). Les travaux de Comeau et al. (2017) mettent en évidence la distribution inégale des données dans la région avec la plupart de données sous le 55ème parallèle et aucune dans la province du sud-est de Churchill. Par conséquent, la carte de flux de chaleur développée par Majorowicz et al. (2015a) est basée sur l'extrapolation de données peu abondantes (l'évaluation du flux de chaleur la plus proche de Kuujjuaq se situe à une distance d'environ 420-430 km), ce qui peut conduire à des erreurs de calcul lors d'une évaluation de la ressource géothermique à l'échelle d'une communauté (Figure 1.24b).

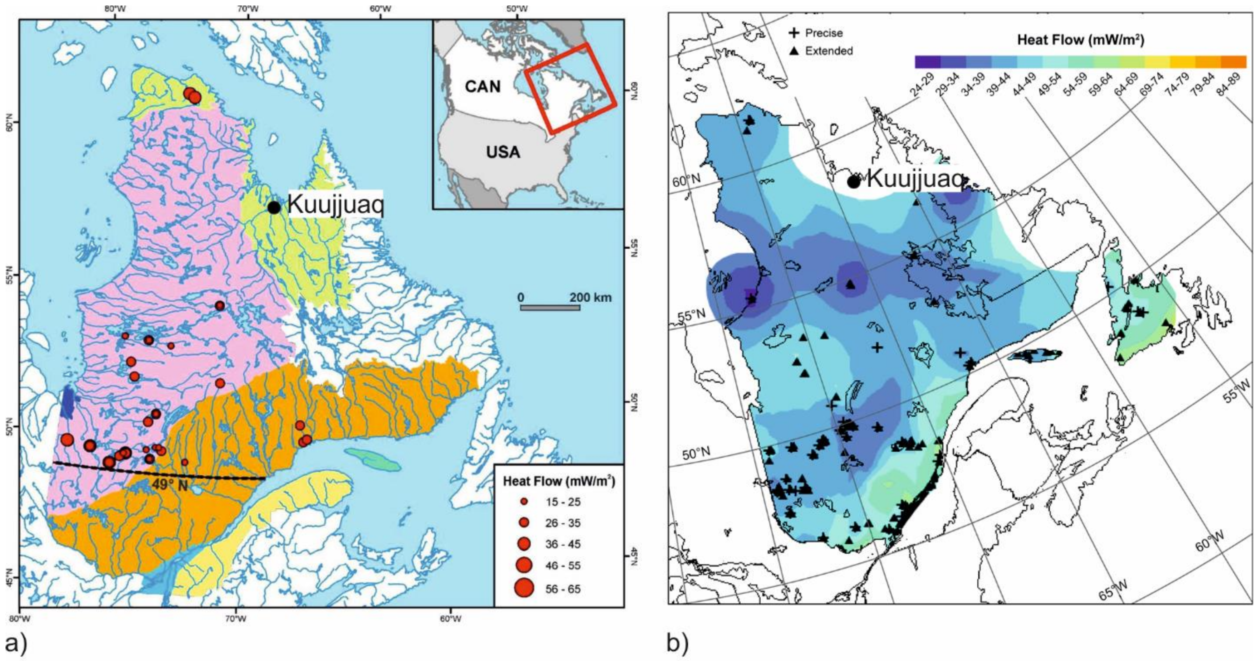

Figure 1.24 **a) Répartition des données de flux de chaleur disponibles et b) densité de flux de chaleur terrestre dans le nord du Québec. En a) rose - Province du Supérieur, vert - Province de Churchill, orange - Province de Grenville, jaune - Province des Appalaches, bleu foncé - Plate-forme de la baie d'Hudson et bleu clair - Basses terres du Saint-Laurent, redessiné selon Majorowicz et al. (2015a) et Comeau et al. (2017).**

Objectifs et questions de recherche

Cette importante lacune des données met en évidence la nécessité de développer des approches originales et d'adapter les méthodes existantes afin de mettre à la disposition des communautés nordiques éloignées des outils d'exploration géothermique non conventionnels abordables et tenter de répondre aux questions suivantes (Glassley, 2010) :

- La ressource géothermique profonde est-elle suffisamment abondante pour répondre à un pourcentage significatif de la demande du marché ?
- La ressource géothermique profonde peut-elle être utilisée à un coût compétitif par rapport au diesel ?

Les travaux réalisés peuvent être considérés comme une première étape pour justifier si des forages d'exploration doivent ou non être réalisés et si des campagnes supplémentaires sur le terrain sont à entreprendre. Dans ces régions éloignées, les forages d'exploration peuvent coûter 2 à 5 fois plus cher qu'au sud du Canada. Le développement de nouvelles méthodes d'exploration utilisant des affleurements comme analogues aux réservoirs, des puits peu profonds de surveillance des eaux souterraines pour évaluer le flux de chaleur, la modélisation numérique et la quantification des incertitudes semblent essentielles pour réduire les risques avant d'enclencher de tels travaux de forage. Finalement, des forages profonds et d'autres campagnes de terrain offriront une évaluation plus exacte du potentiel géothermique si les communautés choisissent d'explorer les développements possibles associés à cette ressource.

Par conséquent, cette thèse vise à fournir des réponses de premier ordre aux questions clés qui se posent lors de l'exploration initiale des ressources géothermiques profondes dans les régions éloignées, soit :

1) Comment caractériser les ressources géothermiques associées aux systèmes pétrothermaux[1] à partir de données de surface ?
2) Comment déduire le flux de chaleur terrestre à partir de profils de température inférieurs à 100 m de profondeur et perturbés par les événements climatiques anciens ?
3) Quels paramètres géologiques et techniques affectent la capacité d'évaluer les ressources géothermiques profondes et quelle est leur influence ? Les ressources géothermiques profondes peuvent-elles localement répondre à la demande en chaleur et électricité d'une communauté type comme Kuujjuaq ?
4) Quel est le régime de contrainte qui prévaut dans le Bouclier canadien au niveau de Kuujjuaq ? Y a-t-il suffisamment de fractures orientées de manière optimale pour permettre leur mouvement lors de stimulations hydrauliques ? Quelle est la pression critique de fluide pour réactiver les fractures ?
5) La technique de stimulation hydraulique permettra-t-elle de maintenir un écoulement des fluides au sein d'un réseau de fractures bien connectées à Kuujjuaq ? Quelle est la meilleure conception de système pour atteindre cet objectif ? Quelles autres données géologiques et thermo-hydro-mécaniques locales sont nécessaires pour des prévisions plus exactes ? Les ressources géothermiques profondes potentiellement exploitables avec un système géothermique ouvragé à Kuujjuaq sont-elles compétitives par rapport aux combustibles fossiles ?

[1] Systèmes petrothermaux – terme utilisé lorsque le fluide caloporteur doit être injecté car le réservoir du système géothermique ne contient pas suffisamment de volume de fluide pour l'extraction de chaleur (Moeck, 2014).

Contexte géographique et demande d'énergie

Les travaux de cette thèse ont été réalisés au niveau de la communauté de Kuujjuaq utilisée en guise d'exemple et située au Nunavik, Québec, Canada (Figure 1.14). Kuujjuaq est la capitale administrative du Nunavik et la plus grande communauté du territoire qui compte 2 754 habitants, dont la majorité est inuit (Statistics Canada, 2019). Le Nunavik est un territoire d'environ 507 000 km^2 au nord du $55^{ème}$ parallèle et qui abrite 11 000 habitants répartis dans 14 communautés dispersées le long de la côte sans accès routier. L'immensité du territoire et la dispersion des communautés font qu'il est préférable d'effectuer une évaluation de ressources géothermiques profondes axée sur chaque communauté pour favoriser le développement local de la géothermie profonde. L'idée est d'éviter l'extrapolation de données éparses sur un vaste territoire pour ne pas fausser l'évaluation du potentiel local par des anomalies régionales éloignées des communautés.

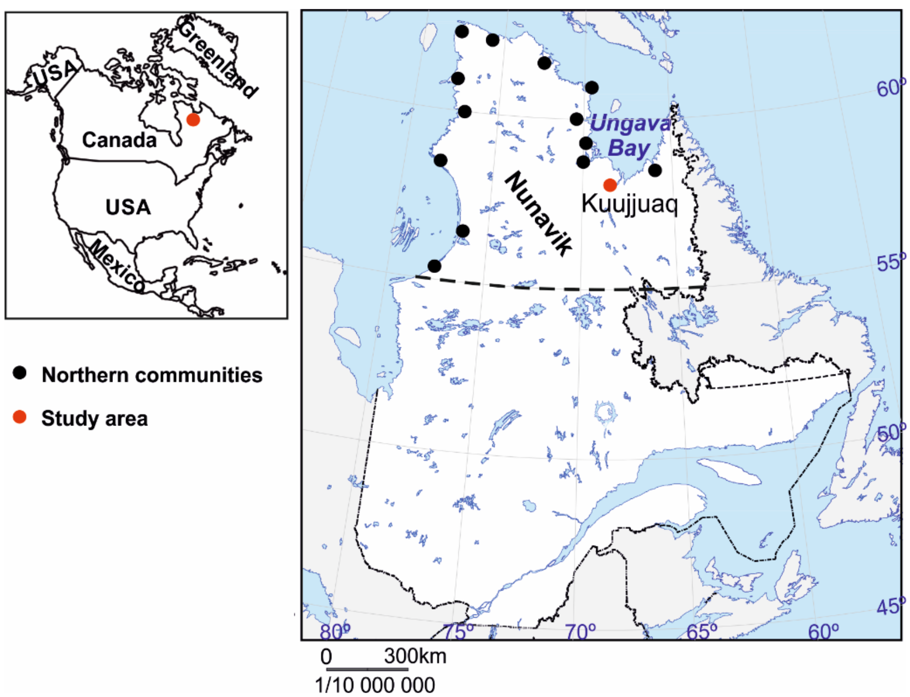

Figure 1.14 Localisation géographique de Kuujjuaq et des autres communautés au Nunavik.

Une centrale au diesel est actuellement utilisée dans chaque communauté pour produire l'électricité et répondre à leurs besoins de base. L'ensemble des centrales au diesel du Nunavik totalisent une consommation annuelle de pétrole d'environ 25 millions de litres (pour 2009 ; KRG et al., 2010). 28 millions de litres supplémentaires de mazout (pour 2009 ; KRG et al., 2010) sont consommés annuellement pour le chauffage au Nunavik. Le coût de production de l'électricité est environ 0,6 $ kWh^{-1} et le coût du chauffage à Kuujjuaq a été évalué à environ 0,19 $ kWh^{-1}, selon le prix du diesel livré sur place (Belzile et al., 2017 ; Giordano et al., 2018).

La communauté de Kuujjuaq connaît une température annuelle moyenne d'environ -5,4 ºC (Figure 6.3 ; Gunawan et al., 2020). Bien que les logements résidentiels soient construits pour répondre à certaines normes réglementaires d'isolation, le climat rigoureux entraîne des exigences élevées en matière de chauffage des bâtiments (Figure 6.3 ; Gunawan et al., 2020).

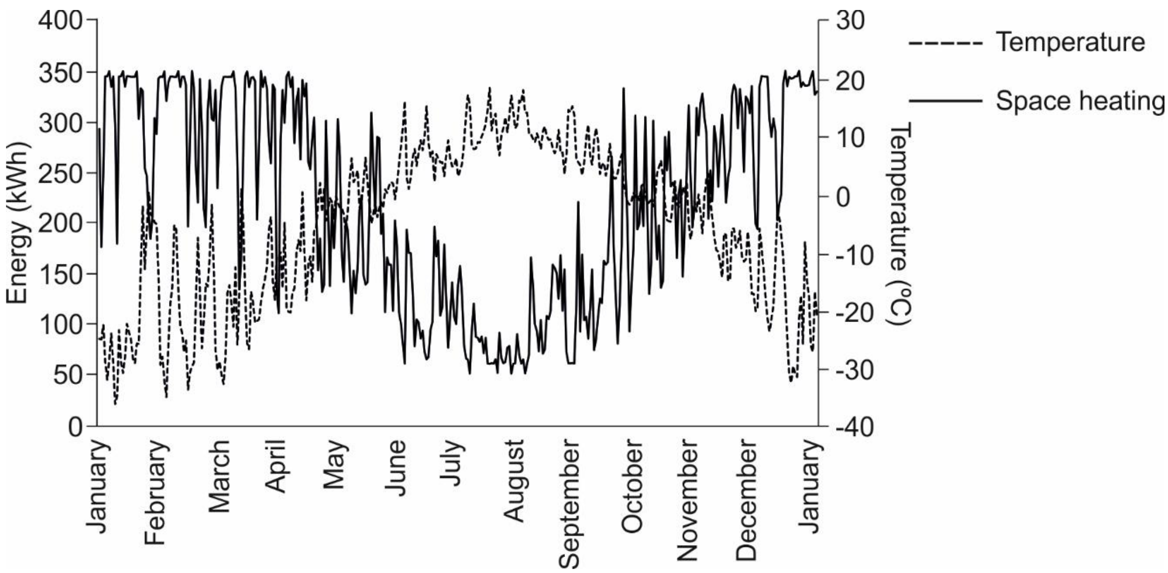

Figure 6.3 Température quotidienne moyenne et profil de chauffage d'un logement résidentiel typique à Kuujjuaq, redessiné selon Gunawan et al. (2020).

La consommation annuelle moyenne de diesel d'un logement résidentiel typique à Kuujjuaq a été estimée à environ 3 100 à 8 180 litres (Yan et al., 2019 ; Gunawan et al., 2020). Cela représente environ 28 à 32 L m^{-2}, considérant la surface au sol d'un bâtiment. Il y a actuellement environ 973 logements résidentiels à Kuujjuaq (Statistics Canada, 2019), ce qui suggère une consommation totale de 3 à 8 millions de litres de mazout pour le chauffage. La charge de pointe en chauffage pour un logement résidentiel est d'environ 7 kW (Yan et al., 2019), en fonction de la charge de chauffage du bâtiment et la surface de plancher, ce qui suggère une charge de pointe pour la communauté d'environ 7 MW. La demande annuelle d'énergie pour le chauffage a été estimée entre 21,6 et 71,3 MWh par logement, selon la surface au sol (Yan et al., 2019 ; Gunawan et al., 2020). Ainsi, la demande de chauffage de la communauté est d'environ 21 à 69 GWh par an. De plus, en 2000, la demande annuelle d'électricité à Kuujjuaq était d'environ 12 000 MWh (Hydro-Québec, 2002), passant à 15 100 MWh en 2011 (NRCan, 2011). Ces valeurs de demande et de coût de production d'énergie fournissent une première perspective afin de proposer une solution d'énergie alternative viable à cette communauté hors réseau basée sur l'utilisation des ressources géothermiques profondes.

Contexte géologique

Kuujjuaq est située au niveau du Bouclier canadien, la plus ancienne (*ca*. 4-1 Ga) et la plus grande région physiographique du Canada couvrant environ 48 % de la surface du pays (Acton et al., 2015). Le Bouclier canadien offre une grande exposition de Laurentia, le centre géologique du continent nord-américain (p.ex., Whitmeyer et al., 2007 ; Darbyshire et al., 2017), et est le résultat des collisions paléoprotérozoïques de fragments cratoniques archéens. Le Sud-est de la Province de Churchill, où se situe Kuujjuaq, est composé de la Zone noyau qui est délimitée par l'Orogéne des Torngat et la Fosse du Labrador (Wardle et al., 1990 ; James et al., 1996 ; Wardle et al., 1996 ; Wardle et al., 2002 ; MERN, 2020a) et a été divisée en 6 domaines lithotectoniques (Lafrance et al., 2018 ; MERN, 2020a). La communauté de Kuujjuaq est située dans la partie nord du domaine lithotectonique de Baleine. Cette section a également été appelée « Terrane de Kuujjuaq » par Perreault et al. (1990) et « Kuujjuaq Tectonic Zone » par Bardoux et al. (1998). Les structures régionales NO-SE à N-S observé dans la région sud-ouest de la baie d'Ungava résultent de la collision entre les zones noyau et supérieure (Simard et al., 2013). Trois phases principales de déformation (D_1 à D_3) ont été identifiées dans cette région, correspondant à un processus de déformation continu lié au développement de la Fosse du Labrador (Moorhead, 1989 ; Perreault et al., 1990 ; Poirier et al., 1990 ; Goulet, 1995 ; Simard et al., 2013).

La communauté de Kuujjuaq est établie principalement sur la Suite de False (paragneiss migmatisé et paragneiss migmatisé à grenat) et le Complexe de Kaslac (diorite et diorite quartzifère à amphibole). Des affleurements mineurs appartenant à la Suite de Ralleau (gabbro et diorite amphibolitisés), la Suite d'Aveneau (tonalite et granite blancs) et la Suite de Dancelou (granite rose massif et granite pegmatitique massif) sont également présents. Le pluton de Kuujjuaq (orthogneiss tonalitique à granodioritique) et le Complexe d'Ungava (gneiss tonalitique à rubans blanchâtres) affleurent loin de la communauté. L'unité Essaim de Falcoz (gabbro, gabbronorite et norite) est également présente en petite quantité. Toutes ces lithologies ont été échantillonnées dans le cadre de cette thèse (Figure 2.2). Les failles Pingiajjulik et Gabriel sont des failles qui ont un mouvement dextre inverse synchrone avec la troisième phase de déformation (D_3 ; p.ex., Perreault et al., 1990 ; Simard et al., 2013 ; SIGÉOM, 2019). Ce mouvement est indiqué par des ombres de pression autour des porphyroblastes en rotation et par des plis de cisaillement (p.ex., Perreault et al., 1990).

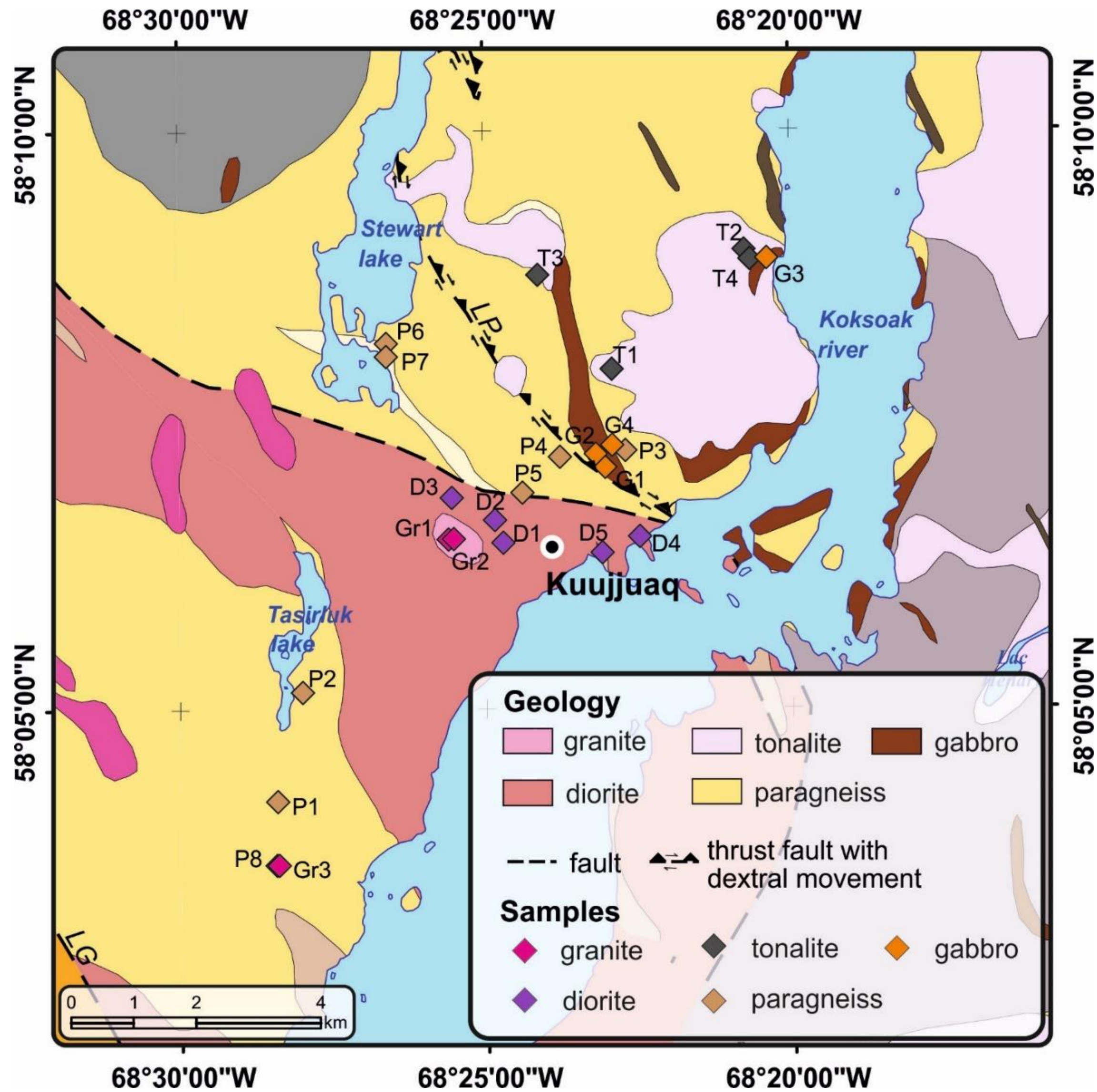

Figure 2.2 **Carte géologique de la zone d'étude. *LP* – faille Pingiajjulik, *LG* – faille Gabriel, P – paragneiss, D – diorite, G – gabbro, T – tonalite, Gr – granite, adapté de SIGÉOM (2019).**

Structure de la thèse

La caractérisation géologique d'un site est une étape clé de la conception d'un système géothermique ouvragé (Nakatsuka, 1999). Pour cette raison, cette thèse présente une caractérisation de premier ordre de la structure thermomécanique de la lithosphère et du réseau de fractures sous Kuujjuaq en utilisant des méthodes d'exploration géothermique abordables pour la communauté. De plus, une évaluation du potentiel technico-économique des systèmes géothermiques ouvragés est présentée. La structure thermique de la croûte sous Kuujjuaq est discutée dans le premier, deuxième et troisième article. Le réseau de fractures et le régime de contraintes sont examinés dans le quatrième article. L'analyse technico-économique de systèmes géothermiques ouvragés à Kuujjuaq est analysée dans le cinquième article.

Premier article : Les propriétés thermophysiques des roches de surface : un outil pour caractériser les ressources géothermiques des régions nordiques éloignées

Le but de ce premier article est de répondre à la question « Comment caractériser les ressources géothermiques associées aux systèmes pétrothermaux à partir de données de surface ? ». Cette question est soulevée en raison du manque de données probantes en profondeur. Pour y arriver, les affleurements rocheux ont été utilisés comme analogues des réservoirs profonds. De plus, la variabilité induite par les méthodes de laboratoire pour caractériser les propriétés thermophysiques est également évaluée dans l'estimation de la température actuelle en profondeur. Ce premier article fournit aussi les informations de base en termes de propriétés thermophysiques, de la concentration des éléments chimiques et des phases minérales principales pour l'ensemble des d'échantillons de roche analysés dans cette thèse.

Les roches échantillonnées ont été analysées pour connaitre les propriétés thermiques (conductivité et capacité thermique) en utilisant les techniques du compteur de flux de chaleur (p.ex., Raymond et al., 2017 ; Ruuska et al., 2017 ; TA Instruments, 2019) et du balayage optique avec un scanneur infrarouge (Popov et al., 2016 et références). La concentration des éléments chimiques et radiogéniques a été évaluée par spectrométrie de masse (p.ex., Hou et al., 2008) et gamma avec un détecteur NaI(Tl) (p.ex., Lamas et al., 2017). Les phases minérales principales des roches ont été évaluées à l'aide de lames minces. Les propriétés hydrauliques (porosité et perméabilité) ont été évaluées en utilisant un perméamètre-porosimètre au gaz (Raymond et al., 2017 ; Coretest System, Inc., 2019).

Les résultats suggèrent que le feldspath et le quartz sont les phases minérales principales dans les roches leucocratiques (tonalite et granite) tandis que les minéraux mafiques dominent les lithologies de paragneiss, de diorite et de gabbro. Les analyses géochimiques indiquent que le SiO_2 et le Al_2O_3 sont les éléments majeurs principaux, quelle que soit l'unité lithologique. Les analyses de conductivité thermique effectuées avec les deux techniques mentionnées ci-dessus montrent une différence moyenne de -9.8 %, allant jusqu'à 30 % et -58 %. La technique du compteur de chaleur donne les résultats les plus bas. Les analyses des éléments radiogéniques indiquent que la concentration d'uranium est 20 % à 60 % inférieure lorsqu'elle est évaluée par spectrométrie de masse. La concentration de thorium diminue de 11 % pour le paragneiss, mais augmente jusqu'à 70 % pour les deux groupes des roches ignées lors de l'évaluation par spectrométrie de masse. La concentration de potassium augmente de plus de 60 % pour toutes les lithologies étudiées lorsqu'elle est évaluée par spectrométrie de masse. Ces résultats, par conséquent, ont une influence sur la production de chaleur radiogénique. Selon la méthode d'analyse, les résultats obtenus augmentent de plus de 50 % pour les groupes de roches ignées, mais diminuent de 9 % pour le paragneiss. La porosité des échantillons varie entre 3 % et 6 % et sa perméabilité est inférieure à 10^{-19} m^2.

Des modèles de distribution de température en profondeur ont ensuite été développés en considérant la géologie régionale et les résultats obtenus à partir des différentes méthodes de laboratoire. Ces modèles ont été résolus numériquement à l'aide du logiciel COMSOL Multiphysics en supposant une conduction de chaleur 2D en régime permanent. Les modèles ont une géométrie rectangulaire d'une largeur de 8 km et d'une profondeur de 10 km. Le centre du modèle correspond au changement de lithologie entre le paragneiss et la diorite. Cette dernière a été considérée comme ayant une épaisseur variable entre 1 et 5 km de façon à évaluer comment les changements lithologiques avec différentes épaisseurs peuvent influencer la distribution verticale et horizontale de la température. La profondeur du Moho a été estimée à 37,5 km, la croûte supérieure a été supposée être composée de paragneiss et a été considérée comme ayant une épaisseur de 26,5 km et la croûte inférieure, supposée être constituée de roches de faciès granulitiques, a été considérée comme ayant une épaisseur d'environ 11 km (p.ex., Christensen et al., 1975 ; Moorhead et al., 1989 ; Poirier, 1989 ; Mareschal et al., 1990 ; Seguin et al., 1990 ; Hall et al., 1995 ; Wardle et al., 1996 ; Telmat, 1998 ; Telmat et al., 1999 ; Bourlon et al., 2002 ; St-Onge et al., 2002 ; Vervaet et al., 2016). La production de chaleur radiogénique estimée par Ashwal et al. (1987) pour les roches granulitiques est de 0,45 μW m^{-3} et la contribution du Moho au flux de chaleur a été considérée équivalente à 15 mW m^{-2} (p.ex., Jaupart et al., 2007 ; Mareschal et al., 2013 ; Jaupart et al., 2014 ; Jaupart et al., 2016). Une température de surface constante de -1 ºC (p.ex., Comeau et al., 2017 ; ECCC, 2019) a été défini comme condition limite supérieure. Toutefois, les changements de la température de surface, qui ont eu lieu durant les épisodes glaciaires, ont un effet sur la distribution de la température du sous-sol et se propagent par diffusion vers le bas (p.ex., Birch, 1948 ; Jessop, 1990 ; Mareschal et al., 1999 ; Beardsmore et al., 2001 ; Beltrami et al., 2005 ; Chouinard et al., 2007 ; Chouinard et al., 2009 ; Rath et al., 2012 ; Suman et al., 2017 ; Bédard et al., 2018 et références). Ainsi, les prévisions de température du sous-sol ont été corrigées pour les effets paléoclimatiques. Les résultats suggèrent que les événements climatiques du Pléistocène ont principalement perturbé la température entre 1 et 2 km de profondeur et leur influence devient minime à 5 km de profondeur avec un facteur de correction d'au plus 1 ºC. Le flux de chaleur à 10 km de profondeur a été défini comme condition limite inférieur et les deux limites latérales du modèle sont supposées adiabatiques. La conductivité thermique et la production de chaleur radiogénique ont été définies selon des lithologies, en supposant des valeurs uniformes.

Les résultats de cet article indiquent un flux de chaleur en surface de 23 à 58 mW m^{-2}, avec une valeur moyenne de 33 – 38 mW m^{-2}. Les différents scénarios simulés suggèrent une température à 5 km de profondeur variant entre une valeur minimale de 31 – 49 ºC et une valeur maximale de 85 – 168 ºC. La valeur moyenne de la température a été estimée à 57 – 88 ºC. Ces plages de température sont dues aux différentes méthodes utilisées pour évaluer la conductivité thermique et la génération de chaleur radiogénique. Les travaux réalisés à Kuujjuaq portent à croire que combiner la spectrométrie gamma et le balayage optique donne des prévisions de température plus faibles par rapport à la spectrométrie de masse combinée au compteur de flux de chaleur. Les simulations de température ont aussi montré qu'une couche de diorite de 1 km a une influence négligeable sur la température à 5 km. Toutefois, pour une couche de 5 km d'épaisseur les isothermes montrent une légère diminution de température dans la couche de diorite par rapport au paragneiss adjacent. Ceci est dû au contraste de conductivité thermique entre ces deux lithologies.

Deuxième article : Une approche numérique pour déduire le flux de chaleur terrestre à partir des profils de température peu profonds dans les régions nordiques éloignées

Cet article vise à répondre à la question « Comment déduire le flux de chaleur terrestre à partir de profils de température inférieurs à 100 m de profondeur et perturbés par les événements climatiques anciens ? ». Dans les régions éloignées, des puits d'exploration profonds à côté des communautés sont inexistants, donc une méthodologie adaptée aux contextes de ces communautés est nécessaire. Ainsi, une approche numérique a été développée pour simuler les événements climatiques et déduire le flux de chaleur terrestre en reproduisant un profil de température de 80 m de profondeur. Le flux de chaleur terrestre a été simulé avec la méthode des éléments finis considérant un problème de conduction de chaleur inverse en 1D, où l'algorithme de Nelder-Mead a été utilisé pour minimiser la somme des moindres carrés et trouver le flux de chaleur optimal pour reproduire le profil de température mesuré dans un puits d'observation hydrogéologique. En plus, une relation expérimentale a été déduite pour décrire l'effet de la température et la pression sur la conductivité thermique et ceci a été implémenté dans le modèle numérique.

Le profil de température évalué et utilisé dans cette thèse a été mesuré à l'aide de capteurs de température et de pression submersible connectés à un enregistreur de données (RBRduet) avec une exactitude de ± 0.002 °C et ± 0.25 cm. La sonde a été insérée dans le puits environ 20 min avant le début de l'enregistrement pour assurer l'équilibre thermique entre la sonde et l'eau souterraine du puits. Les températures ont ensuite été enregistrées à un rythme continu de 1 m sur 10 s. Un total de 6 étalonnages de profondeur ont été effectués le long du profil en corrélant les mesures de pression avec la profondeur exacte mesurée avec un câble gradué. Le puits présentait une légère inclinaison (inférieure à 20°) et une correction de profondeur verticale a été effectuée.

La formulation mathématique du problème de conduction de chaleur inverse avec un flux de chaleur basal inconnu est donnée par :

$$\frac{\partial}{\partial z}\left(\lambda \frac{\partial T}{\partial z}\right) + RHP = \rho c \frac{\partial T}{\partial t} \quad \text{pour} \quad 0 < z < z_{\mathrm{n}}, \quad 0 < t \leq t_{\mathrm{n}} \tag{3.1a}$$

$$-\lambda \frac{\partial T}{\partial z} = q = ?\,(\text{inconnu}) \quad \text{à} \quad z = z_{\mathrm{n}}, \quad t = t_{\mathrm{n}} \tag{3.1b}$$

$$T = T(t) \quad \text{à} \quad z = 0, \quad 0 < t \leq t_{\mathrm{n}} \tag{3.1c}$$

$$T = T(z) \quad \text{pour} \quad t = 0, \quad \text{et} \quad 0 \leq z \leq z_{\mathrm{n}} \tag{3.1d}$$

où λ (W m^{-1} K^{-1}) est la conductivité thermique, *RHP* (W m^{-3}) est la production de chaleur radiogénique, ρc (J m^{-3} K^{-1}) est la capacité thermique volumétrique, *T* (ºC) est la température, *t* (s) est le temps, *z* (m) est la profondeur, *q* (W m^{-2}) est le flux de chaleur et l'indice n signifie final.

Puisque la conductivité thermique dépend de la température, ce problème de conduction de chaleur inverse devient non linéaire. Une condition limite supérieure de température variant dans le temps a été imposée pour représenter les événements climatiques avec une fonction en escalier implémentée dans COMSOL. La condition initiale de température a été calculée avec la solution analytique de l'équation (3.1a) en régime permanent. Les simulations de diffusion de chaleur décrites ont été résolues numériquement avec la méthode des éléments finis à l'aide du module d'optimisation du logiciel COMSOL Multiphysics.

Le problème inverse mentionné ci-dessus a été résolu par optimisation mathématique :

$$\begin{cases} \underset{q}{min} O_f(q) \\ lb_q \leq q \leq ub_q \end{cases} \tag{3.4}$$

où O_f est la fonction objective à valeur scalaire, *lb* représente la limite inférieure et *ub* représente la limite supérieure.

Ces deux limites sont des contraintes d'inégalité sur le degré de liberté de la variable de contrôle (c'est-à-dire le flux de chaleur) qui ont été limitées à l'intervalle 10 et 70 mW m^{-2}. Aucune autre contrainte n'a été utilisée. La méthode des moindres carrés a été choisie comme fonction objective et le flux de chaleur optimal a été trouvé en minimisant la somme des résidus carrés :

$$q_{\mathrm{optimal}} = \sum [T_{\mathrm{measured}} - T_{\mathrm{simulated}}]^2 \tag{3.5}$$

où $T_{measured}$ est le profil de température mesuré et $T_{simulated}$ représente la température simulée.

L'algorithme Nelder-Mead (Nelder et al., 1965) a été sélectionné pour échantillonner la fonction objective à chaque itération et trouver son minimum selon le degré de liberté imposé à la variable de contrôle.

La géométrie du profil calculé a une longueur de 10 km et est stratifié près de la surface avec les premiers 20 m composés de sédiments marins, suivis de 20 m de till glaciaire et le reste est du paragneiss. La profondeur de 0 m dans le modèle a été considérée comme correspondant à la surface actuelle du sol. Les changements causés par la sédimentation et/ou l'érosion n'ont pas été pris en considération dans cette étude.

La conductivité thermique d'échantillons a été évaluée dans la plage de températures de 20 à 160 ºC. Cela a permis de définir une relation expérimentale pour décrire l'effet de la température sur la conductivité thermique des échantillons de roche. Une relation linéaire entre la température et la résistivité thermique a été ajustée pour reproduire les données expérimentales (p.ex., Schatz et al.,1972). L'effet de la pression sur la conductivité thermique a été évalué indirectement à partir de la dépendance de la pression sur la porosité en considérant la moyenne géométrique comme modèle qui décrit le mieux la relation entre la conductivité thermique et la porosité (p.ex., Beck, 1976). Les deux relations expérimentales ont été combinées pour obtenir une fonction qui décrit l'effet de la température et de la pression sur la conductivité thermique.

Les simulations suggèrent que la température en surface durant les événements glaciaires influence l'évaluation du flux de chaleur. Ce dernier, évalué à 10 km de profondeur, varie entre

32,1 mW m^{-2} et 54,5 mW m^{-2} pour le scénario de climat froid et entre 31,8 mW m^{-2} et 52,3 mW m^{-2} pour le scénario de climat chaud. De plus, la saturation des roches en eau influence le flux de chaleur de 7 à 25 % et les effets de température et pression sur la conductivité thermique conduisent à une diminution du flux de chaleur inférieure à 0,1 %. En résumé, le flux de chaleur terrestre à 10 km de profondeur varie entre 31,8 et 69,4 mW m^{-2}, selon l'historique paléoclimatique et les propriétés thermophysiques considérées.

Troisième article : Évaluation d'incertitude et des risques liés à la ressource géothermique profonde pour la production de chaleur et d'électricité dans les régions nordiques éloignées

Le troisième article répond aux questions « Quels paramètres géologiques et techniques affectent la capacité d'évaluer les ressources géothermiques profondes et quelle est leur influence ? » et « Les ressources géothermiques profondes peuvent-elles localement répondre à la demande en chaleur et électricité d'une communauté type comme Kuujjuaq ? ».

Pour répondre à ces questions, des modèles de conduction de chaleur en 2D avec une condition limite supérieure qui varie dans le temps ont été utilisés pour simuler la distribution de la température en profondeur. La condition limite supérieure a été supposée variable dans le temps pour reproduire les effets des événements climatiques qui affectent la température en profondeur. La condition limite inférieure de ces modèles est le flux de chaleur terrestre obtenu dans le deuxième article et l'effet de température et pression sur la conductivité thermique a aussi été considéré dans les modèles. De plus, la méthode du volume (Muffler et al., 1978) a été utilisée pour évaluer l'énergie thermique en place considérant la température de référence comme la température d'abandon du réservoir au lieu de la température de surface annuelle moyenne. La température d'abandon du réservoir dépend de l'application prévue et a été considérée comme égale à 30 – 50 ºC pour le chauffage (Lindal, 1973 ; Sarmiento et al., 2013) et 120 – 140 ºC pour la production d'électricité (Tomarov et al., 2017). Des analyses de sensibilité basées sur la méthode de Monte Carlo (p.ex., Scheidt et al., 2018) ont été réalisées avec le logiciel @Risk (Palisade, 2019) pour déterminer les principales incertitudes géologiques et techniques. Des analyses de risque ont été réalisées avec le même logiciel pour prévoir la production d'énergie et évaluer la probabilité que la ressource géothermique profonde puisse répondre à la demande de chaleur et d'électricité de la communauté de Kuujjuaq.

Les résultats de cet article indiquent que la température du réservoir et le facteur de récupération sont les paramètres plus influents, suivis par la durée du projet. La température d’abandon du réservoir à une influence importante pour une profondeur de 2 – 3 km pour le chauffage et 5 – 6 km pour la production d’électricité, mais cette variable perd de l’importance en fonction de la profondeur du réservoir.

La probabilité que les ressources géothermiques profondes puissent répondre à la demande en chaleur de l’ensemble de la communauté de Kuujjuaq est supérieure à 98 % à une profondeur supérieure à 4 km si les paramètres incertains (principalement la température du réservoir et le facteur de récupération) se situent dans les plages de distribution définies. D’un autre côté, la probabilité que les ressources géothermiques profondes puissent répondre à la demande en électricité est de 13,6 – 20,2 % à 5 km de profondeur et de 88 – 91,2 % à 10 km de profondeur, selon les événements climatiques et les propriétés thermophysiques considérées. Une analyse détaillée a indiqué qu’à 5 km de profondeur, la demande d’électricité peut être satisfaite si la température du réservoir est supérieure à son 80ème percentile. À 6 km, la température du réservoir doit être supérieure à son 55ème percentile, le facteur de récupération supérieur à son 40ème percentile et la température d’abandon du réservoir et la durée du projet inférieures à leur 80ème percentile. À 7 km, la demande d’électricité est satisfaite si la température du réservoir est supérieure à son 35ème percentile. À 8 km, la température du réservoir doit être supérieure à son 20ème percentile et à 9 et 10 km, au-dessus de son 10ème percentile. De plus, à des profondeurs supérieures à 7 km, le facteur de récupération doit être supérieur à 2 %.

La cogénération de chaleur et d’électricité peut être une solution pour la communauté de Kuujjuaq en utilisant la chaleur perdue du processus de production d’électricité pour fournir du chauffage (Rybach et al., 2004 ; Lund et al., 2007 ; Saadat et al., 2010 ; Gehringer, 2015). Les résultats révèlent qu’environ 5 à 14 MW_{th} seraient rejetés pour chaque MW_e produit considérant les ressources géothermiques profondes à Kuujjuaq. Bien que 50 – 60 % de cette chaleur perdue puisse être utilisée pour d’autres applications, puisque le reste n’est pas récupérable, le potentiel annuel de production de chaleur associé à la cogénération reste important. Toutefois, la probabilité de répondre à la demande annuelle de chauffage de la communauté est inférieure à 90 % à 5 km de profondeur et moins de 12 % à 10 km de profondeur.

Quatrième article : Réseau de fractures et régime de contrainte : implications pour le développement de systèmes géothermiques ouvragés dans les régions nordiques éloignées

Les questions « Quel est le régime de contrainte qui prévaut dans le Bouclier canadien au niveau de Kuujjuaq ? », « Y a-t-il suffisamment de fractures orientées de manière optimale pour permettre leur mouvement lors de stimulations hydrauliques ? » et « Quelle est la pression critique de fluide pour réactiver les fractures ? » sont posées dans cet article. Une caractérisation de premier ordre du réseau de fractures a été réalisée pour aider à répondre à ces questions en utilisant des affleurements comme analogues de réservoirs profonds. De plus, une analyse de frottement de Mohr-Coulomb et de la tendance au glissement a été réalisée pour évaluer les familles de fractures orientées de manière optimale pour le glissement et pour estimer la pression critique de fluide nécessaire pour réactiver les structures et initier le cisaillement. Comme les principales contraintes in situ sont inconnues dans la zone d'étude et aucune mesure de contraintes n'a été réalisée dans le cadre de ces travaux, un modèle de contraintes *a priori* a été proposé à partir d'indicateurs géologiques, de corrélations empiriques et de modèles analytiques. Le modèle a été calibré avec la carte mondiale de contraintes (Heidbach et al., 2019) et des données de contraintes mesurées dans le Bouclier canadien issues de la littérature. La méthode de Monte Carlo a été utilisée pour déterminer l'ensemble des incertitudes affectant le modèle de contraintes *a priori*. Ces simulations ont été réalisées avec le logiciel @Risk (Palisade, 2019).

Un total de 452 fractures ont été cartographiées dans 6 zones entourant la communauté de Kuujjuaq à l'aide de la méthode d'échantillonnage en ligne ou scanline (p.ex., Zeeb et al., 2013a) après avoir corrigé la boussole considérant 22° de déclinaison magnétique (GCan, 2020b). Avec cette méthode, un ruban décamètre, ou chaîne d'arpentage, est déposé sur la surface de l'affleurement et les propriétés géométriques de chaque fracture interceptant le ruban sont mesurées. Les propriétés géométriques inventoriées sont la direction, l'inclinaison, la longueur, l'espacement, l'ouverture de fractures, le remplissage et altération minérale et l'âge relatif des fractures. Le logiciel Stereonet (Allmendinger et al., 2012 ; Cardozo et al., 2013) a été utilisé pour tracer la direction et le pendage des fractures, évaluer leurs pôles, estimer le contour de l'aire de 1 % et déduire la distribution de von Mises pour les principales familles de fractures. Ces résultats ont révélé quatre familles de fractures principales avec les directions suivantes : F1 (E-O) – N81ºE-N90ºE, F2 (NNO-SSE) – N161ºE-N170ºE, F3 (N-S) – N11ºE-N20ºE et F4 (NO-SE) – N121ºE-N130ºE.

Plusieurs corrections des biais statistiques et analyses statistiques ont été réalisées telles qu'expliquées par Zeeb et al. (2013a) et Sanderson et al. (2019a) pour déduire les paramètres à utiliser afin de développer le modèle stochastique du réseau de fractures. Ces paramètres incluent la direction de pendage et le pendage de chaque fracture, la densité moyenne (0,8 fracture m^{-1}) et la taille minimale et maximale et la dimension fractale de chaque ensemble de fractures. La famille E-O a des longueurs de fractures allant de 2 à 13,2 m et une dimension fractale de 1,7. La famille NNO-SSE a des longueurs de fractures variant entre 2 et 8 m et une dimension fractale de 2,4. La taille de fractures dans la famille N-S varie entre 2 et 12 m, avec une dimension fractale de 1,8. La famille NO-SE révèle des fractures de longueurs allant de 2 à 16 m avec une dimension fractale de 1,7. Les dimensions fractales déduites sont élevées soulignant un nombre élevé de courtes fractures échantillonnées par rapport aux fractures plus longues.

Le modèle stochastique du réseau de fractures a été généré utilisant le logiciel FRACSIM3D (Jing et al., 2000). Une distribution de Poisson a été utilisée pour placer uniformément au hasard les fractures dans un volume deux fois plus grand que le volume du modèle défini en considérant la densité de fractures moyenne évalué (Jing et al., 2000). Le concept de géométrie fractale de Watanabe et al. (1995) a été appliquée pour générer les longueurs aléatoires de fracture en considérant la taille minimale et maximale et la dimension fractale déduite (Willis-Richards et al., 1996). La direction de pendage et le pendage ont été attribués au hasard à chaque fracture générée sur la base des données échantillonnées.

Une première étape du processus d'évaluation des contraintes in situ consiste à rassembler les informations disponibles sur les contraintes dans la région et à développer le modèle de contrainte selon la meilleure estimation (ou modèle de contrainte *a priori* ; Hudson et al., 2003 ; Stephansson et al., 2012 ; Zhang, 2017). Cela comprend la carte mondiale de contraintes (Heidbach et al., 2019), la sismotectonique, les indicateurs géologiques, la littérature publiée sur les mesures de contraintes précédemment effectuées, des corrélations empiriques et des modèles analytiques. Toutefois, l'utilisation de corrélations empiriques et de modèles analytiques est basée sur deux hypothèses : 1) l'état de contrainte peut être décrit par trois composantes : une composante verticale et deux composantes horizontales liées par le coefficient du ratio de contrainte et 2) la composante verticale et les composantes horizontales correspondent aux contraintes principales. Les mesures de contraintes réalisées dans le Bouclier canadien suggèrent que la contrainte verticale n'est pas une contrainte principale (Herget, 1993 ; Arjang et al., 1997 ; Arjang, 1998 ; Young et al., 2015). Cela limite l'utilisation de corrélations empiriques. Cependant, en raison de l'absence de mesures de contraintes in situ dans la zone d'étude, la contrainte verticale sera considérée dans cette étude comme une contrainte principale pour cette caractérisation de premier ordre de l'état de contrainte.

L'orientation des failles Pingiajjulik et Gabriel est approximativement NNO-SSE indiquant une compression ENE-OSO qui correspond à la tendance régionale proposée par Adams (1989). De plus, l'analyse des principales familles de fractures, supposant ici que les contraintes principales sont orientées dans des directions divisant en deux les angles entre ces familles, indique une tendance de la contrainte principale horizontale maximale de N210ºE-N220ºE, corrélée à la tendance régionale. En supposant que la contrainte principale horizontale minimale forme un angle droit avec la contrainte principale horizontale maximale, sa direction serait donc N300ºE-N310ºE.

Les fonctions empiriques proposées par Herget (1987), Herget (1993) et Arjang et al. (1997) ont été utilisés dans cette étude pour calculer le coefficient du ratio de contrainte. Ainsi, les résultats révèlent que la contrainte principale verticale pour Kuujjuaq peut être décrite par l'équation suivante :

$$\sigma_V = 0.0271z \tag{5.25}$$

Les expressions suivantes ont été obtenues pour les contraintes principales minimales et maximales :

$$\sigma_h = 0.0251z + 4.94 \tag{5.26a}$$

$$\sigma_H = 0.0430z + 8.62 \tag{5.26b}$$

Les modèles de McCutchen (1982) et Sheorey (1994) ont aussi été utilisés pour déduire la contrainte horizontale principale moyenne, mais les résultats ont révélé une différence de -32 % (modèle de McCutchen) et -4 % (modèle de Sheorey) entre les valeurs déduites et la valeur mesurée par Herget (1982) et Herget (1987). Comme les contraintes ne peuvent pas dépasser la résistance des roches, des limites théoriques pour les contraintes minimale et maximale ont été définies en supposant la théorie de l'équilibre de frottement (p.ex., Zoback, 2007). Cette analyse a révélé que les contraintes à 1 km de profondeur sont plus proches des conditions critiques qu'à de plus grandes profondeurs. La pression du fluide in situ a été évaluée considérant le ratio entre la pression de fluide dans les fractures et la pression lithostatique (facteur pore-fluide ; Zoback et al., 2001 ; Sibson, 2004). Ce paramètre est d'environ 0,4 en supposant un régime hydrostatique et les résultats indiquent l'équation suivante :

$$P_{\text{pore}} = 0.0108z \tag{5.29}$$

Une nouvelle méthode pour estimer le ratio entre les contraintes in situ et la tectonique a été proposée par González de Vallejo et al. (2008) et utilisé dans cette étude. La méthode est basée sur la relation linéaire entre le coefficient du ratio de contraintes et l'indice de contrainte tectonique, qui considère les paramètres géologiques et les propriétés élastiques des roches. Le coefficient du ratio de contrainte dans cette expression a été obtenu sur la base des simulations de Monte Carlo plutôt que sur des mesures de contrainte in situ comme décrite par González de Vallejo (2008). Des travaux futurs axés sur des mesures de contraintes in situ seront nécessaires pour obtenir des valeurs plus précises pour les constantes expérimentales de cette méthode.

De plus, un profil rhéologique (p.ex., Byerlee, 1978 ; Brace et al., 1980 ; Ranalli, 1991 ; Burov, 2011) préliminaire et théorétique a été développé pour Kuujjuaq. Ce profil a été essentiellement construit sur la base d'une connaissance approximative de la composition des couches lithosphériques, d'informations structurales et d'une estimation de la température en profondeur. La croûte continentale semble avoir une composition stratifiée et donc le profil rhéologique peut être considéré comme un modèle de type « jelly sandwich » (Burov, 2011) avec la croûte inférieure en régime ductile et la croûte supérieure en régime fragile. La partie supérieure du manteau est également considérée comme une couche en régime fragile. Un régime hydrostatique a été considéré pour la pression de fluide in situ. Une vitesse de déformation de 10^{-18} s^{-1} a été supposée pour la croûte inférieure et les autres paramètres de fluage utilisés ont été tirés des travaux de Mareschal et al. (2006). La délimitation des zones de transition fragile-ductile a considéré que le comportement en frottement prédomine si la résistance au cisaillement fragile est inférieure à la résistance au fluage ductile (Ranalli, 1991). Les résultats suggèrent que la contrainte est répartie sur une grande épaisseur de lithosphère élastique, ce qui indique qu'une stimulation hydraulique efficace dans cette zone d'étude peut être plus difficile à réaliser que si la contrainte était concentrée sur une épaisseur plus petite de la lithosphère élastique. De plus, la contrainte déviatorique déduite dans ce travail est environ 60 à 207 % inférieure à celle déduite pour le glissement des fractures orientées de manière optimale selon le profil rhéologique théorique. Cela suggère que la pression du fluide dans les fractures doit être augmentée de 50 % pour favoriser le glissement ou que la pression in situ dans la zone d'étude est plus proche du régime lithostatique que du régime hydrostatique. Ainsi, la condition thermomécanique de la zone d'étude, considérant le niveau actuel des connaissances, ne semble pas favorable au développement de systèmes géothermiques ouvragés. Néanmoins, une incertitude élevée existe et des études complémentaires pourraient fournir une évaluation plus adéquate.

L'analyse de frottement de Mohr-Coulomb et de la tendance au glissement a été effectuée à l'aide du logiciel MohrPlotter (Allmendinger, 2020) en supposant une pression de fluide in situ dans le régime hydrostatique et le modèle *a priori* proposé. Ces analyses ont été réalisées pour évaluer si les plans de fracture sont à un état critique de contrainte et à quelle pression critique de fluide ces plans peuvent être réactivés. Cette analyse a aussi indiqué quelles familles de fractures sont orientées de manière optimale pour glisser. En plus, cinq coefficients de frottement statique hypothétiques ont été supposés pour évaluer leur influence sur la réactivation des fractures. Les résultats de ces analyses suggèrent que les fractures et failles ne sont pas à un état critique de contrainte en supposant le régime hydrostatique. De plus, ces analyses indiquent que les fractures qui auront tendance à être réactivées appartiennent aux familles E-O, NNO-SSE et N-S. Les fractures et failles commencent à avoir une forte tendance au glissement, en termes qualitatifs, lorsque les contraintes effectives sont réduites de 50 %. Cependant, si la pression de fluide in situ est plutôt dans le régime lithostatique, alors les fractures sont à un état critique de contrainte et moins de pression de fluide est nécessaire pour réactiver ces structures.

Cinquième article : Analyse technico-économique des systèmes géothermiques ouvragés pour des applications à usage direct dans les communautés hors réseau de l'Arctique : incertitude des paramètres et études de sensibilité

Ce dernier article vise à répondre aux questions « La technique de stimulation hydraulique permettra-t-elle de maintenir un écoulement des fluides au sein d'un réseau de fractures bien connectées à Kuujjuaq ? Quelle est la meilleure conception de système pour atteindre cet objectif ? Quelles autres données géologiques et thermo-hydro-mécaniques locales sont nécessaires pour des prévisions plus exactes ?» et « Les ressources géothermiques profondes potentiellement exploitables avec un système géothermique ouvragé à Kuujjuaq sont-elles compétitives par rapport aux combustibles fossiles ? ». La réponse à ces questions est toutefois limitée par une incertitude élevée en raison de la faible connaissance actuelle de la géologie et des données thermo-hydro-mécaniques locales. Ainsi, aucune donnée n'existe pour calibrer les simulations numériques réalisées dans ce travail. Néanmoins, une approche hypothétique a été utilisée pour fournir une gamme de possibilités et aider à concevoir un système géothermique ouvragé pour chacun des scénarios possibles. Ces systèmes visent à fournir de l'énergie thermique nécessaire à la communauté de Kuujjuaq, en maintenant les pertes d'eau inférieures à 20 %, l'impédance d'écoulement du réservoir inférieure à 0,1 MPa L^{-1} s^{-1} et le rabattement thermique inférieur à 1 ºC par an. En plus, une évaluation préliminaire du coût actualisé de l'énergie a été réalisée à l'aide du logiciel @Risk (Palisade, 2019) pour évaluer la rentabilité économique des systèmes géothermiques ouvragés dans les régions nordiques éloignées.

Les simulations thermo-hydro-mécaniques ont été réalisées avec le logiciel FRACSIM3D (Jing et al., 2000) mis à jour selon de nouvelles lois de comportement des fractures. Une relation déplacement-dilatation de cisaillement, dans laquelle l'angle de dilatation de cisaillement est en fonction du déplacement plutôt que constante, a été formulée et mise en œuvre. De plus amples détails sur les lois de comportement des fractures, les solutions de stimulation et d'écoulement, l'approximation de la perte d'eau et l'extraction de l'énergie thermique sont donnés par Jing et al. (2000). Un modèle de 4 km^3 de volume discrétisé en une grille de 200 pour 200 pour 200 cellules a été utilisé pour effectuer les simulations numériques. Les limites du modèle sont supposées fermées à l'écoulement régional et ont été maintenues à une température constante. Au temps zéro, le modèle est supposé rempli de fluide et la distribution de pression est supposée hydrostatique. La perméabilité in situ initiale et les contraintes sont définies par l'utilisateur. Au-delà des limites du modèle, la pression est supposée hydrostatique lors des calculs de stimulation et de circulation. De plus, la perméabilité in situ, au-delà du volume stimulé, est supposée non perturbée.

Le système géothermique ouvragé a été conçu en doublet, avec un puits injecteur et un producteur, tous deux verticaux. Deux configurations de puits ont été étudiées pour identifier le meilleur emplacement en considérant la présence de la faille Pingiajjulik. Différentes possibilités d'espacement des puits et de longueur de trou ouvert ont été envisagées. Le rayon du puits de forage a été défini à 0,11 m suivant l'exemple du système géothermique ouvragé de Soultz-sous-Fôrets (p.ex., Genter et al. 2010). Le volume de stimulation a été considéré comme variable. Une stimulation a été appliquée dans chaque puits et différentes pressions de stimulation et de circulation ont été étudiées. La durée du projet a été définie pour 30 ans. Des calculs préliminaires ont été effectués pour évaluer un débit de référence que les simulations doivent répondre. Les résultats révèlent que, pour le meilleur scénario thermo-hydro-mécanique considéré, des débits de l'ordre de 14 à 45 L s^{-1} sont nécessaire pour extraire suffisamment d'énergie thermique afin de répondre à la demande d'énergie de Kuujjuaq. Pour le scénario de base, la plage de débit nécessaire est de 27 à 89 L s^{-1}, tandis que pour le pire scénario thermo-hydro-mécanique considéré, le débit nécessaire est supérieur à 200 L s^{-1}.

L'analyse de l'ouverture des fractures avant le processus de stimulation, de la rigidité au cisaillement des fractures et du déplacement de cisaillement des fractures suggère que le développement d'un réservoir géothermique hydrauliquement stimulé est favorisé dans un milieu mécaniquement faible (c'est-à-dire de faible amplitude pour les contraintes principales et avec des fractures peu résistantes à la déformation) et hydrauliquement conducteur. De plus, cette analyse indique également que les fractures plus petites ont tendance à moins glisser, ce qui rend la circulation du fluide plus difficile. L'énergie thermique extraite dans le meilleur scénario thermo-hydro-mécanique considéré et dans le scénario de base avec des fractures plus longues que celles observées sur le terrain peut répondre à la demande d'énergie de chauffage prévue pendant les 30 années de fonctionnement du système géothermique profond.

Une étude supplémentaire a été effectuée pour évaluer si le système géothermique ouvragé peut être utilisée pour la cogénération une fois que certaines conceptions dépassent largement les besoins en chauffage au cours des premières années. Les résultats révèlent que, pour certaines conceptions envisagées, la production combinée de chaleur et d'électricité peut être une solution pendant environ les 10 à 15 premières années de la durée du projet.

Le coût actualisé de l'énergie a été évalué en considérant les coûts proposés par Sanyal et al. (2007) comme le scénario optimiste, ces coûts augmentés par un facteur de 2 comme le scénario le plus probable et augmentés par un facteur de 5 comme le scénario pessimiste. Ainsi, le coût actualisé de l'énergie pour la production de chaleur seulement varie entre une valeur minimale de 54 \$ MWh^{-1} et une valeur maximale de 145 \$ MWh^{-1} pour le scénario optimiste, entre 83 \$ MWh^{-1} et 265 \$ MWh^{-1} pour le scénario le plus probable et entre 170 \$ MWh^{-1} et 626 \$ MWh^{-1} pour le scénario pessimiste. Le coût actualisé de l'énergie pour la production combinée de chauffage et d'électricité varie entre une valeur minimale de 120 \$ MWh^{-1} et une valeur maximale de 143 \$ MWh^{-1} pour le scénario optimiste, entre 218 \$ MWh^{-1} et 262 \$ MWh^{-1} pour le scénario le plus probable et entre 510 \$ MWh^{-1} et 617 \$ MWh^{-1} pour le scénario pessimiste. De plus, une étude probabiliste a été réalisée pour évaluer si la ressource géothermique profonde est compétitive par rapport au statu quo, où le chauffage est assuré par de fournaises au mazout et l'électricité par une centrale au diesel. Les résultats indiquent qu'un système géothermique à la probabilité de fournir de la chaleur avec un cout de production de 8 à 91 % moins importants que les systèmes actuels. La probabilité de fournir de l'électricité et de la chaleur avec une centrale géothermique moins dispendieuse qu'une centrale au diesel est supérieure à 99 %.

Discussion générale et conclusions

La forte dépendance au diesel est une réalité dans les communautés arctiques et subarctiques du Canada. Ces communautés peuvent jouer un rôle important dans le développement de solutions énergétiques et participer aux défis national et mondial posés par les changements climatiques. Un investissement dans le secteur de l'énergie géothermique, par exemple, pourrait soutenir le développement économique local de façon durable en créant des opportunités commerciales, en améliorant la sécurité énergétique, en garantissant la stabilité des prix de l'énergie et en contribuant à réduire les émissions de gaz à effet de serre (p.ex., Serdjuk et al., 2013). Pour y arriver, il existe des défis importants à relever dans les régions nordiques éloignées qui doivent être surmontés, notamment pour franchir un premier stade d'exploration géothermique dans ces communautés. D'importantes lacunes existent au niveau des connaissances et données en profondeur dans les régions éloignées. Ainsi, il est apparu nécessaire d'adapter les méthodes existantes et de définir des lignes directrices pour fournir une évaluation de premier ordre du potentiel géothermique dans les régions nordiques éloignées avec des outils abordables pour les communautés. Ceci est primordial pour stimuler l'intérêt de financier de nouveaux développements et aider à avancer le stade de maturité des activités d'exploration des ressources géothermiques, principalement dans le Bouclier canadien. Cette province géologique est supposée comme moins favorable au développement géothermique par rapport aux bassins sédimentaires et à la ceinture volcanique de l'Ouest canadien (Majorowicz et al., 2010a ; Majorowicz et al., 2010b ; Grasby et al., 2012 ; Grasby et al., 2013). Cependant, ces évaluations sont basées sur l'extrapolation de données de flux de chaleur limités et inégalement distribués. Ainsi, ce travail ciblant les ressources géothermiques profondes réalisé à l'échelle de la communauté et basé sur des méthodes d'exploration géothermique non conventionnelles représente une contribution importante pour aider à avancer la recherche et le développement des ressources géothermiques dans les régions nordiques éloignées. Néanmoins, ce travail présente des points faibles et de points forts qui ont été décrits dans cette thèse.

Contributions

Cette thèse a apporté plusieurs contributions scientifiques qui ont permis de mieux comprendre si l'énergie géothermique peut être une solution hors réseau viable pour diminuer la consommation de diesel dans la communauté de Kuujjuaq. Les recherches entreprises ont permis de mieux comprendre les conditions thermomécaniques et les ressources géothermiques sous la communauté de Kuujjuaq. De plus, le potentiel de récupération de l'énergie thermique par des systèmes géothermiques ouvragés a été étudié et son coût par rapport au diesel a été évalué. Les principales contributions de cette thèse sont énumérées ci-dessous :

1. Évaluation de l'incertitude associée aux différentes techniques de laboratoire pour déterminer les propriétés thermophysiques et l'hétérogénéité intrinsèque des lithologies et leur impact dans les modèles de conduction de chaleur

2. Développement de relations expérimentales pour décrire l’effet de la température, de la pression et de la saturation en eau sur la conductivité thermique
3. Développement d’un modèle numérique pour corriger numériquement les événements paléoclimatiques et déduire simultanément le flux de chaleur terrestre à partir de profils de température inférieurs à 100 m de profondeur
4. Analyse de sensibilité pour déterminer de l’influence de la température en surface lors d’un événement glaciaire sur l’évaluation du flux de chaleur et la température en profondeur
5. Évaluation de la distribution de la température en profondeur en considérant les événements paléoclimatiques
6. Évaluation de l’énergie thermique en place sous Kuujjuaq à l’aide d’une analyse de sensibilité et prévisions de la production de chaleur et d’électricité.
7. Caractérisation du réseau de fractures à Kuujjuaq basée sur un échantillonnage en ligne et une analyse de la topologie pour évaluer la connectivité du réseau
8. Estimations du régime de contraintes in situ à partir des indicateurs géologiques, des corrélations empiriques et des modèles analytiques
9. Élaboration d'un modèle géologique conceptuel préliminaire pour la lithosphère sous Kuujjuaq sur la base de publications géologiques et géophysiques régionales et proposition d'un profil rhéologique théorique 1D considérant les informations structurales et les estimations de température
10. Évaluation de la présence de fractures orientées de manière optimale, de leur état de contrainte et de la pression critique du fluide pour leur réactivation en considérant le régime de contraintes déduit
11. Mise en évidence du rôle clé joué par la pression du fluide in situ et le coefficient de frottement statique lors de l'évaluation de l'état de contrainte des fractures
12. Évaluation de la performance des systèmes géothermiques ouvragés sur la base d’une approche hypothétique pour faire face à l'incertitude des paramètres et évaluer les conditions thermomécaniques optimales pour une procédure de stimulation hydraulique efficace
13. Évaluation du coût actualisé de l'énergie selon des hypothèses de coûts d’installation optimistes, les plus probables et pessimistes, et évaluation probabiliste de la fourniture de chaleur et d'électricité à un coût inférieur à celui des fournaises au mazout et d’une centrale au diesel actuellement utilisée

Conclusions

Les communautés canadiennes hors réseau dépendent fortement des combustibles fossiles et leur transition vers un approvisionnement en énergie propre est actuellement une priorité gouvernementale. Bien que cette thèse ait été entreprise dans la communauté de Kuujjuaq (Canada), les méthodes décrites dans chaque chapitre et l'approche globale suivie dans cette thèse sont des contributions importantes pour évaluer le potentiel des ressources géothermiques profondes avec des outils d'exploration abordables pour les communautés nordiques. De plus, une série d’autres méthodes sont proposées pour améliorer cette évaluation de premier ordre. Ces méthodes peuvent également être utilisées lors d'autres évaluations des ressources d'énergie géothermique profonde à l’endroit d’autres communautés. Cette thèse fournit un guide utile, présentant des méthodes nouvelles et adaptées, fournissant des informations de base et discutant des voies futures possibles, pour évaluer le potentiel d'énergie géothermique profonde dans les milieux cristallins fracturés à faible perméabilité et dans les régions confrontées à des défis énergétiques importants faisant toutefois face à une maque d’information ou d’observations géologiques en profondeur.

L'évaluation des propriétés thermophysiques des lithologies affleurantes a révélé qu'à Kuujjuaq, la combinaison de la spectrométrie gamma et du balayage optique donne des prévisions de température de base plus faibles que la combinaison de la spectrométrie de masse avec un compteur de flux de chaleur. Par conséquent, il est conseillé de combiner ces méthodes pour éviter des prévisions biaisées de la température en profondeur. Le modèle numérique développé pour simuler les événements paléoclimatiques et déduire le flux de chaleur terrestre à partir d'un profil de température de 80 m de profondeur indique que le flux de chaleur terrestre à 10 km de profondeur varie entre 31,8 et 69,4 mW m^{-2}, selon les conditions paléoclimatiques et propriétés thermophysiques considérées. De plus, la quantification de l'incertitude et l'analyse de sensibilité ont révélé que la température en profondeur et le facteur de récupération sont les paramètres les plus influents sur l'énergie thermique disponible sous Kuujjuaq. Les prévisions de production potentielle de chaleur et d'électricité indiquent que la production d'électricité et la production combinée de chaleur et d'électricité sont des applications à risque élevé à moyen, tandis que la production de chaleur est à faible risque entre les profondeurs de 4 à 10 km. À ces profondeurs, la probabilité de répondre à la demande annuelle moyenne de chauffage estimée à Kuujjuaq est supérieure à 98 %.

La caractérisation des fractures à Kuujjuaq a révélé quatre familles de fractures principales : N81°E-N90ºE (E-O – F1), N161°E-N170ºE (NNO-SSE – F2), N11°E-N20ºE (N-S – F3) et

N121°E-N130ºE (NO-SE – F4). La densité des fractures se situait entre un minimum de 0,3 fracture m^{-1} et un maximum de 3,7 fractures m^{-1}, avec une valeur médiane de 0,8 fracture m^{-1}. Le coefficient de variation calculé pour chaque famille a révélé des valeurs de 0,4 pour les familles N-S et NO-SE et de 0,7 pour les familles E-O et NNO-SSE. L'hétérogénéité de la distribution évaluée par la méthode de Kuiper a révélé une valeur de 15 %. La longueur des fractures varie entre 2 à 28 m et la dimension fractale entre 1,7 à 2,4. Les indicateurs géologiques suggèrent que les contraintes principales horizontales maximales et minimales sont respectivement orientées N210ºE-N220ºE et N300ºE-N310ºE. L'inclinaison est supposée horizontale. Les trois contraintes principales (verticale et horizontales) peuvent être décrites par les relations suivantes :

- $\sigma_{\mathrm{V}} = 0.0271z$
- $\sigma_{\mathrm{H}} = 0.0430z + 8.62$
- $\sigma_{\mathrm{h}} = 0.0251z + 4.94$

Les analyses de frottement de Mohr-Coulomb et de tendance au glissement ont révélé que, bien que la plupart des plans de fracture soient orientés de manière optimale pour le glissement, ceux-ci ne sont pas à un état critique de contrainte en supposant un régime hydrostatique in situ. Les contraintes principales effectives doivent être diminuées de plus de 50% pour réactiver ces fractures. De plus, les analyses indiquent que les familles de fractures E-O, NNO-SSE et N-S ont la plus forte tendance au glissement, tandis que les fractures NO-SE ne seront pas réactivées. L'analyse des conditions thermomécaniques sous Kuujjuaq semble défavorable pour le développement de systèmes géothermiques ouvragés bien qu'il existe une incertitude à ce niveau. Les simulations d'opération de systèmes géothermiques ouvragés ont principalement été réalisées pour des systèmes d'intérêt considérant le meilleur scénario, où le réservoir a été supposé à haute température, hydrauliquement conducteur et mécaniquement faible. Dans ce cas, les simulations numériques suggèrent que la production combinée de chaleur et d'électricité est possible pendant les 10 à 15 premières années de fonctionnement du système géothermique. Le coût actualisé de l'énergie en supposant uniquement la production de chaleur a été estimé entre 54 \$ MWh^{-1} et 626 \$ MWh^{-1}, tandis que le coût de la cogénération varie entre 120 \$ MWh^{-1} et 617 \$ MWh^{-1} (en USD). De plus, les systèmes géothermiques ouvragés ont de 8% à 91% de probabilité de fournir de l'énergie à un coût inférieur à celui des fournaises au mazout et plus de 99% de chances de fournir de l'électricité à un coût inférieur à celui de la centrale au diesel actuellement en place.

Les résultats de cette thèse, bien que comportant des incertitudes analysées de façon exhaustive dans ce travail en raison du manque de forages d'exploration et d'observations géologiques profondes, suggèrent que le Bouclier canadien sous la communauté de Kuujjuaq a le potentiel de répondre à la demande moyenne d'énergie de chauffage de ces 2 754 habitants. De plus, les systèmes d'énergie géothermique ouvragés peuvent être une solution potentielle pour exploiter les ressources géothermiques profondes à un coût compétitif, lorsque comparé avec celui des fournaises au mazout et des centrales diesel actuelles. Ainsi, en réalisant les travaux de cette thèse pour mettre en lumière le problème de valeur de l'information typique aux régions nordiques, les résultats obtenus suggèrent que l'exploration des ressources géothermiques vaut la peine se poursuivre afin d'affiner les estimations réalisées et d'envisager son exploration dans un futur proche. Cette thèse met également en évidence le besoin d'évaluation des ressources géothermiques axées sur la communauté plutôt que des évaluations régionales basées sur une extrapolation de données peu abondantes. Il est toutefois important de souligner l'importance de forages profonds d'exploration géothermique. Ces forages permettront d'évaluer la température en profondeur, le flux de chaleur, les fractures et les contraintes in situ et de valider les résultats obtenus dans cette thèse.

En conclusion, l'énergie géothermique peut être une solution hors réseau viable sur le plan technique et économique pour soutenir la transition énergétique des collectivités nordiques éloignées avec une source d'énergie locale, durable et sans carbone.

CONTENTS

FIGURES

TABLES

EQUATIONS

NOTATION

	Variable	Unit
a, b, c', d	Experimental constants	---
A	Constant	MPa^{-n} s^{-1}
A'	Area	m^2
c	Specific heat	J kg^{-1} K^{-1}
C	Cost	$
C_B	Connections per branch	---
C_f	Connections per fracture	---
C_H	Hydraulic connectivity	---
C_L	Connections per line	---
C_N	Connections per node	---
CV	Coefficient of variation	%
D	Fractal dimension	---
e	Energy	J, MWh, J mol^{-1}
E	Young's modulus	Pa
erfc	Error function	---
f	Function	---
F	Factor	%
g	Gravitational acceleration	m s^{-2}
G	Gravitational constant	m^3 kg^{-1} s^{-1}
h	Thickness	(m)
H	Hydraulic impedance	MPa L^{-1} s^{-1}
H'	Heat generated by the radioisotope	W kg^{-1}
i	Imputed interest rate	%
I	Intensity	fractures m^{-1}
*I**	Injection well	---
j	Distance	m
J	Total capital investment	$
JRC	Joint roughness coefficient	---
k	Stress ratio coefficient	---
K	Maximum departure from the uniform distribution	---
K'	Hydraulic conductivity	m s^{-1}
l	Length	m
L	Maximum lithostatic load	m
lb	Lower bound	---
LCOE	Levelized cost of energy	$ MWh^{-1}
M	Mass	kg
MRE	Mean value of the relative error	%
n	Stress and temperature-independent parameter	---
N	Number of fractures, number of samples, number of wells	---
NC	Coefficient of seismotectonic activity	---
O	Operation & maintenance cost	$ year
O_f	Scalar-valued objective function	---
P'	Specific abundance of the radioisotope	Wt %
P	Pressure	Pa
PO	Power output	W
q	Heat flux	W m^{-2}

Q	Flow rate	$m^3\ s^{-1}$; $L\ s^{-1}$
r	Radius	m
R	Gas constant	$J\ K^{-1}\ mol^{-1}$
R^*	Recovery well	---
RHP	Radiogenic heat production	$W\ m^{-3}$
S	Fracture spacing	m
SC	Coefficient of topographic influence	---
t	Time	s, years
T	Temperature	ºC, K
T'	Termination	%
T^*	Transmissivity	$m^2\ s^{-1}$
TDS	Total dissolved solids	$kg\ L^{-1}$
TSI	Tectonic stress index	---
u	Darcy velocity	$m\ s^{-1}$
U	Shear displacement	m
ub	Upper bound	---
v	Kinematic viscosity	$m^2\ s^{-1}$
V	Volume	m^3
V'	Heterogeneity parameter	---
V^*	Parameter to test the null hypothesis of uniformity	---
w	Aperture	m
W_{loss}	Water loss	%
x	Spatial variable	m
X	Parameter under evaluation	---
z	Spatial variable, depth	m, km
	Greek letter	
α	Thermal diffusivity	$m^2\ s^{-1}$
β	Coefficient of linear thermal expansion	$ºC^{-1}$
Δ	Variation	---
$\acute{\varepsilon}$	Strain rate	s^{-1}
η	Thermal efficiency	%
ι	Random number	---
κ	Permeability	m^2
λ	Thermal conductivity	$W\ m^{-1}\ K^{-1}$
μ^*	Arithmetic mean	---
μ	Friction coefficient	---
ν	Poisson's ratio	---
ρ	Density	$kg\ m^{-3}$
ρc	Volumetric heat capacity	$J\ m^{-3}\ K^{-1}$
σ^*	Population standard deviation	---
σ	Stress	Pa
σ'	Effective stress	Pa
σ_n	Normal stress	Pa
σ'_n	Effective normal stress	Pa
σ_{SB}	Stefan-Boltzmann constant	$W\ m^{-2}\ K^{-4}$
τ	Shear stress	Pa
φ	Porosity	%
ϕ	Angle	º
χ	Median	---
ω	Dynamic viscosity	$kg\ m^{-1}\ s^{-1}$

	Symbol	
[X]	Concentration of an element	mg kg^{-1}, %
∇P	Pressure gradient	Pa m^{-1}
∇T	Geothermal gradient	ºC m^{-1}
	Subscript	
0	Surface, ambient pressure, initial	
1	Maximum principal stress	
2	Intermediate principal stress	
3	Minimum principal stress	
10	10 km depth	
20	Room temperature	
a	Apparent	
amb	Ambient, surface air	
circ	Circulation	
dry	Dry conditions	
e	Electrical	
emp	Empirical	
f	Fluid	
fract	Fracture	
g	Ground, ground surface	
GPP	Geothermal power plant	
h	Horizontal minimum principal stress	
H	Horizontal maximum principal stress	
H, average	Average horizontal principal stress	
hyd	Hydraulic	
i	Index	
I	I-node	
inj	Injection	
LC	Lower crust	
m	Mechanical	
M	Moho	
max	Maximum	
min	Minimum	
n	Final	
n_ref	Reference stress for 90% closure	
p-f	Pore-fluid	
rec	Recovery, recovered	
res	Reservoir	
ref	Reference	
s	Well scaling	
stim	Stimulation	
th	Thermal	
UC	Upper crust	
V	Vertical principal stress	
wet	Water-saturation conditions	
X	X-node	
Y	Y-node	

Abbreviation

ASTM	American Society for Testing and Materials
BDF	Backward differentiation formula
B.P.	Before present
CCB	Continuing calibration blank
CCV	Continuing calibration verification
CGPP	Combined gas permeameter-porosimeter
CHP	Combined heat and power
CRM	Certified reference material
DBHE	Deep borehole heat exchangers
DFN	Discrete fracture network
ECSOOT	Eastern Canadian Shield Onshore-Offshore Transect
EGS	Enhanced/Engineered Geothermal Systems
ERT	Electrical resistivity tomography
FEM	Finite element method
GHFM	Guarded heat flow meter
GPP	Geothermal power plant
GSHP	Ground-source heat pumps
GRS	Gamma-ray spectrometry
GSTH	Ground Surface Temperature History
HSD	Hydrothermal spallation drilling
IAEA	International Atomic Energy Agency
ICP-MS	Inductively Coupled Plasma – Mass Spectrometry
IHCP	Inverse heat conduction problem
JRC	Joint roughness coefficient
LGM	Last Glacial Maximum
LIS	Laurentide Ice Sheet
MIS	Marine Isotope Stage
OECD	Organization for Economic Co-operation and Development
PE	Percent equilibrium
SE	Semi-equilibrium
TCS	Thermal conductivity scanner
TE	Temperature equilibrium
USD	US dollars
USGS	United States Geological Survey

1 INTRODUCTION

1.1 Context

Canada is a vast country, and its electrical grid connects only the southern part of the country where most of the population lives, leaving 280 communities off the grid (Figure 1.1a). Of these, 239 settlements located mostly in the northern part of Canada are currently relying exclusively on fossil fuels for electricity and space heating (Grasby et al., 2013; Arriaga et al., 2017). Electricity is locally generated in diesel-powered power plants while space heating is provided by oil furnaces. This leads to a consumption of more than 90 million liters of diesel per year in the remote regions of Canada (Figure 1.1b; Lovekin et al., 2019a). In the communities without year-round road access, the diesel must be purchased and shipped once a year and stored for long-term usage, with increasing risks of spills (Arriaga et al., 2017). Moreover, to keep energy affordable in the northern regions, large subsidies are required (CER, 2018). For example, in Nunavik (Québec, Canada), in 2018, the price of diesel increased from 1.79 to 2.03 $\$ L^{-1}$, and the local government subsidizes it at 40 ¢ L^{-1}, reducing the price to 1.63 $\$ L^{-1}$ (Makivik Corporation, 2018). These prices are in Canadian dollars (CAD).

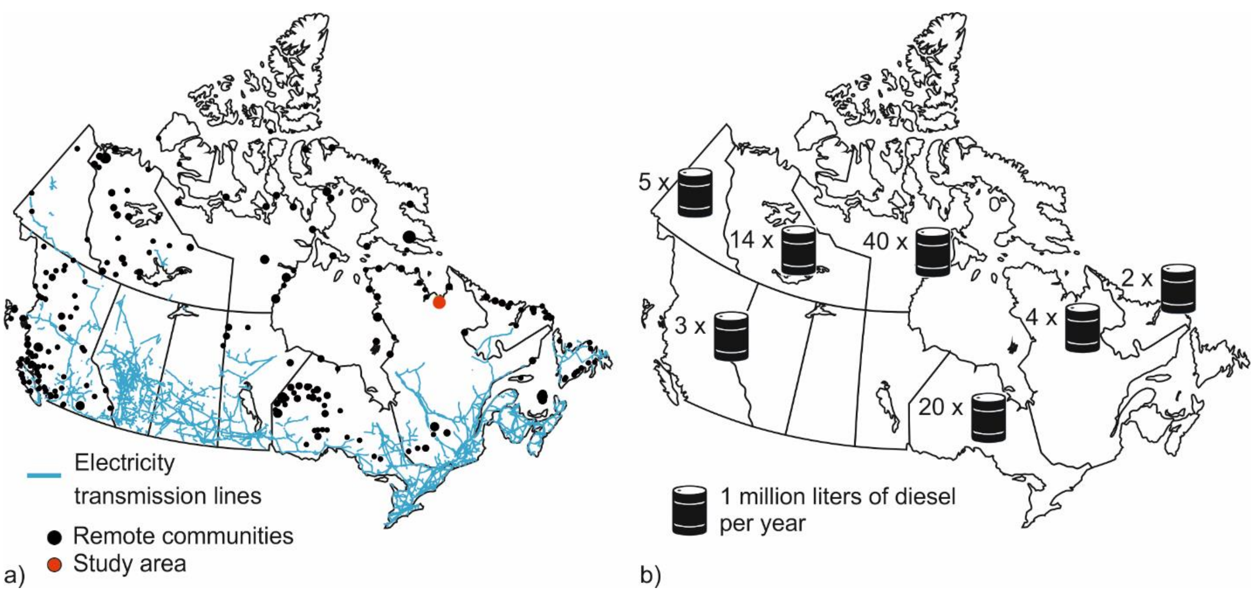

Figure 1.1 a) Canadian off-grid communities and b) annual diesel consumption per province and territory, redrawn from Arriaga et al. (2017) and Lovekin et al. (2019a).

Thus, the energetic framework of the diesel-based communities entails 1) high costs to buy, transport, and store the diesel, 2) greenhouse gas emissions during heat production and power generation that damage the local environment and contribute for the climate change, and 3) low energy security, opposite to the three main axes that constitute the concept of sustainable energy markets: economic affordability, environmental compatibility, and energy security (Figure 1.2; Frick et al., 2010; Zweifel et al., 2017). A sustainable energy market intends to maintain and improve living standards at an affordable cost by replacing the consumption of environmentally harmful sources of energy by more environmentally friendly alternatives.

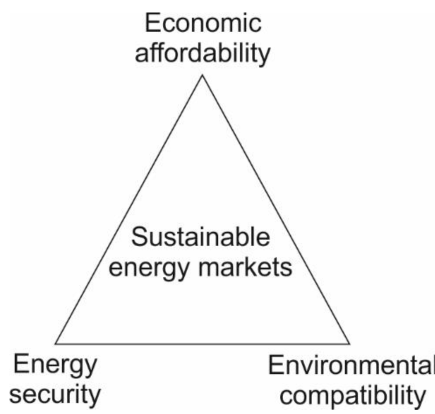

Figure 1.2 Strategic triangle of sustainable energy markets, redrawn from Frick et al. (2010).

Therefore, promoting the energy transition of these communities is the nowadays watchword and off-grid renewable technologies, including stand-alone and micro-grids, can be a viable solution. Paraphrasing Adnan Z. Amin, "*Off-grid renewable energy systems have transformed our ability to deliver secure, affordable electricity to rural communities all over the world, and are playing a vital role in breaking a cycle of energy poverty that has held back socio-economic progress for hundreds of millions of people*" (IRENA 2019). Beyond electricity generation, space heating is also an important issue for the 200 000 people living in northern Canada. Although the residential dwellings are built to meet strict regulatory standards of insulation, the harsh climate with more than 8 000 heating degree days results in high heating energy consumption. For example, in Kuujjuaq (Nunavik, Canada), the annual average heating demand has been estimated to range between 22 and 71 MWh per residential dwelling (Yan et al., 2019; Gunawan et al., 2020). Therefore, the optimal off-grid renewable energy solution should be capable to fulfill not only the electricity needs, but the space heating as well. However, such a system might be utopian with the current level of technology and combining several renewable technologies may be more tangible options.

Among the renewable sources possible to develop in northern regions, deep geothermal has increased interest due to its fuel cycle independency, its base load nature, i.e. geothermal power plants are capable to produce heat and generate power 24h per 7 days a week regardless of the weather conditions and diurnal cycles, and its ubiquitous and versatile character (Kagel et al., 2005; Glassley, 2010). Nevertheless, integrating deep geothermal energy systems with other technologies (renewables or nonrenewable) can improve their individual efficiency in such cold climates (Mahbaz et al., 2020). Thus, assessing if the deep geothermal energy sources[2] can supplant or displace reliance on fossil fuels is of utmost importance. The viability of geothermal energy as an alternative solution for the off-grid diesel-based communities is evaluated through a number of geologic, technical, socio-economic, environmental and policy criteria (e.g., Glassley, 2010; Young et al., 2018). The research undertaken in this thesis within the community of Kuujjuaq aims at providing first-order answers to the following questions through an original approach that uses geothermal exploration tools affordable to the northern and remote communities:

- Is it sufficiently abundant to meet a significant percentage of the market demand?
- Can it be obtained at a cost competitive with the diesel?

The work carried out can be seen as a first step to justify whether deep exploration drilling should be completed. In these remote areas, exploration drilling is expected to be 2 to 5 times more expensive than in the south such that development of new exploration methods using outcrops as subsurface analogues, shallow groundwater monitoring wells, numerical modeling and uncertainty quantification appear essential to reduce risks. Ultimately, deep drilling will provide a more accurate prediction of the potential if local communities choose to explore their geothermal energy sources.

1.2 **Literature review**

1.2.1 Canada's energy outlook and climate actions

Canada is an energy-intensive country. Data shows that the average Canadian consumes 5.1 times as much energy as the average world citizen and 23% more than the average American (Hughes, 2018). Currently, 16% of Canada's total primary energy supply comes from renewable sources, mostly hydro (68%) and solid biomass (23%), with wind, ethanol and other biodiesel, municipal waste/landfill gas, solar and tidal accounting for a small share (Figure 1.3; GCan, 2020a). However, fossil fuels are still Canada's primary energy source (Figure 1.3; Hughes, 2018). Furthermore, Canada emits more greenhouse gases (GHGs) than triple the

---

[2] Geothermal energy source – "*thermal energy contained in a body of rock, sediment and/or soil, including any contained fluids, which is available for extraction and conversion into energy products. (…) The Geothermal Energy Source results from any influx to outflux from or internal generation of energy within the system over a specified period of time*" (UNECE, 2016).

world average mainly due to upstream oil and gas production (26%) and transportation (24%). However, the emissions in buildings, electricity generation and industrial sectors are also important (around 11%; Hughes, 2018).

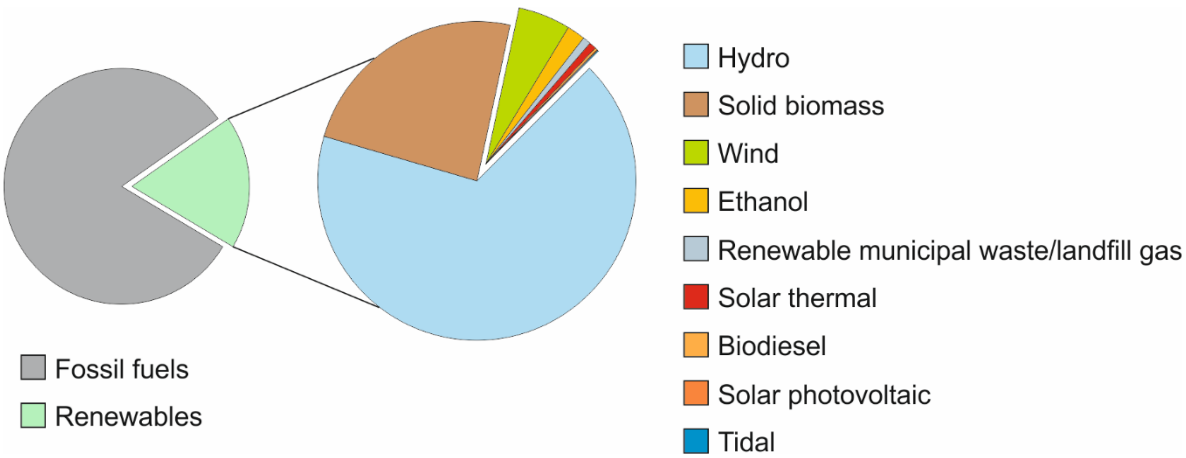

Figure 1.3 Canada's primary energy sources, based on Hughes (2018) and GCan (2020a).

Therefore, Canada is making strong commitments to embrace energy transition and fight climate change. In 2015, Canada joined the Paris Agreement pledging to reduce carbon emissions 30% below 2005 levels by 2030 (Generation Energy, 2018). This agreement is a legally binding international treaty on climate change that aims to limit global warming preferably to 1.5 ºC (UNFCCC, 2021). To achieve this goal, the 196 participating countries agree on reaching global peaking of GHG emissions to reach a climate neutral world by mid-century (UNFCCC, 2021). For Canada to achieve the proposed goal, federal territorial and provincial governments agreed to the Pan-Canadian Framework on Clean Growth and Climate Change, which is built upon four main pillars (GCan, 2016):

- Pricing carbon pollution
- Complementary measures to further reduce emissions across the economy
- Measures to adapt to the impacts of climate change and build resilience
- Actions to accelerate innovation, support clean technology, and create jobs

The Pan-Canadian Framework is not only a collective plan for economic growth while reducing emissions, but also aims at building resilience to adapt to a changing climate (GCan, 2016). Moreover, the Pan-Canadian Framework aims at respecting the rights of Indigenous Peoples, with robust and meaningful engagement drawing on their Traditional Knowledge (GCan, 2016). Furthermore, it intends to take into account the unique circumstances and opportunities of Indigenous Peoples and northern, remote and vulnerable communities (GCan, 2016). In fact, the impacts of climate change are already being felt across Canada and they are magnified in

Canada's Arctic, posing significant risks for the communities with significant social, cultural, ecological and economic implications (GCan, 2016). Thus, the remote northern communities are at the front line of climate change and can play a leading role in providing solutions for Canada's successful energy transition (Generation Energy, 2018).

1.2.2 Canadian northern communities and energy transition

Canada's northern communities critically depend on energy services for their safety, sustainability, and economic growth (Gilmour et al., 2018). Their diesel dependency has been promoting a cycle of energy poverty that has been holding back their socio-economic progress. The economic development of a region relies on the accessibility to markets and raw materials and availability of a reliable energy source. In Nunavik, for example, despite the regional proximity to vast hydroelectric potential, the 14 Inuit communities are still compelled to rely on non-renewable energy sources (KRG et al., 2010). This results on a regional cost of living higher than in southern Québec (e.g., food costs 57% more in Nunavik than elsewhere in Québec) and on an unemployment rate of 25-30% (KRG et al., 2010). Although this diesel-based structure entails a major expense for basic living needs, the "true cost" of such energetic framework is even higher (Lovekin et al., 2019b). In addition to the diesel and energy cost, transportation and maintenance costs need to be accounted, not to mention the negative environmental and health impacts and the largely unknown financial liability of diesel spill clean-up and remediation (Lovekin et al., 2019b).

One of the actions proposed on the Pan-Canadian Framework aims at reducing reliance on fossil fuels in the diesel-based communities, by "*accelerating and intensifying efforts to improve the energy efficiency of diesel generating units, demonstrate and install hybrid or renewable energy systems, and connect communities to electricity grids*" (GCan, 2016). These actions bring significant benefits for the communities by creating the potential for locally owned and sourced power generation (GCan, 2016). Although a study conducted by Denis et al. (2009) highlights that most communities prefer policies and programs centered on increasing energy efficiency and conservation rather than switching to renewables, smaller and more remote settlements may be the most willing to lead the introduction of renewable energy systems. Furthermore, promoting renewable energy development can lead to drastic reductions in carbon emissions, the decommissioning of the diesel power plants and opportunities for sustainable development at the community level (Krupa, 2012). Nevertheless, certain barriers (e.g., cash, capacity, clarity, circumstance and lack of legitimacy and equality) must be overcome for Indigenous Peoples to reach their full potential and shape the debate (Krupa, 2012).

Extensive research has been carried out evaluating diverse renewable energy options for the Canadian remote northern communities, such as wind (e.g., Khan et al., 2005; Weis et al., 2008; Thompson et al., 2009; Weis et al., 2010; Guo et al., 2016), hydro (e.g., Ranjitkar et al., 2006), solar (e.g., Thompson et al., 2009), biomass (e.g., Thompson et al., 2009; Stephen et al., 2016; Yan et al., 2019), biofuels (e.g., McFarlan, 2008), waste gasification (e.g., Yan et al., 2019) and geothermal (e.g., Majorowicz et al., 2010a; Majorowicz et al., 2010b; Belzile et al., 2017; Minnick et al., 2018; Kanzari et al., 2019; Kinney et al., 2019; Gunawan et al., 2020; Mahbaz et al., 2020). Microgrid hybrid (or integrated) systems (fully or partially renewable) are seen as the most favorable to address the challenges of off-grid energy (e.g., Mahbaz et al., 2020; Quitoras et al., 2020). Such systems usually offer better energy security as they can compensate for the fluctuating and intermittent nature of some of the renewable energy technologies and are designed to meet the peak demand (Dincer et al., 2014). Additionally, the efficiency of renewable technologies may improve if coupled with energy storage (e.g., Ibrahim et al., 2011; Brenna et al., 2017; Giordano et al., 2019a). Despite all these options, few communities are actually embracing the energy transition with projects being developed. A series of reviews on the recent development in renewable energy in the Canadian remote communities have been produced for Yukon (Karanasios et al. 2016a), Northwest Territories (Karanasios et al. 2016b), Nunavut (Karanasios et al., 2016c), British Columbia (Karanasios et al., 2016d), Ontario (Karanasios et al., 2016e), Québec (Karanasios et al., 2016f) and Newfoundland and Labrador (Karanasios et al., 2016g). Geothermal energy is only being considered and identified as a viable option in Yukon (Karanasios et al., 2016a), Northwest Territories (Karanasios et al., 2016b) and British Columbia (Karanasios et al., 2016d).

Deep geothermal energy, although the perception of high-cost and high-risk, is a reliable source of energy that can produce base-load power, which is an advantage compared to the intermittent production by wind and solar. Furthermore, deep geothermal is produced locally, which is an advantage compared to biomass that has to be transported and stored. Moreover, deep geothermal energy is versatile and can be used for both heat and power, an advantage compared to renewable energy technologies that can only produce electricity (e.g., hydro, solar photovoltaic and wind) or used for heating (e.g., solar thermal). Nevertheless, although deep geothermal energy sources are a local alternative to provide base load heat and electricity, an auxiliary system is more likely to be used together with the geothermal power plant to supply energy during peak conditions.

1.2.3 Geothermal energy

1.2.3.1 Definition

Geothermal energy is the energy stored in the form of heat within the Earth. The word comes from the Greek *geo* and *therme* that mean earth and heat, respectively (e.g., Watchel, 2010). There are several external and internal sources that contribute for the Earth's heat income (Pater et al., 2001; Clauser, 2006; Jaupart et al., 2011). The external sources are mainly the electromagnetic energy from the solar radiation and the gravitational energy due to external bodies (i.e. the sun and the moon; Clauser 2006). The internal sources are the radiogenic heat from the decay of the unstable radioisotopes, the heat originated during the formation of the planet, the potential energy released by geodynamic processes, and the frictional heat released during earthquakes (Clauser, 2006). Of these, the radiogenic heat and the release of the primordial heat are believed to be the main contributors for the terrestrial heat flux (e.g., Barbier, 2002; Clauser, 2006).

Unstable radioisotopes tend to decay into more stable and nonradioactive isotopes. During this process, energetic particles (α and β) and gamma-rays are emitted, and the kinetic energy released is absorbed by the surrounding rock mass, thus, generating heat. The radioactive isotopes contributing for the radiogenic heat production are mainly ^{238}U, ^{232}Th, and ^{40}K. These isotopes are abundant, have a half-life comparable to the age of the Earth (^{238}U, $t^{1/2}$ = 4.5 Ga; ^{232}Th, $t^{1/2}$ = 13.9 Ga; ^{40}K, $t^{1/2}$ = 1.4 Ga), and most of their decay energy is converted to heat (Pater et al., 2001; Barbier, 2002; Clauser, 2006).

The ^{238}U undergoes a series of 14 radioactive decays, emitting 8 α-particle and 6 β- particles, until it becomes ^{206}Pb. This process releases approximately 4.27 MeV gamma-radiation and generates about 91.7 μW kg^{-1} of heat. The ^{232}Th decays to ^{208}Pb in a series of 10 radioactive decays, emitting 7 α-particle and 4 β-particles, and releasing approximately 4.08 MeV gamma-radiation and producing approximately 25.6 μW kg^{-1} of heat. ^{40}K becomes the nonradioactive daughter-isotope in a single-step decay. The energy released during its decay is 1.31 MeV gamma-radiation if ^{40}K decays to ^{40}Ca, or 1.46 MeV if it decays to ^{40}Ar. This single-step decay generates about 30.0 μW kg^{-1} of heat (Pasquale et al., 2014).

Potassium is a major element and occurs in the main mineral phases, such as feldspars and micas. Uranium and thorium, in turn, are trace elements enclosed in the crystal lattice of accessory minerals, such as zircon and monazite. The concentration of these two elements in a rock mass depends on the composition of the molten rock. The magma partial melting and fractional crystallization processes enables uranium and thorium to be concentrated in the liquid phase and become incorporated into more silica-rich products (Uosif et al., 2015). Thus, the concentration of uranium and thorium increases as a function of the silica content and felsic rocks, such as granites, tend to have higher concentration of both these elements than mafic rocks (e.g., Hasterok et al., 2018). Moreover, uranium is highly mobile in the presence of fluids and weathering. Therefore, surficial rocks tend to have lower concentrations of uranium than core samples (e.g., Jaupart et al., 2014; Lamas et al., 2017). Moreover, this element can be an indicator of groundwater circulation in subsurface faults (e.g., Lamas et al., 2017) and its daughter-isotope radon can be used to infer the fluid residence time (e.g., Richards et al., 1991) and the aperture of the joints (e.g., Andrews et al., 1986; Hussain, 1991).

The primordial heat accumulated within Earth's interior is believed to be a consequence of both accretional and differentiation energy (Pater et al., 2001; Breuer, 2011). The former is a result of the accretion of material during the formation of the planet (Pater et al., 2001). The collision of bodies leads to a gain in energy. This energy gain is equal to the difference between the gravitational energy acquired with the accretion and the energy radiated away (Pater et al., 2001):

$$\rho c(T(r) - T_0)dr = \left(\frac{GM(r)}{r} - \sigma_{\mathrm{SB}}(T^4(r) - T_0^4)\right) \tag{1.1}$$

where ρc (J m^{-3} K^{-1}) is the volumetric heat capacity, T (°C) is the temperature, G (m^3 kg^{-1} s^{-1}) is the gravitational constant, M (kg) is the mass, r (m) is the radius and σ_{SB} (W m^{-2} K^{-4}) is the Stefan-Boltzmann constant ($\sigma_{\mathrm{SB}} \approx 5.67\text{x}10^{-8}$ W m^{-2} K^{-1}). During rapid accretion, the energy is stored faster than it is radiated away, leading to an increase of temperature on the inner part of the planetary body and to differentiation (Pater et al., 2001).

1.2.3.2 Technologies and applications

The heat existing in the planet has long been recognized, either by the volcanic eruptions and all other demonstrations of the planet's geodynamics, or by the thermal springs that gave origin to the ancient spas and hot baths. However, the industrial exploration of geothermal energy sources started only in the 20$^{\text{th}}$ century, with the first experimental installation built at Larderello

(Italy) in 1913 (e.g., Minissale, 1991; Watchel, 2010). In the United States, the first geothermal power plant opened in 1922 near the Geysers (e.g., Watchel, 2010). In Canada, no geothermal power plant is under operation to date. However, geothermal research and exploration are underway to install the first geothermal power plant in the southern part of Saskatchewan (e.g., DEEP; Hickson et al., 2020; Somma et al., submitted). DEEP's project is targeting the Williston Basin, more specifically, the Early Paleozoic basal clastic reservoirs of Deadwood Formation and the fractured Precambrian granite. Cleveland et al. (2014) presents a comprehensive chronology of geothermal energy main developments worldwide throughout the history.

The first areas to be considered of geothermal interest, from an industrial point of view, were zones of active volcanism and tectonic activity. Nowadays, geothermal energy is explored in a number of different geological contexts, from young volcanics to sedimentary basins and basement rocks (Moeck, 2014) and at several depths, from few hundreds of meters (e.g., ground-source heat pumps; Banks, 2012) to kilometers deep (e.g., deep borehole heat exchangers and engineered geothermal energy systems[3]; Stober et al., 2013).

Ground-source heat pumps is an inclusive term to describe heat pump systems that uses the ground or groundwater as a heat source and/or sink (Figure 1.4). These can be categorized as having closed or open loops, and those loops can be installed in three ways: horizontally, vertically, or in a water body (pond/lake; IGSHPA, [2021]). These systems have the advantage of being capable to work in dual mode, providing heating and/or cooling depending on the season. A reversing valve is used to switch between the modes by reversing the refrigerant flow direction (Figure 1.4; IGSHPA, [2021]).

[3] The term engineered geothermal energy systems is used in this work to refer the technology to extract geothermal energy sources from low permeability crystalline fractured rocks and the term encompasses, not only the hydraulic stimulation of the subsurface, but the connection of the reservoir by the injection and recovery wells, the circulation of the fluid through the heat exchanger created and the energy extracted. The concept of artificially enhancing the wells and subsurface productivity via chemical, thermal, and/or hydraulic stimulation techniques, regardless the geological environment, is termed in this work as Enhanced Geothermal Systems.

Petrothermal systems is a term applied when the heat carrier fluid must be injected since the formation of the geothermal system does not contain enough fluid volume for heat extraction (e.g., Moeck, 2014).

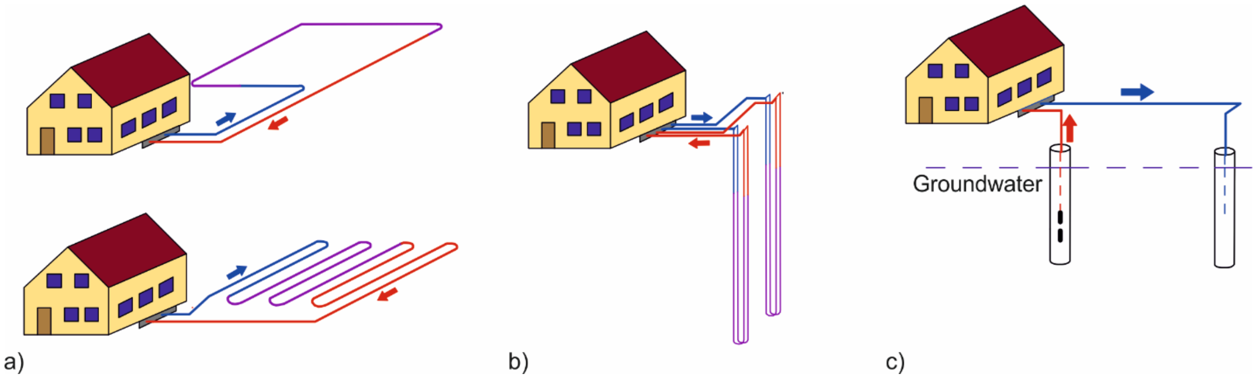

Figure 1.4 **Ground-source heat pumps configurations: a) Horizontal closed-loop, b) vertical closed-loop and c) vertical open-loop, redrawn from Sanner (2014).**

Hydro-geothermal low-enthalpy systems, such as the hydrothermal doublet (or SedHeat systems; e.g., Mahbaz et al., 2021), uses the heat stored in warm/hot water of deep aquifers (Stober et al., 2013). Such a system was designed to operate at Regina University campus (Saskatchewan, Canada), but the project was abandoned in 1979. The system would have involved the production of hot water from the geothermal reservoir, passing it through a heat exchanger, and transferring the heat to a fresh-water circuit that would carry the heated fresh water to the utilization point, i.e., the sports complex. The cooled brine would then be re-injected into the producing reservoir about a kilometer away from the producing well (Figure 1.5; Vigrass et al., 2007).

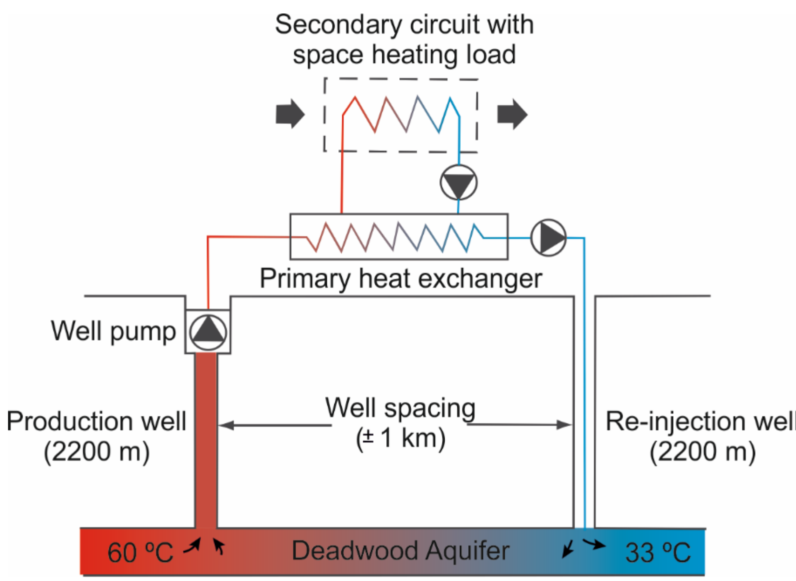

Figure 1.5 **Scheme of the doublet system planned for University of Regina, redrawn from Vigrass et al. (2007).**

Deep borehole heat exchangers extract the thermal energy using a closed loop system with a coaxial pipe configuration (Figure 1.6). Particularly well suited for installation of these types of systems are existing old abandoned deep wellbores from oil and gas industry, for example (e.g., Mehmood et al., 2019; Shah et al., 2019). In these systems, the heat transfer occurs by conduction from the surrounding medium through the grouting and casing of the borehole to the advecting heat transfer fluid (e.g., water, ammonia). As the cool fluid flows downwards in the outer side of the coaxial pipe at a velocity of approximately 5 – 65 m min^{-1} (Stober et al., 2013), it is gradually heated by the surrounding medium. The warm fluid is recovered through the inner side of the coaxial pipe. At the surface, the heat is extracted from the warm ascending fluid via a heat exchanger. The cooled fluid is then re-injected in the system at a temperature of approximately 15 ºC (Stober et al., 2013). This system is advantageous since it does not require permeable rocks and thus can be installed almost everywhere. However, the heat extraction process cools the vicinity of the borehole and the fluid descending velocity must be adequate for the thermal extraction. These are two key parameters that must be considered when designing the system (Stober et al., 2013).

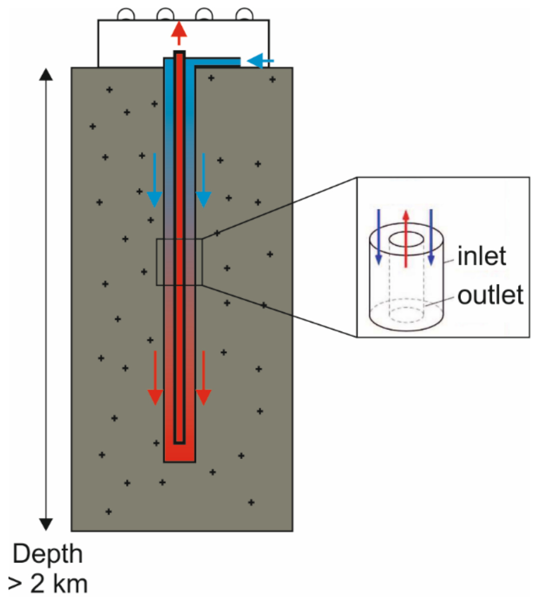

Figure 1.6 Scheme of a coaxial deep borehole heat exchanger (or deep geothermal probe), redrawn from Stober et al. (2013).

The concept of Enhanced Geothermal Systems aims at increasing well(s) productivity through chemical, thermal, and/or hydraulic stimulation techniques (e.g., Schulte et al., 2010; Grant et al., 2011). Hydraulic stimulation techniques were first employed at Los Alamos National Laboratory in New Mexico to improve the subsurface permeability of the Fenton Hill crystalline rock mass (e.g., Brown et al., 2012). Broadly, a high-pressure fluid is injected into a crystalline rock mass over a certain period of time. This process leads to the shearing and dilation of the natural joints, permanently increasing the subsurface permeability. Afterward, fluid can be circulated through the newly developed geothermal reservoir and the sheared joints act as natural heat exchangers (Figure 1.7).

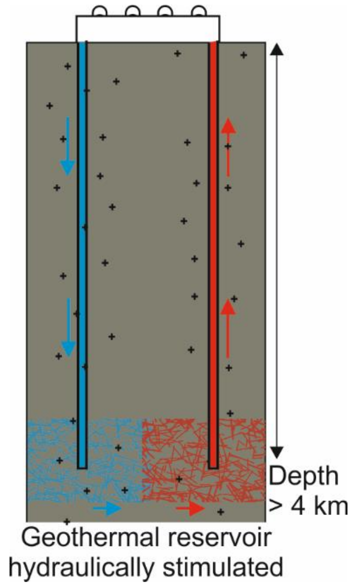

Figure 1.7 Scheme of a doublet engineered geothermal energy system, redrawn from Brown et al. (2012).

Although primarily developed for crystalline rocks, the concept of Enhanced Geothermal Systems is nowadays being applied in different geological environments (e.g., sedimentary basins; Morgan, 2013; Richard, 2016; Kazemi et al., 2019) and to boost production in already productive areas, such as the Coso geothermal project (US; Rose et al., 2004), the Geysers project (US; Walters et al., 2010) and the Desert Peak geothermal field (US; Zemach et al., 2017).

A new technology to harvest deep geothermal energy sources has been proposed by Eavor^{TM} (Eavor Technologies Inc., 2021). The Eavor-Loop is a buried-pipe closed system that acts as a heat exchanger and within which a working fluid is contained and circulated to harvest the heat from the surrounding medium. The system consists of connecting two vertical wells several kilometers deep with many horizontal multilateral wellbores several kilometers long that act as pipes and not producing wells (Figure 1.8). The working fluid naturally circulates without requiring an external pump due to the thermosiphon effect of a hot fluid rising in the outlet well and a cool fluid falling in the inlet well. This fluid brings the thermal energy to the surface where it is harvested for direct-use applications and electricity generation. The suitability of this system is, however, limited to sedimentary basins environments because of the ease of drilling. Western Canada Sedimentary Basin, Yukon Territory basins and St. Lawrence Lowlands, for example, can be possible targets for the development of the Eavor-Loop (Eavor Technologies Inc., 2021).

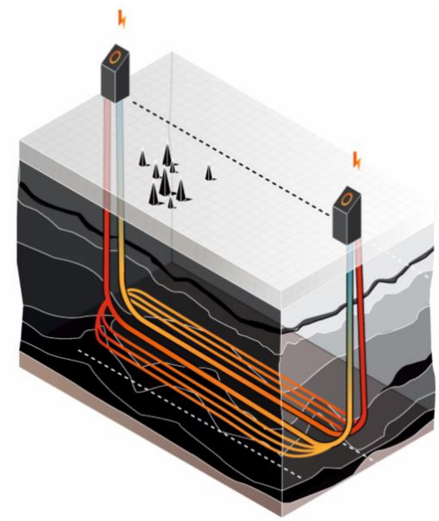

Figure 1.8 Eavor-Loop scheme, redrawn from Eavor Technologies Inc. (2021).

A new enhanced and integrated geothermal system concept was introduced by Mahbaz et al. (2020) has a promising solution for Canada's northern communities. This concept can be seen as analogue to a hybrid car. It involves large-scale and seasonal heat storage in geo-repositories, with shallow geothermal heat pumps to complement the deep system (Figure 1.9). Depending on "grade", temperature differences, and design, heat may be stored in the deep geothermal system or the shallow repository in appropriate proportions to meet the profound heat needs of the October to April months (Mahbaz et al. 2020).

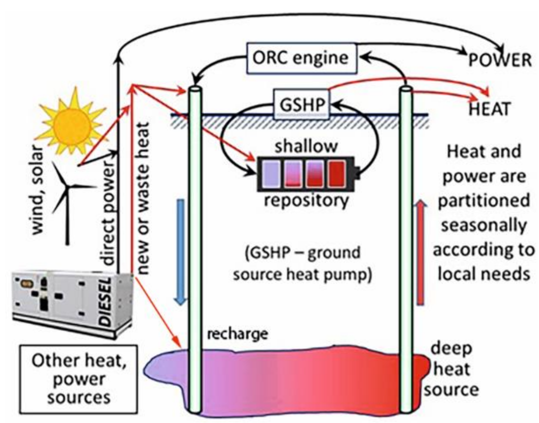

Figure 1.9 Enhanced and integrated geothermal system concept, redrawn from Mahbaz et al. (2020).

Geothermal energy has a vast number of applications depending on the temperature of the geothermal energy source (Figure 1.10; Lindal, 1973). Of these, space heating and electricity are the envisioned applications to offset the consumption of diesel in the off-grid communities (e.g., Grasby et al., 2013; Minnick et al., 2018).

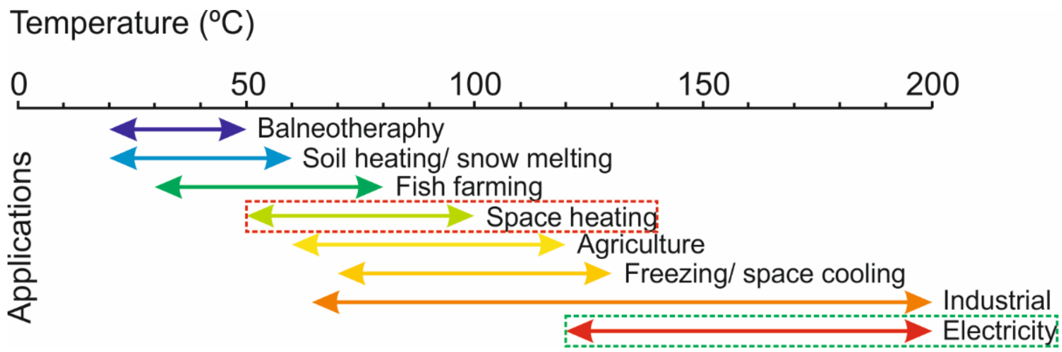

Figure 1.10 **Lindal diagram relating the main types of geothermal application with the geothermal energy source temperature. The red and green squares indicate the envisioned applications of the deep geothermal energy source for the community of Kuujjuaq, redrawn from Lindal (1973).**

Additionally, the waste heat from the power conversion can be applied in other low-temperature applications (e.g., space heating, greenhouses), increasing the sustainability of the deep geothermal system (e.g., Rybach et al., 2004; Saadat et al., 2010; Gehringer, 2015). The extracted deep geothermal energy source can be used in a district heating system (e.g., Tester et al., 2016) and, in this way, providing space heating for the community through a distribution network.

Moreover, deep geothermal energy systems can be integrated with other technologies (renewables or non-renewables) to improve their efficiency in cold climates (e.g., Mahbaz et al., 2020). A new concept of hybrid geothermal energy systems has been developed by Mahbaz et al. (2020) and involves energy storage in georepositories to complement the deep geothermal systems. Furthermore, binary cycle geothermal power plants with Organic Rankine Cycle using an optimized working fluid are currently enabling electricity generation from geothermal energy sources with temperatures lower than 120 ºC (e.g., Liu et al., 2017; Tillmanns et al., 2017; Tomarov et al., 2017; Shi et al., 2019; Chagnon-Lessard et al., 2020; Imre et al., 2020).

1.2.3.3 The Canadian potential

Canada has a long and rich history in geothermal research and exploration. Names such as Alan Jessop, Andrew Nevin, Jacek Majorowicz, Tim Sadlier-Brown and many other geothermal pioneers in Canada have greatly contributed to unravel this ubiquitous energy source. Their contribution has been inspiring generations, and within the time span 1990-2018, about 1229 publications have been made by authors affiliated in Canada, providing an outstanding contribution to geothermal science in general and to the Canadian geothermal industry in particular (Raymond et al., 2015; Hickson et al., 2020). Moreover, the increasing interest for geothermal energy sources in Canada is also noticed by the number of publications per year. For example, from 1990 to 2013, 765 publications have been made (Raymond et al., 2015), meaning an average of 33 publications per year. Recently, between 2014 and 2018, 464 publications were made (Hickson et al., 2020), which gives an average of 116 publications per year. Thus, indicating an increase of approximately 72% on the annual number of publications.

The Canadian interest for the development of geothermal energy sources started around 1972/73 as a consequence of the diesel price rise and reserves decline forecasts (Souther, 1976; Jessop et al., 1991a; Jessop, 1998; Jessop, 2008). Prior to the 70s, geothermal energy sources were restricted to direct use applications, such as hot springs and spas in western Canada (Thompson, 2010). The first governmental program to investigate the geothermal potential of Canada, the Geothermal Energy Program, began in 1976 but was terminated a decade later in 1986 motivated mostly by the oil price dropped, but also due to the perception of geothermal energy as a high capital risk (Jessop et al., 1991a; Jessop, 1998; Allen et al., 2000; Jessop, 2008; Thompson, 2010). Nevertheless, important advances were made to unravel the Canadian hidden geothermal potential. The two main projects funded by the Geothermal Energy Program were the power generation project at Mt. Meager (Jessop, 2008) and the direct use project at University of Regina (Jessop et al., 1989; Vigrass et al., 2007; Jessop, 2008). Beyond these, the Geothermal Energy Program also aided other proposals throughout the country, from deep to shallow sources. These included (Jessop et al., 1991a):

- Power generation geothermal project at Mt. Cayley (British Columbia; e.g., Lewis et al., 1981; Souther et al., 1984; Jessop et al., 1991a; Jessop, 2008).
- Direct use geothermal project at Hot Springs Cove (British Columbia; Jessop, 2008).
- Direct use geothermal project for the greenhouses at Summerland (British Columbia; Jessop et al., 1991b; Jessop, 2008).
- Direct use geothermal project for a resort development nearby Jasper National Park (Alberta; Jessop, 2008).
- Direct use geothermal project in Hinton-Edson area (Alberta; e.g., Lam et al., 1985).
- Direct use geothermal project at Mayo (Yukon Territory; Jessop, 2008)
- Direct use and aquifer thermal energy storage project at Carleton University campus (Ottawa, Ontario; e.g., Jessop, 1998; Allen et al., 2000)

- Direct use geothermal project at Springhill (Nova Scotia; e.g., Jessop et al., 1995; Jessop, 1998; Allen et al., 2000; Jessop, 2008).

Almost 5 decades have passed since Canada started seeing geothermal energy sources from an industrial point of view, rather than for ludic activities only. The use of shallow geothermal energy sources for heating and cooling has grown steadily (Allen et al., 2000; Thompson, 2010; Raymond et al., 2015). Ground-source heat pump systems, for example, are installed almost all over the southern part of the country with the largest markets in the provinces of Ontario, Québec, and British Columbia (Figure 1.11; Raymond et al., 2015).

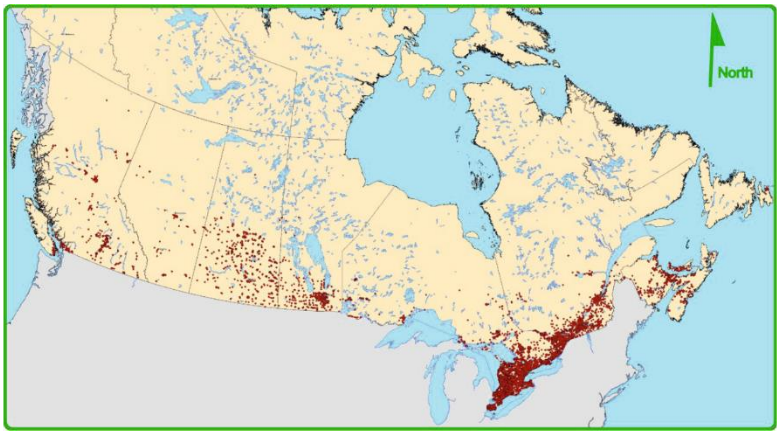

Figure 1.11 Distribution of ground-source heat pumps certified by the Canadian GeoExchange Coalition, redrawn from Raymond et al. (2015).

The total installed capacity in 2013 was estimated to be 1 458 MW_{th} with an annual use of 11 338 TJ, in which the residential sector accounts for approximately 60% of the installed capacity (Raymond et al., 2015). The remaining 40% is associated with the commercial sector. Moreover, within the residential sector, the systems are closed loop, with 56% horizontal and 24% vertical (Raymond et al., 2015). Industry surveys and market analysis undertaken between 2008 and 2012 reveal a growth rate of 40% during 2006 to 2008 followed by a sharp decreased in 2010 (Raymond et al., 2015). The peak installation was observed in 2009, corresponding to 15 913 units (Raymond et al., 2015). In 2013, the units installed are estimated to be half this value (Raymond et al., 2015). Assuming the same trend as for air-source heat pumps (AHRI, 2021), currently a cumulative of about 166 000 units may be installed throughout the country, with a total of approximately 63 000 new units installed since 2013 until 2019.

Per contra, the perception of high costs and low deep geothermal potential in more than 90% of the territory (Figure 1.12; Grasby et al., 2012) have been delaying geothermal projects using deep sources for both heat and power. Times are, however, changing, and several private and provincial and territorial government joint initiatives are underway to assess the potential to explore this renewable energy source (Richter et al., 2012; Hickson et al., 2020).

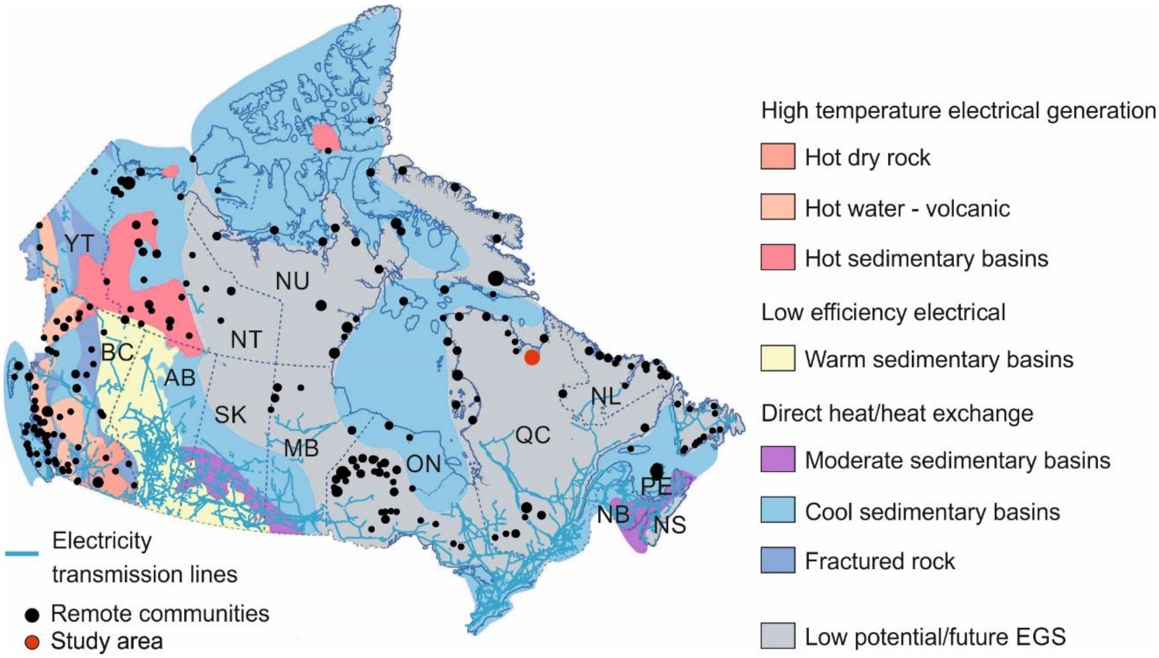

Figure 1.12 Distribution of geothermal potential in Canada based on end use and location of the electrical grid and remote communities. Provinces: BC – British Columbia, AB – Alberta, SK – Saskatchewan, MB – Manitoba, ON – Ontario, QC – Quebec, NL – Newfoundland and Labrador, NB – New Brunswick, NS – Nova Scotia, PE – Prince Edward. Territories: YT – Yukon, NT – Northwest Territories, NU – Nunavut. The reader is referred to the original source for further details, redrawn from Grasby et al. (2012) and Arriaga et al. (2017).

In the Western Canadian Sedimentary Basin, three major deep geothermal direct-use and power projects are progressing (Figure 1.13; Hickson et al., 2020): the Clarke Lake geothermal project, the Alberta #1 Greenview project, and the DEEP project. The Clarke Lake field is a 127 km^2 depleted natural gas reservoir located near the Indigenous community of Fort Nelson First Nation that has been redeveloped for its geothermal energy potential (e.g., Hickson et al. 2020). This geothermal project is targeting the middle Devonian dolomite aquifer that exhibits relatively high permeability, water saturation and temperatures over 110 °C (Hickson et al., 2020). The Alberta #1 Greenview project aims to provide both electricity and thermal energy to the Tri-Municipal Industrial Park of the County of Grande Prairie and Municipal District of Greenview. This project is targeting the units from the Beaverhill Lake Group to the top of the Precambrian basement, where temperatures have been inferred above 120 °C at 3.5 km (Hickson et al., 2020; Huang et al., 2021). The DEEP project is located in the province of Saskatchewan along the United States border and aims to provide power sales to the provincial grid as well as direct large-scale heating opportunities for industries such as greenhouses.

Drilling and testing have confirmed an extensive hot sedimentary resource of 125 °C at 3.5 km depth (e.g., Hickson et al., 2020).

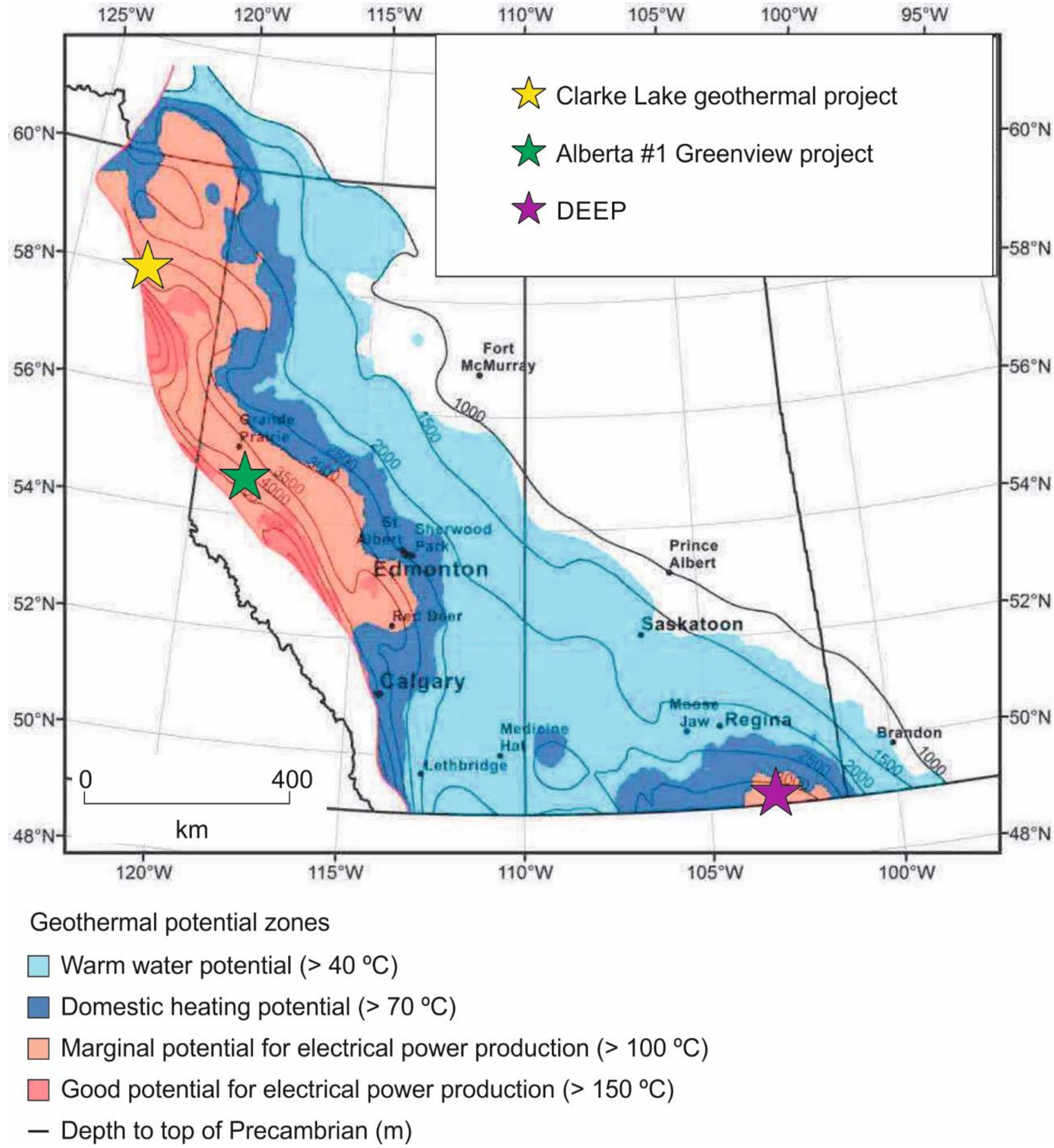

Figure 1.13 Possible geothermal applications based on the temperature at the top of the Precambrian basement in the Western Canadian Sedimentary Basin. The stars mark the location of the three geothermal projects currently underway in the Western Canadian Sedimentary Basin, redrawn from Weides et al. (2014) and Hickson et al. (2020).

It is important to highlight the key role played by NRCan in supporting commercial geothermal development. In fact, NRCan provided financial support to these and other projects through several programs that aim at making Canada a world leader in clean power. Nearly $40.5 million in federal investments were provided in March 2021 to the Clarke Lake geothermal project (NRCan, 2021). In August 2019, Alberta #1 Greenview project received $25.4-million investment (NRCan, 2021). In January 2019, a funding of $25.6 million in support for the DEEP Earth Energy Production geothermal project was announced (NRCan, 2021). This funding is part of the Emerging Renewable Power Program.

Studies have been also carried out to define a geothermal favorability maps for British Columbia (e.g., CanGEA, 2021a), Alberta (e.g., CanGEA, 2021b), Yukon (e.g., CanGEA, 2021c) and Nunavut (Minnick et al., 2018; CanGEA, 2021d). Moreover, further research is ongoing at Mt. Meager using a multidisciplinary approach to decrease exploration risks (e.g., Grasby et al., 2020). Yukon is currently carrying out field investigations and drilling temperature gradient wells in selected areas to assess the potential of the southern part of the territory for direct use applications (e.g., Fraser et al., 2019). The Northwest Territories Geological Survey undertook studies to build a favorability map where possible areas of interest were identified in the southern part of the territory (e.g., EBA Engineering Consultants Ltd, 2010). Recently, the geothermal energy potential of Nova Scotia has been revisited and potential areas for direct use and electricity applications were identified (Comeau et al., 2020). Regarding Québec's geothermal energy source assessment, the St. Lawrence Lowlands has also been targeted of extensive research to identify areas of possible deep geothermal energy production (Bédard et al., 2018; Bédard et al., 2020; Gascuel et al., 2020). Moreover, Hubert et al. (2019) carried out an evaluation of the geothermal energy source potential on Îles-de-la-Madeleine. The northern Québec geothermal potential has been evaluated by Majorowicz et al. (2015a) and Comeau et al. (2017).

1.2.4 Kuujjuaq's geothermal potential

This thesis was undertaken in the community of Kuujjuaq located in Nunavik, Québec, Canada (Figure 1.14). Nunavik is a territory north of the 55º parallel of about 507 000 km^2 and home to 11 000 inhabitants spread by 14 communities dispersed along the shore without road access connecting them. Each community currently operate its own diesel power plant with annual oil consumption of approximately 25 million liters (for 2009; KRG et al., 2010) that only meet their basic electricity needs. In Nunavik, the daily electricity consumption below 30 kWh is 0.07 $ kWh^{-1}, increasing between 0.27 to 0.58 $ kWh^{-1} if the 30-kWh threshold is surpassed (KRG et al., 2010). Such high costs prevent the use of electricity other than lighting and strict domestic needs (KRG et al., 2010; Hydro-Québec, 2019). An additional 28 million liters of oil (for 2009; KRG et al., 2010) is consumed annually for space heating of residential dwellings and other facilities. Mines are also important oil consumers. For example, the Raglan mine site consumes approximately 40 million liters of oil per year (for 2008; KRG et al., 2010).

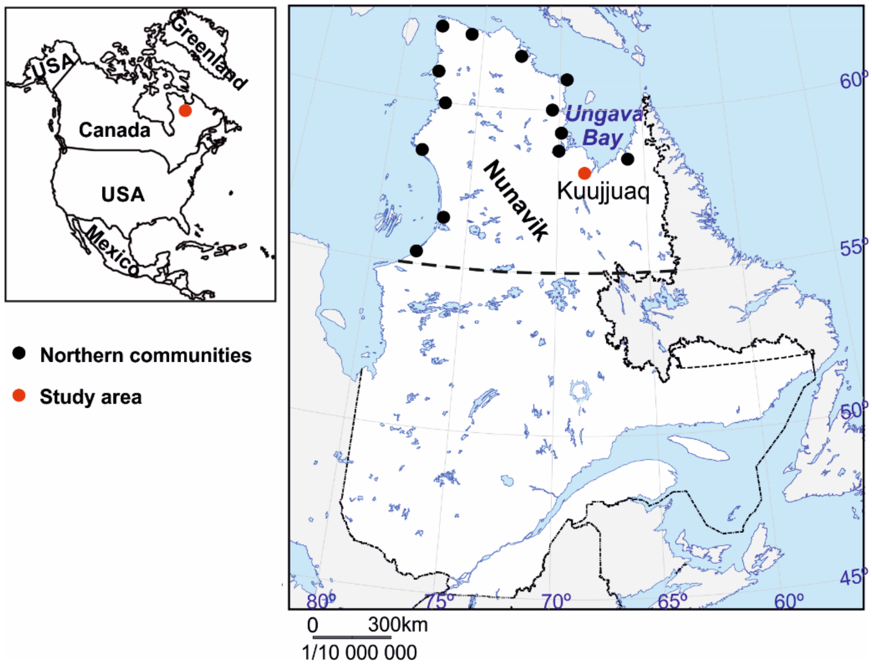

Figure 1.14 Geographical location of Kuujjuaq and remaining communities in Nunavik.

The vastness of the territory and the dispersion of the settlements makes it preferable to carry out a community-focused deep geothermal energy source assessment to foster local deep geothermal development. This avoids the extrapolation of sparse data over a large territory and blinding the local potential by regional anomalies far away from the communities and useless for their energy transition. Kuujjuaq, the selected study case, is the administrative capital of Nunavik and the largest community within the territory. Kuujjuaq is home to 2 754 inhabitants (Statistics Canada 2019). In 2000, the annual electricity demand in Kuujjuaq was about 12 000 MWh (Hydro-Quebec, 2002), increasing to 15 100 MWh in 2011 (NRCan, 2011). Furthermore, the simulated heating load of typical residential dwellings can range between 21.6 and 71 MWh, depending on the residence floor area (Yan et al., 2019; Gunawan et al., 2020). Electricity production price in Kuujjuaq is about 0.6 USD kWh^{-1} and space heating around 0.19 USD kWh^{-1} (Belzile et al., 2017; Giordano et al., 2018). These values provide a gross, first-order perspective of the energy demand and cost that deep geothermal systems need to meet in order to be a viable alternative energy solution for this off-grid diesel-based community.

1.2.4.1 Regional setting

Canada is composed by seven physiographic regions defined based on the geologic structure, land relief attributes, the permafrost distribution and treeline position. These are: Arctic Lands, Cordillera, Interior Plains, Hudson Bay Lowland, Canadian Shield, St Lawrence Lowlands and Appalachian (Figure 1.15; Acton et al., 2015). The Canadian Shield is the oldest (*ca*. 4-1 Ga) and largest physiographic region covering about 48% of Canada's land surface (Acton et al., 2015).

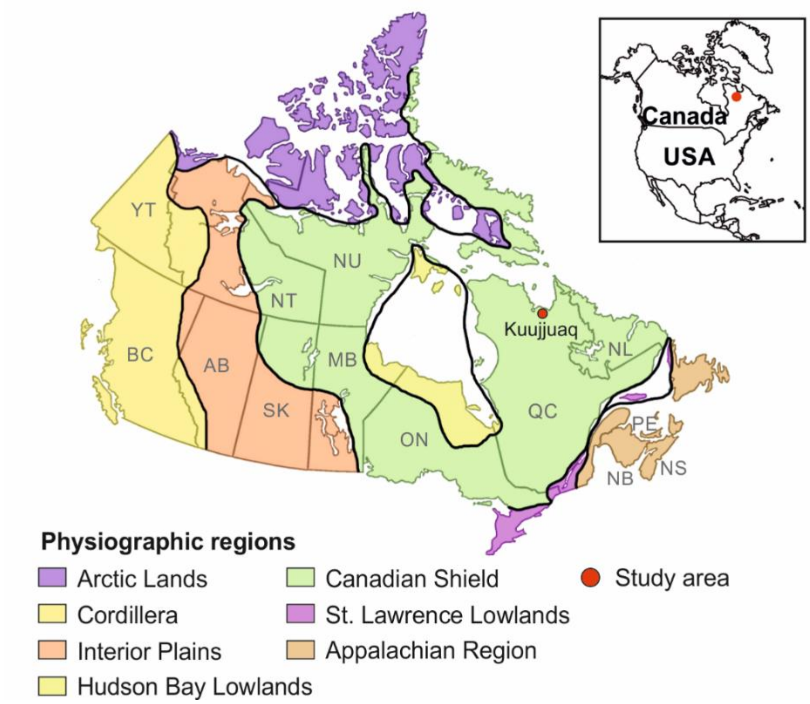

Figure 1.15 **Physiographic regions of Canada. Provinces: BC – British Columbia, AB – Alberta, SK – Saskatchewan, MB – Manitoba, ON – Ontario, QC – Quebec, NL – Newfoundland and Labrador, NB – New Brunswick, NS – Nova Scotia, PE – Prince Edward. Territories: YT – Yukon, NT – Northwest Territories, NU – Nunavut, redrawn from Acton et al. (2015).**

The Canadian Shield is a large exposure of Laurentia, the geologic core of the North American continent (e.g., Whitmeyer et al., 2007; Darbyshire et al., 2017), and is a result of Paleoproterozoic collisional amalgamation of Archean cratonic fragments that occurred diachronously from *ca.* 1.96 to 1.83 Ga and from 1.83 to 1.80 Ga (Figure 1.16; e.g., Hoffman, 1988; Percival et al., 2004; Whitmeyer et al., 2007; Hammer et al., 2010). This amalgamation gave origin to several orogenic belts, among them the Trans-Hudson Orogen (1.83-1.80 Ga; Figure 1.16), a Paleoproterozoic arc-continent to continent-continent collisional zone (e.g., Corrigan et al., 2005; Whitmeyer et al., 2007; Corrigan et al., 2009; Darbyshire et al., 2017), joined the northwestern Canadian Shield cratonic block with the southeastern block (Figure 1.16).

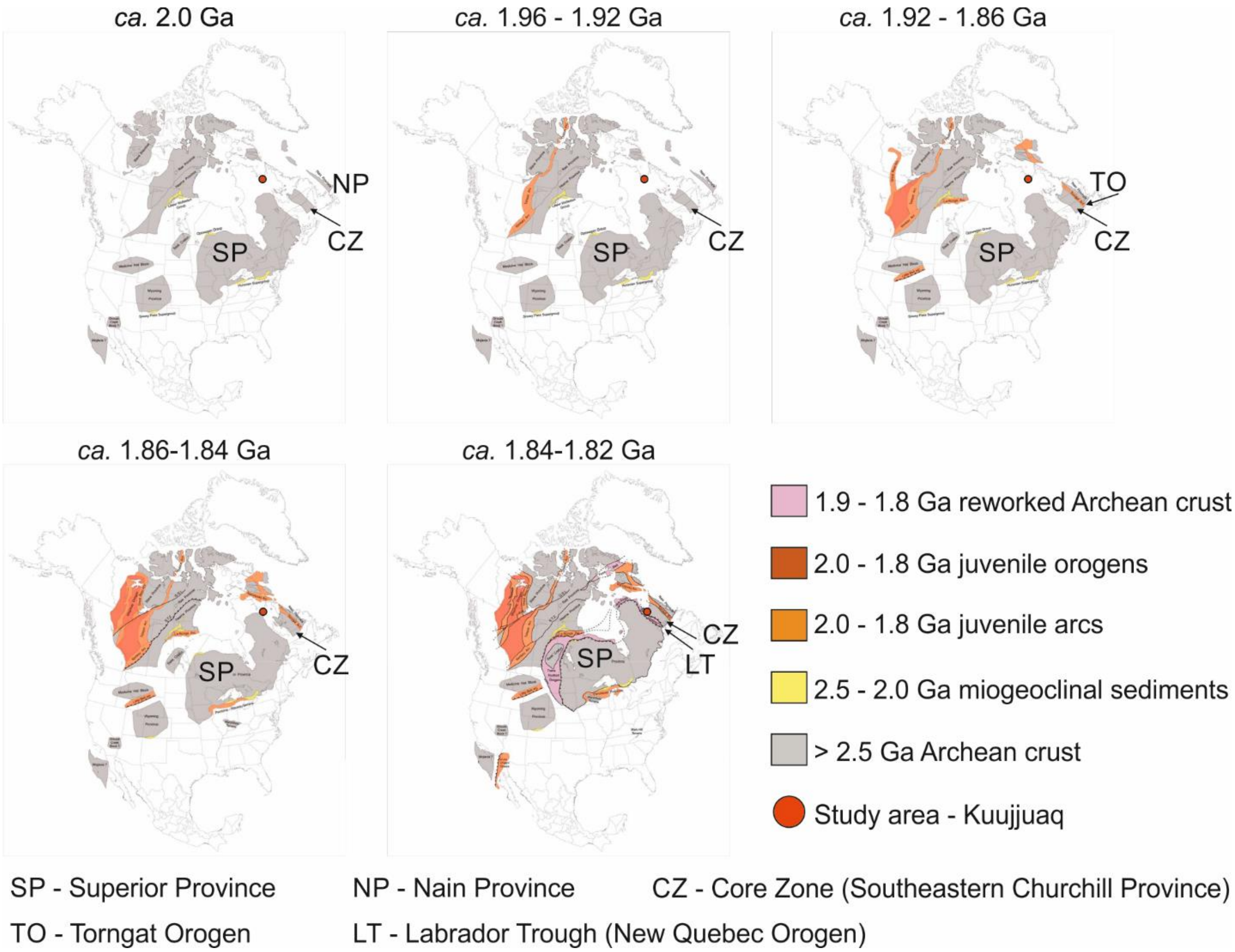

Figure 1.16 **Geodynamic assembly of the Canadian Shield. The position, orientation and separation of the Archean cratons are only approximations due to the poor knowledge of pre-collisional (pre-1.9 Ga) paleogeographies. The reader is referred to the original plate-scale model for further details, redrawn from Whitmeyer et al. (2007).**

Prior to and during the formation of the Trans-Hudson Orogen, the nowadays northeastern Canadian Shield experienced collisions between Nain Province and Core Zone (*ca.* 1.87-1.85 Ga; Figure 1.16) and between Core Zone and Superior Province (*ca.* 1.82-1.77 Ga; Figure 1.16). The Nain/Core Zone collision resulted in the Torngat Orogen, a fold-and-thrust belt dominated by an extensive sinistral shear system developed in granulite-facies crust that is an excellent analogue for modern crustal-scale transcurrent fault system (Wardle et al., 1990; Wardle et al., 1996; Wardle et al., 2002). The Core Zone/Superior collision resulted in an 800-km-long, SW-vergent, thin-skinned volcanic-sedimentary foreland fold-and-thrust belt dominated by dextral transcurrent shearing, commonly termed Labrador Trough or New Quebec Orogen (Figure 1.17; Hoffman, 1988; Wardle et al., 1990; Wardle et al., 1996; Wardle et al., 2002). This suture involved whole-crustal shearing in the Core Zone, linked to thin-skinned deformation in the Labrador Trough (or New Quebec Orogen; Hall et al., 2002).

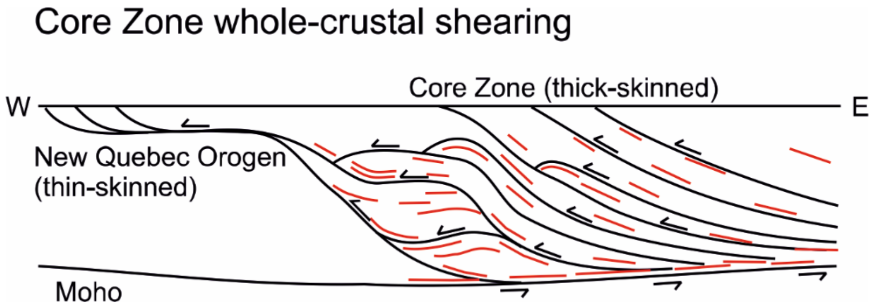

Figure 1.17 **Schematic representation of the thick-skinned shortening of the Core Zone involving shearing along Moho and linked to the west with thin-skinned deformation observed at surface in the Labrador Trough (or New Québec Orogen). The reader is referred to the original interpretation for further details, redrawn from Hall et al. (2002).**

Both Torngat Orogen and Labrador Trough have a mirror-image symmetry. The Core Zone is a 200-km-wide and 35-40 km thick cratonic fragment mostly underlain by Archean tonalitic to granitic gneiss and granitoid rocks and characterized by a pervasive E-dipping fabric related to westerly thrusting (James et al., 1996; Wardle et al., 2002; Corrigan et al., 2018). This craton has been correlated with the Meta Incognita micro-continent (Scott et al., 1998; Bourlon et al., 2002; Wardle et al., 2002; Corrigan et al., 2009) and was previously thought as an allochthonous Archean hinterland of the Rae province (Hoffman, 1988; Wardle et al., 1990; Wardle et al., 1996).

The Eastern Canadian Shield Onshore-Offshore Transect (ECSOOT) is part of the Canadian Lithoprobe program which was developed with the goal of determining how the northern North American continent was formed (e.g., Hall et al., 2002; Hammer et al., 2010). This transect includes 1200 km of normal-incidence seismic profiles and seven wide-angle seismic profiles across Archean and Proterozoic rocks of Labrador, northern Quebec, and the surrounding marine areas (Hall et al., 2002). The interpretation of the profiles revealed Archean crust with 33-44 km thickness and P-wave velocities increasing downwards from 5.9 to 7.0 km s^{-1} (Figure 1.18; Hall et al., 2002).

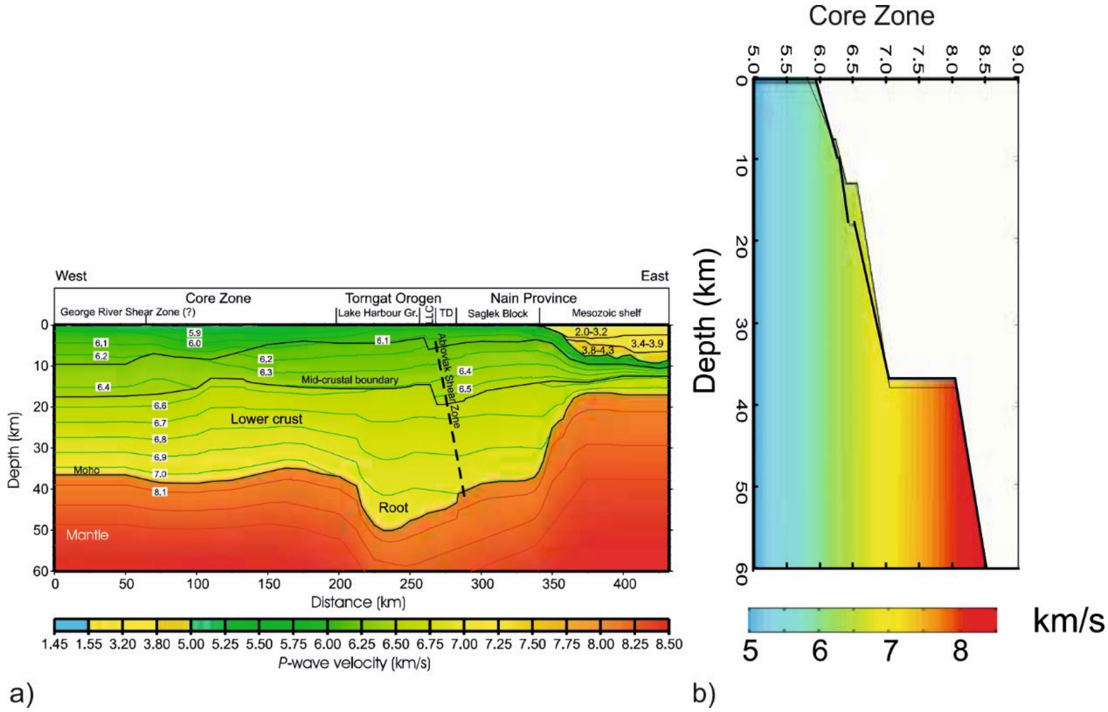

Figure 1.18 **a) Seismic P-wave velocity model along the Line 5 of the ECSOOT and b) seismic velocity cross section. The reader is referred to the original model for further details, redrawn from Hall et al. (2002).**

The Torngat Orogen, Core Zone and Labrador Trough form the nowadays termed Southeastern Churchill Province (Wardle et al., 1990; James et al., 1996; Wardle et al., 1996; Wardle et al., 2002; MERN, 2020a). This province is a 415- to 615-km-long and 250- to 380-km-wide rare example of a two-sided orogenic belt, oriented NNW-SSE, in which both flanks record transpressional development due to the oblique collisions that led to its assemblage (Wardle et al., 1990; Wardle et al., 1996; Wardle et al., 2002; MERN 2020a). The principal stages of its development are (Figure 1.16; Wardle et al., 2002):

1. Rifting of Nain and Superior cratons (2.2-2.1 Ga)
2. Subduction under eastern Nain craton (*ca.* 1.9 Ga)
3. Collision of Nain craton and Core Zone to form the Torngat Orogen (*ca.* 1.87-1.85 Ga)
4. Sinistral transpression in the Torngat Orogen and subduction under the western Core Zone (1.845-1.820 Ga)
5. Collision of Superior craton and Core Zone to form the Labrador Trough in association with dextral transpression (1.82-1.77 Ga).

The Southeastern Churchill Province is divided into 6 lithotectonic domains, which are (from W to E): Labrador Trough, Rachel-Laporte, Baleine, George, Mistinibi-Raude and Falcoz (Figure 1.19; Lafrance et al., 2018; MERN, 2020a). The community of Kuujjuaq is located within the northern section of the Baleine lithotectonic domain (Figure 1.19). This section has also been termed Kuujjuaq terrane by Perreault et al. (1990) and Kuujjuaq tectonic zone by Bardoux et al. (1998).

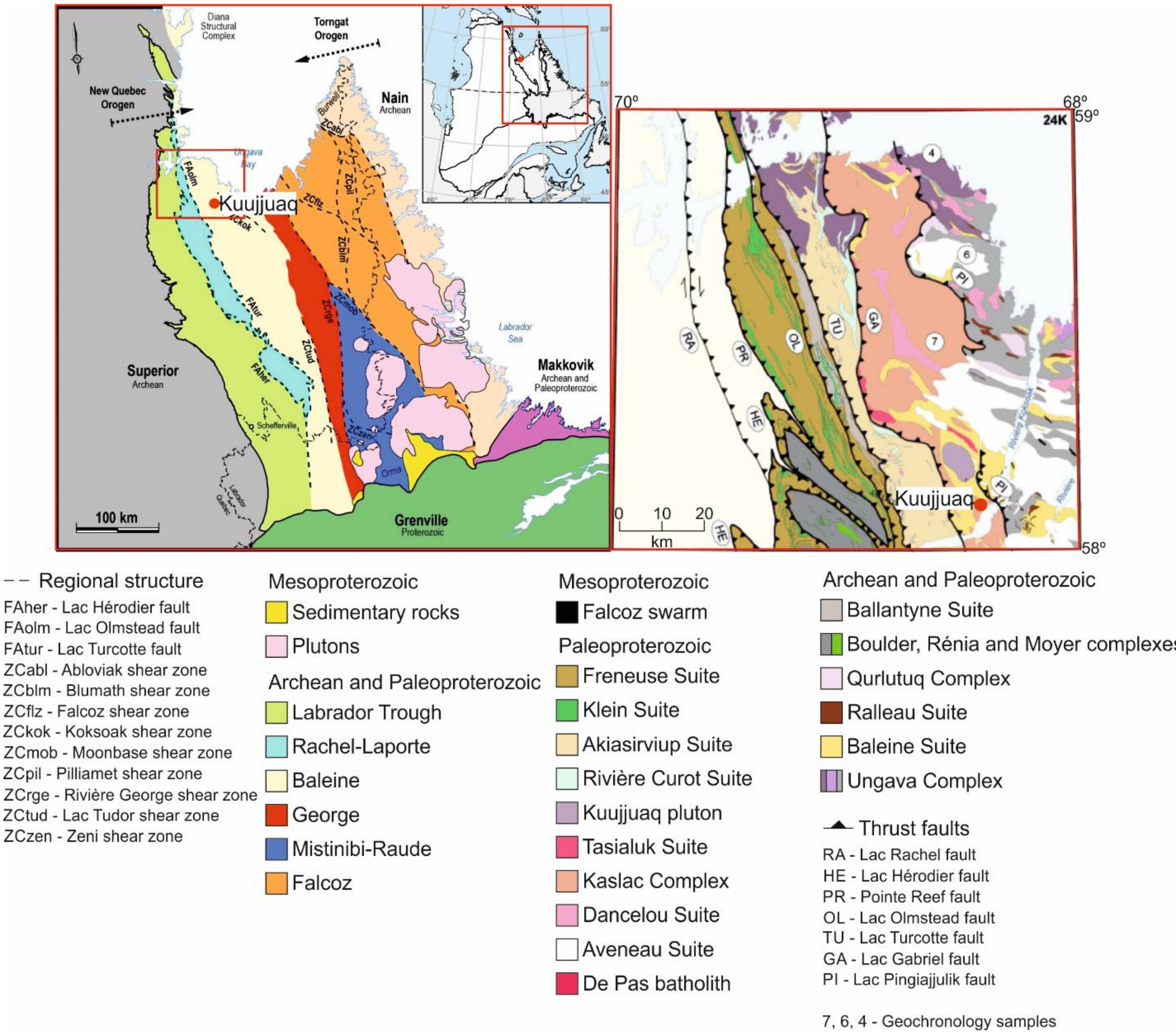

Figure 1.19 **Major lithotectonic geological divisions, faults and major deformation corridors of the Southeastern Churchill Province and simplified geology of Kuujjuaq and Ungava Bay area. The reader is referred to the original geological map (sheet 24K) for further details, redrawn from Simard et al. (2013) and MERN (2020a).**

The Baleine lithotectonic domain is 615 km long and 15 to 100 km wide and is oriented generally NNW-SSE (MERN, 2020b). The northern section of this lithotectonic domain is mainly composed by Archean gneiss (Ungava Complex), migmatite (Qurlutuq Complex) and anatectic granite (Aveneau suite) derived from partial melting of gneiss (Figure 1.19; MERN, 2020b). Mafic to intermediate intrusive complex (Kaslac Complex) and volcano-sedimentary sequences (Curot and Akiasirviup suites) are also observed (Figure 1.19; MERN, 2020b). The geological evolution of the Baleine lithotectonic domain begins in the Archean with the emplacement of the Ungava and Qurlutuq gneissic and migmatitic complexes, with crystallization ages ranging from 2.8 to 2.6 Ga. These units correspond to the bedrock on which metasedimentary rocks of the Akiasirviup suite were deposited (Lafrance et al., 2018; MERN, 2020b). Moreover, gneissic rocks of the Ungava Complex also underwent an anatexis process that originated part of the Aveneau Suite. Nevertheless, some aspects of the Baleine lithotectonic domain evolution during Archean times still remain unclear. For example, it is generally accepted that both Rachel-Laporte and Baleine domains were attached to the Superior craton prior to rifting of the Archean continent along its NE margin at *ca.* 2.2 Ga (MERN, 2020b and references therein). This hypothesis is based on geochronology and composition of units observed in both Southeastern Churchill and Superior provinces, as well as on E-W magnetic anomalies on either side of the Labrador Trough (Lafrance et al., 2018; MERN, 2020b).

The regional structural grain NW-SE to N-S observed in the southwestern Ungava Bay area resulted from the Core Zone/Superior collision (Figure 1.20, Figure 1.21; Simard et al., 2013). The poles to plans of the main fabric observed in the domain delimited by Lac Gabriel and Lac Pingiajjulik faults is N338º/30º (Figure 1.19; Simard et al., 2013). Three main deformation phases (D_1 to D_3) have been identified in this region, corresponding to a continuous deformation process linked to the Labrador Trough development (Moorhead, 1989; Perreault et al., 1990; Poirier et al., 1990; Goulet, 1995; Simard et al., 2013). D_1 and D_2 phases are associated with the compression during the collision of the cratons and D_3 corresponds to the oblique component of the collision (Simard et al., 2013).

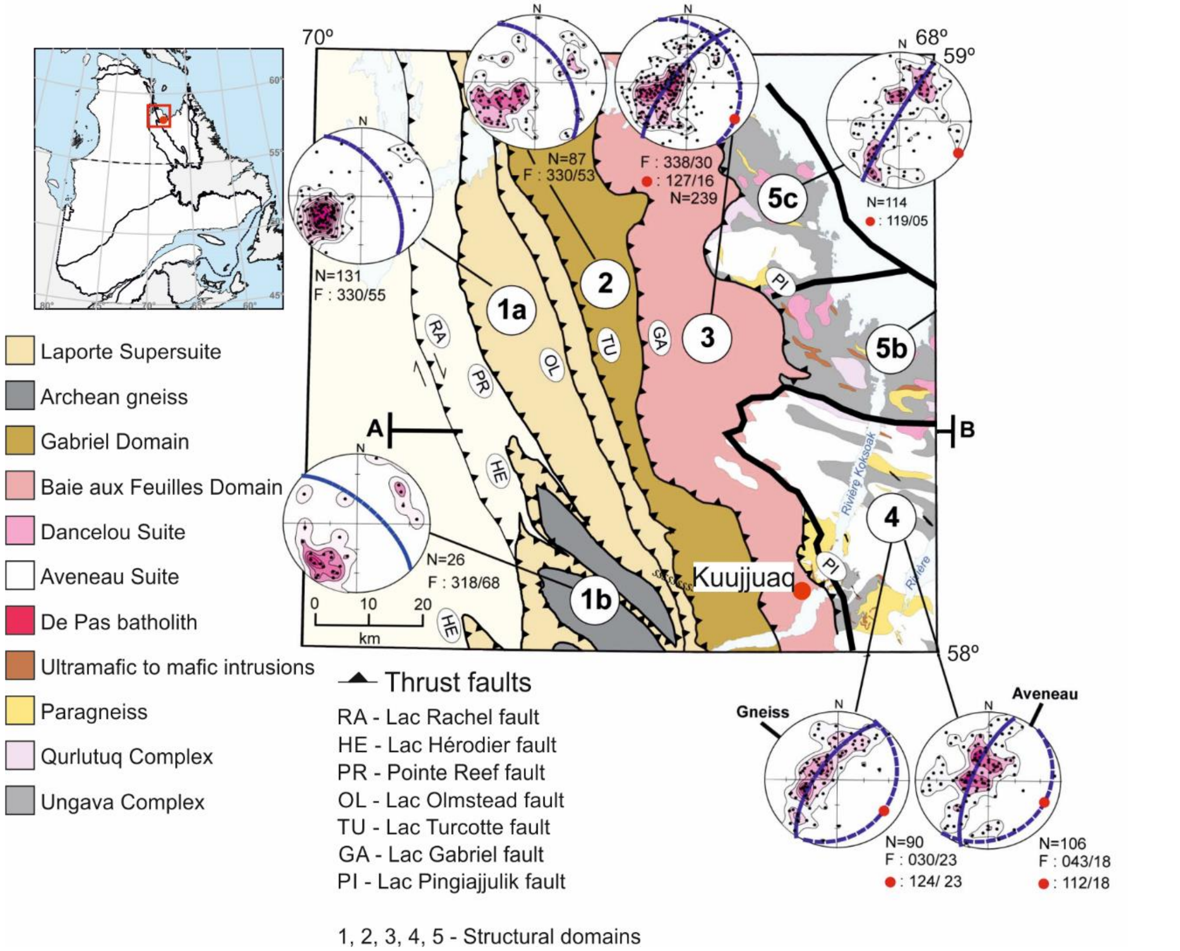

Figure 1.20 Structural domains and structural analysis of the southwestern Ungava Bay region. A and B indicate the cross-section in Figure 1.20. The reader is referred to the original structural map for further details, redrawn from Simard et al. (2013).

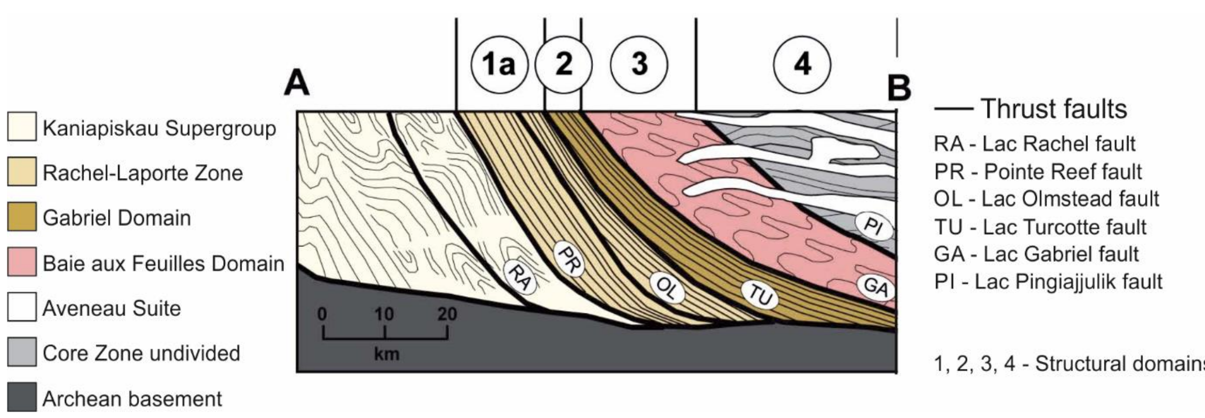

Figure 1.21 Schematic structural cross-section. A and B in Figure 1.19. The reader is referred to the original structural cross-section for further details, redrawn from Simard et al. (2013).

1.2.4.2 Kuujjuaq geology

The community of Kuujjuaq is settled mainly on the False Suite (migmatized paragneiss and migmatized garnet paragneiss) and Kaslac Complex (amphibole diorite and quartz diorite and gabbro, gabbronorite and clinopyroxenite). Smaller outcrops belonging to the Ralleau Suite (amphibolitized gabbro and diorite), Aveneau Suite (white tonalite and granite) and Dancelou Suite (massive pink granite and massive pegmatitic granite) are also present (Figure 1.22). The Kuujjuaq Pluton (tonalitic to granodioritic orthogneiss) and Ungava Complex (tonalitic gneiss containing whitish bands) outcrop far from the community (Figure 1.22). Dikes of the Falcoz Swarm are also present in small amount (Figure 1.22).

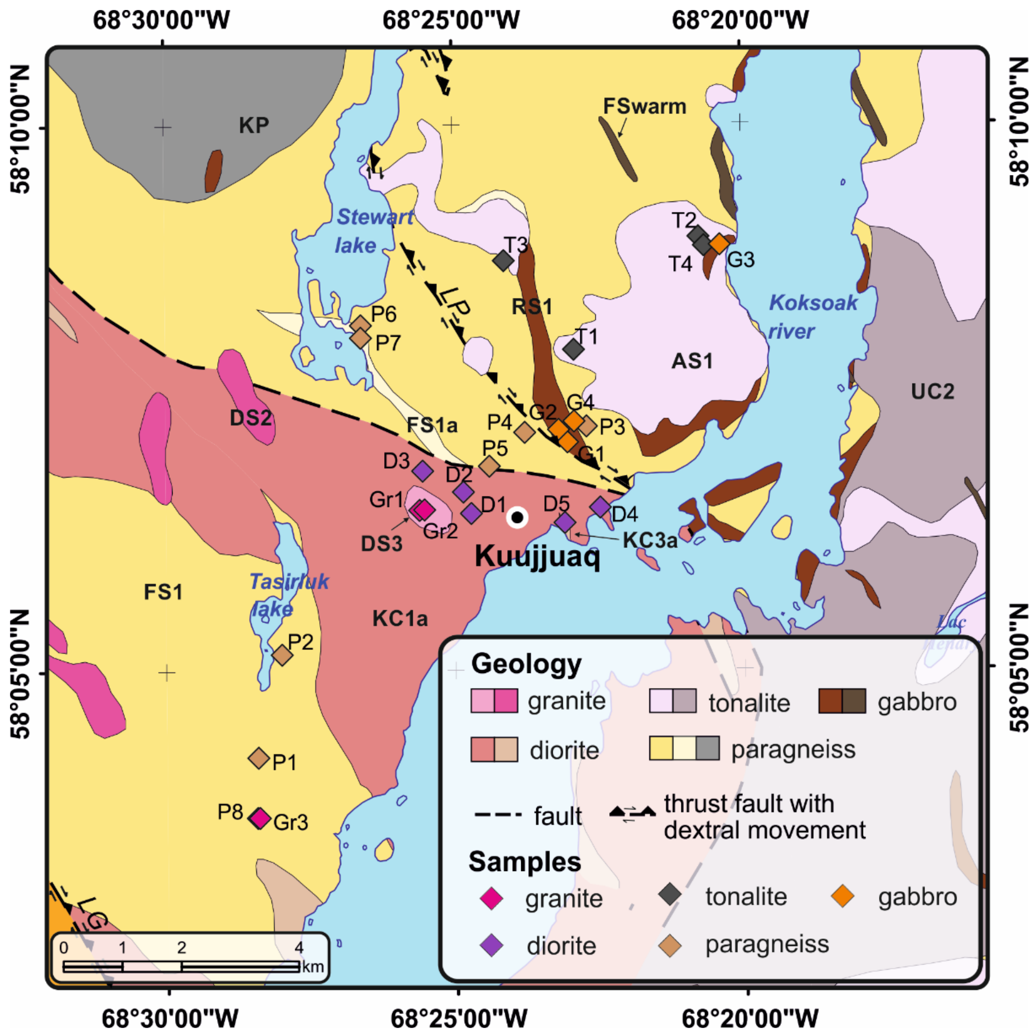

Figure 1.22 Geological setting of the community of Kuujjuaq and surrounding area. UC2 – Ungava Complex 1, FS1 – False Suite 1, FS1a – False Suite 1a, KP – Kuujjuaq Pluton, AS1 – Aveneau Suite 1, KC1a – Kaslac Complex 1a, KC3a – Kaslac Complex 3a, RS1 – Ralleau Suite 1, DS2 – Dancelou Suite 2, DS3 – Dancelou Suite 3, FSwarm – Falcoz Swarm, *LP* – Lac Pingiajjulik fault, *LG* – Lac Gabriel fault. The points P, D, G, T and Gr are the locations of the samples collected in the framework of this thesis, redrawn from SIGÉOM (2019).

The Ungava Complex 2 (*ca.* 2.95-2.66 Ga; Archean) is a gneiss with tonalitic composition, changing locally to quartz diorite (MERN, 2020c). 5 to 30% millimeter- to centimeter-wide whitish tonalite bands are present (MERN, 2020c). It has a light- to medium-grey color, it is fine- to medium-grained and presents foliation (MERN, 2020c). Ferromagnesian minerals (8-20%) are mainly brown biotite and amphiboles (green hornblende or actinolite). K-feldspar is also observed (up to 5%). Apatite, epidote, opaque minerals, zircon, sphene, muscovite, chlorite, allanite and rutile also occur (MERN, 2020c).

The False Suite 1 (*ca.* 2.68 Ga; Neoarchean) is a migmatized fine- to medium-grained paragneiss with grey (fresh) to brownish (altered) color and has well-developed granoblastic texture (MERN, 2020d). A millimeter- to centimeter-wide whitish mobilisate of tonalitic composition can be observed as well as banding with amounts of ferromagnesian minerals varying between 10-30% (MERN, 2020d). These minerals include brown to red biotite associated with hornblende (up to 15%). Apatite, zircon, opaque minerals and allanite are frequent. Muscovite can represent up to 15% of the rock. Sphene, chlorite, epidote, garnet and sillimanite may also occur (MERN, 2020d). The unite False Suite 1a (*ca.* 2.7 Ga; Neoarchean) occurs in areas where paragneiss and mobilisate contain more than 5% of pink or red garnet (MERN, 2020d).

The Kuujjuaq pluton (*ca*. 1.87-1.83 Ga; Paleoproterozoic) is orthogneiss varying in composition from tonalitic to granodioritic, with locally dioritic and granitic phases (MERN, 2020e). The orthogneiss is whitish grey or pink and contains 40-70% of quartz and 20-40% of feldspar (MERN, 2020e). Ferromagnesian minerals are rare (5%) and include biotite and hornblende (MERN, 2020e). Sphene, allanite, zircon, apatite and magnetite are also observed (MERN, 2020e).

The Aveneau Suite 1 (*ca.* 1.85-1.82 Ga; Paleoproterozoic) is a fine- to coarse-grained whitish tonalite and granite (MERN, 2020f). These rocks are massive to foliated (MERN, 2020f). The ferromagnesian minerals are sparse (1-8%) and consist mainly in brown biotite (MERN, 2020f). Muscovite is frequent (1-5%) and opaque minerals, sphene, epidote, zircon, garnet, sericite and carbonate can occur (MERN, 2020f).

The Kaslac Complex 1a (*ca.* 1.83 Ga; Paleoproterozoic) is characterized by the absence of pyroxenes (MERN, 2020g). The rocks belonging to this complex are amphibole diorite and quartz diorite, locally tonalite, granoblastic and medium-grained (MERN, 2020g). This unit can have gneissic banded and homogeneous appearance (MERN, 2020g). The banded facies consist of alternating light grey to dark grey millimetric to centimetric bands. The diorite is light grey to brown and well foliated to mylonitic in the homogeneous facies. The ferromagnesian minerals (10-30%) form clusters stretched parallel to foliation and consist of amphiboles (hornblende and actinolite) and dark brown to red biotite locally altered to a mixture of chlorite and opaque mineral dusts (MERN, 2020g). Occurrences of coronitic, clinopyroxene and orthopyroxene are observed (MERN, 2020g). Epidote, garnet, chlorite, muscovite, tourmaline, allanite, sphene, magnetite and ilmenite are also present (MERN, 2020g). The subunit Kaslac Complex 3a (*ca.* 1.83 Ga; Paleoproterozoic) contains 50% to 70% ferromagnesian minerals which confer to these rocks a black to dark green color (MERN, 2020g). They are well foliated and medium- to fine-grained (MERN, 2020g). The ferromagnesian minerals are mainly clinopyroxene and brown/green amphiboles (hornblende and fibrous actinolite), but orthopyroxene can occur locally (MERN, 2020g). Biotite, magnetite, sphene, ilmenite, apatite and carbonate are accessory minerals (MERN, 2020g).

The Ralleau Suite 1 (Archean to Paleoproterozoic) consists mainly of amphibolitized gabbro and diorite, locally gabbronorite and quartz gabbro (MERN, 2020h). The rocks from this subunit are homogeneous, medium- to fine-grained with granoblastic texture and they can be massive to foliated (MERN, 2020h). Their color is dark grey to black, locally greenish (fresh) to black-and-white-speckled (altered). The amount of ferromagnesian minerals is 35-65% in which mostly are green to brown hornblende, clinopyroxene (1-20% and brown biotite (1-10%). Opaque minerals, apatite, sphene and epidote are abundant accessory minerals, and these are accompanied locally by quartz (< 5%), garnet, chlorite, carbonate and zircon (MERN, 2020h).

The Dancelou Suite 2 (*ca.* 1.77-1.75 Ga; Paleoproterozoic) is a pinkish medium-grained granite with low ferromagnesian minerals (< 5%) that consist mainly of brown biotite and chlorite containing zircon (MERN, 2020i). Muscovite (up to 2%), hematite, epidote and apatite can occur locally in low amounts (MERN, 2020i). The subunit Dancelou Suite 3 (*ca.* 1.81-1.78 Ga; Paleoproterozoic) is a pegmatitic granite intruding into other units of the Dancelou Suite (MERN, 2020i). The granite is light pink with less than 5% of ferromagnesian minerals (MERN, 2020i). These consist mainly of brown-red chloritized biotite (MERN, 2020). Muscovite is frequent (< 5%), plagioclase is weakly sericitized and epidote, hematite, apatite, garnet and zircon are sparse (MERN, 2020i).

The Falcoz Swarm (Mesoproterozoic) is mainly subophitic olivine gabbro, but can include some gabbro, gabbronorite, olivine norite and troctolite outcrops (MERN, 2020j). The olivine gabbro is fine-grained with weakly to moderately sericitized plagioclase laths and mafic minerals (30-

40%). These are majority olivine, clinopyroxene and magnetite (2-5%). Biotite and apatite are accessory minerals (MERN, 2020j).

The Lac Pingiajjulik and Lac Gabriel faults are regional thrust faults with dextral motion synchronous with the third deformation phase (D_3; e.g., Perreault et al., 1990; Simard et al., 2013; SIGÉOM, 2019). This movement is indicated by asymmetric pressure shadows around rotated porphyroblasts and by shear folds (e.g., Perreault et al., 1990). Neither fault is visible in the field (Simard et al., 2013) and, thus, their position on the geological map was based on aeromagnetic data (Simard et al., 2013).

1.2.4.3 Thermal structure

The surface air annual mean temperatures in Nunavik range approximately from -9 to -4 ºC (Figure 1.23a; Comeau et al., 2017) while the ground surface temperature is inferred to range between -4 and 1 ºC (Figure 1.23a; Comeau et al., 2017). Furthermore, permafrost within this territory ranges from continuous above the 60º parallel to discontinuous/scatter at the 55º parallel (Figure 1.23b; Comeau et al., 2017).

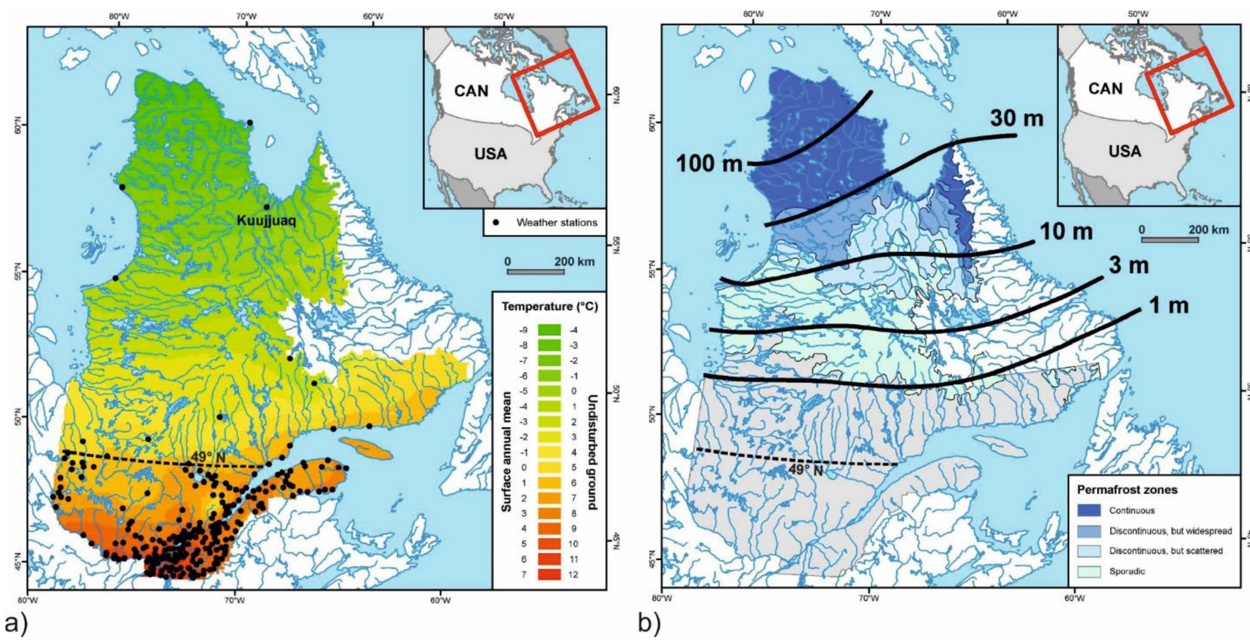

Figure 1.23 **a) Surface air and ground surface annual mean temperatures distribution and b) permafrost distribution and depth in Québec province, redrawn from Lemieux et al. (2016) and Comeau et al. (2017).**

Comeau et al. (2017) carried out a compilation of heat flow assessments available for northern Québec (Figure 1.24a). Their work highlights the uneven distribution of data points within the region, with most of the data below the 55º parallel and none at the Southeastern Churchill

Province. Therefore, the heat flow map developed by Majorowicz et al. (2015a) is based on extrapolation of scarce data (the closest heat flow assessment to Kuujjuaq lies at a distance of approximately 420-430 km) that can lead to miscalculations at a community-scale geothermal energy source assessment (Figure 1.24b). Moreover, this map reveals no information for Kuujjuaq. Nevertheless, the existing data points reveal that the heat flow above the 55º parallel ranges between a minimum of 22 mW m^{-2} at Voisey Bay (Newfoundland and Labrador; Mareschal et al., 2000) and a maximum of 38 mW m^{-2} at Asbestos Hill (Nunavik; Taylor et al., 1979; Drury, 1985). Based on the extrapolation trend of Majorowicz et al. (2015a) map, the heat flow in Kuujjuaq may be in the interval 44 – 49 mW m^{-2}. However, large uncertainty exists due to the lack of heat flow assessments.

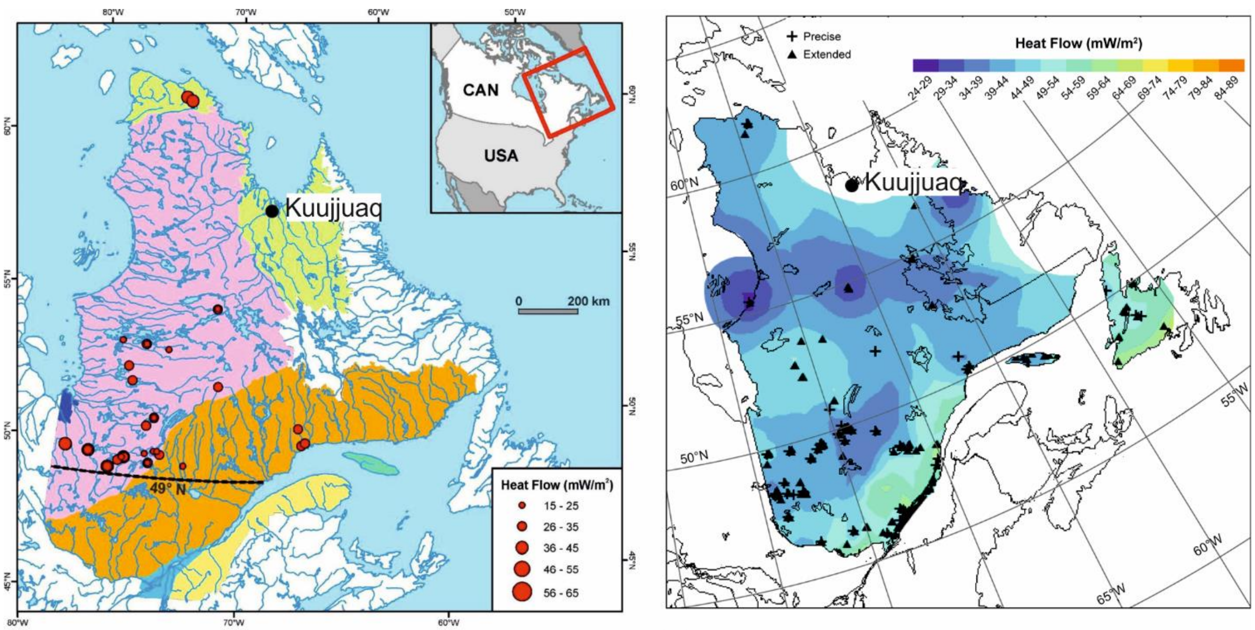

a) b)

Figure 1.24 **a) Distribution of heat flow data available and b) geothermal heat flow density for Northern Québec. In a) pink – Superior Province, green – Churchill Province, orange – Grenville Province, yellow – Appalachian Province, dark blue – Hudson Bay Platform and light blue – St Lawrence Lowlands, redrawn from Majorowicz et al. (2015a) and Comeau et al. (2017).**

Furthermore, Comeau et al. (2017) inferred the 1D subsurface temperature distribution among the different geologic provinces and their results reveal that at 5 km depth the temperature in the Churchill Province ranges from 49 to 53 ºC (Figure 1.25). However, only two data points exist for the Churchill Province, and these lie at a distance of almost 500 km from Kuujjuaq.

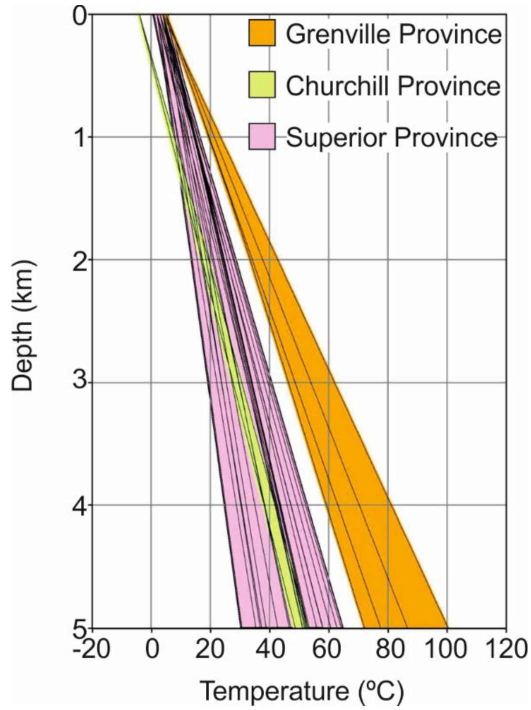

Figure 1.25 **Temperature profiles of northern Québec based on the available heat flow data, redrawn from Comeau et al. (2017).**

Curie point depth has been mapped in the province of Québec by Drolet et al. (2017; Figure 1.26) and is a useful tool to calibrate subsurface temperature distribution models (e.g., Tanaka et al., 1999). Drolet et al. (2017) maps indicate a Curie point depth in Kuujjuaq area within the interval 20 – 30 km (Figure 1.26). Although at a community-scale large uncertainty exists in using such regional maps, these are useful for a first-order calibration of both heat flux and subsurface temperature.

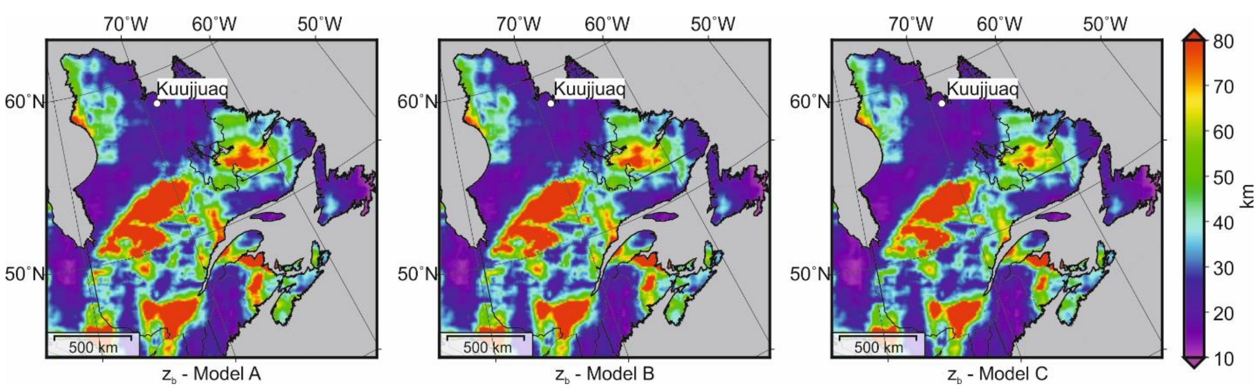

Figure 1.26 **Curie point depth maps for Quebec province. z_b – Curie point depth. The reader is referred to the original source for further details, redrawn from Drolet et al. (2017).**

1.2.4.4 Stress regime

The World Stress Map (Heidbach et al., 2019) is a global database of contemporary tectonic stress of the Earth's crust and a useful tool to infer the orientation of the maximum horizontal stress. However, the World Stress Map does not have information on the study area. The lack of deep exploratory boreholes associated with the absence of earthquake data with magnitude higher than 3 (Figure 1.27) contributes for this important gap. In fact, only three seismic events with magnitudes between 2.2 and 3.4 and at depths of 18 km have been recorded at distances of 10 to 53 km away from Kuujjuaq since 1985 until present (GCan, 2021) and none seem to be associated with the fault planes crossing Kuujjuaq. Thus, the only information available is the regional stress trend proposed by Adams (1989). This author compiled stress data available at depths shallower than 9 km and concluded that Canada, east of the Cordillera physiographic region, is being compressed NE-SW with the maximum principal stress σ_1 being horizontal (Figure 1.27a). This has also been supported by others. For example, Hashizume (1974) examined an earthquake in northwestern Hudson Bay and the results suggest a thrust fault type with maximum compressional direction nearly NE-SW. Adams et al. (1989) compiled earthquakes that occurred in Canada's eastern margin and craton and concluded that, although most of the area is aseismic, there are several zones of intense seismicity along the eastern continental margin and some clusters within the craton (Figure 1.27b). These earthquakes appear to be occurring within a regional stress field dominated by ENE compression. Moreover, the majority of large earthquakes have occurred near Paleozoic or younger rift structures that surround or break the integrity of the North American craton (Adams et al., 1989). Bell et al. (1997) analyzed borehole breakouts in wells in Hudson Bay and concluded that the Paleozoic section is subject to maximum horizontal compression about a NE-SW axis, with some local deflection in horizontal stress orientation related to faults. Furthermore, leak-off tests suggest contemporary horizontal stress magnitudes above 1500 m depth exceeding present-day overburden loads (Bell et al., 1997). However, Bent (1994) studied an earthquake that occurred in Ungava Peninsula and the results indicated the earthquake consisted of two sub-events, a thrust subevent on a NE-SW striking plane followed by a strike-slip subevent on a NNE-SSW striking plane. A NW compression, consistent with the focal mechanisms of other recent northeastern Canadian events, was inferred from the fault plane solution (Bent, 1994). Moreover, Steffen et al. (2012) investigated five earthquakes that occurred northern Hudson Bay which exhibit thrust-fault mechanism. These authors found that the maximum horizontal stress direction strikes roughly NNW-SSE, deviating from regional stresses due to the existence of a roughly E-W oriented zone of faulting. In summary, published literature on focal mechanism in eastern Canada indicates thrust faulting as the dominant regime. However, normal-fault type earthquakes are more common along the northeast coast of Baffin Island and strike-slip faulting predominates in the northeastern United States (Wu et al., 1996 and references therein).

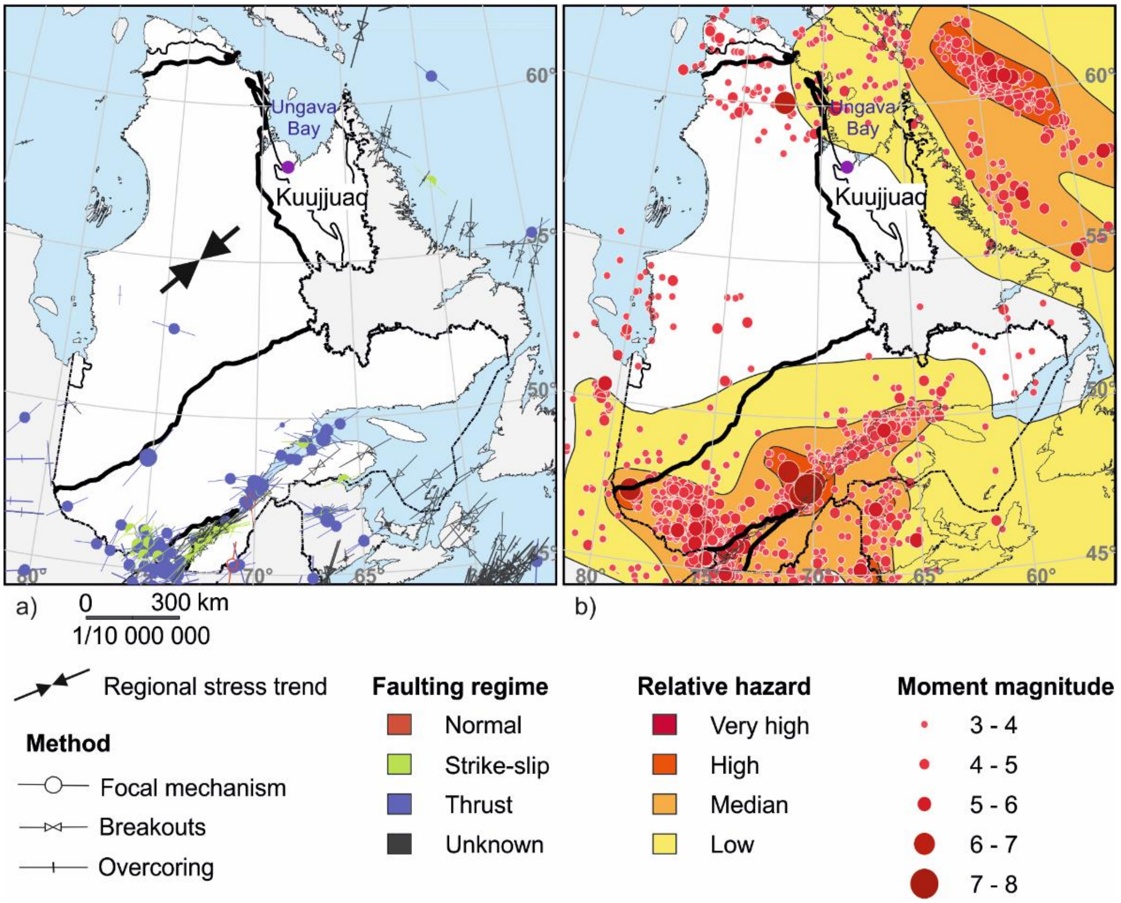

Figure 1.27 **a) Stress and b) seismic hazard maps of Québec province. The arrows in a) indicate the regional trend of the contemporary stress field and the orientation of the maximum horizontal compression based on Adams (1989), redrawn from NRCan (2018a) and Heidbach et al. (2019).**

The earthquakes occurring in the North Atlantic Ocean, Labrador Sea and Baffin Bay are mostly concentrated at the ocean-continent transitions and are believed to be caused by reactivation of the Mesozoic rift faults created during the formation of the North Atlantic (Adams et al., 1989). Moreover, the earthquakes at the Labrador Sea are believed to occur on the extinct spreading ridge and the associated transform faults (Adams et al., 1989). The earthquakes occurring on Baffin Island and along the arcuate band Boothia-Ungava are spatially associated with Cretaceous normal faults and with steep gradients in the postglacial uplift rate (Adams et al., 1989). Moreover, seismicity along the Boothia uplift-Bell arch appears to be related with Paleozoic structures reactivated by the recent glacial episode (Hasegawa et al., 1989). Glacial loading centers flanking both sides of this curvilinear trend would generate an extensional stress component that could reactivate weakened faults (Hasegawa et al., 1989). In summary, seismicity, steep gradients in free-air gravity anomaly and steep gradients in postglacial uplift along the northeastern periphery of the Canadian Shield suggest a causal correlation between seismicity, postglacial rebound and lateral variations in crustal structure in this region (Adams et al., 1989; Hasegawa et al., 1989). In fact, glaciation-deglaciation episodes can influence earthquake activity in eastern Canada depending on how weakened features in structures created by tectonic activity react to glacially induced stress and strain (Hasegawa et al., 1989). Wu et al. (1996) propose a time-dependent relationship to evaluate the likelihood of faulting (negative *dFSM*) or fault stability (positive *dFSM*) of optimally oriented pre-existing faults that are close to, but not at, failure:

$$dFSM(t) = \frac{1}{2}\left[\left(\sigma_1(t_0) - \sigma_3(t_0) - \sigma_1(t) - \sigma_3(t)\right)\right] + \mu\left[\frac{\sin(\arctan(\mu))}{2\mu}\right] \times \left[\left(\sigma_1(t) - \sigma_3(t)\right) - \left(\sigma_1(t_0) - \sigma_3(t_0)\right)\right] \tag{1.2}$$

where σ_1 and σ_3 (Pa) are the maximum and minimum principal stresses, t (s) is the time under consideration, t_0 (s) is the time before the onset of glaciation and μ is the friction coefficient (usually $0.6 < \mu > 1$).

According to Wu et al. (1996), the onset of thrust faulting and maximum earthquake activities started shortly after deglaciation is complete (i.e., when rebound rates were at a maximum). Nowadays, although rebound stresses have been decreasing in magnitude, they continue to act as a trigger mechanism for optimally oriented pre-existing faults that are on the verge of failure. Thus, limiting the existence of such near-slip conditions to lie within the pre-weakened zones of eastern Canada explains the spatial distribution of current earthquakes (Wu et al., 1996).

Several authors have been measuring and compiling in situ stresses in the Canadian Shield, mainly in underground mines located in Manitoba, Ontario and Quebec. Herget (1974) carried out tectonic fabric analysis and stress determinations at the MacLeod Mine (Ontario), NE shore of Lake Superior. This area consists of Archean volcanics (*ca.* 2.5 Ga) and sedimentary rocks of the Superior Province (Herget, 1974). The results of Herget (1974) revealed that the compression developing the major synclines and anticlines was oriented NNW-SSE and subhorizontal, but shearing along late Precambrian diabase dikes, development of kink-bands and quartz-filled fractures suggest a compression in a NE-SW direction (*ca.* 1.0-2.1 Ga). Furthermore, stresses determined between 365 m and 560 m below surface indicate the minimum principal compressive stress σ_3 approximately vertical. The maximum principal compressive stress σ_1 does not possess a uniform direction and the magnitude of both maximum and intermediate principal stresses present little variation (Herget, 1974).

Herget (1982) and Herget (1987) present vertical and average horizontal principal stress estimations based on measurements carried out in mines in Ontario and Manitoba (Table 1.1, Table 1.2). The lithologies analyzed belong to the Superior and Southern Province and consist of Archean and Proterozoic volcanics, metamorphosed sediments and granites (Herget, 1982). Arjang (1991) carried out overcoring strain relief measurements at several mine sites within depths between 60 and 1890 m (Table 1.1). Herget (1993) carried out a compilation of stress data obtained at mining locations in Ontario, Manitoba and Quebec (Table 1.1, Table 1.2). These sites are mainly located in the Superior and Southern Province. Analysis of 165 tensors indicates that the direction of the maximum principal stress σ_1 correlates with the regional NE to ENE trend (Herget, 1993) and that the vertical principal stress is higher than the minimum principal compressive stress (Herget, 1993). Arjang et al. (1997) compiled data from 39 Canadian deep hardrock mine sites (Table 1.1, Table 1.2). The stress measurements in their compilation were carried out in medium to high strength rocks with elastic moduli of 43 to 100 GPa and Poisson's ratio ranging from 0.16 to 0.30 and within depths between 12 to 2134 m below the surface. The stress results are from overcoring strain recovery measurements (Arjang et al., 1997). The maximum and minimum horizontal stresses are equivalent to the maximum and intermediate principal stresses, and exceed the vertical principal stress (Arjang et al., 1997). Moreover, the statistics on horizontal stress ratios revealed that the maximum horizontal principal stress is, on average, 1.7 times higher than the minimum horizontal principal stress (i.e., $\sigma_{\mathrm{H}} = 1.7 \times \sigma_{\mathrm{h}}$; Arjang et al., 1997). Arjang (1998) presents a database of stress measurements carried out to depths of 6000 m (Table 1.1). For the Canadian Shield, the results of frequency analysis for orientation of the principal compressive stresses and linear regression analysis on the magnitudes of principal compressive stresses reveal that both maximum and minimum horizontal principal stresses exceed the vertical principal stress (Arjang, 1998). Young et al. (2015) present an update stress database for the Canadian Shield. This compilation includes 199 stress measurements from operating mines in Ontario and covers a range of depths between 12 and 2552 m below ground surface (Table 1.1, Table 1.2). The maximum horizontal principals stress trends, on average, ENE-WSW, consistent with the regional trend (Young et al., 2015).

Table 1.1 Principal stresses in the Canadian Shield.

Principal stress	Orientation	Magnitude	Observations		Reference
σ_V	--	(0.0260-0.0324)z	$0 < z <$ 2200 m		Herget (1982), Herget (1987)
$\sigma_{V,\ extreme}$	--	0.0603z			
$\sigma_{H,\ average}$	--	9.86+0.0371z	$0 < z <$ 900 m	$\sigma_V < \sigma_{H,\ average}$	
		33.41+0.0111z	$900 < z <$ 2200 m		
$\sigma_{H,\ average,\ extreme}$	--	12.36+0.0586z	--		
σ_V	--	(0.0266±0.008)z	$60 < z <$ 1890 m	$\sigma_V < \sigma_h < \sigma_H$	Arjang (1991)
$\sigma_{H,\ average}$	--	5.91+0.0349z			
σ_H	--	8.18+0.0422z			
σ_h	--	3.64+0.0276z			
σ_V	--	0.0285z	$0 < z <$ 2200 m	$\sigma_3 < \sigma_V < \sigma_2 < \sigma_1$	Herget (1993)
σ_1	N248º/10º	12.1+(0.0403±0.0020)z			
σ_2	N300-340º/0º	6.4+(0.0293±0.0019)z			
σ_3	vertical	1.4+(0.0225±0.0015)z			
σ_V	--	0.0260z	$0 < z <$ 6000 m	$\sigma_3 < \sigma_2 \leq \sigma_V < \sigma_1$	Arjang (1998)
σ_1	NE/horizontal	13.50+0.0344z			
σ_2	NW/sub-horizontal	8.03+0.0233z			
σ_3	vertical	3.01+0.0180z			
σ_V	--	(0.0258-0.0263)z	$12 < z <$ 2552 m	$\sigma_3 < \sigma_V < \sigma_2 < \sigma_1$	Young *et al.* (2015)
σ_1	N227º/02º	(0.040±0.001)z-(9.185±1.5)			
σ_2	N310º/08º	(0.029±0.001)z+(4.617±1.159)			
σ_3	N270º/88º	(0.021±0.001)z-(0.777±0.872)			

σ_V – vertical principal stress, $\sigma_{V,\ extreme}$ – extreme vertical principal stress, $\sigma_{H,\ average}$ – average horizontal principal stress ($\sigma_{H,\ average} = \frac{\sigma_H + \sigma_h}{2}$), $\sigma_{H,\ average,\ extreme}$ – extreme average horizontal principal stress, σ_H – maximum horizontal principal stress, σ_h – minimum horizontal principal stress, σ_1 – maximum principal stress, σ_2 – intermediate principal stress, σ_3 – minimum principal stress, z – depth.

Table 1.2 Stress ratio coefficient in the Canadian Shield.

Stress ratio coefficient		Observations	Reference
$k_{maximum}$	$\frac{357}{z}+1.46$	--	Herget (1987)
$k_{average}$	$\frac{267}{z}+1.25$	--	
$k_{minimum}$	$\frac{167}{z}+1.10$	--	
$k_{maximum}$	$\frac{272\pm 8}{z}+1.72$	--	Herget (1993)
$k_{average}$	$\frac{141\pm 6}{z}+1.18$	--	
$k_{minimum}$	$\frac{30\pm 4}{z}+0.86$	--	
$k_{maximum}$	$1.2-7.8$	0 < z < 1000 m	Arjang (1997)
$k_{maximum}$	≥ 2.2	z > 1000 m	
$k_{minimum}$	$0.6-4.6$	0 < z < 1400 m	
$k_{minimum}$	1.0	z > 1400 m	
$k_{maximum}$	$7.44z^{-0.198}$	--	
$k_{minimum}$	$2.81z^{-0.120}$	--	
$k_{maximum}$	$-0.0007z+3.284$	--	Young et al. (2015)
$k_{intermediate}$	$-0.0003z+2.074$	--	
$k_{minimum}$	$-0.0001z+1.641$	--	

$k_{maximum}$ – ratio maximum horizontal principal stress/principal vertical stress, $k_{average}$ – ratio average horizontal principal stress /principal vertical stress, $k_{minimum}$ – ratio minimum horizontal principal stress/principal vertical stress, $k_{intermediate}$ – ratio intermediate principal stress/minimum principal stress, z – depth.

1.2.4.5 Geothermal play type

Moeck (2014) introduced the concept of categorizing geothermal play types according to the geologic controls. Based on Moeck's (2014) catalog and given the geological context of the study area previously described the geothermal play fits within the conduction-dominated category. These geothermal plays occur mainly in passive continental margins and intracontinental tectonically inactive areas (Moeck, 2014). Furthermore, according to Moeck's (2014) classification, the study area is a conduction-dominated geothermal play of basement type, also referred as petrothermal systems (Figure 1.28). The typical targets are crystalline basement rocks and fracture zones therein with permeability lower than 10^{-15} m^2 (Figure 1.28; Sass et al., 2012; Moeck, 2014).

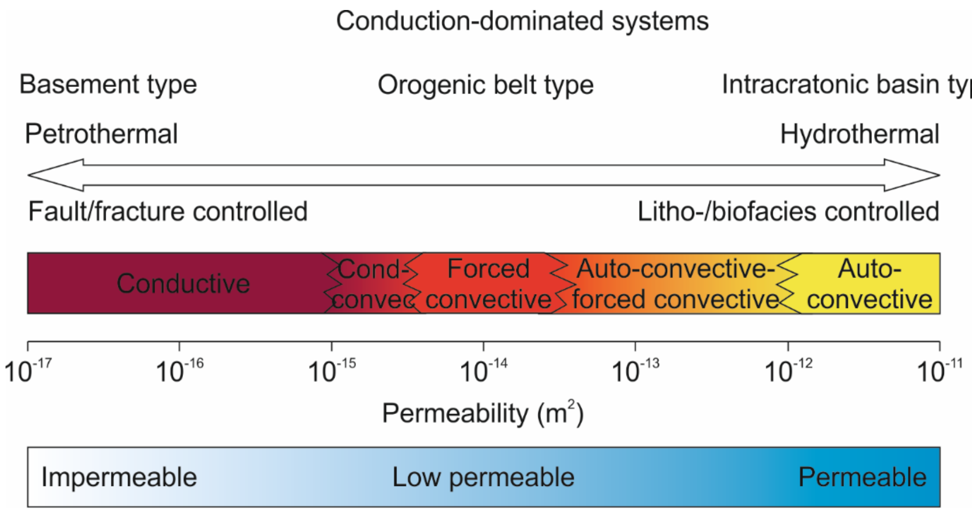

Figure 1.28 **Conduction-dominated geothermal play types with correlation to geologic controls, heat transfer mechanism and subsurface permeability, redrawn from Sass et al. (2012) and Moeck (2014).**

Alternative (and unconventional) geothermal systems, such as engineered geothermal energy systems and, more recently, deep borehole heat exchangers, are the commonly used to harvest the deep geothermal energy source in this type of geothermal plays. The choice between deep boreholes heat exchangers or engineered geothermal energy systems depend on the intended end use (Stober et al., 2013), i.e., heat supply only (deep borehole heat exchangers) or both power generation and heat production (engineered geothermal energy systems).

1.2.4.6 Engineered geothermal energy systems

Hydraulic fracturing has been widely applied in the oil and gas industry to boost production since 1947 (e.g., Gidley et al., 1989). Given the success of this technique, researchers at Los Alamos National Laboratory (New Mexico, US) decided to apply it in crystalline rocks for the first time in 1973 (Brown et al. 2012). This new concept of recovering the Earth’s heat via a pressurized closed-loop circulation of fluid from the surface through a hydraulically stimulated and confined reservoir several kilometers deep made in crystalline basement rocks represented a turn point in the geothermal energy industry, opening new opportunities to explore geothermal energy sources in areas that were considered unviable (e.g., crystalline rocks with very low permeability).

These engineered geothermal energy systems consist of the stimulated reservoir, the injection boreholes, the recovery borehole(s), the surface pipping, and the injection pumps (Brown et al., 2012). The term reservoir in engineered geothermal energy systems shall not be confused with hydrocarbon or conventional geothermal reservoirs, where the resource is naturally present within the porosity of the rock mass. In these geothermal systems, the reservoir consists of a network of pre-existing pressure-dilated joints and naturally flowing faults forming a dendritic pattern of interconnections between wells within an unlimited extent of rock mass (e.g., Richards et al., 1994; Brown et al., 2012; Genter et al., 2010).

However, this reservoir perception only became established in the 1980s, when further research carried out at several test sites led to the recognition that hydraulic stimulation was not breaking intact crystalline rock against its inherent tensile strength, but rather opening the pre-existing sealed natural joints (e.g., Garnish, 1985; Richards et al., 1994; Parker, 1999; Brown et al., 2012). Prior to the 1980s, it was thought that the crystalline rock was unjointed, homogeneous and isotropic and that the maximum principal stress was vertical. Thus, the application of hydraulic pressure was believed to induce an artificial fracture by tensile failure. This fracture would be held open by jacking forces due to the water pressure. Moreover, this induced fracture should be vertical, planar and would open normal to the least principal stress. The continued pressurization of this fracture was believed to lead it to extend radially outward from the borehole for approximately 2-km-width and upwards, since the compressive stress increases with depth at a rate greater than the hydrostatic gradient. This gave rise to the “penny-shaped vertical fracture” concept (Garnish, 1985; Brown et al., 2012). The natural fractures were ignored in the preliminary conventional theory of hydraulic stimulation, mostly because of the poor understanding on how jointed crystalline basement would behave under pressurization and the quality of the diagnostic tools available at that time (Brown et al., 2012).

Since the 70s, several projects started worldwide, applying different stimulation techniques and in geological contexts going from crystalline to sedimentary rocks (e.g., Tester et al. 2006; Breede et al., 2013; Lu, 2018). Of these, 23 were considered of interest given the similarities with the study area regarding the rock type (crystalline basement rocks) and engineering interventions (Table 1.3, Table 1.4, Table 1.5).

Table 1.3 Engineered geothermal energy systems – abandoned or suspended projects.

Project	Start date	End date	Location	Rock type	Stimulation method	References
Fenton Hill	1974	1995	New Mexico, US	Gneissic, schistose, granitoid and pegmatoid rocks	Hydraulic	Brown et al. (2012), Kelkar et al. (2016)
Bad Urach	1977 1989	1980 --	Germany	Gneiss	Hydraulic	Haenel (1982)
Le Mayet de Montagne	1978	1986	France	Granite	Hydraulic, proppant	Cornet (1987)
Fjällbacka	1984	1995	Sweden	Granite	Hydraulic, chemical	Sundquist et al. (1988)
Hijiori	1985	2002	Japan	Granodiorite	Hydraulic	Matsunaga et al. (2005)
Ogachi	1989	2002	Japan	Granodiorite	Hydraulic	Kaieda et al. (2005)
Habanero/Cooper Basin	2003	2015	Australia	Granite	Hydraulic	Hogarth et al. (2017)
Paralana	2005	2014	Australia	Metasediments, granite	Hydraulic	Reid et al. (2010)
Basel	2005	2006	Switzerland	Granite	Hydraulic	Häring et al. (2008)
Pohang	2010	2019	South Kora	Granite/granodiorite	Hydraulic	DESTRESS [2020a]
Haute-Sorne	2017	2018	Switzerland	Granite	Hydraulic	DESTRESS [2020b]

On – ongoing project, -- - unknown.

Table 1.4 Engineered geothermal energy systems – research and development and commercial projects.

Project	Start date	End date	Location	Rock type	Stimulation method	References
Soultz	1987	On	France	Granite	Hydraulic, chemical	Genter et al. (2010)
Landau	2003	On	Germany	Granite	Hydraulic	Schindler et al. (2010)
Rittershoffen	2016	On	France	Granite	Hydraulic, chemical	Mouchot et al. (2018)
Rosemanowes	1977	1991	UK	Granite	Hydraulic, proppant	Richards et al. (1994), Parker (1999)
	2009	On				Somma et al. (2021)
DEEP	2018	On	Canada	Sedimentary and crystalline rocks	Hydraulic	Somma et al. (2021)

On – ongoing project.

Table 1.5 Engineered geothermal energy systems – research and development projects and field scale laboratories.

Project	Start date	End date	Location	Rock type	Stimulation method	References
Falkenberg	1977	1986	Germany	Granite	Hydraulic	Kappelmeyer et al. (1987)
Äspö Hard Rock Laboratory	2015	On	Sweden	Crystalline basement rock	Hydraulic	Zang et al. (2019)
Grimsel	2015	On	Switzerland	Granodiorite and granite	Hydraulic	Amann et al. (2018), Gischig et al. (2020)
EGS Collab	2017	On	South Dakota, US	Crystalline basement rock	Hydraulic	Dobson et al. (2017), Kneafsey et al. (2019)
Utah FORGE	2018	On	Utah, US	Granitoid rocks	Hydraulic	Moore et al. (2019), Moore et al. (2020)
Los Humeros & Acoculco	2016	On	Mexico	Sedimentary and crystalline rocks	Hydraulic	GEMex [2020]
Bedretto	2018	On	Switzerland	Granite	Hydraulic	DESTRESS [2020c]

On – ongoing project.

Engineered geothermal energy systems can be represented by learning curves (Figure 1.29). The mistakes made and the lessons learned from the historical stimulated geothermal projects, such as Fenton Hill, Rosemanowes and Soultz, helped to gain great knowledge on the behavior of rock masses and joints subjected to hydraulic stimulation. The information obtained improved the quality of further ventures and nowadays successful commercial projects (e.g., Soultz, Landau, Rittershoffen) are built upon this previous gained know-how. Furthermore, field-scale underground laboratories (e.g., Grimsel, EGS Collab, Utah FORGE) are tackling hydro-thermal-mechanical questions that have remained unresolved in the past. Moreover, although only a few sites are actually generating geothermal energy power (e.g., Soultz, Landau, Rittershoffen), all the abandoned, suspended and ongoing projects are still nowadays important research facilities, providing a huge scientific database.

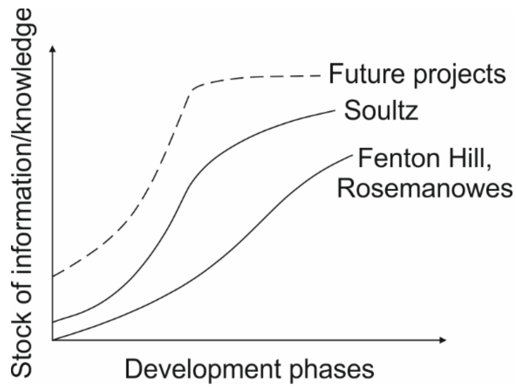

Figure 1.29 Learning curve of engineered geothermal energy systems, redrawn from Nakatsuka (1999).

Enormous amount of literature has been published overviewing the geology and development phases and discussing the results obtained, future directions, and key lessons at each test site. For example, the Fenton Hill venture is described in great detail by Brown et al. (2012). Moreover, a complete description of the Fenton Hill site selection process, geological setting, petrographic description of the drilling cuts, fracture analysis and temperature-gradient measurements is presented by Laughlin et al. (1983). A compilation of the development phases of the Rosemanowes geothermal project, problems faced, and unresolved issues are provided by, for example, Garnish (1985), MacDonald et al. (1992), Parker (1999). Richards et al. (1991) reviewed the geological investigations carried out. Moreover, Richards et al. (1994) discuss the performance and characteristics of the Rosemanowes hydraulically stimulated geothermal reservoir. These authors also discuss the fundamental parameters controlling the impedance, thermal performance and water losses. The contribution of the Soultz project for the scientific community and its development phases are described in detail by, for instance, Genter et al. (2010). Furthermore, the information gathered in all these test sites has been reviewed and the lessons learned on the creation, engineering, operation and geotechnical issues of engineered geothermal energy systems have been compiled by, for instance, Tester et al. (2006), Breede et al. (2013), Xie et al. (2015), Kelkar et al. (2016), Olasolo et al. (2016a), Lu (2018) and Kumari et al. (2019).

Nevertheless, and although the high global estimate engineered geothermal energy systems potential (e.g., Aghahosseini et al., 2020), the utilization of engineered geothermal energy systems is still nowadays controversial. Despite the social, economic and environmental benefits, the potential environmental impacts associated with for example the induced seismicity, water use and footprint and water and air quality need to be carefully addressed to not severely compromised the project (e.g., Lacirignola et al., 2013; Pan et al., 2019). Moreover, several barriers for the development of geothermal systems still exist and need to be overcome. Pan et al. (2019) highlight some of these barriers and propose strategies to overcome them. Knoblauch et al. (2018) carried out a cost-benefit analysis of engineered geothermal energy systems in terms of heat benefits and induced seismicity risks. According to these authors, from both private and social perspectives, engineered geothermal energy systems should be placed where considerable heat can be sold but damage due to induced seismicity remains limited. Moreover, according to Mignan et al. (2019), seismic risk mitigation should also be considered when evaluating the levelized cost of energy of engineered geothermal energy systems.

One key step prior to the development of the stimulated geothermal reservoir is the field characterization. This constitutes the basis of any development planning, strongly influencing the decision-making process (Nakatsuka, 1999). In fact, since reservoir engineering procedures are site-specific (Evans et al., 1999), an accurate field characterization is needed for the accurate design of the system. Parameters such as regional and local geology control the thermal structure, the fracture network and the stress and rock mechanics, which, in turn, have a profound influence on the design of engineered geothermal energy systems (Figure 1.30).

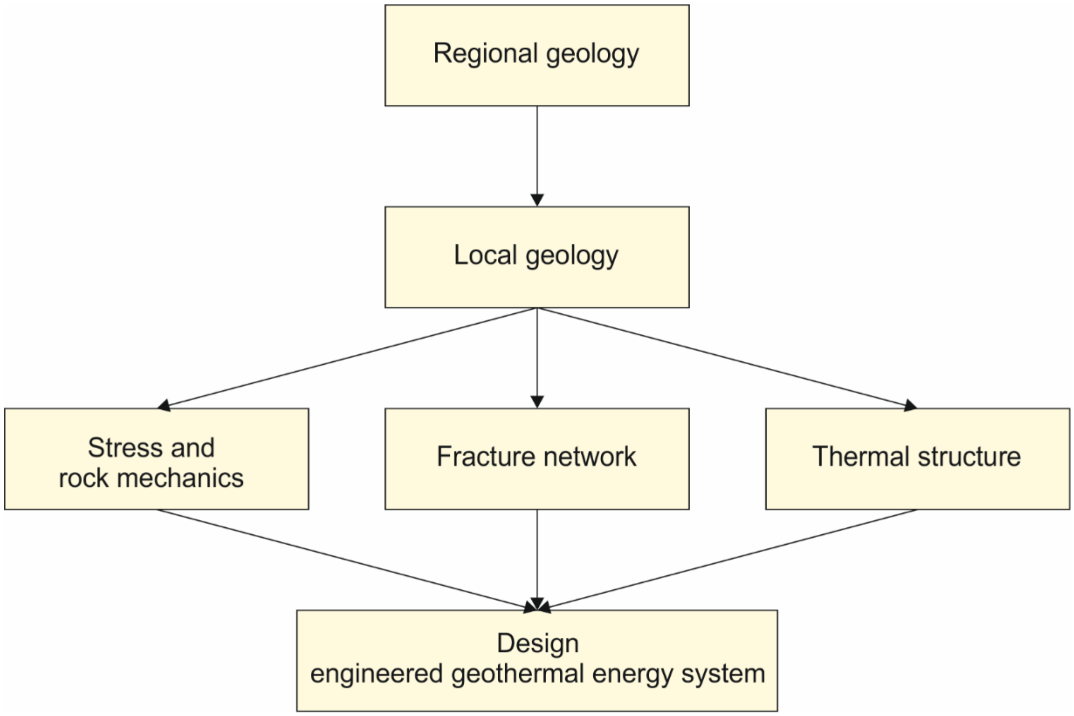

Figure 1.30 Structure of field characterization of engineered geothermal energy systems, adapted from Nakatsuka (1999).

Knowledge of temperature at depth and the thermo-mechanical signature of the lithosphere and crust provide critical constraints affecting the crustal stress field, heat flow and temperature gradients. Moreover, the assessment of the distribution and geometrical properties of the natural fractures within a rock mass is imperative to inform the design of the fracturing stimulation (Hashida, 2015). The available data is then used to build a conceptual model, which is translated into a numerical representation, and calibrated to the unexploited, initial thermodynamic state of the reservoir (Hashida, 2015). Modeling and simulation of thermo-hydro-mechanical processes are a critical part to predict the effects of fracturing and stimulation and design the optimum strategy (Hashida, 2015). In fact, numerical models should be able to solve the following objectives (e.g., Willis-Richards, 1995):

1) Help to understand the performance of the actual field experimental system and help to design measures to improve inadequate system performance
2) Predict the effect of different reservoir creation strategies
3) Predict the thermal performance with time (i.e. thermal drawdown curve)
4) Predict the hydraulic performance (i.e. impedance, water loss)
5) Optimize well placement and operating strategy in relation to both reservoir creation and circulation

Two main categories of models to simulate the processes occurring within engineered geothermal energy systems and help answer those questions have been developed: continuum methods (effective continuum model, dual-continuum or multiple continuum model and stochastic-continuum model) and discrete methods (single-fracture model, discrete fracture network and fracture-matrix model; e.g., Augustin et al., 2014). All these numerical methods have advantages and limitations and the choice between these approaches depends on the compromise between reservoir geometry and description of its behavior.

1.3 Thesis structure

Assessing the deep geothermal energy source potential of remote northern communities is challenging due to remoteness and important data gaps. As highlighted on the previous section, no heat flow data is available for the study area and no in situ stress regime information exists. These are key parameters for the accurate design of engineered geothermal energy systems, as aforementioned. Therefore, this thesis aims at answering to a series of research questions by following an original approach and adapting existing methodologies using geothermal exploration tools affordable to the northern and remote communities. The work undertaken in this thesis is a significant contribution for a first-order evaluation of the deep geothermal energy source as an alternative energetic solution for the off-grid diesel-based communities.

The first of these research questions, “How to characterize geothermal energy sources associated to petrothermal systems based on surficial data?”, is answered in **Chapter 2. Thermophysical properties of surficial rocks: A tool to characterize geothermal resources in remote northern regions.** This chapter highlights how outcrops can be used as deep subsurface analogues. Furthermore, it studies how the variability induced by laboratory methods to characterize thermophysical properties can influence estimates of the present-day temperature at depth and surface terrestrial heat flux. A simplified conceptual model for the crust was built to help carrying out these calculations.

Chapter 3. A numerical approach to infer terrestrial heat flux from shallow temperature profiles in remote northern regions aims at answering the research question “How to infer the terrestrial heat flux from temperature profiles shallower than 100 m depth and perturbed by climate events?”. A model was developed in this chapter to numerically correct paleoclimate and simultaneously infer terrestrial heat flux with inverse numerical simulations. A multi-layer temperature profile with time-varying upper boundary condition, known thermal properties that are both temperature- and pressure-dependent and unknown basal heat flux was simulated and compared to a temperature profile measured in the field. The Nelder-Mead algorithm and least-squares method were then applied for function comparison and to obtain the optimal basal heat flux.

Chapter 4. Uncertainty and risk evaluation of deep geothermal energy source for heat production and electricity generation in remote northern regions uses the inferred basal heat flux in Chapter 3 as a lower boundary condition for the transient 2D heat conduction models simulated to estimate the subsurface temperature distribution. The goals of this chapter are to identify the most influential geological and technical uncertainties on the thermal energy available and evaluate if the deep geothermal energy source in-place can meet Kuujjuaq's community heat and power demand. Beyond simulations of the subsurface temperature distribution, the thermal energy in-place was calculated based on the volumetric method and Monte Carlo simulations. While global sensitivity analysis enabled to rank the uncertain parameters by order of importance, probabilistic analysis revealed the chances of the deep geothermal energy source beneath Kuujjuaq to meet the 2700 inhabitants heating and power needs.

These previous chapters correspond to the description of the thermal structure considering the field characterization of engineered geothermal energy systems proposed by Nakatsuka (1999; Figure 1.30). The following chapter, in turn, encompasses the field characterization parameters related to fracture network and stress and rock mechanics (Figure 1.30).

The research questions "What is the stress regime prevailing in Kuujjuaq? Are there sufficient fracture planes optimally oriented for slip at sufficiently low fluid pressure? What is the critical fluid pressure to reactivate the fracture planes?" are answered in **Chapter 5. Fracture network and stress regime: Implications for the development of engineered geothermal energy systems in remote northern regions.** A statistical fracture network was generated based on a homogeneous Poisson process and fractal dimension, calibrated by field data measurements to help answer these questions. A mixture of von Mises distributions was applied to identify the fracture sets. Furthermore, geological indicators were used to define the orientation of the principal stresses and empirical correlations and analytical modeling, together with Monte Carlo simulations, were used to define the magnitude of the principal stresses. An a priori stress model was inferred for Kuujjuaq based on these evaluations. A theoretical rheological profile is also proposed based on literature structural information and temperature simulations to study the thermo-mechanical conditions of the lithosphere. Mohr-Coulomb friction and slip tendency analyzes enabled to understand if the fracture planes are optimally oriented to slip and at critical state of stress, given the a priori stress model inferred. Moreover, it allowed to study at which fluid pressure the fracture planes can be reactivated.

The thermal structure, fracture network and stress and rock mechanics discussed in the previous chapters were then combined and used to design an engineered geothermal energy system, which is the goal of the following chapter.

Chapter 6. Techno-economic analysis of engineered geothermal energy systems for direct-use applications in Arctic off-grid communities: Parameter uncertainty and sensitivity studies has the purpose of providing answers to "Will the hydraulic stimulation technique applied in crystalline basement rocks develop a well-connected flowing system in Kuujjuaq? How can this be done? What further local geological and thermo-hydro-mechanical data is required for more accurate predictions?" and "Are the deep geothermal energy sources harvested by engineered geothermal energy systems in Kuujjuaq cost-competitive compared to fossil fuels?". Thermo-hydro-mechanical modeling with a shear-dilation-based model following a "what-if" approach is used to answer these research questions. Engineered geothermal energy systems capable to fulfill the community heating energy needs were designed, keeping the water losses lower than 20%, the reservoir flow impedance lower than 0.1 MPa L^{-1} s^{-1} and the thermal drawdown lower than 1 ºC/year. Furthermore, a first-order evaluation of the levelized cost of energy together with Monte Carlo simulations was carried out.

2 THERMOPHYSICAL PROPERTIES OF SURFICIAL ROCKS: A TOOL TO CHARACTERIZE GEOTHERMAL RESOURCES OF REMOTE NORTHERN REGIONS

Propriétés thermophysiques des roches de surface : un outil pour caractériser les ressources géothermiques des régions nordiques éloignées

Authors:

Mafalda M. Miranda (M.M.M.), Nicolò Giordano (N.G), Jasmin Raymond (J.R.)

Institut national de la recherche scientifique, Canada

Alcides J. S. C. Pereira (A.J.S.C.P.)

Centre for Earth and Space Research of the University of Coimbra, Portugal

Chrystel Dezayes (C.D.)

Bureau de recherches géologiques et minières, France

Journal title:

Geothermal Energy

05 February 2020, Volume 8, article 4

https://doi.org/10.1186/s40517-020-0159-y

Author’s contribution:

Conceptualization, M.M.M., N.G., J.R., A.J.S.C.P. and C.D.; methodology, M.M.M.; validation, M.M.M.; formal analysis, M.M.M.; investigation, M.M.M.; resources, M.M.M., N.G, J.R., A.J.S.C.P. and C.D.; data curation, M.M.M.; writing – original draft preparation, M.M.M., N.G, J.R., A.J.S.C.P. and C.D.; writing — review and editing, M.M.M., N.G., J.R., A.J.S.C.P and C.D.; visualization, M.M.M.; supervision, J.R. and C.D.; project administration, J.R.; funding acquisition, J.R.

Graphical abstract:

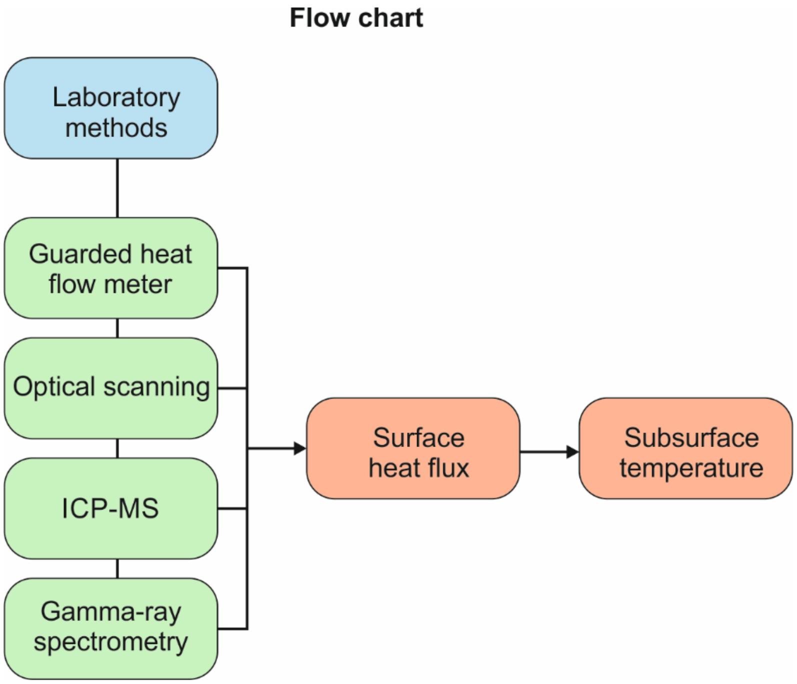

2.1 Introduction

Remote and off-grid communities of northern Canada rely on fossil fuels for electricity generation, space heating and domestic hot water (NRCan, 2018b). At a time of increasingly environmental awareness and in order to assure energy security and offset the use of fossil fuels, the search for local sources of environmentally friendly energy is of fundamental interest. Amongst the renewable energy options, geothermal resources have the advantage of providing continuous heating and base-load power generation regardless of the weather conditions.

In Canada, the utilization of geothermal energy is growing annually. From 1990 to 2013, the ground-source heat pump (GSHP) market experienced a significant increase from 450 to 8250 installed units. In total, more than 110 000 GSHP units were installed throughout the southern part of the country until 2013 (Raymond et al., 2015). Assuming a linear growth of this market, more than 180 000 units might have been installed by 2019. Deep geothermal resources have been the target of recent research (e.g., Majorowicz et al., 2010a; Grasby et al., 2012; Majorowicz et al., 2012a; Ferguson et al., 2014; Hofmann et al., 2014; Majorowicz et al., 2014a; Majorowicz et al., 2015b; Bédard et al., 2018; Nasr et al., 2018), but no geothermal power plant is yet producing electricity.

Geothermal investigations with a focus on the Canadian northern communities facing critical energy challenges have additionally been carried out (e.g., Grasby et al., 2013; Majorowicz et al., 2014b; Majorowicz et al., 2015a; Comeau et al., 2017; Minnick et al., 2018; Giordano et al., 2019a; Gunawan et al., 2020). These studies indicate promising geothermal energy development for the off-grid communities due to the cold climate and the high energy cost. Shallow geothermal resources are seen as viable short-term alternative solutions whereas deep geothermal development can be a long-term objective. However, the uncertainty about the depth and temperature of geothermal resources in northern Canada is considered as the main obstacle for their exploitation. Due to the lack of heat flow data in such remote regions, it is difficult to accurately assess the extent of the geothermal resources. Majorowicz et al. (2015a) presented an evaluation of the geothermal resources for northern Québec based on sparse heat flow data and assumptions regarding the subsurface thermophysical properties. These authors mention that a temperature of 100 °C can be reached at a depth greater than 5 km, making electricity generation difficult. However, in such remote areas, where fossil fuels are the only source of energy, it is crucial to carry out detailed and local studies to avoid extrapolating sparse heat flow data over a large territory. As additionally highlighted by Eppelbaum et al. (2014), the use of average published literature values of rock thermophysical properties can indeed lead to miscalculations of the geothermal potential of a target area. Perhaps an accurate knowledge of rock thermophysical properties from surface outcrops can help better assess temperature at depth and provide the critical information to directly use deep geothermal resources for space heating and to offset fossil fuel consumption.

Deep boreholes with equilibrium temperature measurements and thermal properties assessment located near northern communities of Canada are rarely available. For example, the territory of Nunavik covering 507 000 km^2 and enclosing parts of the Superior and Churchill geological provinces only has three locations at which heat flow has been evaluated (Comeau et al., 2017): Raglan mine, Asbestos Hill mine and Coulon (Figure 2.1).

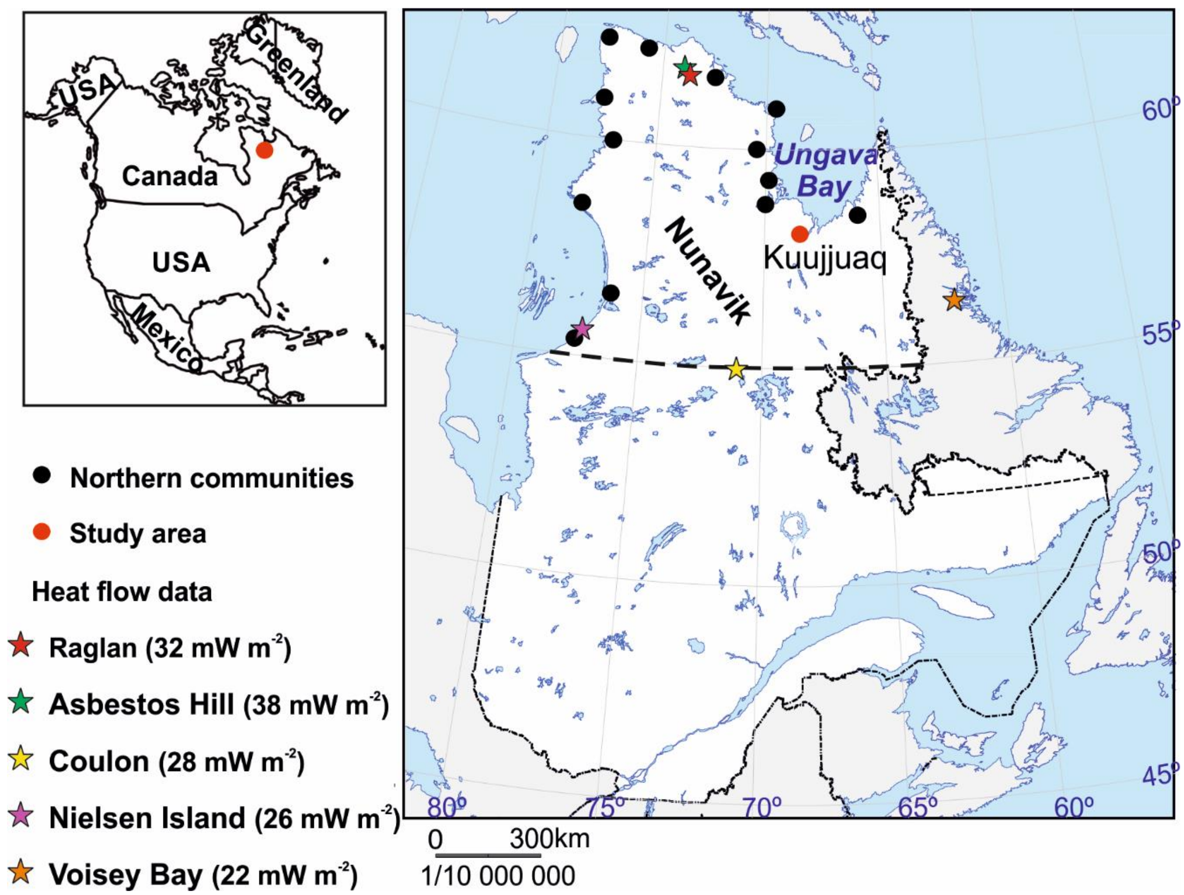

Figure 2.1 **Geographical location of the community of Kuujjuaq and remaining communities of Nunavik (Canada) and of the heat flow assessments: Nielsen Island (Jessop, 1968), Voisey Bay (Mareschal et al., 2000), Camp Coulon (Lévy et al., 2010), Raglan and Asbestos Hill mining sites (e.g., Comeau et al., 2017).**

These locations are far from the communities. Raglan and Asbestos Hill mines lie at a distance of almost 500 km from Kuujjuaq and Coulon at a distance of 420 km (Figure 2.1). Additionally, two other heat flow measurements located in Nunavut (Nielsen Island; Figure 2.1) and Newfoundland and Labrador (Voisey Bay; Figure 2.1) lie at a distance of approximately 500 km and 430 km, respectively, from Kuujjuaq. Similarly, Nunavut is facing a data gap challenge as outlined by Minnick et al. (2018), that conducted a geothermal potential assessment for this region. This raises the question: how to evaluate the depth and temperature of geothermal resources when only surface data is available? This evaluation, even if only preliminary, might trigger the interest of stakeholders for deep drilling nearby the communities. An option for overcoming the subsurface data gap problem is to use outcrops as surface analogues. Although exposed to weathering and erosion processes, outcrops can be easily accessed at low cost and provide reliable data to build geothermal conceptual models (e.g., Cumming, 2009; Homuth et al., 2014; Bauer et al., 2017; Blázquez et al., 2017a; Blázquez et al., 2017b; Weydt et al., 2018). In the absence of any sign of geothermal activity (e.g., thermal springs) and in the presence of low-permeability crystalline rocks, conduction is the main heat transfer mechanism expected for petrothermal systems of the Canadian Shield. Therefore, the estimation of the depth and temperature of geothermal resources is mainly controlled by the heat flux, the surface temperature and the thermal conductivity and internal heat generation of the geological materials.

The work presented in this study is focused on Kuujjuaq, where geothermal evaluation has been conducted to define guidelines for other communities facing the same data gap and exploration challenges. Thermal conductivity of the field samples collected in this community was evaluated by steady-state and transient methods. The concentration of heat-producing elements was determined in the laboratory by mass and radiometric spectrometry. Additionally, hydraulic properties have been evaluated in the laboratory with transient methods to confirm the petrothermal regime assumption. The subsurface temperature distribution was then evaluated numerically by 2D steady-state heat conduction simulations. The use of the aforementioned laboratory methods was essential to assess the variability induced by the laboratory analyzes on the temperature extrapolations, and, thus, define lower and upper bounds for the temperature field at depth.

2.2 Geology

Kuujjuaq is the administrative capital of Nunavik (Figure 2.1). This village is also the largest Inuit community in Nunavik, with about 2750 inhabitants. Given its high energy demand compared to the remaining smaller communities, it is the most suitable target to carry out a geothermal energy feasibility study in northern Québec. The main lithological units outcropping nearby the community of Kuujjuaq are paragneiss and diorite, with smaller occurrences of gabbro, tonalite and granite (Figure 2.2). These lithologies are of two main origins: metamorphic/metasedimentary, comprising the paragneiss rocks; and igneous, enclosing diorite, gabbro, tonalite and granite lithologies. These rocks belong to the Southeastern Churchill Province of the Canadian Shield (e.g., Wardle et al., 2002) and are Archean to Paleoproterozoic in age (SIGÉOM, 2019).

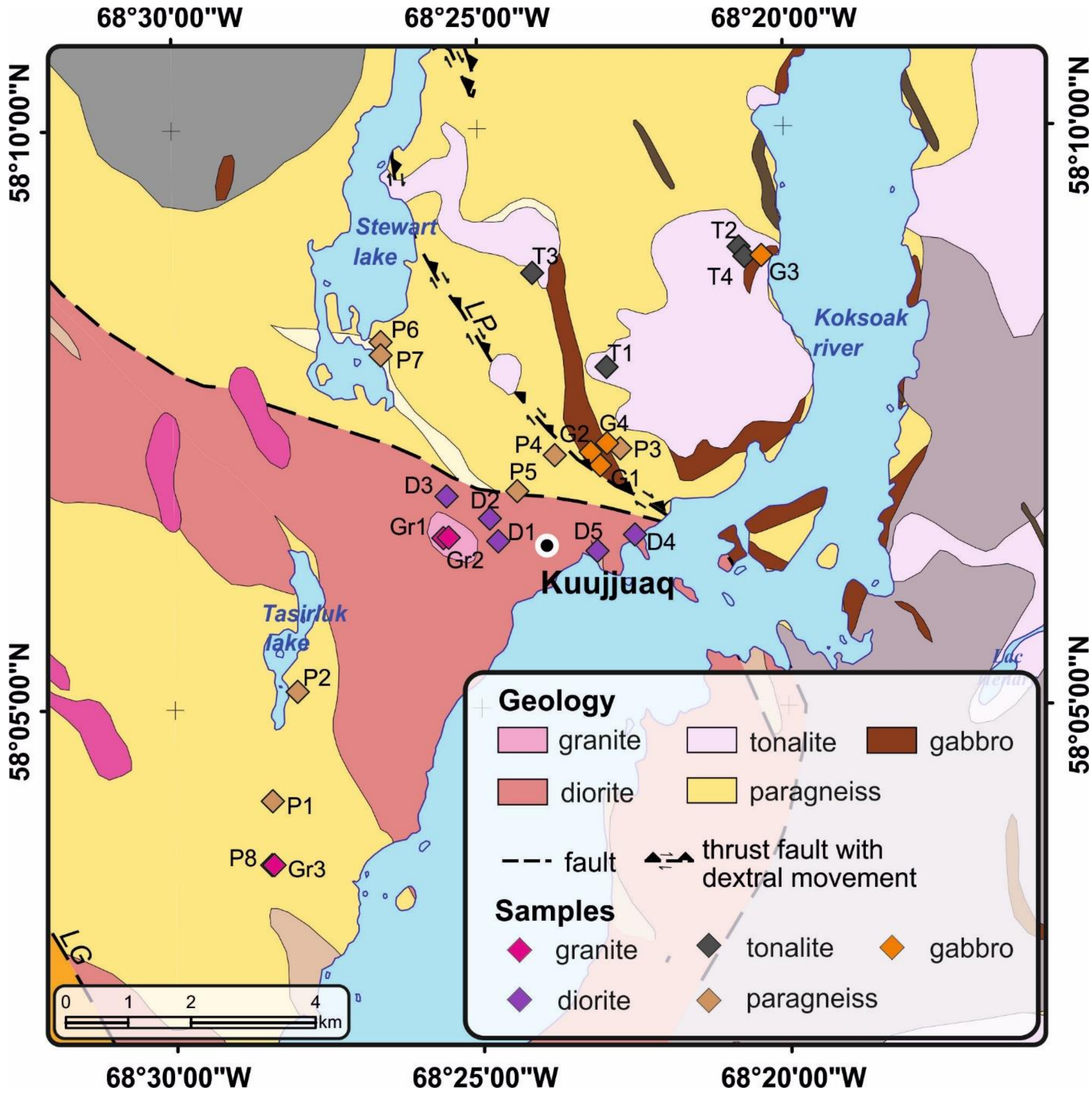

Figure 2.2 Geological map of the study area. *LP* – Lac Pingiajjulik fault, *LG* – Lac Gabriel fault, P – paragneiss, D – diorite, G – gabbro, T – tonalite, Gr – granite, adapted from SIGÉOM (2019).

The paragneiss unit is described as a biotite-rich migmatitic paragneiss, with occurrences of millimetric garnet minerals (Lafrance et al., 2014). The diorite unit is described by Simard et al. (2013) as a very foliated to mylonitic granoblastic diorite and quartz diorite rich in hornblende and actinolite. The gabbro unit is, according to Simard et al. (2013), an amphibolite-rich granoblastic gabbro and diorite. The tonalite unit is defined as a white color tonalite and granite of mobilize type (Simard et al., 2013). The granite intrusions are described as two-mica pink-color granite to pegmatitic granite (Simard et al., 2013).

The Lac Pingiajjulik fault (Figure 2.2) is described in Simard et al. (2013) and SIGÉOM (2019) as a regional thrust fault with dextral movement. The fault is characterized by a broad zone of highly recrystallized mylonite, separating different lithologies (Poirier, 1989). The dextral movement was determined from pressure shadows around the porphyroblasts (Simard et al., 2013 and references therein).

2.3 Methods and techniques

A total of 24 samples were collected in the Kuujjuaq field area (Figure 2.2) and core plugs with 20-mm-radius and thicknesses of 20 to 30 mm were drilled from the specimens, taking into account the observed anisotropy. Core plugs were used for laboratory experiments to infer thermal and hydraulic properties at INRS. Different laboratory methods were used to evaluate the influence of the chosen laboratory approach on the numerical modeling of the temperature distribution at depth. In all cases, the mean value of the relative error (*MRE*; %) between laboratory results with different methodologies was calculated as:

$$MRE = \sum \frac{X_1 - X_2}{X_1} \times 100 \qquad (2.1)$$

where X stands for the parameter under evaluation and the subscripts 1 and 2 stand for the applied methodology.

A total of 14 samples were selected as representative of the different lithologies and analyzed for the radioisotopes ^{238}U, ^{232}Th and ^{40}K to estimate the radiogenic heat production. These analyzes were carried out at the University of Coimbra. The samples selection took into account the concentrations of U and Th obtained through ICP-MS, their geographical position (Figure 2.2) and the weathering degree.

2.3.1 Thermal conductivity

Thermal conductivity of dry samples was evaluated at room temperature using the guarded heat flow meter (GHFM) technique (e.g., Raymond et al., 2017; Ruuska et al., 2017; TA Instruments, 2019), with a FOX50 Heat Flow Meter from TA Instruments having an accuracy of 3%. The instrument has two plates, two heat flow meters and two protective casings to prevent heat losses. The analysis is made when temperature across the sample reaches steady state. A temperature difference is imposed on both plates and successive data acquisition cycles grouped in blocks are run until the temperature of the upper and lower plates and transducer signals satisfy all the necessary equilibrium criteria to declare the sample in thermal equilibrium. Then, thermal conductivity is evaluated. Each plate must meet each equilibrium criterion independently. These criteria are (TA Instruments, 2019):

1. Temperature equilibrium (TE) criterion. The average temperature of each plate must be equal to the setpoint temperature within the chosen TE value. The default is 1 °C.
2. Semi-equilibrium (SE) criterion. This criterion is met when transducers average signals are equal within the SE chosen value. The default is 200 μV.
3. Percent equilibrium (PE) criterion. The average signal of the transducers must be equal to the value of the PE criterion chosen. The default value is 2%.
4. Number of blocks of PE refers to the number of blocks satisfying the PE criterion required to declare that thermal equilibrium has been reached and results can be calculated.
5. Inflexion criterion. To meet this criterion, the transducers average signal of successive data acquisition cycles cannot change only in one direction. The difference between a block and a previous one must change its sign or be equal to zero. Only when this final criterion is met, the equilibrium is declared, and the results are calculated.

A film of silicone paste of about 0.1 mm was smeared on both samples surfaces to improve the contact between rock sample and heating plates.

Additionally, 18 samples from the same lithological units as the core plugs were analyzed by the optical scanning technique (Popov et al. 2016 and references therein) with an infrared thermal conductivity scanner (TCS) from LGM Lippmann having an accuracy of 3%. These measurements took into account the observed anisotropy. Thermal conductivity is evaluated transiently based on solutions of the heat conduction equation for a quasi-stationary temperature field in a movable coordinate system OXYZ (Popov et al., 2016). The main elements of the TCS are a focused, mobile and continuously operated optical heat source mounted on an array of three infrared temperature sensors (Popov et al., 2016). The cold sensor passes first and records the temperature of both standards and sample before the thermal perturbation. Then, the optical heat source disturbs the temperature and, finally, the two hot sensors record the temperature after the perturbation. The sample thermal conductivity is evaluated taking into account this temperature variation and the thermal conductivity of both standards.

2.3.2 Radiogenic elements and heat production

The concentration of naturally occurring radioisotopes ^{238}U, ^{232}Th and ^{40}K was determined by gamma-ray spectrometry (GRS) using a NaI(Tl) detector (7.62×7.62 cm) connected to a multichannel pulse-height analyzer (1024 channels) equipped with a spectrum stabilizer for automatic compensation of gain shift. The detector is surrounded by a 5-cm-thick lead shield to smoothen background gamma-radiation (ORTEC 2015). The isotope concentrations are measured using the three-window method. This involves the detection of the gamma-radiation emission on the decay of ^{214}Bi (^{238}U decay chain), ^{208}Tl (^{232}Th series) and ^{40}K. The analyzed portion of the gamma-ray spectrum ranges in energy from 0 to 3000 keV. ^{40}K as an energy peak of 1460 keV. ^{214}Bi has an energy peak of 1764 keV. ^{208}Tl has the most energetic peak with 2614 keV (e.g., Lamas et al., 2017). The system is calibrated with standard solutions certified by the International Atomic Energy Agency (IAEA) for K, U and Th activity measurements. The potassium calibration standard is extra-pure potassium sulphate (99.8%) and uranium and thorium content lower than 0.001 mg kg^{-1} and 0.01 mg kg^{-1}, respectively. The uranium standard is U-ore diluted with silica, containing a negligible amount of K ($<$ 0.00234 mg kg^{-1}) and Th ($<$ 1 mg kg^{-1}). The thorium standard is Th-ore diluted with silica, with trace content of uranium and potassium. The background gamma-radiation subtraction is performed for each measurement. The counting time for each sample was increased for 24 h due to the results from the trace elements concentration (Table 2.1). The elemental concentration on U, Th and K is then calculated based on the daughter isotopes activity.

Additionally, GRS results were compared with those obtained from ICP-OES/MS (Table 2.1), as mass spectrometry methods are referred to be more accurate by six orders of magnitude than radiometric methods (Hou et al., 2008). In ICP, the chemical elements contained in the sample solution are decomposed into their atomic constituents in an inductively coupled argon plasma. Then, the positively charged ions are extracted from the inductively coupled plasma into a high vacuum via an interface. These ions are then separated by mass filters and finally measured by an ion detector (e.g., Hou et al., 2008). Quality control procedures were considered during the analyzes to guarantee the accuracy of laboratory measurements. First, the ICP was calibrated using a blank and the working calibration standard. Then, the initial calibration verification standard was run, and the percent of recovery was ± 10%. Following the initial calibration verification, the initial calibration blank was analyzed. The concentration was verified to be less than the reporting limit for each element. The reporting limit standard was run, followed by the spectral interference check solution, the continuing calibration verification (CCV) and the continuing calibration blank (CCB). Afterwards, the method blank, the laboratory control samples, and the samples themselves were analyzed. The CCV/CCB was run every 10 samples. At the end of the analytical sequence, a final CCV/CCB was analyzed. The following certified reference materials (CRM) were used:

- WPR-1a – CRM for a peridotite with rare earth and platinum group elements
- QLO-1 – CRM for quartz latite
- SGR-1 – CRM for green river shale
- SY-4 – CRM for diorite gneiss

Radiogenic heat production (*RHP*; W m^{-3}) was calculated afterwards knowing that:

$$RHP = \rho \sum P'H'[X] \tag{2.2}$$

where ρ (kg m^{-3}) is the density, P' (wt %), H' (W kg^{-1}) and $[X]$ (mg kg^{-1}; %) are the specific abundance, heat generated and concentration of each radioisotope, respectively.

The constants P' and H_0 for each element were estimated with Rybach (1976) approach, transforming Equation (2.2) in the following empirical function (Rybach, 1988):

$$RHP = 10^{-5}\rho(9.51[U] + 2.56[Th] + 3.50[K]) \tag{2.3}$$

where potassium concentration was converted from its oxide form to the elemental form by:

$$[K] = 0.830 \times [K_2O] \tag{2.4}$$

2.3.3 Hydraulic properties

Porosity was evaluated using the combined gas permeameter–porosimeter AP-608 from Core Test following Boyle’s law (e.g., Raymond et al., 2017; Coretest Systems, Inc., 2019). This law states that the pressure exerted by a given mass of an ideal gas is inversely proportional to the volume it occupies (Raymond et al., 2017 and references therein).

Permeability was also evaluated using the AP-608. The analysis follows the transient pressure decay method, and the permeability is inferred by Darcy’s law. Klinkenberg correction is then applied to convert the gas to liquid permeability (Raymond et al., 2017 and references therein). Density of solid grains was evaluated with the AP-608 grain volume chamber.

2.3.4 Temperature field at depth

Preliminary estimation of the present-day temperature at depth was solved numerically using the COMSOL Multiphysics software assuming 2D steady-state heat conduction:

$$\frac{\partial}{\partial x}\left(\lambda\frac{\partial T}{\partial x}\right)+\frac{\partial}{\partial z}\left(\lambda\frac{\partial T}{\partial z}\right)+RHP=0 \tag{2.5}$$

where λ (W m^{-1} K^{-1}) is the thermal conductivity, T (°C) is the temperature and x (m) and z (m) are the spatial variables.

Geological models of the lithosphere stratigraphy and thickness in Kuujjuaq were built based on available regional literature data (e.g., Christensen et al., 1975; Moorhead et al., 1989; Poirier, 1989; Mareschal et al., 1990; Seguin et al., 1990; Hall et al., 1995; Wardle et al., 1996; Telmat, 1998; Telmat et al., 1999; Bourlon et al., 2002; St-Onge et al., 2002; Vervaet et al., 2016). Moho is placed at 37.5 km depth. The upper crust is mainly composed by paragneiss and has a thickness of 26.5 km. The lower crust is assumed to be made of granulitic facies rocks with a thickness of about 11 km. Its radiogenic heat production is estimated to be 0.45×10^{-6} W m^{-3} (Ashwal et al., 1987). The Moho contribution to the heat flow is estimated to be, on average, 15×10^{-3} W m^{-2} (e.g., Jaupart et al., 2007; Mareschal et al., 2013; Jaupart et al., 2014; Jaupart et al., 2016).

The temperature distribution was modeled for a rectangular geometry with a width of 8 km and a depth of 10 km (Figure 2.3). The center of the 2D model corresponds to a change in lithology between paragneiss and diorite (Figure 2.2). The diorite layer thickness is considered to vary within 1 to 5 km. This geometry was selected to evaluate how lithological changes with different thicknesses of the diorite can influence the temperature at depth. A constant surface temperature of -1 °C (climate normals 1981–2010; Comeau et al., 2017; ECCC, 2019) was set as the upper boundary condition. The lower boundary condition is the heat flux at 10 km depth. This parameter is calculated as:

$$q=q_{\mathrm{M}}+\int_{z_{\mathrm{M}}}^{10}RHP(z)dz \Leftrightarrow q_{10}=q_{\mathrm{M}}+RHP_{\mathrm{LC}}\times h_{\mathrm{LC}}+RHP_{\mathrm{UC}}\times(h_{\mathrm{UC}}-h_{\mathrm{model}}) \tag{2.6}$$

where q (W m^{-2}) is the heat flux, z (m) is depth and h (m) is thickness. The subscript 10 stands for 10-km depth and M for Moho. LC and UC are, respectively, lower and upper crustal layers.

Both lateral boundaries are assumed adiabatic. Thermal conductivity and radiogenic heat production were defined according to lithologies, assuming uniform values.

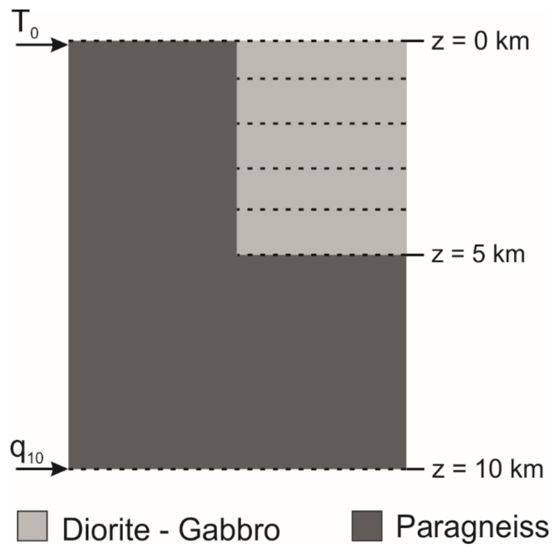

Figure 2.3 Simplified geological model of the upper 10 km lithosphere stratigraphy in Kuujjuaq.

Several scenarios were studied with the goal of assessing the influence of the different laboratory methods in the prediction of the temperature field at depth. These are: (1) scenario GHFM – GRS, (2) scenario TCS – GRS, (3) scenario GHFM – ICP-MS, and (4) scenario TCS – ICP-MS. The thermophysical properties of each geological material were, thus, varied according to the applied method. It is important to highlight that only the samples evaluated by the four methods were considered for the numerical simulations to avoid a misinterpretation of the results. The worst and best temperature predictions were calculated within each scenario considering the statistical distribution of thermal properties.

Long-lasting changes in surface temperature, which can occur during glacial episodes, have an effect on the subsurface temperature distribution due to downwards thermal diffusion (e.g., Birch, 1948; Jessop, 1990; Mareschal et al., 1999; Beardsmore et al., 2001; Beltrami et al., 2005; Chouinard et al., 2007; Chouinard et al., 2009; Rath et al., 2012; Suman et al., 2017; Bédard et al., 2018 and references therein). The temperature predictions were therefore corrected to evaluate by how much the temperature at 5 km depth can have been misestimated by assuming a constant Dirichlet condition in the numerical simulations. The temperature correction was based on Carslaw et al. (1959) solution:

$$\Delta T = T_0 \times erfc\left(\frac{z}{2\sqrt{\alpha t}}\right) \quad (2.7)$$

where ΔT (°C) is the departure from original equilibrium temperature at depth z (m) and time t (s) after an instantaneous change in surface temperature T_0 (°C), α ($m^2\ s^{-1}$) is the thermal diffusivity of the geological materials (assumed as $1 \times 10^{-6}\ m^2\ s^{-1}$) and $erfc(x)$ is the complimentary error function.

The duration and surface temperature perturbations of each Pleistocene climate events in Northern Canada are still debatable and several models have been proposed (e.g., Birch, 1948 and references therein; Mareschal et al., 1999; Beltrami et al., 2003; Majorowicz et al., 2005; Chouinard et al., 2009; Jaume-Santero et al., 2016; Pickler et al., 2016a). Therefore, three different ground surface temperature histories (GSTH) were used based on Birch (1948) and Jessop (1990) model of the Pleistocene glaciations (Figure 2.4). For the first scenario, the temperature during a glacial cycle was considered as 10 °C colder than today. The second assumes a temperature of 5 °C colder and, for the third, a temperature of 1 °C colder than current times was considered (Figure 2.4).

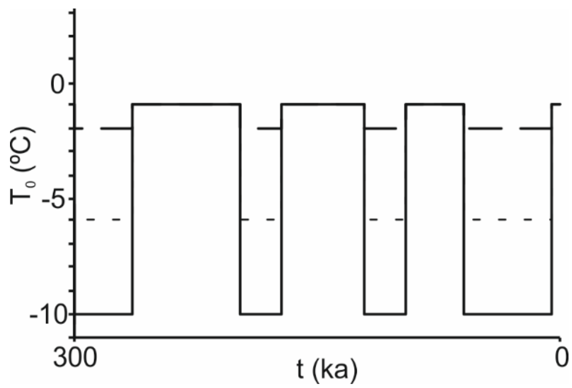

Figure 2.4 **Timeline of Pleistocene and Holocene climate events and temperature step. Solid line — temperature during glacial episode assumed as 10 °C colder than today; pointed line — temperature during glacial episode assume 5 °C colder than today; dashed line — temperature during glacial episode 1 °C colder than today.**

2.4 Results

2.4.1 Rock samples description and geochemistry

The paragneiss samples (P1 – P8; Figure 2.2) collected present high content in amphibole and biotite minerals, in a fine- to medium-grained matrix. The feldspar minerals are weathered showing a brown to light-brown tone. The main mineral phases identified in thin sections are, on average, 16% quartz, 29% feldspar and 55% mafic minerals. The diorite samples (D1 – D5; Figure 2.2) are a fine- to medium-grained matrix and do not have evidence of weathering. They have an averaged content of 17% quartz, 23% feldspar and 59% mafic minerals. The gabbro samples (G1 – G4; Figure 2.2) have a fine- to medium-grained texture and their feldspar minerals have signs of weathering given by their brownish tone. The analyzed samples from this unit have 25% quartz, 24% feldspar and 51% mafic minerals content. The tonalite samples (T1 – T4; Figure 2.2) collected are coarse-grained, and their color varies from white to pinkish. The samples analyzed are characterized by a higher content of quartz (41%) and feldspar

(51%) than of mafic minerals (8%). The granite samples (Gr1 – Gr3; Figure 2.2) are composed, on average, of 35% quartz, 55% feldspar and 10% mafic minerals. One of the granite samples collected presents foliation. Based on the similar texture and mineralogical content, the rock samples collected can be classified in three main groups: paragneiss, diorite–gabbro and tonalite–granite.

The content of major and trace elements of rock samples were analyzed by inductively coupled plasma (ICP) techniques, more precisely, optical emission spectrometry (OES) and mass spectrometry (MS) at INRS (Table 2.1). The paragneiss samples have an average composition of 63% SiO_2, 14% Al_2O_3, 8% Fe_2O_3, 4% MgO, 3% K_2O, CaO and Na_2O, and < 1% TiO_2. The diorite–gabbro has an average composition of 63% SiO_2, 13% Al_2O_3, 8% Fe_2O_3, 5% MgO and CaO, 2% Na_2O, 1.5% K_2O, and < 1% TiO_2. Regarding the tonalite–granite, this group has an average composition of 73% SiO_2, 14% Al_2O_3, 4% K_2O and Na_2O, 1% CaO, and < 1% Fe_2O_3, MgO and TiO_2.

Table 2.1 Whole-rock geochemistry of the samples collected in Kuujjuaq.

ID			Major elements (%)								Trace elements (mg kg^{-1})	
			SiO_2	TiO_2	Al_2O_3	Fe_2O_3	MgO	CaO	Na_2O	K_2O	U	Th
Metamorphic/ metasedimentary		P1	69.4	0.41	15.1	4.27	1.75	2.93	4.07	1.46	1.71	4.34
		P2	63.7	0.64	17.0	4.65	1.68	3.57	5.15	1.90	0.25	0.79
		P3	58.9	0.57	14.1	6.71	7.50	6.56	1.94	2.24	0.55	1.30
		P4	61.6	0.62	13.4	5.12	1.99	1.91	3.14	3.51	1.83	18.04
		P5	42.8	1.62	13.0	17.50	11.70	0.95	0.17	7.65	1.56	1.71
		P6	79.6	0.26	10.3	5.16	1.46	1.59	2.21	1.34	1.20	7.08
		P7	67.3	0.95	13.7	7.57	2.40	1.69	2.28	3.07	1.82	15.10
		P8	63.5	0.93	14.8	8.59	3.37	3.17	2.70	2.34	2.55	5.34
Igneous	Mafic	D1	64.8	0.94	14.3	9.30	2.37	2.67	2.91	2.50	1.13	16.70
		D2	57.6	0.44	16.0	6.88	4.96	5.83	3.76	1.96	0.21	0.61
		D3	71.3	0.77	12.3	5.80	1.50	2.43	2.54	1.71	1.36	10.90
		D4	47.4	0.43	6.5	12.80	19.50	7.84	0.90	0.12	0.33	1.06
		D5	60.2	1.15	16.5	10.40	1.53	4.70	4.35	2.17	0.71	1.22
		G1	48.5	1.44	15.4	14.40	7.40	8.58	1.71	1.42	0.35	0.27
		G2	94.0	0.04	2.2	0.91	0.69	0.82	0.44	0.18	0.32	1.01
		G3	47.1	1.04	12.5	11.80	10.00	11.30	1.31	0.11	0.06	0.24
		G4	73.0	0.03	14.0	0.51	0.12	1.35	3.76	3.40	0.75	2.21
	Felsic	T1	63.6	0.31	14.2	1.87	0.69	2.94	4.71	1.03	0.33	0.83
		T2	73.9	0.11	14.7	0.71	0.44	1.46	4.08	3.78	0.19	0.34
		T3	74.9	0.02	15.0	0.59	0.07	1.51	5.47	2.15	2.04	1.72
		T4	75.0	0.03	12.9	0.43	0.08	1.14	3.78	4.21	1.57	4.09
		Gr1	73.2	0.02	14.8	0.20	0.02	0.09	2.20	10.2	0.63	0.87
		Gr2	78.8	0.01	13.5	0.72	0.04	1.33	5.76	0.80	2.61	26.0
		Gr3	70.0	0.02	12.6	0.18	0.03	0.96	3.32	5.07	14.80	25.0

P – Paragneiss, D – Diorite, G – Gabbro, T – Tonalite, Gr – Granite.

2.4.2 Thermal properties

The paragneiss samples are characterized by an average thermal conductivity of 2.32 W m^{-1} K^{-1} when evaluated with the steady-state method (GHFM) and 2.52 W m^{-1} K^{-1} with the transient method (TCS; Table 2.2; Figure 2.5). For the igneous mafic group (diorite – gabbro), both steady-state and transient methods give a similar value of 2.83 W m^{-1} K^{-1} and 2.84 W m^{-1} K^{-1}, respectively. Thermal conductivity of igneous felsic samples evaluated by the steady-state method is, on average, 3.08 W m^{-1} K^{-1} and 3.36 W m^{-1} K^{-1} when evaluated by the transient method. The lower *MRE* is obtained for the igneous mafic group (diorite – gabbro), with a value of -2%, considering the steady-state value at the denominator. Regarding the paragneiss samples and the felsic igneous rocks, the *MRE* is -15% and -13%, respectively. On average, the relative error between steady-state and transient methods for all the lithologies is −9.8%, ranging from a maximum of 30% to a minimum of -58%.

Table 2.2 Thermal conductivity statistics of the main lithologies in Kuujjuaq.

	λ_{GHFM} (W m^{-1} K^{-1})	λ_{TCS} (W m^{-1} K^{-1})	*MRE* (%)
Paragneiss (*N* = 7)			
Arithmetic mean	2.32	2.52	-15
Standard deviation	0.61	0.30	
Median	2.10	2.55	
Min – Max	1.62 – 3.15	2.07 – 2.90	
Diorite-gabbro (*N* = 9)			
Arithmetic mean	2.83	2.84	-2
Standard deviation	0.58	0.51	
Median	2.72	2.57	
Min – Max	2.07 – 3.70	2.26 – 3.51	
Tonalite-granite (*N* = 6)			
Arithmetic mean	3.08	3.34	-13
Standard deviation	0.59	0.70	
Median	3.09	3.57	
Min – Max	2.34 – 3.73	2.25 – 4.43	

***λ* – thermal conductivity, *N* – number of samples, Standard deviation – population standard deviation, Min – minimum, Max – maximum.**

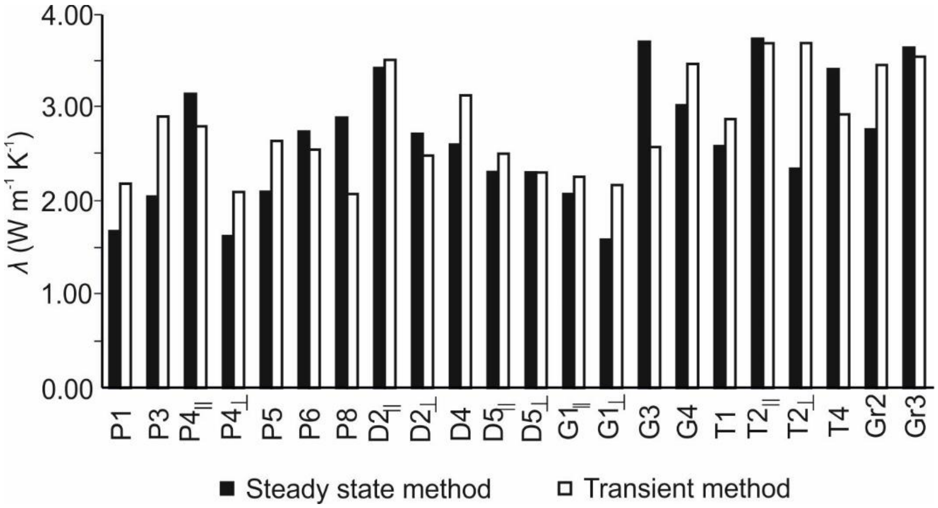

Figure 2.5 Thermal conductivity evaluated by steady-state and transient methods for Kuujjuaq samples.

2.4.3 Radiogenic elements and heat production

Results obtained for radiogenic elements from radiometric (GRS) and mass (ICP-MS) spectrometry methods allowed to estimate the internal heat generation with Equation (2.2) for the main lithologies in Kuujjuaq (Table 2.3; Figure 2.6). The results of GRS reveal that, on average, paragneiss samples are characterized by a uranium concentration of 1.50 mg kg^{-1}, a thorium concentration of 3.75 mg kg^{-1} and a potassium concentration of 0.50%. Lower values are found for diorite–gabbro group with average concentration in uranium, thorium and potassium of 0.38 mg kg^{-1}, 1.94 mg kg^{-1} and 0.47%, respectively. The igneous felsic group is characterized by higher uranium and potassium concentration of 1.3 mg kg^{-1} and 0.88%, respectively, than the igneous mafic, but a similar concentration in thorium of 1.82 mg kg^{-1}. The evaluation of the heat-producing elements by ICP-MS leads to a decrease on uranium concentration of about 60% and 20% for the paragneiss and tonalite–granite groups, respectively. The igneous mafic group reveals an increase of 50% for uranium. Thorium concentration decreased by 11% for the paragneiss samples when evaluated by ICP-MS, whereas for both igneous groups, this element increased up to 70%. Potassium concentration, in turn, increased by more than 60% when evaluated by ICP-MS for all the lithological groups under study.

Table 2.3 **Heat-producing elements, density and radiogenic heat production statistics of the main lithologies in Kuujjuaq.**

	U_{GRS}	$U_{ICP\text{-}MS}$	Th_{GRS}	$Th_{ICP\text{-}MS}$	K_{GRS}	$K_{ICP\text{-}MS}$	RHP_{GRS}	$RHP_{ICP\text{-}MS}$	ρ
	(mg kg^{-1})		(mg kg^{-1})		(%)		($\times 10^{-6}$ W m^{-3})		(kg m^{-3})
Paragneiss (*N* = 4)									*N* = 8
Arithmetic mean	1.50	0.93	3.75	3.38	0.50	1.44	0.70	0.64	2721
Standard deviation	1.27	0.66	3.36	2.92	0.45	0.34	0.59	0.32	118.36
Median	1.30	0.88	3.10	2.82	0.47	1.39	0.62	0.67	2711
Min – Max	0.40 – 3.00	0.25 – 1.71	0.60 – 8.20	0.79 – 7.08	0.04 – 1.02	1.11 – 1.86	0.15 – 1.41	0.30 – 0.94	2464 – 2879
Diorite-gabbro (*N* = 5)									*N* = 9
Arithmetic mean	0.38	0.75	1.94	6.29	0.47	1.62	0.27	0.79	2752
Standard deviation	0.18	0.50	1.96	7.18	0.79	0.98	0.24	0.64	166.58
Median	0.40	0.75	1.50	2.21	0.12	1.63	0.23	0.63	2700
Min – Max	0.20 – 0.60	0.21 – 1.36	0.40 – 5.20	0.61 – 16.7	0.03 – 1.86	0.15 – 2.82	0.09 – 0.66	0.16 – 1.67	2571 – 3108
Tonalite-granite (*N* = 5)									*N* = 6
Arithmetic mean	1.30	1.07	1.82	6.43	0.88	3.32	0.51	1.03	2565
Standard deviation	1.73	1.02	1.64	11.04	0.62	3.15	0.48	0.85	40.03
Median	0.60	0.63	1.50	0.87	0.79	3.14	0.31	1.03	2573
Min – Max	0.20 – 4.30	0.19 – 2.61	0.40 – 4.60	0.34 – 26.00	0.04 – 1.74	0.66 – 8.47	0.11 – 1.29	0.23 – 2.39	2505 – 2626

***RHP* – radiogenic heat production, *ρ* – density.**

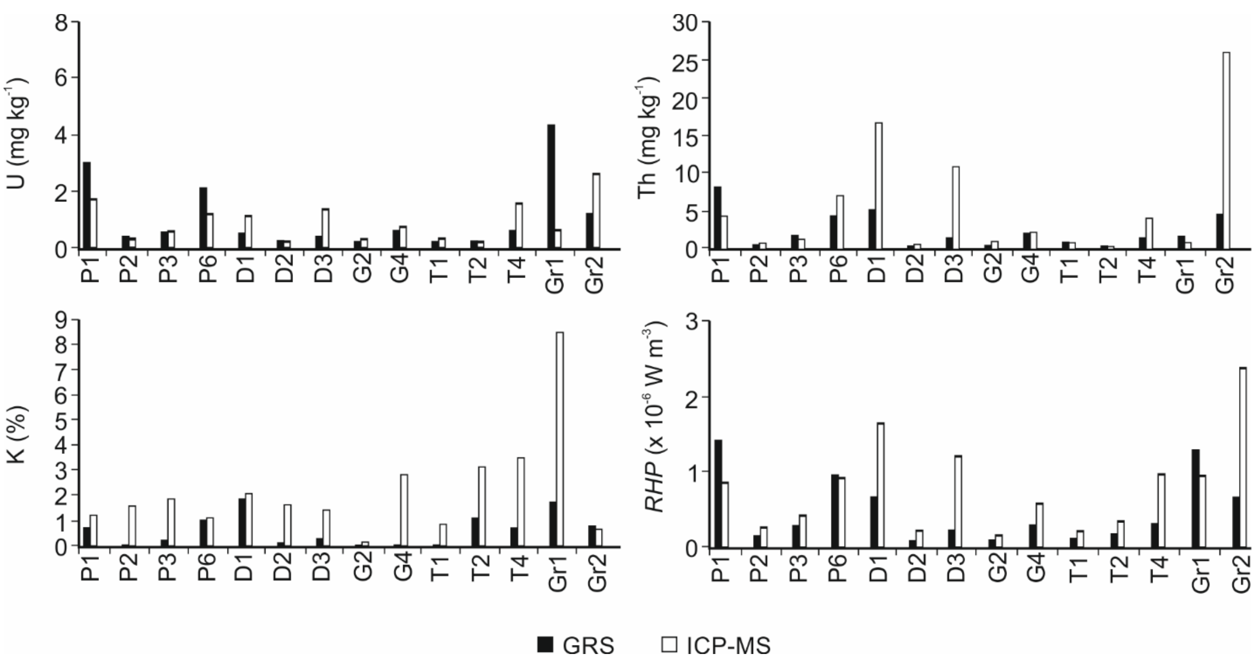

Figure 2.6 **Comparison of radiogenic element concentration between gamma-ray spectrometry (GRS) and ICP-MS.**

2.4.4 Hydraulic properties

Paragneiss samples are characterized by an averaged porosity value of about 6%, whereas the igneous specimens have an averaged porosity of 4% for the diorite – gabbro group and 3% for the tonalite – granite. The matrix permeability for all the samples analyzed is below 10^{-19} m^2, which is beyond the detection limit of the instrument used.

2.4.5 Temperature field at depth

Thermal conductivity and internal heat generation were varied according to the analysis method (Table 2.4) to study the variability induced by laboratory methods on the steady-state temperature extrapolation. Moreover, due to uncertainty on the diorite – gabbro thickness, this layer was considered to vary from a minimum of 1 km to a maximum of 5 km (Table 2.4).

Table 2.4 Thermal property scenarios used in the numerical model to define the temperature at depth.

			Paragneiss	Diorite – gabbro ($1 < z > 5$ km)
Scenario GHFM – GRS	λ_{GHFM} (W m^{-1} K^{-1})	Min	1.62	2.07
		Median	2.10	2.72
		Max	3.15	3.70
	RHP_{GRS} (×10^{-6} W m^{-3})	Min	0.15	0.09
		Median	0.62	0.23
		Max	1.41	0.66
Scenario TCS – GRS	λ_{TCS} (W m^{-1} K^{-1})	Min	2.07	2.26
		Median	2.55	2.57
		Max	2.90	3.51
	RHP_{GRS} (×10^{-6} W m^{-3})	Min	0.15	0.09
		Median	0.62	0.23
		Max	1.41	0.66
Scenario GHFM – ICP-MS	λ_{GHFM} (W m^{-1} K^{-1})	Min	1.62	2.07
		Median	2.10	2.72
		Max	3.15	3.70
	RHP_{ICP-MS} (×10^{-6} W m^{-3})	Min	0.30	0.16
		Median	0.67	0.63
		Max	0.94	1.67
Scenario TCS – ICP-MS	λ_{TCS} (W m^{-1} K^{-1})	Min	2.07	2.26
		Median	2.55	2.57
		Max	2.90	3.51
	RHP_{ICP-MS} (×10^{-6} W m^{-3})	Min	0.30	0.16
		Median	0.67	0.63
		Max	0.94	1.67

Results reveal that a high temperature is found when combining the minimum value obtained for thermal conductivity with the maximum of internal heat generation. This corresponds to the best-case scenario of Table 2.6. The worst-case scenario is obtained by using the maximum thermal conductivity with the minimum heat production. The median values of the thermophysical properties were used to calculate the base-case scenarios. This choice took into account the population standard deviation calculated for each thermophysical parameter (Table 2.2, Table 2.3). The median was considered to be statistically more robust than the population average value.

The heat flux at surface estimated from Equation (2.6) varies between 23×10^{-3} W m^{-2} and 58×10^{-3} W m^{-2}, with an average value of $33–38 \times 10^{-3}$ W m^{-2} (Table 2.5). Internal heat generation in the diorite layer contributes with 1% to 3% for the total surface heat flux whereas the paragneiss with up to 48% (Table 2.5).

Table 2.5 **Inferred heat flux and contribution from each layer.**

			$q_{0, GRS}$ ($\times 10^{-3}$ W m^{-2})	$q_{0, ICP-MS}$ ($\times 10^{-3}$ W m^{-2})	$q_{10, GRS}$ ($\times 10^{-3}$ W m^{-2})	$q_{10, ICP-MS}$ ($\times 10^{-3}$ W m^{-2})	Contribution (%)
Paragneiss		Min	24.0	28.1	22.4	24.9	
		Average	36.7	38.0	30.2	31.0	48
		Max	58.0	45.3	43.2	35.5	
Paragneiss + Diorite	1-km-thick diorite	Min	23.9	27.8	22.4	24.9	
		Average	33.3	38.0	30.2	31.0	46:1
		Max	50.3	46.8	43.2	35.5	
	5-km-thick diorite	Min	23.2	27.2	22.4	24.9	
		Average	33.1	37.8	30.2	31.0	39:3
		Max	49.9	49.7	43.2	35.5	

Using GHFM to evaluate thermal conductivity and GRS for the internal heat generation, the temperature at 5 km can vary from a minimum of 31 – 39 °C to a maximum of 129 – 168 °C. The base-case scenario of this simulation points towards temperatures of 66 – 85 °C (Table 2.6). These temperature values change when TCS is used instead of GHFM. For the scenario TCS – GRS, at 5 km depth, temperature is predicted to vary from 33 – 43 °C to 105 – 132 °C, with an average of 57 – 71 °C (Table 2.6). For the GHFM – ICP-MS simulation, the base-case scenario gives temperatures of 68 – 88 °C at 5 km depth, ranging from a minimum of 35 – 45 °C to a maximum of 105 – 134 °C (Table 2.6). Finally, TCS combined with ICP–MS indicates temperature of 38 – 49 °C to 85 – 105 °C at 5 km depth, with an average of 59 – 73 °C (Table 2.6).

Table 2.6 **Temperature at depth scenarios based on the thermal properties of the geological materials.**

		Scenario GHFM – GRS		Scenario TCS – GRS		Scenario GHFM – ICP-MS		Scenario TCS – ICP-MS	
Diorite-gabbro thickness		1 km	5 km	1 km	5 km	1 km	5 km	1 km	5 km
T (ºC) at 5 km depth	Worst-case scenario	32 - 39	31 - 38	35 - 43	33 - 41	36 - 45	35 - 43	40 - 49	38 - 47
	Base-case scenario	69 - 85	66 - 80	58 - 71	57 - 70	72 - 88	68 - 84	60 - 73	59 - 73
	Best-case scenario	137 - 168	129 - 158	108 - 132	105 - 129	109 - 134	105 - 129	86 - 105	85 - 104

Another interesting aspect is the influence of the diorite – gabbro layer. A thin diorite – gabbro layer of 1 km has a negligible influence on the temperature at 5 km. However, for a 5-km-thick layer, the isotherms show a slight decrease in this layer when compared to the adjacent paragneiss (Figure 2.7). This is due to the contrast in the thermal conductivity between the paragneiss and diorite – gabbro. The only exception occurs for the base-case scenarios with TCS – GRS and TCS – ICP-MS, since both median thermal conductivity values are similar (Table 2.4).

However, the simulations carried out indicate that the thickness of the diorite–gabbro layer induces a variability of about 4% only on the temperature field at depth. This variability is 12% to 14% when the two different techniques to evaluate the internal heat generation and the thermal conductivity are considered. A higher variability, of more than 50%, is obtained as a result of the lithological intrinsic heterogeneity associated to the statistical distribution of rock thermal properties.

Considering the base-case scenarios, the laboratory methods can be ranked in terms of temperature field at depth such that (Table 2.6; Figure 2.7):

TCS – GRS < TCS – ICP-MS < GHFM – GRS < GHFM – ICP-MS.

However, considering the variability induced by the intrinsic heterogeneous character of each lithological unit, the rank is:

TCS – ICP-MS < GHFM – ICP-MS < TCS – GRS < GHFM – GRS.

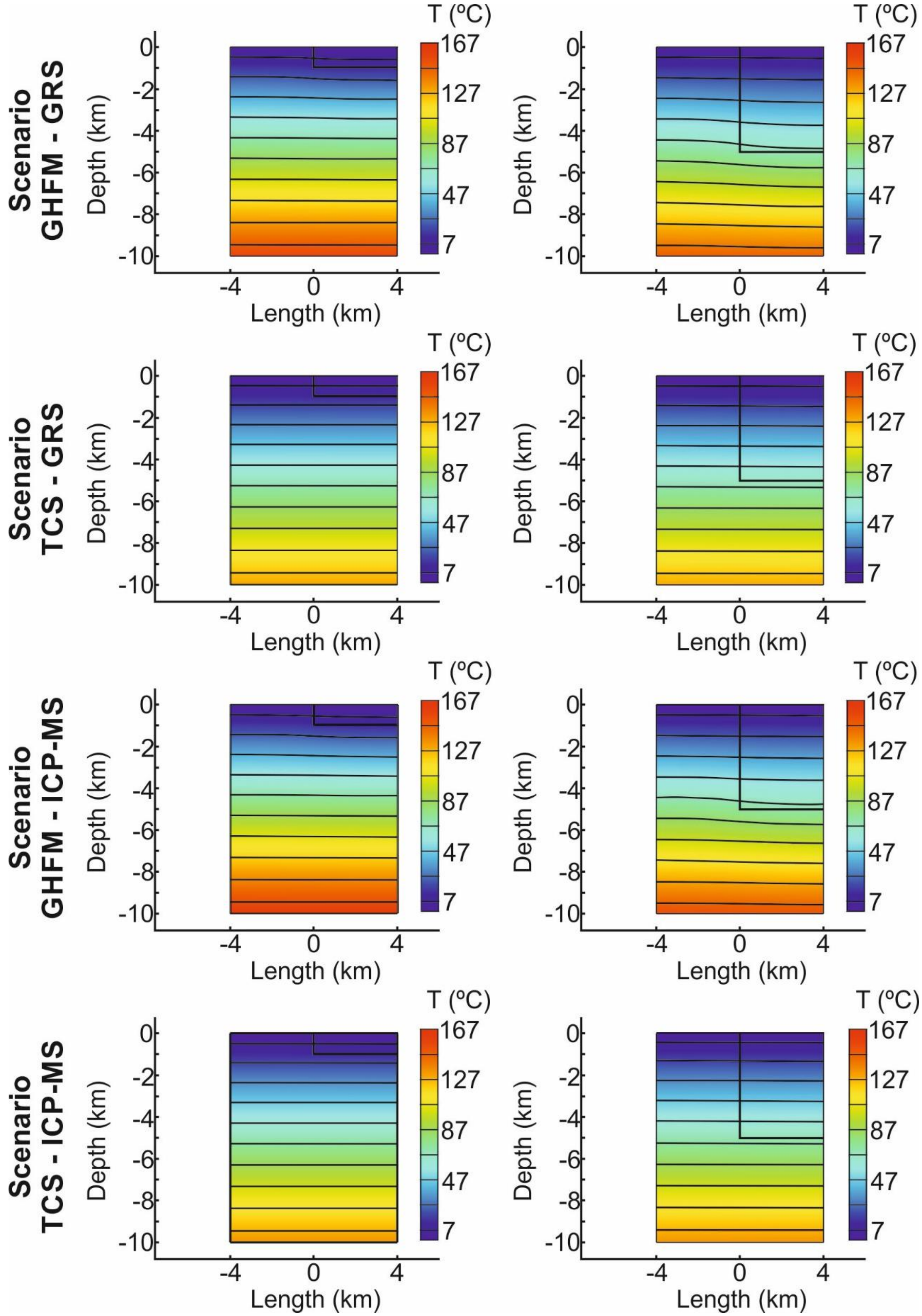

Figure 2.7 **2D steady-state simulations of the present-day temperature distribution at depth.**

Pleistocene climate events appear to have disturbed the temperature in the shallower part of the crust by up to 4.5 °C when considering Equation (2.7) to correct the simulated temperature profiles (Figure 2.8). At 5 km depth, the influence of the thermal perturbation induced by the GSTH becomes minimal with correction factor up to 1 °C. However, this correction is dependent on the assumed temperature steps between climate events (Figure 2.8). For example, considering the glacial episodes with a temperature of 10 °C lower than nowadays, the necessary correction is 1 °C. However, a temperature difference of 1 °C for the glacial episodes leads to a correction factor of 0.03 °C (Figure 2.8).

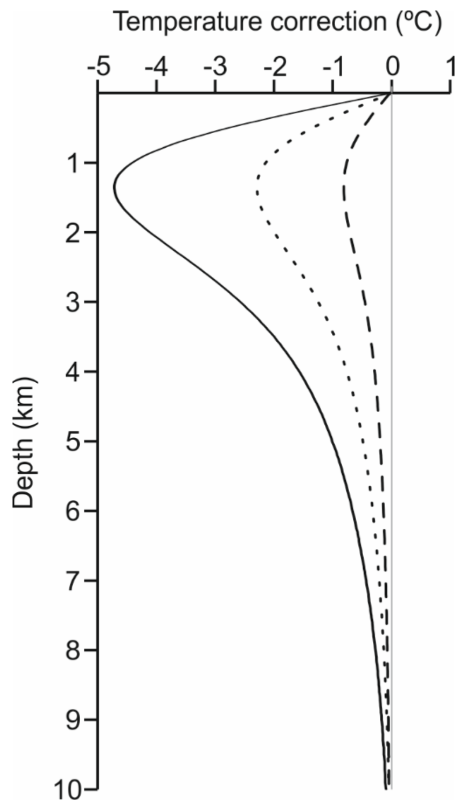

Figure 2.8 **Subsurface temperature perturbation caused by Pleistocene climate events. Solid line — temperature during glacial episode assumed as 10 °C colder than today; pointed line — temperature during glacial episode assume 5 °C colder than today; dashed line — temperature during glacial episode 1 °C colder than today.**

2.5 Discussion

2.5.1 Thermal properties

The thermal conductivity of the different lithologies (Table 2.2) is within the values presented in the database of Schön (2011 and references therein) and Eppelbaum et al. (2014 and references therein). Moreover, the thermal conductivity results are in accordance with the mineralogical composition of the rock samples. Specimens with a higher percentage of quartz minerals, i.e., tonalite–granite group, reveal higher thermal conductivity (3.1 to 3.3 W m^{-1} K^{-1}; Table 2.2) than the samples with lower content in quartz (paragneiss and igneous mafic group; Table 2.2).

Two methods were applied to evaluate the thermal conductivity: steady state (GHFM) and transient (TCS). The average *MRE* between the two methods is -9.8% for all lithologies (Table 2.2; Figure 2.5). Giordano et al. (2019b) compared the same methods using a different dataset and obtained a mean absolute value of the relative error of 9.8%, ranging from a minimum value of 1.7% to a maximum of 23.1%. These authors proposed that the differences can be caused by sample preparation and inherent heterogeneity associated with the rock itself, rather than the intrinsic accuracy of the device. It should also be noticed that the transient method is to evaluate the thermal conductivity on a larger sample length but on a smaller volume than the steady-state method. For the latter, a volume of rock sample of 2.4 to 1.6×10^{-3} cm^3 was used. Taking into account the results of this work, both steady-state and transient methods can be compared together to avoid a biased evaluation of the thermal conductivity.

2.5.2 Radiogenic elements and heat production

Studies found in the literature mentioned that both gamma-ray and mass spectrometry should give similar results when evaluating the radiogenic elements concentration (Chiozzi et al., 2003; Zhu et al., 2017). However, we obtained *MRE* between -61 and 49% for U, -11 to 72% for Th and more than 60% for K. The standards for each method were analyzed before and during the analyzes to assure the calibration of both devices. These differences may be related to the analytical error of each method and to the low concentration of the radioisotopes common to Precambrian rocks. Few samples fell within the minimum detectable activity of gamma-ray spectrometry. The analytical error for gamma-ray spectrometry for the analyzed dataset is, on average, 6% for K, 35% for Bi and 21% for Tl. Regarding ICP-MS, the analytical error varies within 2 – 3%, increasing up to 30% if closed to the detection limit. However, the most appropriate method cannot be determined from the sole results of this work. A larger dataset including equilibrium temperature profile is needed to do so, but this falls outside of the scope of the present work. Moreover, even if ICP-MS technique has been reported as more accurate by six orders of magnitude than radiometric methods (Hou et al., 2008), the results obtained by the NaI(Tl) system (GRS) are better correlated with the range of values found for similar Canadian Shield rocks (e.g., Rolandone et al., 2002; Perry et al., 2006; Phaneuf et al., 2014). Additionally, the radiogenic heat production evaluated by the two laboratory methods is in accordance with the rock samples' geochemistry. An increase of both U and Th as a function of the SiO_2 content (Table 2.1) is observed. Based on these results, it can be highlighted that both methods must be compared together in order to prevent a misestimation of the internal heat generation, mainly in such old Precambrian rocks common to the Canadian northern regions.

2.5.3 Hydraulic properties

Porosity and permeability of the analyzed samples show low values, less than 6% and 10^{-19} m^2, respectively. These values justify the use of dry samples for the thermal conductivity analysis. A matrix permeability lower than 10^{-19} m^2 and a thermal conductivity in the range of 2.3 to 3.3 W m^{-1} K^{-1} (Table 2.2) constrain the heat transfer mechanisms naturally occurring in the subsurface to conduction-dominated. Taking into account the thermofacies concept proposed by Sass et al. (2012), the characterization of thermophysical properties confirms a petrothermal regime. According to Moeck (2014) classification, the study area is a conduction-dominated geothermal play of basement type. Therefore, technologies such as Engineered Geothermal Systems (EGS) and deep borehole heat exchangers (DBHE) are more adequate to exploit the geothermal resources. Permeability needs to be increased to induce advection and operate an EGS, while DBHE can be operated taking advantage of heat conduction only.

2.5.4 Temperature field at depth

The lack of subsurface geological knowledge (e.g., geophysical data, well logs) and detailed geochemical analyzes of the mineral phases makes it difficult to accurately constrain the thickness of the diorite – gabbro layer. However, the temperature simulations reveal that the influence of this layer is minimal (about 4%) when compared to the variability originating from the laboratory methods (12 – 14%) and the heterogeneity of each lithological unit (more than 50%).

The heat flux inferred at surface (Table 2.5) is within the range of typical values found in the Superior, Nain and Churchill geological provinces north of the 55th parallel (Figure 2.1). Nielsen Island and Camp Coulon are in the Superior geological province, while Kuujjuaq, Raglan and Asbestos Hill are in the Churchill province. Voisey Bay belongs to the Nain geological province. These few heat flux assessments suggest a value that is about 10 mW m^{-2} higher in the Churchill province than in Superior and Nain. This can be related with the age, structure and composition of the geological provinces (e.g., Jaupart et al., 2007). Within Churchill province, Raglan and Asbestos Hill are located in the Ungava orogen while Kuujjuaq is in the limit of Labrador Trough, where heat flux has never been assessed through borehole measurements. Based on the obtained results, both orogens appear characterized by similar heat flux values.

The evaluation of both thermal conductivity and radiogenic heat production is influenced by the laboratory method (Table 2.2, Table 2.3), which, consequently, induces variability on the predictions of the temperature field at depth (Table 2.6). Without deep boreholes to evaluate the prevailing temperature at depth, it is critical to consider this variability. For the Kuujjuaq dataset, TCS and GRS lead to lower temperature values at 5 km than GHFM and ICP-MS. In the former scenario, the base-case temperature ranges from 57 to 71 °C, whereas for the latter it varies between 68 and 88 °C (Table 2.6; Figure 2.7). This corresponds to a difference of about 18%. Nevertheless, the highest variability on the temperature prediction is undoubtedly caused by the intrinsic heterogeneous character of each lithological unit. Scenario GHFM – GRS presents the maximal value (77%) whereas TCS – ICP has the minimal variability (55%).

Surface temperature variations indeed disturbed the subsurface temperature at shallow depths, but their effect diminishes by about 80% at 5 km depth, becoming almost negligible (Figure 2.8). At such depths, the paleoclimate effect is minimal when compared with the uncertainty related to the analytical methods, or to the intrinsic heterogeneous character of each lithological unit. In the absence of borehole temperature data, the assumption of a constant surface temperature seems justifiable for a preliminary characterization of heat flux and subsurface temperature.

Considering the worst-case scenarios, the exploration of deep resources is nonviable (Figure 2.9a). Temperatures of 50 °C are predicted to be found at depths greater than 5 km. On the other hand, the best-case scenarios provide temperature estimates that are suitable for electricity generation representing an option for further exploration (Figure 2.9c). Assuming that the base-case scenarios are the most likely to occur, then direct heat production is the most logical option to develop geothermal energy in the community of Kuujjuaq (Figure 2.9b).

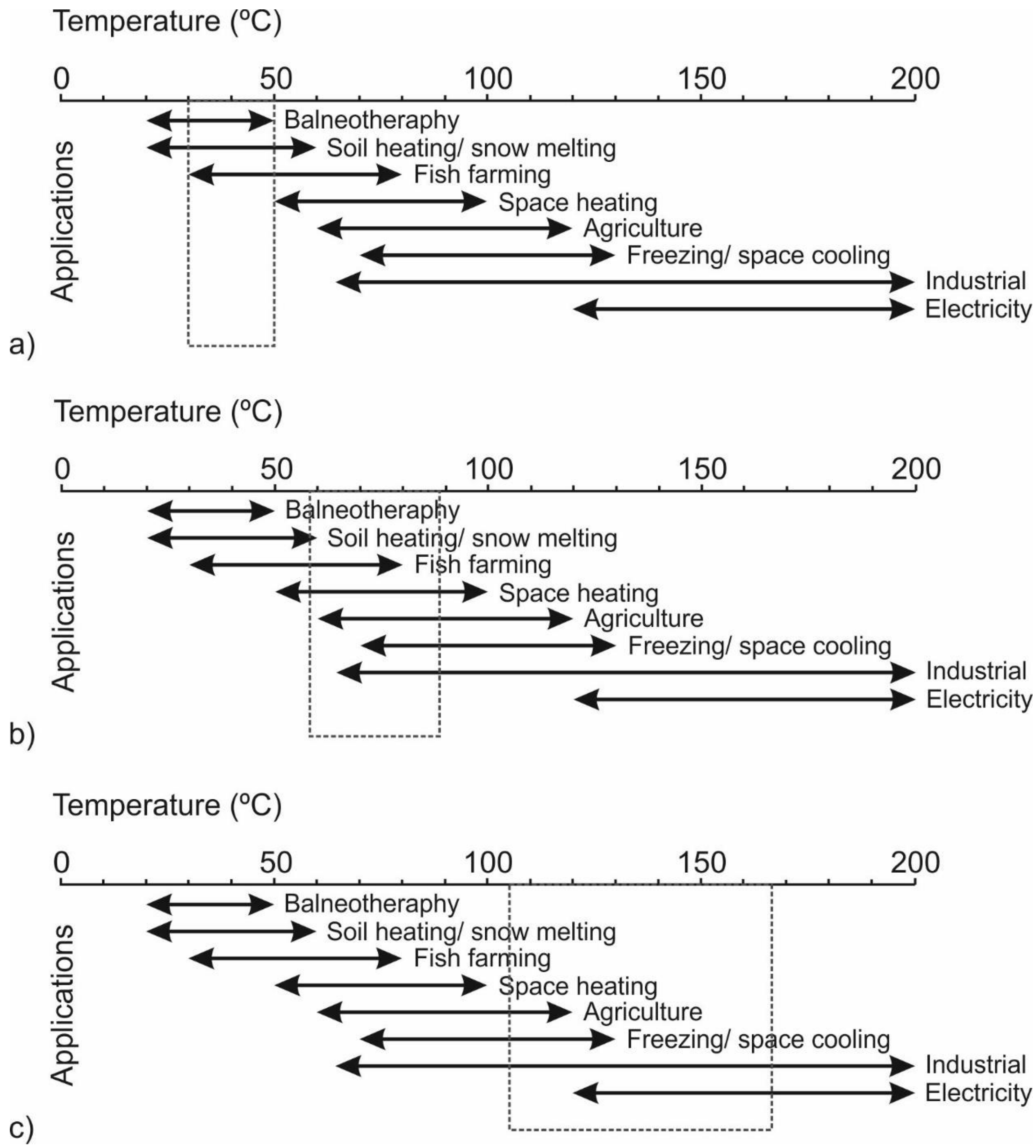

Figure 2.9 **Lindal diagram correlating geothermal resource temperature in Kuujjuaq with possible utilizations: a) worst-case scenario, b) base-case scenario, c) best-case scenario. The square highlights the temperature range at 5 km obtained by the different temperature simulations, adapted from Lindal (1973).**

An average drilling depth of 4 to 7 km is estimated to reach the temperature interval 50–100 °C (Table 2.7). This can have an impact on the potential geothermal project's rate since drilling cost increases nonlinearly with depth (e.g., Augustine et al., 2006). For example, in Nunavut territory, northern Canada, the drilling of a full-size production well can cost approximately $12 million USD for 4 km depth and up to $30 million USD if the well has a length of 8 km (e.g., Minnick et al., 2018).

Table 2.7 **Drilling depth to reach the temperature interval 50–100 °C.**

	Scenario GHFM – GRS		Scenario TCS – GRS		Scenario GHFM – ICP-MS		Scenario TCS – ICP-MS	
Diorite-gabbro thickness	1 km	5 km	1 km	5 km	1 km	5 km	1 km	5 km
Base-case scenario z (km)	3.5 – 6.5	4 – 7	4 – 8	4 – 8	3 – 6	3.5 – 7	4 – 7.5	4 – 8

This new evaluation of the temperature field at depth based on local rock sampling and outcrop analogues points towards potential development of deep geothermal resources for direct use. Moreover, this work demonstrates that the study of outcrop analogues is essential to build geothermal conceptual models, especially in remote areas away from locations with heat flow assessment. However, there is still an epistemic uncertainty in the temperature predictions that can only be overcome with deep temperature measurements. This is a key to advance to the stage of geothermal resource exploration.

2.6 **Conclusions**

The energetic framework of remote and off-grid communities in northern Canada, heavily relying on fossil fuels, needs to change. Geothermal energy is considered a potential solution, but a profound data gap exists. While it can be difficult to accurately define geothermal resources in such remote regions, the critical energy situation raises a key question that was addressed in Kuujjuaq. How can the depth and temperature of geothermal resources be evaluated when only surface data is available?

The guidelines drawn from the work conducted in Kuujjuaq are an example to other remote communities of Nunavik, Nunavut and Nunatsiavut facing the same energy development challenges. The estimation of the steady-state temperature field at depth requires an evaluation of the thermal conductivity and internal heat generation of the geological materials. In the lack of subsurface data, rock samples are collected from outcrop analogues. Often, the evaluation of the thermal conductivity is carried out either by steady-state or transient methods. Similarly, radiogenic heat production is usually estimated based on gamma-ray or mass spectrometry. The variability induced to the prediction of the temperature field at depth and originating from the laboratory methods was assessed in this study. The use of the four aforementioned methods indicates that thermal conductivity and radiogenic heat production are affected by laboratory analysis. The results revealed that thermal conductivity evaluated by TCS is 8% higher than by GHFM. Similarly, radiogenic heat production estimated based on ICP-MS results is, on average, 36% higher than based on GRS. This, consequently, influences the temperature predictions. In this case, the TCS combined with GRS gives lower base-case temperature predictions at depth, while upper base-case temperature predictions are found with the GHFM and ICP-MS. However, the variability induced by the laboratory methods is smaller (less than 15%) than the one resulting from the intrinsic heterogeneity of each lithological unit (more than 50%). The simulation TCS – ICP-MS reveals lower variability (55%) between the worst- and best-case scenarios when compared to GHFM – GRS (77%).

Regional geophysical data and local geological mapping are useful to build geological conceptual models, essential to carry out the temperature simulations at depth. The absence of local subsurface geological model is another source of uncertainty such that the thickness of the diorite – gabbro layer cannot be accurately constrained. Nevertheless, more detailed geochemistry analyzes on the mineral phases can overcome this data gap. Geobarometry allows to infer the pressure at which a mineral or mineral assemblage formed (e.g., Wendlandt, 1999; Mukherjee, 2011). If reasonable assumptions are made to convert pressure to depth, then, this methodology together with the erosion rate can help narrowing the range of possibilities for the present-day thickness of the diorite–gabbro layer (e.g., Burbank, 2002). Such analyzes were out of the scope of the present work but will be envisioned for further studies. However, as the simulations reveal, its influence on the temperature field is minimal (about 4%). In Kuujjuaq, the preliminary steady-state simulations reveal a base-case temperature varying between 57 and 88 °C at 5 km depth, pointing to a minimum drilling depth of 3 – 4 km to reach the necessary temperature to use the geothermal resources for space heating.

In conclusion, this work demonstrates that, even with the arising uncertainty due to the lack of subsurface temperature data and geophysical studies, it is possible to characterize the temperature of deep geothermal resources in remote regions. The study of outcrop analogues is essential to provide a reliable evaluation of the temperature conditions that can prevail in petrothermal systems hosted in ancient, here Precambrian, rocks. Further numerical modeling will address if deep enhanced geothermal systems are technically suitable to replace the fossil fuels consumption and provide higher energy security for the communities north of the 55^{th} parallel.

3 A NUMERICAL APPROACH TO INFER TERRESTRIAL HEAT FLUX FROM SHALLOW TEMPERATURE PROFILES IN REMOTE NORTHERN REGIONS

Une approche numérique pour déduire le flux de chaleur terrestre à partir des profils de température peu profonds dans les régions nordiques éloignées

Authors:

Mafalda M. Miranda (M.M.M.), Maria Isabel Velez Marquez (M.I.V.M.), Jasmin Raymond (J.R.)

Institut national de la recherche scientifique, Canada

Chrystel Dezayes (C.D.)

Bureau de recherches géologiques et minières, France

Journal title:

Geothermics

02 March 2021, Volume 93, article 102064

https://doi.org/10.1016/j.geothermics.2021.102064

Author's contribution:

Conceptualization, M.M.M., M.I.V.M., J.R. and C.D.; methodology, M.M.M., M.I.V.M. and J.R.; validation, M.M.M.; formal analysis, M.M.M.; investigation, M.M.M.; resources, M.M.M., M.I.V.M., J.R. and C.D.; data curation, M.M.M. and M.I.V.M.; writing – original draft preparation, M.M.M., J.R. and C.D.; writing – review and editing, M.M.M., J.R. and C.D.; visualization, M.M.M.; supervision, J.R. and C.D.; project administration, J.R.; funding acquisition, J.R.

Link between the previous article and the next:

The previous chapter provides the background information on the rock samples collected from outcrops in terms of main mineral phases, major, minor and trace geochemical elements, thermal properties and radiogenic heat production. It also discusses how different laboratory techniques to evaluate thermal conductivity and radiogenic elements introduce variability on heat conduction models. Moreover, a preliminary evaluation of the terrestrial heat flux based on a "bottoms-up" approach was carried out. However, such methodology requires a deep knowledge of the local crustal composition from Moho discontinuity to the surface for an accurate assessment. An evaluation based on regional literature data introduces uncertainty and may lead to misestimations. Therefore, in this chapter, a numerical approach was developed to infer terrestrial heat flux from temperature profiles measured in shallow boreholes, such as groundwater monitoring wells with 80 m depth. The method described in the previous chapter is useful if only surficial rock samples are available to carry out a preliminary evaluation of the deep geothermal energy potential. However, if a borehole exists and in good conditions for temperature measurements, then, the assessment can be complemented with the methodology described in this chapter. Furthermore, the terrestrial heat flux assessed on the previous chapter provides the initial values to carry out the numerical simulations discussed in this chapter. The previous chapter also indicates the depth-distribution of the paleoclimate effects, helping to define the total length of the temperature profile simulated in this chapter.

Graphical abstract:

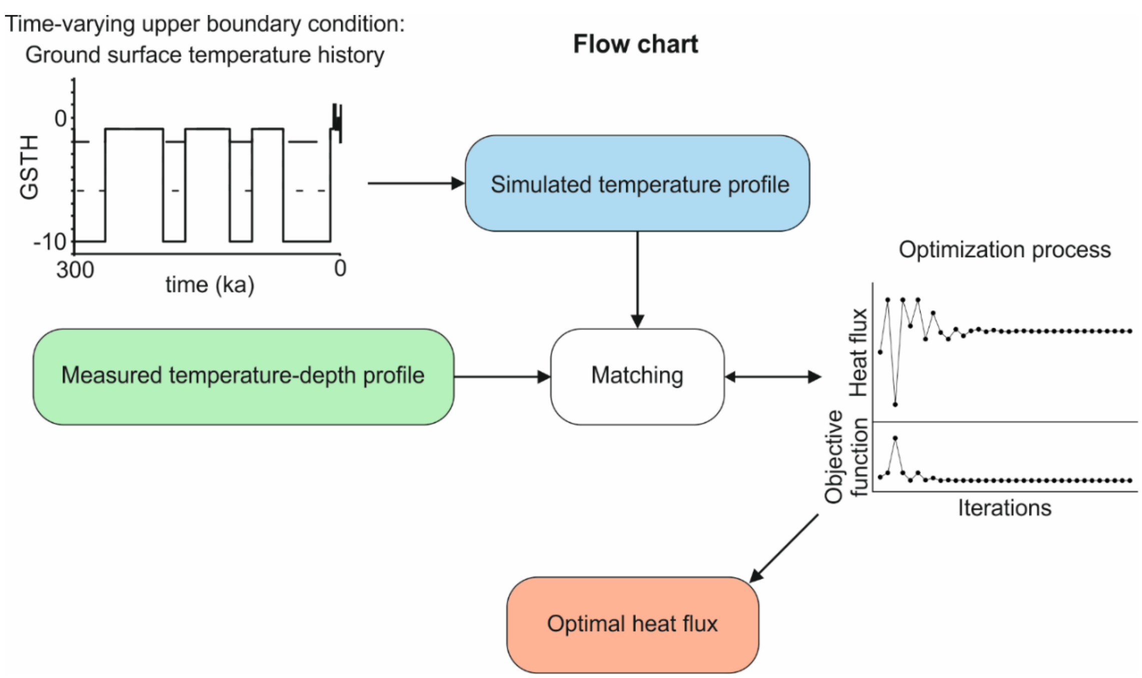

3.1 Introduction

Heat flux, together with the thermophysical properties of the geological materials and the geothermal gradient, plays a major role in the evaluation of the subsurface temperature and, hence, in assessing the geothermal potential of a target area (e.g., Bédard et al., 2018; Gascuel et al., 2020). Two main methods have been developed to infer heat flux from temperature-depth (T-z) profiles: the interval/product method and the Bullard method (e.g., Powell et al., 1988; Jessop, 1990; Beardsmore et al., 2001). However, the application of these methods implies T-z profiles that are deep enough to observe the linear increase in temperature with depth and that are corrected for both artificial and natural disturbances (e.g., drilling, true-vertical depth, free thermal convection, groundwater flow, topography, climate change, etc.; Powell et al., 1988; Jessop, 1990; Beardsmore et al., 2001). Neglecting the corrections for these features, mainly topography and climate, may lead to important misestimations of heat flux (Powell et al., 1988; Jessop, 1990; Beardsmore et al., 2001). For example, ignoring the effects of paleoclimate has been shown to underestimate the heat flux by 10% or more (e.g., Birch, 1948; Crain, 1968; Jessop, 1971; Beck, 1977; Beck et al., 1989; Majorowicz et al., 2011; Westway et al., 2013; Suman et al., 2017; Bédard et al., 2018; Mather et al., 2018). This is due to the downward diffusion of the surface temperature variations with larger amplitudes and duration than daily or annual cycles (Jessop, 1990; Beardsmore et al., 2001; Bodri et al., 2007). Solutions to quantitatively correct paleoclimate effects and to reconstruct the ground surface temperature history (GSTH) have received attention since the first observations of the impact of climate events on T-z profiles (e.g., Birch, 1948; Crain, 1969; Clauser, 1984; Nielsen et al., 1989; Mareschal et al., 1992; Shen et al., 1992; Huang et al., 1996; Harris et al., 1998). However, the application of such methods to invert both the heat flux and the GSTH requires a temperature profile that is deep, at least 300 m, to reach a depth were paleoclimate perturbations are less important (e.g., Beltrami et al., 2011). In remote territories, where only shallow boreholes are available (e.g., boreholes drilled for groundwater monitoring), a different methodology is needed to provide a first reliable estimate of heat flux and justify further work to drill deep geothermal exploration boreholes. Therefore, a numerical approach was developed in this work to correct a shallow temperature profile for past and recent surface temperature variations and, thus, infer the present-day heat flux. The approach is based on the work of Velez Marquez et al. (2019) and has been improved to numerically consider both quaternary glaciations and Holocene climate events as an upper boundary condition to the model. The method was used to infer heat flux in the community of Kuujjuaq (Nunavik, Canada) where a temperature profile was measured in a groundwater monitoring borehole having 80 m depth that has been drilled prior to this study. The present numerical approach does not address topography effect since changes in surface elevation in the study area are negligible, neither groundwater advection effect since no groundwater flow perturbation was detected in the temperature profile. Moreover, it does not deal with sedimentation and/or erosion through time that affect the surface and induce terrain effect. Furthermore, the present study does not intend to reconstruct the GSTH since the temperature profile measured is unfortunately too shallow to carry out such reconstructions. The goal of this work is to provide a tool for a first-order assessment of the present-day terrestrial heat flux by numerically correct a shallow temperature profile for literature-based surface temperature variations considering heat conduction only. The idea is to provide new geothermal exploration methods using means that are affordable to remote communities and adapted to northern regions facing data gap challenges, trying to advance geothermal exploration to the benefit of the indigenous population.

The heat flux is solved numerically with the finite element method (FEM) as a 1D inverse heat conduction problem (IHCP), considering known transient surface temperature and thermophysical properties. A shallow T-z profile acquired during a field campaign is used to find the control variable, i.e. the heat flux at the base of the model, that minimizes the objective function. In other words, the goal is to find the heat flux for simulated temperature to best match measured temperature. An arising problem of carrying out climate corrections is linked with the imperfect knowledge about the duration and temperature of each Pleistocene event. Flint (1947) and Emiliani (1955) proposed a fourfold chronology for the Quaternary glaciations that has been used by Jessop (1971) and Jessop (1990) to correct heat flow measurements in Canada. The same chronology has been used, for instance, by Bédard et al. (2018) and Velez Marquez et al. (2019) to correct T-z profiles in southern Québec. Although more recent literature proposes a different timeframe with the beginning and end of the glaciations at an older time (e.g., Ehlers et al., 2011; Jennings et al., 2013), the same fourfold stratigraphic framework was used in this work for the numerical simulations. The basal temperature during a glaciation episode can vary regionally. For instance, the surface temperature during the last glacial maximum (LGM) has been evaluated 10 ºC colder than present in eastern Canada, while in central Canada studies point 5 ºC, or less, colder than current times (e.g., Sass et al., 1971; Sugden, 1977; Mareschal et al., 1999; Rolandone et al., 2003; Chouinard et al., 2009; Majorowicz et al., 2012b; Majorowicz et al., 2015c; Pickler et al., 2016b). Hence, a sensitivity analysis was undertaken to assess the impact of the different temperature signals during glacial periods on the heat flux estimate. Moreover, an extensive literature review was carried out to define the timeframe and temperature of the major Holocene events that can influence the subsurface temperature. Additionally, the effect of temperature, pressure and water-saturation on thermal conductivity was considered and implemented in the numerical model. These thermal conductivity conditions have been shown to influence the heat flux (e.g., Lerche, 1991; Nasr et al., 2018; Harlé et al., 2019; Förster et al., 2020; Norden et al., 2020). Furthermore, the influence of the statistical distribution of the thermophysical properties on heat flux cannot be neglected (Miranda et al. 2020a) and this uncertainty was considered in the numerical model as well.

The methodology described in this work was used to estimate heat flux in the context of geothermal energy sources assessment. In northern Canada, 239 remote communities spread over a territory of more than 3 500 000 km^2 rely exclusively on diesel fuel for electricity and oil for space heating (Arriaga et al., 2017). This unsustainable energetic framework needs to change and local and clean source of energy, such as geothermal, might be a solution (Majorowicz et al, 2010a; Majorowicz et al., 2010b; Grasby et al., 2012; Grasby et al., 2013; Majorowicz et al., 2014b; Majorowicz et al., 2015a; Minnick et al., 2018; Giordano et al., 2019a; Kanzari, 2019; Kinney et al., 2019; Gunawan et al., 2020; Mahbaz et al., 2020; Majorowicz et al., 2020). However, a large data gap exists in such remote areas. For example, in Nunavik, a 507 000 km^2 territory, only 3 locations have boreholes deep enough to evaluate heat flux in a conventional manner: Raglan mine, Asbestos Hill mine and Coulon exploration camp, and these lie at a distance of approximately 420 km (camp Coulon) to 500 km (Raglan mine and Asbestos Hill mining sites) from Kuujjuaq (Figure 3.1). Two other deep boreholes, one in Nunavut (Nielsen Island; Figure 3.1) and another in Newfoundland and Labrador (Voisey Bay; Figure 3.1), are also located around 500 km and 430 km, respectively, from Kuujjuaq.

This data gap highlights the need to adapt methodologies for the data sources that are available in a small radius (< 4 km) from the northern remote communities. The numerical approach described was applied to Kuujjuaq (Nunavik, Canada) as a case study, but is versatile enough to be utilized in other remote northern communities facing the same data gap and geothermal exploration challenges.

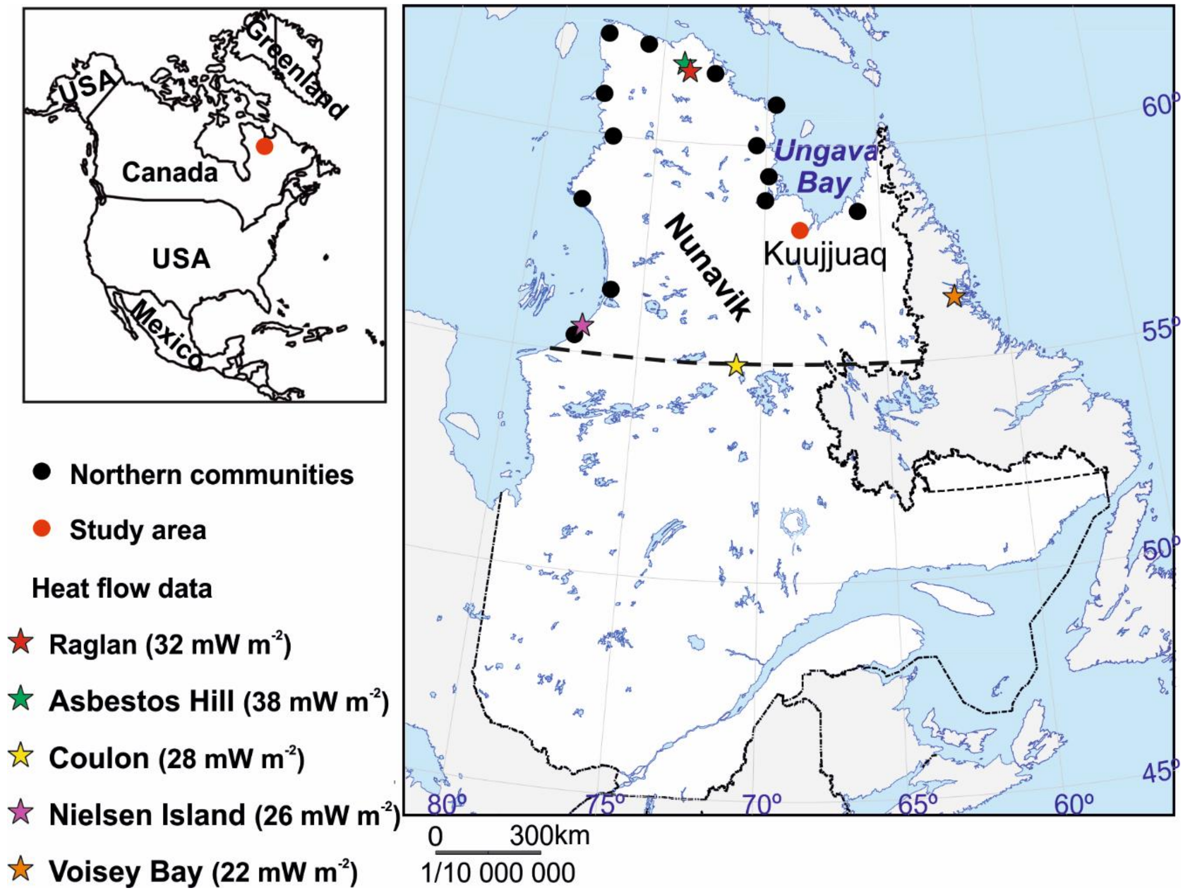

Figure 3.1 **Geographical location of the community of Kuujjuaq and remaining communities of Nunavik (Canada) and of the heat flow assessments: Raglan (Perry et al., 2006) and Asbestos Hill mining sites (Taylor et al., 1979; Drury, 1985), Camp Coulon (Lévy et al., 2010), Nielsen Island (Jessop, 1968) and Voisey Bay (Mareschal et al., 2000), redrawn from Miranda et al. (2020a).**

3.2 Geological setting

The Inuit community of Kuujjuaq is the administrative capital of Nunavik and home for more than 2 500 inhabitants (Figure 3.1). The study area (Figure 3.2) is located in the Southeastern Churchill geological province of the Canadian Shield (e.g., Wardle et al., 2002). The main lithological units outcropping are paragneiss and diorite. The former has been sampled in the framework of this study (Figure 3.2). The paragneiss unit is Neoarchean and the diorite unit is Paleoproterozoic in age (SIGÉOM, 2019). A detailed description of these units and of the samples collected can be found in Miranda et al. (2020a and references therein). The two main geological structures present are Lac Pingiajjulik and Lac Gabriel faults (Figure 3.2). Both are described as regional thrust faults with dextral movement (SIGÉOM, 2019).

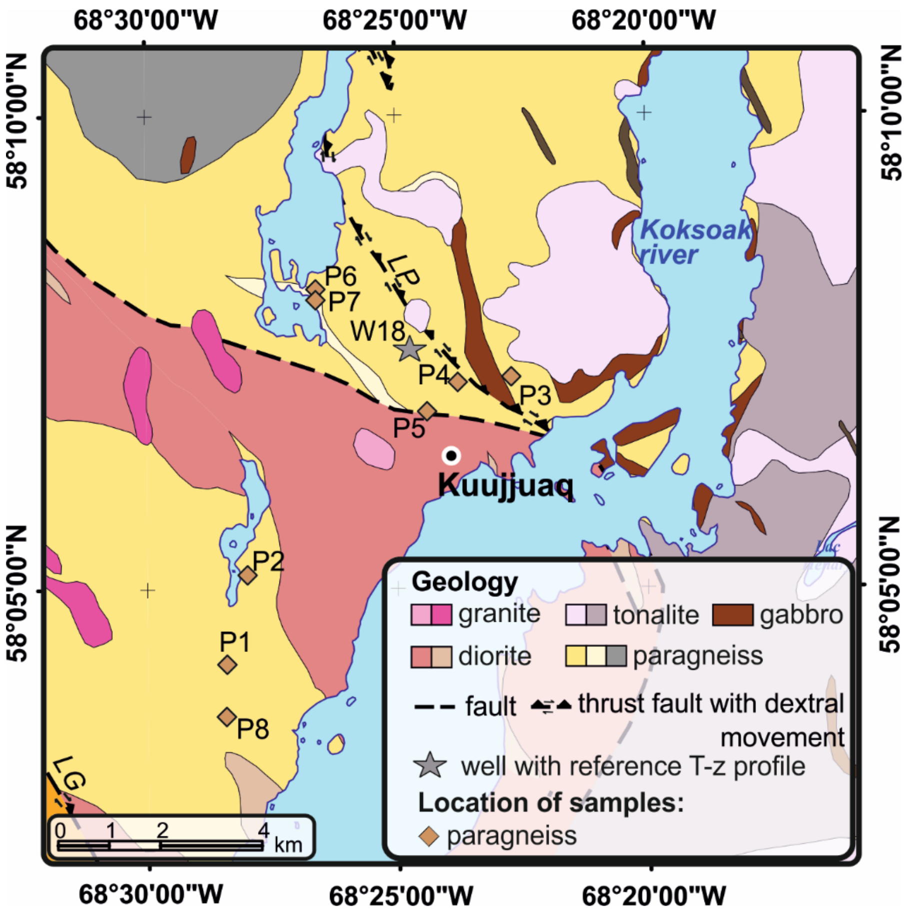

Figure 3.2 Geological map of the study area. *LP* – Lac Pingiajjulik fault, *LG* – Lac Gabriel fault, P- paragneiss, W18 – well with reference T-z profile, adapted from SIGÉOM (2019) and Miranda et al. (2020a).

The W18 well was drilled with the scope of groundwater monitoring at least five years before this study has been undertaken. Moreover, the well is not artesian, and neither is disturbed by drilling effect or pumping. Unfortunately, no drilled core is available to carry out thermophysical properties analyzes. The altitude in the area range between a minimum of 1 m at the Koksoak river and a maximum of approximately 125 m at the tonalite outcropping units. The W18 well was drilled in an area of flat topography where the altitude is approximately 47 m. Thus, topography corrections on heat flux assessment were neglected due to this weak topographic variation.

The intercepted geological units were interpreted based on electrical resistivity tomography (ERT) profiles carried out close to the wells (Giordano et al., 2017). These indicate that 40 m of Quaternary sediments overlies the bedrock made of paragneiss. This information was used to build the geometry of the 1D numerical model. The marine deposits found in the first 20 m of the interpreted stratigraphic succession are composed of unconsolidated sediments and believed to have been deposited during the Iberville sea marine transgression (Allard et al., 1989; Fortier et al., 2011). In Kuujjuaq, the marine elevation limit of the Iberville sea reached approximately 185 m (Lauriol, 1982). The 20-m-thick glacial till encountered below the marine deposits are also believed to be associated with the marine transgression (e.g., Dubé-Loubert et al., 2015). The Iberville sea transgression is synchronous with the last glacial ice sheet regression around 7500 to 7000 years before present (B.P.) in Ungava (Gray et al., 1980; Allard et al., 1989). Following the ice sheet retreat, crustal rebound due to glacio-isostatic relaxation has taken place (Gray et al., 1980). On the Ungava Bay west shore, for instance, 75-85% of the total postglacial uplift occurred between 7 and 5 ka B.P. at an average rate of 4-5 cm per year (Gray et al., 1980). The remaining 15-25% over the subsequent 5 ka at an average rate of 0.3-1 cm per year (Gray et al., 1980). Mean uplift rates around 0.6 m per century have also been referred (Lauriol, 1982). This postglacial rebound led to the uplifting of the marine deposits that were consequently eroded and colonized by vegetation (Fortier et al., 2011). The thickness of the eroded material was roughly estimated as about 138 m at an erosion rate of 2 cm per year, considering 7 ka of postglacial rebound.

3.3 Inverse heat conduction problem

The aim in direct heat conduction problems is to determine the temperature distribution within the medium by prescribing a set of known boundary and initial conditions, internal heat generation rate and thermophysical properties of the geological materials (e.g., Özisik, 1993). A pair of boundary conditions is conveniently defined by setting the temperature *T* (ºC) as the upper boundary condition and the heat flux *Q* (W m^{-2}) as the lower boundary condition. The initial condition specifies the temperature distribution *T*(z) in the medium at time zero. However, if one condition is unknown, finding its solution becomes an inverse problem (e.g., Beck et al., 1985; Özisik, 1993; Alifanov, 1994; Taler et al., 2006; Özisik et al., 2017).

The mathematical formulation of such IHCP with unknown basal heat flux is given by:

$$\frac{\partial}{\partial z}\left(\lambda \frac{\partial T}{\partial z}\right) + RHP = \rho c \frac{\partial T}{\partial t} \quad \text{in} \quad 0 < z < z_\mathrm{n}, \quad 0 < t \le t_\mathrm{n} \tag{3.1a}$$

$$-\lambda \frac{\partial T}{\partial z} = q = ?\,(\text{unknown}) \quad \text{at} \quad z = z_\mathrm{n}, \quad t = t_\mathrm{n} \tag{3.1b}$$

$$T = T(t) \quad \text{at} \quad z = 0, \quad 0 < t \le t_\mathrm{n} \tag{3.1c}$$

$$T = T(z) \quad \text{for} \quad t = 0, \quad \text{in} \quad 0 \le z \le z_\mathrm{n} \tag{3.1d}$$

where z (m) is the spatial variable and t (s) is time. The variables λ (W m^{-1} K^{-1}), *RHP* (W m^{-3}), ρc (J m^{-3} K^{-1}) are thermal conductivity, radiogenic heat production and volumetric heat capacity, respectively. The subscript n stands for final.

Since thermal conductivity is temperature-dependent, the IHCP becomes nonlinear (Beck, 1970; Beck et al., 1985). A time-varying upper boundary condition (Equation 3.1c) is imposed to represent the GSTH and the initial condition (Equation 3.1d) is given by the analytical solution of Equation (3.1a) in steady state:

$$T(z) = T_0 + \frac{q_0}{\lambda} z - \frac{RHP}{2\lambda} z^2 \tag{3.2a}$$

$$q_0 = q_{z_n} + RHP \times z_n \tag{3.2b}$$

where subscript 0 stands for surface.

The inverse problem stated above was solved through mathematical optimization. The least-squares method is applied to find the unknown heat flux by minimizing the sum of squared differences between measured and simulated temperature. A directional search derivative-free algorithm was used in this work to find the optimal heat flux while the heat diffusion simulations described with Equation (3.1a) were solved numerically with the FEM.

3.3.1 Upper boundary condition

The fourfold stratigraphic framework proposed by Flint (1947) and Emiliani (1955) to characterize the late Pleistocene (300 – 11.6 ka B.P.) climate events was adopted in this study. Although each glacial and interglacial episode is composed by several substages, these were not considered in this study. Instead, a constant temperature during each glacial and interglacial period was assumed (Birch 1948; Crain 1967; Jessop 1990). This is a simple approximation that can be further improved. The temperature at the base of the Laurentide Ice Sheet (LIS) is still debatable. GSTH inversion from deep T-z profiles in Canada points towards an average temperature of -5 ºC during the LGM, though lower temperatures were simulated in eastern Canada than in central Canada (e.g., Sass et al., 1971; Sugden, 1977; Mareschal et al., 1999; Rolandone et al., 2003; Chouinard et al., 2009; Majorowicz et al., 2012b; Majorowicz et al., 2015c; Pickler et al., 2016b). During the LGM, the LIS reached a maximum thickness higher than 3 km (Peltier, 2002; Peltier, 2004) and may suggest that under such thick ice the temperature was close to the freezing point (-1 to -2 ºC; Jessop, 1971; Jessop, 1990).

Furthermore, permafrost studies also suggest that the base of the ice sheet above subarctic Quebec was roughly at the melting temperature (Allard et al., 1987).

The Holocene epoch is composed by several substages that, contrarily to the Pleistocene, were considered within the GSTH reconstruction. The interglacial Holocene thermal maximum occurred *ca.* 7 – 5.8 ka B.P. (Renssen et al., 2012; Gajewski, 2015; Richerol et al., 2016 and references therein) and is referred to have been 1 – 2 ºC warmer than the present-day temperature (Dahl-Jensen et al., 1998; Kaufman et al., 2004; Renssen et al., 2012; Gajewski, 2015). The temperature during the interstadial Roman and Medieval warm periods (*ca.* 3.2 – 1 ka B.P.; Richerol et al., 2016 and references therein) were estimated to have been 1 – 1.5 ºC warmer than at present (Dahl-Jensen et al., 1998; Easterbrook, 2016). During the stadial Little Ice Age (*ca.* 500 – 270 years B.P.; Richerol et al., 2016 and references therein), the temperature is estimated to have been 1 ºC lower than today (Cermak, 1971; Dahl-Jensen et al., 1998). Majorowicz et al. (2005) and Chouinard et al. (2007) identified a warming of about 1.4 – 2 ºC during the pre-industrial and industrial revolution (*ca.* 270 – 80 years B.P.). This episode was followed by a short cooling episode (80 – 30 years B.P.), where temperature decreased around 0.4 ºC (Chouinard et al., 2007). Nowadays, meteorological data (ECCC, 2019) can be converted empirically to undisturbed ground surface temperature following the relation proposed by Ouzzane et al. (2015):

$$T_{\mathrm{g}} = 17.898 + 0.951T_{\mathrm{amb}} \tag{3.3}$$

where T (K) is temperature and the subscripts g and amb are used for ground surface and surface air temperature, respectively.

Ouzzane et al. (2015) developed two different empirical correlations. One is a function of surface air temperature, wind velocity, global solar radiation on a horizontal surface and sky temperature. This equation revealed the surface air temperature as the dominant parameter on the undisturbed ground surface temperature. Thus, these authors developed a second simplified empirical correlation that is only a function of the surface air temperature (Equation 3.3). However, these authors did not consider the precipitation character and the duration of snow cover that can influence the relation between mean annual surface air temperature and ground surface temperature (Cermak, 1971). Nevertheless, Equation (3.3) provides a first-order approximation to convert meteorological data into undisturbed ground surface temperature. The application of this empirical correlation in Kuujjuaq revealed a sharp increase on the temperature of about 2 ºC for the last 30 years (Figure 3.3). Moreover, this correlation allowed to infer the reference undisturbed ground surface temperature based on temperature from climate normal of the 1981-2010 period (ECCC, 2019). The value is -1 ºC (Figure 3.3).

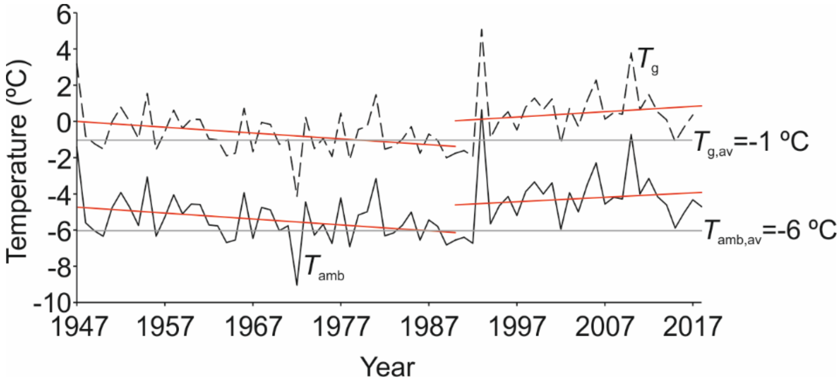

Figure 3.3 Annual average surface air and ground surface temperature in Kuujjuaq. Surface air temperature from meteorological data (ECCC, 2019). Ground surface temperature estimated based on Ouzzane et al. (2015) relation. Red lines – annual average temperature trend lines between 1947-1990 and 1990-2018. Black solid line – annual average surface air temperature, black dashed line – annual average ground surface temperature.

3.3.2 Mathematical optimization

The formulation of the optimization problem in this study is (e.g., Allaire, 2007):

$$\begin{cases} \min_{\mathrm{q}} O_{\mathrm{f}}(q) \\ lb_{\mathrm{q}} \leq q \leq ub_{\mathrm{q}} \end{cases} \tag{3.4}$$

where O_f is the scalar-valued objective function, *lb* and *ub* stand for lower bound and upper bound, respectively.

These are inequality constraints on the control variable degree of freedom (i.e., heat flux). No other constraints were used. The least-squares method was chosen as objective function since the eight standard statistical assumptions are met (Beck et al., 1977). The optimal heat flux is found by minimization of the sum of the squared residuals:

$$q_{\text{optimal}} = \sum[T_{\text{measured}} - T_{\text{simulated}}]^2 \tag{3.5}$$

where T_{measured} is the measured T-z profile, while $T_{\text{simulated}}$ represents the model function holding the constrained range of control variables to simulate.

Direct search derivative-free algorithms were applied to sample the objective function at each iteration and find its minimum within the degree of freedom imposed to the control variable (Equation 3.4). Such algorithms do not have any explicit or implicit derivative approximation (contrarily to gradient-based algorithms), so the descent towards the optimal value is solely based on the scalar-valued objective function (e.g., Conn et al., 2009). The algorithms are based on function comparison and move in the direction away from the worst value. The Nelder-Mead algorithm (Nelder et al., 1965) was selected after testing different methods to solve the inverse optimization problem stated above. The method tracks the optimal control variable by function comparison at the vertices of a simplex. Firstly, the simplex is expanded to the defined upper bound of the control variable (ub_q; Equation 3.4). Then, it tries the lower bound (lb_q; Equation 3.4) by reflection. A series of reflections and contractions take place by vertex replacement until the scalar value of the objective function is minimal (i.e., the optimal heat flux) and the stopping parameters are reached (Figure 3.4).

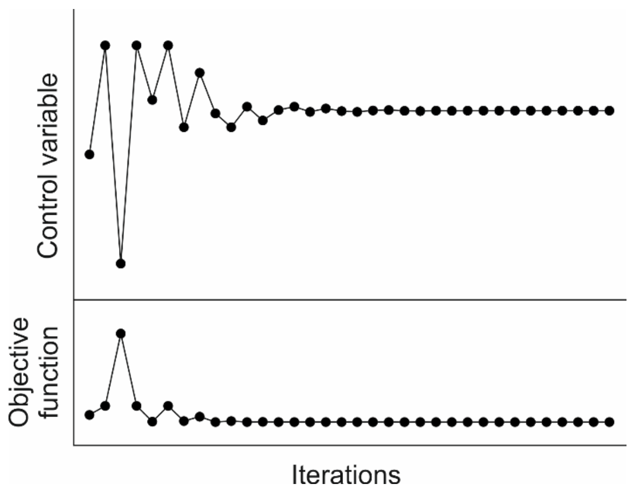

Figure 3.4 Example of the optimization process.

3.4 Methodology

3.4.1 Temperature surveys

Three groundwater monitoring wells exist within the area of the community of Kuujjuaq. However, two of these wells were artesian and, thus, showed a temperature profile influenced by groundwater flow and advective heat transfer. Moreover, one of these artesian wells only reached 44 m. Only well W18 revealed a temperature profile characteristic to heat conduction. Further details on these three temperature profiles are given in Miranda et al. (2018a). The T-z profile was measured in a groundwater well in Kuujjuaq using a submersible temperature and pressure data logger (RBRduet) with an accuracy of ± 0.002 ºC and ± 0.25 cm. This well has been drilled prior to this study, it is not artesian and has no pump installed. Thus, the temperature was recorded under equilibrium conditions. Moreover, the probe was inserted in the well about 20 min before the beginning of the recording to ensure the thermal equilibrium between the probe and the groundwater in the well. The temperatures were then recorded in a continuous temperature logging pace of 1 m per 10 seconds. A total of 6 depth calibrations were made along the profile by correlating the pressure measurements with the exact depth measured with the wire. As the well shows a slight inclination (less than 20º), a true vertical depth correction was made.

3.4.2 Thermophysical properties

3.4.2.1 Measurement methods

A total 24 rock samples were collected from outcrops in the study area, in which 8 correspond to the paragneiss unit, 5 to the diorite unit, 4 to the gabbro unit, 4 to the tonalite unit and 3 to the granite unit (see Miranda et al., 2020a for further details). Of these, only the 8 rock samples belonging to the paragneiss unit (Figure 3.2) were used in this study, since it is the relevant lithology for the present work. Furthermore, the evaluated inhomogeneous factor for these samples ranges from a minimum of 0.068 to a maximum of 0.443, indicating their quasi-homogeneous character. Unfortunately, no core is available from the groundwater monitoring well to carry thermophysical properties analyzes. The rock sampling took into account the spatial distribution of the outcrops (Figure 3.2) and the textural, fabric and mineralogical variability of the lithological unit of interest (see Miranda et al., 2020a for further details on the rock samples characterization). Hand samples were initially analyzed for thermal conductivity and diffusivity with an optical scanner (TCS method) after a black-silicone scanline was painted on a smooth surface. Core plugs with 20-mm-radius and 20 to 30-mm-thickness were drilled from the hand samples and analyzed for thermal conductivity and volumetric heat capacity with a guarded heat flow meter (GHFM). The evaluation was undertaken at both dry and water-saturation state. For the latter, the samples were placed in a vacuum chamber and immersed in water for 24 h. Additionally, porosity was evaluated with a combined gas permeameter-porosimeter (CGPP).

Thermal conductivity and volumetric heat capacity of the geological materials evaluated in the laboratory using a FOX50 from TA Instruments (GHFM technique) and a TCS from LGM Lippmann were compared. The application of both methods is advisable to avoid biased results (cf. Miranda et al., 2020a). Both devices have an accuracy of 3% reported from the manufacturers. Analyzes with the former method are made when the temperature across the sample reaches the steady state. For thermal conductivity, a temperature difference of 10 °C is imposed on each plate. For volumetric heat capacity, in turn, both plates are set with the same temperature, but two runs are necessary, one at lower temperature and other at higher. Successive data acquisition cycles grouped in blocks are run until all the necessary equilibrium criteria are reached and the sample is considered in thermal equilibrium. A preliminary evaluation of the accuracy of the GHFM was undertaken by analyzing a pyrex standard provided by the manufacturer. The results reveal a difference of 3.6% between the analyzed and certified value. The TCS technique evaluates thermal conductivity and thermal diffusivity transiently based on solutions for the heat conduction in a quasi-stationary temperature field with a movable coordinate system (Popov et al., 2016). Two gabbro standards provided by the manufacturer are placed in series with the sample under analysis. The unknown thermal conductivity of the sample is evaluated based on the thermal conductivity of the two standards and the temperature difference recorded by the temperature sensors. Furthermore, thermal conductivity was evaluated at a sampling interval of 0.1 mm in a straight line along the whole length of the sample surface (longer than 10 cm) and three analyzes per sample were done to ensure reproducibility (less than 4% difference was inferred).

The concentration of the naturally occurring radioisotopes ^{238}U, ^{232}Th and ^{40}K was determined by gamma-ray spectrometry (GRS) and inductively coupled plasma - mass spectrometry (ICP-MS) to avoid biased results (cf. Miranda et al., 2020a). The Ortec GRS detector used for this purpose is NaI(Tl) with 7.62 × 7.62 cm, surrounded by a 5-cm-thick lead shield. The concentration of the radioisotopes was measured using the three-window method taking into account the emitted gamma-radiation. The system is calibrated with standard solutions certified by the International Atomic Energy Agency (IAEA). The ICP-MS method, where the chemical elements passed through a decomposition into their atomic constituents, was also used. The positively charged ions are extracted and separated, being finally measured by an ion detector. A quality control protocol was followed, and certified reference materials used to guarantee the reliability of the analyzes (see Miranda et al., 2020a for further description of both methods).

Radiogenic heat production was then calculated by applying Rybach's (1988) empirical function:

$$RHP = 10^{-5}\rho(9.51[U] + 2.56[Th] + 3.50[K]) \tag{3.6}$$

where ρ (kg m^{-3}) is the density and *[U], [Th]* and *[K]* are the concentrations of each element (U and Th in mg kg^{-1} or ppm and K in %).

A thin layer of Quaternary deposits was inferred at the borehole site by geophysical methods (ERT; Giordano et al., 2017). A total of 8 samples of marine sediments and 3 samples of glacial till were collected and their thermal properties evaluated with the transient line source technique (e.g., Bristow et al., 1994; Raymond et al., 2017). The thermal conductivity was evaluated with a needle probe using the infinite line source equation to analyze the heat injection experiments. Further details on the laboratory analyzes and description of the Quaternary sediments can be read in Kanzari (2019).

3.4.2.2 Effect of temperature and pressure on thermal conductivity

The GHFM was used to evaluate thermal conductivity of dry samples within the temperature range 20 ºC to 160 ºC. This allowed to define an experimental relationship to describe the effect of temperature on thermal conductivity of the rock samples. The linear relationship between temperature and thermal resistivity was used to fit the experimental data (e.g., Schatz et al.,1972):

$$\frac{1}{\lambda(T)} = \frac{1}{\lambda_{20}} + b(T-20) \Leftrightarrow \lambda(T) = \frac{1}{(\lambda_{20})^{-1} + b(T-20)} \tag{3.7}$$

where the coefficient *b* controls the temperature dependence of the thermal conductivity and the subscript 20 stands for room-temperature.

The effect of pressure on thermal conductivity was assessed indirectly from the pressure-dependence on porosity. The CGPP AP-608 was used to evaluate porosity at different confining pressures from 2.8 to 69 MPa. The evaluation of porosity follows Boyle's law, which states that the pressure exerted by a given mass of an ideal gas is inversely proportional to the volume it occupies (e.g., Raymond et al., 2017 and references therein). Porosity decays logarithmically as a function of the confining pressure in the form:

$$\varphi(P) = a\,ln(P) + \varphi_0 \tag{3.8}$$

where φ (%) is the porosity and P (Pa) is the confining pressure. The coefficient a controls the pressure dependence of the porosity and the subscript 0 stands for ambient pressure.

Considering the geometric mean as the mixing model that best describes the relationship between thermal conductivity and porosity (e.g., Beck, 1976), then:

$$\lambda(\varphi) = \lambda_{\mathrm{f}}^{\varphi} \lambda_{\mathrm{s}}^{1-\varphi} \tag{3.9}$$

where the subscripts f and s are thermal conductivity of the fluid filling the pores and the thermal conductivity of the solid rock matrix, respectively.

The effect of pressure on thermal conductivity was determined by plotting Equation (3.9) as a function of pressure. The best fit is given by the function:

$$\lambda(P) = d\, ln(P) + \lambda_{20} \tag{3.10}$$

where *d* is an experimental coefficient that controls the pressure dependence of thermal conductivity.

The following relationship was then obtained when combining Equation (3.10) with Equation (3.7) to describe the effect of both temperature and confining pressure on thermal conductivity:

$$\lambda(T,P) = \frac{1}{(d\, ln(P)+\lambda_{20})^{-1}+b(T-20)} \tag{3.11}$$

3.4.3 Numerical model

3.4.3.1 Model description

The 1D nonlinear IHCP described in section 3.3 was solved numerically by FEM using the optimization module of COMSOL Multiphysics software. The geometry of the computed profile has a length of 10 km and is layered near the surface accordingly to the interpreted ERT profiles (see Giordano et al., 2017 for further details). The first 20 m is composed by marine sediments, followed by 20 m of glacial till and the remaining is paragneiss (Figure 3.5). The simulations took into consideration the subsurface temperature perturbation caused by the Pleistocene climate events. At 10 km depth, their effect is minimum compared to shallower depths (cf. Bédard et al., 2018; Miranda et al., 2020a). Therefore, the lower boundary condition was defined at a depth of 10 km. Changes caused by sedimentation and/or erosion were not considered in this study. The depth 0 m in the model was considered to match the present ground surface.

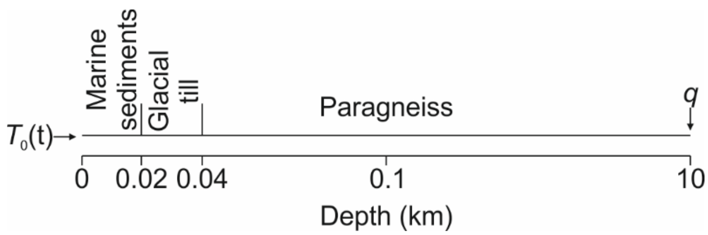

Figure 3.5 **Geometry of the model. T_0(t) – time-varying upper boundary condition, q – unknown heat flux.**

The initial temperature of the model was inferred from the last 20 m of the measured T-z profile. This last part of the profile is less influenced by the temperature variations. The initial temperature condition to run the transient simulations was calculated using Equation (3.2a) and Equation (3.2b). Both dry and water-saturated state of the thermophysical properties were considered to assess their influence on heat flux. Additionally, the effect of temperature and pressure on thermal conductivity was implemented in the model. The statistical distribution of rock thermal conductivity was also taken into account. The unknown heat flux was set as the lower boundary condition and a time-varying upper boundary condition was imposed to represent the GSTH. COMSOL's piecewise function was used to implement the climate events (Table 3.1). To deal with the uncertainty on the temperature at the base of the LIS (see section 3.3 for further details) and its influence on heat flux, a sensitivity study was undertaken assuming different temperature scenarios for the glacial episodes (Table 3.1). Moreover, due to the shallow length of the reference T-z profile, a sensitivity analysis was also carried out to understand which epoch has the major impact on the heat flux.

Table 3.1 Time and temperature steps of the major Pleistocene and Holocene climate events considered for GSTH in this work.

Event	Time step (years B.P.)	Temperature step (ºC) Cold scenario	Average scenario	Warm scenario
Nebraskan (MIS 14*)	300000 - 265000	-10	-5	-1
Aftonian (MIS 13 – 11*)	265000 - 200000	0	0	0
Kansan (MIS 10*)	200000 - 175000	-10	-5	-1
Yarmouth (MIS 9 – 7*)	175000 - 125000	0	0	0
Illinoian (MIS 6*)	125000 - 100000	-10	-5	-1
Sangamonian (MIS 5*)	100000 - 75000	0	0	0
Wisconsinan (MIS 4 – 2*)	75000 - 11600	-10	-5	-1
Holocene (MIS 1)	11600 – present		---	
---	11600 - 7000		0	
Holocene thermal maximum	7000 – 5800		+2	
---	5800 - 3200		0	
Roman and Medieval warm periods	3200 – 1000		+1	
---	1000 - 500		0	
Little Ice Age	500 – 270		-1	
Pre-industrial and Industrial Revolution	270 – 80		+1.4	
Present-day global warming	30 - present		+2	

*** Based on Emiliani (1955), MIS – Marine Isotope Stage, B.P. – before present.**

The transient simulations were carried out for 300 ka with yearly time step to ensure a smooth solution for the effect of the more recent and short episodes of surface temperature changes. The backward differentiation formula (BDF) was chosen for the time step method. The steps taken by the solver were set as free after a step-independency study have been undertaken. The results reveal no difference in the optimal value of the control variable regarding the time step used: free or strict.

A mesh-dependency study was carried out to guarantee the reliability of the results. The mesh was gradually refined until a constant temperature at a given depth was obtained. This study started with a normal mesh (26 elements) until a constant temperature at 100 m was reached for an extremely fine mesh with 121 elements. However, a mesh with 959 elements was used instead to guarantee the correct distribution of the elements throughout the geometry (Table 3.2). In the first 40 meters, the mesh is more refined than at the bottom of the model. For the former, an element at each 0.10 m was defined. From 40 m beyond, the maximum element size was set as 100 m with a maximum element growth of 1.3 and resolution of 1.1 in narrow regions.

Table 3.2 Verification of the mesh independence.

Number of elements	T(100) (ºC)	Relative difference (%)
26	0.95	-
62	0.85	-11.8
110	0.75	-13.3
112	0.65	-7.5
121	0.65	0
959	0.65	0

To solve the inverse problem stated in section 3.3, the Nelder-Mead algorithm and the least-squares method were selected for optimization of the heat flux (e.g., Frankel, 1996; Manesh et al., 2015). An algorithm independency-study was carried and both Nelder-Mead and coordinate search (e.g., Conn et al., 2009) gave the same optimal heat flux. The optimally tolerance to stop the iterations was set to 10^{-6} and the maximum number of model evaluations was defined to 100. The latter was chosen since the optimal solution was found at 28 to 42 iterations. The heat flux degree of freedom was constrained to the interval 10 and 70 mW m^{-2}.

3.4.3.2 Model validation

The reliability of the inverse numerical approach was validated using a synthetic temperature profile with thermal conductivity of 2.70 W m^{-1} K^{-1}, surface temperature of -9.8 ºC and heat flux of 40 mW m^{-2}. The simulations were run in steady state. The degree of freedom of the control variable was set between 20 and 60 mW m^{-2}. The least-squares objective function gave the best-fit to the value 40 mW m^{-2} (Figure 3.6).

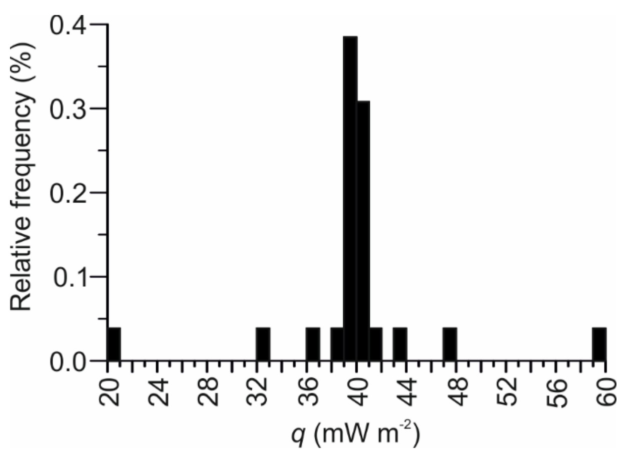

Figure 3.6 Heat flux values tried by the Nelder-Mead solver to minimize the objective function for model validation.

3.5 **Results**

3.5.1 Temperature surveys and thermophysical properties

The T-z profile W18, although shallow with only 80 m, displays a typical geothermal gradient inversion caused by climate variations. As previously described, before reaching the bedrock, 20 m of marine sediments followed by 20 m of glacial till were observed (Figure 3.7).

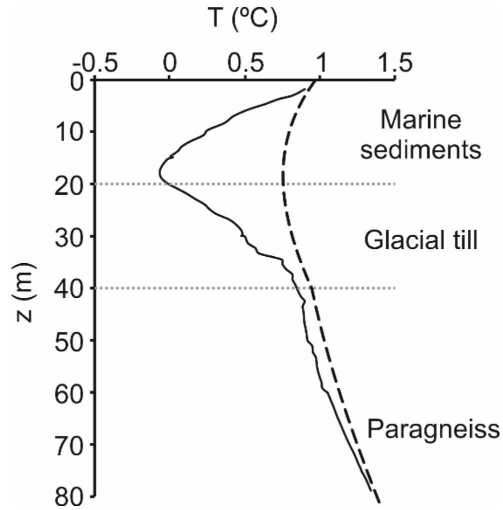

Figure 3.7 Measured (solid line) and simulated (dashed line) T-z profile near the community of Kuujjuaq (see Figure 4.2 for geographical location). The simulated profile corresponds to a heat flux of 41.6 mW m^{-2}.

The marine sediments have a median thermal conductivity of 1.17 W m^{-1} K^{-1} and a median volumetric heat capacity of 2.31 MJ m^{-3} K^{-1} at in situ conditions (Figure 3.8a; Kanzari, 2019). The glacial till presents an in situ median thermal conductivity of 1.09 W m^{-1} K^{-1} and an in situ median volumetric heat capacity of 2.01 MJ m^{-3} K^{-1} (Figure 3.8b; Kanzari, 2019). Two methods (GHFM and TCS) were used to evaluate the thermophysical properties. Therefore, the results from these methods were averaged to obtain the minimum, median and maximum values. At dry conditions, the paragneiss samples are characterized by a median thermal conductivity of 2.37 W m^{-1} K^{-1}, ranging from a minimum of 1.82 W m^{-1} K^{-1} to a maximum of 2.97 W m^{-1} K^{-1} (Figure 3.8a). The median volumetric heat capacity is 2.30 MJ m^{-3} K^{-1}, varying within 2.12 to 2.90 MJ m^{-3} K^{-1} (Figure 3.8b).

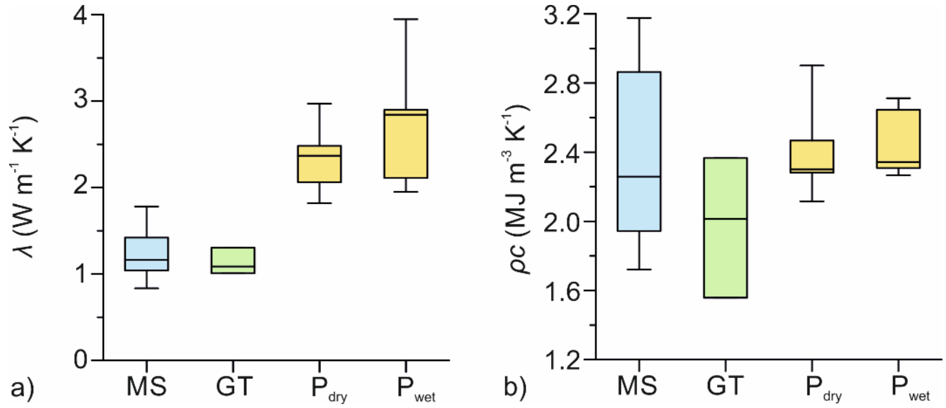

Figure 3.8 **a) Thermal conductivity and b) volumetric heat capacity boxplots with whiskers from minimum to maximum. MS – marine sediments (*N* = 8), GT – glacial till (*N* = 3), P – paragneiss (*N* = 8), dry – dry conditions, wet – water-saturation conditions.**

Only GHFM was used to evaluate the thermophysical properties at water-saturation conditions. The results reveal a median thermal conductivity of 2.84 W m^{-1} K^{-1}, with a minimum of 1.95 W m^{-1} K^{-1} and a maximum of 3.95 W m^{-1} K^{-1} (Figure 3.8a). A minimum of 2.27 MJ m^{-3} K^{-1} and a maximum of 2.71 MJ m^{-3} K^{-1} were evaluated for the volumetric heat capacity. The median value is 2.34 MJ m^{-3} K^{-1} (Figure 3.8b). Two methods (GRS and ICP-MS) were used to evaluate the concentration on radiogenic elements. Therefore, the results from both methods were averaged to obtain the minimum, median and maximum values. The median internal heat generation for the paragneiss is 1.16 μW m^{-3}, varying between 0.21 to 1.99 μW m^{-3}.

The thermal conductivity of the paragneiss samples at dry conditions was evaluated within the temperature range 20 – 160 ºC. The results reveal a decrease between 18 – 40% as a function of temperature (Figure 3.9a). The evaluation of porosity as a function of pressure reveals a decrease of 52 – 82% within the pressure range 2.8 – 48.3 MPa (Figure 3.9b). The effect of pressure on thermal conductivity was evaluated indirectly (Equation 3.10). The results reveal an increase of thermal conductivity of 3 to 15% within the same pressure range (Figure 3.9c). The experimental coefficient *b* (Equation 3.7) is found to range between 0.0003 – 0.002. The coefficient *a* of Equation (3.8) varies within -0.2 to -1.1. Coefficient *d* (Equation 3.10) ranges between 0.02 and 0.20.

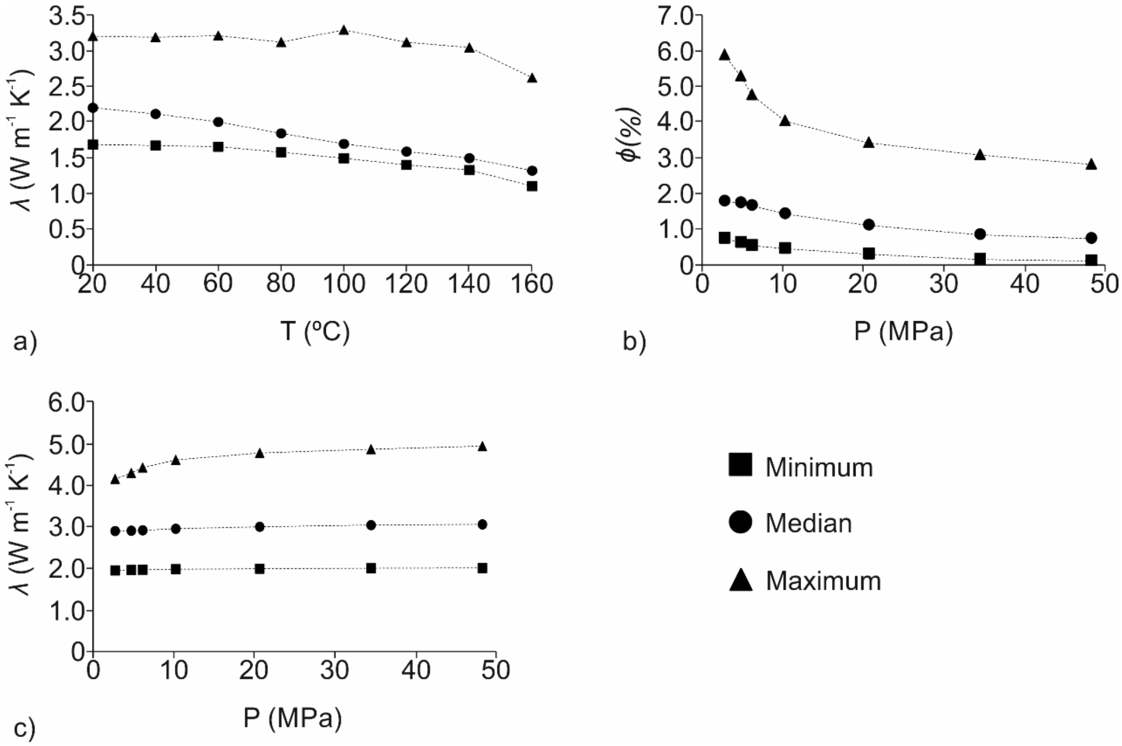

Figure 3.9 **a) Thermal conductivity as a function of temperature, b) porosity as a function of pressure and c) thermal conductivity as a function of pressure. Minimum, median and maximum refer to the values evaluated for the thermophysical properties.**

3.5.2 Heat flux simulations

Sensitivity analyzes were carried out to assess the influence of GSTH and thermophysical properties conditions on heat flux. The minimum heat flux was obtained by using the minimum value evaluated for thermal conductivity and heat generation with the maximum value of volumetric heat capacity. In turn, the maximum heat flux was obtained by using the inverse combination. The same stopping parameters and degree of freedom of the control variable were used in all the simulations for a better comparison of the results. These are described in the following sections.

3.5.2.1 Heat flux as a function of the GSTH

The different scenarios for the LIS basal temperature (Table 3.1) influence the heat flux (Figure 3.10). The cold climate scenario reveals a heat flux ranging from a minimum of 32.1 mW m^{-2} to a maximum of 54.5 mW m^{-2} (Figure 3.10a). The minimum, median and maximum heat flux values depend on the minimum, median and maximum values of the thermophysical properties as aforementioned. A heat flux varying between 32.0 and

53.3 mW m^{-2} was inferred for the average climate scenario (Figure 3.10b). The warm climate scenario, in turn, reveals a heat flux ranging from 31.8 to 52.3 mW m^{-2} (Figure 3.10c). The difference between cold and warm scenarios ranges from 0.9% for the minimum heat flux value to 4.0% for the maximum heat flux.

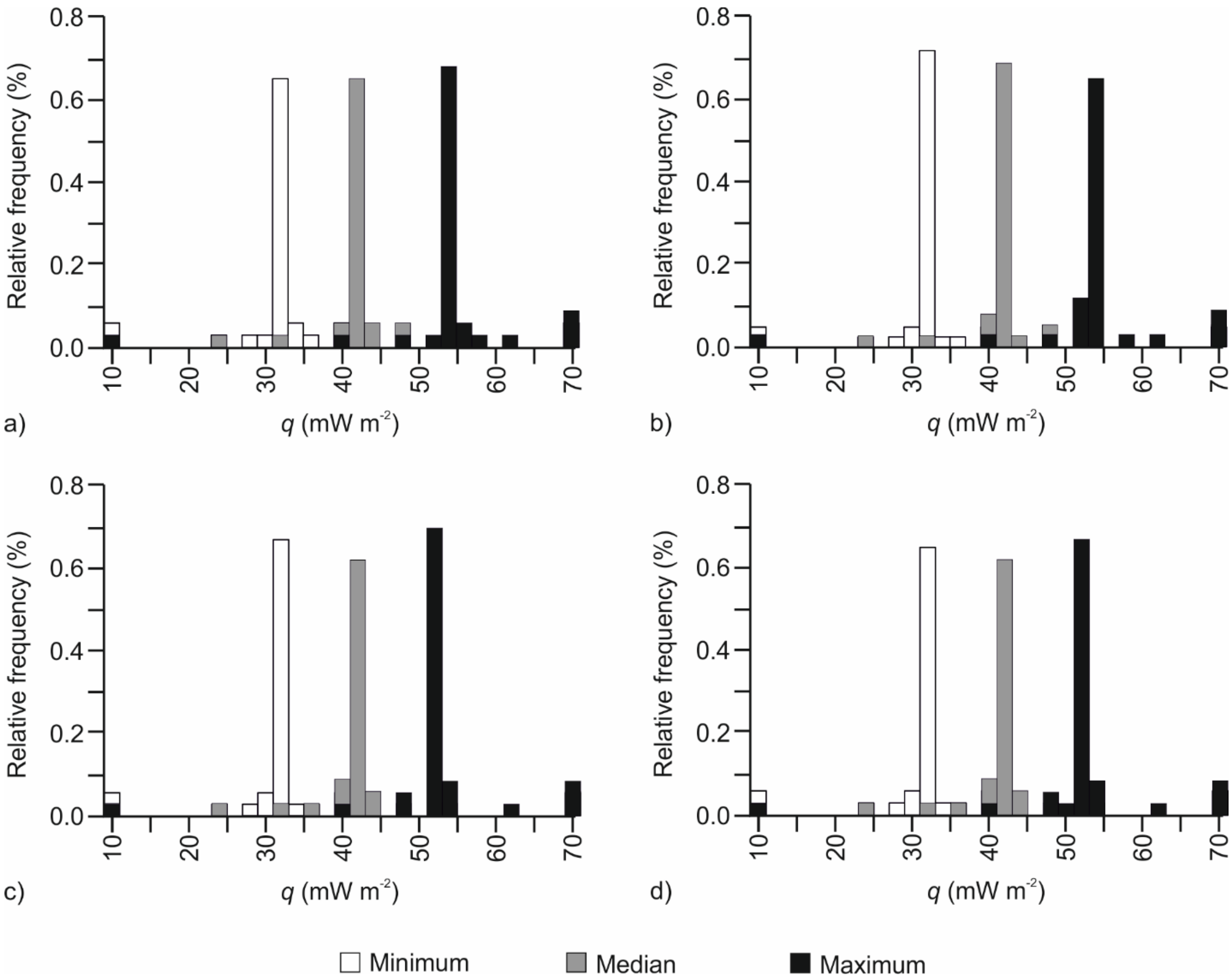

Figure 3.10 **Heat flux values tried by the Nelder-Mead solver to minimize the objective function: a) cold climate scenario, b) average climate scenario, c) warm climate scenario and d) Holocene events only. The reader is referred to Table 3.1 for further information on the climate scenarios. Minimum, median and maximum refer to the values evaluated for the heat flux considering varying thermophysical properties in each climate scenario.**

An additional study was undertaken to evaluate which epoch, Pleistocene or Holocene, has the major influence on the heat flux. The results reveal that taking into account the Holocene events only leads to a heat flux ranging from 31.8 – 52.1 mW m^{-2} (Figure 3.10d). However, considering the Pleistocene climate events only, the results are the same as stated above: 32.1 – 54.5 mW m^{-2} for the cold climate scenario, 32.0 to 53.3 mW m^{-2} for the average climate scenario and 31.8 – 52.3 mW m^{-2} for the warm climate scenario. The difference between the heat flux values obtained for the Pleistocene and the ones obtained for the Holocene ranges from a minimum of 0.1%, corresponding to the warm climate scenario and minimum heat flux value, to a maximum of 4.4% that corresponds to the cold climate scenario and maximum heat flux.

Although the climate scenarios and epochs have an influence on the inferred heat flux, the main uncertainty is found to be associated with the heterogeneous character of the lithological units, which influences the statistical variability of the heat flux. The difference between the maximum and minimum values varies between 39 – 41%. Moreover, an influence of the climate scenarios on the objective function fitting is also observed (Figure 3.11). For the cold climate scenario, the scalar value of the objective function decreases from 134 to 107 for the maximum heat flux and from 87 to 35 for the minimum heat flux (Figure 3.11a). For the average climate scenario, the decrease is from 67 to 38 for the maximum heat flux and from 33 to 14 for the minimum heat flux (Figure 3.11b). The warm climate scenario reveals a decrease on the objective function from 58 to 8 for the maximum heat flux and from 33 to 5 for the minimum heat flux (Figure 3.11c). Considering the Holocene events only, the decrease is from 56 to 4 for the maximum heat flux and from 29 to 3 for the minimum heat flux (Figure 3.11d).

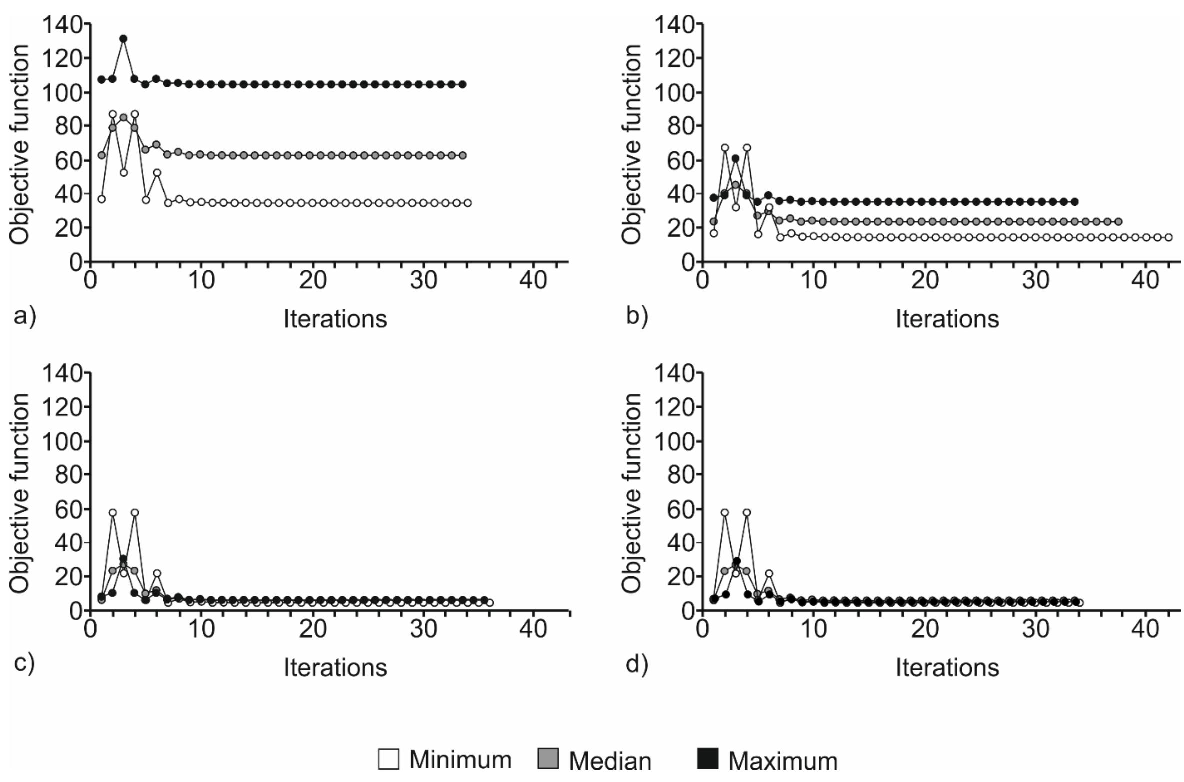

Figure 3.11 **Minimization of the objective function with number of iterations: a) cold climate scenario, b) average climate scenario, c) warm climate scenario, d) Holocene only. The reader is referred to Table 3.1 for further information on the climate scenarios. Minimum, median and maximum refer to the values evaluated for the heat flux considering varying thermophysical properties in each climate scenario.**

Furthermore, a study was undertaken to assess the heat flux misestimation if surface temperature variations, past or recent, are neglected. The heat flux is inferred to vary between 31.2 to 51.8 mW m^{-2}. This represents an underestimation of 1 – 5% when compared with the cold scenario, 0.6 – 3% for the average scenario and 0.2 – 1% for the warm scenario.

3.5.2.2 Heat flux as a function of the thermophysical properties

a. Effect of water-saturation

Given the lower objective function obtained for the warm scenario (Figure 3.11), this was selected to carry out the simulations of this section. Considering the thermophysical properties at dry conditions, the heat flux is found to vary within a minimum of 31.8 mW m^{-2} and a maximum of 52.3 mW m^{-2}, with a median value of 41.6 mW m^{-2} (Figure 3.12a). The water saturation of the samples led to an increase in thermal conductivity of 7 – 25% and in volumetric heat capacity of 1 – 9% (Figure 3.8). Thus, this resulted in an increase of the heat flux. At water-saturation conditions, the heat flux ranges between 34.1 mW m^{-2} to 69.4 mW m^{-2}, with a median value of 49.7 mW m^{-2} (Figure 3.12b). Moreover, considering the thermophysical properties at dry conditions, the scalar value of the objective function decreases from 58 to 8 for the maximum heat flux and from 33 to 5 for the minimum heat flux (Figure 3.12c). In turn, assuming the water-saturation state, the decrease on the objective function is from 46 to 8 for the maximum heat flux and from 15 to 5 for the minimum heat flux (Figure 3.12d).

The uncertainty introduced by the dry and water-saturation conditions on the heat flux ranges from 7% to 25% while the one associated with the statistical variability of the lithological units is 39% at dry conditions, increasing to 51% at water-saturation state. This corresponds to the difference between the maximum and minimum values evaluated for the heat flux.

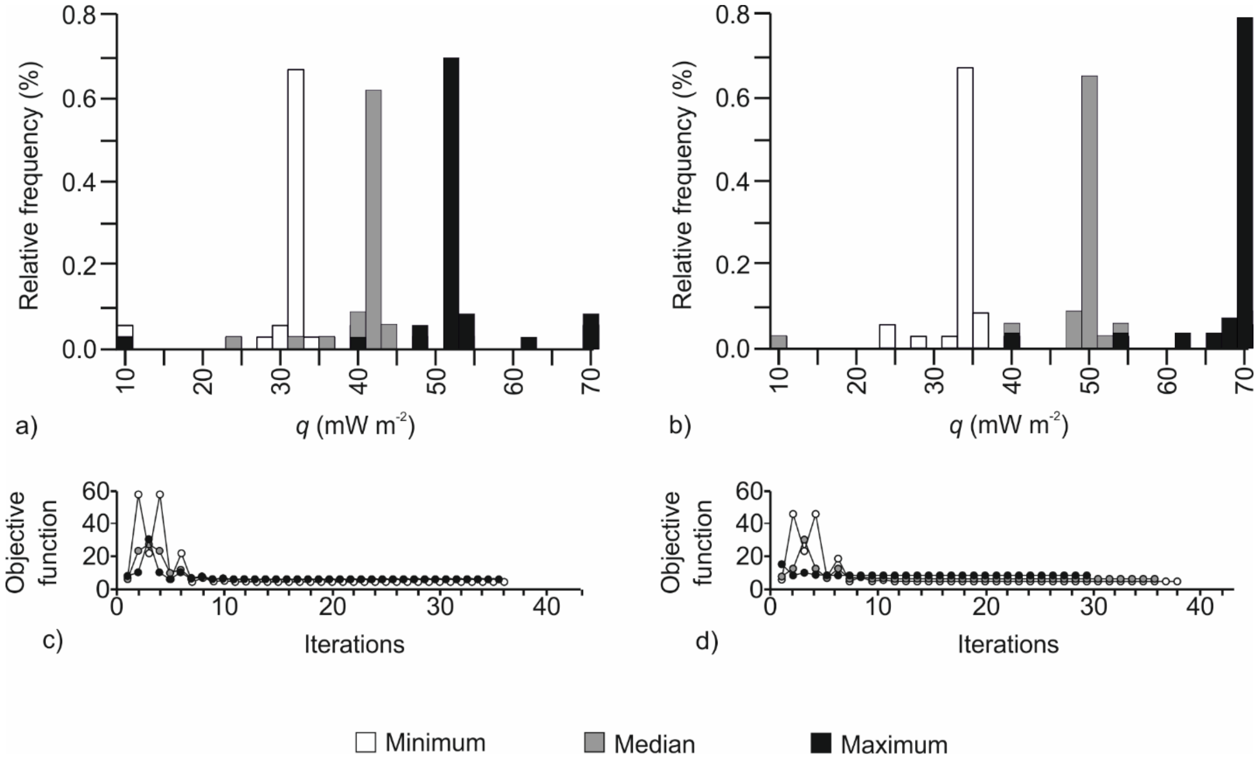

Figure 3.12 **Heat flux values tried by the Nelder-Mead solver to minimize the objective function with thermal conductivity under a) dry and b) water-saturation conditions. Minimization of the objective function as a function of iterations for c) dry and d) water-saturated thermal conductivity. Minimum, median and maximum refer to the values evaluated for the heat flux considering varying thermophysical properties.**

b. Effect of temperature and pressure

Thermal conductivity at dry state decreases by 18–40% as temperature increases and increases 3 – 15% as pressure increases (Figure 3.9). However, the results reveal that the effect of temperature and pressure on thermal conductivity leads to a decrease in the heat flux of less than 0.1%. The obtained temperature- and pressure-dependent heat flux for dry conditions ranges from 31.8–52.3 mW m^{-2} (dry hot heat flux; Figure 3.13). Neglecting these effects reveals heat flux ranging within the same values (dry heat flux; Figure 3.13). Including water-saturation, temperature and pressure leads to heat flux varying within 34.1–69.4 mW m^{-2} (wet hot heat flux; Figure 3.13). Neglecting temperature and pressure leads to a heat flux ranging within the same values (wet heat flux; Figure 3.13).

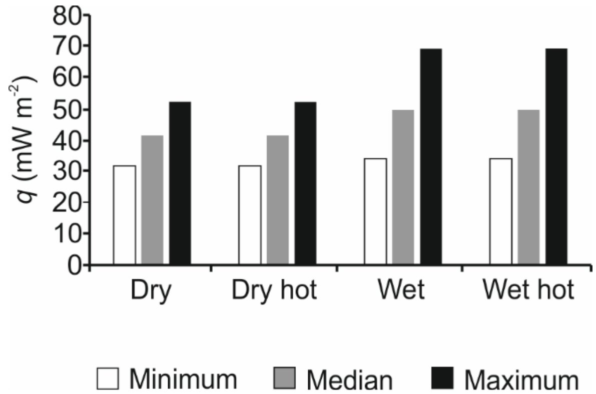

Figure 3.13 **Heat flux as a function of thermal conductivity conditions. Minimum, median and maximum refer to the values evaluated for the heat flux considering varying thermophysical properties.**

3.6 Discussion

3.6.1 Thermophysical properties

The results obtained for the thermophysical properties are in the range of values mentioned in databases (e.g., Clauser et al., 1995; Vilà et al., 2010; Eppelbaum et al., 2014; Hasterok et al., 2018) and they are in accordance with the mineralogical composition and geochemistry of the rock samples (see Miranda et al., 2020a for further details). The effect of temperature on thermal conductivity led to its decrease, agreeing with other authors that carried out similar experimental evaluation (e.g., Vosteen et al., 2003; Abdulagatov et al. 2006; Miao et al. 2014). The linear relationship between temperature and thermal resistivity (e.g., Schatz et al., 1972) was used to fit the experimental data solely for the purpose of the present computation. Other function can be used and implemented in the numerical model (e.g., Chapman et al., 1984; Sass et al., 1992; Seipold, 1998; Furlong et al., 2013). In fact, the different relationships lead to significant thermal conductivity variations when comparing evaluated and inferred values (e.g., Lee et al., 1998). This consequently has an impact on both subsurface temperature distribution and basal heat flux (Norden et al., 2020). A sensitivity study to assess the influence of these different relationships on the inferred heat flux and to quantify the associated uncertainty can be envisioned for future developments of this numerical approach. The effect of pressure on thermal conductivity indirectly inferred reveal a similar increasing trend as referred from experimental evaluation (e.g., Abdulagatov et al., 2006; Emirov et al., 2017). Moreover, the results also show the twofold effect of pressure on thermal conductivity mentioned by Clauser et al. (1995). An increase in thermal conductivity up to 15 MPa, which is related with the decrease of porosity, followed by an insignificant variation until 48 MPa (Figure 3.9).

3.6.2 Heat flux simulations

The numerical approach described in this study enables to evaluate heat flux from shallow T-z profiles. Although applied to one of Nunavik's communities (Kuujjuaq), this methodology is versatile enough to be used at any other community facing the same deep data gap. About 239 communities spread over northern Canada and exclusively relying on diesel fuel face this same geothermal exploration challenge (Arriaga et al., 2017). Thus, this study represents a step forward in the assessment of deep geothermal resources, especially those related to petrothermal systems, in remote northern regions.

Heat flux was solved with FEM as a 1D IHCP with unknown lower boundary condition and a time-varying upper boundary condition. The solution to this inverse problem was found through mathematical optimization. The Nelder-Mead algorithm and the least-squares method were chosen to track the optimal heat flux. A piecewise function was implemented for the upper boundary condition to represent the GSTH. However, it is important to highlight that this GSTH is highly qualitative and based upon global and regional proxy climate published data. Any change in the surface temperature affects the geothermal gradient due to downwards thermal diffusion (e.g., Jessop, 1990; Beardsmore et al., 2001). This consequently has an impact on heat flux. Despite the limitations associated with the shallow depth of the T-z profile used for inversion (Figure 3.7), the temperature simulation and the resulting heat flux assessment is sensitive to climate variations. The sensitivity study carried out for different scenarios of the LIS basal temperature (Table 3.1) reveals a variation of 0.9 – 4% between cold and warm climate scenarios. Additionally, a simulation was run neglecting the climate events. The results reveal a misestimation of heat flux ranging within -0.2 to -5%. Although this variation is smaller than the 10% or more that has been reported (e.g., Jessop, 1971), it is important to keep in mind that the T-z profile used for comparison is only 80-m-long. Deeper temperature measurements can result in larger differences. The results also suggest the Pleistocene events as the main climate disturbances to the basal heat flux. The Holocene climate episodes can be neglected without affecting the inferred basal heat flux. However, if the Pleistocene events are discarded, the heat flux decreases by -0.1 to -4.5%. An observation already mentioned by others (e.g., Gosnold et al. 2011; Beltrami et al. 2014; Bédard et al. 2018). Moreover, the minimum scalar value of the least-squares method is found for the warm climate scenario (1 °C difference), which is considered more reliable for the observed temperature profile. This agrees with Jessop (1971) that suggested that under thick ice the temperature might have been close to the freezing point. However, a deeper T-z profile is required to support this observation and provide more accurate conclusions regarding paleoclimate. As pointed by Hartmann et al. (2005a) and Beltrami et al. (2011), shallow T-z profiles (< 300 m) can introduce a bias on the climate reconstruction. Nevertheless, it is shown here to be sufficient for a first estimate of heat flux in the scope of geothermal resource evaluation.

The influence on heat flux of the thermophysical properties at different conditions was also investigated. The effect of temperature, pressure and water-saturation on thermal conductivity are known to influence the estimation of basal heat flux (e.g., Lerche 1991; Nasr et al. 2018; Harlé et al. 2019; Norden et al. 2020). The effect of water-saturation on thermal conductivity led to a 7 to 25% increase in the heat flux. This observation agrees with Harlé et al. (2019), which calculated heat fluxes up to 43% higher if water-saturation is considered. Although the water-saturation at depth cannot be readily observed, this effect shall not be ignored when inferring heat flux, even in low porosity rocks such as the ones studied for Kuujjuaq. Harlé et al. (2019) evaluated a decrease up to 11% of heat flux caused by the effect of temperature on thermal conductivity of sedimentary rocks. Nasr et al. (2018), in turn, obtained a neglectable variation caused by the temperature effect alone. However, these authors reported a significant increase (about 10%) of heat flux if pressure and temperature are considered together. Norden et al. (2020) mentioned minor influence of these thermal conductivity conditions on the surface heat flux, but notable differences in the calculated subsurface heat flux (10 to more than 20% at 4 km depth). However, the results from this study reveal a minimal decrease on the heat flux, less than 0.1%, when implementing in the model a thermal conductivity varying with temperature and pressure. This can be caused by the weak geothermal gradient and the small counter effect of temperature and pressure on thermal conductivity evaluated experimentally and indirectly. It can also be related with the relationship used for temperature correction of thermal conductivity. Lerche (1991) argued that the linear increase of thermal conductivity with increasing thermal resistance might not be an adequate approximation and need to be replaced with a more exact exponential increase. Further developments can be envisioned by applying different temperature and pressure corrections for thermal conductivity and assess the associated uncertainty. Nevertheless, the model was capable of tracking thermal conductivity changes and vary the heat flux accordingly.

Current uncertainties can be reduced with further geothermal exploration development, such as deep temperature measurements. Per contra, the main source of uncertainty is introduced by the statistical distribution of the thermophysical properties. This falls within the aleatory variability uncertainty category (e.g., Witter et al., 2019 and references therein) and is difficultly predictable with the current level of knowledge. The lithological units are intrinsically heterogeneous, which is reflected in the spatial variability of the thermophysical properties. Such uncertainty is difficult to predict, even with a high number of samples collected for analysis but can be accounted for when modeling the subsurface temperature for geothermal research and development. A source of uncertainty not dealt with in this study is associated with vertical lithological changes. The numerical model assumed a homogeneous lithology from 40 m beyond due to the insufficient subsurface knowledge. However, a multilayered geometry can be implemented as information on deep geological structures become available with further geothermal exploration.

3.6.3 Representativeness of the heat flux evaluation

Surface heat flux inferred in the deep boreholes of Raglan and Asbestos Hill mining sites, Camp Coulon, Nielsen Island and Voisey Bay (see Figure 3.1 for geographic location) indicate values ranging from a minimum of 22 mW m^{-2} at Voisey Bay (Mareschal et al., 2000) to a maximum of 38 mW m^{-2} at Asbestos Hill mining site (Taylor et al., 1979). Majorowicz et al. (2015a) estimated a surface heat flux of 40.26 ± 9.38 mW m^{-2} based on 67 wells drilled in northern Québec, but only 3 are located in Nunavik and none are in the Southeastern Churchill geological province. The geothermal heat flow density map in northern Québec presented by these authors indicate a surface heat flux in Kuujjuaq of approximately 44 – 49 mW m^{-2}. Applying Equation (3.2b) to estimate the surface heat flux based on the basal heat flux and radiogenic heat production obtained in this study indicates values ranging from a minimum of 33.9 mW m^{-2} to a maximum of 72.2 mW m^{-2}, with a median value of 53.2 mW m^{-2}. These results refer to the heat flux obtained considering the warm climate scenario and the thermophysical properties at dry conditions. The difference between the median value obtained in this study and the surface heat flux estimated by Majorowicz et al. (2015a) is 8 to 17%. Although this difference seems high, it is convenient to highlight that there is no deep borehole in Kuujjuaq to accurately assess heat flux. Moreover, the heat flux of Majorowicz et al. (2015a) is based on extrapolation from sparse data (the closest heat flow assessment to Kuujjuaq lies at a distance of approximately 420-430 km), which induce further uncertainty. Additionally, Drolet et al. (2017) mapped the Curie point depth in Québec province and their results indicate a value within the interval 20 to 30 km in Kuujjuaq area. Considering the median thermal conductivity (2.37 W m^{-1} K^{-1}) and median surface heat flux (53.2 mW m^{-2}) obtained in this study, then the median geothermal gradient inferred using Fourier's law is 22.4 ºC km^{-1}. If Curie point temperature is assumed 580 ºC, then the Curie point depth calculated based on the median geothermal gradient is approximately 26 km, clearly within the interval of Drolet et al. (2017) map. Moreover, according to a regional literature review, a simplified conceptual model for the crustal stratigraphy can be built. Vervaet et al. (2016) estimated crustal thickness varying from 33 to 49 km with the thickest crust in the Ungava region. The granulitic-facies lower crust has an approximate thickness of 26 km and a minimum average radiogenic heat production of 0.4 – 0.5 μW m^{-3} (Christensen et al., 1975; Ashwal et al. 1987; Seguin et al., 1990). Seguin et al. (1990) mention an average upper crustal thickness of 20 km. The Moho contribution to the heat flux is approximately 15 mW m^{-2} (e.g., Mareschal et al., 2013). The surface heat flux for a lithosphere in thermal steady-state is given by the sum of Moho and crustal contributions (e.g., Mareschal et al., 2013). Thus, applying this relationship and assuming the aforementioned conceptual model and the median radiogenic heat production obtained in this study, indicates a median heat flux at 10 km depth of 38.3 mW m^{-2}. This corresponds to a difference of 8% between the numerical and analytical heat flux. However, there is uncertainty associated with this regional literature-based conceptual model. Furthermore, using the same regional literature-based conceptual crustal model and the median heat flux at 10 km depth and median radiogenic heat production inferred in this study points toward a radiogenic heat production for the granulitic-facies lower crust of 0.6 μW m^{-3}. This corresponds to a difference of 17 – 33% when compared to the values proposed by Ashwal et al. (1987). However, as referred by these authors, their values are minimum radiogenic heat production, and the granulitic-facies lower crust may have higher values.

Additionally, the paleoclimate corrections to the temperature profile were carried out analytically using the approach described in Birch (1948), a harmonic mean thermal diffusivity inferred from the thermal conductivity and volumetric heat capacity obtained in this study and Fourier 1D heat conduction equation. The analytical results reveal a median surface heat flux of 54.3 mW m^{-2} assuming the warm climate scenario (Table 3.1) and the thermophysical properties at dry conditions. Comparing numerical (53.2 mW m^{-2}) and analytical (54.3 mW m^{-2}) results reveals a difference of -2%. Although the harmonic mean thermal diffusivity was used in the analytical approach in order to reproduce a layered subsurface medium, the heterogeneity of the medium cannot be fully represented in opposite to the numerical model developed in this study. Thus, the numerical approach here described provides a more representative evaluation compared to the analytical approach.

Therefore, the comparison between literature and the numerical heat flux indicates reliability of the results presented in this study. Nevertheless, higher accuracy on the heat flux can be obtained with further geothermal developments such as drilling of deep exploratory boreholes

(> 300 m) to carry out temperature measurements and analyze thermal conductivity from core samples.

3.6.4 Future improvements of the numerical approach

The numerical approach presented in this study considers only heat conduction and aims to infer heat flux by applying paleoclimate correction. However, another 94-m-long groundwater monitoring well in Kuujjuaq was discarded due to the effect of groundwater flow (see Miranda et al., 2018a for further details) and, thus, future developments can be foreseen to include the advection effect. Groundwater flow has been observed to perturb T-z profiles and, thus, heat flux (e.g., Mansure et al., 1979; Kukkonen et al., 1994; Popek et al., 2011). The direct effect of groundwater flow on heat flux determinations can be caused by water movement within the borehole, transient loss or gain of water into or out of fractures during drilling and water flow though porous or fractured bedrock surrounding the borehole (Drury, 1984). Low permeability rocks, such as the paragneiss bedrock analyzed in this study having a permeability around 10^{-19} m^2 (Miranda et al., 2020a), and gentle topography (groundwater monitoring well drilled in a flat area with an altitude of approximately 47 m), indicate that groundwater velocity is small enough for advective heat transfer to be negligible (Powell et al., 1988 and references therein). The screening tool proposed by Ferguson (2015) was applied to confirm this hypothesis. This method is based on the relationship between the specific discharge and the Peclet Number and between hydraulic gradient and hydraulic conductivity. The specific discharge is calculated based on the hydraulic conductivity and hydraulic gradient. The permeability inferred for the paragneiss is 10^{-19} m^2. Assuming fresh water with a density of 1000 kg m^{-3} and a dynamic viscosity of 10^{-3} kg m^{-1} s^{-1}, results on a hydraulic conductivity of 10^{-13} m s^{-1}. A hydraulic gradient of 10^{-2} is obtained assuming the water level in the well at the ground surface (i.e. 47 m above sea level) and averaging the water level in the Koksoak river (FOC, 2020) which is located about 3 km away from the well. However, this hydraulic gradient is highly speculative due to the lack of sufficient information to build a piezometric map. Nevertheless, this rough approximation is useful to evaluate the main heat transfer mechanism using Ferguson (2015) approach. The specific discharge is inferred to be 10^{-14} m s^{-1}. The Peclet Number was calculated as referred in Ferguson (2015) assuming the borehole length (i.e 80 m). The fresh water specific heat was assumed 4184 J kg^{-1} K^{-1}. Thus, the inferred Peclet Number is 10^{-6}. Considering the plots in Ferguson (2015), it is observed that the values of specific discharge, Peclet Number, hydraulic gradient and hydraulic conductivity clearly indicate that conduction is the dominated heat transfer mechanism, and therefore advection can be neglected. Nevertheless, the groundwater effect may be more important near surface where the temperature profile intercepts the marine deposits and glacial till (Figure 3.7). Giordano et al. (2019a) evaluated the hydraulic conductivity of the marine deposits and obtained a value of 10^{-5} m s^{-1}. This hydraulic conductivity is 67% higher than the hydraulic conductivity inferred for the paragneiss unit. Assuming the same hydraulic gradient of 10^{-2}, results on a specific discharge of 10^{-6} m s^{-1}. The Peclet Number is 10^{2}. These values place the heat transfer mechanism in the lower limit of advection. However, large uncertainty is associated with the hydraulic gradient. Lower values will place conduction as the main heat transfer mechanism while higher values will favor advection. Moreover, assuming the hydraulic conductivity of the glacial till ranging from 10^{-11} to 10^{-8} m s^{-1} (e.g., Ferris et al., 2020), indicates heat conduction as the main heat transfer mechanism within this lithological unit.

The topography effect was neglected in this study due to the gentle topography of the study area. Nevertheless, implementation of topography corrections can be foreseen in further improvements of this numerical approach to confirm the assumption of neglecting topography effects. A detailed explanation of modeling topographic disturbances is provided by, for instance, Blackwell et al. (1980), Powell et al. (1988), Lee (1991) and Kohl (1999) that can be followed to implement such effects on numerical models. Furthermore, sedimentation and erosion effects were not considered in this study. The surface of the model was assumed constant through the 300 ka of paleoclimate simulation. However, glacial erosion and deposition of the Quaternary sediments may influence the present-day heat flux. England (1978), for example, refer that in deep boreholes where a significant deviation of heat flux from the steady state has not been observed it may be due to the erosion that accompanies the glaciation periods. According to this author, small amounts of erosion during a cold period of surface temperature can result in nearly constant, or smooth with depth, perturbations to heat flux that damp the climate signal and render it undetectable. Furthermore, according to England (1978), ignoring the erosion effect on the topographic correction in valley glaciation regions may result in large errors in the estimates, particularly for shallow measurements. This author assumed that erosion results in a lowering of surface temperature of 14 mK per meter of erosion. The amount of glacial erosion is still poorly defined. Flint (1947) suggests that about 3 m of material has been removed from the Canadian Shield during each glacial period. Sugden (1976), Sugden (1977) and Sudgen (1978) also supports the hypothesis of only tens of meters of material removal. Although evidence suggests unlikely more than 100 m of erosion (England, 1978), Bell et al. (1985), supported by seismic reflection data, inferred an average erosion of 120 m. Thus, with these values in mind, glacial erosion may affect the surface temperature by a minimum of 0.042 ºC (assuming 3 m of erosion and a reduction of surface temperature of 14 mK per meter of erosion) to a maximum of 1.4 ºC (considering 100 m of erosion and surface temperature decrease of 14 mK per meter of erosion). Following England's (1978) approach, these surface temperature decrements shall be applied to the glacial period to simulate erosion. This was analytically applied in the temperature profile studied and reveals that the difference between considering and discarding glacial erosion varies between 4 and 1%. If glacial erosion leads to a lowering of the surface temperature, then the deposition of the Quaternary sediments is expected to have the opposite effect. Assuming the same 14 mK value, but this time per meter of sedimentation, the deposition of sediments may affect the surface temperature by 2.6 ºC (assuming 185 m as the marine elevation limit and sedimentation synchronous with marine transgression; see section 3.2 for further details). However, these deposits were eroded through time (approximately 138 m of erosion; see section 3.2 for further details). Thus, the erosion of the Quaternary sediments may affect the surface temperature by 1.9 ºC. However, this sedimentation and erosion values are only very rough approximations and are bounded by high uncertainty. The effect of glacial erosion and deposition of the sediments can cancel each other. Neglecting these effects in this first-order assessment of heat flux seems acceptable and would likely induce marginal errors in the numerical model. Nevertheless, further developments may be foreseen to consider these effects. For example, England et al. (1980) and Ehlers (2005) present solutions that can be implemented on the numerical model to address the erosion and sedimentation effects.

Finally, Figure 3.7 reveals a mismatch between measured and simulated temperature profiles at the depths of 0 to 40 m. The observed discrepancy is believed to be caused by the large temporal intervals of the GSTH imposed as upper boundary conditions (Table 3.1). A more discretized GSTH for the last 120 years, for example, associated with seasonal/annual temperature variations may lead to a better approximation between measured and simulated temperature profile. In fact, an annual temperature variation cycle is inferred to reach a theoretical maximum depth of approximately 20 m. Furthermore, a detailed GSTH can be obtained with a deeper temperature profile than the 80-m-long used in this study, that unfortunately is currently nonexistent in the study area or proximities. Moreover, analysis of climate proxies, such as, tree rings, pollen, dinoflagellate cyst assemblages and other organisms (e.g., Majorowicz et al., 2005; Richerol et al., 2016; SERC, 2020) can help to build a more detailed climate history for further studies in the Kuujjuaq area. However, although it may lead to a better matching at surface, a discretized GSTH for recent periods of time will have neglectable influence on the heat flux at 10 km depth. As the results of this work suggest, the Pleistocene surface temperature variations have the main impact on the heat flux at depth.

3.7 **Conclusions**

Remote northern communities in Canada are not connected to the provincial electrical grid or natural gas infrastructure (e.g., Grasby et al., 2013; Arriaga et al., 2017). Such communities need to produce energy locally to improve their sustainability. At present, several renewable projects are being developed to offset the diesel dependency, but fossil fuels are still their main source of energy (e.g., Grasby et al. 2013; Arriaga et al. 2017; Minnick et al. 2018). Geothermal resources may help to change this energetic framework due to their ubiquity, abundance, and versatility. However, in such remote regions, where most of the communities are only accessible by airplane, boat, or winter road (e.g., Nunavik, Nunavut), characterizing the geothermal resources is challenging. Not only in terms of remoteness but challenges are also connected to data availability. The presence of deep boreholes with equilibrium temperature profiles is one such data gap. Often, existing wells have been drilled for other purposes rather than geothermal exploration, as in the case of the groundwater well used in this study. This leads to a need for adapting available methodologies for the situation at hand. The numerical approach described in this study is versatile, quick and provides a reliable evaluation of the heat flux. Any GSTH, thermophysical properties and time stepping can be used to adapt the model for the situation of the temperature profile. A major advantage of this approach is the possibility to invert the heat flux from shallow T-z profiles, typical of remote northern regions.

Heat flux was solved with FEM as a 1D IHCP with unknown lower boundary condition and a time-varying upper boundary condition representing climate episodes for the Kuujjuaq example provided with this study. The solution to this inverse problem was found through mathematical optimization. The Nelder-Mead algorithm and the least-squares method were chosen to track the optimal heat flux. The numerical model was proved capable to evaluate heat flux variations caused by Pleistocene and Holocene climate episodes, even if a shallow temperature profile (80 m) was used for function comparison. A simple GSTH with only the main climate events, each with a constant temperature amplitude was used in this study. Nevertheless, the numerical approach is versatile enough to deal with different and more detailed GSTH. The median heat flux obtained in this study ranges between 41.6 and 42.4 mW m^{-2}, depending on the temperature at the base of the Laurentide ice sheet. The water-saturation effect on thermal conductivity led to a 17% increase, on average, of heat flux. The median heat flux at water-saturation conditions is inferred to be 49.7 mW m^{-2}. The temperature and pressure effect, per contra, led to less than 0.1% decrease on heat flux. The main source of uncertainty on heat flux is found to be associated with the intrinsic heterogenous character of the lithological units (39 – 51%). Moreover, the current numerical approach does not consider advection, neither topography, nor sedimentation/erosion effects. Future developments can be foreseen to account for these disturbances to heat flux.

Nevertheless, the inferred heat flux, regardless of the climate scenarios and thermal conductivity conditions, is within the average calculated for Nunavik's territory. The difference between literature and numerically inferred heat flux is lower than 20%. Thus, suggesting robustness of the numerical calculations. Moreover, this numerical approach helps to provide information at low cost and move forward with costly decisions implying deep borehole as a second step to continue or abort geothermal research in such territories heavily dependent on fossil fuels.

4 UNCERTAINTY AND RISK EVALUATION OF DEEP GEOTHERMAL ENERGY SOURCE FOR HEAT PRODUCTION AND ELECTRICITY GENERATION IN REMOTE NORTHERN REGIONS

Évaluation d'incertitude et des risques liés à la source d'énergie géothermique profonde pour la production de chaleur et d'électricité dans les régions nordiques éloignées

Authors:

Mafalda M. Miranda (M.M.M.), Jasmin Raymond (J.R.)

Institut national de la recherche scientifique, Canada

Chrystel Dezayes (C.D.)

Bureau de recherches géologiques et minières, France

Journal title:

Energies

14 August 2020, Volume 13, number 16, article 4221

https://doi.org/10.3390/en13164221

Author's contribution:

Conceptualization, M.M.M., J.R. and C.D.; methodology, M.M.M.; validation, M.M.M.; formal analysis, M.M.M.; investigation, M.M.M.; resources, M.M.M., J.R. and C.D.; data curation, M.M.M.; writing – original draft preparation, M.M.M., J.R. and C.D.; writing – review and editing, M.M.M., J.R. and C.D.; visualization, M.M.M.; supervision, J.R. and C.D.; project administration, J.R.; funding acquisition, J.R.

Link between the previous article and the next:

The previous chapter presents a numerical approach developed to infer the terrestrial heat flux. The values obtained in the previous chapter are used as the lower boundary condition of the transient heat conduction models developed in this chapter to infer the subsurface temperature distribution. These two chapters complete each other.

Graphical abstract:

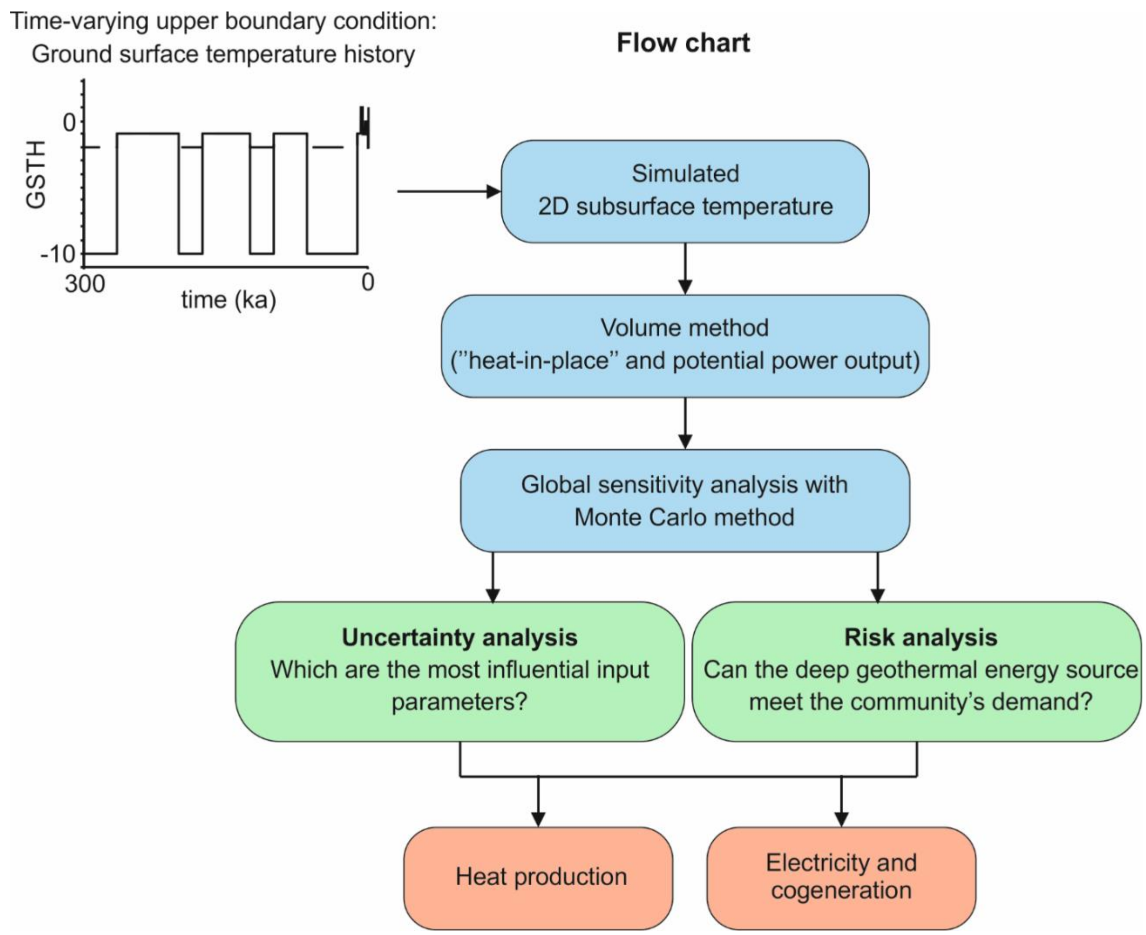

4.1 Introduction

The access to electricity is still a global challenge nowadays. In 2016, there were about 1 billion people off-grid worldwide (IRENA, 2019). In Canada, 239 communities rely solely on fossil fuels for electricity, space heating, and domestic hot water (Grasby et al., 2013; Arriaga et al., 2017). In most of these communities, the fuel is shipped only once a year with long-term storage period in sometimes old facilities having a risk of spill (Arriaga et al., 2017). Moreover, the electricity cost is volatile and more than 50% higher than in southern Canada (Arriaga et al., 2017; Makivik Corporation, 2018). Therefore, the volatility and high cost of the diesel price, the will for higher energy security, and the severe environmental consequences brought interest to develop local, sustainable, and carbon-free energy resources, not only in the Canadian remote communities but also in other off-grid areas worldwide (e.g., Schallenberg, 2002; Kanase-Patil et al., 2010; Palit et al., 2011; Chmiel et al., 2015; Bhattacharyya et al., 2016; Görgen, 2016; IRENA, 2016; World Bank, 2016; Islam et al., 2017; Wu et al., 2017; Rud et al., 2018; Selosse et al., 2018; IRENA, 2019; Viteri et al., 2019; World Bank, 2019; Ringkjob et al., 2020). Geothermal energy can be one of such renewable options to replace diesel consumption and provide electricity and heating/cooling for both Arctic/subarctic (e.g., Hjartarson et al., 2010; Majorowicz et al., 2014b; Midttome et al., 2015; Eidesgaard et al., 2019; Gascuel et al., 2020) and non-Arctic (e.g., Franco et al., 2019; GEOENERGY, 2020; Koon et al., 2020; Rajaobelison et al., 2020) remote and off-grid regions. Compared with other sources of renewable energy, geothermal has a high-capacity factor and is available indefinitely regardless of weather conditions (Kagel et al., 2005). Ground-coupled heat pumps are believed to be an interesting heating alternative for the residential dwellings (Kanzari, 2019; Gunawan et al., 2020) and to support greenhouses food production (Kinney et al., 2019) in such arctic and subarctic climate. Borehole thermal energy storage has also been studied and can be a promising technology to help improve energy and food security in the arctic/subarctic environment (Giordano et al., 2019a). Furthermore, geothermal systems of all kinds can be integrated with other renewable sources and technologies, enhancing their individual efficiency in cold climates (Mahbaz et al., 2020). Technological advances in the geothermal energy sector now allow to envision the exploitation of deep geothermal energy source in geological environments other than hydrothermal systems. For example, the engineered geothermal systems (EGS) concept (e.g., Tester et al., 2006), together with binary cycle geothermal power plants (GPP), can generate electricity from low-temperature resources (e.g., DiPippo, 2016).

Unfortunately, an important data gap exists in northern territories to accurately assess the local and deep geothermal energy source potential (cf. Grasby et al. 2013; Comeau et al., 2017; Minnick et al., 2018). For this reason, efforts have been made to adapt methodologies and draw guidelines using outcrops as subsurface analogs to provide initial data for preliminary geothermal energy source assessment associated with petrothermal systems. Thus, an evaluation of the geothermal energy source and potential heat and power output is presented in this work to forecast future energy production. It is convenient to highlight that the term geothermal energy source was utilized in this work to follow the United Nations Framework Classification on fossil energy and mineral reserves and resources 2009 to geothermal energy resources (UNECE, 2016).

Guidelines to carry out geothermal energy source and potential power output assessment associated with petrothermal systems have been proposed in the literature (e.g., Tester et al., 2006; Beardsmore et al., 2010; Limberger et al., 2014) and were adopted in this work to account for heat production and cogeneration. These previous studies differ in terminology and somewhat calculation methods. Tester et al. (2006) followed the resources terminology of Muffler et al. (1978), while Beardsmore et al. (2010) and Limberger et al. (2014) followed the geothermal potential classification of Rybach (2015). Moreover, Limberger et al. (2014) extended Beardsmore et al. (2010) protocol and evaluated the levelized cost of energy and the economic potential. Regardless of the protocol followed, the basic element of the geothermal energy source and potential heat and power output assessment is the estimation of the available thermal energy, or “heat-in-place”. The volume method introduced by USGS (United States Geological Survey) researchers (e.g., Bolton, 1973; White et al., 1975; Muffler et al., 1978) is the most widely used evaluation technique to infer the available thermal energy (e.g., Tester et al., 2006; Blackwell et al., 2007; Tester et al., 2007; Williams et al., 2008; Beardsmore et al., 2010; Sarmiento et al., 2013; Limberger et al., 2014; Busby et al., 2017; Agemar et al., 2018; Minnick et al., 2018). This method is based on the evaluation of the heat stored in a certain volume of rock at specified depths in relation to the mean annual surface temperature (Muffler et al., 1978). However, many authors argued that, for a more realistic assessment, the reference temperature should be equivalent to the reservoir abandonment temperature. This is dependent on the intended application (space heating and/or electricity generation) and on the type of GPP to be installed (e.g., Beardsmore et al., 2010; Sarmiento et al., 2013; Garg et al., 2015). The second key element is the recoverable fraction. This concept was introduced since only a fraction of the available thermal energy can be harvested. This is mostly due to technical and economic constraints, such as drilling depth and cost, the active stimulated volume, the allowed reservoir thermal drawdown, and the surface land area available (Tester et al., 2006; Tester et al., 2007; Beardsmore et al., 2010). Finally, the conversion of thermal energy to power output takes into account the project lifetime, the availability of the GPP throughout the year, and the cycle thermal efficiency (Tester et al., 2006; Beardsmore et al., 2010; Sarmiento et al., 2013).

An evaluation of the subsurface temperature distribution is imperative to calculate the available thermal energy accordingly with the volume method. Thus, 2D transient heat conduction models were solved numerically with finite element method (FEM). Several climate episodes have occurred throughout Earth's history (e.g., Crowell, 1982) that propagates downwards by thermal diffusion influencing the subsurface temperature (e.g., Jessop, 1990; Beardsmore et al., 2001) and these shall not be ignored. Additionally, the effect of temperature and pressure on thermal conductivity was considered and implemented in the numerical models used to simulate the subsurface temperature. The variability of the rock thermal conductivity has been shown to influence these predictions (e.g., Lemenager et al., 2018; Velez Marquez et al., 2018a; Norden et al., 2020).

Then, the assessment of the available thermal energy was constrained by the envisioned applications: heat production and electricity generation. The minimum temperature for space heating is about 30 – 50 °C (Lindal, 1973; Sarmiento et al., 2013) and for electricity generation using a binary cycle GPP designed for an Arctic climate is about 120 – 140 °C (Tomarov et al., 2017).

Thus, these were used as reservoir abandonment temperatures. Nevertheless, Organic Rankine Cycle with an optimized working fluid may generate electricity from geothermal energy source lower than 120 °C (e.g., Liu et al., 2017; Tillmanns et al., 2017; Shi et al., 2019; Chagnon-Lessard et al., 2020). The thermal energy was assessed every 1 km in depth for a total depth of 10 km, for the land surface area occupied by the community of Kuujjuaq (*ca.* 4 km^2). Finally, a range of theoretical recovery factors was investigated. The planar fracture method developed by Bodvarsson (1951) and Bodvarsson et al. (1982), later modified by Williams (2007), has been widely used to predict theoretical recovery factors values for fracture-dominated systems (8 to 20%; Williams, 2014). Sanyal et al. (2005), however, simulated recovery factors of about 40% for a stimulated rock volume higher than 0.1 km^3. In this work, a conservative range between 2% and 20% was preferred following the recommendations of Tester et al. (2006), Tester et al. (2007) and Beardsmore et al. (2010).

Afterward, thermal energy was converted to heat and power output. For the latter, a cycle net thermal efficiency correlation equation has been proposed by Tester et al. (2006) and was used in this study. This equation estimates quantitatively the percentage of heat that can be converted to electricity by binary GPP, thus allowing for a first-order evaluation of the potential power output. The project lifetime is constrained by several economic and technical factors, such as the minimum economic limit, design life, reservoir sustainable management, maintenance, contract, and entitlement periods (Sarmiento et al., 2013; UNECE, 2016). Often, a 30-year life cycle is assumed for the evaluation of the geothermal potential (Tester et al., 2006; Beardsmore et al., 2010). However, technical aspects may dictate a longer or shorter lifetime, and this needs to be considered to evaluate the potential heat and power output and plan future energy production. Therefore, project lifetimes of 20 to 50 years were examined in this study. The GPP factor usually varies between 90% and 97% (Sarmiento et al., 2013) and this range was considered in this study.

Lastly, global sensitivity analysis with Monte Carlo simulations was undertaken in this study for uncertainty and risk evaluation (Sarmiento et al., 2008; Williams, 2014). The global sampling and probabilistic approach were preferred to account for the current geological and technical uncertainties considered in this study. Detailed explanations of the Monte Carlo method and global sensitivity analysis can be found in, for example, Rubinstein et al. (2008), Graham et al. (2013), Thomopoulos (2013), and Scheidt et al. (2018). Broadly, global sensitivity analysis based on Monte Carlo simulates the possible scenarios by random sampling the input variables jointly, within the defined span of the probability distribution functions. The use of these methods enabled to infer the most influential uncertainties and assess the probability of the deep geothermal energy source to meet the community's heat and power demand.

The influence of the statistical distribution of the bedrock thermophysical properties cannot be neglected (Miranda et al., 2020a) when doing such geothermal energy source assessment and this uncertainty was considered throughout this study. Moreover, the effect of water saturation on the thermophysical properties was considered as well. Although the water saturation cannot be readily observed at depth, its effect may lead to significant miscalculations and shall not be ignored (e.g., Harlé et al., 2019).

Thus, this study is the first of its kind undertaken in the Canadian Shield and represents an initial step to assess if deep geothermal energy source can be a viable alternative for remote northern communities settled in that physiographic region. Nevertheless, the approach followed in this study can be extended to other remote areas facing the same off-grid challenges (e.g., Svalbard, Faeroe Islands, Greenland, and other Arctic and non-Arctic communities). The thermal energy and potential output for heat production and electricity and cogeneration were examined and the main current geological (both epistemic and aleatory variability) and technical uncertainties were determined by the sensitivity analysis carried out. The statistical distribution of the thermophysical properties due to their intrinsic heterogeneous character is an aleatory variability type. The subsurface temperature, the conditions of the thermophysical properties (dry and water saturation), and the climate signal during a glacial period are epistemic uncertainties that can be decreased with further geothermal exploration development. Reservoir abandonment temperature, recovery factor, project lifetime, and GPP factor are technical uncertainties that can be optimized to maximize the energy production. The outcomes of this first-order assessment are useful to plan further geothermal developments and forecast future energy production, hence, helping remote northern communities to move toward a more sustainable energetic framework.

4.2 Geographic and geological setting

Nunavik is home to 14 communities that are independent of the southern provincial electrical grid and rely exclusively on diesel for electricity, space heating, and domestic hot water, like the majority of communities in northern Canada (Grasby et al., 2013; Arriaga et al., 2017). In this region, the price of fuel oil per liter amounted to $2.03 in 2018, which was subsidized to $1.63 by the local government (Makivik Corporation, 2018). Therefore, geothermal energy sources may be a solution for this unfavorable energetic framework. However, in Nunavik, a territory of about 507 000 km^2, only three deep boreholes exist to evaluate heat flux. Those are Raglan mine, Asbestos Hill mine, and camp Coulon, which are located away from the Inuit communities (Figure 4.1; Comeau et al., 2017 and references therein). This highlights the need of adapting geothermal exploration methodologies to use outcrops treated as subsurface analogs to obtain a first estimate of the geothermal potential.

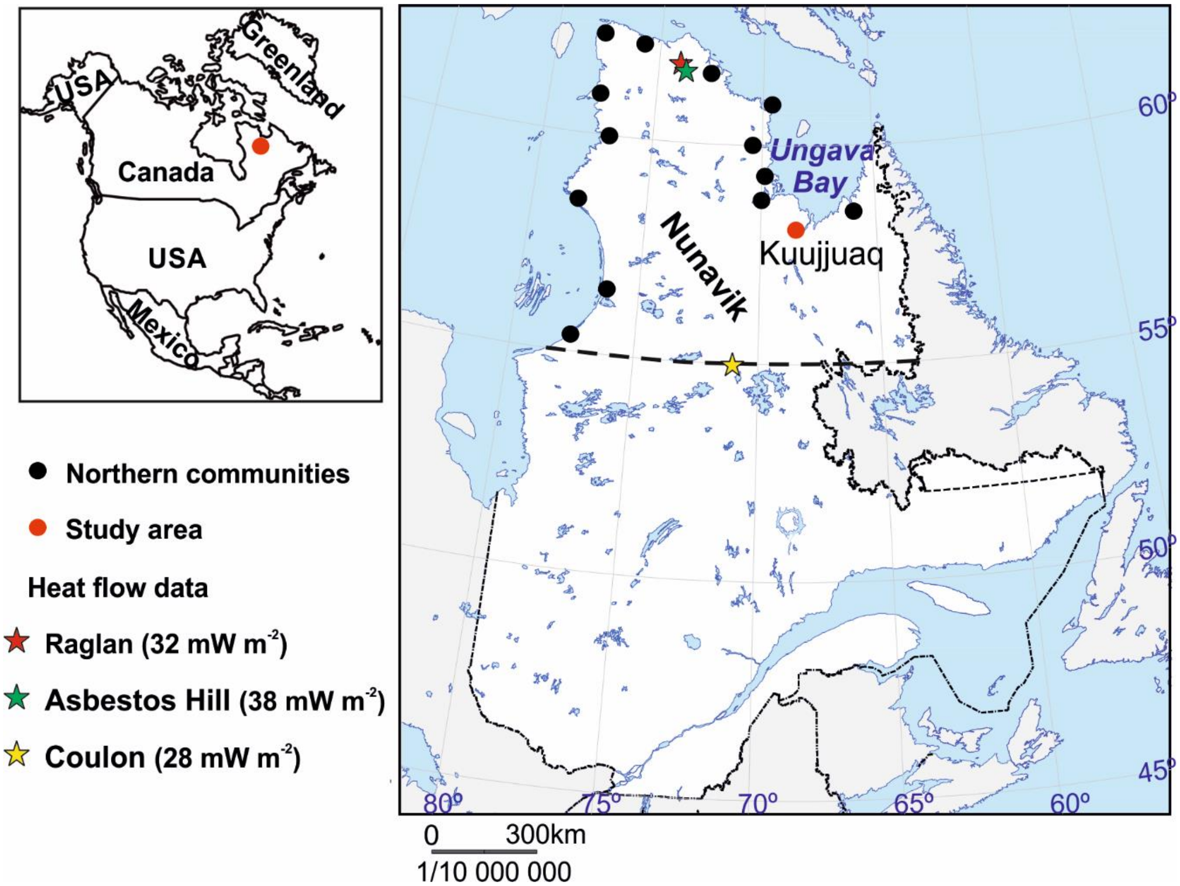

Figure 4.1 **Geographical location of Kuujjuaq and the remaining Nunavik communities (Canada) along the shore of a vast territory with few heat flow assessments: Camp Coulon, Raglan, and Asbestos Hill mining sites (Comeau et al., 2017 and references therein), adapted from Miranda et al. (2020a).**

Nunavik is a vast territory, with the communities dispersed along the shore (Figure 4.1), and for that reason, a community-focused assessment was preferred to foster local deep geothermal development. Thus, avoiding to (1) extrapolate sparse data over such a large region and (2) blind the local potential by regional anomalies far away from the communities and useless for their energy transition. Kuujjuaq (Figure 4.1) is used as a case study and an example for the remaining communities. This village is the administrative capital of Nunavik and the largest within that territory, enclosing about 2 750 inhabitants and 518 private dwellings (Statistics Canada, 2016) in a surface land area of approximately 4 km^2 (KRG, 2019). In 2000, the annual electricity demand in Kuujjuaq was about 12 000 MWh (Hydro-Quebec, 2002), increasing to 15 100 MWh in 2011 (NRCan, 2011). The daily electricity consumption amounts typically to 15 to 22 kWh per dwelling, depending on the season, and is used exclusively for lighting and electrical household appliances (Hydro-Quebec, 2019). Gunawan et al. (2020) simulated the heating load of a typical 5-occupants residential dwelling in Kuujjuaq. Their results reveal an annual heating energy demand of about 71 MWh per residence. These values provide a gross, first-order perspective of Kuujjuaq heat and power demand.

The main lithologic units outcropping near Kuujjuaq are paragneiss and diorite that were sampled in the framework of this study (Figure 4.2). These rocks belong to the Canadian Shield and are Neoarchean to Paleoproterozoic in age (SIGÉOM, 2019). A detailed description of these units and the samples collected can be found in Miranda et al. (2020a and references therein). The two main structures present in the study area are Lac Pingiajjulik and Lac Gabriel faults (Figure 4.2). Both are described as regional thrust faults with dextral movement (SIGÉOM, 2019).

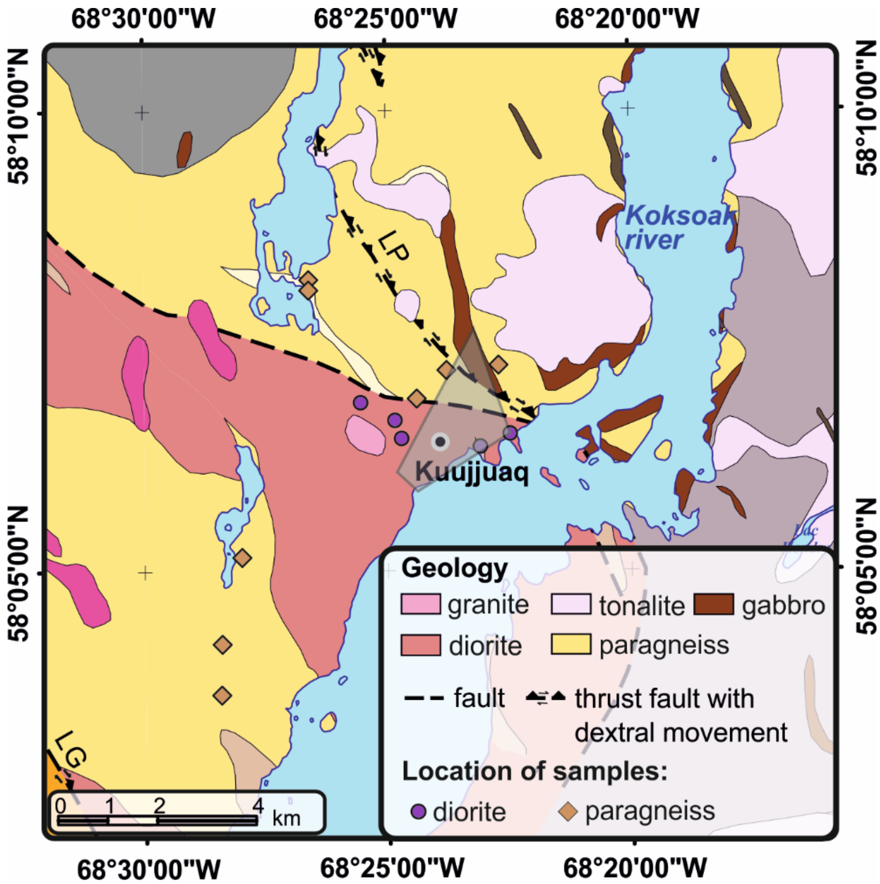

Figure 4.2 Geological map of the study area. LP—Lac Pingiajjulik fault, LG—Lac Gabriel fault. The grey polygon represents the surface land area occupied by Kuujjuaq's community (KRG, 2019), adapted from SIGÉOM (2019) and Miranda et al. (2020a).

4.3 Materials and methods

4.3.1 Thermophysical properties

A total of 13 rock samples were collected in the study area (Figure 4.2) and prepared for the laboratory analyzes. Core plugs with 20-mm-radius and 20 to 30-mm-thickness were drilled from the hand samples. Then, the core plugs were analyzed for thermal conductivity and volumetric heat capacity at dry conditions with a guarded heat flow meter. In a second time, the plugs were placed in a vacuum chamber and immersed in water for 24 h to reach the water saturation state. Thermal conductivity and volumetric heat capacity were re-evaluated considering water-saturation. Porosity was additionally evaluated as a function of pressure to indirectly infer the effect of pressure on thermal conductivity. The concentration in uranium (U), thorium (Th), and potassium (K) was determined by gamma-ray spectrometry and inductively coupled plasma-mass spectrometry (ICP-MS).

Thermal conductivity and volumetric heat capacity were evaluated at both dry and water-saturated conditions in the laboratory using a FOX50 device from TA Instruments that has an accuracy of 3%. The device consists of two plates, two heat flow meters, and two insulating casings to prevent heat losses. The method follows the ASTM (American Society for Testing and Materials) standard C1784-13 (2013). The sample is placed between the plates and the temperature is allowed to reach equilibrium. A temperature difference of 10 °C is imposed on each plate for thermal conductivity assessment. The temperature of the plates is changed instantaneously for volumetric heat capacity evaluation and the time to reach equilibrium is needed to evaluate this property based on the energy conservation equation (Ruuska et al., 2017). For both properties, successive data acquisition cycles grouped in blocks are run until all the necessary equilibrium criteria are reached and the sample is considered in thermal equilibrium (see Miranda et al., 2020a for further details). Thermal conductivity was additionally evaluated within the temperature range of 20–160 °C to define an experimental relationship that describes the effect of temperature on thermal conductivity (e.g., Schatz et al., 1972):

$$\frac{1}{\lambda(T)} = \frac{1}{\lambda_{20}} + b(T-20) \Leftrightarrow \lambda(T) = \frac{1}{(\lambda_{20})^{-1} + b(T-20)} \quad (4.1)$$

where λ (W m^{-1} K^{-1}) is thermal conductivity, T (°C) is temperature, and b is an experimental coefficient that controls temperature dependence of the thermal conductivity. The subscript 20 stands for room temperature.

The effect of pressure on thermal conductivity was assessed indirectly from the pressure dependence on porosity. The combined gas permeameter-porosimeter AP-608 was used to evaluate porosity at different confining pressures from 2.8 to 69 MPa. The evaluation of porosity follows Boyle's law, which states that the pressure exerted by a given mass of an ideal gas is inversely proportional to the volume it occupies (e.g., Raymond et al., 2017 and references therein). The results from this analysis were used to indirectly infer the effect of pressure on thermal conductivity, which is described by the following function:

$$\lambda(P) = d\, ln(P) + \lambda_{20} \tag{4.2}$$

where *P* (Pa) is pressure and *d* is an experimental coefficient that controls the pressure dependence of thermal conductivity.

The following relationship was then obtained when combining Equation (4.2) with Equation (4.1) to describe the effect of both temperature and confining pressure on thermal conductivity:

$$\lambda(T) = \frac{1}{(d\, ln(P)+\lambda_{20})^{-1}+b(T-20)} \tag{4.3}$$

The concentration in U, Th, and K was evaluated by both gamma-ray spectrometry and ICP-MS to avoid biased results (*cf*. Miranda et al., 2020a). The Ortec gamma-ray spectrometer detector used for this purpose is NaI(Tl) with 7.62 × 7.62 cm, surrounded by a 5-cm-thick lead shield. The concentrations of the radioisotopes were measured using the three-window method taking into account the emitted gamma radiation. The system is calibrated with standard solutions certified by the International Atomic Energy Agency (IAEA). The ICP-MS method, where the chemical elements passed through decomposition into their atomic constituents, was also used. The positively charged ions are extracted and separated, being finally measured by an ion detector. A quality control protocol was followed, and certified reference materials used to guarantee the reliability of the analyzes (see Miranda et al., 2020a for further details).

Radiogenic heat production was then calculated by applying Rybach's empirical function (Rybach, 1988):

$$RHP = 10^{-5}\rho(9.51[U] + 2.56[Th] + 3.50[K]) \tag{4.4}$$

where *RHP* (W m^{-3}) is the radiogenic heat production, ρ (kg m^{-3}) is the density, and *[U], [Th]* and *[K]* (mg kg^{-1}; %) is the concentration of each radioisotope.

4.3.2 2D subsurface temperature distribution

The temperature-at-depth was solved numerically by FEM in COMSOL Multiphysics® with the 2D transient heat conduction equation:

$$\frac{\partial}{\partial x}\left(\lambda\frac{\partial T}{\partial x}\right)+\frac{\partial}{\partial z}\left(\lambda\frac{\partial T}{\partial z}\right)+RHP=\rho c\frac{\partial T}{\partial t} \quad (4.5)$$

where *x* (m) and *z* (m) are spatial variables, ρc (J m^{-3} K^{-1}) is the volumetric heat capacity, and *t* (s) is time.

The geometry of the model is rectangular with width of 32 km and depth of 10 km (Figure 4.3) and takes into account the regional geological cross-section of Simard et al. (2013).

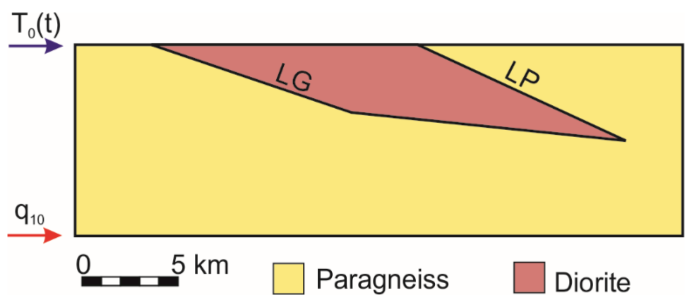

Figure 4.3 Simplified geological cross-section and model's geometry. LP—Lac Pingiajjulik fault, LG—Lac Gabriel fault; $T_0(t)$—time-varying upper boundary condition, q_{10}—basal heat flux, based on Simard et al. (2013).

The initial temperature condition to run the transient simulations was calculated using the 1D analytical solution of Equation (4.5) in steady-state:

$$T(z)=T_0+\frac{q}{\lambda}z-\frac{RHP}{2\lambda}z^2 \quad (4.6)$$

The lateral boundary conditions were assumed adiabatic. The lower boundary condition is the basal heat flux. A numerical approach has been developed by Velez Marquez et al. (2019) and improved by Miranda et al. (2021) to simulate climate events and find the basal heat flux that best matches a measured temperature log. The results of the latter were used in this work. The temperature profile was measured in an 80-m-deep groundwater monitoring well drilled prior to any of these studies. Considering the thermophysical properties at dry conditions, Miranda et al. (2021) estimated the basal heat flux to range between 31.8 to 52.3 mW m^{-2}, with an average value of 41.6 mW m^{-2}. In turn, the thermophysical properties evaluated at water saturation conditions led to an increase of the heat flux: 34.1 to 69.4 mW m^{-2}, with an average value of 49.7 mW m^{-2} (Miranda et al., 2021). The heat flux estimates of Miranda et al. (2021) were used as the lower boundary condition in the present work.

A time-varying upper boundary condition was imposed to represent the ground surface temperature history (GSTH). COMSOL Multiphysics® piecewise function was used to implement the climate events (Table 4.1). The fourfold stratigraphic framework proposed by Flint (1947) and Emiliani (1955) to characterize the late Pleistocene (300–11.6 ka before present (B.P.)) climate events were considered in this study. The temperature at the base of the Laurentide Ice Sheet is still debatable. GSTH inversion from deep temperature profiles in Canada points toward an average temperature of −5 °C during the last glacial maximum, though lower temperatures were simulated in eastern Canada than in central Canada (Sass et al., 1971; Mareschal et al., 1999; Rolandone et al., 2003; Majorowicz et al., 2015c; Pickler et al., 2016b). During the last glacial maximum, the Laurentide Ice Sheet reached a maximum thickness higher than 3 km (Jaupart et al., 2011), highlighting that under such thick ice the temperature was close to the freezing point (−1 to −2 °C; Jessop, 1971; Jessop, 1990). A sensitivity study was undertaken to deal with the uncertainty of the Laurentide Ice Sheet basal temperature and its influence on the subsurface temperature (Table 4.1).

Table 4.1 Time and temperature steps of the major Pleistocene and Holocene climate events considered for ground surface temperature history (GSTH) in this work.

Event	Time Step (Years B.P.)	Temperature Step (°C)	
		Cold Scenario	Warm Scenario
Nebraskan (MIS 14 *)	300,000–265,000	−10	−1
Aftonian (MIS 13–11 *)	265,000–200,000	0	0
Kansan (MIS 10 *)	200,000–175,000	−10	−1
Yarmouth (MIS 9–7 *)	175,000–125,000	0	0
Illinoian (MIS 6 *)	125,000–100,000	−10	−1
Sangamonian (MIS 5 *)	100,000–75,000	0	0
Wisconsinan (MIS 4–2 *)	75,000–11,600	−10	−1
Holocene (MIS 1)	11,600–present		
Holocene thermal maximum	7000–5800	+2	
Roman and Medieval warm periods	3200–1000	+1	
Little Ice Age	500–270	−1	
Pre-industrial and Industrial Revolution	270–80	+1.4	
Present-day global warming	30–present	+2	

* **Based on Emiliani (1955), MIS—Marine Isotope Stage, B.P.—before present.**

The interglacial Holocene thermal maximum occurred *ca.* 7 – 5.8 ka B.P. (Renssen et al., 2012; Gajewski, 2015; Richerol et al., 2015 and references therein) and is referred to have been 1 – 2 °C warmer than the present-day temperature (Dahl-Jensen et al., 1998; Kaufman et al., 2004; Renssen et al., 2012; Gajewski, 2015). The temperature during the interstadial Roman and Medieval warm periods (*ca.* 3.2–1 ka B.P.; Richerol et al., 2016 and references therein) were estimated to have been 1 – 1.5 °C warmer than at present (Dahl-Jensen et al., 1998). During the stadial Little Ice Age (*ca.* 500 – 270 years B.P.; Richerol et al., 2016 and references therein), the temperature is estimated to have been 1 °C lower than today (Dahl-Jensen et al., 1998).

Majorowicz et al. (2005) and Chouinard et al. (2007) identified warming of about 1.4 – 2 °C during the pre-industrial and Industrial Revolution (*ca.* 270 – 80 years B.P.). This episode was followed by a short cooling episode (80 – 30 years B.P.), where temperature decreased around 0.4 °C (Chouinard et al., 2007). Nowadays, meteorological data (ECCC, 2019) can be converted empirically to undisturbed ground temperature with (Ouzzane et al., 2015):

$$T_{\mathrm{g}} = 17.898 + 0.951 T_{\mathrm{amb}} \tag{4.7}$$

where the subscripts g and amb are used for ground and ambient (air), respectively.

This was done with Kuujjuaq historic weather data and revealed a sharp increase in the temperature of about 2 °C for the last 30 years.

The thermal properties of the geological materials were assumed at both dry and water-saturated state and the effect of temperature and pressure on thermal conductivity (Equation 4.3) was implemented in the model. The statistical distribution of the thermophysical properties was also taken into account. The transient simulations were carried out for 300 ka with yearly time step to ensure a smooth solution for the effect of the more recent and short episodes of surface temperature changes. The backward differentiation formula was chosen for the time step method (e.g., Beck et al., 1965). The steps taken by the solver were set as free after a step-independency study have been undertaken.

4.3.3 Geothermal energy source and potential power output

4.3.3.1 Volume method

The available thermal energy content was assessed within the limits of Kuujjuaq land surface area covering 4 km^2 (Figure 4.2) down to 10 km. Volumetric heat capacity at both dry and water-saturated state was used in the calculations and its statistical distribution was considered as well. The available thermal energy was inferred with (e.g., Muffler et al., 1978):

$$e_{\mathrm{th}} = V\rho c (T_{\mathrm{res}} - T_{\mathrm{ref}}) F_{\mathrm{rec}} \tag{4.8}$$

where e_{th} (J) is the thermal energy, V (m^3) is the volume, and F_{rec} (%) is the recovery factor. The subscripts res and ref stand for reservoir and reference temperature, respectively.

The former was obtained through the 2D temperature simulations previously described and for the latter, the following hypotheses were assumed:

1. The reservoir abandonment temperature for space heating is about 30 – 50 °C (Lindal, 1973; Sarmiento et al., 2013)
2. The minimum temperature to generate electricity by a binary GPP considering an Arctic design is around 120 – 140 °C (Tomarov et al., 2017)

The recovery factor is not yet well constrained at this early stage of the geothermal exploration and, therefore, a theoretical range of 2 – 20% was used (Tester et al., 2006; Tester et al., 2007; Beardsmore et al., 2010). The conversion of the thermal energy to potential heat and power output (*PO*; $W_{th,\ e}$) was calculated with (Tester et al., 2006; Beardsmore et al., 2010; Sarmiento et al., 2013):

$$PO = \frac{e_{\mathrm{th}} \eta_{\mathrm{th}}}{F_{\mathrm{GPP}} t} \tag{4.9}$$

where η (%) is the cycle efficiency and F_{GPP} (%) is the GPP factor related with its availability throughout the year. The subscript th stands for thermal.

The cycle net thermal efficiency was calculated as indicated by Tester et al. (2006):

$$\eta_{\mathrm{th}} = 0.0935 T_{\mathrm{res}} - 2.3266 \tag{4.10}$$

The cycle thermal efficiency was only used to estimate the theoretical potential for electricity generation. The heat production evaluation did not consider this parameter since the heat energy is used directly (e.g., Glassley, 2010). A range between 20 to 50 years of project lifetime was assumed. The GPP factor was varied between 90% and 97% (Sarmiento et al., 2013). It is important to highlight that no temperature loss was considered in this study (Beardsmore et al., 2010).

4.3.3.2 Global sensitivity analysis with Monte Carlo method

A global sensitivity analysis was undertaken to assess the joint effect of each parameter (and respective uncertainty; Table 4.2) on the potential heat and power output based on Monte Carlo method (Scheidt et al., 2014). The simulations were carried out with @Risk (Palisade, 2019) using Latin Hypercube sampling (Mackay, 1998) and the pseudorandom number generator Marsenne Twister (Matsumoto et al., 1998). The Latin Hypercube sampling was chosen since it is referred to be more reliable and efficient than Monte Carlo sampling (Vose, 2008). A total of 10,000 iterations (i.e., possible scenarios) were run per simulation to assure output stability. Moreover, the initial random number seed was fixed to 1 in all the simulations carried out. A total of 3 simulations without changing any of the inputs were run to confirm the solidity of the randomness of the sampling (Vose, 2008). This approach was followed after carrying out an analysis of the stochasticity component of the response (Scheidt et al., 2018). Five simulations were run and the difference in the output was less than 10%, indicating that the spatial uncertainty of the input parameters will have a minor impact on the deep geothermal energy source and potential heat and power output, and therefore can be neglected.

Table 4.2 Monte Carlo method input parameters and their uncertainty.

Parameter Code	Parameter Description	Variable Type	Distribution
Geological uncertainties			
V	Reservoir volume		Single value
T_{res}	Reservoir temperature	Continuous	Triang(min,median,max)
ρc	Volumetric heat capacity	Continuous	Normal(μ*,σ*)
Technical uncertainties			
T_{ref}	Reservoir abandonment temperature	Continuous	Uniform(min,max)
F_{rec}	Recovery factor	Continuous	Uniform(min,max)
η_{th}	Cycle thermal efficiency		$f(T)$
F_{GPP}	GPP factor	Continuous	Uniform(min,max)
t	Project lifetime	Continuous	Triang(min,most,max)

Triang—Triangular probability distribution, min and max—minimum and maximum values, respectively, *μ—arithmetic mean, *σ**—population standard deviation, *f*—function, most—most likely value.**

The existent GSTH and conditions of the thermophysical properties (dry or water-saturated) are unknown at this early stage of the geothermal development. Therefore, three hypotheses for the reservoir temperature were analyzed separately:

1. Thermophysical properties at dry conditions and warm GSTH
2. Thermophysical properties at dry conditions and cold GSTH
3. Thermophysical properties at water saturation conditions and warm GSTH

The outcomes from the uncertainty analysis can be translated to risk, enabling to forecast the probability of the deep geothermal energy source to meet the community's heat and power demand (Witter et al., 2019).

4.4 Results

4.4.1 Thermophysical properties

At dry conditions and room temperature, the paragneiss samples are characterized by lower thermal conductivity than the diorite samples. The former has an average value of 2.26 W m^{-1} K^{-1}, while the latter is characterized by an average thermal conductivity of 2.78 W m^{-1} K^{-1} (Table 4.3). Per contra, the volumetric heat capacity is higher for the paragneiss samples than for the diorite (Table 4.3). An average value of 2.32 MJ m^{-3} K^{-1} was inferred for the diorite while a value of 2.36 MJ m^{-3} K^{-1} was evaluated for the paragneiss. At water saturation conditions, the same trend is observed. The paragneiss samples have lower thermal conductivity but higher volumetric heat capacity than the diorite (Table 4.3). Likewise, higher concentration of radiogenic elements (U, Th, K) was evaluated for the paragneiss samples than for the diorite. This consequently influenced the inferred internal heat generation (Table 4.3). An average value of 1.08 μW m^{-3} was inferred for the paragneiss while an average value of 0.53 μW m^{-3} was evaluated for the diorite. These are average values from the two methods used in this work to evaluate the radiogenic element concentrations (gamma-ray spectrometry and ICP-MS).

Table 4.3 Results of the thermophysical properties analyzes.

	Paragneiss		Diorite	
	Dry	Wet	Dry	Wet
	λ (W m^{-1} K^{-1})			
μ^*	2.26	2.67	2.78	3.08
σ^*	0.55	0.64	0.65	0.82
χ	2.10	2.84	2.60	2.82
[min–max]	1.62–3.15	1.95–3.95	2.12–3.98	2.08–4.54
	ρc (MJ m^{-3} K^{-1})			
μ^*	2.36	2.44	2.32	2.36
σ^*	0.10	0.18	0.14	0.12
χ	2.37	2.34	2.31	2.33
[min–max]	2.20–2.47	2.27–2.71	2.16–2.53	2.22–2.59
	RHP (μW m^{-3})			
μ^*	1.08		0.53	
σ^*	0.59		0.41	
χ	1.16		0.44	
[min–max]	0.21–1.99		0.16–1.14	

λ **– thermal conductivity,** ***ρc*** **– volumetric heat capacity,** ***RHP*** **– radiogenic heat production,** ***μ**** **- arithmetic mean,** ***σ**** **- population standard deviation,** ***χ*** **– median, min and max – minimum and maximum values, respectively.**

The thermal conductivity analysis of both paragneiss and diorite samples evaluated at dry conditions within the temperature range of 20 to 160 °C reveal a decrease between 18 to 40% as a function of temperature for the paragneiss samples (Table 4.4), while for the diorite samples the decrease is 34 to 52% (Table 4.5). The effect of pressure on thermal conductivity indirectly inferred (Equation 4.2) revealed an increase of 3 to 15% for the paragneiss samples (Table 4.4) and 2 to 5% for the diorite samples (Table 4.5). The experimental coefficient *b* (Equation 4.1) is found to range between 0.0003 and 0.002 for the paragneiss samples and between 0.0011 and 0.0051 for the diorite. The coefficient *d* (Equation 4.2) varies within 0.02 and 0.20 and between 0.02 and 0.09 for the paragneiss and diorite samples, respectively.

Table 4.4 **Thermal conductivity of the paragneiss samples as a function of temperature and pressure.**

Paragneiss								
				λ (W m^{-1} K^{-1})				
T (°C)	20	40	60	80	100	120	140	160
μ^*	2.32	2.28	2.22	2.11	2.05	1.95	1.88	1.63
σ^*	0.63	0.63	0.66	0.66	0.76	0.72	0.71	0.63
χ	2.20	2.12	2.00	1.84	1.70	1.59	1.49	1.32
[min–max]	1.69–3.21	1.67–3.20	1.66–3.22	1.58–3.13	1.49–3.30	1.40–3.13	1.33–3.05	1.10–2.63
				λ (W m^{-1} K^{-1})				
P (MPa)	2.8	4.8	6.2	10.3	20.7	34.5	48.3	
μ^*	2.32	2.32	2.33	2.34	2.40	2.43	2.44	
X	2.15	2.16	2.17	2.19	2.22	2.25	2.26	
[min–max]	1.64–3.32	1.64–3.43	1.65–3.53	1.66–3.67	1.67–3.79	1.70–3.86	1.68–3.92	

λ – thermal conductivity, *T* – temperature, *P* – pressure, μ^* - arithmetic mean, σ^* - population standard deviation, χ – median, min and max – minimum and maximum values, respectively.

Table 4.5 **Thermal conductivity of the diorite samples as a function of temperature and pressure.**

Diorite								
				λ (W m^{-1} K^{-1})				
T (°C)	20	40	60	80	100	120	140	160
μ^*	2.39	2.33	2.25	2.10	1.96	1.86	1.78	1.49
σ^*	0.87	0.83	0.81	0.78	0.80	0.77	0.76	0.68
χ	2.58	2.57	2.53	2.36	2.24	2.12	2.02	1.70
[min–max]	1.41–3.73	1.39–3.60	1.30–3.42	1.18–3.16	1.01–2.91	0.94–2.75	0.87–2.67	0.68–2.33
				λ (W m^{-1} K^{-1})				
P (MPa)	2.8	4.8	6.2	10.3	20.7	34.5	48.3	
μ^*	2.83	2.86	2.87	2.90	2.94	2.96	2.98	
χ	2.65	2.67	2.68	2.71	2.75	2.76	2.78	
[min–max]	2.13–4.10	2.14–4.11	2.15–4.12	2.16–4.16	2.17–4.23	2.17–4.29	2.18–4.33	

λ – thermal conductivity, *T* – temperature, *P* – pressure, μ^* - arithmetic mean, σ^* - population standard deviation, χ – median, min and max – minimum and maximum values, respectively.

4.4.2 2D subsurface temperature distribution

Sensitivity analyzes were carried out to assess the influence of GSTH and conditions of the thermophysical properties (dry and water-saturated state) on the subsurface temperature distribution. The statistical distribution of the thermophysical properties was taken into account to run these simulations. Moreover, the effect of pressure and temperature on thermal conductivity was implemented in the models. A deterministic approach was followed, and the minimum subsurface temperature was obtained by combining the maximum value evaluated for thermal conductivity with the maximum value of volumetric heat capacity and radiogenic heat production. The maximum temperature was obtained by using the inverse combination.

4.4.2.1 Influence of model mesh

A mesh-dependency study was carried out to guarantee the reliability of the results. The free-triangular mesh was gradually refined until a constant temperature at a given point (x, z) in the model was obtained. This study started with an extremely coarse mesh (22 elements) until a constant temperature at (17,999, −4999.5) was reached for an extremely fine mesh with 8544 elements. However, a mesh with 13,725 elements was used instead to guarantee the correct distribution of the elements throughout the geometry (Table 4.6). The maximum and minimum element size was set as 250 and 0.5 m, respectively, with a maximum element growth of 1.1 and resolution of 1 in narrow regions.

Table 4.6 Verification of the mesh independence.

Number of Elements	T(17,999,−4999.5) (°C)	Relative Difference (%)
22	98.71	-
289	98.56	−0.15
758	98.52	−0.04
2223	98.53	0.01
8544	98.55	0.02
9750	98.55	0
13,725	98.55	0

4.4.2.2 Influence of GSTH

The following temperature simulations were run considering the samples at dry state. The comparison between dry and water saturation conditions is discussed in the next section. The different scenarios for the Laurentide Ice Sheet basal temperature (Table 4.1) reveal a minimal influence on the subsurface temperature distribution at the base of the model. The difference between the warm and the cold scenarios is up to 1% (Figure 4.4; Table 4.7). In the first kilometers, however, the difference is about 80% for the minimum temperature simulated and 14% for the maximum (Figure 4.4, Table 4.7). The climate scenarios reveal no influence on the median temperature simulated (Figure 4.4, Table 4.7). The uncertainty of the subsurface temperature due to the heterogeneous character of the lithological units is 78% (Figure 4.4, Table 4.7). This corresponds to the difference between the maximum and minimum simulated temperatures.

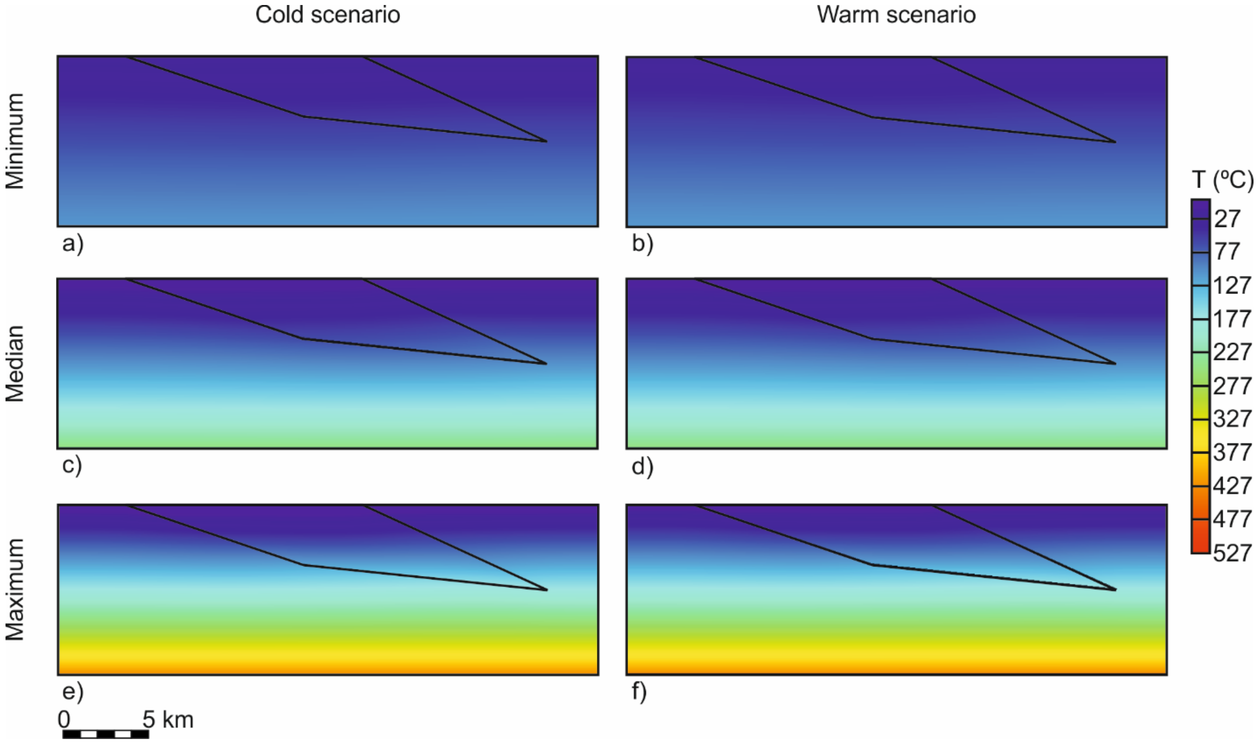

Figure 4.4 2D subsurface temperature distribution: (a) minimum temperature considering the cold scenario; (b) minimum temperature considering the warm scenario; (c) median temperature considering the cold scenario; (d) median temperature considering the warm scenario; (e) maximum temperature considering the cold scenario; (f) maximum temperature considering the warm scenario. The reader is referred to Table 4.1 for further information on the climate scenarios. Minimum, median, and maximum refer to the values evaluated for the temperature considering varying thermophysical properties in each climate scenario.

Table 4.7 Subsurface temperature distribution as a function of the GSTH.

Depth (km)	T_{min} (°C)		T_{median} (°C)		T_{max} (°C)	
	Cold	Warm	Cold	Warm	Cold	Warm
0–1	1	5	13	13	19	22
1–2	10	15	38	38	62	65
2–3	20	24	63	63	105	107
3–4	30	33	88	88	148	150
4–5	39	42	113	113	191	193
5–6	49	52	137	137	234	235
6–7	59	61	162	162	277	278
7–8	68	70	187	187	320	321
8–9	78	79	212	212	363	363
9–10	88	89	237	237	406	406

***T* – temperature, min – minimum, max – maximum. Minimum, median, and maximum refer to the values evaluated for the temperature considering varying thermophysical properties in each climate scenario. The reader is referred to Table 4.1 for further information on the climate scenarios.**

4.4.2.3 Influence of thermophysical properties conditions

The warm climate scenario was chosen to run the following temperature simulations since it revealed the best match between measured and simulated temperature profiles when evaluating the basal heat flux (Miranda et al., 2021). The water saturation of the thermophysical properties leads to a decrease of the simulated temperature in the minimum and median scenarios (on average, 17 – 10%, respectively; Figure 4.5, Table 4.8). Per contra, the maximum temperature scenario reveals an average increase of 10% (Figure 4.5, Table 4.8). The difference between the maximum and minimum temperature is, on average, 78% for the simulations at dry conditions. This difference increases to 84% in the simulations considering water saturation.

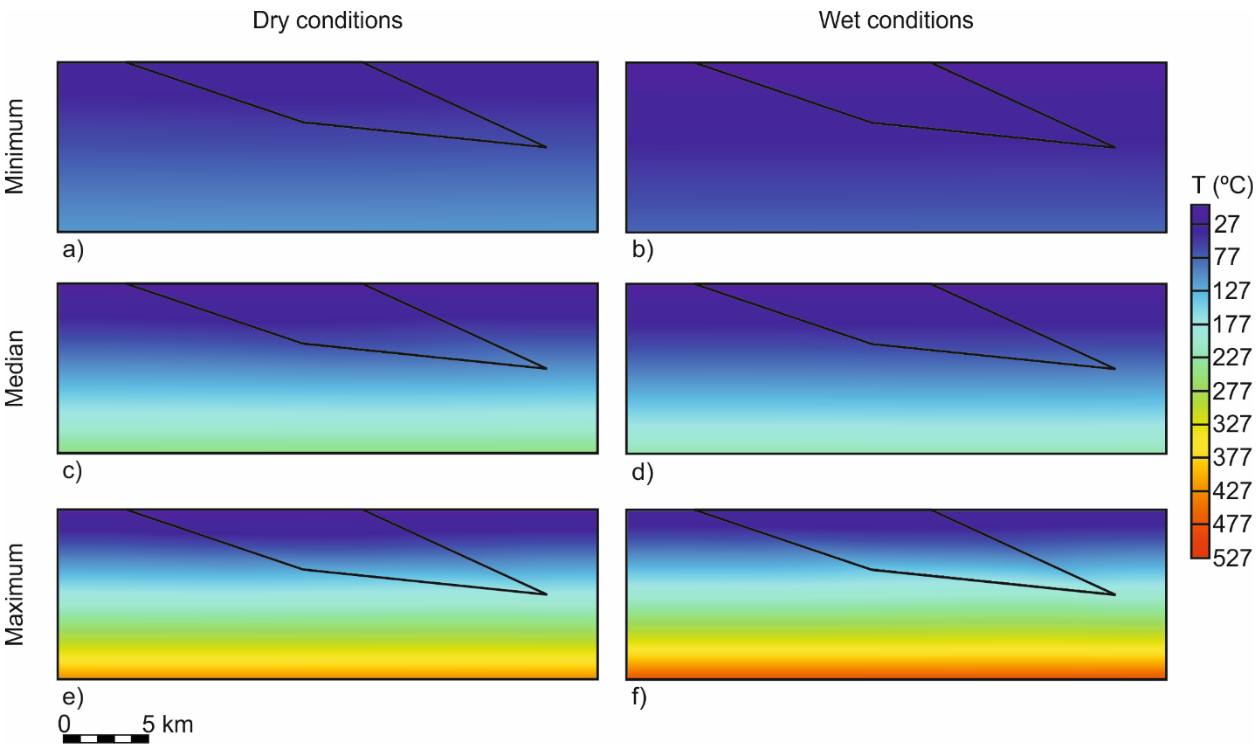

Figure 4.5 **2D subsurface temperature distribution: (a) minimum temperature considering the thermophysical properties at dry conditions; (b) minimum temperature considering the thermophysical properties at water saturation conditions; (c) median temperature considering the thermophysical properties at dry conditions; (d) median temperature considering the thermophysical properties at water saturation conditions; (e) maximum temperature considering the thermophysical properties at dry conditions; (f) maximum temperature considering the thermophysical properties at water saturation conditions. Dry and wet conditions refer to the state at which the thermophysical properties were evaluated. Minimum, median, and maximum refer to the values evaluated for the temperature considering varying thermophysical properties.**

Table 4.8 **Subsurface temperature distribution as a function of the thermophysical properties. conditions**

Depth (km)	T_{min} (°C)		T_{median} (°C)		T_{max} (°C)	
	Dry	Wet	Dry	Wet	Dry	Wet
0–1	5	5	13	12	22	25
1–2	15	12	38	34	65	72
2–3	24	20	63	57	107	120
3–4	33	28	88	79	150	167
4–5	42	36	113	102	193	215
5–6	52	43	137	124	235	262
6–7	61	51	162	147	278	310
7–8	70	59	187	169	321	358
8–9	79	67	212	191	363	405
9–10	89	74	237	214	406	453

***T* – temperature, min – minimum, max – maximum. Dry and wet conditions refer to the state at which the thermophysical properties were evaluated. Minimum, median, and maximum refer to the values evaluated for the temperature considering varying thermophysical properties.**

4.4.3 Geothermal energy source and potential heat and power output

The geothermal energy source and potential output are examined in two different sections considering the envisioned applications. Results obtained for heat production are first described, followed by electricity generation. Two key questions are answered in both sections:

1. Which geological and technical uncertainties are the most influential input parameters?
2. Can the deep geothermal energy source meet the heat/power demand in Kuujjuaq?

4.4.3.1 Heat production

The depth of 1 km was excluded from the following analyzes since the 2D subsurface temperature models revealed lower reservoir temperature than the defined reservoir abandonment temperature (30 – 50 °C; Table 4.7 and Table 4.8).

Sensitivity analyzes were carried out to infer the consistency of the input-output relationship and to compare the relative importance of the input parameters, and thus answering the first aforementioned key question. The Spearman correlation coefficient was evaluated to obtain a qualitative measure of the effect of the uncertain parameters in the potential heat output. A strong positive or negative correlation (i.e., high correlation coefficient) indicates high influence of the input parameter in the output. Per contra, a weak correlation (i.e., low correlation coefficient) suggests a minor influence. The results reveal that volumetric heat capacity and GPP factor have a very weak correlation with the potential heat output, regardless the depth, GSTH, and conditions of the thermophysical properties. The obtained Spearman coefficients range between −5% and 1% for the GPP factor and −1% and 11% for the volumetric heat capacity. The project lifetime and reservoir abandonment temperature are weakly to moderately correlated with the potential heat output. The former has correlation coefficients ranging between −1% at 2 km depth and −27% at 10 km depth. The correlation coefficients of the latter vary from −44% at 2 km depth to −4% at 10 km depth. The recovery factor and reservoir temperature reveal a moderate to very strong correlation with the potential heat output. The reservoir temperature has correlation coefficients varying between 82% and 48% as a function of depth, while for the recovery factor the coefficients increase with depth from 42% to 80%.

Therefore, due to their low correlation coefficients, any change in the GPP factor and volumetric heat capacity will have a minimal influence on the potential heat output (Figure 4.6). At 2 km depth, the potential heat output is sensitive to the reservoir abandonment temperature, but this variable loses importance as a function of depth (Figure 4.6). The significance of the project lifetime increases with depth (Figure 4.6). Nonetheless, reservoir temperature and recovery factor are clearly the most influential input parameters, regardless of the depth, GSTH, and conditions of the thermophysical properties (Figure 4.6). The results indicate a switch of rank between reservoir temperature and recovery factor (Figure 4.6) with the increase of the minimum reservoir temperature when reaching values above the minimum reservoir abandonment temperature (30 °C). Moreover, the results highlight that decreasing the reservoir abandonment temperature and the project lifetime and increasing the recovery factor led to an increase in the potential heat output.

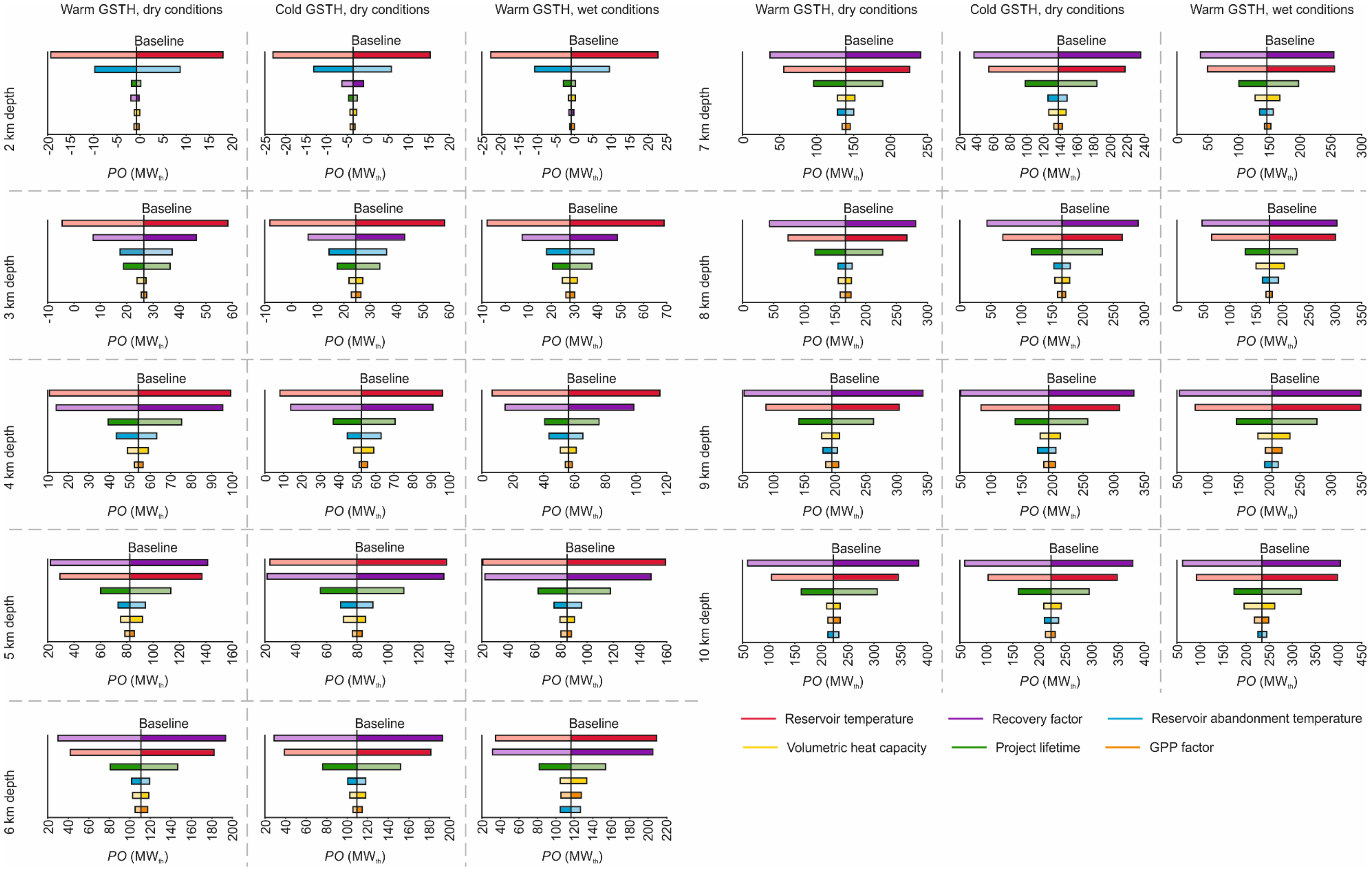

Figure 4.6 **Input parameters ranked according to their influence on the geothermal energy source and potential heat output. The reader is referred to Table 4.1 for further information on the climate scenarios. Dry and wet conditions refer to the state at which the thermophysical properties were evaluated. Baseline – overall simulated mean value; solid color – positive impact on the output; transparency – negative impact on the output.**

The probabilistic approach together with the following assumptions helps to answer the second key question: “Can the deep geothermal energy source meet the heating demand in Kuujjuaq?”:

- The average annual heating need is approximately 71 MWh per residential dwelling in Kuujjuaq (Gunawan et al., 2020)
- The total number of dwellings is 518 (Statistics Canada, 2016)

Thus, this corresponds to an average annual heat consumption of about 37 000 MWh (or, 37 GWh). This value was used as the threshold to assess the probability of the geothermal energy source to meet the community’s estimated heating demand (Figure 4.7). It is convenient to highlight, however, that this approach neglected peak loads as an auxiliary system is more likely to be used to supply heat during peak conditions.

The probability of meeting the estimated heating demand is higher than 98% at a depth of 4 km and below, considering the current geological and technical uncertain parameters along with their distribution span and regardless of the GSTH and conditions of the thermophysical properties (Figure 4.7d–i). At 2 km depth, the probability of meeting the heating demand ranges from 24.8%, for the cold GSTH, to 33.0%, for the water saturation scenario (Figure 4.7a). The geothermal energy source at 2 km depth will fulfill the community’s needs only if the reservoir temperature is above its 65^{th}–70^{th} percentile and the reservoir abandonment temperature is decreased to values below its 15^{th}–30^{th} percentile (Figure 4.8). Although the probability of meeting the heating demand at 3 km depth is 80.5 to 83.7% (Figure 4.7b), the reservoir temperature is required to be higher than its 15^{th} percentile and the recovery factor cannot be lower than the minimum value defined (2%; Figure 4.8). At 4 km and below, the heating needs are met if the uncertain parameters (mainly reservoir temperature and recovery factor) are within the defined distribution spans (Figure 4.8).

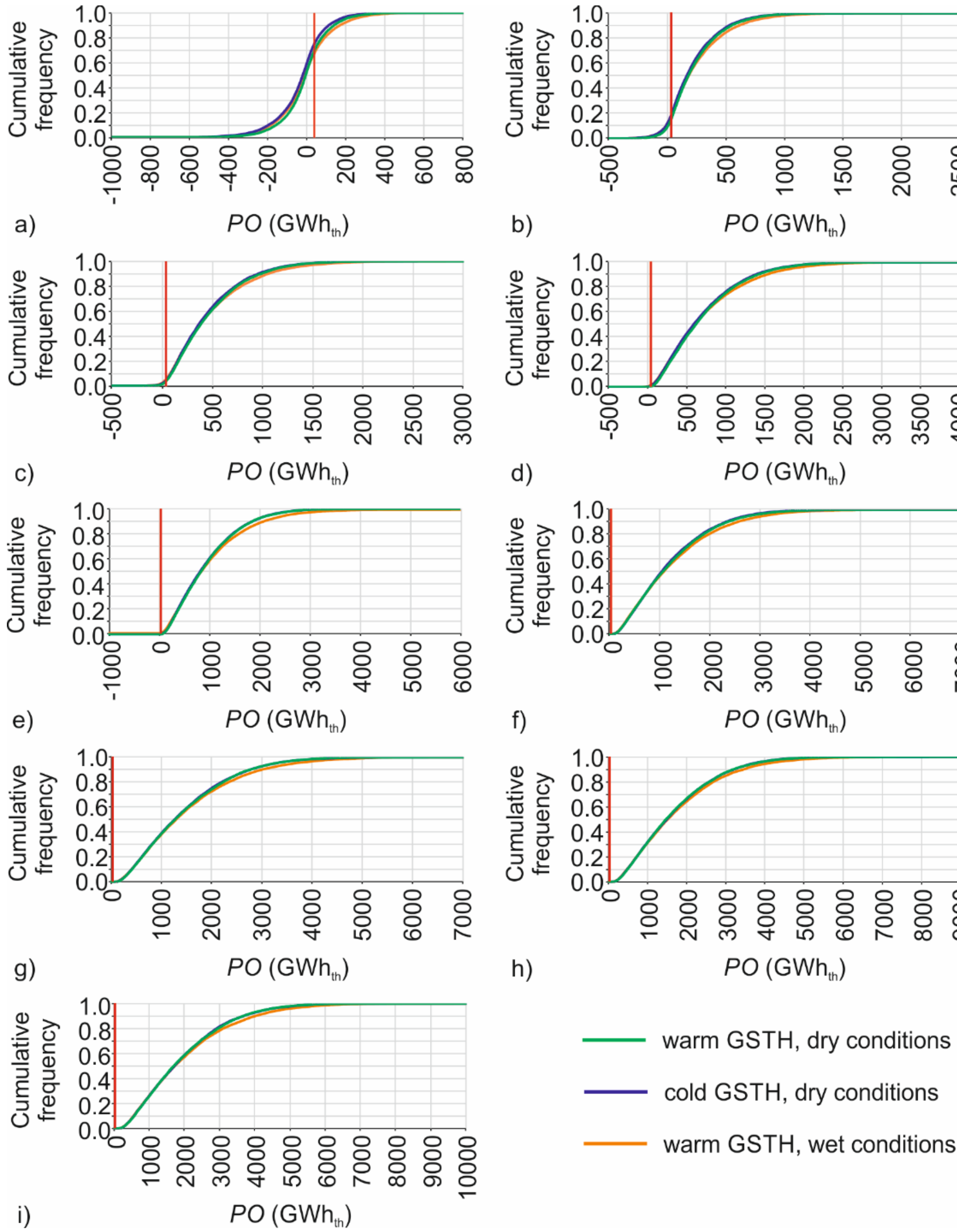

Figure 4.7 **Annual geothermal heat output potential and probability of meeting the community's annual average heating demand: (a) 2 km depth; (b) 3 km depth; (c) 4 km depth; (d) 5 km depth; (e) 6 km depth; (f) 7 km depth; (g) 8 km depth; (h) 9 km depth and (i) 10 km depth. Red line – community's estimated heating demand (see text for further details). The reader is referred to Table 4.1 for further information on the climate scenarios. Dry and wet conditions refer to the state at which the thermophysical properties were evaluated.**

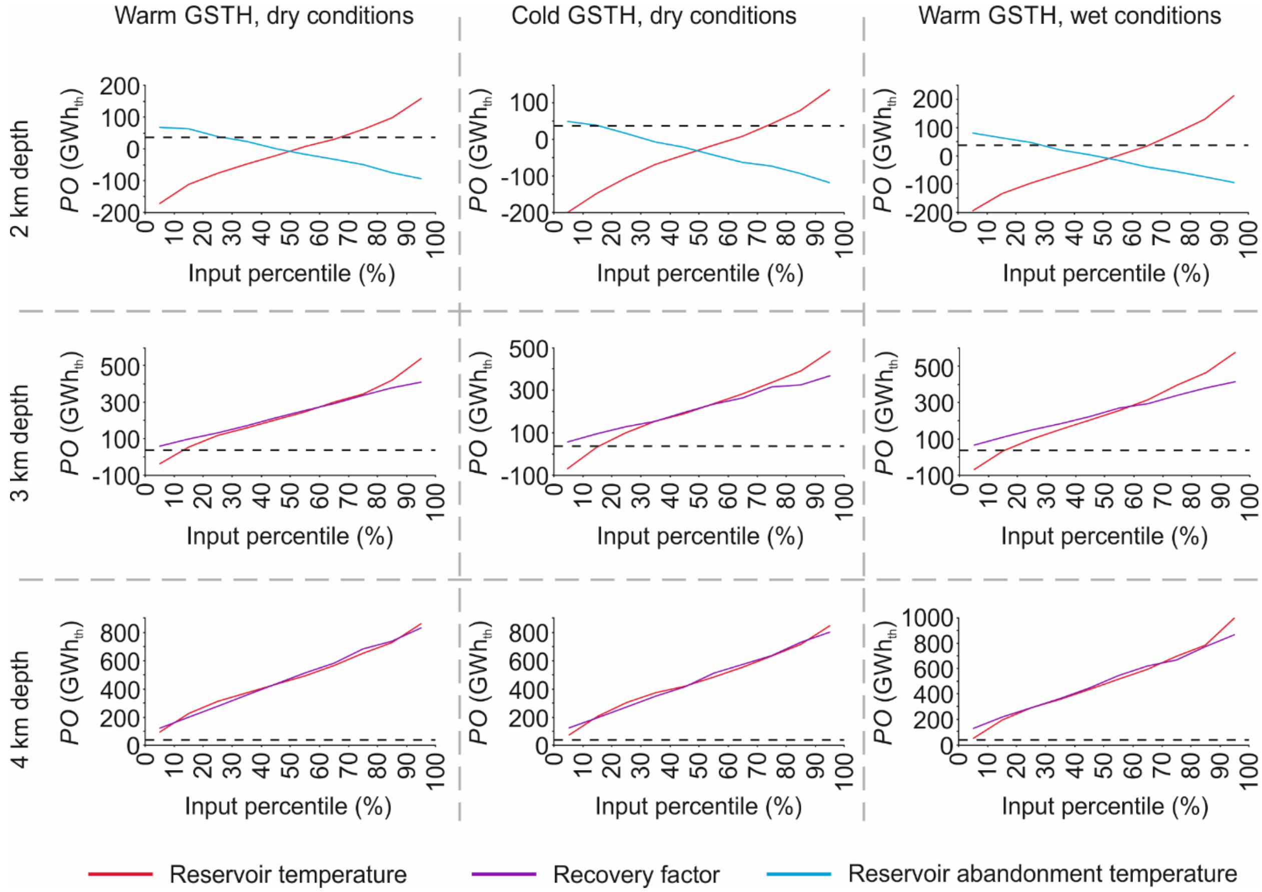

Figure 4.8 **Annual geothermal heat output potential as a function of the uncertain parameters' percentile. Dashed line – community's estimated heating demand (see text for further details). The reader is referred to Table 4.1 for further information on the climate scenarios. Dry and wet conditions refer to the state at which the thermophysical properties were evaluated.**

4.4.3.2 Electricity generation

The following analysis was made at a depth of 5 km and below since the 2D subsurface temperature models revealed lower reservoir temperature than the reservoir abandonment temperature defined for electricity generation (120 – 140 °C; Table 4.7 and Table 4.8). Moreover, although the maximum temperature simulated at 4 km is higher than 120 °C (Table 4.7 and Table 4.8), the potential power output predominantly falls within the negative values leading to biased results.

Similarly to heat production, the Spearman correlation coefficient was also inferred in this section to qualitatively evaluate the input-output relationship. Higher positive/negative correlation coefficient implies more consistency in the relationship than lower coefficient. The relative importance of the input parameters was likewise illustrated with tornado charts.

The results reveal that volumetric heat capacity and GPP factor have a very weak correlation, with the potential power output, regardless the depth, GSTH, and conditions of the thermophysical properties. The correlation coefficients vary within −2% and 2% for the GPP factor and −2% and 5% for the volumetric heat capacity. Hence, the influence of these uncertainties is minimal (Figure 4.9). The project lifetime has a weak negative correlation with the potential power output ranging between 8% and −16%. The significance of this parameter increases as a function of depth (Figure 4.9). The reservoir abandonment temperature is negatively weakly correlated to the potential power output, with coefficients varying between −20% and −5%, losing importance as a function of depth (Figure 4.9). The recovery factor is moderately correlated with the potential power output. The Spearman coefficient ranges between −26% and 48%. This uncertain parameter becomes more influential as a function of depth (Figure 4.9). Lastly, the reservoir temperature has a moderate to very strong correlation with the potential power output, with coefficients ranging within 37% and 94% and is clearly the most influential parameter for the electricity generation potential (Figure 4.9). Moreover, the results highlight that decreasing the reservoir abandonment temperature and the project lifetime and increasing the recovery factor leads to an increase in the potential power output.

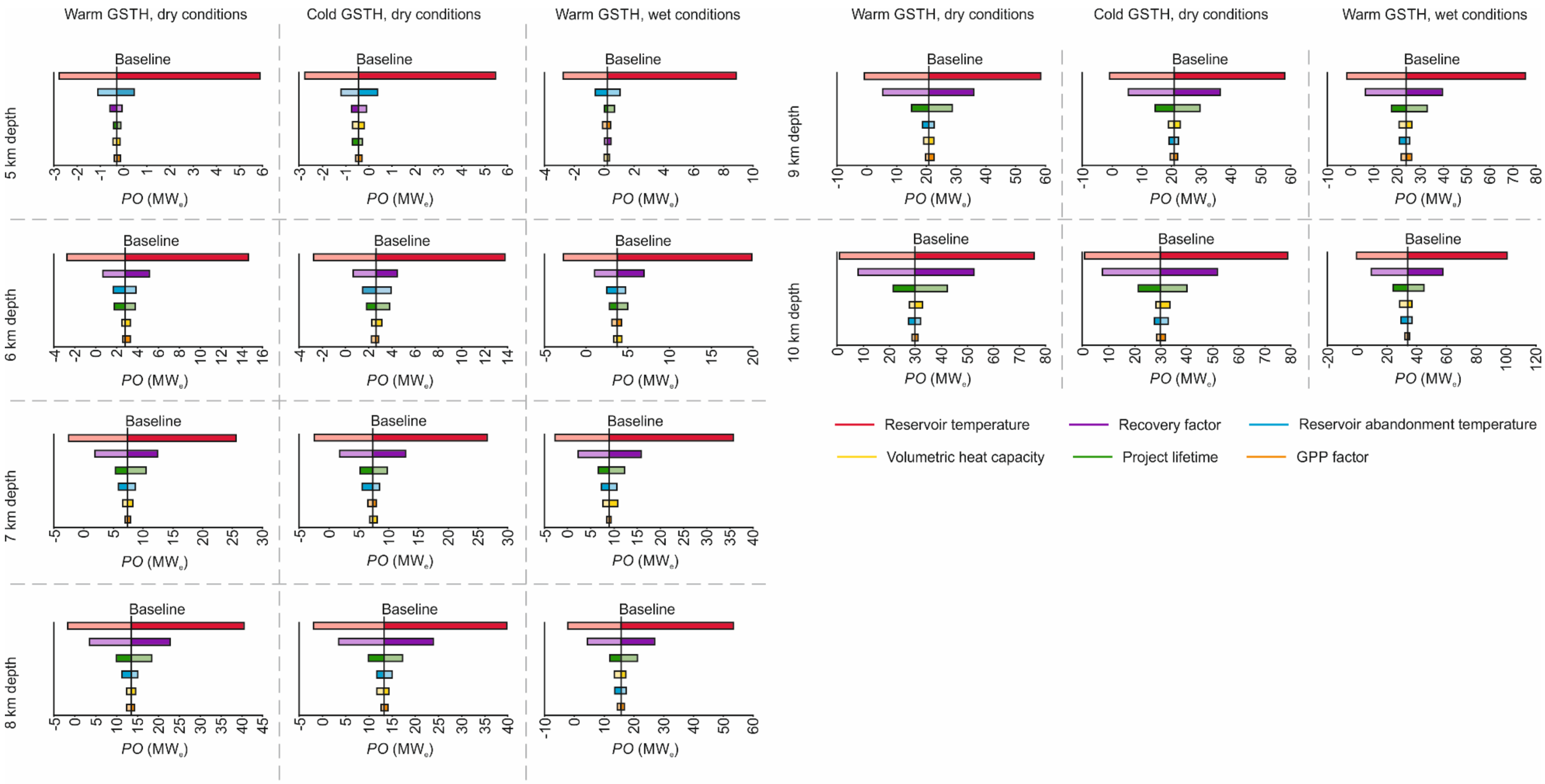

Figure 4.9 **Input parameters ranked according to their influence on the geothermal energy source and potential power output. The reader is referred to Table 4.1 for further information on the climate scenarios. Dry and wet conditions refer to the state at which the thermophysical properties were evaluated. Baseline – overall simulated mean value; solid color – positive impact on the output; transparency – negative impact on the output.**

Combining the probabilistic approach with the following assumptions enables to answer the question: “Can the deep geothermal energy source meet the power demand in Kuujjuaq?”:

- In 2011, the electricity consumption in Kuujjuaq was 15 100 MWh (NRCan, 2011)
- The population in the community of Kuujjuaq increased about 14% from 2011 to 2016 (Statistics Canada, 2016)

Hence, assuming the same growth rate in terms of electricity needs, this corresponds to the current annual consumption of approximately 18 900 MWh (or, 18.9 GWh). This value was used as the threshold to assess the probability of the geothermal energy source to meet the community’s estimated power needs (Figure 4.10). It is important to highlight that the electricity produced and consumed in the community of Kuujjuaq is only for lighting, electrical household appliances, and other electrical devices in service buildings (Hydro-Québec, 2019). The space heating and domestic hot water are provided by oil furnaces (Hydro-Québec, 2019).

The probability of meeting the power demand ranges from 13.6 to 20.2% at 5 km depth (Figure 4.10) and is between 38.4% and 40.8% at 6 km (Figure 4.10), considering the current geological and technical uncertain parameters and their distribution span. The highest percentage was obtained for the water saturation conditions while the lowest percentage is associated to the cold GSTH. At depths of 7 km and below, the probability of meeting the power demand is higher than 50% but lower than 100% (Figure 4.10). The probability is 88 to 91.2% at 10 km, depending on the GSTH and the conditions of the thermophysical properties (Figure 4.10). The lowest value was obtained for the water saturation state while the highest value for the dry conditions.

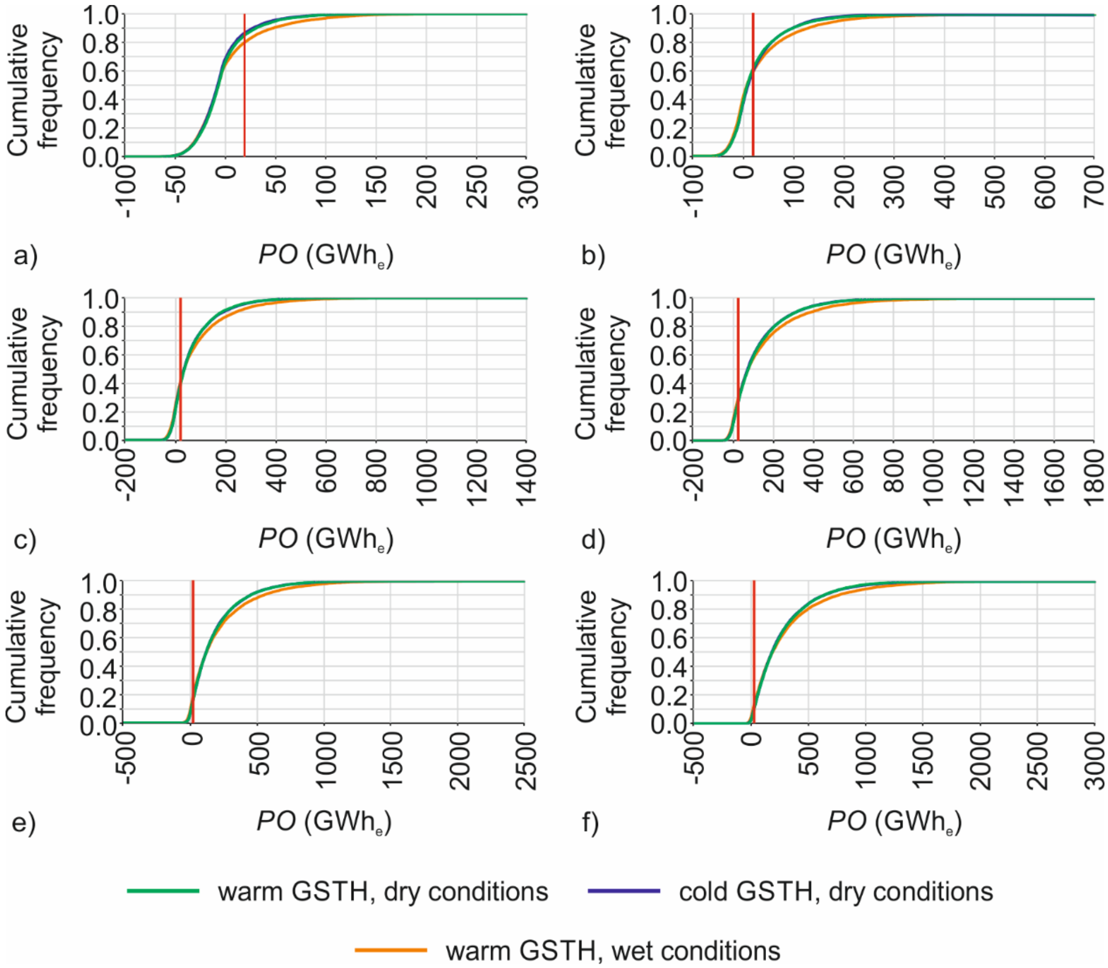

Figure 4.10 **Annual geothermal power output potential and probability of meeting the community's electricity demand: (a) 5 km depth; (b) 6 km depth; (c) 7 km depth; (d) 8 km depth; (e) 9 km depth and (f) 10 km depth. Red line – community's estimated electricity demand (see text for further details). The reader is referred to Table 4.1 for further information on climate scenarios. Dry and wet conditions refer to the state at which the thermophysical properties were evaluated.**

Moreover, a detailed analysis was carried out indicating that at 5 km depth, the power demand will be met if the reservoir temperature is higher than its 80th percentile, regardless of the GSTH and the conditions of the thermophysical properties (Figure 4.11). At 6 km, the reservoir temperature must be higher than its 55th percentile, the recovery factor higher than its 40th percentile, and the reservoir abandonment temperature and the project lifetime lower than their 80th percentile (Figure 4.11). At 7 km, the demand is met if the reservoir temperature is above its 35th percentile (Figure 4.11). At 8 km, the reservoir temperature needs to be higher than its 20th percentile and at 9 and 10 km, above its 10th percentile (Figure 4.11). At 7 km and below, the recovery factor is required to be higher than the minimum defined value (2%; Figure 4.11).

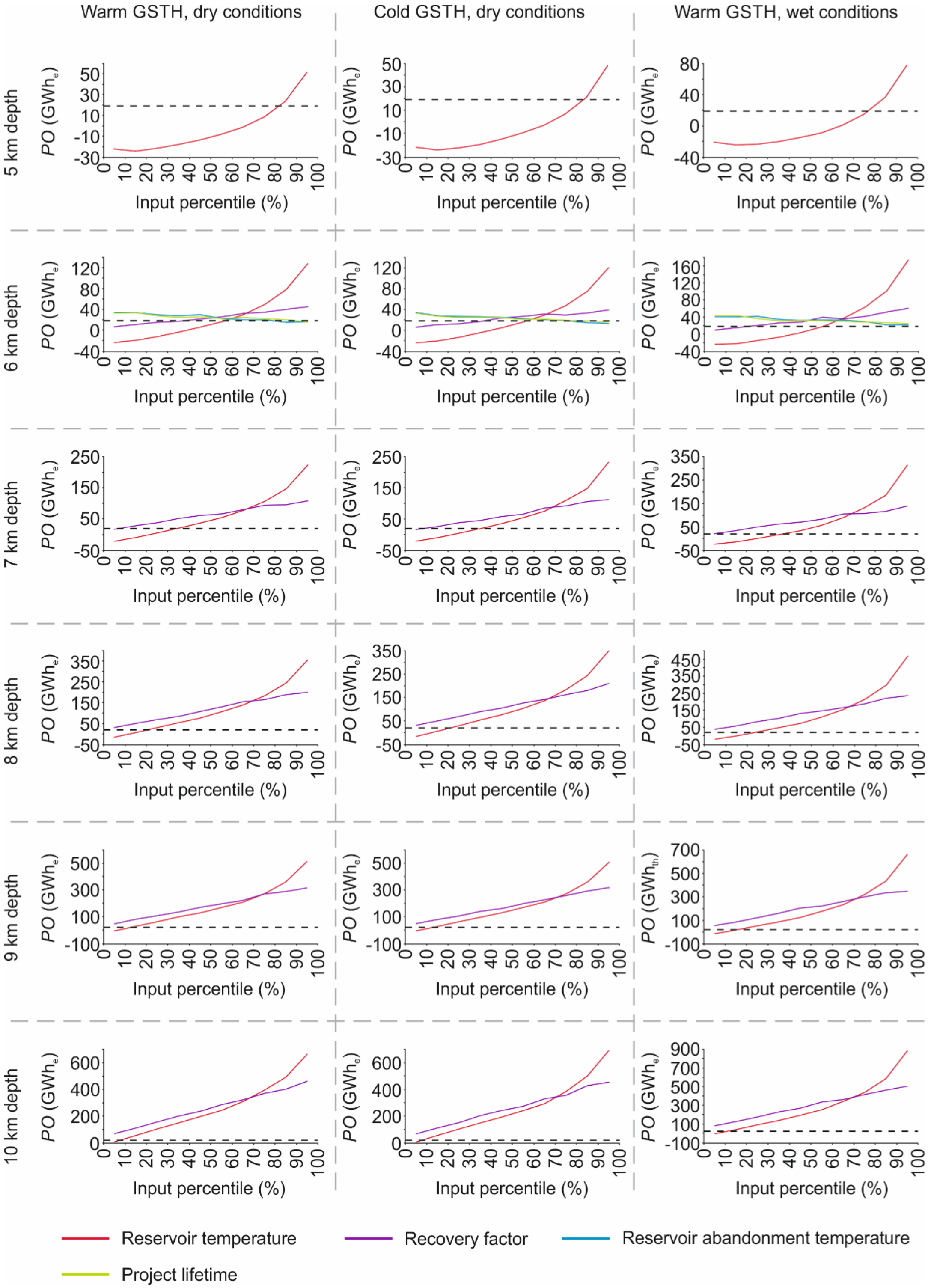

Figure 4.11 Annual geothermal power output potential as a function of the uncertain parameters' percentile. Dashed line – community's estimated power demand (see text for further details). The reader is referred to Table 4.1 for further information on the climate scenarios. Dry and wet conditions refer to the state at which the thermophysical properties were evaluated.

Cogeneration of heat and electricity, or combined heat and power (CHP), can potentially improve the efficiency of the geothermal energy source. The waste heat from the conversion process can be used for heat supply instead of being discharged to the environment (Rybach et al., 2004; Lund et al., 2007; Saadat et al., 2010; Gehringer, 2015). Thus, an analysis was carried out for a depth of 5 km and below to assess if CHP can be an alternative to supply both heat and power.

The results reveal that about 5 to 14 MWth are rejected per each MWe produced when considering geothermal energy sources in Kuujjuaq (Table 4.9). The waste heat decreases as a function of depth as the cycle thermal efficiency increases as a function of the reservoir temperature. Although 50% to 60% of this waste heat can only be used for other applications (Gehringer, 2015) as the remaining is utilized by parasitic equipment requirements (Lund et al., 2007), the annual heat output potential associated to CHP is significant (Table 4.9). However, the probability of fulfilling the community's annual heating demand is lower than 90% at 5 km depth, decreasing to less than 12% at 10 km depth (Figure 4.12).

Table 4.9 Waste heat produced per unit electric capacity (MW_{th}/MW_e) and combined heat and power (CHP) heat output potential considering 50% of the waste heat is recovered.

Depth (km)		Waste Heat (MW_{th})			CHP (GWh_{th})		
		Warm GSTH, Dry	Cold GSTH, Dry	Warm GSTH, Wet	Warm GSTH, Dry	Cold GSTH, Dry	Warm GSTH, Wet
5	*μ**	13	14	14	58	62	62
	*σ**	6	7	8	26	32	37
	[min–max]	6–51	6–72	6–93	28–222	28–317	25–406
6	*μ**	10	11	11	46	47	48
	*σ**	4	5	6	19	21	25
	[min–max]	5–39	5–42	5–58	22–169	23–185	20–254
7	*μ**	8	9	9	37	38	38
	*σ**	3	4	4	15	16	19
	[min–max]	4–29	4–31	4–39	19–126	19–134	17–172
8	*μ**	7	7	7	31	32	32
	*σ**	3	3	3	12	13	15
	[min–max]	4–23	4–24	3–30	16–102	16–106	14–132
9	*μ**	6	6	6	27	27	28
	*σ**	2	2	3	10	10	13
	[min–max]	3–19	3–20	3–25	14–85	14–87	12–108
10	*μ**	5	5	6	24	24	24
	*σ**	2	2	2	9	9	11
	[min–max]	3–17	3–16	3–21	12–72	12–72	11–91

μ **- arithmetic mean, *σ** - standard deviation, min – minimum, max – maximum. The reader is referred to Table 4.1 for further information on the climate scenarios. Dry and wet conditions refer to the state at which the thermophysical properties were evaluated.**

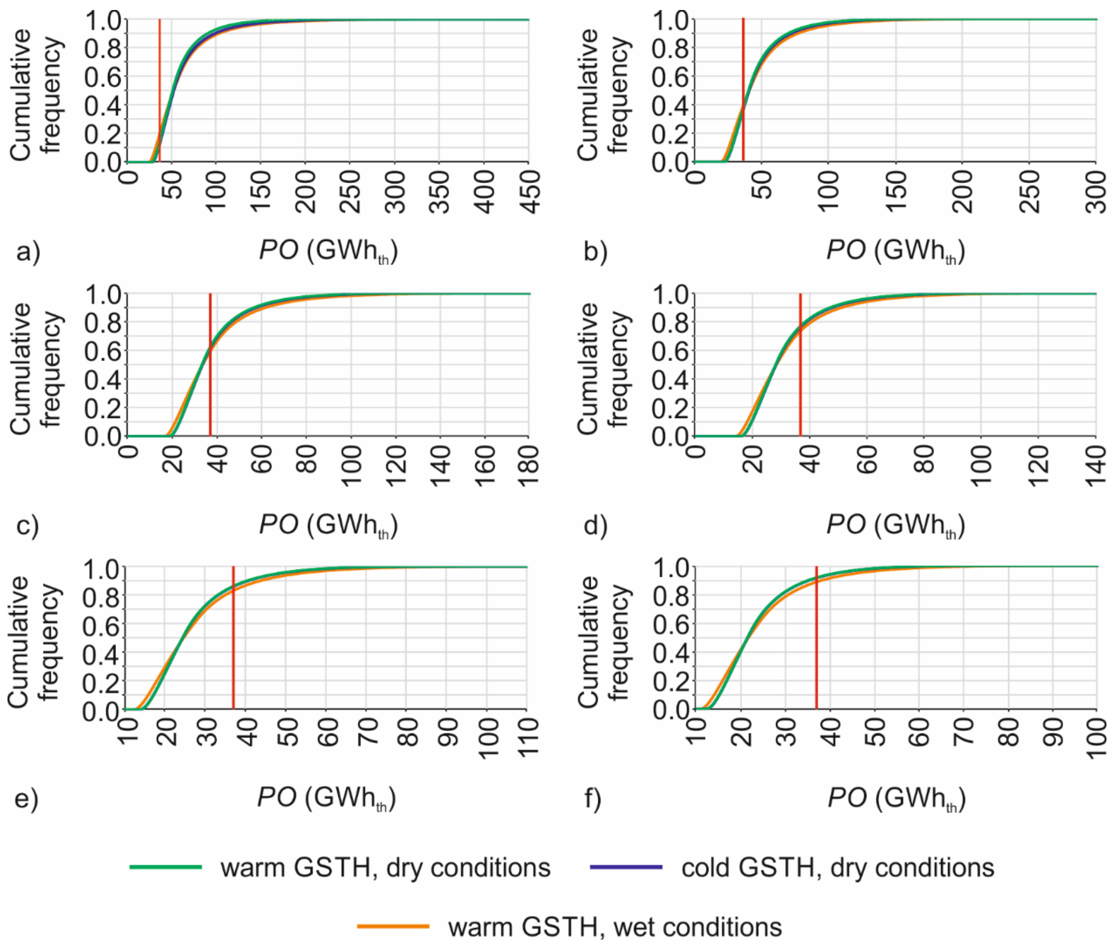

Figure 4.12 Annual CHP heat output potential and probability of meeting the community's heating demand: (a) 5 km depth; (b) 6 km depth; (c) 7 km depth; (d) 8 km depth; (e) 9 km depth; and (f) 10 km depth. Red line – community's estimated heating demand (see text for further details). The reader is referred to Table 4.1 for further information on the climate scenarios. Dry and wet conditions refer to the state at which the thermophysical properties were evaluated.

4.5 Discussion

The exclusive reliance on diesel for electricity, space heating, and domestic hot water is a reality in Canada, not only in Nunavik but also in the remaining 225 communities spread over Northwest Territories, Nunavut, Yukon, and in the northern part of the provinces of British Columbia, Manitoba, Ontario, and Newfoundland and Labrador (Arriaga et al., 2017). These Arctic and subarctic communities are at the front line of climate change and can play a leading role in providing energy solutions to this national and global challenge. The investment in the geothermal energy sector, for instance, can support local and sustainable economic development by creating business opportunities, improve energy security, ensure price stability, and help reducing greenhouse gas emissions (Serdjuk et al. 2013). However, there are still significant challenges in remote northern regions that need to be overcome, for example, at the level of the early stage of geothermal research and development. As mentioned in this study, important data gaps exist in remote areas. Deep boreholes suitable for geothermal energy source assessment are limited to areas of interest for oil and gas and mining exploration (Grasby et al., 2013; Comeau et al., 2017), and thus often located away from the communities where the targeted energy customers are. Therefore, there is a growing need to adapt methodologies and define guidelines in the remote northern regions using outcrops treated as subsurface analogs and shallow data for a first-order assessment of the deep geothermal energy source. This is paramount to stimulate interest to finance further developments and help to advance the stage of exploration, mainly in the Canadian Shield. This geological province has been assumed less favorable for geothermal development when compared to the western sedimentary basins (Majorowicz et al., 2010a; Majorowicz et al., 2010b; Grasby et al., 2012; Grasby et al., 2013). However, these previous geothermal energy source assessments have been based on the extrapolation of limited and uneven distributed heat flux data. Thus, this first-order community-scale research targeting deep geothermal energy source based on surface geological information is an important contribution to help advance the stage of geothermal research and development in remote northern regions. The work has been undertaken in the community of Kuujjuaq (Nunavik, Canada) as a case study to define guidelines that can be further used in the remaining Canadian remote northern communities.

In the following subsections are discussed the weaknesses and strengths of this work, highlighting not only additional envisioned work and future directions but also data limitations that require further geothermal exploration developments for a more accurate evaluation of the deep geothermal energy source. Moreover, the contribution of this work is discussed in the context of the energy transition of remote northern communities located in unconventional geological settings with respect to geothermal energy, and the advantages of deep geothermal energy are compared with other renewable energy sources.

4.5.1 Thermophysical properties

In the lack of borehole cores, the thermophysical properties of surficial rocks treated as subsurface analogs are essential for a first-order characterization of the deep geothermal energy source (Miranda et al., 2020a and references therein). Therefore, these properties were evaluated, and the results obtained are in the range of values mentioned in literature for similar lithologies of Canadian Shield rocks (e.g., Rolandone et al., 2002; Perry et al., 2006; Phaneuf et al., 2014; Comeau et al., 2017). Moreover, the values are in accordance with the mineralogical composition and geochemistry of the rock samples (see Miranda et al., 2020a for further details). The obtained decrease of thermal conductivity as a function of temperature (Table 4.4 and Table 4.5) and its increase as a function of pressure (Table 4.4 and Table 4.5) and water saturation (Table 4.3) also agree with other experimental studies (e.g., Vosteen et al., 2003; Abdulagatov et al., 2006; Nagaraju et al., 2014).

4.5.2 2D subsurface temperature distribution

The subsurface temperature distribution was simulated numerically in COMSOL Multiphysics® with the FEM solving the 2D transient heat conduction equation. The geometry of the conceptual model (Figure 4.3) is based on a schematic regional cross-section of the Ungava Bay area proposed by Simard et al. (2013) and thus simplified. Further geothermal exploration developments, such as drilling of exploratory wells and geophysical campaigns (e.g., borehole logging, magnetotellurics; Kana et al., 2015) will be needed to obtain a more complex subsurface geological model.

Nevertheless, this simplified geological conceptual model is helpful for this first-order assessment of the deep geothermal energy source. Moreover, by imposing a time-varying upper boundary condition, the model is capable to reproduce the variations in the surface temperature caused by the several climate events that have been occurring since late Pleistocene (Table 4.1; Flint, 1947; Emiliani, 1955; Jessop, 1971; Sass et al., 1971; Dahl-Jensen et al., 1998; Mareschal et al., 1999; Rolandone et al., 2003; Kaufman et al., 2004; Majorowicz et al., 2005; Chouinard et al., 2007; Jaupart et al., 2011; Renssen et al., 2012; Gajewski, 2015; Majorowicz et al., 2015c; Pickler et al., 2016b; Richerol et al., 2016; ECCC, 2019).

These climate disturbances propagate downwards by thermal diffusion, disrupting the steady-state geothermal gradient and affecting not only the present-day heat flux (Miranda et al., 2021 and references therein) but the subsurface temperature as well (as supported by this work; Table 4.7). The amplitude of the climate events exponentially decay with depth and their signal attenuates (Beardsmore et al., 2001). Therefore, at a depth below 5 km, the disturbance caused by the paleoclimate is expected to be in phase with the subsurface temperature, as demonstrated by the analytical solution to correct temperature profiles for the paleoclimate effects (Birch, 1948). The two GSTH scenarios simulated to address the uncertainty associated with the Laurentide Ice Sheet basal temperature (cold and warm; Table 4.1) revealed a difference between scenarios up to 80% at the surface, progressively decreasing to 1% at the base of the model (Figure 4.4, Table 4.7). Therefore, agreeing with the climate signal attenuation with depth. Moreover, the model also reveals that the effects of the climate events are stronger than the lateral variation of the thermophysical properties. The temperature distribution is laterally uniform throughout the model.

The existent subsurface conditions (dry or water saturation) are an unknown that cannot be readily observed at depth. Therefore, two possible scenarios were simulated and compared to deal with this uncertainty. The difference between them is −20 to 10% (Figure 4.5, Table 4.8), agreeing with Harlé et al. (2019) and highlighting that both scenarios shall be considered when evaluating the deep geothermal energy source.

Beyond the uncertainty imposed by the GSTH and subsurface conditions, the aleatory variability associated with the statistical distribution of the bedrock thermophysical properties was also considered. The three-point estimation technique was used to infer the variability of both the heat flux (Miranda et al., 2021) and the thermophysical properties and, therefore, to presume a minimum, median, and maximum scenarios for the subsurface temperature. The associated uncertainty ranges from 78% to 84%. Deep temperature profiles will enable to ascertain more accurately the heat flux and, subsequently, the subsurface temperature and more complex geostatistical tools can then be applied for the uncertainty quantification (Caers, 2011; Scheidt et al., 2018; Athens et al., 2019). Nevertheless, the adopted methodology developed by Velez Marquez et al. (2019) and improved by Miranda et al. (2021) to infer heat flux from shallow temperature logs (80 m), together with the thermophysical properties of the surficial rock samples, is a valuable tool to carry out a first-order assessment of the deep geothermal potential in remote northern communities.

Finally, the effect of both pressure and temperature on thermal conductivity was implemented in the numerical models. The volumetric heat capacity, however, was assumed independent of temperature and a uniform distribution of the radiogenic heat production as a function of depth was considered. Nevertheless, further developments can be envisioned to account for the effect of temperature on the volumetric heat capacity (e.g., Vosteen et al., 2003) and the possible exponential decay of heat production with depth (Lachenbruch, 1970).

4.5.3 Geothermal energy source and potential heat and power output

In this study, the volume method together with a Monte Carlo-based sensitivity analysis was used to evaluate the deep geothermal energy source. The approach followed considered both current geological and technical uncertainties and evaluated the deep geothermal potential in terms of heat production and electricity and cogeneration at each 1 km depth. Three different scenarios were assumed separately to deal with the uncertainty imposed by the GSTH and the conditions of the thermophysical properties (dry vs. water saturation) on the subsurface temperature. The recovery factor is considered a technical uncertainty in this work rather than a geological one (Witter et al., 2019) since reservoir active volume and flow rate can be optimized by engineering interventions (Tester et al., 2006). A key point in the Monte Carlo method is the correct specification of the distribution functions of the input parameters (Vose, 2008; Scheidt et al., 2018), as these determine the output response. A single value was defined for the reservoir volume as the goal of this work was to evaluate the deep geothermal energy source at each 1 km depth and within the land surface area occupied by the community (Figure 4.2). Reservoir simulation and optimization can help to infer the potential microseismic cloud and thus provide a better constraint for the reservoir volume. The triangular distribution function was chosen for the reservoir temperature in the three studied scenarios since the three-point estimation technique was used to define the worst-case, most likely, and best-case subsurface temperature estimations (Vose, 2008). The Gaussian (normal) distribution was specified for the volumetric heat capacity based on the results from the laboratory analyzes. However, the triangular distribution has been commonly assigned for this thermophysical property (e.g., Sarmiento et al., 2008). Further work can be envisioned to compare the outcomes from both distribution functions and evaluate the associated variability. The technical uncertainties related to reservoir abandonment temperature, recovery factor, and GPP factor were assumed to follow a uniform distribution bounded by common minimum and maximum values mentioned in literature. This choice was based on the assumption that, within the defined limit, each outcome of the random variable has equal probability of occurring. The triangular distribution, however, was specified for the project lifetime, assuming 30 years as the most likely value (Tester et al., 2006; Beardsmore et al., 2010; Sarmiento et al., 2013; Limberger et al., 2014).

The sensitivity of the input parameters in this work was determined through a linear regression-based global sensitivity method, using the Spearman correlation coefficient. Moreover, the input parameters were compared and ranked according to their relative importance. This provides a gross, first-order qualitative assessment of the most influential parameters on the deep geothermal energy source and potential heat and power output. Future directions of this work can be envisioned to quantitatively measure the sensitivity through other linear methods, such as the standardized regression coefficients, or through variance-based methods or regionalized sensitivity analysis (Scheidt et al., 2018). Nevertheless, the qualitative results reveal that reservoir temperature and recovery factor are clearly the most influential parameters, and further geothermal exploration should be focused on decreasing their uncertainty (Figure 4.6 and Figure 4.9).

4.5.4 Deep geothermal energy as a viable solution to reduce fossil fuels dependency of remote communities

The following criteria, based on Glassley (2010), can be used to evaluate if geothermal energy is a viable alternative solution to fossil fuels in remote northern communities:

1. Is the deep geothermal energy source sufficiently abundant to meet the local heat and power demand?
2. Is the deep geothermal energy source cost-competitive compared to fossil fuels?
3. Will the deep geothermal energy source help to reduce or eliminate greenhouse gas emissions?

The ultimate goal of this work is obviously related to the first fundamental question. A probabilistic approach, accounting for the current geological and technical uncertainties, was used for this purpose and the results revealed deep geothermal energy as a promising solution for the community of Kuujjuaq, especially for heat production. Moreover, the estimated annual average potential power output at 6 km depth (11 GWh_e; Figure 4.10b) is within the range of values inferred by Majorowicz et al. (2014b) for the northwestern sedimentary basins (10 – 15 GWh).

In the present work, the threshold value used as the community's heating demand did not consider the heat consumed by service buildings (health clinic, shops, hotels, etc.). Only the total residential dwellings (518; Statistics Canada, 2016) were accounted. Moreover, these were considered as typical 5-occupant household with an annual average heating need of approximately 71 MWh per dwelling (Gunawan et al., 2020). However, 157 of those are single-family houses with an annual average heating demand of about 22 MWh per dwelling (Yan et al., 2019). This reduces the estimated annual average consumption from 37 to 29 GWh. In any case, service buildings were left outside from the estimate such that the threshold value represent a fair starting point to evaluate the risk of meeting the heating demand. Thus, the results reveal that, at 4 km depth and below, heat production from deep geothermal energy source is a low-risk application with more than 98% probability of fulfilling the community's heating demand (Figure 4.7). Moreover, the results show that heat production can be possible at shallower depths of 2 and 3 km if the reservoir temperature is above its 65^{th}–70^{th} percentile and its 15^{th} percentile, respectively (Figure 4.8). This can help to narrow estimates of a project's capital costs, mainly associated with well drilling. In Nunavut (Canada), a 4 km deep full-size production well can cost approximately $12 million USD (US dollars), increasing up to $30 million USD for an 8 km deep well (Minnick et al., 2018).

A reservoir abandonment temperature of 120 – 140 °C was selected for the electricity generation analysis based on the operational binary cycle GPP of Kamchatka Peninsula (Russia; Tomarov et al., 2017). However, Organic Rankine Cycle using an optimized working fluid has helped to achieve favorable electricity generation from lower geothermal energy source of about 80 °C (Liu et al., 2017; Tillmanns et al., 2017; Shi et al., 2019; Chagnon-Lessard et al., 2020; Imre et al., 2020). Although the efficiency of the GPP with such low heat source is lower than 10% (Tester et al., 2006), this can be advantageous for remote northern regions where deep drilling cost is high ($12 million USD for a 4-km-well; Minnick et al., 2018). Moreover, decreasing the reservoir abandonment temperature leads to an increase in the potential power output. Furthermore, Organic Rankine Cycle has been capable of generating electricity from even lower temperature sources. For example, power generation from waste energy during the process of liquified natural gas regasification was achieved with a source temperature of 100 to 30 °C (e.g., Dutta et al., 2018; Yu et al., 2019). Thus, Organic Rankine Cycle can be a promising technology for northern regions. However, compared to heat production, electricity generation produced by deep geothermal energy source is a high to medium risk application. The probability of meeting the power needs is low (0.1% at 3 km depth and 94% at 10 km depth), even if the reservoir abandonment temperature is reduced to 80 °C.

Considering the reservoir abandonment temperature threshold of 120 – 140 °C, the probability of meeting the community's annual power demand is lower than 95% at 10 km depth, with reservoir temperature and recovery factor playing the major roles in constraining the feasibility of such application (Figure 4.11). A first-order assessment of CHP viability was also undertaken. The waste heat from the power conversion process has low probability to fulfill the community's total heating demand assuming the 37 GWh threshold (Figure 4.12). However, if this waste heat is only used to provide space heating to half of the residential dwellings, for instance, then the probabilities increase substantially. For example, at 10 km depth, it increases from less than 12% to more than 67%.

Beyond geothermal energy, other alternative solutions to supplant the northern communities' reliance on fossil fuels have been studied. Yan et al. (2019) carried out a multi-criteria decision analysis based on the preference ranking organization method for enrichment evaluation method to evaluate the possibility of replacing the traditional heating oil-based systems in

Kuujjuaq by either natural gas, biomass, or gasification of domestic waste. Their analysis took into account environmental considerations, social improvements, and economic feasibility and concluded that biomass (using wood pellets) is the favored solution. Thompson et al. (2009) compared the economic and environmental costs of electricity generation by biomass CHP, wind, and solar with the traditional diesel engine for off-grid Canadian communities. Their results revealed biomass CHP as the most competitive renewable energy technology. However, in both studies, geothermal energy (shallow or deep systems) was not considered. Often, biomass resources need to be transported and stored similarly to fossil fuels, which is a disadvantage compared to local geothermal energy exploitation (Yan et al., 2019). Moreover, wind and solar are highly dependent on weather conditions (Bremen, 2010). Ground-coupled heat pumps and underground thermal energy storage can be viable alternative heating solutions (Giordano et al., 2019a; Kanzari, 2019; Gunawan et al., 2020). However, the energy taken from the subsurface with such shallow systems is generally no more than 50% of the heat needed by a building, requiring an auxiliary system to cover the remaining load (Giordano et al., 2019a; Gunawan et al., 2020). Deep geothermal energy sources are the only local alternatives to provide base load heat and electricity, as indicated by this study. Nevertheless, it can be more economic to use an auxiliary system in conjunction with a GPP to supply heat during peak conditions. Future activities can be planned to follow Thompson et al. (2009) or Yan et al. (2019) methodology comparing biomass resources with deep geothermal energy sources to evaluate which renewable technology is economically, socially, and environmentally best suited for the Canadian remote northern communities.

4.6 **Conclusions**

Geothermal energy source assessment is an iterative process and imperative to forecast future energy production. In this work, a first-order evaluation of the geothermal energy source and potential heat and power output in a remote northern community of Canada was undertaken based on shallow data and outcrops treated as subsurface analogs. Monte Carlo-based sensitivity analyzes were carried out to deal with the current geological (both epistemic and aleatory variability) and technical uncertainties. The statistical distribution of the thermophysical properties due to their intrinsic heterogeneous character is an aleatory variability type. The subsurface temperature, the conditions of the thermophysical properties (dry and water saturation), and the climate signal during a glacial period are epistemic uncertainties. The reservoir abandonment temperature, recovery factor, project lifetime, and GPP factor are technical uncertainties. The study was focused on the community of Kuujjuaq (Nunavik) to provide an example for the remaining off-grid northern communities relying on an unsustainable energetic framework, where fossil fuels are their main source of energy for electricity and space heating.

Thus, a new and alternative approach to conduct geothermal energy source assessment at the community scale based on surface geological information was presented. The knowledge gained can advance the stage of geothermal exploration to take decision on deep drilling. The uncertainty analysis revealed the parameters that have a major impact on the potential heat and power output and the risk analysis highlighted promising geothermal development despite the outcoming uncertainties. Reservoir temperature and recovery factor are the most influential geological and technical uncertainties on the potential heat and power output. Thus, these parameters need to be accurately assessed. Given the current state of knowledge and the high uncertainty, electricity generation, and hence CHP, is high to medium risk applications with less than 92% probability of fulfilling this community with 2 750 inhabitants' needs. Heat production, per contra, is a low-risk application at depths of 4 km and below. The probability of meeting the estimated annual average heating demand of the community of Kuujjuaq is higher than 98%, regardless of the GSTH and the conditions of the thermophysical properties.

The results obtained with this study indicate that, although found at a significant depth of at least more than 4 km, the old Canadian Shield beneath the community of Kuujjuaq can host significant geothermal energy source for space heating applications. This is especially important for remote northern communities like Kuujjuaq since this source of energy appears as the only local alternative that can fulfill their heating needs.

To conclude, it is important to highlight that this analysis was based on shallow data and surficial rock samples treated as subsurface analogs. These are low-cost geothermal exploration tools useful for a first-order assessment of the deep geothermal energy source, as indicated by this study. Nonetheless, the stage of geothermal exploration in remote northern regions needs to advance. Deep exploratory wells are essential and the step missing to accurately infer the deep geothermal energy source and potential heat and power output. Thus, helping remote northern communities to move toward a more sustainable and green energetic future.

5 FRACTURE NETWORK AND STRESS REGIME: IMPLICATIONS FOR THE DEVELOPMENT OF ENGINEERED GEOTHERMAL ENERGY SYSTEMS IN REMOTE NORTHERN REGIONS

Réseau de fractures et régime de contrainte : implications pour le développement de systèmes géothermiques ouvragés dans les régions nordiques éloignées

Authors:

Mafalda M. Miranda (M.M.M.), Jasmin Raymond (J.R.)

Institut national de la recherche scientifique, Canada

Jonathan Willis-Richards (J.W-R)

Fracture and Reliability Research Institute, Tohoku University, Japan

Chrystel Dezayes (C.D.)

Bureau de recherches géologiques et minières, France

Journal title:

Journal of Structural Geology

To submit

Author's contribution:

Conceptualization, M.M.M., J.R., J.W-R and C.D.; methodology, M.M.M. and J.W-R; validation, M.M.M. and J.W-R; formal analysis, M.M.M.; investigation, M.M.M.; resources, M.M.M., J.R., J.W-R and C.D.; data curation, M.M.M.; writing – original draft preparation, M.M.M., J.R., J.W-R and C.D.; writing – review and editing, M.M.M., J.R., J.W-R and C.D.; visualization, M.M.M.; software, J.W-R; supervision, J.R. and C.D.; project administration, J.R.; funding acquisition, J.R.

Link between the previous articles and the next:

The previous chapters provide a first-order characterization of the thermal structure in Kuujjuaq. This chapter, in turn, aims at characterizing the fracture network and stress regime, key parameters for the development of engineered geothermal energy systems in Kuujjuaq. Moreover, the geothermal gradient evaluated in the previous chapter is used in the theoretical rheological model developed in this chapter.

Graphical abstract:

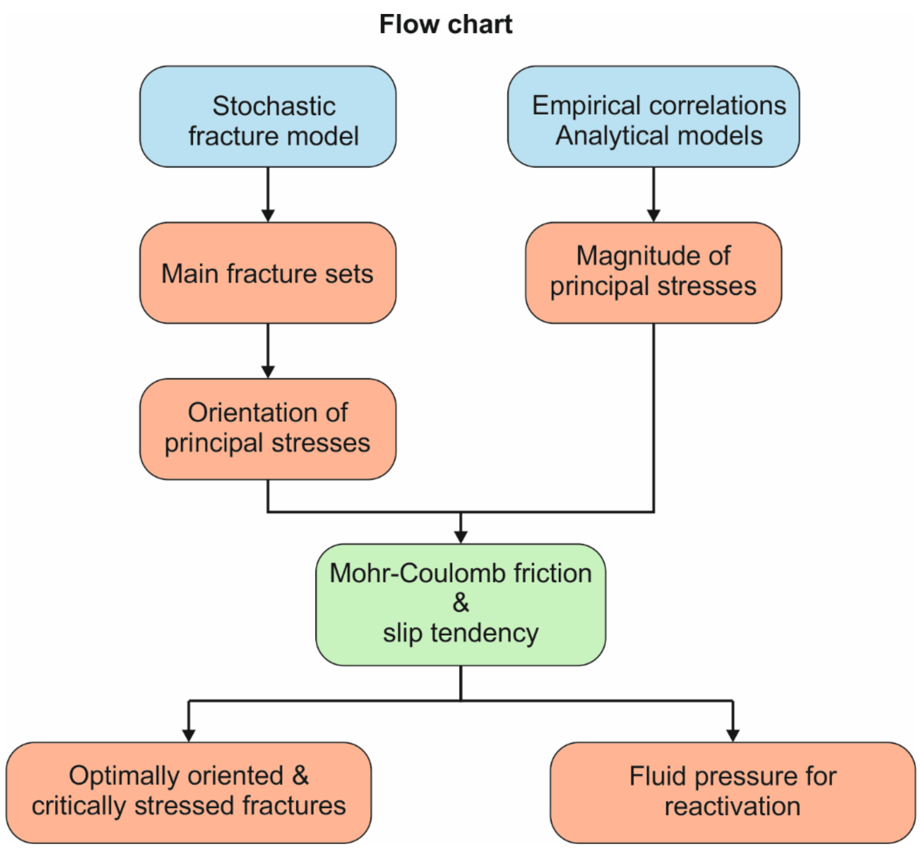

5.1 Introduction

Ensuring access to affordable, reliable, sustainable and modern energy for all is one of the sustainable development goals of the United Nations (UN, 2020). Although Canada, compared to most OECD (Organization for Economic Co-operation and Development) countries, has a high share of renewables in its energy supply (renewable energy sources currently provide 16% of Canada's total primary energy supply; GCan 2020a), there are still 239 communities relying solely on fossil fuels to generate electricity in diesel power plants and to produce space heating with oil furnaces (Grasby et al. 2013; Arriaga et al. 2017). This represents about 200 000 inhabitants with no clean energy supply that critically depend on energy services for their safety and economic growth. Therefore, there is a growing interest in developing other sources of energy to improve the living standards (well-being, environment and economy) of these off-grid settlements. Thompson et al. (2009) and Yan et al. (2019) indicate biomass as the most favorable and competitive renewable energy technology compared to natural gas, gasification of domestic waste, wind and solar. Furthermore, Stephen et al. (2016) carried out a study to determine the techno-economic feasibility of biomass utilization for space heating and concluded that biomass has the potential to reduce heat costs, reduce the cost of electricity subsidizations for electrical utilities, reduce greenhouse gas emissions and increase energy independence. However, biomass resources need to be transported and stored similarly to diesel, which is disadvantageous compared with the development of a local source of energy. Wind and solar can also be a solution, as for example the fully hybrid wind-solar-battery-diesel system proposed by Quitoras et al. (2020), but these remain weather-dependent and, therefore, their supply of energy is intermittent (Bremen, 2010). McFarlan (2018) conducted a techno-economic assessment of replacing diesel for electricity generation with clean biofuels (methanol and dimethyl ether) and showed potential socioeconomic benefits from switching to these energy sources. However, biofuels are still in a nascent stage and more research and development are needed. Ground-source heat pumps can be viable to supply heat (Kanzari, 2019; Gunawan et al., 2020). However, the extracted energy with such shallow systems (100 to 300 m) is generally insufficient to fulfill the heating demand of a single residential dwelling, relying on auxiliary systems to cover the remaining load. Micro-hydropower systems in off-grid communities have been proved as a favorable solution to displace the use of diesel and reduce greenhouse gas emissions (Ranjitkar et al., 2006). The majority of these systems are run-of-river without a need for a dam or reservoir and, therefore, the best geographical locations are steep rivers, streams, creeks, or spring flowing year-round (Ranjitkar et al., 2006). Although water resources may not be a current issue throughout Canada, climate change may impact existing and proposed hydropower projects especially in the boreal, sub-Arctic and Arctic unique and complex environments (Cherry et al., 2017). Deep geothermal energy sources are currently receiving increased attention as a local renewable alternative source of energy capable to provide base-load heat and power for off-grid communities (e.g., Majorowicz et al., 2010a; Majorowicz et al., 2010b; Kunkel et al., 2012; Grasby et al., 2013; Walsh, 2013; Majorowicz et al., 2014b; Majorowicz et al., 2015a; Majorowicz et al., 2020; Majorowicz et al., 2021). The heat supply during peak conditions can also be met by the deep geothermal energy sources. However, renewable, or non-renewable, auxiliary systems together with the geothermal power plant might be more economic to meet the peak loads in such cold climates (e.g., Mahbaz et al. 2020).

A geothermal energy source assessment was undertaken in Canada (Grasby et al., 2012), indicating high geothermal potential for electricity generation and heat production using conventional hydrothermal systems in the Garibaldi Volcanic Belt, northwestern sedimentary basins and the Western Canada Sedimentary Basin (Figure 5.1). This geothermal assessment considered the Canadian Shield physiographic region as promising for geothermal energy production through unconventional concept, such as enhanced geothermal systems (EGS; Figure 5.1). Recently, a geothermal energy feasibility study carried out in Nunavut (Minnick et al., 2018) also suggested EGS as a possible solution to extract the deep geothermal energy source in the Canadian Shield.

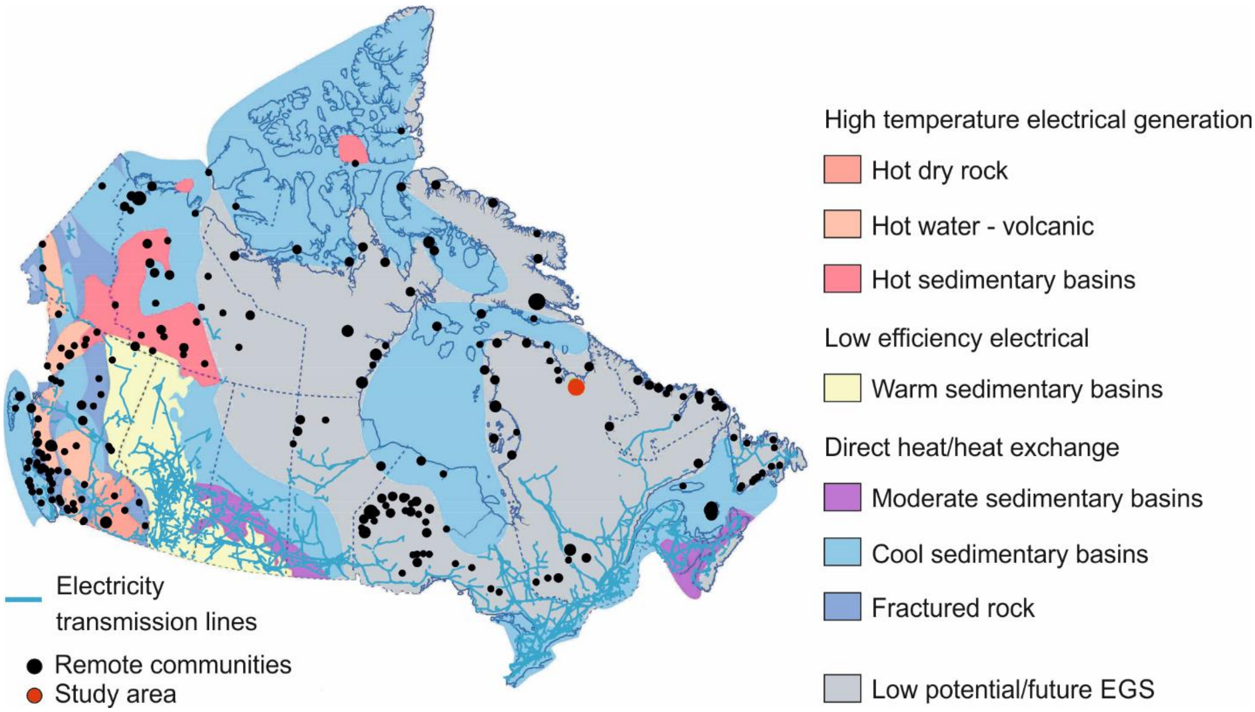

Figure 5.1 **Canadian geothermal potential based on end use and off-grid communities, adapted from Grasby et al. (2012) and Arriaga et al. (2017).**

Thus, studying the feasibility of EGS in remote northern communities settled in the Canadian Shield is of utmost interest. However, prior to design an engineered geothermal energy system, characterizing the natural fracture network and in situ principal stresses are critical (e.g., Richards et al., 1994; Evans et al., 1999; Brown et al., 2012; Ghassemi, 2012). Fractures are not only the main flow pathways, but their orientation relative to the contemporary stress field determines which fractures will shear and at what pressure, thus, defining the shape of the stimulated geothermal reservoir (e.g., Evans et al., 1999; Brown et al., 2012; Ghassemi, 2012). The reservoir tends to be an elliptical shape, with the major axis parallel to the maximum principal stress and normal to the least principal stress, reflecting the tendency of the reservoir to grow in the direction of the least energy configuration (e.g., Hubbert et al., 1957; Evans et al., 1999; Brown et al., 2012). Moreover, the appropriate position and orientation of the wells depend on the fracture network and stress field (Richards et al., 1994; Brown et al., 2012). Beyond the orientation of the principal stresses, their magnitude and differential are also key components of a comprehensive geomechanical model, together with the knowledge of the in-situ fluid pressure (e.g., Jaeger et al., 2007; Zoback, 2007). The in-situ stress regime constraints the fractures shear strength and, thus, the necessary fluid pressure for the slippage of the optimally oriented fractures (i.e., the reduction of effective normal stress along fractures that support shear stress). Moreover, if a fracture is critically stressed (i.e., the ratio between shear stress and normal effective is similar to the friction angle – Amonton's law) and, thus, is on the verge of failing, then less fluid pressure is required to reactivate the structure (e.g., Evans et al., 1999; Jaeger et al., 2007; Zoback, 2007). A linear Coulomb friction law with a friction coefficient ranging between 0.6 and 0.8 has been observed to provide a good first-order approximation for the upper limit of the shear strength necessary to reactivate structures and initiate shearing (e.g., Evans et al., 1999; Jaeger et al., 2007; Zoback, 2007). However, laboratory experiments demonstrated that the friction coefficient is time- and velocity-dependent (Dieterich, 1978; Dieterich, 1979). A static friction coefficient higher than the Mohr envelope friction coefficient can be applied as an upper limit for the pre-existing joints (e.g., Zoback, 2007). Two mechanisms based on asperity behavior have been proposed to explain the higher static friction coefficient when compared to the dynamic coefficient (Scholz et al., 1976). It can be a result of locked asperities fail by brittle fracture at the onset of sliding (e.g., Scholz et al., 1976). It can additionally be related with the so-called "indentation creep" that causes an increase in the asperities contact area (Scholz et al., 1976; Dieterich, 1978; Dieterich, 1979). A large indentation time suggests a large asperity contact area and, thus, a large static friction coefficient.

The present work undertaken in the community of Kuujjuaq (Figure 5.1) has the objective of providing guidelines to develop EGS in remote diesel-based settlements having to cope with data scarcity and can be used as an example for remaining communities located in a similar geological context. The following fundamental questions were addressed through this work:

1. What is the stress regime prevailing in Kuujjuaq?
2. Are there sufficient fracture planes optimally oriented for slip at sufficiently low fluid pressure?
3. What is the critical fluid pressure to reactivate the fracture planes?

A first-order characterization of the natural fracture network based on outcrops as subsurface analogues was carried out to help answer these questions. The in-situ stress is currently unknown in the study area and no stress measurements were carried out in the scope of this work due to the absence of deep exploratory boreholes. Thus, an a priori stress model was proposed. This resorts on geological indicators to approximate the orientation of the principal stresses and on empirical correlations and analytical models to estimate their magnitude. Furthermore, since rheological parametrization is an important issue to be considered in models for stress prediction in general, and in geothermal exploration where the reservoir permeability is controlled by faults and fractures (e.g., Limberger et al., 2017), a 1D theoretical rheological profile was developed based on structural and compositional literature-based data and temperature estimates carried out by Miranda et al. (2020b). Finally, Mohr-Coulomb friction and slip tendency analyzes were carried out to assess the fracture sets that are optimally oriented to slip and to estimate the required fluid pressure to reactivate the fractures and initiate shearing. Although the potential error associated with the use of outcrops as subsurface analogues as well as literature-based and empirical data, a first-order characterization of the thermo-mechanical conditions of the subsurface is crucial to advance the knowledge and the stage of the geothermal exploration in such remote northern regions.

5.2 Geographical and geological setting

The current work was undertaken north of the 55th parallel in the remote community of Kuujjuaq, the administrative capital of Nunavik and home of 2750 habitants, the majority being Inuits (Statistics Canada, 2019). Kuujjuaq is located in the periphery of northern Labrador Trough in the Southeastern Churchill Province. This province is an orogenic belt, oriented NNW-SSE with both flanks (Torngat Orogen and Labrador Trough) recording transpressional development associated with the oblique collisions that led to its assemblage (e.g., Wardle et al., 2002). The collision between the Core Zone (central part of the Southeastern Churchill Province) and the Superior Province occurred about 1.82-1.77 Ga before present. The Core Zone is a cratonic fragment mostly consisting of Archean tonalitic to granitic gneiss and granitoid rocks and is characterized by a pervasive E-dipping fabric related to westerly thrusting (e.g., Wardle et al., 2002). A regional structural grain NW-SE to N-S is observed and believed to be associated with the Core Zone/Superior collision (Simard et al., 2013).

The crustal thickness in northern Québec was estimated by Vervaet et al. (2016) to vary within 33 to 49 km with a Moho depth of about 37 km beneath Kuujjuaq terrane (Telmat et al., 1999; Hall et al., 2002; Hammer et al., 2010). Seismic profiles acquired in the east coast of Ungava Bay in the context of the Lithoprobe project suggest P-wave velocities ranging between 5.9 to 6.2 km s^{-1} for the upper crustal levels (from 0 to 10 km depth), between 6.2 and 6.5 km s^{-1} for the mid-crust (from 10 to about 17 km depth) and between 6.6 and 7.0 km s^{-1} for the lower crust (from around 17 to 37 km depth; Hall et al., 2002; Hammer et al., 2010). The P-wave velocities in the mantle are higher than 8.0 km s^{-1} (Hall et al., 2002; Hammer et al., 2010). Both upper and mid-crust have also been interpreted as one single layer (Hall et al., 2002).

Effective elastic thickness of the Canadian Shield estimated with the maximum entropy method by Audet et al. (2004) suggest a value ranging between 70 and 85 km within Kuujjuaq area. Taking into consideration the approximated effective elastic thickness and crustal thickness, the ratio between these parameters reveals to be 1.9-2.3. Thus, suggesting a strong “dried jelly sandwich” rheology where the lower crust is strong and both crust and mantle are mechanically coupled (Burov, 2011).

The study area is characterized mainly by outcrops of the False Suite (migmatized paragneiss and migmatized garnet paragneiss; SIGÉOM, 2019) and Kaslac Complex (amphibole diorite and quartz diorite and gabbro, gabbronorite and clinopyroxenite; SIGÉOM, 2019). Smaller outcrops belonging to the Ralleau Suite (amphibolitized gabbro and diorite; SIGÉOM, 2019), Aveneau Suite (white tonalite and granite; SIGÉOM, 2019), Dancelou Suite (massive pink granite and massive pegmatitic granite; SIGÉOM, 2019) and Falcoz Swarm (subophitic gabbro; SIGÉOM, 2019) are also present (Figure 5.2). The outcrops of paragneiss and diorite lithologies were analyzed and the existing fractures were sampled in the framework of this study (Figure 5.2). A detailed description of these lithologies is given in SIGÉOM (2019) and the petrographic and geochemistry characteristics of samples collected within the study area are given in Miranda et al. (2020a).

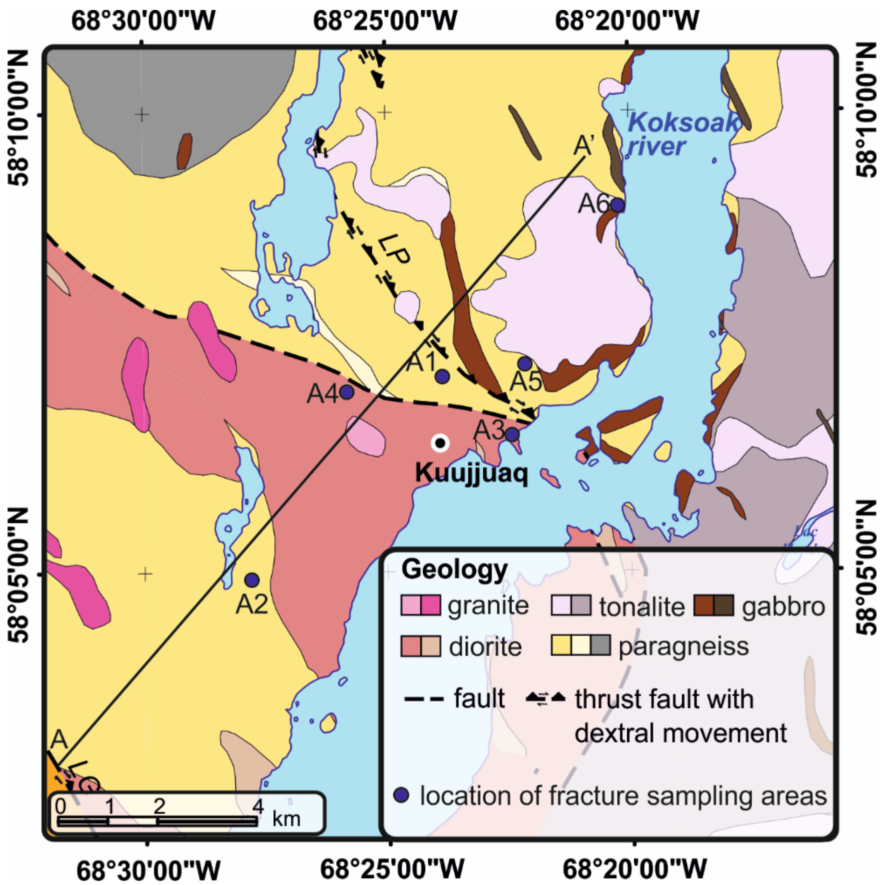

Figure 5.2 **Geological map of the study area indicating the location of fracture sampling. LP – Lac Pingiajjulik fault, LG – Lac Gabriel fault, adapted from SIGÉOM (2019) and Miranda et al. (2020a).**

The two main structures indicated in the geological map, Lac Pingiajjulik and Lac Gabriel faults (Figure 5.2), are mostly not visible in the field (Simard et al., 2013) and their position on the geological map was based on aeromagnetic data as explained by Simard et al. (2013). Nevertheless, they are indicated as regional thrust faults with dextral motion synchronous with the third deformation phase (D_3; e.g., Perreault et al., 1990; Simard et al., 2013; SIGÉOM, 2019). This movement is indicated by asymmetric pressure shadows around rotated porphyroblasts and by shear folds in places where the faults are visible in the field (e.g., Perreault et al., 1990). A cross-section for the southwestern part of Ungava Bay has been proposed by Simard et al. (2013) and adapted in Miranda et al. (2020b) to build a conceptual model for the study area (Figure 5.3).

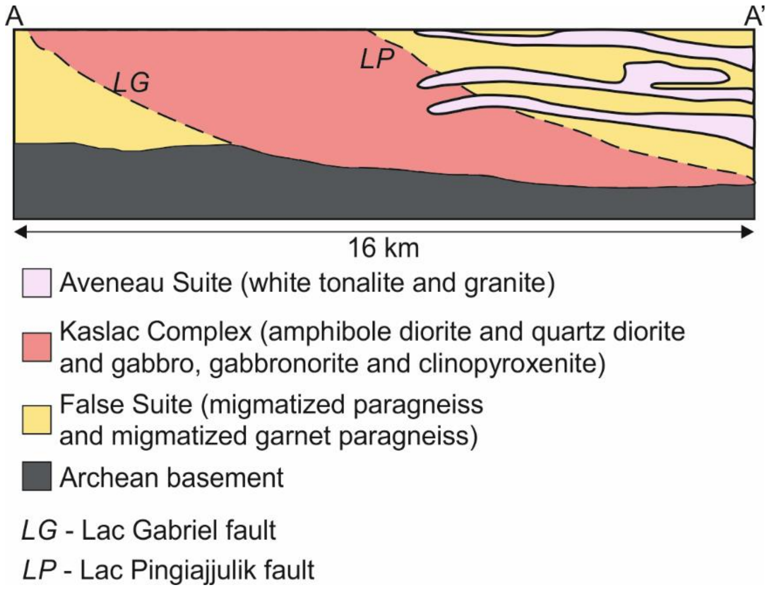

Figure 5.3 Conceptual cross-section. A and A' in Figure 5.2. Vertical scale unknown, based on Simard et al. (2013).

5.3 Stress regime

5.3.1 World Stress Map and seismotectonics

The World Stress Map (Heidbach et al., 2019) is a global database of contemporary tectonic stress of the Earth's crust and a useful tool to infer the orientation of the maximum horizontal stress. However, the World Stress Map does not have information on the study area. The lack of deep exploratory boreholes associated with the absence of earthquake data with magnitudes higher than 3 (Figure 5.4) contributes for this important gap. However, it is important to highlight that the absence of earthquake data does not necessary mean that seismicity is not occurring. In fact, about three seismic events with magnitudes between 2.2 and 3.4 and at a depth of 18 km were recorded at a distance of 10 to 53 km away from Kuujjuaq (GCan, 2021). However, these events seemed to have occurred in different fault planes than the ones crossing the community. Nonetheless, these events may be related to the brittle-ductile transition, indicating its possible depth. Perhaps microseismic monitoring can provide greater insights on the stress release in the study area. Such analyzes are however currently out of the scope of this work.

Adams (1989) compiled the available stress data in Canada shallower than 9 km and suggests that, east of the Cordillera physiographic region of Canada, the compression is NE-SW with the principal stress σ_1 being horizontal (Figure 5.4a). This compression azimuth has been supported by others (e.g., Hashizume, 1974; Adams et al., 1989; Zoback et al., 1989; Bell et al., 1997). Furthermore, published literature on focal mechanism in eastern Canada indicate upper- to midcrustal earthquakes with mostly thrust faulting mechanism (Lamontagne, 2008). Analysis of the 6.3 magnitude Ungava earthquake that occurred in 1989 indicated two subevents (a thrust subevent on a NE-SW striking plane followed by a strike-slip subevent on a NNE-SSW striking plane) at a depth of 3 km (Bent, 1994). Other main earthquake events with magnitudes higher than 4.5 occurred onshore west of Ungava Bay and revealed depths ranging from 5 to 18 km (USGS, 2021). This agrees with seismic observations indicating that in old continental lithosphere seismicity is confined to the upper 20 km of the crust (e.g., Ranalli et al., 1987).

Shallow and deep stress measurements (maximum depth of 2 km) carried out in the Canadian Shield support thrusting as the dominant regime. However, normal-fault type earthquakes are more common along the northeast coast of Baffin Island and strike-slip faulting predominates in the northeastern United States (Wu et al., 1996 and references therein).

The earthquakes occurring in the North Atlantic Ocean, Labrador Sea and Baffin Bay (Figure 5.4b) are mostly concentrated at the ocean-continent transitions and are believed to be caused by reactivation of the Mesozoic rift faults created during the formation of the North Atlantic (Adams et al., 1989). The earthquakes occurring on Baffin Island and along the arcuate band Boothia-Ungava are spatially associated with Cretaceous normal faults and with steep gradients in the postglacial uplift rate (Adams et al., 1989). In summary, seismicity, steep gradients in free-air gravity anomaly and steep gradients in postglacial uplift along northeastern periphery of the Canadian Shield suggest a causal correlation between seismicity, postglacial rebound and lateral variations in crustal structure in this region (Adams et al., 1989; Hasegawa et al., 1989). Nowadays, although rebound stresses have been decreasing in magnitude, they continue to act as a trigger mechanism for optimally oriented pre-existing faults that are otherwise on the verge of failure. Thus, limiting the existence of near-slip conditions to lie within the pre-weakened zones of eastern Canada explain the spatial distribution of current earthquakes (Wu et al., 1996).

Additionally, the infrequent intraplate earthquakes may also be related with the low ductile strain rate in the lower crust and upper mantle (e.g., Zoback et al., 2001; Zoback, 2007). In intraplate regions, sufficient plate-driving force (about 3×10^{12} N m^{-1}) is available to maintain the upper crust in a state of frictional failure equilibrium (e.g., Zoback et al., 2001; Zoback, 2007). Moreover, the distribution of the earthquakes along the edges of the craton may indicate accumulation of tectonic stresses in those areas and that these intraplate earthquakes are occurring in a weak lithosphere or near the edges of strong cratonic block (Tesauro et al., 2015). Aseismic deformation can also be one of the reasons for the absence of earthquake data in the study area. In fact, Ojo et al. (2020) observed that less than 20% of the accumulated strain in Canada is released by earthquakes. In summary, several causative factors can be invoked to explain the intraplate seismicity, or the absence of it in the study area (e.g., local reduction of crustal and/or upper mantle strength caused by thermal, mechanical or chemical anomalies, local increases in differential stresses related to density contrasts, local topography or kinks and intersections in a fault system; e.g., Mazzotti, 2007). Studying them is, however, beyond the scope of the present work. The sole purpose of referring the earthquake data is to illustrate that there is little published data for the study area and, thus, focal mechanisms cannot be used in the present study as a tool to help infer the stress regime.

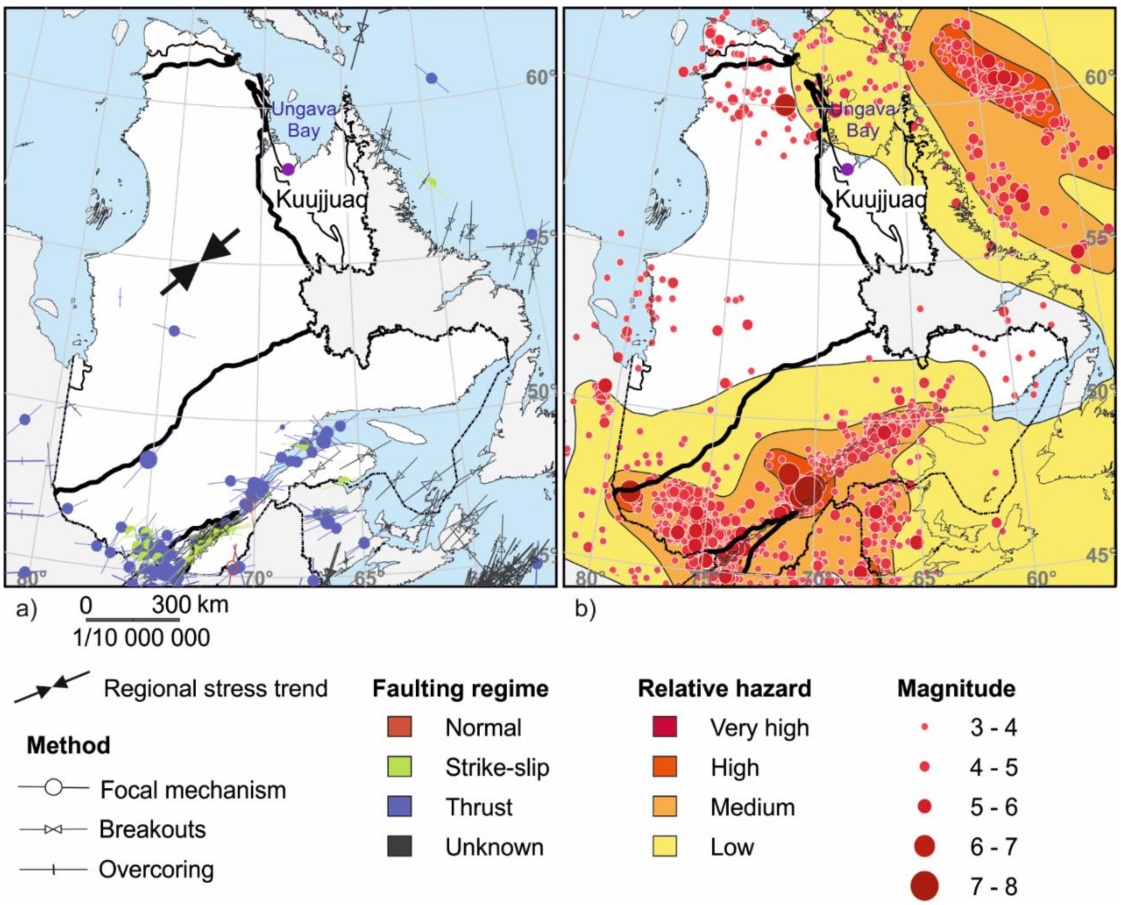

Figure 5.4 **a) Stress and b) seismic hazard maps of Québec province. The arrows in a) indicate the regional trend of the contemporary stress field and the orientation of the maximum horizontal compression based on Adams (1989), redrawn from NRCan (2018a) and Heidbach et al. (2019).**

5.3.2 Stress data in the Canadian Shield

Several authors have been measuring and compiling in situ stresses in the Canadian Shield, mainly in underground mines located in Manitoba, Ontario and southern Quebec (Table 5.1).

Their compilations indicate that the direction of the maximum principal stress (σ_1) correlates with the regional NE to ENE trend (Herget, 1993; Young et al., 2015). Moreover, the vertical principal stress (σ_V) is often higher than the minimum principal compressive stress (σ_3) but smaller than the intermediate (σ_2) and maximum (σ_1) principal stresses (Herget, 1993; Arjang et al., 1997; Arjang, 1998; Young et al., 2015), implying that the vertical stress is not a principal stress. This constrains the application of empirical functions and analytical models to infer the principal stresses since these are based on the assumption that the vertical stress is a principal stress.

Arjang et al. (1997) observed that the maximum (σ_1) and intermediate (σ_2) principal stresses are equivalent to the maximum (σ_H) and minimum (σ_h) horizontal principal stresses and that the former is 1.7 times higher than the latter. These stress compilations indicate that thrust faulting regime is dominant in the Canadian Shield (Herget, 1982; Herget, 1987; Arjang, 1991; Herget, 1993; Young et al., 2015), however strike-slip regime might occur (Arjang, 1998). Furthermore, at depths greater than 2000 m, extrapolation of Herget (1982) and Herget (1987) data indicates normal faulting regime.

Table 5.1 Principal stresses in the Canadian Shield.

Principal stress	Orientation	Magnitude	Observations		Reference
σ_V	--	(0.0260-0.0324)z	$0 < z < 2200$ m	$\sigma_V < \sigma_{H,\ average}$	Herget (1982), Herget (1987)
$\sigma_{H,\ average}$	--	9.86+0.0371z	$0 < z < 900$ m		
		33.41+0.0111z	$900 < z < 2200$ m		
σ_V	--	(0.0266±0.008)z	$60 < z < 1890$ m	$\sigma_V < \sigma_h < \sigma_H$	Arjang (1991)
$\sigma_{H,\ average}$	--	5.91+0.0349z			
σ_H	--	8.18+0.0422z			
σ_h	--	3.64+0.0276z			
σ_V	--	0.0285z	$0 < z < 2200$ m	$\sigma_3 < \sigma_V < \sigma_2 < \sigma_1$	Herget (1993)
σ_1	N248º/10º	12.1+(0.0403±0.0020)z			
σ_2	N300-340º/0º	6.4+(0.0293±0.0019)z			
σ_3	vertical	1.4+(0.0225±0.0015)z			
σ_V	--	0.0260z	$0 < z < 6000$ m	$\sigma_3 < \sigma_2 \leq \sigma_V < \sigma_1$	Arjang (1998)
σ_1	NE/horizontal	13.50+0.0344z			
σ_2	NW/sub-horizontal	8.03+0.0233z			
σ_3	vertical	3.01+0.0180z			
σ_V	--	(0.0258-0.0263)z	$12 < z < 2552$ m	$\sigma_3 < \sigma_V < \sigma_2 < \sigma_1$	Young et al. (2015)
σ_1	N227º/02º	(0.040±0.001)z-(9.185±1.5)			
σ_2	N310º/08º	(0.029±0.001)z+(4.617±1.159)			
σ_3	N270º/88º	(0.021±0.001)z-(0.777±0.872)			

σ_V – vertical principal stress, $\sigma_{H,\ average}$ – average horizontal principal stress ($\sigma_{\mathrm{H,\ average}} = \frac{\sigma_H + \sigma_h}{2}$), σ_H – maximum horizontal principal stress, σ_h – minimum horizontal principal stress, σ_1 – maximum principal stress, σ_2 – intermediate principal stress, σ_3 – minimum principal stress, z – depth.

5.4 Methods

5.4.1 Fracture sampling and statistical analyzes

A total of 452 natural fractures, mostly opening-mode fractures, were mapped in 6 areas surrounding the community of Kuujjuaq (Figure 5.2) using the scanline sampling method (e.g., Zeeb et al., 2013a) after correcting the compass for the 22º of magnetic declination (GCan, 2020b). In this method, a tape is laid down on the outcrop surface and the geometrical properties of each fracture intersecting the tape are collected. The geometrical properties encompass orientation, dip, length, linear intensity (or density) and spacing. The data sampled was posteriorly corrected for censoring and orientation biases (Zeeb et al., 2013a) and used to generate the stochastic discrete fracture network (DFN).

Censoring and truncation biases were corrected by applying the chord method to truncate the minimum fracture length. The descending cumulative frequency of the fracture was plotted as a function of fractures length in a log-log chart. A line going from the minimum to the maximum fracture size was calculated and the data point farther away from this line marks the lower cutoff length (e.g., Zeeb et al., 2013a).

The Stereonet software version 11.3.0 (Cardozo et al., 2013; Allmendinger et al., 2012) was used to plot the strike and dip of the fractures, evaluate their poles, estimate the 1% area contouring and infer the von Mises distribution for the main fracture sets. The geometrical properties of the fractures were sampled in horizontal outcrop surfaces that are common to the area and thus both dip and dip direction are unclear. Only the outcrop in area A6 (Fig. 2) had vertical surfaces to correctly evaluate the dip and dip direction of the fractures. Therefore, random numbers were used to generate the dip of the remaining sampling areas based on the observed range. Dip direction was calculated based on recorded orientations and regional and local dipping trends and random numbers were used to arbitrary define the direction of the dip of each fracture. The data obtained from A6 sampling area revealed dips ranging between 68º and 80º and NNW- and NNE-dipping structures. Moreover, a E-dipping fabric has also been observed for the Archean basement rocks underlying the Core Zone craton (Wardle et al., 2002). The two probable faults (Lac Pingiajjulik and Lac Gabriel; Fig. 2) are probably oriented roughly NW-SE and with a probable dip of 45º or less since they are thrust faults. Based on the geological map, proposed cross-section and their geodynamic history, these faults can be assumed dipping towards NE.

The intensity and spacing were calculated as (Sanderson and Peacock, 2019):

$$I = \frac{N}{l} \tag{5.1a}$$

$$S = \frac{l}{N} = \frac{1}{I} \tag{5.1b}$$

where *I* (fractures m^{-1}) is the linear intensity, *N* is the number of fractures, *l* (m) is the length of the scanline and *S* (m) is the fracture spacing.

The effects of unmeasured spacing at the extremities of the scanlines were removed as explained in Sanderson et al. (2019a):

$$I = \frac{1}{S} = \frac{(N-1)}{(j_n - j_1)} \tag{5.2}$$

where j_n and j_1 (m) are the distance measured from the last fracture and from the first fracture, respectively.

Orientation bias was avoided by placing the scanline normal to the strike of the fracture set and by applying the Terzaghi correction when such was not possible (e.g., Zeeb et al., 2013a):

$$S = S_a \cos \phi \tag{5.3}$$

where ϕ (º) is the acute angle of the normal of the fracture to the scanline and the subscript a stands for apparent.

The fracture clustering was evaluated as the coefficient of variation of fractures spacing and corresponds to the ratio between the standard deviation of the fracture spacing and the mean (e.g., Sanderson et al., 2019a). This parameter was calculated after correction for the censoring and orientation biases. A coefficient of variation equal to 1 is characteristic of a negative exponential spacing distribution that results due to the random intersection of fractures along the scanline. A coefficient of variation smaller than 1 indicates regularly spaced fractures, and equal to 0 means uniformly spaced fractures. Coefficient of variations higher than 0 and smaller than 1 usually indicate a log-normal distribution of spacing. A coefficient of variation higher than 1 is characteristic of irregularly spaced fractures and may indicate fracture clustering. If the coefficient of variation is much higher than 1, the fracture distribution can be approximated by a power-law (Sanderson et al., 2019a).

The heterogeneity of the distribution was evaluated following Kuiper's method (e.g., Sanderson et al., 2019a). The ascending cumulative frequency of the fractures was plotted against their percentage distance. In this plot, the sum of the maximum departure measured from above (K^+) and below (K^-) the uniform distribution line indicates the heterogeneity. The heterogeneity parameter (V') is calculated as:

$$V' = |K^+| + |K^-| \quad (5.4)$$

A heterogeneity parameter close to 0 indicates uniform distribution. A small value of this parameter (i.e., approximately between 0 and 30%) indicates random distribution. For values higher than 30%, the fractures present a corridor or fractal distribution (Sanderson et al., 2019a). Additionally, the statistical significance of the departure from a uniform distribution was evaluated as (Sanderson et al., 2019a):

$$V^* = V'\left(\sqrt{N} + 0.155 + \frac{0.24}{\sqrt{N}}\right) \quad (5.5)$$

where *V** is the parameter to test the null hypothesis of uniformity and *N* is the number of samples.

According to Stephens (1970), if $V^* > 1.75$, 2.0 and 2.3, the null hypothesis of uniformity can be rejected at 95%, 99% and 99.9% levels, respectively.

Lognormal, exponential and power law are commonly used distributions to explain the fracture length distributions (e.g., Gutierrez et al., 2015). In this study, the power law distribution was used to produce random fracture length distributions and evaluate the fractal dimension (or the power law exponent). In situ studies have been confirming the validity of the physical basis of this probability distribution function, which is based on the self-similarity or fractal behavior of fracturing (Gutierrez et al., 2015). The fractal dimension (or the power law exponent) for the length of the fractures was estimated based on the log-log plot of fracture length against descending cumulative frequency. This parameter was estimated for each fracture set after correction for censoring bias.

5.4.2 Fracture network modeling

The DFN was generated using FRACSIM3D (Jing et al., 2000). The model simulates a stochastic network of circular fracture planes within a specified volume based on statistical information sampled in field campaigns. A spatial homogeneous Poisson process is used to uniformly random place the fracture centers within a volume twice larger than the defined model volume (Jing et al., 2000). The fractures' generation process finishes when the stopping parameter, volumetric fracture density (or intensity), is met.

The fractal geometry concept of Watanabe et al. (1995) is applied to generate the random fractal fracture lengths considering the smallest and largest fractures measured on the field and the inferred fractal dimension (Willis-Richards et al., 1996):

$$r_i = \left[(1-\iota)r_{\min}^{-D} + \iota r_{\max}^{-D}\right]^{-\frac{1}{D}} \tag{5.6}$$

where r (m) is the fracture radius, ι is a random number between [0,1] and D is the fractal dimension (or the power law exponent). The subscript i stand for the ith fracture and the subscripts min and max mean smallest and largest fracture sampled in the field, respectively.

The set dip and dip direction are attributed randomly to each generated fracture based on the field sampling data.

5.4.3 A priori stress model

An early step in the process of estimating in situ stress consists of gathering available information on rock stress in the region and develop the best estimate stress model (or a priori model; Hudson et al., 2003; Stephansson et al., 2012; Zhang, 2017). This includes the World Stress Map (Heidbach et al., 2019), seismotectonics, geological indicators, published literature on stress measurements previously made, and the application of empirical correlations and analytical models to estimate in situ stress.

However, the a priori model is only informative and shall not substitute in situ stress measurements. Nevertheless, it is useful for this first-order characterization of the state of stress. The World Stress Map, seismotectonics and published data were discussed in section 5.3. Therefore, the focus on this section is on how to infer principal stresses from geological indicators and on how to infer their magnitude from empirical correlations and analytical models.

5.4.3.1 Geological indicators

Geological structures, such as faults, folds, joints, dikes, sills, slickensides, among others, provide first-order approximations to the paleostress (Amadei et al., 1997 and references therein). However, care must be taken when using such indicators. The stresses that created the geological structures, and the geological structures themselves, may have been modified over time and, thus, the current rock fabric may or may not be correlated with the current in situ stress field (Terzaghi, 1962).

The orientation of in situ stress components can be inferred from fault orientation by comparing the fault with one of the three faulting modes (e.g., Friedman, 1964; Zoback et al., 1987). Lac Pingiajjulik and Lac Gabriel are referred as thrust faults with late dextral motion and are roughly oriented NNW-SSE (Figure 5.2). These faults are a result of the transpressional deformation occasioned by the Core Zone/Superior collision (1.82-1.77 Ga). Unfortunately, these structures were not observed in the field within the study area which limits the number of methods that can be applied to infer the principal stresses.

Analysis of veins and dikes are also helpful to infer the principal stress directions since these structures are commonly emplaced parallel to the maximum compressive stress, representing the least resistance path (Parker, 1973; Nakamura et al., 1977). Joint sets have also been used in the paleostress estimations. The principal stresses are assumed oriented in directions bisecting the angles between major joint sets (Mattauer, 1973; Scheidegger, 1982; Scheidegger, 1995). However, these geological indicators only provide a rough approximation and may not reflect the present-day orientation of the principal stresses, highlighting the need of in situ stress measurements for a more accurate evaluation.

5.4.3.2 Empirical correlations and analytical models

Estimating the state of stress from empirical correlations and analytical models is based on two assumptions (Amadei et al., 1997):

- The state of stress can be described by three components: a vertical component due to the weight of the overlying rock and two horizontal components that are equal to stress ratio coefficient times the vertical stress
- Both vertical and horizontal components are principal stresses

Thus, assuming that the three principal stresses act in vertical and horizontal directions, according to Anderson (1951) relationship between stresses and faults, makes possible to estimate the magnitudes of these stresses using correlations between vertical and horizontal stresses and depth (e.g., Zhang, 2017). However, these correlations are only approximations. The measured in situ value can differ from these predictions (e.g., Amadei et al., 1997; Zhang, 2017). Moreover, as aforementioned in section 5.3.2, the stress measurements in the Canadian Shield suggest that the vertical stress is not a principal stress, which limits the use of empirical correlations and analytical models. However, due to the absence of in situ stress measurements in the study area, the vertical stress will be assumed in this study as a principal stress for a first-order characterization of the state of stress. However, the authors are aware of the implications of such assumption.

The vertical stress was approximated as (Hoek et al., 1980):

$$\sigma_{\mathrm{V}} = \rho_{\mathrm{rock}} g z \tag{5.7}$$

where σ_V (Pa) is the vertical principal stress, ρ_{rock} (kg m^{-3}) is the density of the geological materials, g (m s^{-2}) is the gravitational acceleration (= 9.81 m s^{-2}) and z (m) is depth.

The horizontal and vertical stresses were assumed related by the following relationship for depths greater than 0 (e.g., Zhang, 2017):

$$\begin{cases} \sigma_{\mathrm{h}} = k\sigma_{\mathrm{V}} \\ \sigma_{\mathrm{H}} = k\sigma_{\mathrm{V}} \end{cases} \tag{5.8}$$

where σ_h (Pa) is the minimum horizontal principal stress and σ_H (Pa) is the maximum horizontal principal stress. k is the stress ratio coefficient derived from in situ measurements.

The stress ratio coefficient is greater than unity at shallow depths but becomes less than unity approaching a constant value at great depths (Hoek et al., 1980). Several empirical functions have been proposed to infer this parameter (e.g., Heim, 1878; Terzaghi et al., 1952; Hoek et al., 1980; Rummel et al., 1986; Zhang, 2017). In this study, the functions proposed by Herget (1987), Herget (1993) and Arjang et al. (1997) for the Canadian Shield were used (Table 5.2).

Table 5.2 Empirical functions to infer the stress ratio coefficient.

Expression	Reference
$\frac{167}{z} + 1.10 < k < \frac{357}{z} + 1.46$	Herget (1987)
$\frac{30 \pm 4}{z} + 0.86 < k < \frac{272 \pm 8}{z} + 1.72$	Herget (1993)
$2.81z^{-0.120} < k < 7.44z^{-0.198}$	Arjang et al. (1997)

***k* – stress ratio coefficient, *z* – depth.**

Spherical shell models, such as the ones proposed by McCutchen (1982) and Sheorey (1994), where the Earth is modeled as a self-gravitating spherical shell consisting of one or several concentric layers have been considered as a more global approach for the analytical prediction of in situ stresses (Amadei et al., 1997). McCutchen (1982) simplified model is:

$$\sigma_{\mathrm{H,\,average}} = \frac{r_{\mathrm{outer}} - r_{\mathrm{Moho}}}{4\mathrm{r}_{\mathrm{outer}}}\rho_{\mathrm{rock}}g(r_{\mathrm{outer}} - r_{\mathrm{Moho}}) + \left(\frac{1.697}{z} + 0.3\right)\rho_{\mathrm{rock}}gz \tag{5.9}$$

where r_{outer} (m) is the outer radius of the Earth (= 3.9 × 10^6 m at 2 km; Amadei et al., 1997) and r_{Moho} (m) is the radius of the crust/mantle interface (or Moho depth).

Sheorey (1994) extended McCutchen (1982) model and proposed an elasto-static thermal stress model that considers the variation of elastic constants, density and thermal expansion coefficients through the crust and mantle. The model is:

$$\sigma_{\mathrm{H,\,average}} = \frac{\nu}{1-\nu}\sigma_{\mathrm{V}} + \frac{\beta E \nabla T}{1-\nu}(z + 1000) \tag{5.10}$$

where β ($\times 10^{-6}$ ºC^{-1}) is the coefficient of linear thermal expansion of the geological materials, E (Pa) is the Young's modulus, v is the Poisson's ratio and ∇T (ºC m^{-1}) is the geothermal gradient.

Since the stresses in the Earth cannot exceed the strength of rocks, theoretical boundaries for both maximum and minimum principal stresses were defined assuming the frictional equilibrium theory as (e.g., Zoback, 2007):

$$\frac{\sigma_1 - P_{\text{pore}}}{\sigma_3 - P_{\text{pore}}} \leq \left[\sqrt{\mu^2 + 1} + \mu\right]^2 \tag{5.11}$$

where σ_1 (Pa) is the maximum principal stress and σ_3 (Pa) is the minimum principal stress. P_{pore} (Pa) is the fluid pressure in the fractures (or in situ fluid pressure) and μ is the friction coefficient (= 0.6 – 1.0; Zoback, 2007).

The vertical stress is assumed a principal component. The previous equation can also aid on the prediction of the differential stress as a function of depth in a crust in frictional equilibrium (e.g., Zoback et al., 2001).

The in-situ fluid pressure was approximated based on the ratio of fluid pressure in the fractures to lithostatic pressure (pore-fluid factor; Zoback et al., 2001; Sibson, 2004):

$$F_{\text{p-f}} = \frac{P_{\text{pore}}}{P_{\text{rock}}} \tag{5.12}$$

where $F_{\text{p-f}}$ is the pore-fluid factor and P_{rock} (Pa) is the lithostatic pressure.

The factor is approximately 0.4 assuming hydrostatic regime and the lithostatic pressure can be approximated as equal to the vertical principal stress. This relationship provides a first-order evaluation of the in-situ fluid pressure. The in-situ fluid salinity was not considered in this analysis. The hydrostatic regime was assumed in this first-order assessment based on data from several deep boreholes that suggest that fluid pressures are hydrostatic up to 12 km depth (e.g., Townend et al., 2000; Zoback et al., 2001).

5.4.3.3 Monte Carlo simulations

Monte Carlo simulations were carried out to create an ensemble of the uncertainties and develop the a priori stress model (Table 5.3). The horizontal principal stresses were inferred based on the horizontal-vertical principal stress relationship (Equation 5.8) considering the different expressions for the stress ratio coefficient (Table 5.2) and considering the models proposed by McCutchen (1982; Equation 5.9) and Sheorey (1994; Equation 5.10). Both vertical and horizontal a priori stress models were posteriorly compared with the published literature data for the Canadian Shield (Table 5.1) and the relative difference between observation and simulation was calculated. Furthermore, the results from the Monte Carlo analyzes were used to calculate the theoretical boundaries for both maximum and minimum principal stresses (Equation 5.11) and to estimate the in-situ fluid pressure (Equation 5.12).

Table 5.3 Monte Carlo method input parameters and uncertainty.

Parameter code	Parameter description	Variable type	Distribution
	Estimate vertical principal stress		
ρ_{rock}	Rock density	Continuous	Triang(min,median,max)
	Estimate maximum and minimum horizontal principal stresses		
σ_V	Vertical principal stress	Continuous	Triang(min,median,max)
k	Stress ratio coefficient		
	Herget (1987)	Discrete	Uniform
	Herget (1993)	Discrete	Uniform
	Arjang et al. (1997)	Discrete	Uniform
r_{outer}	Earth's outer radius		Single value
r_{Moho}	Moho depth	Continuous	Triang(min,mean,max)
E	Young's modulus	Continuous	Uniform(min,max)
v	Poisson's ratio	Continuous	Uniform(min,max)
β	Coefficient of linear thermal expansion	Continuous	Uniform(min,max)
∇T	Geothermal gradient	Continuous	Triang(min,median,max)

Triang – triangular distribution function.

The density of the outcropping geological materials was inferred by Miranda et al. (2020a) and revealed values ranging between 2465 and 2880 kg m^{-3} for the paragneiss, between 2590 and 3108 kg m^{-3} for the diorite, between 2571 and 2994 kg m^{-3} for the gabbro, between 2546 and 2626 kg m^{-3} for the tonalite and between 2505 and 2592 kg m^{-3} for the granite. Since diorite and paragneiss are the main lithologies, the density values used in this study were assumed to range between a mean minimum value of 2528 kg m^{-3} and a maximum mean value of 2994 kg m^{-3}, with a mean median value of 2697 kg m^{-3}. Arjang et al. (1997) inferred a Poisson's ratio of 0.16 – 0.30 and a Young's modulus of 43 – 100 GPa in Canadian Shield crystalline basement rocks. The Moho depth in northern Québec has been inferred by Vervaet et al. (2016) to range between 33 and 49 km. However, Telmat et al. (1999), Hall et al. (2002) and Hammer et al. (2010) suggest that below Kuujjuaq, Moho might be at a depth of about 37 km. Therefore, Moho was considered to vary within the range of 37 km ± 10%. The coefficient of thermal expansion typical for granitic rocks was used in this study. The value range between 6×10^{-6} and 9×10^{-6} ºC^{-1} (Sheorey et al. 2001). However, this parameter is a function of the content in SiO_2, decreasing with the decrease of the latter and therefore the literature values may not correspond to the values for the lithologies existing in Kuujjuaq. Further studies are needed to decrease this uncertainty. The geothermal gradient was inferred based on the subsurface temperature simulations carried out in Miranda et al. (2020b). A total of 1000 possible scenarios were run for the Monte Carlo analyzes and the software @RISK (Palisade, 2019) was used to run the simulations. The a priori stress model was developed for depths between 1 and 10 km. However, the comparison between inferred and literature values was carried out for a depth of 2 km to match the maximum depth of stress measurements in the Canadian Shield (Table 5.1).

5.4.4 Tectonic stress index

The Tectonic Stress Index (TSI) is a new method to estimate the ratio between in situ rock stresses and tectonics proposed by González de Vallejo et al. (2008). The method is based on the linear relationship between the stress ratio coefficient inferred from stress measurements and the TSI. The latter considers geological parameters and elastic properties of the rocks and is expressed as (González de Vallejo et al. 1988; González de Vallejo et al., 2008):

$$TSI = log\left(\frac{t}{E \cdot L}\right) NC \cdot SC \tag{5.13}$$

where *t* (years) is the age of the first orogenic cycle or main folding period affecting the rock mass, *L* (m) is the maximum lithostatic load supported throughout its geological history, *NC* is the coefficient of seismotectonic activity and *SC* is the coefficient of topographic influence.

Parameters *NC* and *SC* were considered 1 in this work given the absence of seismotectonic activity (Figure 5.4b) and the flat topography that characterizes the study area. The time *t* was assumed equal to the collision between Core Zone and Superior at 1.82 – 1.77 Ga before present. The variable *L* for high-grade metamorphism rocks, such as the paragneiss found in the study area, ranges within 12 to 20 km (González de Vallejo et al. 2008). Monte Carlo simulations were carried out to deal with the ensemble of uncertainties on the time, Young's modulus and maximum lithostatic load input parameters (Table 5.4).

Table 5.4 Monte Carlo method input parameters and uncertainty.

Parameter code	Parameter description	Variable type	Distribution
t	Time	Continuous	Uniform(min,max)
E	Young's modulus	Continuous	Uniform(min,max)
L	Lithostatic load	Continuous	Uniform (min,max)

The TSI is related with the stress ratio coefficient as (González de Vallejo et al. 2008):

$$k = a \cdot TSI + b \tag{5.14}$$

where *a* and *b* are experimental constants.

The stress ratio coefficient in this expression corresponds to (González de Vallejo et al. 1988; González de Vallejo et al., 2008):

$$k = \frac{\sigma_H}{\sigma_V} \tag{5.15}$$

The experimental constants *a* and *b* were inferred by plotting the calculated stress ratio coefficient as a function of the TSI. Each possible TSI value was randomly assigned to the stress ratio coefficient calculated based on the stresses inferred in this study.

5.4.5 Lithospheric strength profile

The rheological properties of the lithosphere can be approximated through the concept of strength envelopes (e.g., Byerlee, 1978; Brace et al., 1980). Rheological profiles are essentially constructed based on an approximate knowledge of the composition of lithospheric layers, structural information, and an estimate of temperature as a function of depth (Ranalli, 1991). A brittle regime prevails at low to moderate temperature and pressure and the frictional shear fracture criterion is (e.g., Byerlee, 1978; Ranalli, 1991):

$$(\sigma_1 - \sigma_3) \geq F_{\text{emp}} \rho g z \left(1 - F_{\text{p-f}}\right) \tag{5.16}$$

where F_{emp} (-) is an empirical factor.

This parameter is equal to 3 for compression and to 0.75 for tension assuming a coefficient of friction of 0.75 (e.g., Ranalli, 1991). The ductile regime, on the other hand, is characterized by creep strength of rocks and the steady-state nonlinear power-law creep equation is commonly used as the flow law (e.g., Brace et al., 1980; Ranalli, 1991):

$$(\sigma_1 - \sigma_3) = \left(\frac{\dot{\varepsilon}}{A}\right)^{\frac{1}{n}} exp\left(\frac{e_{creep}}{nRT}\right) \tag{5.17}$$

where $\acute{\varepsilon}$ (s^{-1}) is the strain rate, *A* ($MPa^{-n}\ s^{-1}$) is a constant characteristic of the material, *n* (-) is a stress and temperature-independent parameter, e_{creep} ($J\ mol^{-1}$) is the activation energy for creep, *R* ($J\ K^{-1}\ mol^{-1}$) is the gas constant ($8.314\ J\ K^{-1}\ mol^{-1}$) and *T* (K) is the absolute temperature.

The P-wave velocities inferred from the Lithoprobe eastern Canadian Shield onshore-offshore transect (e.g., Hall et al., 2002; Hammer et al., 2010) suggest two main crustal layers – upper and lower crust. Whole-rock geochemistry analysis supported with thin-sections (see Miranda et al., 2020a for further details) suggest feldspar and mafic minerals as the main mineral phases of the outcropping lithologies. Thus, the upper crust may be assumed as feldspar-dominated rheology. The lower crust composition has been assumed as granulite-facies (e.g., Ashwal et al., 1987). Thus, the continental crust seems to be internally stratified in composition and the lithospheric strength profile can be assumed as a “jelly sandwich” model (Burov, 2011), which in its simplest form, is composed by a brittle upper crust down to a depth of about 20-25 km, ductile lower crust and brittle upper 30-40 km of mantle (Ranalli et al., 1987). Moreover, the upper mantle of a thermally stabilized and old cratonic lithosphere is generally assumed stronger than the strong part of the upper crust (e.g., Cloetingh et al., 2010).

The rheological profile in this study was constructed until Moho depth to provide a first-order approximation of the distribution strength expected in the upper lithosphere beneath Kuujjuaq. The pore-fluid factor was assumed 0.4 implying in situ fluid pressure in hydrostatic regime (Sibson, 2004). The strain rate was assumed 10^{-18} s^{-1} and the remaining creep parameters for the lower crust were taken from the work of Mareschal et al. (2006). The geothermal gradient and heat flux were inferred by Miranda et al. (2020b) and Miranda et al. (2021). The subsurface temperature was assumed to increase linearly with depth for simplification in this preliminary analysis. The delimitation of the brittle-ductile transition zones took into account that frictional behavior predominates if the brittle shear strength is less than the ductile creep strength (Ranalli, 1991). The rheological profile developed in this work is theoretical and was made to provide a first order estimate of the lithosphere strength.

Additionally, the strength of the lithosphere until Moho depth was inferred as (Ranalli, 1997):

$$\sigma_{\mathrm{total}} = \int_0^{h_{\mathrm{M}}} (\sigma_1 - \sigma_3)\,(z)dz \tag{5.18}$$

where σ_{total} (N m^{-1}) is the strength of the lithosphere and h_{M} (m) is the mechanical thickness of the lithosphere until the Moho depth.

5.4.6 Mohr-Coulomb friction and tendency analyzes

Fracture reactivation analyzes are commonly done based on the Mohr-Coulomb criterion. The MohrPlotter software version 3.0.0 (Allmendinger, 2020) was used in this study to help assess the state of stress of the mapped fractures and the critical fluid pressure required to reactivate these structures, taking into account the a priori stress model proposed. The trend and plunge of the principal stresses were entered in the software in the geographic coordinate system format assuming a North-East-Down coordinate system for the stress tensor. The effect of in situ fluid pressure was also considered:

$$\begin{cases} \sigma'_1 = \sigma_1 - P_{\text{pore}} \\ \sigma'_2 = \sigma_2 - P_{\text{pore}} \\ \sigma'_3 = \sigma_3 - P_{\text{pore}} \end{cases} \tag{5.19}$$

where σ_2 (Pa) is the intermediate principal stress and σ'_1, σ'_2 and σ'_3 (Pa) are the effective maximum principal stress, effective intermediate principal stress and effective minimum principal stress, respectively.

Although several friction laws have been proposed in literature (e.g., Byerlee, 1978; Barton, 2013), a linear Coulomb friction law was assumed in this study for the failure criterion as:

$$\tau = \sigma'_{\text{n}}\, tan(\phi) \tag{5.20}$$

where τ (Pa) is the shear stress, σ'_{n} (Pa) is the effective normal stress and ϕ (º) is the internal friction angle.

In its simplest form, the internal friction angle is equal to:

$$\phi = tan^{-1}(\mu) \tag{5.21}$$

A constant friction coefficient of 0.6 (Zoback, 2007) can be assumed to simplify the friction analysis. However, a static friction coefficient shall be considered for pre-existing fractures that have been in stationary contact for long periods of time and subject to high normal stresses. This parameter was calculated as (Dieterich, 1978):

$$\mu_{\text{static}} = \mu_0 + c' ln(t) \tag{5.22}$$

where c' is a dimensionless parameter that describes the rate of increase in the static friction coefficient with the natural logarithm of the stick time t (s).

The friction coefficient μ_0 was found to range between 0.7 and 0.8 and parameter c' is 0.0096 for granitic rocks (Dieterich, 1978). The latest seismic event recorded closer to Kuujjuaq (53 km distance) occurred 5 years ago (GCan, 2021) thus the stick time of 1.6×10^8 s can be used as a working hypothesis to study the effect of static friction in the tendency of the fractures to slip. However, since this seismic event did not occur in the fault planes crossing Kuujjuaq, stick times of 3.2×10^9 s, 3.2×10^{10} s, 3.2×10^{13} s and 3.2×10^{16} s were additionally considered as working hypotheses. The fact that none of the three seismic events recorded since 1985 until present (GCan, 2021) occur in the fault planes crossing the community of Kuujjuaq, suggests that the pre-existing fault planes in the community are relative stationary objects with long-term points of contacts between the sliding surfaces and therefore resistant to sliding.

The critical fluid pressure required to induce slip on an optimally oriented fracture considering a friction coefficient of 0.6 has been estimated as (e.g., Rutqvist et al., 2007; Taghipour et al., 2019):

$$P_{\text{pore, critical}} = \frac{3\sigma_3^{'} - \sigma_1^{'}}{2} \tag{5.23}$$

where $P_{\text{pore, critical}}$ (MPa) is the critical fluid pressure.

However, the critical fluid pressure required to overcome the strength of the sliding surfaces considering the different stick times and static friction coefficients assumed was evaluate as:

$$P_{\text{pore, critical}} = \frac{t - \mu_{\text{static}} \sigma'_{\text{n}}}{-\mu_{\text{static}}} \leq \sigma_3 - P_{\text{pore}} = 0 \tag{5.24}$$

The Mohr-Coulomb friction and slip tendency analyzes were carried out considering the minimum, mean and maximum stress scenarios and for a depth of 4 km. The choice of this depth is based on the probabilistic analysis carried out by Miranda et al. (2020b). This study revealed that at 4 km depth the temperature is hot enough for the geothermal energy source to meet the heating needs of the community of Kuujjuaq (approximately 37 GWh) with a 98% probability.

5.5 **Results**

5.5.1 Fracture sampling and statistical analyzes

The fracture data collected was firstly corrected for censoring bias using the chord method (Figure 5.5). The results revealed a lower cutoff length of 2 m. Thus, the fractures smaller than the 2 m threshold were excluded from the analysis. From the total of 452 fractures sampled, only 199 are longer than 2 m, highlighting that scanline sampling method tends to underestimate the length of the fractures.

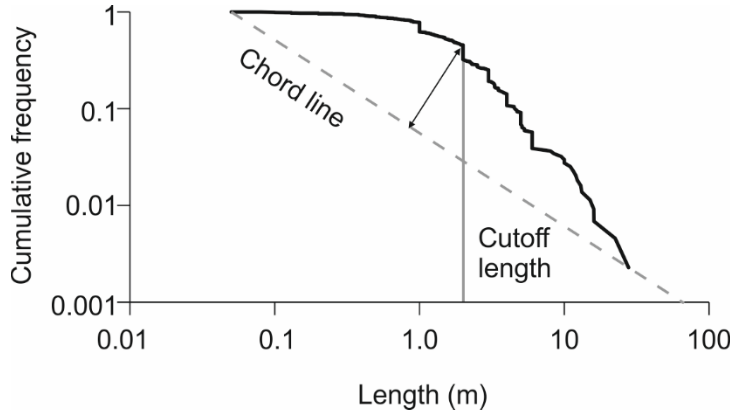

Figure 5.5 **Chord method applied to correct censoring bias in the fracture data sampled. Cutoff length = 2 m.**

The projection of the fracture planes, and posterior von Mises distribution calculation, revealed four main fracture sets striking approximately N81°E-N90ºE (E-W – F1), N161°E-N170ºE (NNW-SSE – F2), N11°E-N20ºE (N-S – F3) and N121°E-N130ºE (NW-SE – F4; Figure 5.6a; Figure 5.6b). Excepting the NW-SE family, all the remaining can be well defined in the histogram of the fracture strike planes grouped in classes of 10º (Figure 5.6c).

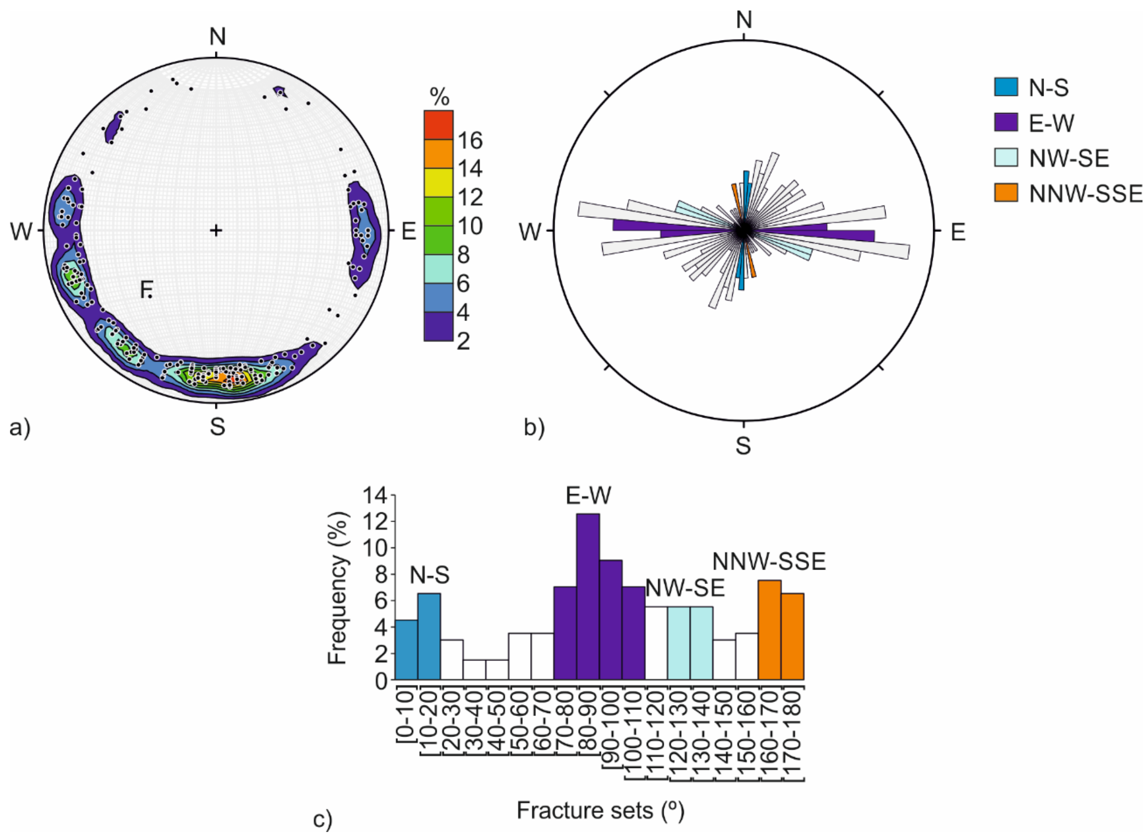

Figure 5.6 **a) Stereographic projection of the poles to planes and 1% area contour, b) rose diagram and c) relative frequency of the fracture strike planes. F – Lac Pingiajjulik and Lac Gabriel fault planes. The colors on a), b) and c) are not related.**

The intensity, after correction for the unmeasured spacing at both ends of the scanlines, for all the fracture planes sampled revealed values ranging from a minimum of 0.3 fracture m^{-1} to a maximum of 3.7 fractures m^{-1}, with a median value of 0.8 fracture m^{-1} (Figure 5.7a). The E-W set revealed a median intensity of 0.5 fracture m^{-1}, the NNW-SSE 0.7 fracture m^{-1}, the N-S 0.9 fracture m^{-1} and the NW-SE 0.9 fracture m^{-1} (Figure 5.7a). NNW-SSE and NW-SE sets revealed outliers with values of 12.5 fractures m^{-1} and 0.03 fracture m^{-1}, respectively, that were discarded from the analyzes. The median fracture spacing for E-W set was inferred as 2.3 m, for the NNW-SSE 1.4 m, for the N-S 1.1 m and for the NW-SE 1.2 m (Figure 5.7b). The coefficient of variation calculated for each set revealed values of 0.4 for N-S and NW-SE sets and 0.7 for E-W and NNW-SSE. These values indicate a log-normal distribution of spacing (e.g., Sanderson et al., 2019a).

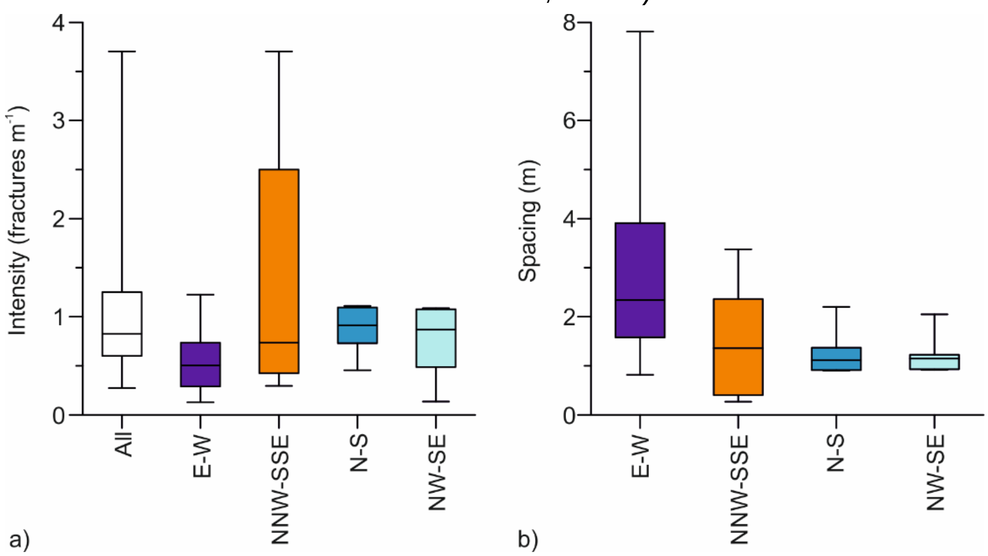

Figure 5.7 **Boxplot with whiskers from minimum to maximum for a) intensity and b) spacing. The number of data points is: All = 37, E-W = 17, NNW-SSE = 7, N-S = 6, NW-SE = 5.**

The heterogeneity of the distribution was evaluated using the Kuiper's method (Figure 5.8). The results reveal a value of 15% considering all the fracture planes (Figure 5.8a). A heterogeneity of 11% was inferred for the E-W set, 31% for the NNW-SSE, 20% for the N-S and 21% for the NW-SE (Figure 5.8b). These results indicate random distribution of the fractures along the scanline. The statistical significance of the departure from a uniform distribution was additionally evaluated and the results revealed values ranging from 1.0 (E-W, N-S and NW-SE) to 1.7 (NNW-SSE). Such results indicate that the null hypothesis of uniformity can be rejected at levels lower than 95%. Considering all the fracture planes, the results revealed a value of 2.1, implying that the null hypothesis of uniformity can be rejected at 99% level.

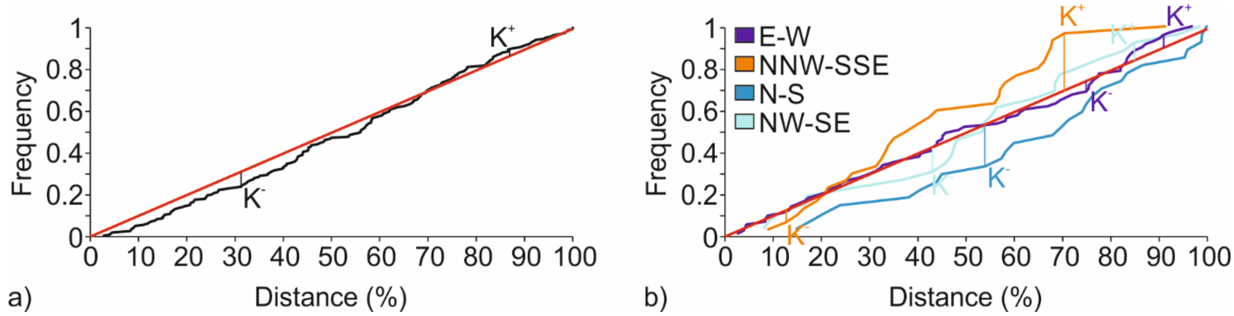

Figure 5.8 Kuiper's method applied in a) all fracture planes and b) each main fracture set. Red line – uniform distribution, K – departure from the uniform distribution.

The length and fractal dimension were inferred for all the fracture planes and for each fracture set (Figure 5.9). Considering all the fracture planes, the length varies within a minimum of 2 m to a maximum of 27.8 m, with a median value of 3 m. The fractal dimension was evaluated as 1.8 (Figure 5.9a). The fracture set E-W have lengths ranging from 2 m to 13.2 m, with a median value of 3.2 m. The fractal dimension is 1.7 (Figure 5.9b). The set NNW-SSE has a median length of 2.8 m, varying between 2 and 8 m. The fractal dimension is 2.4 (Figure 5.9b). N-S set reveals lengths within 2 and 12 m, with a median value of 3 m. The fractal dimension is 1.8 (Figure 5.9b). Lastly, the set NW-SE reveal lengths from 2 to 16 m, with a median of 2 m. The fractal dimension is 1.7 (Figure 5.9b). The high fractal dimension inferred highlight the high number of short fractures sampled compared to the longest ones.

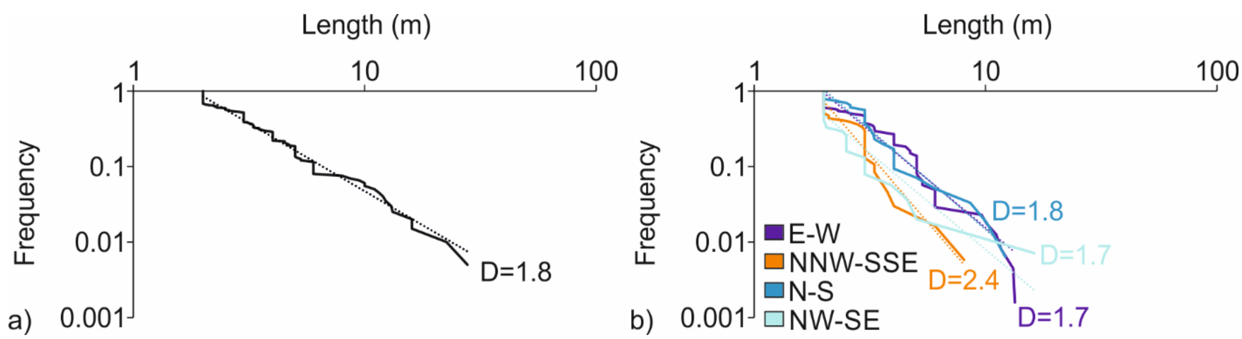

Figure 5.9 Log-log plot of the length of the fractures for a) all the fracture planes and b) each main fracture set. D – fractal dimension.

The apertures of the fractures sampled are biased due to weathering and erosion of the fracture walls. As a recall, only outcrops are available in the study area. Therefore, these were observed to range from minimum values lower than 1 mm up to maximum values wider than 1 cm. The roughness of the fracture walls, assuming the joint roughness coefficient (JRC) profiles of Barton et al., (1977), varied from smooth (JRC = 2-4) to rough (JRC = 10-12). The factures sampled do not show infilling, but this does not mean that infilling does not occur, and it may be present in other fractures not sampled. Moreover, the fracture set E-W seems the oldest set in the region based on a dozen observations of the relative age of the sets. However, further structural work is necessary to prove this theory. Alteration minerals in the walls of the fractures were not observed in the scope of this work. Topology of the fracture networks is further discussed in Miranda et al. (2018b).

5.5.2 Fracture network modeling

The fracture network was generated for a total cubic volume of 4 km^3 and considering the field data sampled, which statistics were discussed in the previous section. The network was generated for the minimum, median and maximum values of fracture intensity. The fracture network includes the four main fracture sets and the fractures not belonging to any of those (hereafter identified as “other”). Each fracture class is defined by the dip and dip direction, by the smallest and largest length sampled and by the fractal dimension. As a recall, the fractures are generated for a volume twice larger than the defined model volume (Jing et al., 2000). Of the fractures included in the model, 34% belong to the set E-W, 24% to the NNW-SSE, 12% to the N-S, 9% to the NW-SE and 20% to the set “other”.

For a fracture intensity of 3.7 fractures per meter, more than 1 000 000 000 fractures were generated and included in the defined model volume. For a fracture intensity of 0.8 fracture m^{-1}, a total of 105 246 818 fractures were generated and, of these, 96 788 246 fractures included in the defined model volume (Figure 5.10a; Figure 5.10d). A fracture intensity of 0.3 fracture m^{-1} leads to the generation of a total of 29 613 593 fractures, accepting 27 233 225 fractures.

An alternative fracture network was also generated by increasing both smallest and largest fractures by a factor of 10 as a working hypothesis to correct the effect of size bias (Figure 5.10b; Figure 5.10e). This fracture network was generated considering the median fracture intensity of 0.8 fracture m^{-1} and the fractal dimension inferred for each fracture set. A total of 1 413 691 fractures were generated and 681 979 fractures included in the defined model volume.

Additionally, the fractal dimension was decreased by a factor of 2 to favor the generation of largest fractures (Figure 5.10c; Figure 5.10f). This fracture network was generated assuming a fracture intensity of 0.8 fracture m^{-1} and the size of the fractures measured in the field. A total of 45 517 423 fractures were generated and 41 648 558 fractures included within the model volume.

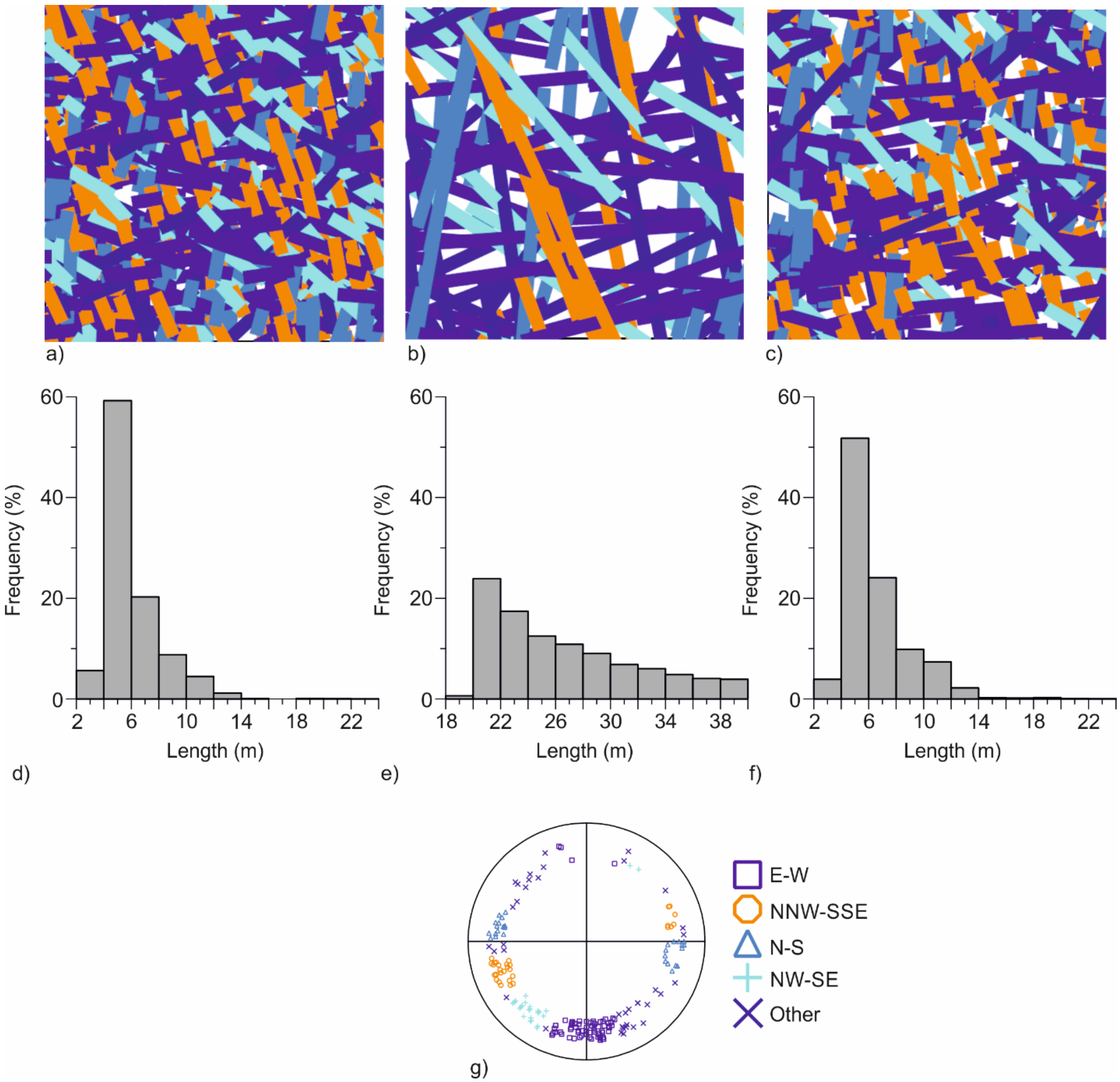

Figure 5.10 **Top view of a 80 m per 80 m section of the total generated fracture network model: a) base-case fracture network, b) fracture network with fracture lengths increased by a factor of 10 and c) fracture network with fractal dimension decreased by a factor of 2. The fracture length distribution is plotted for d) the base-case fracture network, e) the fracture network with fracture lengths increased by a factor of 10 and f) the fracture network with fractal dimension decreased by a factor of 2. g) Wulff projection stereo plot of field fracture data.**

5.5.3 A priori stress model

5.5.3.1 Geological indicators

As aforementioned, Lac Pingiajjulik and Lac Gabriel faults are a result of the transpressional deformation occasioned by the Core Zone/Superior collision (1.82-1.77 Ga). Both structures are thrust faults with late dextral motion (Figure 5.2). Thus, the stress faulting regime seems to be a combination of thrust/strike-slip. The orientation of these faults is roughly NNW-SSE (Figure 5.2) indicating a ENE-WSW compression that correlates with the regional trend proposed by Adams (1989). Observation of the Falcoz Swarm intrusions (Mesoproterozoic) in the geological map (Figure 5.2) suggests a maximum compressive stress oriented roughly NW-SE, thus contrary to the contemporary regional stress trend indicated by Adams (1989). Analysis of the main fracture sets and assuming the principal stresses oriented in directions bisecting the angles between those sets indicates a maximum horizontal principal stress trending N210ºE-N220ºE, correlated with the NE-SW regional trend of Adams (1989). If the minimum horizontal principal stress is assumed to form a right angle with the maximum horizontal principal stress, then the former trends to N300ºE-N310ºE.

5.5.3.2 Empirical correlations, analytical models and Monte Carlo simulations

The results revealed that the vertical principal stress for the study area can be described by the following equation:

$$\sigma_{\mathrm{V}} = 0.0271z \tag{5.25}$$

The relative average difference between the inferred vertical principal stress and the ones published for the Canadian Shield varies between -7.9% and 3.9% (Figure 5.11). The smallest difference of 1.7% was found when compared the inferred stress with the one proposed by Arjang (1991). The highest difference of -7.9% was obtained when compared to the results from this study with the vertical stress referred by Herget (1982) and Herget (1987).

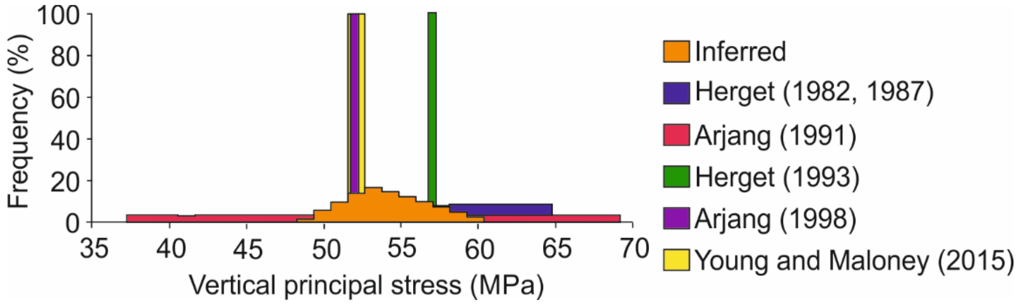

Figure 5.11 **Inferred and literature vertical principal stress.**

The minimum and maximum horizontal principal stresses were evaluated considering the minimum and maximum stress ratio coefficient inferred by Herget (1987), Herget (1993) and Arjang et al. (1997). The following expressions for the minimum and maximum principal stresses were obtained:

$$\sigma_{\mathrm{h}} = 0.0251z + 4.94 \tag{5.26a}$$

$$\sigma_{\mathrm{H}} = 0.0430z + 8.62 \tag{5.26b}$$

The inferred minimum horizontal principal stress revealed relative differences in the range -18% to 0.6% when compared with published literature values for the Canadian Shield (Figure 5.12). The minimum difference was obtained when compared with Arjang (1998) minimum stress and the maximum for Herget (1993) compiled minimum stress (Figure 5.12a). The evaluated maximum horizontal principal stress indicates a minimum relative difference of 2.2% when compared to Herget (1993) stress data while the maximum difference of 25% is obtained comparing inferred value with the Young et al. (2015) stress compilation (Figure 5.12b).

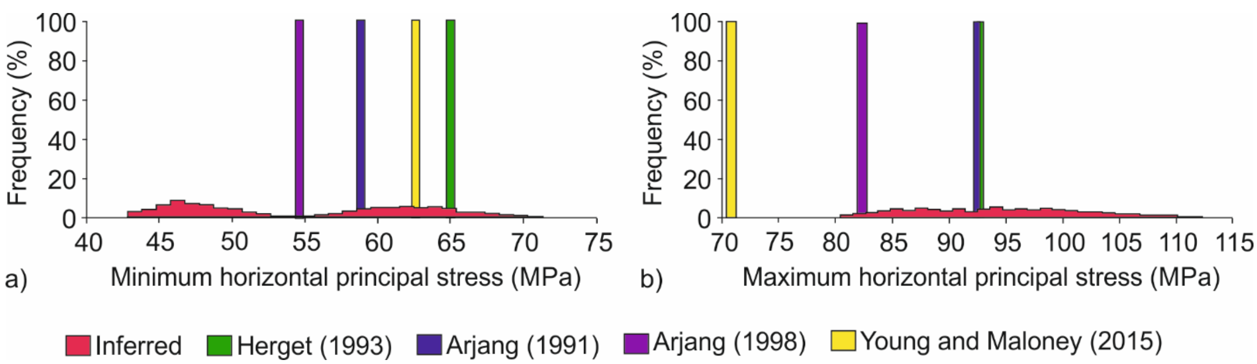

Figure 5.12 **Inferred and literature a) minimum and b) maximum horizontal principal stresses.**

Alternatively, the average horizontal principal stress was estimated based on McCutchen (1982; Equation 5.9) and Sheorey (1994; Equation 5.10) models. The relative difference at 2 km depth between inferred average horizontal principal stress and the stress measurements of Herget (1982) and Herget (1987) is -32% for the McCutchen (1982) model and -4% for the Sheorey

(1994) model (Figure 5.13). While the latter provides a good approximation to the average horizontal principal stress, the former tends to underestimate it.

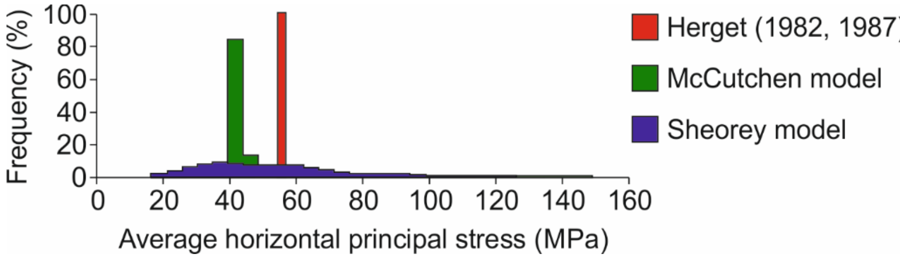

Figure 5.13 Inferred and literature average horizontal principal stress.

Linear-based global sensitivity analysis through Spearman correlation coefficient reveals that, for the McCutchen (1982) model, the density of the geological materials plays a major role on the average horizontal principal stress, with a correlation coefficient of 1.00. The Moho depth and vertical principal stress, per contra, have a weak correlation, with coefficients of 0.02 and 0.03, respectively. For the Sheorey (1994) model, the geothermal gradient has a strong correlation with the average horizontal principal stress with a coefficient of 0.76. The Young's modulus, the coefficient of linear expansion and the Poisson's ratio, in turn, have a medium to weak correlation with coefficients of 0.56, 0.26 and 0.13, respectively. The principal vertical stress is found to have no influence on the average horizontal principal stress. Furthermore, considering this model, the average horizontal principal stress as a function of depth can be described by the following relationship:

$$\sigma_{\mathrm{H,average}} = 0.0178z + 17.81 \tag{5.27}$$

Additionally, a comparison between the minimum and maximum horizontal principal stresses inferred by the stress ratio coefficient and by the Sheorey (1994) model was undertaken for depths up to 10 km (Figure 5.14). Since the latter only evaluates the average horizontal principal stress, the minimum and maximum horizontal principal stresses were calculated assuming that:

$$\begin{cases} \sigma_{\mathrm{H,average}} = \frac{\sigma_{\mathrm{H}}+\sigma_{\mathrm{h}}}{2} \\ \sigma_{\mathrm{H}} = 1.7\sigma_{\mathrm{h}} \end{cases} \tag{5.28}$$

The results reveal that the Sheorey (1994) model leads to a greater dispersion around the mean value and that the mean value is on average 31 to 33% smaller than evaluating the minimum and maximum horizontal principal stresses with the stress ratio coefficient.

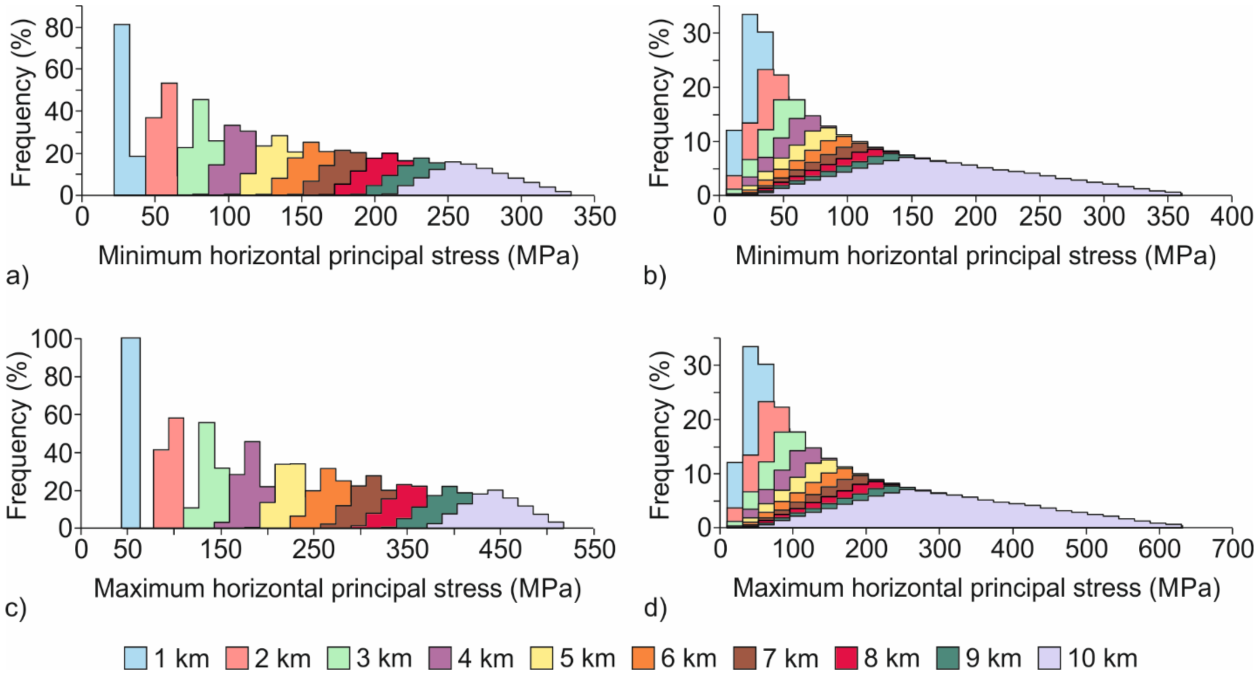

Figure 5.14 Calculated minimum and maximum horizontal principal stresses using the stress ratio coefficient in a) and c) and the Sheorey (1994) model in b) and d).

The vertical and horizontal principal stresses inferred through the stress ratio coefficient reveals that thrust faulting regime is dominant in the maximum stress scenario and up to a depth of 2 km in the mean stress scenario (Table 5.5). Strike-slip faulting regime prevails in the minimum stress scenario and at depths deeper than 2 km in the mean stress scenario (Table 5.5). However, if Sheorey (1994) model is used to infer the horizontal principal stresses, the results reveal that normal faulting regime prevails in the minimum stress scenario, strike-slip/normal in the mean stress scenario and thrust faulting regime in the maximum stress scenario (Table 5.5).

Table 5.5 Magnitude of the principal stresses as a function of depth.

Depth (km)	σ_V (MPa)			Stress ratio coefficient σ_h (MPa)			Stress ratio coefficient σ_H (MPa)			Sheorey model σ_h (MPa)			Sheorey model σ_H (MPa)		
	min	mean	max	min	mean	max	min	mean	max	min	mean	max	min	mean	max
1	24	27	30	22	29	38	45	52	60	5	27	67	9	45	113
2	49	54	61	43	55	72	80	95	112	7	39	101	13	67	171
3	73	81	91	64	79	105	116	138	162	10	53	134	16	89	228
4	97	108	121	84	106	138	152	181	213	13	66	167	21	112	285
5	121	135	152	105	131	173	189	224	264	15	79	201	25	135	341
6	146	162	182	126	156	206	225	267	318	17	93	235	29	157	399
7	170	189	212	147	181	238	263	310	370	20	106	268	34	180	456
8	194	217	243	169	206	269	297	353	421	22	119	301	38	201	513
9	218	244	273	189	231	305	333	396	470	24	132	335	42	224	569
10	243	271	304	209	255	337	372	439	521	27	145	368	45	247	626

Although Sheorey (1994) model provides a good fit for the average horizontal principal stress, the analysis discussed hereafter is focused on the principal stresses inferred through the stress ratio coefficient.

The in-situ fluid pressure was inferred based on the pore-fluid factor (Equation 5.12) and the results revealed the following relationship and results (Table 5.6):

$$P_{\text{pore}} = 0.0108z \tag{5.29}$$

Table 5.6 In situ fluid pressure as a function of depth.

Depth (km)	P_{pore} (MPa) min	mean	max
1	10	11	12
2	19	22	24
3	29	33	36
4	39	43	49
5	49	54	61
6	58	65	73
7	68	76	85
8	77	87	97
9	87	97	109
10	97	108	122

Frictional limit analysis (Equation 5.11) reveals that the probability of the inferred stresses using the stress ratio coefficient below the threshold value considering a friction coefficient of 0.6 and in situ fluid pressure in hydrostatic regime is 98% (Figure 5.15). In this analysis, the distribution span of both maximum and minimum principal stresses and in situ fluid pressure are used together as inputs to assess the frictional limit output.

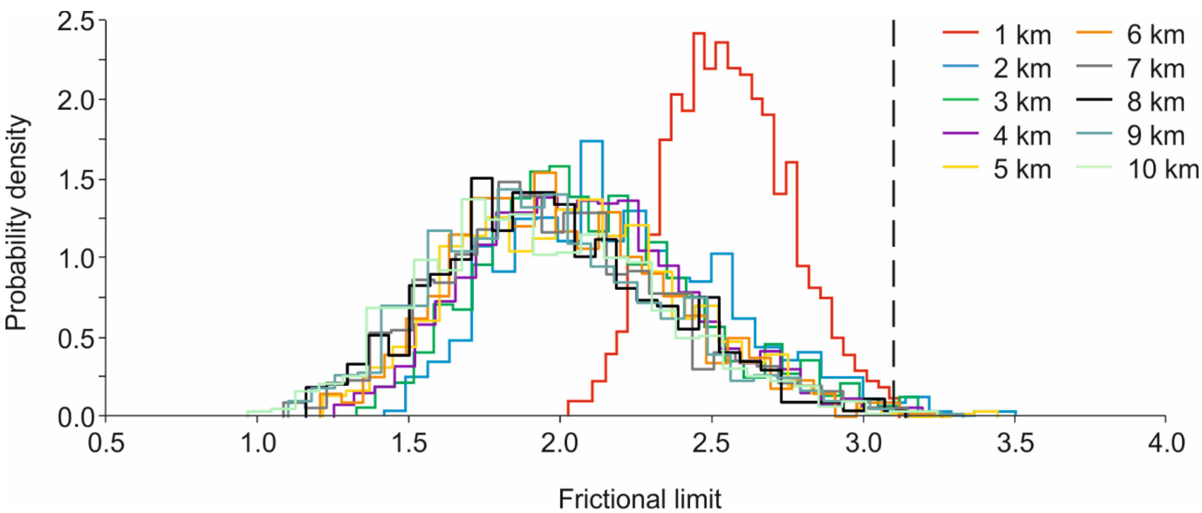

Figure 5.15 Frictional limit as a function of depth. Black dashed line – frictional limit for a friction coefficient of 0.6.

This analysis also reveals that at 1 km depth, the stresses are closer to critical conditions than at greater depths. In fact, theoretical boundaries for the maximum or minimum principal stresses can be evaluated using the frictional limit analysis. Assuming that both minimum principal stress and in situ fluid pressure are known and the maximum principal stress is unknown, the results reveal that the latter should be on average 15 to 22% greater than the one inferred in this study through the stress ratio coefficient (Table 5.7). Per contra, if the minimum principal stress is unknown and both maximum principal stress and in situ fluid pressure are known, the results reveal that the former should be on average 11 to 19% smaller than inferred in this study through the stress ratio coefficient (Table 5.7). It is important to highlight that these results assumed a friction coefficient of 0.6. In fact, increasing the friction coefficient to 0.75 leads to an increase in the theoretical boundaries for the principal stresses (Table 5.7).

Table 5.7 Theoretical maximum and minimum principal stresses.

Depth (km)	Friction coefficient = 0.6						Friction coefficient = 0.75					
	σ_1 (MPa)			σ_3 (MPa)			σ_1 (MPa)			σ_3 (MPa)		
	min	mean	max	min	mean	max	min	mean	max	min	mean	max
1	47	61	68	21	24	27	58	83	116	19	21	24
2	93	121	139	39	46	52	115	154	216	34	40	46
3	138	176	207	57	67	77	169	217	312	51	59	68
4	179	238	272	75	88	102	219	295	405	67	78	90
5	223	293	343	94	109	126	273	362	509	84	97	112
6	269	347	411	112	130	152	330	429	605	100	116	134
7	313	402	479	131	151	177	384	496	697	117	135	156
8	362	456	550	148	173	202	445	563	785	132	154	178
9	403	512	617	166	193	225	495	633	893	149	172	199
10	444	564	686	186	215	251	545	696	982	166	191	222

5.5.4 Tectonic stress index

Monte Carlo simulations revealed that the TSI ranges within a minimum of 2.96 to a maximum of 3.52, with a mean value of 3.21 (Figure 5.16). Linear-based global sensitivity analysis revealed that the Young's modulus is the most influential parameter with a Spearman coefficient of -0.85, followed by the maximum lithostatic load with a coefficient of -0.49. The time input parameter revealed a Spearman coefficient of 0.

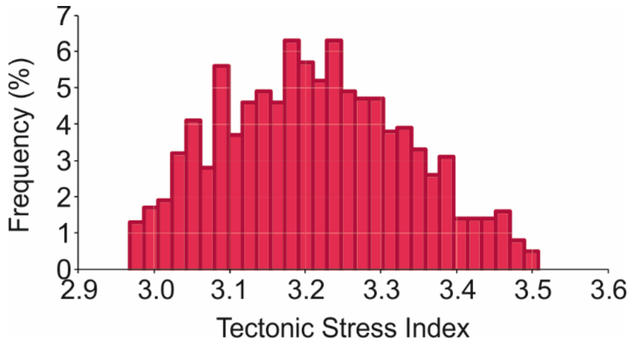

Figure 5.16 Tectonic stress index distribution.

Randomly assigning the TSI to the stress ratio coefficient and plotting the stress ratio coefficient obtained in this work through Equation (5.15) as a function of the TSI (Figure 5.17a), gives the following expression to relate the tectonic stress index with the stress ratio coefficient for the study area:

$$k = -0.01 \cdot TSI + 1.71 \tag{5.30}$$

However, if the TSI is randomly assigned and plotted against the literature-based stress ratio coefficients (Figure 5.17b), then the expression obtained is:

$$k = 0.12 \cdot TSI + 1.11 \tag{5.31}$$

This highlights the uncertainty associated with estimating stresses using the tectonic stress index approach.

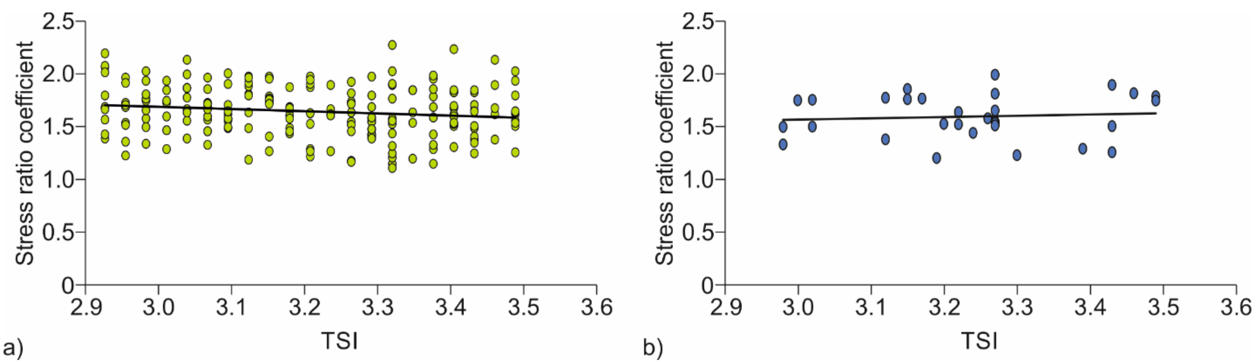

Figure 5.17 **Stress ratio coefficient as a function of the tectonic stress index: a) and b) literature-based inferred stress ratio coefficient.**

5.5.5 Lithospheric strength profile

The theoretical lithospheric strength profile provides a first-order approximation of the stress distribution as a function of depth beneath Kuujjuaq, assuming a pre-fractured crust (Figure 5.18). The profile also provides information on the theoretical deviatoric stresses required for fracture slippage. The profiles were constructed taking into account the subsurface temperature range estimated by Miranda et al. (2020b) and assuming the in-situ fluid pressure in hydrostatic regime. Furthermore, the regional data indicates compression as the main stress regime (Adams, 1989).

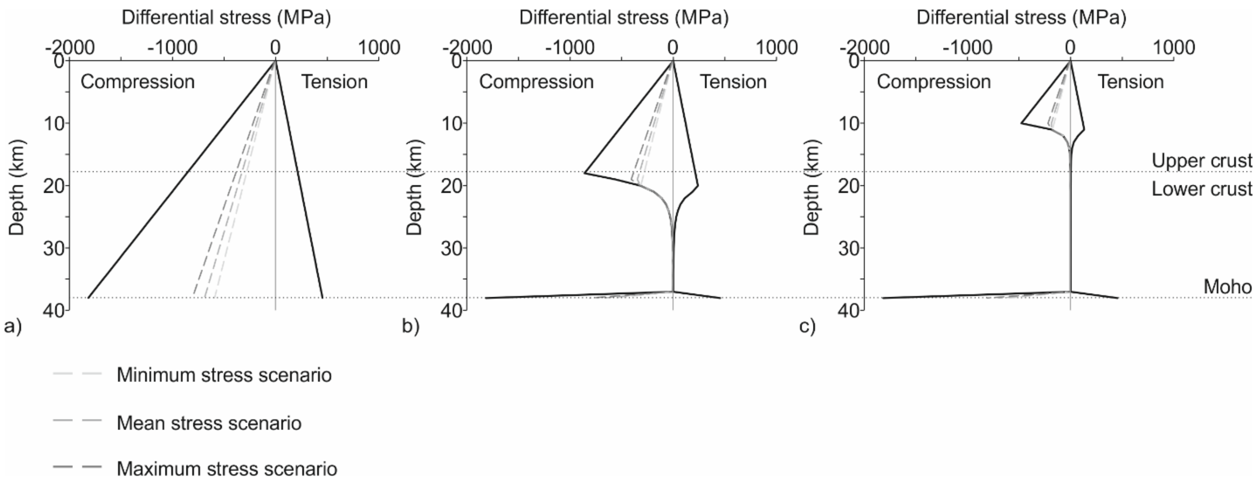

Figure 5.18 Lithospheric strength profile considering the a) minimum, b) median and c) maximum subsurface temperature. Dashed lines – stress scenarios inferred in this work through the stress ratio coefficient.

The rheological profiles clearly highlight the influence of the heat flux and geothermal gradient on the strength of the lithosphere. For a heat flux of 32 – 34 mW m^{-2} at 10 km depth and a geothermal gradient of 8 ºC km^{-1}, the theoretical profile indicates brittle crust up to Moho depth (Figure 5.18a), with the brittle-ductile transition at around 47 km. Moreover, the lithosphere strength evaluated until Moho for this profile reveals a value of 2.04×10^{13} N m^{-1}. This rheological profile can be assumed as the worst-case thermo-mechanical scenario. Per contra, a heat flux at 10 km depth of 52 – 69 mW m^{-2} and a geothermal gradient of 42 ºC km^{-1}, suggests a brittle domain until 10 km depth (Figure 5.18c) and a lithosphere strength of 1.81×10^{11} N m^{-1}. This rheological profile can be considered the best-case thermo-mechanical scenario. The base-case heat flux (42 – 50 mW m^{-2}) and geothermal gradient (22 ºC km^{-1}) suggest brittle crust until 18 km depth, with the brittle-ductile transition matching the upper-lower crust transition (Figure 5.18b) and the depth of the earthquakes recorded nearby Kuujjuaq. Moreover, the lithosphere strength was evaluated about 4.45×10^{11} N m^{-1}. This profile is thus the base-case thermo-mechanical scenario. Additionally, the long-term mechanical base of the lithosphere, which is limited by the 700 – 800 ºC isotherm (Burov, 2011), was evaluated for each rheological profile. This parameter is found to vary between the depth of 17 – 19 km (Figure 5.16c) and 88 – 100 km (Figure 5.16a), with a mean value of 32 – 36 km (Figure 5.16b).

Depicted are also an extrapolation of the differential stresses inferred in this study (Figure 5.18). These results highlight the major role played by the differential stress, indicating that the inferred differential stresses, regardless of the scenario, are lower than the lower limit of strength suggested by the theoretical rheological profiles. At shallow depths, the differential stresses inferred are 60 to 118% lower while deeper in the crust are 125 to 207% lower. In theory, the stress level required to drive suitably oriented faults to slip at the depth of interest, in this case 4 km depth, is 191 MPa according to the theoretical rheological profile (Table 5.8). The differential stresses inferred in this work for a depth of 4 km range between a minimum of 55 MPa and a maximum of 92 MPa, with a mean value of 75 MPa (Table 5.8). These results reveal that the theoretical differential stress is 71 – 52% higher than the inferred values for 4 km depth. In fact, for the differential stress match the theoretical rheological profile, the maximum principal stress needs to be 32 to 45% higher than the one inferred in this study through the stress ratio coefficient. This analysis took into account the minimum principal stress inferred in this study using the stress ratio coefficient.

Table 5.8 Deviatoric stress as a function of depth.

Depth (km)	$(\sigma_1\text{-}\sigma_3)$ (MPa) Rheological profile Compression	Inferred Minimum	Inferred Mean	Inferred Maximum
1	48	21	25	30
2	96	31	41	51
3	143	43	59	71
4	191	55	75	92
5	239	68	93	112
6	287	79	111	136
7	334	93	129	158
8	382	103	147	178
9	430	115	165	197
10	478	129	184	217

An additional analysis of the strength profiles as a function of the pore-fluid factor indicates the key role played by the in-situ fluid pressure (Figure 5.19). If the in-situ fluid pressure is at hydrostatic regime, the fluid pressure in the fractures need to be increased by 50% to trigger slippage considering the inferred stress scenarios. However, if the in-situ fluid pressure beneath Kuujjuaq is near-lithostatic rather than hydrostatic, then less fluid pressure is necessary to induce slippage in optimally oriented fractures. Suprahydrostatic in situ fluid pressures tend to reduce the stresses required for brittle failure (Figure 5.19), and consequently reduces the lithosphere strength. The base-case thermo-mechanical scenario, for a pore-fluid factor of 0.7, reveals a strength of 2.38×10^{11} N m^{-1}, i.e. 87% smaller than assuming hydrostatic regime.

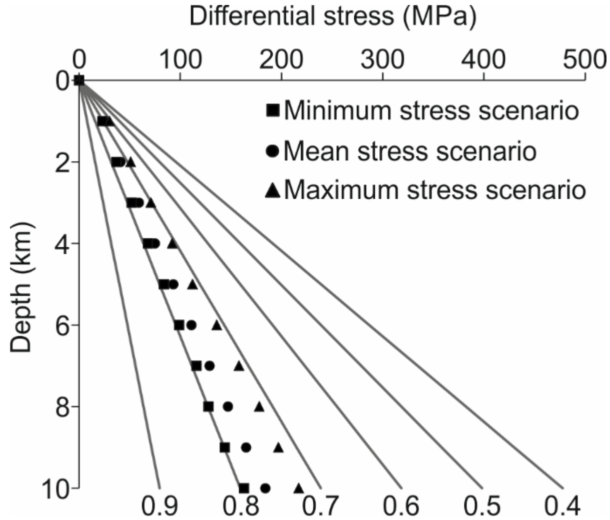

Figure 5.19 **Compression strength profile as a function of the pore-fluid factor.**

5.5.6 Mohr-Coulomb friction and slip tendency analyzes

The analyzes were carried for a depth of 4 km and considering the minimum, mean and maximum values obtained from the Monte Carlo simulations and stress ratio coefficient for the principal stresses (Table 5.5) and in situ fluid pressure at hydrostatic regime (Table 5.6) and their geographic coordinates inferred from the geological indicators. In all the three scenarios, the maximum principal stress corresponds to the maximum horizontal stress with a trend N215ºE, and a plunge assumed 0º. The intermediate principal stress is the vertical principal stress for the minimum and mean stress scenarios and is assumed trending N90º. For these stress scenarios, the minimum principal stress is the minimum horizontal principal stress trending N305ºE and assumed with a horizontal plunge. For the maximum stress scenario, a switch is observed between vertical and minimum horizontal principal stress, the latter becomes the intermediate principal stress and the former the minimum principal stress. For a depth of 4 km, the strike-slip faulting regime is dominant for the minimum and mean stress scenarios while the thrusting system prevails for the maximum stress scenario.

The Mohr-Coulomb friction analysis reveals that the fracture planes are not at critical state of stress considering the effective principal stresses in hydrostatic regime (Figure 5.20). A critically stressed fracture plane has the ratio between shear stress and normal effective stress similar to the coefficient of friction (i.e Amonton's law) which has been assumed with the typical value of 0.6 (e.g., Zoback, 2007), but it can be higher if the stick time is taken into account. The results of the slip tendency analysis reveal coefficient of friction below 0.5 for the minimum stress scenario, below 0.40 for the mean stress scenario and below 0.35 for the maximum stress scenario.

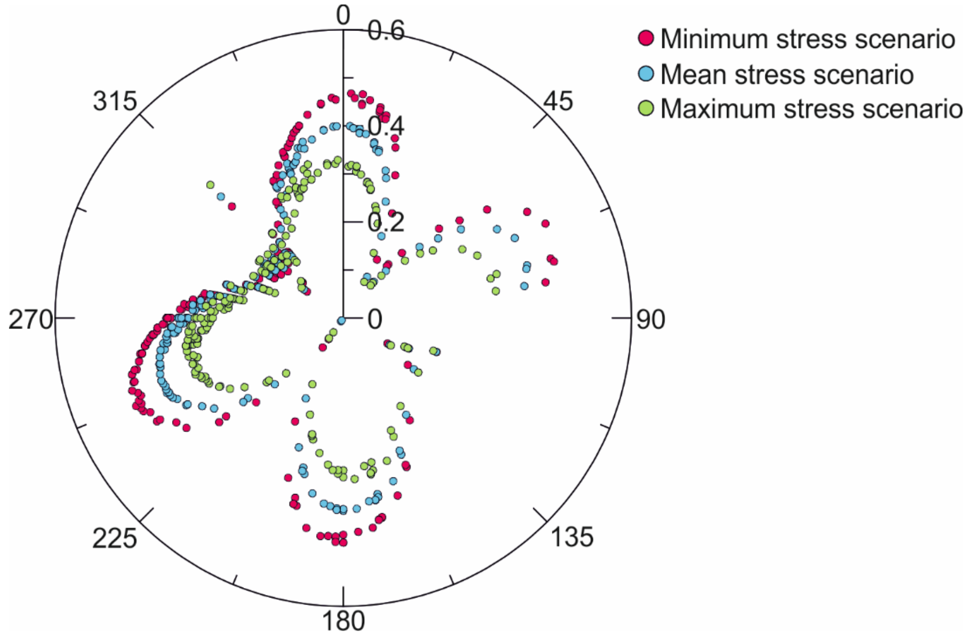

Figure 5.20 Surface frictional characteristics of the fracture planes for each stress scenario. Vertical axis – coefficient of friction, dots – orientation of the fractures.

The critical fluid pressure analysis was carried out considering different static friction coefficients that are related with the working hypotheses for the stick times aforementioned. The results clearly indicate the influence of assuming a friction coefficient of 0.6 or one that is time-dependent on the reactivation of the fracture planes (Figure 5.19). These results also highlight the influence of the stress scenarios on the fluid pressure required to reactivate the fracture planes. Moreover, considering the inferred stress regimes, the fracture set NW-SE will not be reactivated. The set N-S, per contra, have the highest tendency to be reactivated at low fluid pressure and regardless of the friction coefficient. Some of the fracture planes belonging to the sets E-W and NNW-SSE can be reactivated but at higher fluid pressure than the set N-S and only for friction coefficients lower than 0.98.

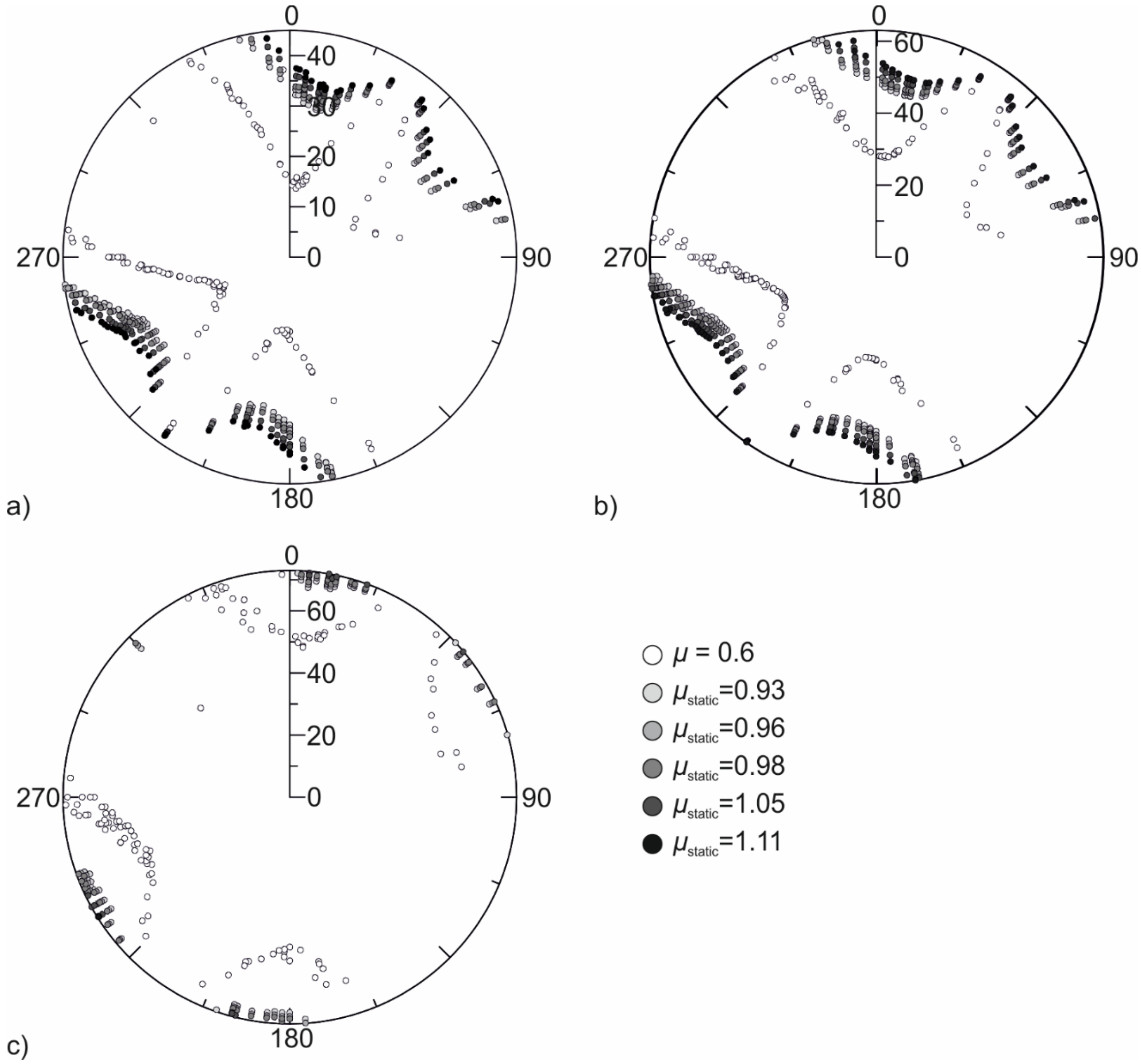

Figure 5.21 Critical fluid pressure to reactivate the fracture planes as a function of the coefficient of friction: a) minimum stress scenario, b) mean stress scenario and c) maximum stress scenario. Vertical axes – fluid pressure in MPa, dots – orientation of the fractures.

However, if the in-situ fluid pressure is near-lithostatic regime rather than hydrostatic, or if the maximum principal stress is higher than inferred in this study through the stress ratio coefficient, then the fracture planes will be at near-critical stress conditions and lower fluid pressure will be necessary to induce slippage.

5.6 Discussion

Canada's northern and remote communities have a critical dependence on energy services for their safety, sustainability, and economic growth (Gilmour et al., 2018) and unconventional geothermal development, such as EGS, have potential to exploit deep geothermal energy sources of petrothermal systems within the Canadian Shield (e.g., Grasby et al., 2012). Given the opportunity that off-grid renewable solutions may provide to Canadian northern communities, this work carried out in the community of Kuujjuaq aims at better understanding the fracture network and stress regime, key points for the successful development of hydraulically stimulated geothermal reservoirs (e.g., Richards et al., 1994; Evans et al., 1999; Brown et al., 2012). The strengths and weaknesses of this study, together with future envisioned work, are discussed in this section.

5.6.1 Fracture sampling and fracture network modeling

Scanline sampling and transit compass are useful and widely applied methods to characterize discontinuities in rock masses (e.g., Priest et al., 1981; Peacock et al., 2003; Priest, 2004; Zeeb et al., 2013a; Chaminé et al., 2015; Fisher et al., 2014; Sanderson et al., 2019a). However, these techniques are subject to a number of biases, such as orientation, size, censoring and truncation (e.g., Park et al., 2002; Zeeb et al., 2013a; Huang et al., 2016). Some of these can be avoided by, for example, placing the scanline normal to each fracture set, or selecting a threshold length for the sampling. However, biases such as censoring and size are difficult to prevent or correct if the outcrop is of poor quality. Methodologies taking advantage of remote sensing, such as terrestrial LiDAR and other photogrammetry techniques (e.g., McLeod et al., 2013; Fisher et al., 2014; Vollgger et al., 2016; Salvini et al., 2017; Menegoni et al., 2018; Sayab et al., 2018), for example coupled with machine learning (e.g., Valera et al., 2018; Bruna et al., 2019; Akara et al., 2020), can be valuable to image larger outcrop areas and, in this way, helping to reduce size and censoring biases. Although a terrestrial LiDAR campaign has been carried out in the community of Kuujjuaq, this data was not used in the present study, but further work can be foreseen to link scanline sampling with LiDAR data. In fact, several workflows have been proposed in the literature that can be followed to apply such techniques (e.g., Bisdom et al., 2017; Wüstefeld et al., 2018; Bistacchi et al., 2020; Larssen et al., 2020; Tavani et al., 2020) and several software and algorithms are nowadays available for automatic/semi-automatic mapping and statistical analysis of large and complex datasets (e.g., Xu et al., 2010; Markovaara-Koivisto et al., 2012; Zeeb et al., 2013b; Vasuki et al., 2014; Hyman et al., 2015; Alghalandis, 2017; Healy et al., 2017; Buyer et al., 2020; Chabani et al., 2020; Lepillier et al., 2020). Nevertheless, although outcrops are widely used as subsurface analogues (e.g., Howell et al., 2014), studies have shown their limitations on predicting the fracture orientation within the reservoir and other important properties as well (Bauer et al., 2017). Additionally, the absence of vertical outcrop surfaces for a 3D characterization provides further biases on the application of scanline sampling technique, for example, in the characterization of the dip and dip direction.

Borehole imaging tools, such as acoustic televiewer, and core analysis can be assets to reduce the uncertainty on these key geometric properties and on others such as orientation, intensity, spacing and aperture (e.g., Genter et al., 1997; Trice, 1999; Massiot et al., 2017; Srinivas et al., 2018). Unfortunately, the groundwater monitoring boreholes available at the study area were not adequate for the application of borehole televiewer, and no core is available from these wells for further fracture network characterization. Nevertheless, although the limitations encountered, the methodology applied in this study is a key step, providing for the first time a first-order characterization of the fracture network in Kuujjuaq. Furthermore, several working hypotheses were considered to deal with uncertainties on the fracture intensity, size and fractal dimension. These networks generated are being applied to design a hydraulically stimulated geothermal reservoir in the community of Kuujjuaq, Canada, using a shear-dilation-based model (FRACSIM3D) developed by Jing et al. (2000) and updated in 2015 for new joint constitutive laws.

Topological analysis can additionally be carried out to characterize the connectivity of fracture networks (e.g., Manzocchi, 2002; Andresen et al., 2013; Sanderson et al., 2015; Saevik et al., 2017). This involves the transformation of the fracture outcrop network into an equivalent network representation made of lines, nodes and branches, following the mathematical concept of graph theory (Andresen et al., 2013; Sanderson et al., 2015; Morley et al., 2016; Sanderson et al., 2019b). A first-order characterization of the fracture network connectivity was carried out in Kuujjuaq (Miranda et al. 2018b) and these preliminary results reveal that fractures terminating against each other (Y-nodes; Sanderson et al., 2015) are dominant. Furthermore, the system studied by Miranda et al. (2018b) suggests a potential hydraulic connectivity of 46%. Miranda et al. (2018b) study, however, was carried out for a small sampling area. LiDAR and other remote sensing techniques can provide further opportunities to enlarge the analyzed area and obtain more accurate description of the potential network connectivity. Moreover, Nyberg et al. (2018) developed an ArcGIS toolbox that can help on the topological analysis of large and complex datasets. Topological analysis can also be helpful to estimate the effective permeability of the fracture network as illustrated on the approaches proposed by Saevik et al. (2017) and Lahiri (2021). The results of the latter indicate that effective permeability of the fracture network increases rapidly with increase in length of the branch segments, suggesting that these play a critical role within the reservoir.

5.6.2 A priori stress model and state of stress

An a priori stress model for the study area is proposed in this study using geological indicators to estimate the orientation of the principal stresses and empirical correlations and analytical models to evaluate the principal stresses. Monte Carlo method was used to deal with the ensemble of uncertainties within the models to infer the stresses. The estimates were calibrated with published data for the Canadian Shield. This model is the first step towards a final rock stress model (Stephansson et al., 2012) and a key input parameter for the simulations of hydraulically stimulated geothermal reservoirs in the absence of new stress measurements. Although the latter are fundamental, these require deep exploratory wells, at least deeper than 300 m, for an accurate evaluation of the in-situ stress field. In remote areas, such deep boreholes are often unavailable in close proximity with the communities. In Kuujjuaq, for example, the closer deep borehole located in Coulon camp lies at a distance of 420 km. Thus, the a priori stress model is of utmost importance to carry out a first-order assessment of engineered geothermal energy systems as viable technologies to harvest the deep geothermal energy source and help to supplant reliance on fossil fuels.

The models used in this work to approximate the a priori stress in Kuujjuaq have strengths and limitations, and without actual measurements to calibrate the results, it is difficult to indicate which one is more representative. Moreover, if the vertical stress is proven not to be a principal stress, then none of the theories stand since they were developed based on the assumption that both vertical and horizontal stresses are principal stresses. Nevertheless, even with all the existing uncertainty, they provide useful information for a first-order analysis of the state of stress in the study area. The relationship between vertical and horizontal stresses through the stress ratio coefficient assuming the empirical equations developed based on measurements undertaken in the Canadian Shield may perhaps provide a closer approximation to the present-day stresses. However, the stress measurements in the Canadian Shield were carried to a maximum depth of 2 km, and therefore extrapolation of the empirical coefficients to greater depths entails additional errors. Perhaps the application of McCutchen (1982) and Sheorey (1994) models can help to avoid such errors. However, each parameter within these models is also bounded by uncertainty and they only provide an estimation of the horizontal average stress magnitude implying that the relation between maximum and minimum horizontal stresses must be known. The frictional equilibrium theory was used in this study with the purpose to assess if the inferred stress values were within the stable domain and if the inferred stress state was near critical conditions. Moreover, this theory was used to infer the theoretical boundaries for the maximum or minimum principal stresses. Although a useful model, the application of the frictional equilibrium theory entails further uncertainties since one of the principal stresses and in situ fluid pressure must be known based on field measurements. Other commonly applied models to infer the in-situ stress are described in Taghipour et al. (2019) and Han et al. (2020), however these models were not currently applied. Further work can be envisioned to compare the results from these models with the ones obtained in this work. Furthermore, Sheorey (1994) model has been modified by Pei et al. (2016) to account for correction factors for the local tectonism and this modification to the original model was not considered in the present work. Moreover, the effects of anisotropy, stratification, geological structures and heterogeneities, topography, erosion, overconsolidation, uplift and glaciation were not taken into account in this work. Nevertheless, Amadei et al. (1997) presents a detail discussion on how these factors influence the in-situ stress field and on how to correct them. Further work can be envisioned to improve the current a priori stress model. Moreover, further gather of information focused on stress measurements can provide more accurate estimates of the principal stresses and help to calibrate the a priori stress model to develop the integrated stress model (e.g., Stephansson et al., 2012; Kruszewski et al., 2021).

A simplified theoretical rheological profile is presented for the study area to illustrate the stress-depth distribution as a function of the different geothermal gradient and heat flux scenarios inferred by Miranda et al. (2020b) and Miranda et al. (2021). This theoretical profile also provides information on the differential stress and fluid pressure to trigger slippage of optimally oriented fractures. The rheological profile highlights the variation of lithosphere strength according to the subsurface temperature. For a colder lithosphere, the crust is 86% stronger than for a hotter lithosphere. Moreover, the base-case thermo-mechanical scenario reveals a crustal strength 58% greater than for the best-case scenario. These observations suggest that hydraulic stimulation treatment may be less effective in both worst- and base-case thermo-mechanical scenarios than in the best-case scenario. Moreover, the low inferred differential stress for all the stress scenarios supports the challenges of developing engineered geothermal energy systems in the study area compared to locations with larger differential stress. Larger differential stress requires less fluid pressure to activate shear slip of natural fractures as illustrated by Xie et al. (2015). Further fundamental research focused on the stress amplification process over time and dependent on applied stresses (e.g., Kusznir et al., 1982; Kusznir et al., 1984a; Kusznir et al., 1984b) shall be envisioned for a detailed characterization of the thermo-mechanical conditions beneath Kuujjuaq and Nunavik in general. Such studies may also provide further insight on the build-up stress and material relaxation rate due to creep, key factors for earthquake occurrence (e.g., Davis, 2017). Furthermore, regional and temporal analysis of the seismic events may provide further information on the lithosphere rheology (e.g., Chen et al., 1983; Ranalli et al., 2005). Studies of the thermo-mechanical conditions beneath other northern villages can help to assess locations more favorable for an effective hydraulic stimulation treatment and, thus, development of engineered geothermal energy systems.

A first-order analysis of the state of stress of the fracture planes suggests that these are not at critical state. The inferred friction coefficient of these structures is lower than 0.6, with the maximum stress scenario revealing lower friction coefficients than the minimum stress scenario. Such observation suggest that the former will increase the challenges of an effective hydraulic stimulation treatment than the latter. Moreover, the Mohr-Coulomb friction and slip tendency analysis revealed that the effective principal stresses must be decreased by more than 50% to reactivate the N-S, E-W and NNW-SSE fracture sets. The minimum critical fluid pressure to reactivate optimally oriented fractures was evaluated and was found to be dependent of the static friction coefficient and stick time assumed. Longer stick times tends to lead to an increase in the shear strength of the fractures (e.g., Mitchell et al., 2013). The logarithmic rate of increase in shear strength with time can be inferred by multiplying the normal stress to the coefficient of friction and the percent increase in coefficient of friction per decade (e.g., Mitchell et al., 2013). Moreover, temperature also plays a role in the static friction coefficient. Laboratory experiments undertaken by Mitchell et al. (2013) suggest that static friction increases linearly with increasing temperature at about 0.02 per 140 ºC. However, these authors also observed that temperature does not significantly change the rate at which static friction increases with time. Moreover, these authors suggested that neglecting the effect of temperature may underestimate fracture strength under dry conditions and that restrengthening rates are weakly temperature dependent under dry conditions. Temperature was not considered in the slip tendency analysis carried out in this work, but further studies can be envisioned to investigate the effect of temperature on the reactivation of the fracture planes. In fact, if the temperature effect on static friction is considered, the best-case thermo-mechanical scenario may lead to fracture planes with higher shear strength compared with the worst- and base-case scenarios.

The in-situ fluid pressure regime also plays a key role in the state of stress of the fractures. The pore-fluid factor tends to increase with increasing cohesive strength of fractures, increasing coefficient of internal friction and increasing fracture angle (e.g., Streit et al., 2001). Although most deep drilling projects in stable crystalline rock medium support in situ fluid pressure within the hydrostatic regime (e.g., Emmermann et al., 1997; Townend et al., 2000), the relative stationarity of the fault planes in Kuujjuaq leads to an increase in their shear strength, as aforementioned, and can lead to an increase of the in-situ fluid pressure. In fact, seismicity in misoriented fault planes has been associated with near-lithostatic fluid pressure conditions (Streit et al., 2001). However, the absence of seismic events recorded in the fault planes crossing Kuujjuaq is a missing evidence to support this theory. Nevertheless, further field investigations are needed for an accurate characterization of the in-situ fluid pressure regime.

Furthermore, the present study does not consider the hydromechanical properties of the geological materials. Aperture, hydraulic conductivity, roughness, dilation, stiffness, among others, play key roles on constraining slippage and reservoir connectivity (e.g., Evans et al., 1999; Ghassemi, 2012). The importance of these parameters on the design of a hydraulically stimulated geothermal reservoir in Kuujjuaq is underway using working hypotheses to overcome the absence of laboratory experimental data and quantify the uncertainty to consider for numerical modeling of reservoir development and circulation.

5.6.3 Practical implications for the design of engineered geothermal energy systems

A hydraulically stimulated geothermal reservoir tends to grow in the direction of the least energy configuration. Therefore, based on the inferred directions for the principal stresses, a reservoir developed in Kuujjuaq will have its major axis parallel to N210ºE-N220ºE while the minor axis will be parallel to N300ºE -N310ºE. Moreover, the performance of the system may be improved if the open hole section of the wells is drilled with its azimuth parallel to the minimum horizontal principal stress (in this case N300ºE-N310ºE). If the azimuths of the open hole section of the wells are drilled at right angles to the minimum horizontal principal stress, this may lead to the interception of few conductive fracture sets. In Kuujjuaq, based on the field data gathered in this work, the fracture sets N-S and E-W are the most optimal oriented to slip followed by the set NNW-SSE. These drilling recommendations are based on the field tests carried out in Rosemanowes (e.g., Pine et al., 1984; Richards et al., 1994). The wrong drilling orientation had severe consequences for this geothermal project.

The direction of shear growth due to hydraulic stimulation of non-horizontal joints within the reservoir can be assessed by the increments of pressure in excess of hydrostatic pressure required to cause shearing above and below the injection point (Pine et al., 1984). Pine et al. (1984) explained how to infer shear growth direction that, although not carry out in this work, can be followed in future studies.

Moreover, the Mohr-Coulomb friction and slip tendency analyzes suggest that a thrust faulting regime with near-vertical fractures and high stress magnitude (i.e., the maximum stress scenario) may increase the challenge of developing an engineered geothermal energy system in the community of Kuujjuaq. In fact, strike-slip regime and low stress magnitude seem to favor the development of such geothermal systems, requiring less fluid pressure to activate the natural fractures. The minimum critical pressure to reactivate the fractures in the study area was found to be about 30 MPa for the minimum stress scenario, 40 MPa for the mean stress scenario and more than 60 MPa for the maximum stress scenario. These values are higher than what is required in other areas with fracture and fault planes at critical state of stress (e.g., Rosemanowes and Soultz; Evans et al., 1999).

5.7 Conclusions

Remote, northern and rural communities in Canada and worldwide can highly benefit from off-grid renewable energy solutions to improve their sustainability and living standards and boost their economic growth. Geothermal energy sources harvested via engineered geothermal energy systems can be one of such viable options if current exploration challenges are overcome. Key parameters for the correct design of such geothermal systems are the fracture network and stress regime. Thus, in this work, a first-order characterization of the fracture network and stress regime was undertaken in an Arctic off-grid community (Kuujjuaq, Canada) to provide guidelines and an example for the remaining settlements located in a similar geological context.

The fracture network was characterized by sampling the geometric properties of each fracture intersecting the scanline, and statistical analyzes were undertaken to assess the main fracture sets, their intensity, spacing and length distribution. The von Mises distribution revealed four main fracture sets striking approximately N81°E-N90ºE (E-W – F1), N161°E-N170ºE (NNW-SSE – F2), N11°E-N20ºE (N-S – F3) and N121°E-N130ºE (NW-SE – F4). The intensity of the fractures was found to range between a minimum of 0.3 fracture m^{-1} and a maximum of 3.7 fractures m^{-1}, with a median value of 0.8 fracture m^{-1}. The coefficient of variation calculated for each set revealed values of 0.4 for N-S and NW-SE sets and 0.7 for E-W and NNW-SSE. The heterogeneity of the distribution evaluated using the Kuiper's method reveal a value of 15%. The length and fractal dimension were inferred to vary in the range 2 – 28 m and 1.7 – 2.4, respectively. This statistical data was used to generate stochastic fracture networks considering the intensity, size and fractal dimension uncertainties.

Additionally, an a priori stress model is proposed for Kuujjuaq in this study by combining geological indicators, literature data, empirical correlations and analytical modeling. Monte Carlo simulations were also carried out to deal with the uncertainties of each input parameter. The geological indicators suggest the maximum and minimum horizontal principal stresses oriented N210ºE-N220ºE and N300ºE-N310ºE, respectively. The plunge is assumed horizontal. The three principal stresses (vertical and horizontal) can be described by the following relationships:

- $\sigma_{\mathrm{V}} = 0.0271z$
- $\sigma_{\mathrm{H}} = 0.0430z + 8.62$
- $\sigma_{\mathrm{h}} = 0.0251z + 4.94$

The a priori stress model suggests thrusting as the dominant faulting regime to depths up to 2 km while strike-slip faulting system may prevail at depths higher than 2 km. This trend is observed for the minimum and mean stress magnitude scenarios. The maximum magnitude scenario indicates thrusting faulting regime only.

Moreover, Mohr-Coulomb friction and slip tendency analyzes reveal that, although most of the fracture planes are optimally oriented to slip, these are not at critical state of stress. The effective principal stresses need to be decreased by more than 50% to reactivate these planes. Furthermore, the analyzes indicate that the fracture sets E-W, NNW-SSE and N-S have the highest tendency to slip, while the NW-SE will not be reactivated.

In conclusion, the results obtained in this work in terms of fracture characterization, stress estimates, rheology and Mohr-Coulomb friction and slip tendency analysis suggest that the thermo-mechanical conditions of the study area, given the current level of knowledge, do not seem to be favorable for the development of engineered geothermal energy systems. Nevertheless, high uncertainty exists, and further studies and field tests can provide a more accurate evaluation.

6 TECHNO-ECONOMIC ANALYSIS OF ENGINEERED GEOTHERMAL ENERGY SYSTEMS FOR DIRECT-USE APPLICATIONS IN ARCTIC OFF-GRID COMMUNITIES: PARAMETER UNCERTAINTY AND SENSITIVITY STUDIES

Analyse technico-économique des systèmes géothermiques ouvragés pour des applications à usage direct dans les communautés hors réseau de l'Arctique : incertitude des paramètres et études de sensibilité

Authors:

Mafalda M. Miranda (M.M.M.)

Institut national de la recherche scientifique, Canada

Jonathan Willis-Richards (J.W.-R.)

Fracture and Reliability Research Institute, Tohoku University, Japan

Jasmin Raymond (J.R.)

Institut national de la recherche scientifique, Canada

Chrystel Dezayes (C.D.)

Bureau de recherches géologiques et minières, France

Journal title:

Natural Resources Research

To submit

Author's contribution:

Conceptualization, M.M.M., J.W.-R., J.R. and C.D.; methodology, M.M.M. and J.W.-R.; validation, M.M.M.; formal analysis, M.M.M.; investigation, M.M.M.; resources, M.M.M., J.W.-R., J.R. and C.D.; data curation, M.M.M.; writing – original draft preparation, M.M.M., J.W.-R., J.R. and C.D.; writing – review and editing, M.M.M., J.W.-R., J.R. and C.D.; visualization, M.M.M.;

software, J.W.-R.; supervision, J.R. and C.D.; project administration, J.R.; funding acquisition, J.R.

Link between the previous article and the next:

The previous chapters provide the background information in terms of thermophysical properties, subsurface temperature, fracture network and stress regime to carry out the thermo-hydro-mechanical modeling discussed in this chapter.

Graphical abstract:

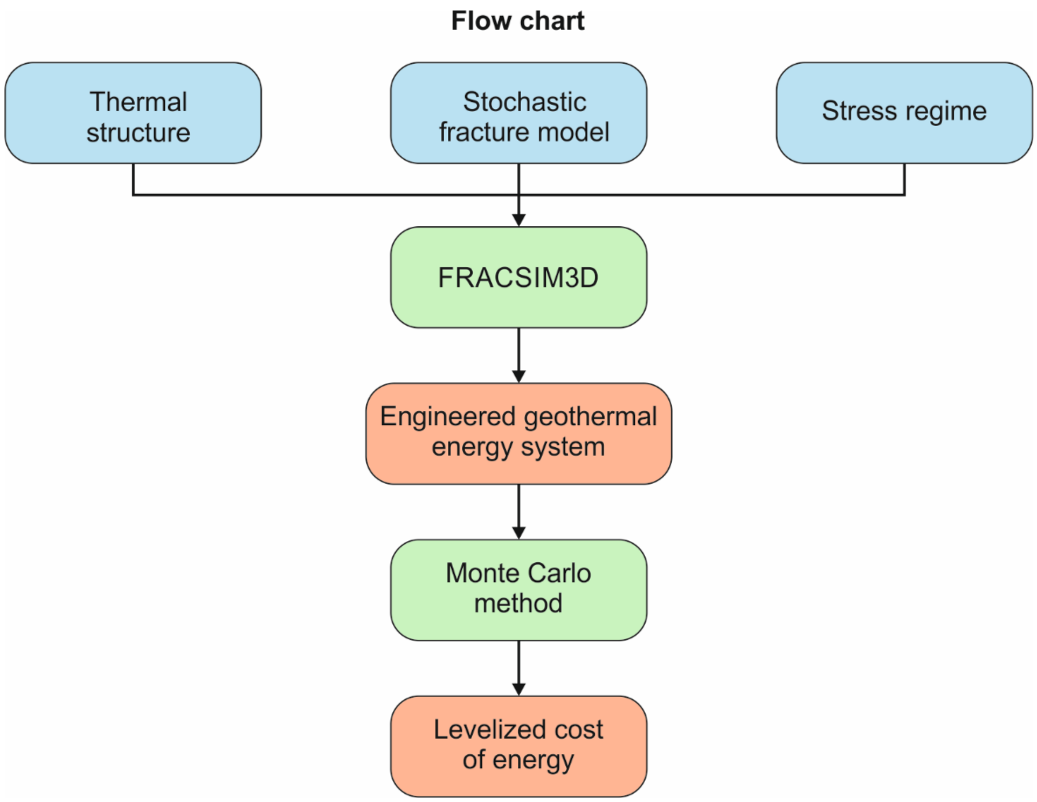

6.1 Introduction

The lack of clean energy supply for electricity, space heating, domestic hot water and cooking is still a reality, not only in the off-grid communities of Canada, but worldwide (UN, 2020). Fossil fuels have been the main sources of electricity, space heating and cooking fuels. However, the current concern on climate change, people's well-being and environment are changing this trend. Clean energy supply and sustainability are nowadays watchwords. The worldwide consumption of renewable energies has increased from 40 EJ in 1990 to 64 EJ in 2017 (UN, 2020). Although smaller than the consumption of non-renewables (304 EJ in 2017; UN, 2020), this is an important increase. Off-grid renewable energy solutions, including stand-alone systems and micro-grids, are a viable electrification solution (IRENA, 2019).

In Canada, for example, from the approximately 280 off-grid communities, 239 rely exclusively on diesel for electricity, space heating, and domestic hot water (CER, 2018). Within the diesel-based settlements without road access, the fuel must be imported during summer and stored for year-round use (Arriaga et al. 2017). Such energy situation entails significant costs, low energy security and a high probability of damaging an already vulnerable ecosystem. Therefore, assessing the potential of renewable sources to feed microgrids in remote communities has increased interest and several studies have been conducted (e.g., Khan et al., 2005; Ranjitkar et al., 2006; Thompson et al., 2009; Ibrahim et al., 2011; Guo et al., 2016; Stephen et al., 2016; Belzile et al., 2017; McFarlan, 2018; Kanzari, 2019; Yan et al., 2019; Gunawan et al., 2020; Mahbaz et al., 2020; Quitoras et al., 2020). Among these options, deep geothermal energy sources can play a key role to provide base-load power and heat to the off-grid settlements (e.g., Majorowicz et al., 2010a; Majorowicz et al., 2010b; Kunkel et al., 2012; Grasby et al., 2013; Walsh, 2013; Majorowicz et al., 2014b; Majorowicz et al., 2015a; Minnick et al., 2018; Majorowicz et al., 2020; Majorowicz et al., 2021). In fact, a first-order community-scale geothermal assessment undertaken in Kuujjuaq (Nunavik, Canada) suggested that the deep geothermal energy source is capable to fulfil the community's annual average heating demand of 37 GWh (Miranda et al., 2020b). This community is settled in the Canadian Shield, a physiographic region that has been considered a target for geothermal exploration through engineered/enhanced geothermal systems (Grasby et al., 2012; Minnick et al., 2018). The feasibility of such systems has been studied in the Western Canadian Sedimentary Basin and Arctic Lands (e.g., Majorowicz et al., 2010a; Majorowicz et al., 2010b; Hofmann et al., 2014; Hofmann et al., 2016; Minnick et al., 2018; Kazemi et al., 2019), but few studies have been conducted in the Canadian Shield (Majorowicz et al., 2015a; Minnick et al., 2018), where there are hundreds of off-grid communities heavily relying on fossil fuels (Grasby et al., 2013; Arriaga et al., 2017). Therefore, there is a need for a detailed prediction of deep engineered geothermal energy systems performance in this physiographic region. In this context, work has been carried out in the community of Kuujjuaq (Nunavik) using limited local surficial and regional data to provide first-order answers to the following key questions:

1. Will the hydraulic stimulation technique applied in crystalline basement rocks develop a well-connected flowing system in Kuujjuaq? How can this be done? What further local geological and thermo-hydro-mechanical data is required for more accurate predictions?
2. Are the deep geothermal energy sources harvested by engineered geothermal energy systems in Kuujjuaq cost-competitive compared to fossil fuels?

The answer to these questions is, however, bounded by high uncertainty due to the current poor knowledge of both geology and thermo-hydro-mechanical local data. Unfortunately, no hydraulic stimulation field experiments have been carried out to date in Kuujjuaq and neither was done in the scope of the present study. Thus, no history matching is available to calibrate the numerical simulations carried out in this work. Nevertheless, a "what-if" approach was used to provide a range of possibilities and help to design an engineered geothermal energy system for each of the uncertain scenarios that provides the thermal energy needed for the community, keeping the water losses lower than 20%, the reservoir flow impedance lower than 0.1 MPa L^{-1} s^{-1} and the thermal drawdown lower than 1 ºC/year. Thus, this study offers a first-order prediction of the performance of such systems as off-grid solutions to help in the energy transition of remote northern communities. Additionally, a preliminary evaluation of the levelized cost of energy was undertaken to forecast the economic potential of engineered geothermal energy systems in remote northern regions. Thus, this study may help trigger interest for further geothermal exploration, fundamental for an accurate evaluation of the deep geothermal energy potential beneath off-grid settlements.

6.2 Geographical and geological setting

The settlement of Kuujjuaq, located north of the 55º parallel, is the administrative capital of the Kativik Regional Government and the largest northern village in the Nunavik region of Quebec, Canada (Figure 6.1a; Statistics Canada, 2019). The 2016 census indicated 2 754 inhabitants (Statistics Canada, 2019). Diorite and paragneiss are the main lithologies, but smaller occurrences of tonalite, gabbro and granite are also observed (Figure 6.1b). A general description of these units is given in SIGÉOM (2019).

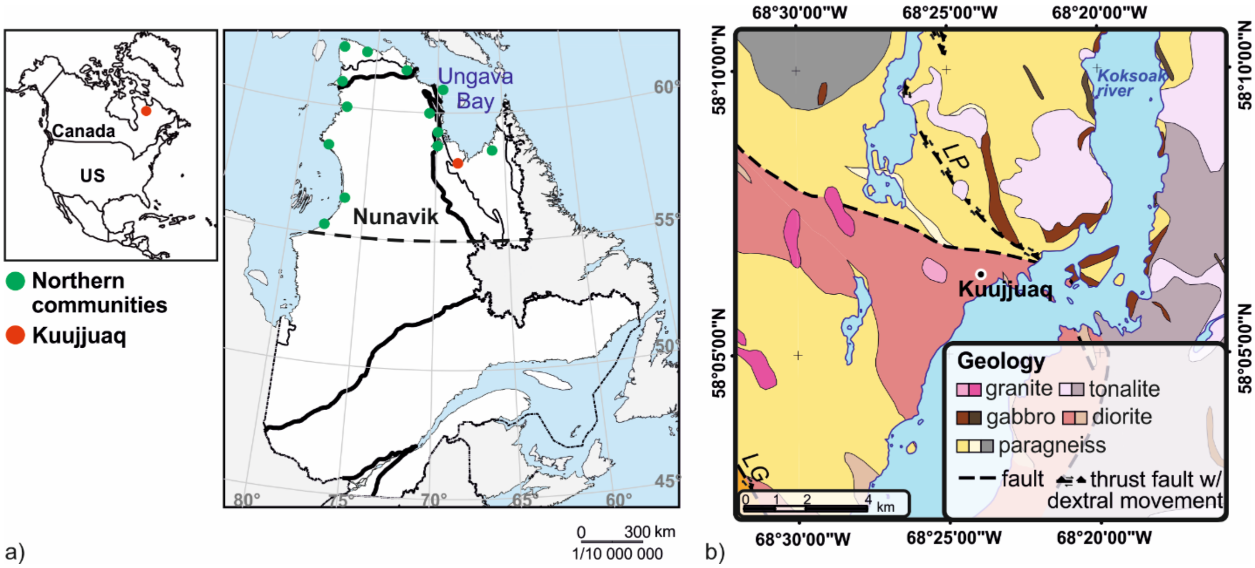

Figure 6.1 a) Geographical location of Kuujjuaq and remaining communities in Nunavik and b) geological setting of the study area. *LP* – Lac Pingiajjulik fault, *LG* – Lac Gabriel fault, adapted from SIGÉOM (2019) and Miranda et al. (2020a).

The lithologies outcropping in Kuujjuaq were sampled and a detailed description in terms of texture, fabric, main mineral phases and major and trace geochemical elements is given in Miranda et al. (2020a). Moreover, Miranda et al. (2020a) and Miranda et al. (2020b) present the results of thermal conductivity, volumetric heat capacity, radiogenic heat production, density, porosity and permeability evaluated for the samples collected. The thermal conductivity and volumetric heat capacity were analyzed considering the samples at dry and water saturation states and for temperatures ranging between 20 and 160 ºC (Miranda et al., 2020b). Furthermore, a temperature profile was measured in a groundwater monitoring well located nearby the community and the terrestrial heat flux evaluated following a 1D inverse heat conduction approach as explained in Miranda et al. (2021). The heat flux assessment considered several hypotheses for the ground surface temperature history and variable conditions for the thermophysical properties. The evaluated subsurface temperature distribution for a depth up to 10 km took into account these previous results and is presented in Miranda et al. (2020b). Miranda et al. (2018b) carried out a preliminary evaluation of the fracture network in terms of geometrical and topological properties that was further improved in chapter 5. Additionally, the latter presents an a priori stress model for Kuujjuaq calibrated with published stress data for the Canadian Shield and built upon geological indicators, empirical correlations, analytical models and Monte Carlo simulations to deal with the ensemble of uncertainties (Figure 6.2). The analyzes of the fracture planes carried out in chapter 5 revealed four main fracture sets but only three of these are optimally oriented to slip. These are: E-W, NNW-SSE and N-S. All these previous results constitute the basis for the numerical simulations carried out in the present study.

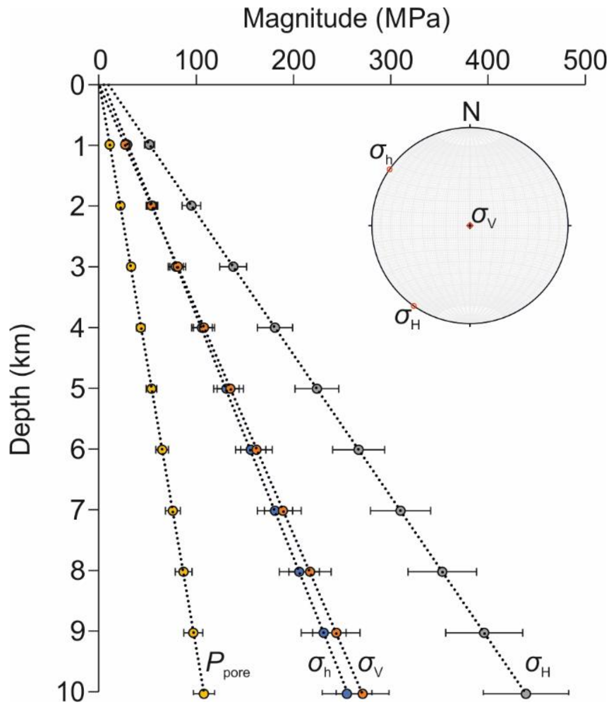

Figure 6.2 **Magnitude and orientation of the principal stresses. The error bar represents the range of values inferred. σ_H – maximum horizontal principal stress, σ_h – minimum horizontal principal stress, σ_V – vertical principal stress, P_{pore} – in situ fluid pressure.**

6.3 **Heating demand**

The community of Kuujjuaq experiences an annual average temperature of about -5.4 ºC and an annual average of 8 520 heating degree days below 18 ºC (Figure 6.3; Gunawan et al., 2020). Although the residential dwellings are built to meet certain regulatory standards of insulation, the harsh climate results in high building heating requirements (Figure 6.3; Gunawan et al., 2020). The annual average fuel consumption of a typical residential dwelling in Kuujjuaq has been estimated about 3 100 to 8 180 liters (Yan et al., 2019; Gunawan et al., 2020). This represents around 28 to 32 L m^{-2}, with respect to the floor area. There are currently about 973 residential dwellings in Kuujjuaq occupied by residents (Statistics Canada, 2019), indicating a total yearly consumption of 3 to 8 million L of oil for space heating. The peak heating load for a residential dwelling is 7 kW (Yan et al., 2019), depending on the building heating load and floor area, indicating a peak load for the community of approximately 7 MW. The annual heating energy demand has been estimated between 21.6 and 71.3 MWh per dwelling, depending on the floor area (Yan et al., 2019; Gunawan et al., 2020). Thus, the community's heating demand is approximately 21 to 69 GWh per year.

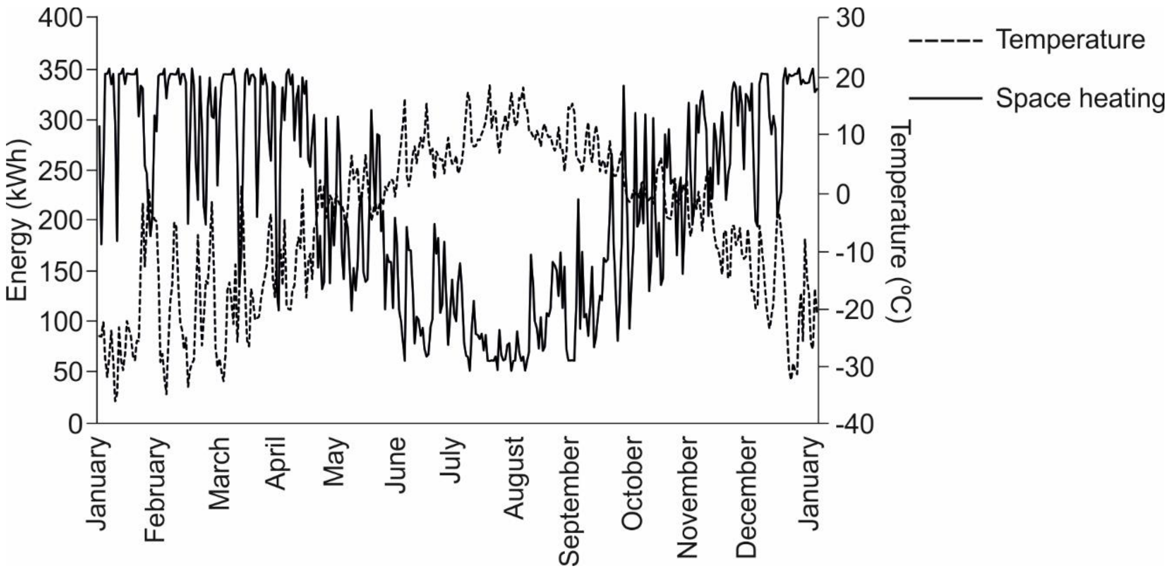

Figure 6.3 Average daily temperature and heating load profile of a typical residential dwelling in Kuujjuaq, redrawn from Gunawan et al. (2020).

The population in Kuujjuaq grew 16% between the years of 2011 and 2016 (Statistics Canada, 2019), representing an annual growth of about 3%. Translating this population increase into heating energy needs, and carrying out projections, suggests that in 30 years the community's heating demand may be 57 to 188 GWh. These values represent the threshold that the geothermal system designed in this study needs to meet during the 30 years of operation.

6.4 Methods

6.4.1 Numerical simulator

The numerical simulator used in this study is the updated version of Jing et al. (2000) FRACSIM3D for new joint constitutive laws. A shear displacement-dilation relationship, in which the shear dilation angle is a function of displacement rather than constant, was formulated and implemented. The most significant aspect of this new sliding/opening law is that the rate of opening with displacement can be made to reduce in line with many experimental papers and geological observations, for example, the work of Lee et al. (2002). FRACSIM3D, however, cannot yet mimic asperity damage from shearing at significant effective normal stress.

Slip occurs when the ratio of the shear stress to the normal stress becomes large enough. This ratio is expressed as the tangent of the total friction angle, which is a property of both rock material and geometry of the fracture surface, and it can be derived from tilted block experiments. The total friction angle is a function of the normal stress and varies with accumulate fracture surface damage from past slip movement. This angle is the sum of the basic friction angle and the shear dilation angle, which is the arctangent of the ratio of the amount of fracture opening per small increment of displacement. The shear dilation angle can be derived from the roughness of the natural fracture surface, and mathematical forms of dilation with slip may be derived for various representations of surface roughness and correlation from one side of the fracture to the other. The fracture opening responds to increased normal stress by closure and the rate of this response is called compliance. Theoretical forms for the closure curve can be derived for specific models of joint roughness and material properties (e.g., Goodman, 1976; Bandis et al., 1983).

The Jing et al. (2000) version of FRACSIM3D aims to capture shear dilation and normal compliance in a single equation as:

$$w = \frac{w_0 + U\,tan(\phi_{\mathrm{dilation}})}{1 + 9\left(\frac{\sigma'_{\mathrm{n}}}{\sigma_{\mathrm{n\_ref}}}\right)} \tag{6.1}$$

where w (m) is the aperture of the compliant fracture and w_0 (m) is the initial aperture before induced slip, U (m) is the amount of slip (or shear displacement), σ'_{n} (Pa) is the effective normal stress, $\sigma_{\mathrm{n\_ref}}$ (Pa) is the reference stress for 90% closure (i.e., closure resistance of the fracture) and ϕ_{dilation} (º) is the shear dilation angle at low normal stress.

The shear dilation angle in Jing et al. (2000) version is assumed constant, meaning that a fracture tends to open up at a constant rate as displacement increases. Although a reasonable approximation, rock mechanics experiments (e.g., Lee et al., 2002) have suggested that the shear dilation angle increases over the first few mm of displacement as asperities of increasing wavelengths become interlocked, reaching a maximum as the asperities climb over each other. Then, the shear dilation angle decreases to lower values after 10s of mm of displacement since the longer wavelength asperities have less relative amplitude than ones with the shorter wavelength. The constant shear dilation angle was substituted by one that is a function of displacement to consider these observations. The relationship is as follows:

- A linear increase from a starting shear dilation angle value to a maximum value over a certain shear displacement distance
- An exponential decay with displacement thereafter to a low constant value at greater displacement at a user specified rate

Furthermore, this new shear displacement-dilation relationship contains elements of "slip weakening" and can be used to calculate which fractures are predicted to slip unstably. Microseismic events in FRACSIM3D are not caused by rapid changes in shear dilation angle with displacement but rather caused by the sudden failure of macroscopic asperities or jogs. These asperities or jogs might be related to fracture intersections, where movement on one fracture interrupts the continuity of another. The amount of shear stress needed to break these asperities is likely to be related to the asperity geometry, the number and extent of such asperities present, the rock strength at the appropriate scale, and the normal stress. Thus, an asperity strength factor was introduced into the code to give the fracture planes extra resistance to slip. The asperity factor is converted to the required rupturing shear stress as:

$$\tau = F_{\text{asperity}} \sigma'_{\mathrm{n}} \, tan(\phi_{\text{basic}}) \tag{6.2}$$

where τ (Pa) is the shear stress, F_{asperity} is the asperity strength factor and ϕ_{basic} (º) is the basic friction angle.

A brief iterative solution provides the fluid pressure in the fracture required to cause asperity rupture via reduction in asperity strength through reduction in effective normal stress. The value of the asperity strength factor is further varied about the mean to create a population of fracture asperity strengths. The introduction of this factor is now allowing the generation of microseismic events of appropriate magnitude and in appropriate number. Asperity strength factor of 0.4 and higher will give rise to large microseismic events, while a value of zero will suppress the seismic events.

The fracture network generated is embedded within a 3D discretization grid, in which the quantity of fluid flow from block to block is controlled by Darcy's law with the transmissivity contribution from each fracture governed by the sum of products of the cubes of the fracture apertures and the fracture intersection length with the block face (Jing et al., 2000):

$$Q_{\mathrm{j}} = \sum_{\mathrm{i}} \frac{w_{\mathrm{i}}^3 l_{\mathrm{i}}}{12\omega} \nabla P, j = x, y, z \tag{6.3}$$

where Q_{j} (m^3 s^{-1}) is the flow rate, l_{i} (m) is the fracture intersection length with the block face, ω (kg m^{-1} s^{-1}) is the fluid dynamic viscosity and ∇P (Pa m^{-1}) is the pressure difference.

In other words, the flow pattern for the discrete fracture network is solved by converting it to an equivalent continuum mesh and the steady state flow through fractures is expressed using the cubic law (i.e., Reynold's equation which is the solution of the Navier-Stokes equation for laminar flow between smooth parallel plates). A ratio of theoretical aperture over laboratory aperture was implemented to compensate the flow overestimation given by the parallel plate assumption and to consider the joint roughness coefficient. Experiments (e.g., Barton et al., 1997; Keller, 1997; Keller, 1998) have suggested that the mechanical aperture of rough fractures overestimates the flow capacity to some extent. A user definable input variable has been implemented to allow for this if desired.

Heat extraction is calculated by finite differences under the assumption that thermal equilibrium is reached instantaneously between each solid element and the water passing through it. Moreover, heat transfer is constrained within the stimulated volume and no heat transfer occurs at the boundaries of the total model volume. Heat is transferred by conduction and advection (Fomin et al., 2004):

$$\rho c \frac{\partial T}{\partial t} = \nabla(\lambda \nabla T) - \rho c_{\text{fluid}} u \nabla T \tag{6.4}$$

where ρc (J m^{-3} K^{-1}) is volumetric heat capacity, T (ºC) is temperature, t (s) is time, λ (W m^{-1} K^{-1}) is thermal conductivity and u (m s^{-1}) is Darcy velocity.

The thermal energy extracted by the circulating fluid is given by:

$$e_{th} = \rho c_{\text{fluid}} Q_{\text{recovered}} \left(T_{\text{reservoir}} - T_{\text{injection}}\right) \tag{6.5}$$

where e_{th} (J) is the thermal energy.

The temperature in the reservoir varies over time as it is cooled down. The thermal drawdown follows the energy conservation equation:

$$\frac{\partial T_{\text{reservoir}}}{\partial t} V_{\text{reservoir}} \rho c_{\text{reservoir}} = -(T_{\text{reservoir}} - T_{\text{water}}) Q \rho c_{\text{water}} + q_0 A'_{\text{reservoir}} \tag{6.6}$$

where $V_{\text{reservoir}}$ (m^3) is the reservoir volume, q_0 (mW m^{-2}) is the heat flux and $A'_{\text{reservoir}}$ (m^2) is the reservoir area.

Further details on the joint constitutive laws, stimulation and steady state flow solutions, water loss approximation and heat extraction are given in Jing et al. (2000).

6.4.2 Model geometry

A cubic model volume of 4 km^3 discretized into a grid of 200 per 200 per 200 cells is used to carry out the numerical simulations. This grid was selected after carrying out a grid dependency study and the results revealed an influence of, on average, 5%. Slippage takes place in the fractures whose centers fall within the current estimate of the stimulated volume. Although this volume is fixed and defined by the user, the shape of the reservoir is adjusted progressively as the estimate of the stimulated permeability tensor is refined. The major axis of the stimulated area is oriented according to the inferred direction of the maximum horizontal principal stress. The boundaries of the model are assumed closed to regional fluid flow and were kept at a constant temperature. At time zero, the model is assumed filled with the in-situ fluid and the pressure distribution is assumed hydrostatic. The initial in situ permeability and state of stress are defined by the user. The far-field, beyond the model boundaries, is assumed at hydrostatic pressure during the stimulation and circulation calculations. Moreover, the in-situ permeability, beyond the stimulated volume, is assumed undisturbed. The pressure within the stimulated volume is higher near the wells, dropping towards the edge of this volume, similarly to a shock wave behavior (e.g., Murphy et al., 1985).

The engineered geothermal energy system was designed as a doublet, with one injector and one producer, with vertical wells. Two configurations for the wells were studied to identify the best location taking into consideration the presence of the Lac Pingiajjulik fault (Figure 6.4). Different possibilities for well spacing and open hole length were considered. The well bore radius was defined as 0.11 m following the example of Soultz engineered geothermal energy system (e.g., Genter et al. 2010). The stimulation volume was considered variable. One stimulation was applied in each well and different stimulation and circulation pressures were studied. The operation time was defined for 30 years.

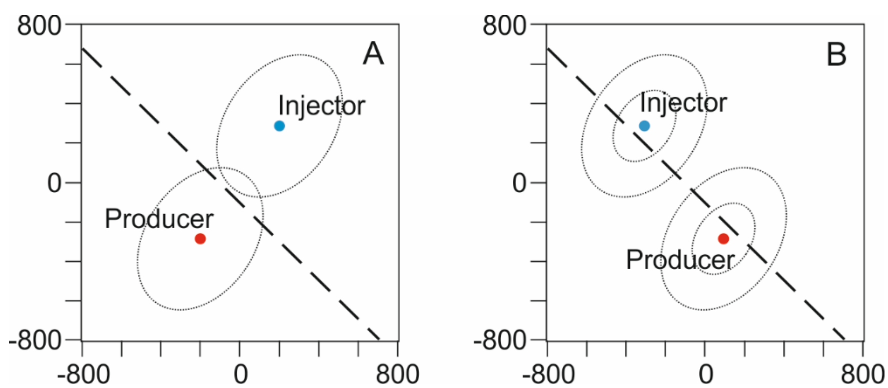

Figure 6.4 **Top view slice cutting the center of the model and illustrating the different wells configuration studied. Dots – vertical wells, dashed line – Lac Pingiajjulik fault trace, ellipsoids – stimulation volume tried (larger ellipsoid, V = 0.4 km^3; smaller ellipsoid, V = 0.2 km^3).**

Three working hypotheses for the fracture network were generated and studied due to the current existing uncertainties as explained in chapter 5. These are:

1. Fracture intensity of 0.8 fractures m^{-1}, fracture length and fractal dimension as sampled in the field (Figure 6.5a)

2. Fracture intensity of 0.8 fractures m^{-1}, fracture length increased by a factor of 10 and fractal dimension as sampled in the field (Figure 6.5b)
3. Fracture intensity of 0.8 fractures m^{-1}, fracture length as sampled in the field and fractal dimension decreased by a factor of 2 (Figure 6.5c)

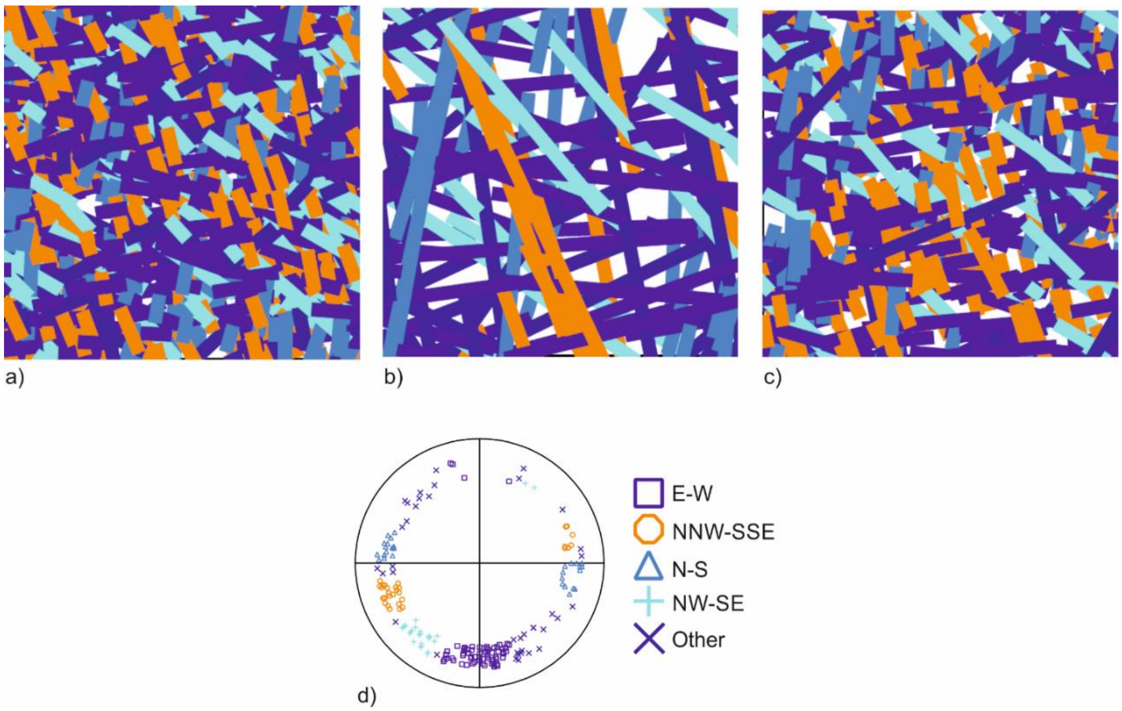

Figure 6.5 Top view of a 80 per 80 m section of the total generated fracture network model. a) base-case fracture network, b) fracture network with fracture lengths increased by a factor of 10, c) fracture network with fractal dimension decreased by a factor of 2 and d) Wulff projection stereo plot of field fracture data.

The influence of the Lac Pingiajjulik fault was assessed by adding the fault plane to the model in a deterministic manner. The fracture was assumed to cut approximately through the middle of the model (Figure 6.4). This structure is described as a thrust fault with late dextral movement (e.g., Simard et al., 2013). Thus, its dip was assumed 45º NE and its dip azimuth N45ºE but its exact orientation at depth in unknown. The radius of this fault was assumed longer than 5 km and the initial fault offset at in situ effective stress was considered variable between 0.001 and 0.10 m.

6.4.3 Properties of the medium

The engineered geothermal energy system was designed for a depth of 4 km since previous analyzes suggest 98% of probability of the deep geothermal energy source in place to meet the community's heating needs (Miranda et al., 2020b). Preliminary simulations were carried out using the three-point estimation technique to define the worst-, base- and best-case scenarios in terms of properties of the medium (Table 6.1).

Table 6.1 Sensitivity analysis for the properties of the medium

Parameter	Symbol	Unit	Worst-case scenario	Base-case scenario	Best-case scenario
Maximum horizontal principal stress	σ_H	MPa	213	181	152
Minimum horizontal principal stress	σ_h	MPa	138	106	84
Vertical principal stress	σ_V	MPa	121	108	97
In situ fluid pressure	P_{pore}	MPa	49	43	39
Reservoir temperature	T_{res}	ºC	33	88	167
Permeability	κ	m^2	10^{-18}	10^{-17}	10^{-16}
Geological materials					
Thermal conductivity	λ_{rock}	$W\ m^{-1}\ K^{-1}$	2.4	2.0	1.5
Volumetric heat capacity	ρc_{rock}	$MJ\ m^{-3}\ K^{-1}$	2.1	2.4	2.7
Young's modulus	E	GPa	100	71.5	43
Poisson's ratio	v	---	0.16	0.23	0.30
Asperity strength factor	$F_{asperity}$	---	0.6	0.5	0.4
Basic friction angle	ϕ_{basic}	º	26	24.5	23
Initial shear dilation angle	$\phi_{dilation,\ 0}$	º	0	2.5	5
Peak shear dilation angle	$\phi_{dilation,\ peak}$	º	5.0	10	20
Ultimate shear dilation angle	$\phi_{dilation,\ ultimate}$	º	2.5	5.0	10
Peak shear displacement	U_{peak}	mm	2.5	5.0	10
Residual shear displacement	$U_{residual}$	mm	1.25	2.5	5
Reference stress for 90% closure	$\sigma_{n,\ ref}$	MPa	40	50	60
In situ fluid					
Density	ρ_{fluid}	$kg\ m^{-3}$	1012	1080	1112
Dynamic viscosity	ω	$kg\ m^{-1}\ s^{-1}$	7.48×-4	3.19×-4	1.62×-4
Circulation fluid					
Re-injection temperature	T_{inj}	ºC	30	30	50
Density	ρ_{fluid}	$kg\ m^{-3}$	993	993	985
Specific heat	c_{fluid}	$J\ kg^{-1}\ K^{-1}$	4180	4180	4180

The magnitude of the principal stresses and in situ fluid pressure were inferred in chapter 5 (Figure 5.2) using empirical correlations, analytical modeling and Monte Carlo simulations calibrated with published literature data for the Canadian Shield. The subsurface temperature distribution was inferred in Miranda et al. (2020b). Hypotheses for the in-situ permeability are based on the results obtained at Rosemanowes and Soultz stimulated geothermal projects (Lanyon et al., 1993; Evans et al., 2005). The thermal conductivity as a function of temperature and pressure and the volumetric heat capacity for water-saturation samples have been inferred by Miranda et al. (2020b). The Young's modulus and Poisson's ratio were defined based on the findings of Arjang et al. (1997) for the Canadian Shield. Asperity strength factor, initial, peak and ultimate shear dilation angle, peak and residual shear displacement and reference stress for 90% closure are working hypotheses to evaluate their influence on the performance of the hydraulically stimulated geothermal reservoir. The basic friction angle was defined according to literature tilt experiments carried out in wet crystalline rock masses (e.g., Alejano et al., 2012).

The density of both in situ and circulation fluids was calculated as (Achtziger-Zupancic et al., 2017 and references therein):

$$\rho_{\text{fluid}}(P,T) = \rho_{\text{fluid}}(T) + \Delta\rho_{\text{fluid}}(P) + 1000 \times TDS \tag{6.7}$$

where *TDS* (kg L^{-1}) is the total dissolved solids and *P* (Pa) stands for pressure.

The effect of temperature and pressure are given by (Achtziger-Zupancic et al., 2017 and references therein):

$$\rho_{\text{fluid}}(T) = \frac{999.84+16.95T+(-7.99\times10^{-3})T^2+(-4.62\times10^{-5})T^3+(1.06\times10^{-7})T^4+(-2.81\times10^{-10})T^5}{1+0.017T} \tag{6.8a}$$

$$\Delta\rho_{\text{fluid}}(P) = (4.0625 \times 10^{-7})P \tag{6.8b}$$

The in-situ fluid was assumed brine with 100 g L^{-1} of total dissolved solids (Bottomley, 1996) and in thermal equilibrium with the geological medium. The dynamic viscosity of the in-situ fluid was approximated as (Achtziger-Zupancic et al., 2017):

$$\omega(T) = (2.414 \times 10^{-5}) \times 10^{\frac{247.8}{T-140}} \tag{6.9}$$

where *T* (K) is the absolute temperature.

Preliminary calculations were carried out to assess a baseline flow rate that the simulations need to meet. This was done as:

$$Q = \frac{e}{\rho c_{\text{fluid}}(T_{\text{reservoir}} - T_{\text{injection}})} \tag{6.10}$$

where *e* (W) is the maximum heating energy demand

The results reveal that, for the best-case scenario, flow rates in the range 14 to 45 L s^{-1} are required. For the base-case scenario, the flow rate range necessary is 27 to 89 L s^{-1}, while for the worst-case scenario is above 200 L s^{-1}. The flow rates estimated for the best- and base-case scenarios have already been achieved in engineered geothermal energy systems (e.g., Soultz and Rittershoffen; Mouchot et al., 2018)

6.4.4 Levelized cost of energy

A first-order evaluation of the levelized cost of energy to build and operate an engineered geothermal energy system in Kuujjuaq at a depth of 4 km was carried out as (e.g., Frick et al., 2010):

$$\mathrm{LCOE} = \frac{A_{\mathrm{total}}}{e_{\mathrm{annual}}} = \frac{O_{\mathrm{annual}} + J_{\mathrm{annual}}}{e_{\mathrm{annual}}} = \frac{O_{\mathrm{annual}} + \frac{i(1+i)^t}{(1+i)^t - 1} J_{\mathrm{total}}}{e_{\mathrm{annual}}} \tag{6.11}$$

where LCOE ($ MWh^{-1}) is the levelized cost of energy, O_{annual} ($/year) is the annual operation and maintenance cost, e_{annual} (MWh) is the energy provided annually, i (%) is the imputed interest rate, t (year) is the project lifetime and J_{total} ($) is the total capital investment.

The latter is estimated as (e.g., Beckens et al., 2019):

$$J_{\mathrm{total}} = C_{\mathrm{wells}} + C_{\mathrm{stimulation}} + C_{\mathrm{plant}} \tag{6.12}$$

where C ($) stands for cost.

Three different well cost models were used. These are (e.g., Limberger et al., 2014 and references therein):

$$\text{WellCost Lite} = F_s \times 10^{-0.67+0.000334(z+h)} \times N \tag{6.13a}$$

$$\text{ThermoGIS} = F_s \times [0.2(z+l)^2 + 700(z+l) + 25000] \times N \times 10^{-6} \tag{6.13b}$$

$$\text{HSD} = 1500 \times z \times N \times 10^{-6} \tag{6.13c}$$

where F_s is the well cost scaling factor, z (m) is depth, l (m) is the possible extra horizontal length of the well and N is the number of wells. HSD stands for hydrothermal spallation drilling.

The parameter F_s was assumed 1 and l was assumed 0 in this work.

The imputed interest rate, stimulation, power plant and other surface facilities and operation and maintenance costs were assumed the same as the values proposed in Sanyal et al. (2007). However, these costs may be underestimated for Kuujjuaq. In fact, due to remoteness, infrastructure cost in Nunavik can be 2 to 5 times more expensive than the regular construction/infrastructure costs in southern areas (Lance, person. comm.). Therefore, a first analysis was carried out using Sanyal et al. (2007) costs and these were posteriorly increased by a factor ranging between 2 and 5 to assess more realistic energy costs for Kuujjuaq (Table 6.2).

Table 6.2 **Sensitivity analysis for the costs.**

Cost		Sanyal et al. (2007) (optimistic scenario)	Factor of 2 (likely scenario)	Factor of 5 (pessimistic scenario)
Stimulation per well (M$)	Minimum	0.5	1.0	2.5
	Mean	0.75	1.5	3.75
	Maximum	1.0	2.0	5.0
Power plant and other surface facilities ($ kWh^{-1})	Minimum	1 800	3 600	9 000
	Mean	2 000	4 000	10 000
	Maximum	2 200	4 400	11 000
Annual operation and maintenance (¢ kWh^{-1})	Minimum	2.0	4.0	10.0
	Maximum	3.5	7.0	17.5

The costs are in USD.

The imputed interest rate was assumed 9% (Sanyal et al., 2007). The annually provided energy was estimated based on the annual average heating (and electricity) consumption inferred for the community. The ensemble of uncertainties was simulated with Monte Carlo method (Table 6.3) using the software @RISK (Palisade, 2019) and the simulations were carried out for each possible engineered geothermal energy system design computed with FRACSIM3D.

Table 6.3 Levelized cost of energy and uncertainty.

Parameter code	Parameter description	Unit	Variable type	Distribution
C_{wells}	Wells cost	$	Discrete	Uniform
$C_{stimulation}$	Stimulation cost	$	Continuous	Triang(min,mean,max)
C_{plant}	Power plant and other surface facilities cost	$ kW^{-1}	Continuous	Traing(min,mean,max)
O_{annual}	Annual operations and maintenance cost	¢ kWh^{-1}	Continuous	Uniform(min,max)
e_{annual}	Annually consumed energy	MWh	Continuous	Uniform(min,max)
i	Imputed interest rate	%	Continuous	Single value
t	Project lifetime	year	Continuous	Single value

6.5 Results

The numerical simulations carried out aimed at 1) studying how the fracture network and properties of the medium influence the initial fracture aperture, fracture shear stiffness and fracture shear displacement, 2) analyze how the stimulation fluid pressure influences the number of sheared fractures and 3) designing an engineered geothermal energy system capable to meet the following targets:

- Flow rates able to harvest enough thermal energy during all system operation time to meet the community's heating demand
- Water loss maximum 20%
- Reservoir flow impedance lower than 0.1 MPa L^{-1} s^{-1}
- Thermal drawdown lower than 1 ºC/year

6.5.1 Initial fracture aperture

The initial fracture aperture is estimated in FRACSIM3D through a predictive model that takes into account the measured average permeability of the undisturbed rock mass, the fracture radius, density, orientation and in situ stresses (Snow, 1969; Willis-Richards et al., 1996; Jing et al., 2000). The results reveal that the hydromechanical properties influence significantly the estimated initial aperture of the fractures (Figure 6.6). The size of the fractures and fractal dimension also play a minor role (Figure 6.6). The observed variability consequently influences the hydraulic conductivity of the medium and the performance of the hydraulic stimulation procedure. It is convenient to indicate that these results were computed assuming the wells in configuration A (Figure 6.4).

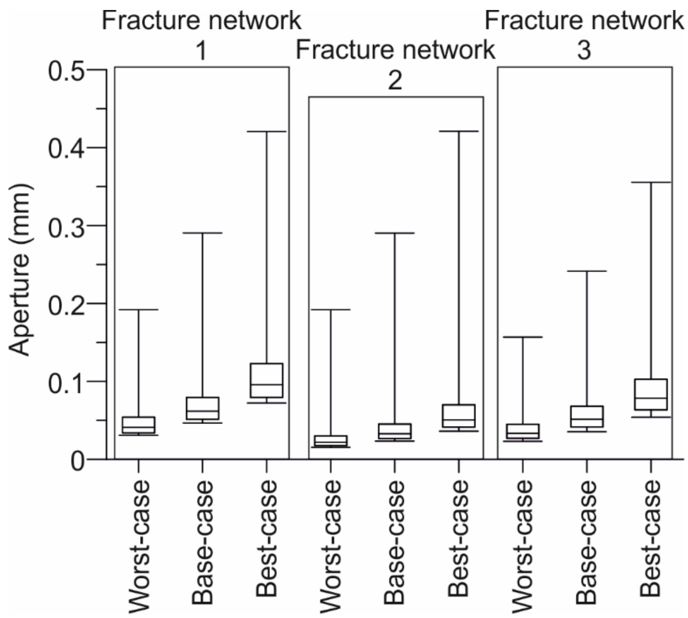

Figure 6.6 **Boxplot of initial fracture aperture with whiskers from minimum to maximum. The reader is referred to section 6.4.2 for further details on the fracture network and to Table 6.1 for further information on the properties of the medium.**

6.5.2 Fracture shear stiffness

The fracture shear stiffness is approximated in FRACSIM3D as the ratio of the shear modulus by the fracture radius multiplied by a geometric parameter (Eshelby, 1957; Jing et al., 2000). The results reveal that longer fractures and small Young’s modulus and high Poisson’s ratio considerably reduce the shear stiffness of the medium (Figure 6.7), thus improving the performance of the hydraulic stimulation procedure. It is convenient to indicate that these results were computed assuming the wells in configuration A (Figure 6.4).

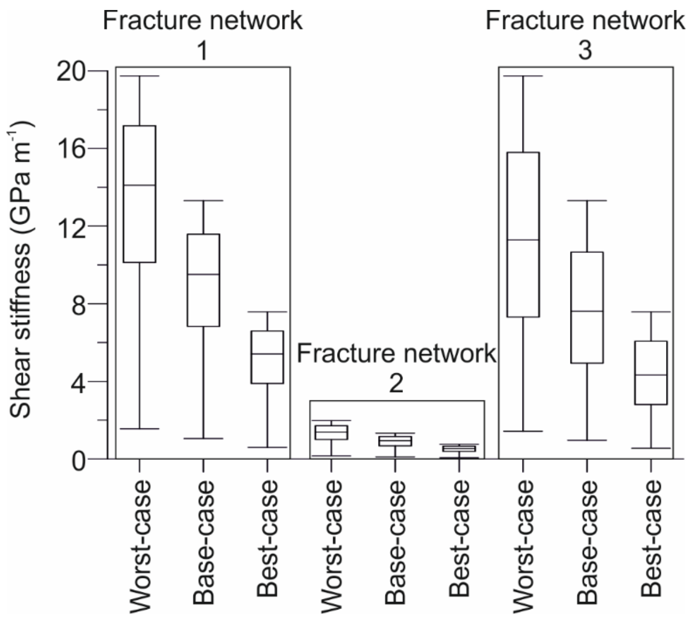

Figure 6.7 **Boxplot of fracture shear stiffness with whiskers from minimum to maximum. The reader is referred to section 6.4.2 for further details on the fracture network and to Table 6.1 for further information on the properties of the medium.**

6.5.3 Fracture shear displacement

The shear displacement is expressed in FRACSIM3D as the ratio of the linear Mohr-Coulomb criterion by the fracture shear stiffness (Jing et al., 2000). Thus, fractures with high shear stiffness tend to experience lower shear displacements and the latter tends to increase as a function of the fluid pressure (Figure 6.8). For the worst-case scenario, slippage occurs at stimulation, or fluid, pressures between 40 MPa and 70 MPa, regardless of the fracture network. For the base-case scenario, slip takes place at stimulation pressures of 20 to 60 MPa while, for the best-case scenario, between the pressures of 5 and 40 MPa. It is convenient to indicate that these results were computed assuming the wells in configuration A (Figure 6.4).

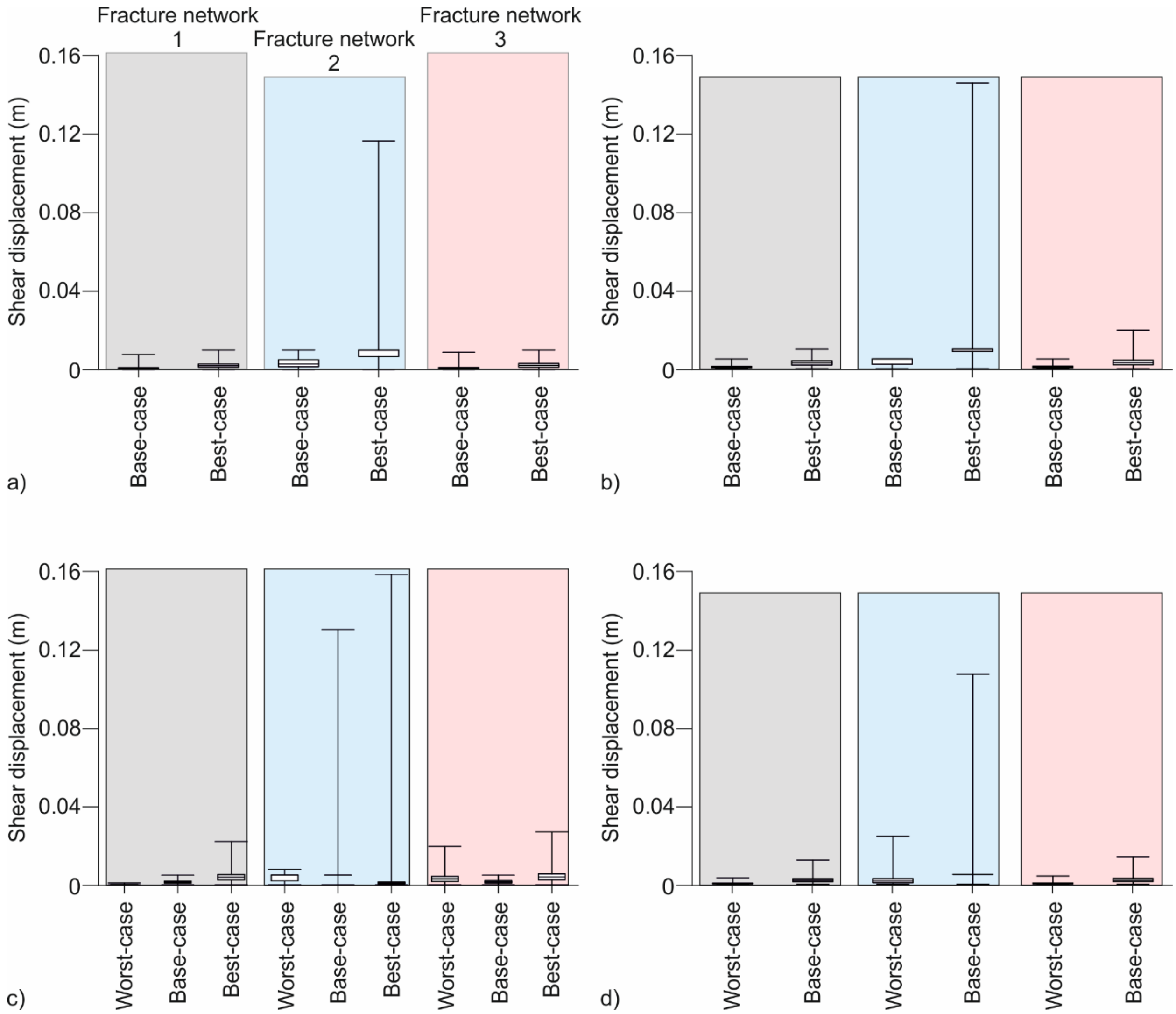

Figure 6.8 **Boxplot of fracture shear displacement with whiskers from minimum to maximum: a) stimulation pressure of 20 MPa, b) stimulation pressure of 30 MPa, c) stimulation pressure of 40 MPa and d) stimulation pressure of 50 MPa. The reader is referred to section 6.4.2 for further details on the fracture network and to Table 6.1 for further information on the properties of the medium.**

6.5.4 Sheared fractures

The optimally oriented fractures to slip belong to the sets E-W and N-S, followed by the set NNW-SSE and the fractures within the other group (Figure 6.9). The set NW-SE is not optimally oriented to slip (Figure 6.9). These observations confirm the Mohr-Coulomb friction and slip tendency analyzes carried out in chapter 5. Moreover, increasing the stimulation fluid pressure led to an increase on the number of fractures that can be reactivated. However, it is important to highlight that the stress regime plays a major role and large uncertainty still exists as discussed in chapter 5. As a note, these results were computed assuming the wells in configuration A (Figure 6.4) and a friction coefficient of 0.6.

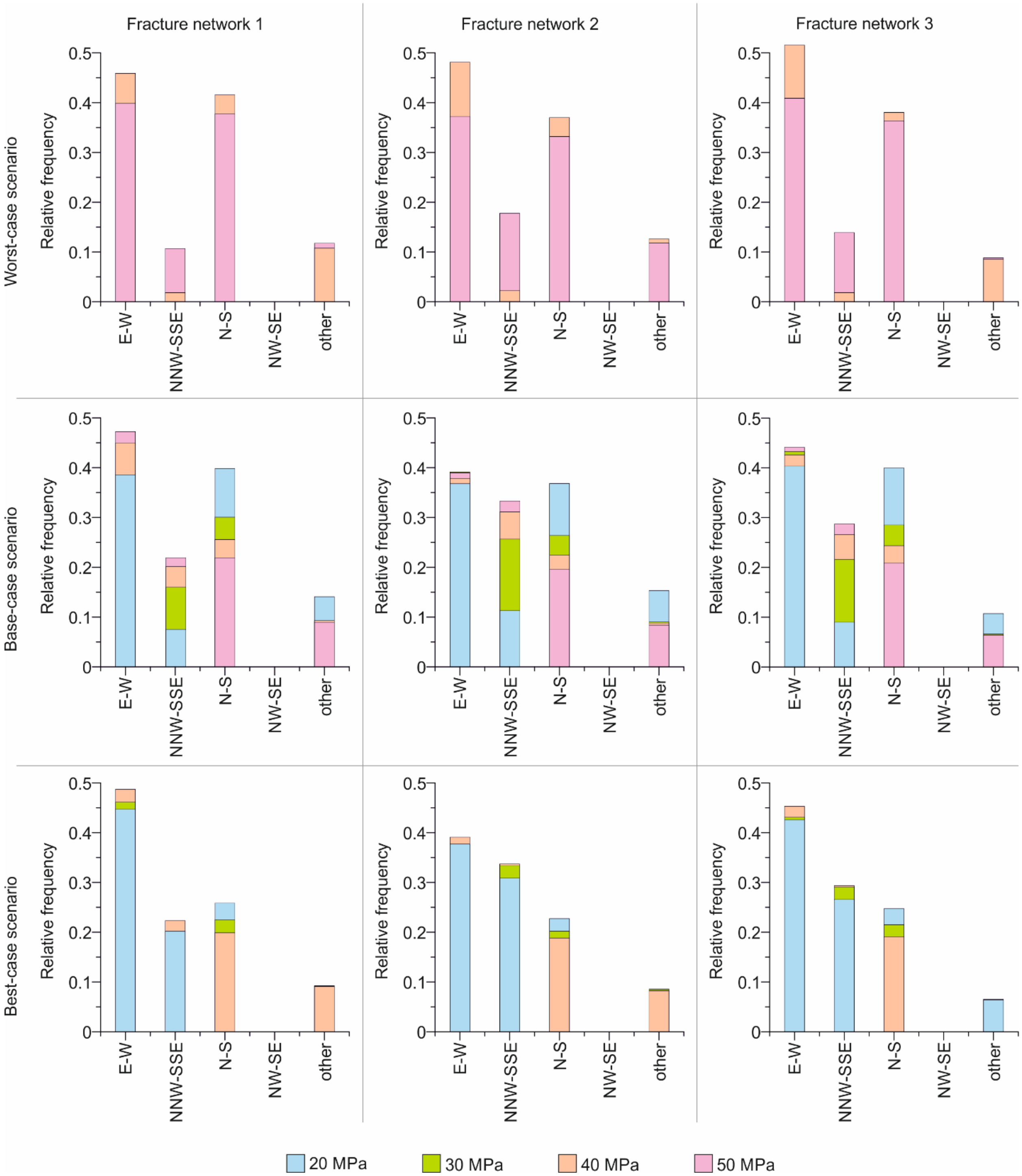

Figure 6.9 **Sheared fractures grouped by sets for different stimulation fluid pressure. The reader is referred to section 6.4.2 for further details on the fracture network and to Table 6.1 for further information on the properties of the medium.**

6.5.1 Engineered geothermal energy system design

The previous results suggest that developing a hydraulically stimulated geothermal reservoir is favored in a mechanically weak (i.e. low magnitude for the principal stresses and fractures with low resistance to deformation and opening) and hydraulically conductive medium. Moreover, they also indicate that smaller fractures tend to slip less, thus, making fluid circulation more difficult. Reservoirs of potential interest were not simulated for the worst-case scenario, firstly, and most important, due to the low reservoir temperature and high flow rates required to meet the demand and secondly due to the high magnitude inferred for the principal stresses and high resistance of the fractures to deformation and opening. Thus, the following sections will be focused on the best- and base-case scenarios, discussing the best simulated design to meet the aforementioned targets. The influence of the Lac Pingiajjulik fault and its initial offset and, thus, hydraulic conductivity, is additionally considered.

6.5.1.1 Best-case scenario

Reservoirs capable to meet the aforementioned targets were simulated in this scenario for the three fracture network hypotheses regardless of Lac Pingiajjulik initial fault offset (Table 6.4). As previously outlined, these simulations were carried out bearing in mind the estimated required flow rate of 14 to 45 L s^{-1}. The simulations reveal that, in this case study, positioning the wells perpendicular to the fault trace (configuration A; Figure 6.4) leads to a better performance and sustainability of the system than placing the wells parallel to the fault trace (configuration B; Figure 6.4). The results also suggest that longer fractures (fracture network 2) tend to improve the performance of the engineered geothermal energy system. Lower stimulation and circulation pressures are required to enhance the transmissivity and circulate the fluid.

Table 6.4 Design parameters and results.

Configuration[1]	Fault offset (m)	Spacing between wells (m)	Open hole length (m)	V_{stim} (km^3)	P_{stim} (MPa)		P_{circ} (MPa)		Q_{rec} (L s^{-1})	W_{loss} (%)	H (MPa L^{-1} s^{-1})	$T_{drawdown}$ (ºC/year)
					*I**	*R**	*I**	*R**				
Fracture network 1												
A	0.10	700	600	0.8	25	28	10	-5	52.9	18.1	0.03	0.16
A	0.01	700	600	0.8	25	28	9	-5	47.4	17.6	0.03	0.12
A	0.001	500	600	0.8	29	35	6	-4	49.0	15.5	0.03	0.10
B	0.10	700	500	0.4	23	28	7	-5	22.4	20.4	0.01	0.60
B	0.01	700	500	0.4	25	30	7	-5	28.8	18.2	0.01	0.73
Fracture network 2												
A	0.10	700	600	0.8	7	14	2	0	55.6	13.7	0.003	0.03
A	0.01	700	600	0.8	4	9	2	-1	56.4	2.1	0.01	0.03
A	0.001	600	600	0.8	5	10	2	-1	50.1	5.3	0.01	0.02
B	0.10	700	600	0.4	2	4	1	-1	22.8	11.8	0.001	0.50
B	0.01	700	600	0.4	3	5	1	-1	26.1	3.4	0.01	0.35
Fracture network 3												
A	0.10	700	600	0.8	23	24	8	-4	50.7	8.0	0.03	0.07
A	0.01	600	600	0.8	23	24	6	-4	46.8	9.9	0.03	0.05
A	0.001	500	600	0.8	26	32	6	-4	51.8	5.0	0.02	0.04
B	0.10	700	600	0.4	22	24	3	-3	22.3	2.9	0.003	0.45
B	0.01	700	600	0.4	22	24	4	-3	22.9	20.5	0.01	0.56

[1] The reader is referred to Figure 6.4 for further details on the configuration. V_{stim} – stimulation volume, P_{stim} – stimulation pressure, P_{circ} – circulation pressure, *I – injection well, *R** – recovery well, Q_{rec} – recovered flow rate, W_{loss} – water loss, H – hydraulic impedance, $T_{drawdown}$ – temperature drawdown. The reader is referred to section 6.4.2 for further details on the fracture network.**

6.5.1.2 Base-case scenario

As previously outlined, these simulations were carried out bearing in mind the estimated required flow rate of 27 to 89 L s^{-1}. Reservoirs of potential interest were only generated considering the fractures longer than sampled in the field (fracture network 2). However, to meet the defined targets, higher stimulation volume and stimulation and circulation pressures are required than for the best scenario previously studied (Table 6.5).

Table 6.5 Design parameters and results.

Configuration[1]	Fault offset (m)	Spacing between wells (m)	Open hole length (m)	V_{stim} (km^3)	P_{stim} (MPa)		P_{circ} (MPa)		Q_{rec} (L s^{-1})	W_{loss} (%)	H (MPa L^{-1} s^{-1})	$T_{drawdown}$ (ºC/year)
					*I**	*R**	*I**	*R**				
Fracture network 2												
A	0.10	700	600	0.8	47	44	14	-2	93.3	0.4	0.09	0.47
A	0.01	700	600	0.8	47	44	16	-4	96.6	10.6	0.10	0.58
A	0.001	700	600	0.8	48	45	16	-4	88.2	18.2	0.11	0.90
B	0.10	700	600	0.8	43	45	3	-1	29.8	9.7	0.003	0.87
B	0.01	700	600	0.8	43	45	4	-2	32.2	2.7	0.03	0.73

[1] The reader is referred to Figure 6.4 for further details on the configuration. V_{stim} – stimulation volume, P_{stim} – stimulation pressure, P_{circ} – circulation pressure, *I – injection well, *R** – recovery well, Q_{rec} – recovered flow rate, W_{loss} – water loss, H – hydraulic impedance, $T_{drawdown}$ – temperature drawdown. The reader is referred to section 6.4.2 for further details on the fracture network.**

6.5.2 Thermal energy and potential heat output

The thermal energy extracted by each design previously studied is capable to fulfill the forecasted heating energy demand during the 30 years of operation (Figure 6.10). Moreover, the results indicate that configuration A (Figure 6.4) is more appropriate to meet the upper bound of the projected demand while configuration B (Figure 6.4) can be used to meet the lower bound of the demand.

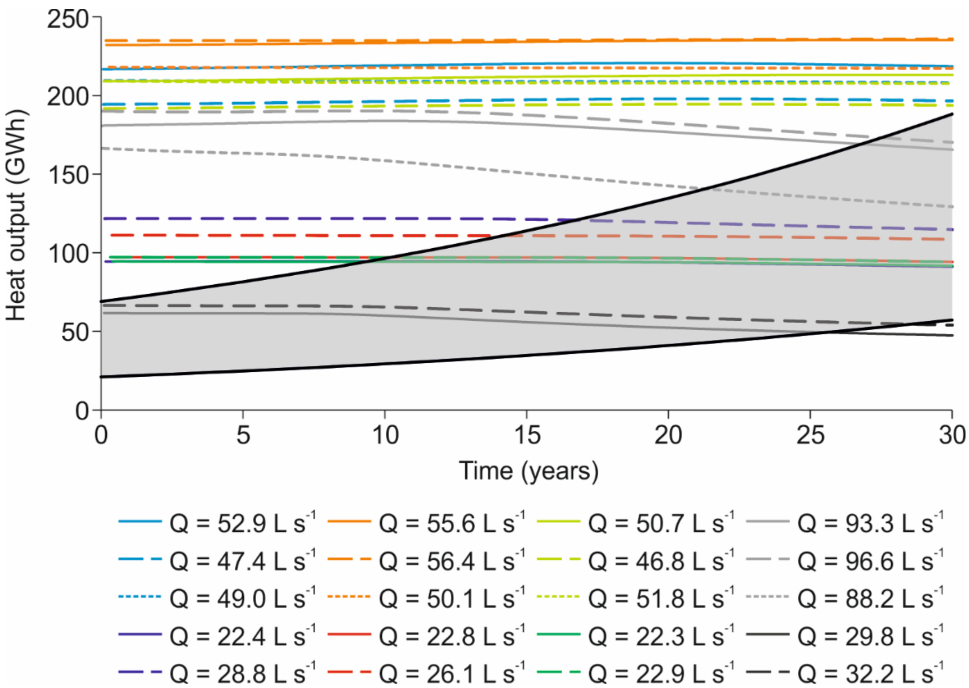

Figure 6.10 **Heating energy produced (color lines) and projected demand (grey polygon). Lower bound of grey polygon – annual heating energy demand estimated based on Yan et al. (2019), upper bound of grey polygon – annual heating energy demand estimated based on Gunawan et al. (2020). The reader is referred to Table 6.4 and Table 6.5 for further details on the flow rates.**

Some of the designs largely exceed the heating needs within the first years of the geothermal system operation. Therefore, an additional study was undertaken to assess if the geothermal system can be used for combined heat and power to improve the sustainability of the system. The electricity consumption in Kuujjuaq was evaluated as 18.9 GWh (see Miranda et al., 2020b for further details) and the yearly growth in energy demand is assumed 3% (Statistics Canada, 2019). The results suggest that about 6 to 8 MW_{th} are rejected per each MW_e produced when considering the deep geothermal energy sources in Kuujjuaq. Assuming that only 50% of the waste heat from power production can be used for space heating, since the remaining is lost from parasitic equipment, engineered geothermal energy system can be designed to operate in combined heat and power mode during approximately 8-15 years of the project lifetime, meeting both power and heating demand (Figure 6.11).

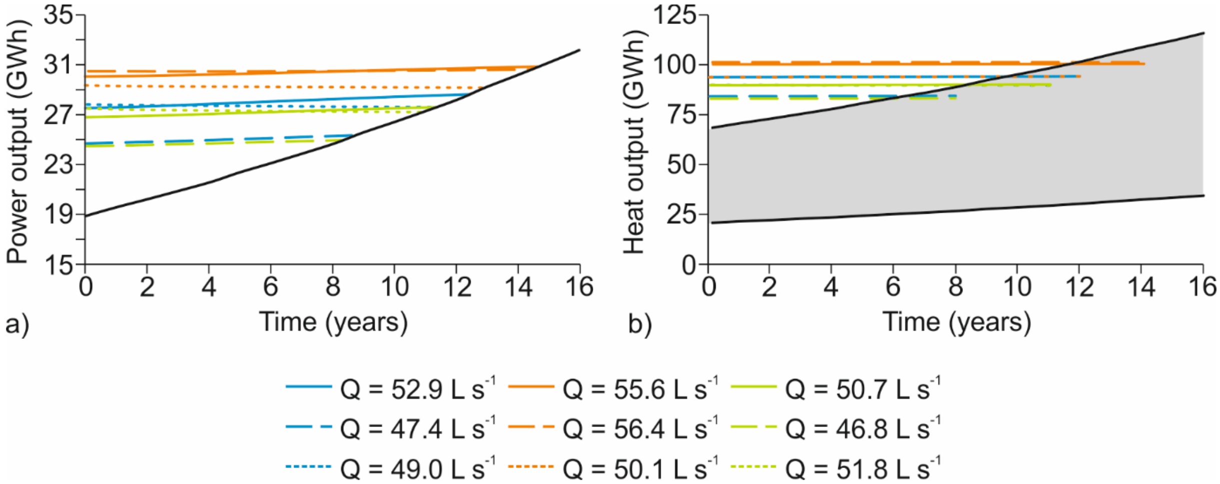

Figure 6.11 **a) Power and b) heating energy produced from the waste heat (color lines) and projected demand (black line and grey polygon). Lower bound of grey polygon – annual heating energy demand estimated based on Yan et al. (2019), upper bound of grey polygon – annual heating energy demand estimated based on Gunawan et al. (2020). The reader is referred to Table 6.4 and Table 6.5 for further details on the flow rates.**

6.5.3 Recovery factor

The thermally active reservoir volume changes over time as heat is being extracted. The recovery factor was calculated as the ratio between the thermally active volume of rock during the 30 years of operation and the stimulated volume defined (Figure 6.12). The recovery factor is commonly assumed to be within the theoretical range of 2 – 20% (e.g., Tester et al., 2006; Beardsmore et al., 2010). The results obtained agree with these values.

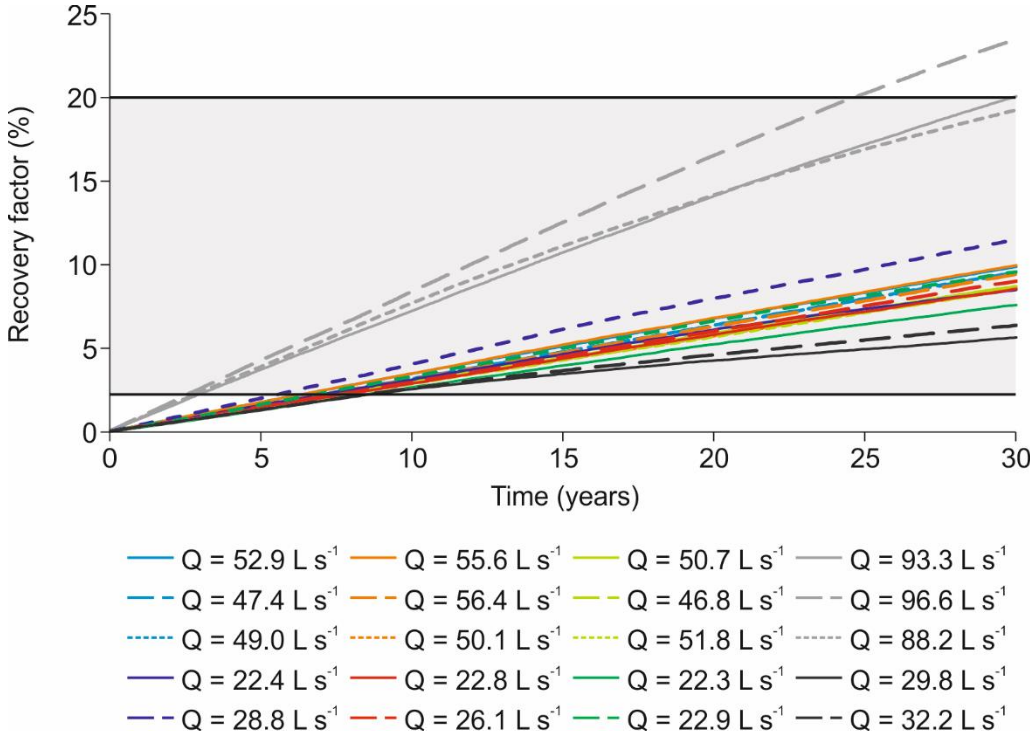

Figure 6.12 **Recovery factor over time. Grey polygon – theoretical values for the recovery factor, lower bound = 2%, upper bound = 20% (e.g., Tester et al., 2006; Beardsmore et al., 2010). The reader is referred to Table 6.4 and Table 6.5 for further details on the flow rates.**

6.5.4 Levelized cost of energy

The three well cost models used in this work suggest that the price of two 4-km-wells can be 9.8 M$ (WellCost Lite model; Equation 6.13a) and 12 M$ (ThermoGIS and HSD models; Equation 6.13b and Equation 6.13c, respectively). Considering the Sanyal et al. (2007) proposed costs, the stimulation of both wells ranges between a minimum of 1 M$ and a maximum of 2 M$, with a mean value of 1.5 M$. The power plant and other surface facilities estimated for each possible design previously studied (Table 6.4 and Table 6.5) is found to vary between an average maximum cost, for configuration A (Figure 6.4), of 54 M$ and an average minimum of 34 M$ (Figure 6.13a). For configuration B (Figure 6.4), the cost varies between an average minimum of 12 M$ and an average maximum of 28 M$ (Figure 6.13b). Thus, the average minimum capital cost estimated for configuration A (Figure 6.4) is 46 M$ while the average maximum is 66.8 M$ (Figure 6.14a). For configuration B (Figure 6.4), the average minimum is 24.8 M$ and the average maximum 40.8 M$ (Figure 6.14b). All these costs are in USD.

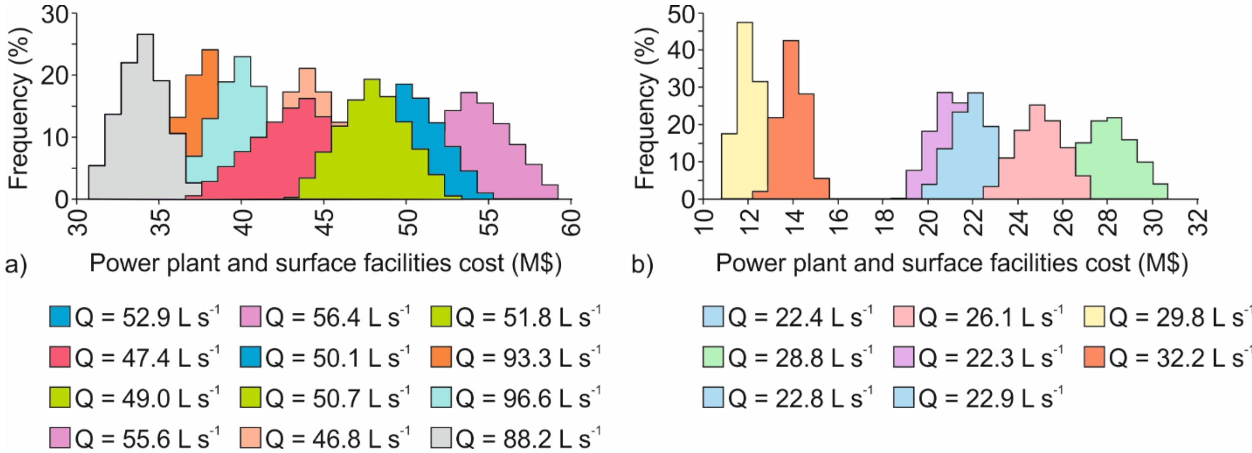

Figure 6.13 **Power plant and other surface facilities cost for each simulated design considering Sanyal et al. (2007) costs: a) configuration A (Figure 6.4) and b) configuration B (Figure 6.4). The cost is in USD. The reader is referred to Table 6.4 and Table 6.5 for further details on the flow rates.**

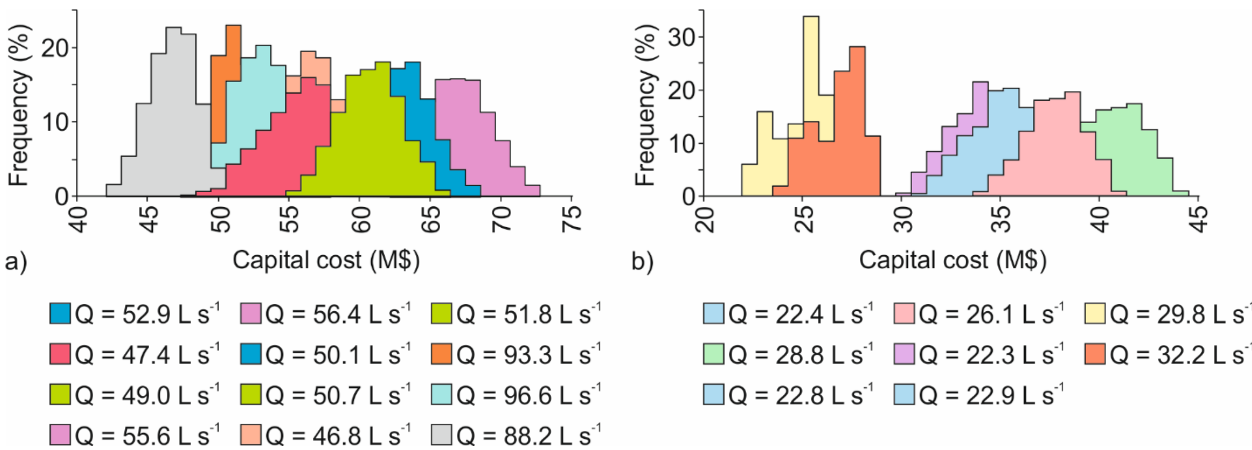

Figure 6.14 **Capital cost for each simulated design considering Sanyal et al. (2007) costs: a) configuration A (Figure 6.4) and b) configuration B (Figure 6.4). The cost is in USD. The reader is referred to Table 6.4 and Table 6.5 for further details on the flow rates.**

However, these costs may be too optimistic since, due to remoteness, infrastructure cost in Nunavik can be 2 to 5 times more expensive than the regular construction/infrastructure costs in southern areas. Therefore, a second analysis was carried out increasing the costs by a factor of 2 and 5 (Table 6.2). The stimulation of both wells is found to vary between 2 M$ and 4 M$, for a factor of 2, and between 5 M$ and 10 M$ if the costs are increased by 5 times. The power plant and other surface facilities, for a factor of 2, can have a cost varying within the average minimum of 24 M$ to the average maximum of 108 M$ (Table 6.6) or between 60 M$ and 270 M$ (Table 6.6) if the cost is 5 times higher than the one proposed by Sanyal et al. (2007).

Table 6.6 **Power plant and other surface facilities cost for each simulated design.**

Design		Power plant and other surface facilities cost (M$)					
		Factor of 2 (likely scenario)			Factor of 5 (pessimistic scenario)		
		Minimum	Mean	Maximum	Minimum	Mean	Maximum
Configuration A	Q = 52.9	90	100	110	225	250	275
	Q = 47.4	79	88	97	198	220	242
	Q = 49.0	86	96	106	216	240	264
	Q = 55.6	97	108	119	243	270	297
	Q = 56.4	97	108	119	243	270	297
	Q = 50.1	90	100	110	225	250	275
	Q = 50.7	86	96	106	216	240	264
	Q = 46.8	79	88	97	198	220	242
	Q = 51.8	86	96	106	216	240	264
	Q = 93.3	68	76	84	171	190	209
	Q = 96.6	72	80	88	180	200	220
	Q = 88.2	61	68	75	153	170	187
Configuration B	Q = 22.4	40	44	48	99	110	121
	Q = 28.8	50	56	62	126	140	154
	Q = 22.8	40	44	48	99	110	121
	Q = 26.1	45	50	55	113	125	138
	Q = 22.3	38	42	46	95	105	116
	Q = 22.9	40	44	48	99	110	121
	Q = 29.8	22	24	26	54	60	66
	Q = 32.2	25	28	31	63	70	77

The cost is in USD. The reader is referred to Figure 6.4 for further details on the configuration. The reader is referred to Table 6.4 and Table 6.5 for further details on the flow rates.

Consequently, the capital cost for each simulated design increase to an average minimum of 38 M$ and an average maximum of 122 M$ if the costs are 2 times higher and to 79 M$ and 289 M$ if the costs are 5 times higher than in Sanyal et al. (2007; Table 6.7).

Table 6.7 **Capital cost for each simulated design.**

Design		Capital cost (M$) Factor of 2 Minimum	Mean	Maximum	Factor of 5 Minimum	Mean	Maximum
Configuration A	Q = 52.9	104	114	124	244	269	294
	Q = 47.4	91	102	112	215	239	261
	Q = 49.0	100	110	121	233	259	283
	Q = 55.6	111	122	134	260	289	315
	Q = 56.4	111	122	134	261	289	315
	Q = 50.1	103	114	125	244	269	295
	Q = 50.7	99	110	121	233	259	283
	Q = 46.8	92	102	112	216	239	260
	Q = 51.8	99	110	121	235	259	284
	Q = 93.3	81	90	99	189	209	228
	Q = 96.6	85	94	104	199	219	239
	Q = 88.2	74	82	90	170	189	208
Configuration B	Q = 22.4	53	58	63	116	129	142
	Q = 28.8	63	70	77	142	159	174
	Q = 22.8	53	58	63	115	129	142
	Q = 26.1	58	64	70	129	144	158
	Q = 22.3	51	56	61	112	124	135
	Q = 22.9	53	58	63	115	129	140
	Q = 29.8	35	38	42	70	79	86
	Q = 32.2	38	42	46	79	89	98

The cost is in USD. The reader is referred to Figure 6.4 for further details on the configuration. The reader is referred to Table 6.4 and Table 6.5 for further details on the flow rates.

Sensitivity analysis carried out indicate that, for configuration A (Figure 6.4), the power plant and surface facilities cost is the most influential parameter on the capital cost followed by the well cost (Figure 6.15). The Spearman correlation coefficient for the former ranges between 0.78 and 0.91, for the latter between 0.28 and 0.54 and for the stimulation cost between 0.02 and 0.13. For configuration B (Figure 6.4), the power plant and surface facilities and well costs have similar influence on the capital cost (Figure 6.15). The Spearman correlation coefficient for the former varies between 0.54 and 0.70, for the latter between 0.59 and 0.73, and for the stimulation cost between 0.11 and 0.20. It is convenient to highlight that although the values displayed in Figure 6.15 correspond to the costs proposed by Sanyal et al. (2007), the same trend is observed if the costs are 2 or 5 times higher.

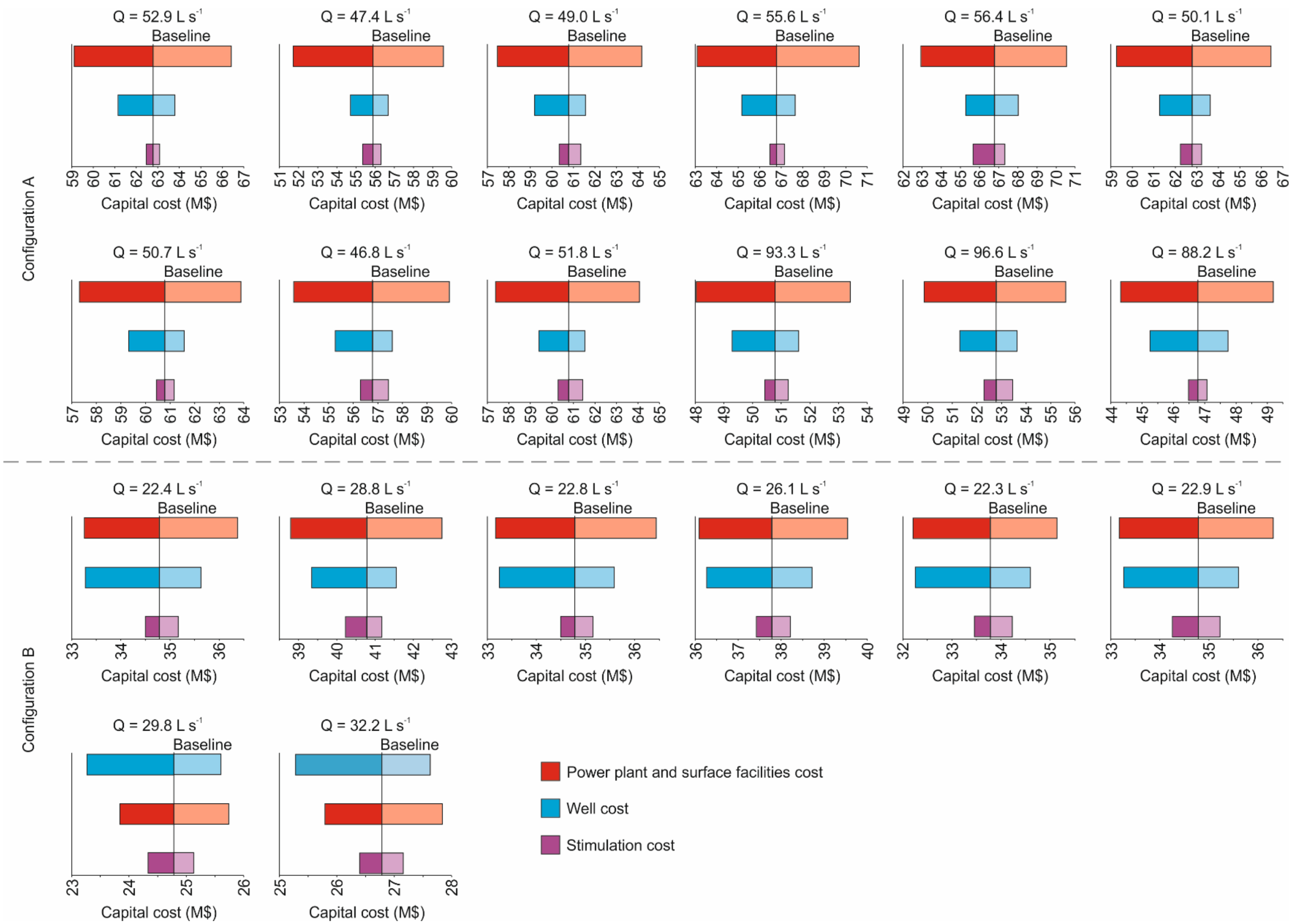

Figure 6.15 **Input parameters ranked according to their influence on the capital cost. Baseline – overall simulated mean value, solid color – positive impact on the output, transparency – negative impact on the output. The cost is in USD. The reader is referred to Table 6.4 and Table 6.5 for further details on the flow rates.**

Considering the results previously discussed, the levelized cost of energy was evaluated considering the Sanyal et al. (2007) costs as the optimistic scenario, the increase by a factor of 2 as the most likely scenario, and the increase by a factor of 5 as the pessimistic scenario. The mean value for each of these hypotheses was used in this analysis. The levelized cost of energy considering configuration A (Figure 6.4) and the best-case scenario (Table 6.4) for heat production only, was evaluated to range between an average minimum of 121 $ MWh^{-1} and an average maximum of 626 $ MWh^{-1} (Table 6.8). These values decreased to 120 $ MWh^{-1} and 617 $ MWh^{-1} if the geothermal system is assumed to work in combined heat and power mode during 10 to 15 years (Table 6.8). The remaining designs can only produce heat. The levelized cost of energy is found to range within an average minimum of 54 $ MWh^{-1} and an average maximum of 475 $ MWh^{-1} (Table 6.8).

Table 6.8 Levelized cost of energy for each simulated design.

Design			Levelized cost of energy ($ MWh^{-1}) Heat Optimistic	Heat Likely	Heat Pessimistic	CHP Optimistic	CHP Likely	CHP Pessimistic
Configuration A	Best-case	Q = 52.9	136	247	584	134	244	576
		Q = 47.4	121	221	517	120	218	510
		Q = 49.0	132	239	561	130	236	553
		Q = 55.6	145	265	625	143	262	616
		Q = 56.4	145	265	626	143	262	617
		Q = 50.1	136	247	584	134	244	577
		Q = 50.7	131	239	561	130	235	553
		Q = 46.8	123	221	517	122	218	510
		Q = 51.8	132	239	563	130	235	555
	Base-case	Q = 93.3	111	195	453	---	---	---
		Q = 96.6	114	205	475	---	---	---
		Q = 88.2	102	178	410	---	---	---
Configuration B		Q = 22.4	75	126	280	---	---	---
		Q = 28.8	88	152	343	---	---	---
		Q = 22.8	75	126	279	---	---	---
		Q = 26.1	82	139	312	---	---	---
		Q = 22.3	73	121	268	---	---	---
		Q = 22.9	75	126	278	---	---	---
		Q = 29.8	54	83	170	---	---	---
		Q = 32.2	58	91	192	---	---	----

CHP – combined heat and power. The reader is referred to Figure 6.4 for further details on the configuration. The reader is referred to Table 6.4 and Table 6.5 for further details on the flow rates.

Currently, the heating energy cost in Kuujjuaq has been evaluated as 0.19 $ kWh^{-1} (or 190 $ MWh^{-1}) while electricity as 0.6 $ kWh^{-1} (or 600 $ MWh^{-1}; Belzile et al., 207; Giordano et al., 2018). Thus, a probabilistic study was undertaken to assess if the deep geothermal energy source, for both heat production and electricity generation, is cost-competitive compared to the business-as-usual, where space heating is provided by oil furnaces and electricity by diesel power plants. The results for heat production reveal that configuration A and the best-case scenario have a probability of 8 to 18% of providing heating energy at a lower energy cost than the business-as-usual (Figure 6.16a). A probability of 25 to 33% was estimated for configuration A and the base-case scenario (Figure 6.16b) while configuration B reveals probabilities of 49 to 91% (Figure 6.16c). Per contra, the probability of combined heat and power to provide electricity at a lower cost than business-as-usual is higher than 99% (Figure 6.16d). This analysis was undertaken by combining the results obtained for the optimistic, most likely and pessimistic scenarios. Considering the most likely scenario only, the engineered geothermal energy system has 13 to 100% probability of providing heating energy at lower cost than the oil furnaces and 100% probability of providing electricity at lower cost than the diesel power plants.

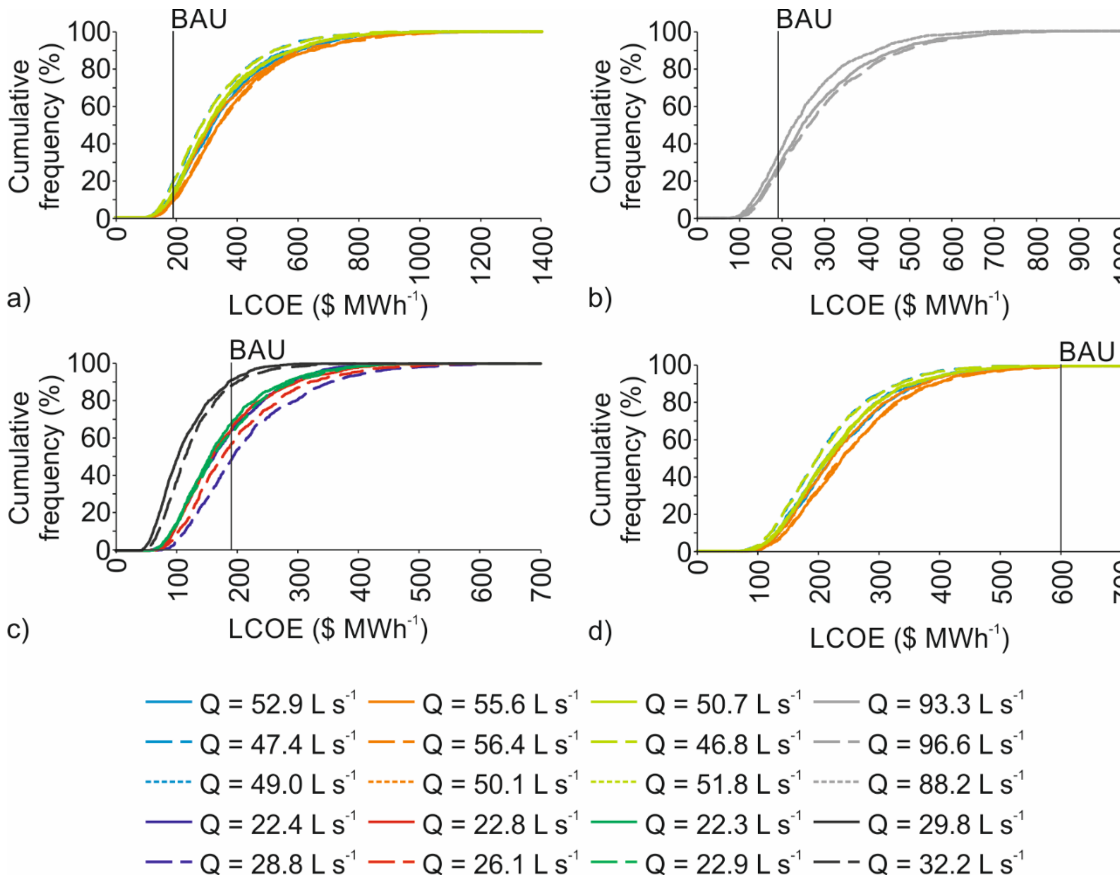

Figure 6.16 **Levelized cost of energy and probability of providing energy at lower cost than the business-as-usual (BAU): a) configuration A and best-case scenario – heat only, b) configuration A and base-case scenario – heat only, c) configuration B – heat only, d) configuration A and best-case scenario – combined heat and power. The cost is in USD. The reader is referred to Table 6.4 and Table 6.5 for further details on the flow rates.**

A deeper analysis was undertaken to assess how can the probability of providing heating energy with an engineered geothermal energy system be increased. The results revealed that the energy consumption and capital cost play the major roles, with Spearman coefficients of, on average, -0.70 and 0.60, respectively. The operation and maintenance costs, per contra, reveal a weak correlation (on average 0.02) with the levelized cost of energy. This trend is observed for all the simulated scenarios (Figure 6.17). In fact, for the best- and base-case scenarios assuming configuration A, if the energy consumption is near or greater than its maximum value and the capital cost near or below its minimum value, then the geothermal systems simulated will have a greater probability of providing heating energy at lower cost than the business-as-usual (Figure 6.18). However, for configuration B, the energy consumption only needs to be greater than its 30th to 50th percentile and the capital cost below its 50th percentile (Figure 6.19). This for the best-case scenario, because for the base-case scenario, the energy consumption can be near its minimum value and the capital cost near its maximum value (Figure 6.19).

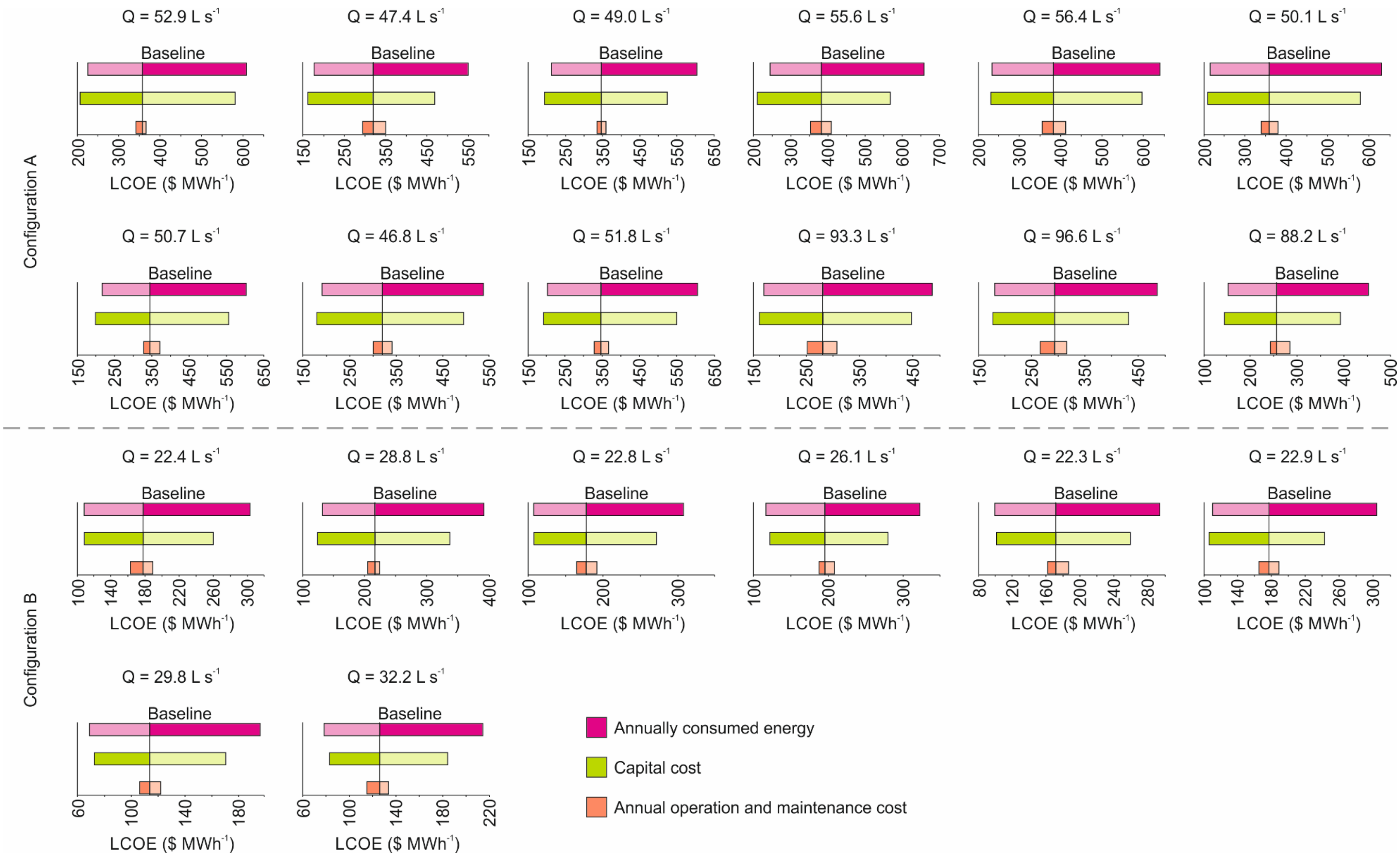

Figure 6.17 Input parameters ranked according to their influence on the levelized cost of energy. Baseline – overall simulated mean value, solid color – positive impact on the output, transparency – negative impact on the output. The cost is in USD. The reader is referred to Table 6.4 and Table 6.5 for further details on the flow rates.

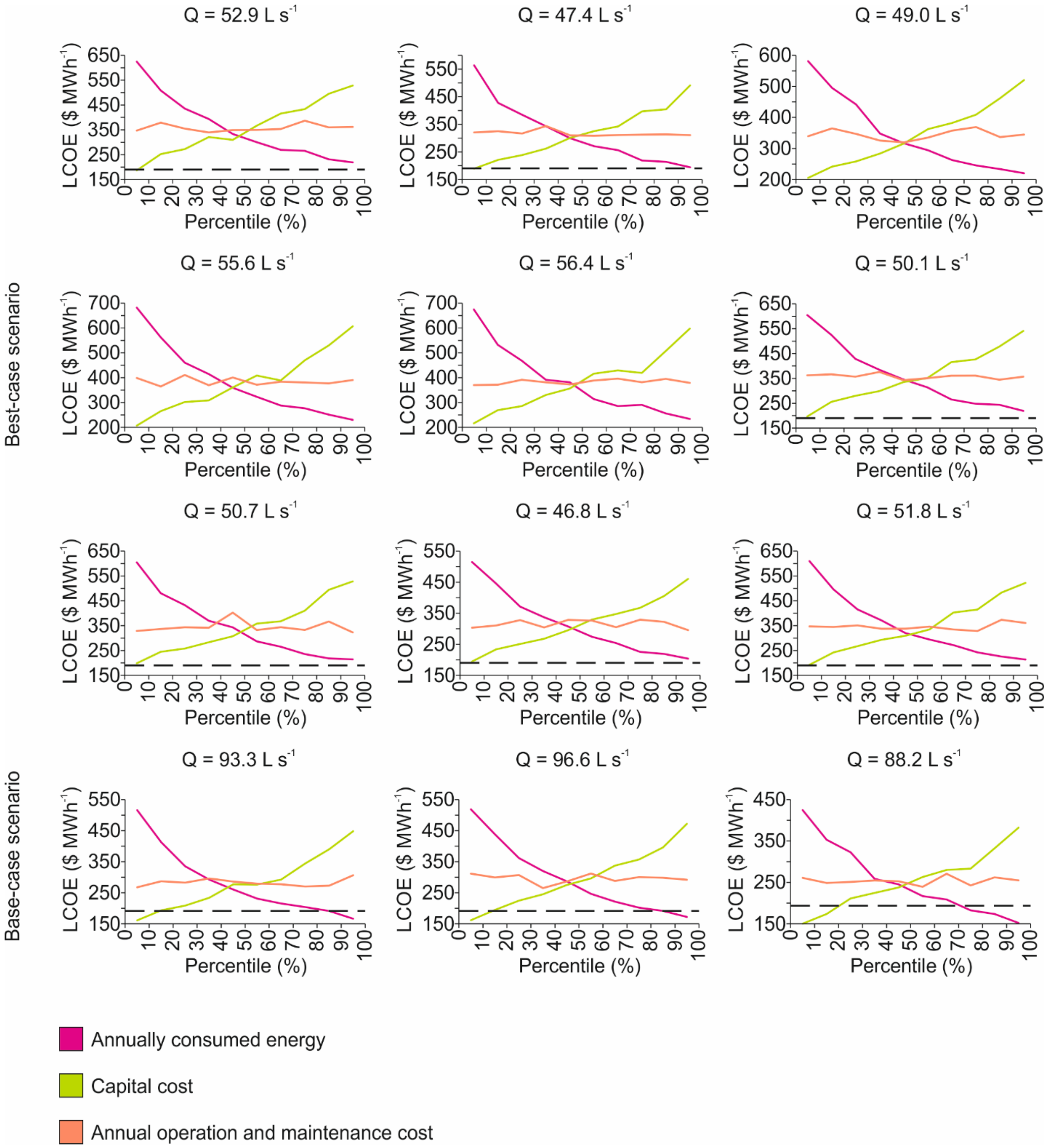

Figure 6.18 **Levelized cost of energy as a function of the uncertain parameters' percentile for configuration A. Dashed line – heating energy cost with oil furnaces (see text for further details). The reader is referred to Table 6.4 and Table 6.5 for further details on the flow rates.**

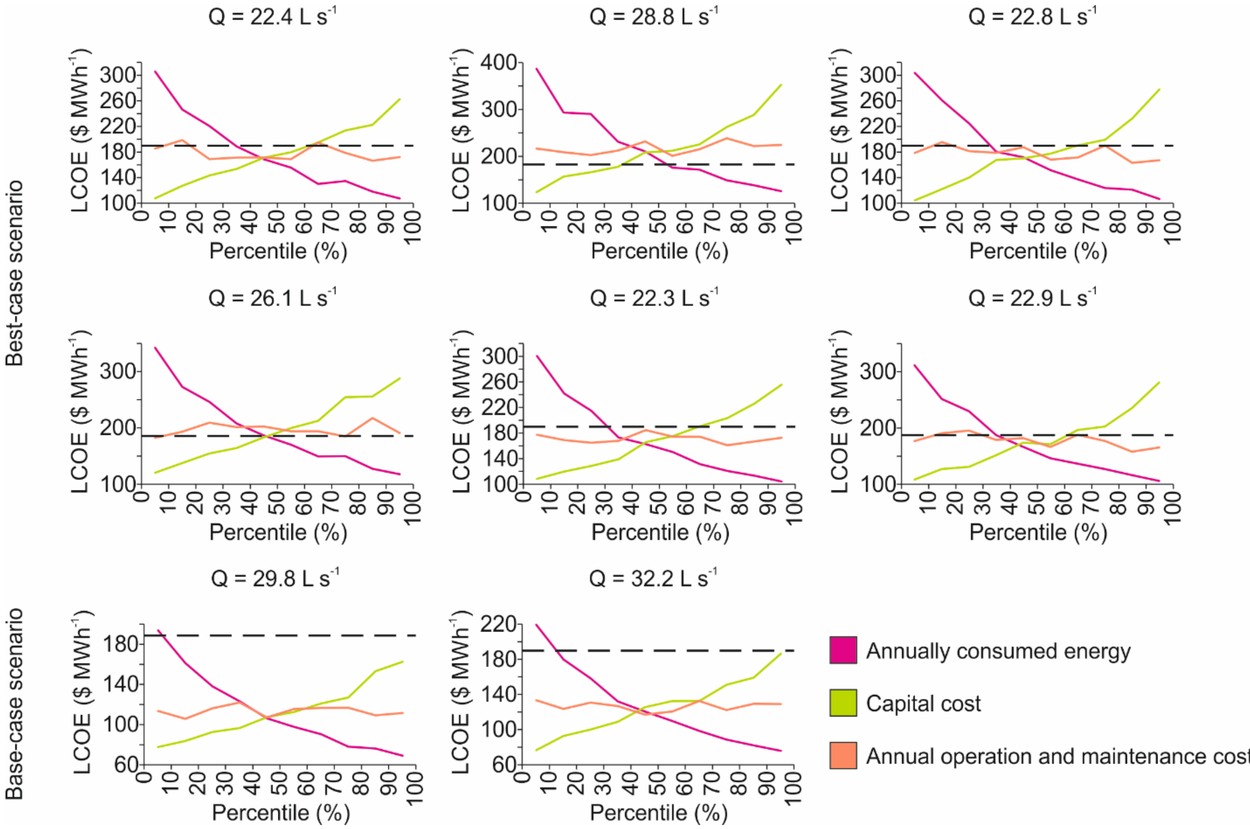

Figure 6.19 Levelized cost of energy as a function of the uncertain parameters' percentile for configuration B. Dashed line – heating energy cost with oil furnaces (see text for further details). The reader is referred to Table 6.4 and Table 6.5 for further details on the flow rates.

6.6 Discussion

The current energetic framework of the 239 Canadian off-grid communities relying solely on diesel entails 1) high costs to buy, transport, and stored diesel, 2) carbon emissions that contribute for climate change, 3) potential spills and leakages that damage the local environment and 4) low energy security that constrains community development (e.g., Karanasios et al., 2018). Thus, opposite to the three main axes that constitute the concept of sustainable energy markets: economic affordability, environmental compatibility and energy security (Frick et al., 2010; Zweifel et al., 2017). A sustainable energy market intends to maintain and improve living standards at an affordable cost by replacing the consumption of environmentally harmful sources of energy by more environmentally friendly alternatives. Therefore, introducing renewable off-grid technologies into the communities can break this energy poverty cycle that has held back their socio-economic progress. Deep geothermal energy can be a viable alternative solution to fossil fuels in remote northern communities, if the following criteria are met (Glassley, 2010):

- It is sufficiently abundant to meet a significant percentage of the market demand
- It can be obtained at a cost competitive with existing energy sources

A previous deep geothermal energy source assessment suggested that the thermal energy stored beneath the community of Kuujjuaq was capable to fulfill an estimated heating energy demand at depths higher than 4 km (Miranda et al., 2020b). Thus, the current study was carried out with the goal of designing an engineered geothermal energy system to harvest this energy and evaluate its economic potential compared with the business-as-usual. However, the results from this study are bounded by high level of uncertainties due to the current poor knowledge of both the geological structures and thermo-hydro-mechanical properties of rock at depth in the area. Nevertheless, this work is a contribution to assess if deep geothermal energy sources can supplant or displace reliance on fossil fuels. Moreover, although this work was undertaken in the community of Kuujjuaq, the methodological approach followed can be extended to other remote northern settlements facing important energy issues and with similar geothermal exploration data gaps.

The first research question of this study was: Will the hydraulic stimulation technique applied in crystalline basement rocks develop a well-connected flowing system in Kuujjuaq? How can this be done? What further local geological and thermo-hydro-mechanical data is required for more accurate predictions? A shear-dilation-based model (FRACSIM3D; Jing et al., 2000), updated for new joint constitutive laws, was used in this work to help on the design of an engineered geothermal energy system for each uncertain geological (fracture network) and thermo-hydro-mechanical (properties of the medium) scenario. Although McClure and Horne (2014) propose different hydraulic stimulation mechanisms (pure opening mode, pure shear stimulation, primary fracturing with shear stimulation leakoff, and mixed-mechanism stimulation), shear displacement is still the widest accepted mechanism to permanently enhance the transmissivity of the natural fractures (e.g., Evans et al., 1999, Genter et al., 2010; Jalali et al., 2018). Jacking (i.e. fracture-normal dilation) can also occur near the open-hole section, but its effect declines over time with the depressurization (e.g. Evans et al., 1999; Jalali et al., 2018). Nevertheless, field observations at the Fenton Hill test site have been supporting mixed-mechanism stimulation, involving propagation of hydraulic splay fractures due to stress changes induced as fractures opened and failed to shear (Norbeck et al., 2018). Thus, highlighting the importance of field tests to better characterize the subsurface and understand stimulation mechanisms.

Studies have shown that considering the effect of thermoelasticity tends to improve the flow rates, decrease water loss, and reduce the hydraulic impedance (e.g., Jing et al., 2014). In this study, although the thermoelasticity module has already been developed for FRACSIM3D, the authors focused only on the hydro-mechanical and thermo-hydro coupling processes. Nevertheless, future improvements can be foreseen to include this module and assess the variability between considering only poroelasticity and considering both thermo and poroelasticity effects. The simulations reveal that the development of hydraulically stimulated geothermal reservoirs is favored in a high temperature, hydraulically conductive and mechanically weak (in terms of low magnitude of the principal stresses and low resistance of fractures to deformation and opening) subsurface, i.e., the best-case scenario assumed in this study. If the reservoir temperature and subsurface hydraulic conductivity are decreased and the magnitude of the principal stresses and the fractures resistance to deformation and opening is increased, then developing engineered geothermal energy systems is more difficult. In fact, the base-case scenario assumed in this study only generated reservoirs of potential interest for fracture longer than sampled in the field. Moreover, if the worst-case scenario is the one prevailing in the study area, then engineered geothermal energy systems are not a viable alternative off-grid technology to offset fossil fuels consumption in the community of Kuujjuaq. Nevertheless, the work conducted suggest it is worth doing additional work to improve these predictions with further geothermal exploration. Exploratory boreholes deeper than 300 m are necessary to carry out more accurate estimations of the subsurface temperature, stress field regime and fracture network. Hydraulic stimulation field tests are also required to obtain more accurate information on the hydromechanical behavior of the subsurface. Although numerical models are fundamental to support the design and operational planning of engineered geothermal energy systems, reservoir simulation is a complex endeavor that requires careful calibration (Gilman et al., 2013). Hydraulic stimulation is accompanied by induced seismicity and the cloud of events is an important monitoring tool to understand the direction in which the reservoir can develop (e.g., Pine et al., 1984; Evans et al., 2005; Brown et al., 2012). Moreover, fracture seismic observations recorded before, during and after hydraulic stimulation enable to build time-lapses to map the fluid flow in the rocks and thus estimate the reservoir connectivity changes over time (e.g., Sicking et al., 2019). The fracture seismic method is based on the recording and analyzing of passive seismic data. Drilling the wells without previous knowledge of the reservoir growth direction, jointing pattern and in situ stress field can severely compromised a stimulated geothermal project (e.g., Pine et al., 1984; Brown et al., 2012). A lesson learned from Rosemanowes stimulated geothermal project is that the wells should be drilled with their azimuths parallel to the minimum in situ horizontal stress direction (e.g., Richards et al., 1994). In the current work, the wells were assumed vertical, but further simulations can be envisioned by changing their azimuth. However, the uncertainty associated with the direction of the stress field must be resolved. Microseismic monitoring can also be used to infer the fracture shear displacement (e.g., Evans et al., 2005). Additionally, an artificial neural network-genetic algorithm-based displacement back analysis has been proposed by Zhang et al. (2015) to estimate fracture stiffness, in situ stresses and elastic parameters from borehole displacements during drilling. Laboratory tests are also an important component to understand the joints behavior (e.g., Chen et al., 2000; Barton, 2013; Frash, 2014; Mao et al., 2017; Deb et al., 2020a; Hu et al., 2020; Deb et al., 2021; Weydt et al., 2021). However, care must be taken due to scaling effects. Nevertheless, the laboratory tests provide first-order calibrations for the fractures opening parameters. Although these were not conducted in the scope of this study, future work can be envisioned to carry out laboratory experiments and modify the input parameters accordingly. Moreover, further simulations can be carried out by changing the configuration from a doublet to a triplet, for instance. Two injectors and one producer may help to develop hydraulically stimulated geothermal reservoirs for the base-case scenario with shorter fractures. This can however impact the capital cost associated to wells.

Chemical mineral dissolution by alkaline or acidic additives was used at Soultz to clean joints, faults and pore volume and, thus, helping to enhance the natural permeability of these structures (Genter et al., 2010; Koelbel et al., 2017). The application of chemical stimulation may be an additional option for further studies in Kuujjuaq if future geothermal exploration reveals the presence of fractures infilling material that can react to this procedure. If this is observed, then a 3D water/rock chemical interaction module has been developed for FRACSIM3D (Jing et al., 2002) that can be used to simulate both hydraulic and chemical stimulations and evaluate the system performance response. Moreover, laboratory experiments with lithologies analogous to the potential reservoir rock in Kuujjuaq can provide further insights of whether or not chemical stimulation may be effective (e.g., Farquharson et al., 2020). Thermal stimulation can also be applied to increase the near-wellbore productivity (e.g., Saadat et al., 2010; Grant et al., 2011).

The numerical simulations carried out considered water as the working fluid. Further improvements can be carried out to assess the change in performance if supercritical CO_2 is used instead. This concept was proposed by Brown (2000) and the advantages of operating engineered geothermal energy systems with supercritical CO_2 are twofold: 1) CO_2 has certain thermophysical and chemical properties that make it an attractive heat transfer medium and 2) such systems can promote geological storage of CO_2 as an ancillary benefit. Numerical simulations have been carried out by several authors, and their results suggest a significant performance improvement compared to water (Pruess, 2006; Pruess, 2008; Guo et al., 2019). Pruess (2006) numerical simulations reveal thermal extraction rates approximately 50% larger for CO_2 compared to water. This suggests that flow rates 50% lower than the ones currently estimated for Kuujjuaq may be enough to extract the same amount of energy. In 2012, the 14 diesel power plants in Nunavik contributed with 65 000 tonnes/year of CO_2 equivalent (Karanasios et al., 2006f). This equals to a flow rate of approximately 2.1 L s^{-1}. Assuming that the required flow rate to meet Kuujjuaq's minimum heating demand threshold is now 7 L s^{-1} instead of 14 L s^{-1} estimated using water as the working fluid, then 3.5 years of capture and storage of CO_2 are needed to reach that flow. This suggests that, although CO_2 can be captured from the thermal plants, used in engineered geothermal energy systems (e.g., Bonalumi, 2018) and its thermal performance was proven superior to water (e.g., Pruess, 2006), this solution is not technically neither economically viable for northern communities. The amount of CO_2 produced by a single diesel power plant is insufficient to meet Kuujjuaq's demand, for example, and shipping additional CO_2 from other communities and southern areas can increase the costs of the geothermal project and may bring additional environmental impacts. In fact, a review of large-scale CO_2 shipping has been undertaken by Baroudi et al. (2021) and the transport costs range between \$10 and \$167 per tonne CO_2, depending on the travel distance and transport capacity. An alternative working fluid, supercritical N_2O, was proposed by Olasolo et al. (2018) due to its thermodynamics properties, but still perhaps not a viable solution for remote northern communities.

The second research question was: Are the deep geothermal energy sources harvested by engineered geothermal energy systems in Kuujjuaq cost-competitive compared to fossil fuels? The levelized cost of energy was estimated based on literature values for US proposed by Sanyal et al. (2007) and increased by factors of 2 and 5 to be more on the range expected in remote northern regions. Empirical well cost models were also used (e.g., Limberger et al., 2014 and references therein). Two 4-km-deep wells were inferred to cost from 9.8 to 12.1 M\$ (in USD). However, Minnick et al. (2018) refer that in Nunavut (northern Canada) a full-size 4-km production well can cost approximately 12 M\$ (in USD). This corresponds to twice the estimated price in this work since Minnick et al. (2018) estimate includes expenses associated to Nunavut's challenging environment. Such difference leads to an increase of 14 to 31% of the capital cost, which in turn increases the levelized cost of energy. The levelized cost of energy, considering the literature well cost models and assuming heat production only, ranges between

83 $ MWh^{-1} and 265 $ MWh^{-1} for the likely scenario. Doubling the well costs that is likely the case in Nunavik leads to values varying between 108 $ MWh^{-1} and 345 $ MWh^{-1} (in USD).

Nevertheless, the first-order evaluation carried out in this study suggests that engineered geothermal energy systems may have commercial interest. The probability of geothermal heat production be lower than the business-as-usual (oil furnaces) ranges from a minimum of 8% to a maximum of 91%. This probability can be increased if the energy consumption of the community is near or above its maximum estimated value and if the capital cost is decreased to its minimum value.

Furthermore, if the best-case scenario prevails in the study area, then combined heat and power may be a viable option to, not only increase the sustainability of the geothermal system, but also to decrease the levelized cost of energy and, thus, increase the economic potential. In fact, combined heat and power have more than 99% of probability to provide electricity at lower cost than the current diesel power plants. It is important to highlight that the geothermal system was assumed to be working 24h per 7 days during the 30 years of project lifetime. The most likely levelized cost of energy, for heat production only, in this study, was found to range between a minimum of 83 $ MWh^{-1} and a maximum of 265 $ MWh^{-1} (in USD). For combined heat and power, the most likely levelized cost of energy ranges between the minimum of 218 $ MWh^{-1} and the maximum of 262 $ MWh^{-1} (in USD). These values are within the range referred by Tester et al. (2006) and Augustine (2011), 100 to 1000 $ MWh^{-1} and 140 to 310 $ MWh^{-1} (in USD), respectively. However, Tester et al. (2006) also mention that with mature and cheaper technology, the levelized cost of energy can reach values as lower as 36 to 92 $ MWh^{-1} (in USD). Nevertheless, it is convenient to highlight that the levelized cost of energy in those aforementioned studies are for electricity generation only and not heat production or combined heat and power.

A previous economic potential assessment of geothermal energy sources in northern Canada undertaken by Majorowicz et al. (2014b) suggest a total cost of the project of 26 M$. These estimations were carried out for a depth of 3 to 5 km, doublet spaced 550-700 m, reservoir temperature of 120 ºC and flow rate of 30 L s^{-1}. The remaining estimations presented by the authors were done for electricity generation only, thus difficult to compare with the results obtained in the current study. Nevertheless, these authors evaluated a cost ranging from 0.50 to 0.84 $ kWh^{-1}. Additionally, Richard (2016) carried out an assessment of the viability of engineered geothermal energy systems for electricity generation in Québec. The base-case estimated production costs were found to vary between a maximum 1.25 $ kWh^{-1} at 4 km and for a reservoir temperature of 100 ºC and a minimum of 0.18 $ kWh^{-1} at 10 km depth, 250 ºC and a reduced drilling cost. In this work, an engineered geothermal energy system in Kuujjuaq for direct-use applications indicates a most likely cost of 0.08 to 0.27 $ kWh^{-1} while combined heat and power is 0.22 to 0.26 $ kWh^{-1}. Thus, deep geothermal energy sources harvested by engineered geothermal energy systems may be cost-competitive compared to fossil fuels, and further gathering of information is worthwhile to improve these predictions.

6.7 Conclusion

Geothermal energy off-grid technologies are a solution to improve the energetic framework of the 239 Canadian remote northern communities that rely solely on diesel for electricity and space heating. Although bounded by high uncertainty, the results of this work suggest that engineered geothermal energy systems are technically and economically viable in the community of Kuujjuaq (Nunavik, Canada) to supplant the reliance on fossil fuels. A "what-if" approach was followed in this study to deal with the poor subsurface knowledge. The engineered geothermal energy systems designed for each uncertain scenario needed to provide enough thermal energy for direct use applications during the 30 years of operation and be within certain defined performance parameters limits. These were: water loss lower than 20%, reservoir flow impedance lower than 0.1 MPa L^{-1} s^{-1} and thermal drawdown lower than 1 ºC/year. The numerical simulations revealed that developing hydraulically stimulated geothermal reservoirs is favored in a high temperature, hydraulically conductive and mechanically weak (in terms of low magnitude of the principal stresses and low resistance of fractures to deformation and opening) subsurface. Decreasing the reservoir temperature and hydraulic conductivity and increasing the magnitude of the principal stresses and fractures resistance to deformation and opening, decreases the performance of the system. Moreover, placing the wells parallel to the inferred direction of the maximum principal stress revealed better performance than if the wells are located parallel to the fault plane. Furthermore, longer fractures tend to improve the performance of the system. Smaller fractures have higher shear stiffness and tend to slip less, making fluid circulation more difficult. Additionally, the best-case scenario suggest that combined heat and power is possible during the first 10 to 15 years of the geothermal system operation.

A first-order evaluation of the capital cost and levelized cost of energy was carried out using Monte Carlo method. Results for capital cost is in the range 25 to 67 M$ for the optimistic scenario, 38 to 122 M$ for the likely scenario and 79 to 289 M$ for the pessimistic scenario (in USD). Global sensitivity analysis based on correlation coefficient reveal that the power plant and surface facilities cost is the most influential parameter on the capital cost followed by the well cost and stimulation cost. The levelized cost of energy, assuming heat production only, was estimated to range within 54 and 145 $\$$ MWh^{-1} for the optimistic scenario, between 83 and 265 $\$$ MWh^{-1} for the likely scenario and between 170 to 626 $\$$ MWh^{-1} for the pessimistic scenario (in USD). Combined heat and power revealed levelized cost of energy varying between 120 and 143 $\$$ MWh^{-1} for the optimistic scenario, 218 – 262 $\$$ MWh^{-1} for the likely scenario and 510 – 617 $\$$ MWh^{-1} for the pessimistic scenario. The probabilistic analysis carried out indicate that engineered geothermal energy systems have 8 to 91% probability of providing heating energy at a lower cost than the current oil furnaces and more than 99% chance of providing electricity at a lower cost than the diesel power plants currently in place. Given that geothermal energy is a local source available for remote community, further geothermal exploration is recommended and indispensable to decrease the existing uncertainties and support decisions to develop this energy alternative. Hence, helping remote northern communities moving towards a greener and sustainable energetic future.

7 GENERAL DISCUSSION AND CONCLUSIONS

Ensuring that rural, remote and Indigenous communities currently relying on diesel have the opportunity to be powered by clean and reliable energy by 2030 is one of Canada's commitments (ECCC, 2020). The transition from diesel to renewable energies can help with the local economic development, improving the communities' living standards and well-being. Furthermore, the energy transition of the off-grid diesel-based settlements can allow to reduce pollution and to achieve the greenhouse gas emissions proposed targets (ECCC, 2020). Therefore, the study of local renewable energy sources capable to meet a significant percentage of the communities' heating and power needs and to be obtained at a competitive cost with diesel has been gaining interest and clean power projects have nearly doubled over the past five years (e.g., Pembina Institute, 2020). Moreover, after a long period of inertia, deep geothermal energy is starting to be seen as a cutting-edge opportunity, with several provincial and territorial projects underway throughout Canada (e.g., Hickson et al., 2020).

However, assessing the deep geothermal energy source potential in remote northern regions is challenging. First, due to remoteness, and second, due to important data gaps as highlighted throughout this thesis. In the southern part of Canada, the interest is to find geothermal anomalous zones that can be developed with power sell on connected electrical grids. In northern regions, however, the interest is to feed micro-grids. Thus, the deep geothermal energy source assessment should be community-focused to avoid extrapolate sparse data over large regions and blind local potential by regional anomalies. Therefore, an original approach was followed in this thesis using unconventional geothermal exploration tools that are affordable for remote northern communities to provide a first-order prediction of the local geothermal energy source potential. The work achieved can be seen as a first step to justify whether or not deep exploration drilling should be completed, and further field campaigns and field tests should be carried out. In such remote areas, exploration drilling, field campaigns and field tests are more expensive than in the south such that development of new exploration methods using outcrops as subsurface analogues, shallow groundwater monitoring wells for heat flux assessment, numerical modeling and uncertainty quantification appear essential to reduce risks. Ultimately, deep drilling and further field campaigns will provide more accurate predictions if local communities choose to explore their geothermal resources.

The viability of geothermal energy as an alternative solution for the off-grid diesel-based communities depends upon an accurate field characterization. Nakatsuka (1999) proposed that, beyond regional and local geology, thermal structure, fracture network and rock mechanics and stress regime are key parameters having a profound influence on the design of engineered geothermal energy systems. Therefore, this thesis aimed at characterizing these parameters and provided first-order answers to key questions that arise during the early-stage exploration of deep geothermal energy sources in remote areas:

1) How to characterize geothermal energy sources associated to petrothermal systems based on surficial data?
2) How to infer the terrestrial heat flux from temperature profiles shallower than 100 m depth and perturbed by climate events?
3) Which geological and technical uncertainties are the most influential parameters affecting the ability to evaluate the deep geothermal energy source? Can the deep geothermal energy source in-place meet the community's heat/power demand?
4) What is the stress regime prevailing in Kuujjuaq? Are there sufficient fracture planes optimally oriented for slip at sufficiently low fluid pressure? What is the critical fluid pressure to reactivate the fracture planes?
5) Will the hydraulic stimulation technique applied in crystalline basement rocks develop a well-connected flowing system in Kuujjuaq? How can this be done? What further local geological and thermo-hydro-mechanical data is required for more accurate predictions? Are the deep geothermal energy sources harvested by engineered geothermal energy systems in Kuujjuaq cost-competitive compared to fossil fuels?

The first of these research questions is answered in **Chapter 2. Thermophysical properties of surficial rocks: a tool to characterize geothermal resources of remote northern regions**. This chapter provides the background information on the rock samples collected from outcrops in terms of main mineral phases, major, minor and trace geochemical elements, thermal properties and radiogenic heat production. Moreover, a preliminary evaluation of the steady state temperature distribution and surface heat flux was carried out based on a simplified conceptual model for the crust beneath Kuujjuaq. Four different laboratory techniques commonly applied to characterize thermal conductivity and radiogenic elements were used in this chapter to assess how the laboratory techniques influence the numerical modeling of the subsurface temperature. Thermal conductivity was analyzed using two devices, the optical scanning and the guarded heat flow meter. The former is based on a transient method while the latter on a steady state. Transient techniques are to evaluate thermal conductivity considering the time-dependent energy dissipation process in a sample (Somerton, 1992). Steady-state methods, in turn, evaluate thermal conductivity by establishing a temperature difference invariable with time under a steady state heat flow through the sample (Somerton, 1992). Radiogenic heat production is often evaluated based on Rybach (1988) empirical relationship considering the concentration of the elements U, Th and K. Laboratory methods and field devices are available to assess the concentration on those elements. In this thesis, inductively coupled plasma – mass spectrometry (commonly ICP-MS) and gamma-ray spectrometry with a NaI(Tl) detector were used. A comparative study between HPGe and NaI(Tl) detectors was carried out by Hossain et al. (2012) and concluded that the HPGe detector has higher resolution than the NaI(Tl), but the latter has higher efficiency. The resolution describes the capacity of the detector in separating two adjacent energy peaks (Hossain et al., 2012). Efficiency is a measure of the percentage of radiation detected from the overall yield that is emitted from the source (Hossain et al., 2012). In situ gamma-ray spectroscopy surveys are also commonly used for geothermal exploration (e.g., McCay et al., 2014). However, factors such as decay series disequilibria, topographical errors and atmospheric influence during surveying can lead to unrepresentative results of the underlying rock (McCay et al., 2014). In fact, an in-situ survey was undertaken in Kuujjuaq and the comparison with laboratory methods reveal a variation of 16% to 57% for U, 16% to 63% for Th and 3% to 34% for K (Appendix II). Sêco et al. (2021) propose a series of procedures to acquire gamma-ray spectrometry data to reduce this variability observed between in situ and laboratory analysis. Although their approach was developed for sedimentary rocks, it can be adjusted for other lithologies.

Chapter 3. A numerical approach to infer terrestrial heat flux from shallow temperature profiles in remote northern regions answers the second research question using the data obtained on the previous chapter. Moreover, based on the laboratory analyzes, empirical relationships were developed for the combined effect of pressure, temperature and water saturation on thermal conductivity and implemented on the numerical model. A key point when evaluating terrestrial heat flux in regions that were covered by ice sheets is related with the paleoclimate. Often, borehole climatology (e.g., Bodri et al., 2007) is the preferred method to reconstruct the ground surface temperature history and simultaneously infer the terrestrial heat flux by temperature inversion techniques (e.g., Mareschal et al., 1999, Beltrami, 2001). However, a literature-based glacial paleoclimate history (e.g., Flint, 1947; Emiliani, 1955) and Birch's (1948) analytical solution have commonly been used for geothermal energy sources evaluation in southern areas (e.g., Bédard et al., 2018; Gascuel et al., 2020). Recently, improvements have been made to consider not only glacial periods corrected analytically as the recent meteorological records corrected numerically (e.g., Velez Marquez et al., 2019).

The numerical approach described in this chapter goes further, considering the Holocene events and carrying out the paleoclimate corrections numerically, allowing the simultaneous evaluation of the terrestrial heat flux. The numerical approach is based on a 1D inverse heat conduction problem simulated with the finite element method, where the Nelder-Mead algorithm and the least-squares method were used to find the optimized heat flux based on function comparison. The coordinate-search algorithm is also available to find the solution for this inverse problem. Both Nelder-Mead and coordinate-search are direct-search derivative-free methods, but the former is simplicial and the later directional. Simplicial direct-search methods are based on simplices and operations over simplices, like reflections, expansions, or contractions (Conn et al., 2009). In directional direct-search methods, sampling is guided by a set of directions with appropriate features (Conn et al., 2009). Both methods are described with details in, for example, Conn et al. (2009). Furthermore, Nelder-Mead algorithm was chosen in this thesis after carrying out preliminary simulations using both algorithms that revealed the same optimized heat flux value.

Chapter 4. Uncertainty and risk evaluation of deep geothermal energy source for heat production and electricity generation in remote northern regions answers the third research question. The thermophysical properties and terrestrial heat flux obtained in the previous chapters were used for the numerical modeling of the 2D subsurface temperature with time-varying upper boundary condition and evaluation of the thermal energy in-place. The volumetric method together with Monte Carlo simulations are often used to evaluate the latter (e.g., Sarmiento et al., 2013; Trota et al., 2019; Wang et al., 2021). Fundamental to uncertainty quantification is to study the influence of each uncertain input parameter and how the input uncertainty impacts the response of the system and affect the reliability of output. A good understanding of how input parameters influence the output response is key to identify high-impacting parameters and aid to select which data to acquire to reduce the uncertainty of said parameters (Scheidt et al., 2018). The Monte Carlo method allows to simulate the ensemble of uncertainties and perform a sensitivity analysis to identify the parameters having the highest impact. Screening techniques based on one-at-a-time method (Scheidt et al., 2018) were used to provide a first evaluation of parameter sensitivity, i.e., to rank the parameters based on their importance via tornado charts. This method however does not define the input parameters as sensitive or insensitive. Therefore, sensitivity analysis was undertaken using linear-based models such as scatter plots and correlation coefficient to assess the relationship between parameter and response (Scheidt et al., 2018). The Spearman correlation coefficient was used to assess which parameters are influential and which are not. A strong correlation coefficient between an input and a response indicates an influential parameter (Scheidt et al., 2018).

The fourth research question was answered in **Chapter 5. Fracture network and stress regime: Implications for the development of engineered geothermal energy systems in remote northern regions**. The former chapters correspond to the thermal structure with reference to the field characterization concept of Nakatsuka (1999). This chapter, in turn, presents the fracture network and stress field characterization. Characterizing the natural fractures is paramount for the development of both statistical and deterministic fracture networks. These constitute the basis when designing engineered geothermal energy systems (e.g, Richards et al., 1994; Genter et al., 2010; Barton et al., 2012). Although studies comparing outcrop and subsurface fractures have revealed some discrepancies (Bauer et al., 2017), outcrops are still widely used to predict natural fracture networks in the subsurface (Howell et al., 2014). The fracture attributes (i.e. orientation, dip, spacing, length, infilling, aperture, frequency, relative age) and topology can be recorded in the field using the scanline and window sampling methods, which was done in the scope of this work. Statistical analyzes and generation of stochastic fracture networks are discussed in the present chapter whereas the results of the topology analysis are examined in Appendix I.

Additionally, the knowledge of the geomechanical behavior of a hydraulically stimulated geothermal reservoir is paramount for the reservoir optimization and to mitigate technological and financial risks (e.g., Evans et al., 1999; Ghassemi, 2012; Amann et al., 2018; Tomac et al., 2018; Kumari et al., 2019). Stress and rock mechanics aspects relevant to engineered geothermal energy systems are discussed in detail in, for example, Evans et al. (1999), Ghassemi (2012), Xie et al. (2015), Amann et al. (2018), Tomac et al. (2018) and Kumari et al. (2019). A lesson learned from Fenton Hill and Rosemanowes geothermal projects was the importance of the accurate knowledge of the in-situ stress regime (e.g., Richards et al., 1994; Brown et al., 2012). The poor knowledge of this parameter can lead to an incorrect design of the engineered geothermal energy system and thus, severely compromise the project. The final rock stress model is derived based on a combination of available stress data from the best estimate stress model, the new stress measurements methods on site and from integrated stress determination using previous data and numerical modeling (Figure 7.1; Stephansson et al., 2012). In fact, before measuring virgin stresses, an attempt should be made to obtain an estimate of the in-situ stress field by applying stress versus depth relationships or observations from past measurements (Amadei et al., 1997). Topography, geology, rock fabric, rock loading history, first motion analysis of earthquakes, occurrence of stress release phenomena, breakouts in boreholes, tunnels and shafts, rock bursts, and the presence of stratification, heterogeneities and geological structures are other important sources of information (Amadei et al., 1997).

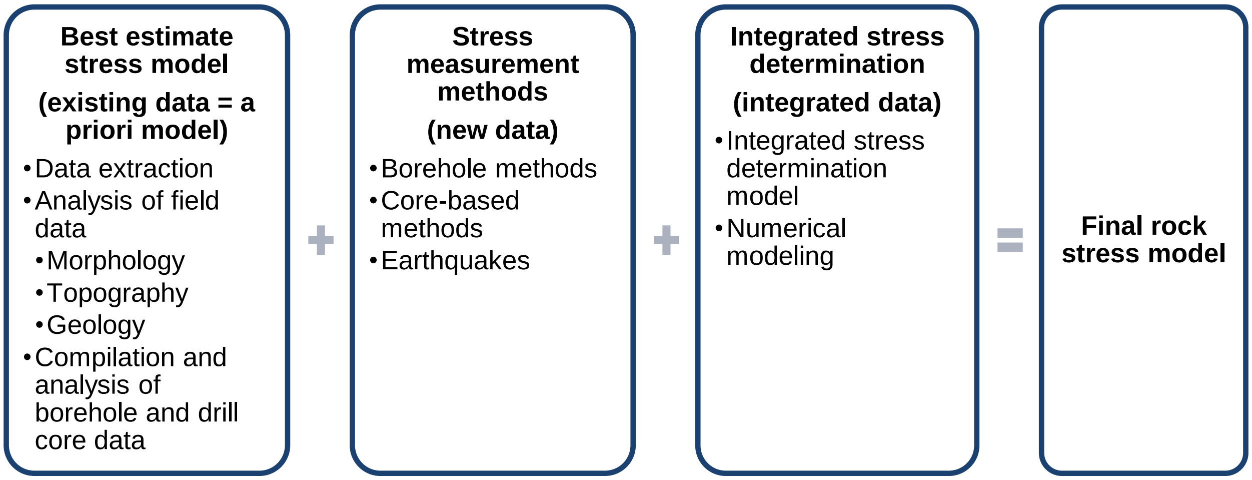

Figure 7.1 Strategy approach to infer the final in situ rock stress model, redrawn from Stephansson et al. (2012).

No stress measurements were carried out in this thesis that rather focused on the estimation of stress model (or a priori stress model; Figure 7.1) using available regional data. This model was built on 1) geological indicators for a first-order characterization of the direction of the principal stresses and 2) empirical correlations and analytical models calibrated with published literature data for the Canadian Shield for a preliminary evaluation of the magnitude of the principal stresses. Monte Carlo simulations were also carried out to deal with the uncertainties of each input parameter. However, it is important to keep in mind that the a priori stress model shall not substitute the in-situ measurements. In fact, the current stress state in an area is the superposition of stress components and the end-product of a series of geological events. Moreover, stresses can vary both spatially due to the inhomogeneity of rock masses and temporally due to tectonic events, erosion, glaciation, etc. Furthermore, the nowadays rock fabric may or may not be correlated with the current stress field (Terzaghi, 1962).

The last research question is addressed in **Chapter 6. Techno-economic analysis of engineered geothermal energy systems for direct-use applications in arctic off-grid communities: parameter uncertainty and sensitivity studies**. The previous chapters provide the inputs for the numerical modeling carried out. Moreover, working hypotheses for the hydromechanical properties were used to define worst-, base- and best-case scenarios. No rock mechanics laboratory experiments neither field tests were carried out in the scope of this work, and therefore large uncertainty exists on the working hypotheses used and on the results of the numerical model. Nevertheless, they provide a first-order approximation for engineered geothermal energy systems as an off-grid solution to offset diesel consumption in remote northern regions.

Engineered geothermal energy systems involve the permeability enhancement of the natural fractures existing in crystalline basement rocks, the forced circulation of a fluid (often water) between injection and recovery wells through the pressurized region, and the thermal energy extraction by conduction and advection mechanisms (e.g., Willis-Richards et al., 1995). Carrying out numerical experimentations of engineered geothermal energy systems are crucial to predict the performance of the reservoir, lending support to the design and operational planning (Willis-Richards et al., 1995). However, the modeling task is demanding due to 1) the strong dependence of reservoir flow properties on the fluid pressures encountered during high pressure injection and 2) the lack of sufficient field data to adequately characterize the rock mass in terms of in situ fracture compliance, shear behavior or fracture length distributions (Willis-Richards et al., 1995).

Over the years, several numerical simulators have been proposed in the literature. For example, Hayashi et al. (1999) reviewed numerical models to simulate hydraulically stimulated geothermal reservoirs by surveying governing factors (i.e. rock stress, joint mechanical properties, flow within fractures and heat transfer) and coupling (thermal, hydraulic, chemical and mechanical). The codes included in Hayashi et al. (1999) discussion are: SFV, FFD, FRIP, ROCK FLOW, FEHM, GEOTH3D, GEOCRACK, FRACTure, Fractal Fracture Networks, FRACSIM2D, FRACAS. These authors concluded that further research was needed to deal with aseismic reservoir growth, modeling of water/rock chemical interaction, modeling of relative permeability for two -phase flow and modeling of change of rock properties with time. Sanyal et al. (2000) carried out a review of numerical simulators focused on the explicit representation of fractures, change in fracture aperture due to effective stress and shear, thermo-elastic effects, relation between fracture aperture and conductivity, channeling of fluid flow within fractures, mineral deposition and dissolution, ability to handle two-phase fluid flow, heat transfer and tracer transport. The review included the following codes: TOUGH2, TETRAD, STAR, GEOCRACK, FEHM, FRACTure, GEOTH3D and FRACSIM3D. According to Sanyal et al. (2000), these numerical models are capable to address almost all of the aforementioned desirable features, but none is able to handle them all. Recently, White et al. (2018) also undertook a review of modern numerical simulation tools. The reviewed codes are: FALCON,

FLAC3D, TOUGH, NUFT, GEOS, FEHM, CFRAC, PFLOTRAN, GeoFrac-Mech, GeoFrac-Stim, STOMP, TOUGHREACT, CFRAC-Stanford, GPRS, CFRAC-UT, MULTIFLUX, THOUGH2 and 3DEC. A suite of benchmark problems was proposed to test the ability of these numerical simulators to solve coupled thermal, hydrologic, geomechanical and geochemical processes (White et al., 2018). The authors concluded that the results from the different codes were comparable, but further research is still needed. Uncertainty, for example, tends to increase with the number of coupled processes in the problem and modeling strong coupled processes remains challenging (White et al., 2018).

The numerical model used in this chapter to carry out the thermo-hydro-mechanical modeling is the updated version of FRACSIM3D of Jing et al. (2000). FRACSIM3D has been shown to be an appropriate approximate model capable to address simultaneously the problems associated with fracture generation, hydraulic stimulation, fluid circulation and heat extraction (Jing et al., 2000; Fomin et al., 2004; Hashida et al., 2015). FRACSIM3D handles the following coupled processes (Hayashi et al., 1999):

- H-M (hydro-mechanical): rock stresses responding to fluid pressure changes
- T-M (thermo-mechanical): rock stresses responding to temperature changes
- M-H (mechanical-hydro): fracture flow apertures responding to stress changes
- H-T (hydro-thermal): heat transfer by fluid flow
- T-H (thermal-hydro): viscosity and flow patterns changing with temperature

Moreover, according to Sanyal et al. (2000), FRACSIM3D is capable to address almost all of the desirable features, with exception of channeling, porous flow in matrix and multi-phase flow. Nevertheless, the code is open-source and improvements can be carried out. The mathematical basis of FRACSIM3D is described in Jing et al. (2000) and Fomin et al. (2004). The accompanying papers of Willis-Richards (1995) and Willis-Richards et al. (1996) and unpublished technical notes written by the authors of the model are also recommended for a full understanding of the mathematical model and assumptions.

A “what-if” approach was used in this chapter to provide a range of possibilities and help to design an engineered geothermal energy system for each of the uncertain scenarios that provides the thermal energy needed for the community, keeping the water losses lower than 20%, the reservoir flow impedance lower than 0.1 MPa L^{-1} s^{-1} and the thermal drawdown lower than 1 ºC/year. The levelized cost of energy was additionally evaluated in this chapter considering optimistic, likely and pessimistic scenarios for stimulation, power plant and other surface facilities and operation and maintenance costs.

7.1 Contributions

This thesis made several scientific contributions that allowed to better understand if geothermal energy can be an off-grid solution to offset diesel consumption in the community of Kuujjuaq. The research undertaken led to a better understanding of the subsurface thermo-mechanical conditions and of the geothermal energy source hosted beneath the community of Kuujjuaq. Moreover, the potential of harvesting this thermal energy by engineered geothermal energy systems was studied and its cost compared to diesel was assessed. The main contributions of this thesis are listed below:

1. Assessment of the uncertainty associated with different laboratory techniques and intrinsic heterogeneity of the lithologies in heat conduction models
2. Development of experimental relationships to describe the effect of temperature, pressure and water-saturation on thermal conductivity
3. Development of a model to numerically simulate paleoclimate events and simultaneously infer the terrestrial heat flux from temperature profiles shallower than 100 m
4. Sensitivity analysis of the influence of the temperature signal during a glacial event on heat flux and subsurface temperature
5. Prediction of 2D subsurface temperature distribution beneath Kuujjuaq considering paleoclimate events
6. Evaluation of the “heat-in-place” beneath Kuujjuaq using a Monte Carlo-based global sensitivity analysis to identify high-impact parameters affecting the assessment of potential heat and power output and the forecast of future energy production through risk analysis
7. Characterization of the fracture network in Kuujjuaq based on scanline sampling and using horizontal outcrop surfaces and topology analysis to evaluate the network connectivity
8. Estimates of the in-situ stress regime considering geological indicators, empirical correlations and analytical models
9. Development of a preliminary conceptual geological model for the lithosphere beneath Kuujjuaq based on regional geological and geophysical published literature and proposal of a 1D theoretical rheological profile considering the structural information and temperature estimates
10. Evaluation of the presence of optimally oriented fractures, their state of stress and critical fluid pressure for their reactivation considering the inferred stress regime

11. Identification of the key role played by the in-situ fluid pressure and static friction angle when evaluating the state of stress of fractures
12. Evaluation of the performance of engineered geothermal energy systems based on a "what if" approach to deal with the uncertainty of the input parameters and assess the optimal thermo-mechanical conditions of the subsurface for the effective hydraulic stimulation procedure
13. Evaluation of the levelized cost of energy assuming optimistic, most likely and pessimistic cost scenarios and probabilistic assessment of providing heat and power at a lower cost than the current oil furnaces and diesel power plants in place

7.2 Summary of the results

The evaluation of the thermophysical properties of the outcropping lithologies using different laboratory techniques revealed that, in Kuujjuaq, combining gamma-ray spectrometry and optical scanning gives lower base-case temperature predictions than combining mass spectrometry with guarded heat flow meter. Therefore, the combination of these methods is advised to avoid biased subsurface temperature predictions. The numerical model developed to simulate paleoclimate events and infer terrestrial heat flux from a 80-m-deep temperature profile indicate a terrestrial heat flux at 10 km depth varying between 31.8 and 69.4 mW m^{-2}, depending on paleoclimate and thermophysical properties conditions. Moreover, uncertainty quantification and sensitivity analysis revealed that subsurface temperature and recovery factor are the most influential parameters on the thermal energy available beneath Kuujjuaq. The potential heat and power output forecasts indicate that, given the current state of knowledge and the high uncertainty, electricity generation and combined heat and power are high to medium risk applications while heat production is low risk at a depth greater than 4 km. The probability of meeting the estimated annual average heating demand of Kuujjuaq is higher than 98%.

Furthermore, the characterization of the fractures surrounding Kuujjuaq revealed four main fracture sets striking approximately N81°E-N90ºE (E-W – F1), N161°E-N170ºE (NNW-SSE – F2), N11°E-N20ºE (N-S – F3) and N121°E-N130ºE (NW-SE – F4). The intensity of the fractures was found to range between a minimum of 0.3 fracture m^{-1} and a maximum of 3.7 fracture m^{-1}, with a median value of 0.8 fracture m^{-1}. The coefficient of variation calculated for each set revealed values of 0.4 for N-S and NW-SE sets and 0.7 for E-W and NNW-SSE. The heterogeneity of the distribution evaluated using the Kuiper's method revealed a value of 15%.

The length and fractal dimension were inferred to vary in the range of 2 – 28 m and 1.7 – 2.4, respectively. Geological indicators suggest the maximum and minimum horizontal principal stresses are oriented N210ºE-N220ºE and N300ºE-N310ºE, respectively. The plunge is assumed horizontal. The three principal stresses (vertical and horizontal) can be described by the following relationships:

- $\sigma_{\mathrm{V}} = 0.0271z$
- $\sigma_{\mathrm{H}} = 0.0430z + 8.62$
- $\sigma_{\mathrm{h}} = 0.0251z + 4.94$

Mohr-Coulomb friction and slip tendency analyzes revealed that, although most of the fracture planes are optimally oriented to slip, these are not at critical state of stress assuming in-situ hydrostatic regime. The effective principal stresses need to be decreased by more than 50% to reactivate these planes. Furthermore, the analyzes indicate that the fracture sets E-W, NNW-SSE and N-S have the highest tendency to slip, while the NW-SE will not be reactivated. The analysis of the thermo-mechanical conditions of the subsurface beneath Kuujjuaq, considering the base-case scenarios, seem unfavorable for the development of engineered geothermal energy systems. In fact, the best-case scenario, where a high temperature, hydraulically conductive and mechanically weak (in terms of low magnitude of the principal stresses and low resistance of fractures to deformation and opening) subsurface was assumed, favors the development of reservoirs of potential interest. In this case, the numerical simulations suggest that combined heat and power is possible during the first 10 to 15 years of the geothermal system operation. The levelized cost of energy assuming heat production only was estimated to range between 54 \$ MWh^{-1} and 617 \$ MWh^{-1} while combined heat and power varies between 120 \$ MWh^{-1} and 617 \$ MWh^{-1} (in USD). Moreover, engineered geothermal energy systems have 8% to 91% probability of providing heating energy at a lower cost than the current oil furnaces and more than 99% chance of providing electricity at a lower cost than the diesel power plants currently in place.

7.3 Future directions

Beyond the future directions discussed within each chapter, this section provides several other pathways that can be followed in the future to improve this first-order geothermal energy assessment.

7.3.1 Thermophysical properties

Although laboratory methods combined with relationships to describe the effect of pressure, temperature and water-saturation provide reliable values for the thermal conductivity, methodologies have been developed to evaluate these properties in situ. Thermal response test, for example, was proposed by Mogensen (1983) as an in-situ method to infer thermal conductivity profiles in shallow borehole heat exchangers and this method has been widely applied (e.g., Velez Marquez et al., 2018b; Zhang et al., 2018). Geophysical well logs are another methodology commonly used to predict thermal conductivity (e.g., Hartmann et al., 2005b; Fuchs et al., 2013; Nasr et al., 2018), and evaluate the concentration of radioelements (e.g., Caldwell et al., 1963; Hertzog et al., 1979). The lack of exploratory boreholes did not allow to use these methodologies, but further geothermal developments encompassing drilling for temperature-gradient wells will enable the application of these in situ exploration tools. Moreover, those temperature profiles can enable the application and improvement of the methodology described in McAliley et al. (2019). In their approach, temperature and heat flux are firstly simulated in a steady-state conductive regime from a known thermal conductivity model, boundary conditions and heat sources. Then, temperature and/or heat flux data are inverted for thermal conductivity to obtain a more general distribution of this parameter.

7.3.2 Heat flux and ground surface temperature history

Future developments of the numerical approach developed to infer terrestrial heat flux may pass by considering the groundwater flow, if detected in the measured temperature profiles, and by taking into account events of erosion and sedimentation. These have been observed to influence the terrestrial heat flux at surface. In fact, the effect of erosion on terrestrial heat flux is twofold: decrease due to removal of heat-producing elements and an increase due to movement of hot rock towards the surface (e.g., England et al., 1980). The low terrestrial heat flux values obtained for the study area suggests that crustal partial melting/metamorphism has driven out most of the crustal radiogenic elements into partial melts/hydrothermal fluids, which can have migrated upward and were incorporated into rocks now eroded.

The commonly used glacial history proposed by Flint (1948) and Emiliani (1955) was used in this thesis. However, the results highlight that the glacial periods have the major influence on the terrestrial heat flux at depth. Therefore, further climate studies can be envisioned to obtain a more reliable glacial history and, thus, more accurate paleoclimate corrections for temperature profiles. In fact, although the glacial paleoclimate history proposed by Flint (1947) and Emiliani

(1955) is widely accepted to carry out borehole-temperature corrections, more recent paleoclimate studies based on diverse climate proxies, glacial landforms and Milankovitch cycles have been enabling to tell a different history for the Quaternary glaciations. For example, studies indicate that the Early Pleistocene (2.6-0.8 Ma) was characterized by climatic fluctuations dominated by 41 ka precession cycles, during which the majority of cold periods were too short to enable the development of ice sheets (e.g., Ehlers et al., 2011; Miller et al., 2013). Only after the transition to the 100 ka cycles was fully established (800 ka), the cold periods started to be long enough to allow ice-sheet development on a continental scale and outside of the polar region (e.g., Ehlers et al., 2011; Miller et al., 2013). Analysis of marine benthic $\delta^{18}O$ records enabled Lisiecki et al. (2005) to construct a 5.3 Ma stack (the "LR04" stack; Figure 7.2) that, although cannot address the relative contributions of ice volume and temperature to the benthic $\delta^{18}O$ signal, it provides an accurate estimate of the total change. Foraminiferal $\delta^{18}O$ is a function of the temperature and $\delta^{18}O$ of the water in which it forms, and the $\delta^{18}O$ of seawater is a function of global ice volume and water salinity (Lisiecki et al., 2005). Thus, high $\delta^{18}O$ signal suggests low temperature and high global ice volume.

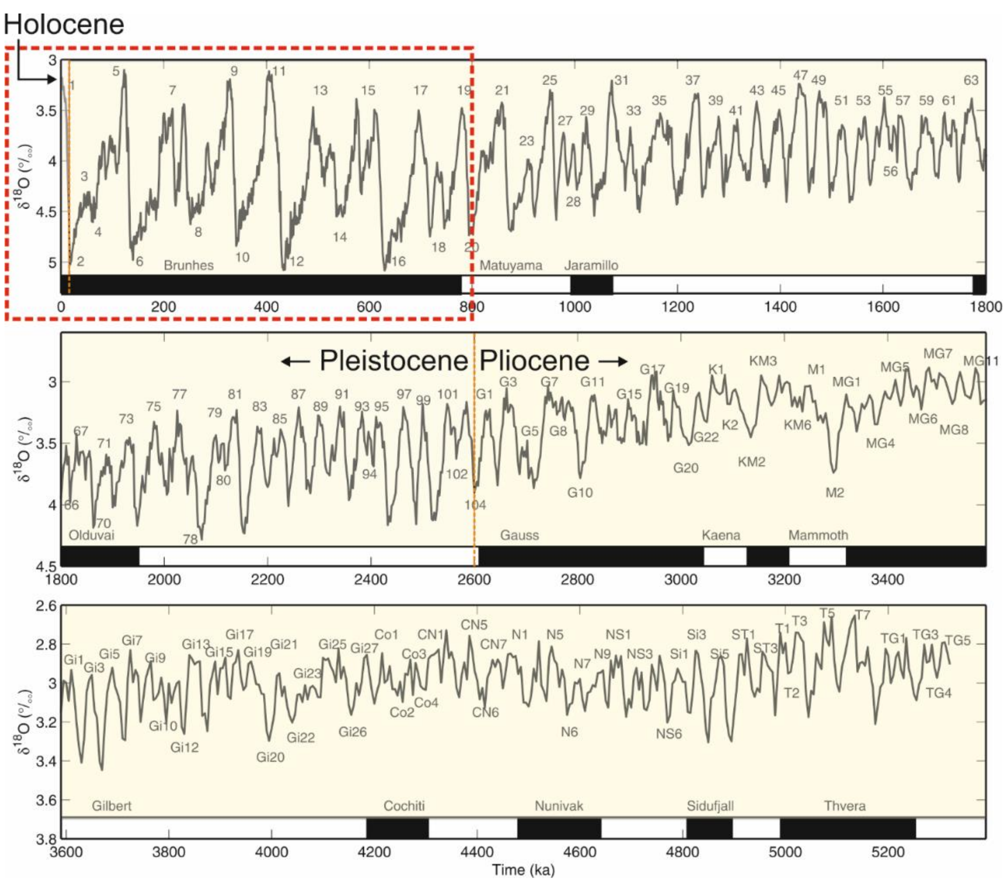

Figure 7.2 **LR04 benthic $\delta^{18}O$ stack. Red square – Late Pleistocene epoch ("Ice-Age"). The reader is referred to the original source for further details, redrawn from Lisiecki et al. (2005).**

The “LR04” stack clearly highlights the drastic climate change occurred after 800 ka (Figure 7.2) and indicates the periods of the later Pleistocene glaciations where substantial ice volumes were developed ($\delta^{18}O$ < 4.5; Figure 7.2). Thus, Marine Isotope Stage 16, 12, 10, 6 and 4-2 correspond to ice-age periods while Marine Isotope Stage 11, 9, 7 and 5 are important interglacial episodes (e.g., Ehlers et al., 2011; Jennings et al., 2013; Miller et al., 2013). The current Holocene epoch is considered itself an interglacial stage. Beltrami et al. (1995) proposed a relationship between oxygen isotope and ground surface temperature history. In Occhietti et al. (2004) and Occhietti et al. (2011) are discussed the Late Pleistocene-Early Holocene decay of the Laurentide Ice Sheet focused on southern Québec-Labrador. Viau et al. (2006) carried out temperature reconstructions and studied the temperature variation in North America during the Holocene. Lang et al. (2011) discusses the last 800 ka climate variability based on ice and terrestrial archives. A detailed 750 ka climate history for the North Atlantic is discussed in Channel et al. (2012). Jennings et al. (2013) and Andrews et al. (2013) discuss the Quaternary period in North America and Miller et al. (2013) present an extensive paleoclimate history of the Arctic. However, few authors discussed the ground temperature prior to the last interglacial Marine Isotope Stage 5e. Temperature trends during the Marine Isotope Stage 11 and its similarities with Holocene interglacial stage are presented by Milker et al. (2013) and Candy et al. (2014) while Vavrus et al. (2018) described similarities between the interglacial Marine Isotope Stage 19 and the Holocene. Marine Isotope Stage 15-13 were analyzed by Hao et al. (2015) who considered it as a continuous interglacial stage. Past Interglacials Working Group of PAGES (2016) reviewed the interglacial periods over the last 800 ka. The Marine Isotope Stage 3 and its effect on the reduction of the Laurentide Ice Sheet is discussed In Dalton et al. (2019).

Future geothermal development involving drilling of exploration boreholes may allow the use of algorithms to invert temperature profiles and provide a more accurate evaluation of the ground surface temperature history. The literature on inversion of temperature profiles is extensive and methods are, for example, described by Vasseur et al. (1983), Shen et al. (1983), Nielsen et al. (1989), Shen et al. (1991), Mareschal et al. (1992), Wang (1992), Shen et al. (1996) and Hopcroft et al. (2009). Moreover, in this thesis, the heat flux sensitivity analysis with respect to the paleoclimate history and the thermophysical properties uncertainties was carried out by defining worst-, base- and best-case scenarios in a deterministic manner. However, a probabilistic approach involving assimilation of paleoclimate uncertainty on estimates of surface heat flux is described by Matther et al. (2018), which can be followed in future work. Future improvements can also be done by additionally considering probability distribution functions for the thermophysical properties.

7.3.3 Subsurface temperature distribution and uncertainty quantification

The subsurface temperature distribution models presented in this thesis can be further improved by considering a probabilistic approach assimilating both paleoclimate and thermophysical properties uncertainties in one model rather than defining the worst-, base- and best-case scenarios in a deterministic manner. Moreover, a deeper temperature profile than the one acquired and used in this thesis may enable to follow and adapt the methodology described by Athens et al. (2019) for uncertainty quantification of temperature predictions in the subsurface.

7.3.4 "Heat-in-place" and uncertainty quantification

The most influential parameters in the "heat-in-place" and potential heat and power output were inferred through tornado plots and correlation coefficient. This method provided a qualitative assessment of the impact of a certain input on the output response. Another linear-based regression method for sensitivity analysis can be done through regression coefficients. The standardized regression coefficients provide a quantitative measure of the impact of the inputs on the output response (Scheidt et al., 2018). A certain input parameter with a large coefficient indicates that a unit change of that input corresponds to a large change in the output. Although this analysis was not carried out in this thesis, it can be envisioned in further studies.

7.3.5 Fracture characterization and network modeling

Although scanline sampling method is a useful tool, new methodologies have been proposed to collect fracture data in the field with larger sampling areas and in inaccessible zones for conventional field work (e.g., high and steep outcrop vertical surfaces) that can be envisioned for future developments. Algorithms for automatic detection of discontinuities and their attributes based on LiDAR, 3D point clouds, photogrammetry and other terrestrial remote sensing methods have been developed by, for example, Mah et al. (2011), Masoud et al. (2011), Sturzenegger et al. (2011), Lato et al. (2012), Vöge et al. (2013), Gomes et al. (2016), Vollgger et al. (2016), Cao et al. (2017), Guo et al. (2017) and Chen et al. (2020). Lato et al. (2013) presents a repository and standards to use LiDAR and photogrammetry to assess rock mass characteristics. Lianheng et al. (2020) describes a workflow to use photogrammetric methods and construct a 3D fracture database. Machine learning has also been applied to train fracture network simulations (e.g., Bruna et al., 2019).

Moreover, software has also been developed to automatically detect discontinuities from photogrammetry methods, to generate fracture networks and to carry out statistical analyzes. Some examples are DigiFract (Hardebol et al., 2013), FraNEP (Zeeb et al., 2013b) and the Matlab open-source toolboxes developed by Alghalandis (2017) and Healy et al. (2017). Moreover, Nyberg et al. (2018) developed NetworkGT, an ArcGIS toolbox to carry out both geometrical and topological analyzes. Future studies can be envisioned to analyze the data from a previous LiDAR campaign undertaken in Kuujjuaq and apply one of the aforementioned software to decrease subjective biases that can impact data gathering and interpretation. These biases are discussed by Andrews et al. (2019). Fisher et al. (2014) compared LiDAR and compass methods and concluded that although both methods are able to identify discontinuities, one joint set was under-represented from the LiDAR data. The utilization of unmanned aerial vehicles coupled with photographic camera is also useful to acquire aerial photographs that can be posteriorly interpreted using one of the aforementioned methods. Future field work can consider the application of this technique.

The stochastic fracture network was generated in this thesis using a homogeneous Poisson process. However, other process models exist to generate statistical fracture network. A comprehensive review of modeling methods developed over the past four decades for the generation of representative fracture networks in rock masses is given by Xu et al. (2021). For example, in FracSim3D (Xu et al., 2010), the user can choose between homogeneous Poisson model, non-homogeneous point process model, cluster point process model or Cox process model to generate the fracture network.

7.3.6 In situ stress regime and lithosphere thermo-mechanical conditions

This thesis presents an a priori stress model for Kuujjuaq based on geometrical indicators, empirical correlations and analytical models. These estimates can be further improved by considering the effects of anisotropy, stratification, topography, glaciation and others as explained in Amadei et al. (1997). Moreover, exploratory drilling and in situ stress measurements are essential to calibrate the a priori model. A series of suggestions are provided by the International Society of Rock Mechanics that shall be followed in future stress estimation campaigns. For example, Hudson et al. (2003) recommends a strategy approach to estimate the rock stress tensor components. Hydraulic fracturing (hydraulic fracturing and hydraulic testing of pre-existing fractures; Haimson et al., 2003) and overcoring (Sjöberg et al., 2003) are the main methods suggested by the International Society of Rock Mechanics. However, there are several other methods to infer the in-situ stresses, such as relief methods, jacking methods, strain recovery methods, borehole breakout methods, fault-slip data analysis, earthquake focal mechanisms, indirect methods, inclusions in time-dependent materials and measurement of residual stresses (Amadei et al., 1997; Zoback, 2007). Additionally, the Kaiser effect has been examined as a laboratory replacement for in situ measurements (e.g., Lehtonen et al., 2012). However, this method needs to follow restrict laboratory procedures and to be supported by geological and other stress measurements information. Finally, an integrated stress model can be developed by combining the a priori model with the new stress measurements as discussed by Stephansson et al. (2012). A methodology to develop this integrated stress model has been proposed by, for example, Kruszewski et al. (2021) and can be followed in future work.

Additionally, a theoretical preliminary rheological profile was developed for Kuujjuaq. This profile provides a qualitative guide to the actual lithosphere strength, indicating the greatest possible stress as a function of depth. Since lithosphere rheology as important consequences for both geodynamic processes and exploitation of geothermal energy (e.g., Ranalli et al., 2005; Cloetingh et al., 2010; Cloetingh et al., 2017; Limberger et al., 2017), future developments can be foreseen to discuss and investigate with greater details the thermo-mechanical structure of the lithosphere beneath Kuujjuaq, the strain-rate and other creep parameters and the vertical distribution of forces applied to the tectonic plate and stress amplification over time. A number of publications have been made over the years discussing the continental lithosphere strength and providing the basis to develop models of lithosphere deformation (e.g., Kusznir, 1982; Kusznir et al., 1982; Kusznir et al., 1984a; Kusznir et al., 1984b; Kusznir et al., 1986; Kusznir, 1991). Moreover, the seismogenic depth was not estimated in this work, but further studies shall be carried out since the total strength of the lithosphere resides in the seismogenic crust. The flexural rigidity is another parameter that is worth further studies.

Furthermore, a detailed regional and local study of the lithosphere strength and thermo-mechanical conditions in Nunavik (Canada) may be helpful to assess the most favorable areas for the development of engineered geothermal energy systems. For example, the presence of seismicity around the 60º parallel may indicate weaker lithosphere, larger deviatoric stresses, or fault planes in the verge of failure and developing geothermal systems for communities in this location may be promising. However, care must be taken due to the induced seismicity that may trigger harmful events. Thus, forecasting induced seismicity with numerical simulations predicting the natural fractures and faults response to hydraulic stimulation is necessary to adapt stimulation procedures and prevent high magnitude seismic events.

7.3.7 Thermo-hydro-mechanical modeling

This thesis used FRACSIM3D to carry out thermo-hydro-mechanical simulations and to assess the performance of engineered geothermal energy systems. However, many other numerical models have been developed as mentioned before and all have strengths and limitations. COMSOL Multiphysics, for example, is a general-purpose finite element numerical simulation software package for solving multi-physics problems. The fracture network generated with one of the aforementioned software can be imported to COMSOL Multiphysics to solve the coupled thermo-hydro-mechanical processes. The results then obtained can be compared with the ones from this thesis and assess the variability induced by simulation methodologies. However, solving thermo-hydro-mechanical models with large and complex fracture geometries in COMSOL is computational expensive (e.g., Xu et al., 2021). A simpler approach is to represent fractures by 2D planar surfaces or generate simpler fracture geometries. Examples of thermo-hydro-mechanical and thermo-hydro and hydro-mechanical coupled models solved with COMSOL Multiphysics are Yao et al. (2018), Lepillier et al. (2019), Kazemi et al. (2019), Zinsalo et al. (2020) and Zinsalo et al. (2021).

Additional “what if” possibilities that should be addressed in further numerical simulations with FRACSIM3D or other numerical simulator are, for example 1) neglect the fault plane and consider only the fracture network, 2) apply a rotation to the well(s), 3) consider a triplet or quadruplet instead of a doublet configuration, 4) assume a slip patch radius rather than continuous slip and 5) generate several equally probable models of the fracture network and assess their influence on the system performance. Moreover, implementation of a Monte Carlo framework in FRACSIM3D could be a possibility for a more comprehensive understanding of the input parameters uncertainty and their impact on the system response. Such a workflow can be useful to predict the performance of engineered geothermal energy systems in regions with sparse data (e.g., Deb et al., 2020b). Another future direction could account for non-linear regimes of fluid flow through fractures (e.g., Zimmerman et al., 2004).

7.3.8 Economic assessment

Although not used in this work, software packages are currently available to carry out sensitivity analysis and estimate the levelized cost of energy. Olasolo et al. (2016b) carried out a comprehensive review of existing models and future work can be envisioned to apply one or several software packages and compare with the results obtained in this thesis.

7.3.9 Other future directions

A future direction of the work carried out in this thesis should pass by the evaluation of deep borehole heat exchangers to harvest the deep geothermal energy source and provide heating energy to the community. These systems can then be compared to engineered geothermal energy systems to study which is more viable for the northern communities in terms of thermal extraction, heat production and costs. Such systems are under evaluation in the Bécancour area (Gascuel et al., 2019). Furthermore, deep borehole heat exchangers have received increased attention and several publications have been made suggesting different models to evaluate their performance and for their optimization (e.g., Chen et al., 2019; Pan et al., 2020; Zhao et al., 2020; Doran et al., 2021). Deep closed-loop ground heat exchangers, similar to Eavor-Loop, has been simulated by Harris (2017) and the approach proposed by this author can be followed to assess its feasibility in crystalline rocks rather than sedimentary environments. Lea (2020) assessed the technical, environmental, and economic feasibility of deep closed-loop geothermal extraction for district cooling applications. The approach described can be followed and modified to account for space heating instead. Additionally, the application of enhanced and integrated geothermal systems concept proposed by Mahbaz et al. (2020) can be envisioned for further work to assess the performance benefits and the cost implications of having a seasonal heat storage system to complement the deep geothermal system. Moreover, a geothermal battery energy storage concept similar to the one proposed by Green et al. (2021) can be foreseen with the difference of using hydraulic stimulation techniques to develop the geo-repository. The concept involves the creation of a reasonable large heat exchange volume via hydraulic stimulation techniques at depths shallower than the required for heat extraction – for example, 2 or 3 km. During summer, water is circulated through a solar heating system with the target of generating warm water at about 40-50 ºC and stored in the created geo-repository. During winter, the water is extracted and run through a distribution network (e.g., district heating system) in which each residential dwelling is equipped with a heat pump system to upgrade the fluid temperature to useful levels. Performance simulations need to be carried out to understand temperature distribution, heat loss, water loss and heat recovery. Large-scale energy storage in underground reservoirs can provide means for a better integration of renewable energy sources, balancing supply and demand and increasing energy security (e.g., Matos et al., 2019). The site selection for underground energy storage is mainly dependent on the geology and structural issues, tectonics and seismicity issues, hydrogeological and geothermal issues and also geotechnical criteria (Matos et al., 2019). Underground energy storage in host rock reservoirs should consider the following criteria and requirements (Matos et al., 2019):

- Geology rock type – intrusive igneous rocks, massive chemical sedimentary rock, and massive nonfoliated metamorphic rocks
- Structure – homogeneous, isotropic rocks; no significant tectonic deformations, rock poorly faulted, fissured, jointed and folded; no discontinuities
- Porosity and permeability – low porosity and low permeability
- Hydraulic conductivity - $< 10^{-8}$ m s^{-1}
- Thermal stability – 4 to 80 ºC

7.4 Concluding remarks

Canadian off-grid communities heavily rely on fossil fuels and their transition to a clean energy supply is nowadays a watchword. Although this thesis was undertaken in the community of Kuujjuaq (Canada), the methodologies outlined in each chapter and the overall approach followed in this thesis are significant contributions to carry out a first-order assessment of the deep geothermal energy source potential with geothermal exploration tools affordable to not only northern communities as to other diesel-based settlements in more tropical regions and outside of the mainland (e.g., Island countries). Moreover, a series of future directions are proposed that can be followed to improve this first-order assessment as to be adopted in other deep geothermal energy assessments currently underway or planned. This thesis provides a useful guide, presenting new and adapted methodologies, providing baseline information and discussing possible future pathways, to evaluate the deep geothermal energy potential in low permeability crystalline fractured media in regions facing energy challenges and with important data gaps.

The results of this thesis, although highly speculative due to the lack of deep geothermal exploration boreholes and subsurface data in general, suggest that the old Canadian Shield beneath Kuujjuaq's community hosts potential to fulfil the average heating energy demand of the 2 754 inhabitants. Moreover, engineered geothermal energy systems may be a potential solution to harvest the deep geothermal energy source at a cost competitive with the current oil furnaces and diesel power plants. Thus, framing this thesis under a value of information problem, the results obtained suggest that, although 2 to 5 times higher than in southern areas, further geothermal exploration is worthwhile to refine the estimations carried out and consider its exploration in the near future. The drilling of geothermal exploration boreholes shall be the next step to improve the assessment carried out in this thesis. Such deep exploratory boreholes will enable to measure temperature, evaluate heat flux, collect fracture data and assess the in-situ stress field, key parameters to calibrate the results obtained throughout this work.

This thesis also highlights the need of community-focused geothermal energy source assessments rather than regional evaluations based on scarce data extrapolation. These regional studies are useful for global geothermal potential maps, but not desirable when the goal is to assess if the local thermo-mechanical conditions of the subsurface are suitable for the local production of deep geothermal energy sources. Hence, geothermal energy may be a technical and economic viable off-grid solution to support the energy transition of remote northern communities with a local, sustainable and carbon-free energy source.

8 REFERENCES

Abdulagatov IM, Emirov SN, Abdulagatova ZZ & Askerov SY (2006) Effect of pressure and temperature on the thermal conductivity of rocks. *Journal of Chemical & Engineering Data* 51:22-33.

Achtziger-Zupancic P, Loew S & Mariéthoz G (2017) A new global database to improve predictions of permeability distribution in crystalline rocks at site scale. *Journal of Geophysical Research: Solid Earth* 122:3513-3539.

Acton DF, Ryder JM, French H, Slaymaker O & Brookes IA (2015) *Physiographic Regions*. https://www.thecanadianencyclopedia.ca/en/article/physiographic-regions (Accessed Oct 14, 2020).

Adams J (1989) Crustal Stresses in Eastern Canada. Gregersen S & Basham PW (Eds.) Earthquakes at North-Atlantic Passive Margins: Neotectonics and Postglacial Rebound, Kluwer Academic Publishers, Dordrecht, pp 289-298.

Adams J & Basham PW (1989) Seismicity and seismotectonics of Canada’s Eastern Margin and Craton. Gregersen S & Basham PW (Eds.) Earthquakes at North-Atlantic Passive Margins: Neotectonics and Postglacial Rebound, Kluwer Academic Publishers, Dordrecht, pp 355-370.

Agemar T, Weber J & Moeck IS (2018) Assessment and Public Reporting of Geothermal Resources in Germany: Review and Outlook. *Energies* 11, 332.

Aghahosseini A & Breyer C (2020) From hot rock to useful energy: A global estimate of enhanced geothermal systems potential. *Applied Energy* 279, 115769.

AHRI – Air-conditioning, Heating, & Refrigeration Institute (2021) *Central air conditioners and air-source heat pumps*. https://www.ahrinet.org/resources/statistics/historical-data/central-air-conditioners-and-air-source-heat-pumps (Accessed Feb 25, 2021).

Akara MEM, Reeves DM & Parashar R (2020) Enhancing fracture-network characterization and discrete-fracture-network simulation with high-resolution surveys using unmanned aerial vehicles. *Hydrogeology Journal* 28:2285-2302

Alejano LR, González J & Muralha J (2012) Comparison of different techniques of tilt testing and basic friction angle variability assessment. *Rock Mechanics and Rock Engineering* 45(6):1023-1035.

Alghalandis YF (2017) ADFNE: Open source software for discrete fracture network engineering, two and three dimensional applications. *Computers & Geosciences* 102:1-11

Alghalandis YF, Xu C & Dowd PA (2013) Connectivity index and connectivity field towards fluid flow in fracture-based geothermal reservoirs. Proceedings, Thirty-Eight Workshop on Geothermal Reservoir Engineering. (Stanford, CA, US, Feb 11 – 13, 2013).

Alifanov OM (1994) *Inverse Heat Transfer Problems*. Springer-Verlag, Berlin, 359 p.

Allard M, Fournier A, Gahé E & Seguin MK (1989) Le Quaternaire de la côte sud-est de la baie d'Ungava, Québec nordique. *Géographie physique et Quaternaire* 43(3):325-336.

Allard M & Seguin MK (1987) Le pergélisol au Québec nordique : bilan et perspectives. *Géographie physique et Quaternaire* 41(1):141-152.

Allen DM, Ghomshei MM, Sadler-Brown TL, Dakin A & Holtz D (2000) The current status of geothermal exploration and development in Canada. Proceedings, World Geothermal Congress 2000. (Kyushu-Tohoku, Japan, May 28-June 10, 2000).

Allaire G. (2007) *Numerical Analysis and Optimization*. Oxford University Press, Oxford, 472 p.

Allmendinger RW (2020) *MohrPlotter.* http://www.geo.cornell.edu/geology/faculty/RWA/programs/mohrplotter.html (Accessed Nov 19, 2020)

Allmendinger RW, Cardozo NC & Fisher D (2012) *Structural Geology Algorithms: Vectors & Tensors*. Cambridge University Press, Cambridge, 302 p.

Amadei B & Stephansson O (1997) *Rock stress and its measurement*. Springer, Dordrecht, 490 p.

Amann F, Gischig V, Evans K, Doetsch J, Jalali R, Valley B, Krietsch H, Dutler N, Villiger L, Brixel B, Klepikova M, Kittilä A, Madonna C, Wiemer S, Saar MO, Loew S, Driesner T, Maurer H & Giardini D (2018) The seismo-hydro-mechanical behaviour during deep geothermal reservoir stimulations: open questions tackled in a decameter-scale in-situ stimulation experiment. *Solid Earth* 9:115-137.

Anderson EM (1951) *The Dynamics of Faulting and Dyke Formation with Applications to Britain*. Oliver and Boyd, Edinburgh, 191 p.

Andresen CA, Hansen A, Goc RL, Davy P & Hope SM (2013) Topology of fracture networks. *Frontiers in Physics* 1:7.

Andrews BJ, Roberts JJ, Shipton ZK, Bigi S, Tartarello MC & Johnson G (2019) How do we see fractures? Quantifying subjective bias in fracture data collection. *Solid Earth* 10:487-516.

Andrews JN, Hussain N, Batchelor AS & Kwakwa K (1986) ^{222}Rn solution by the circulating fluids in a “hot dry rock” geothermal reservoir. *Applied Geochemistry* 1(6):647-657.

Andrews JT & Dyke AS (2013) Late Quaternary in North America. Elias S & Mock C (Eds.) Encyclopedia of Quaternary Science, Elsevier, Netherlands, pp. II:245-II:249.

Arjang B (1998) Canadian crustal stresses and their application in mine design. Singhal RK (Ed) Mine Planning and Equipment Selection 1998, A.A. Balkema, Rotterdam, pp 269-274.

Arjang B & Herget G (1997) In situ ground stresses in the Canadian hardrock mines: an update. *International Journal of Rock Mechanics & Mining Sciences* 34(3-4), 15.

Arjang B (1991) Pre-mining stresses at some hard rock mines in the Canadian Shield. *CIM Bulletin* 84(945).

Arriaga M, Brooks M & Moore N (2017) *Energy access – the Canadian context*. Waterloo Global Initiative’s OpenAcess Energy Blueprint. http://wgsi.org/sites/wgsi-live.pi.local/files/Energy_Access_Canadian_Context_Infographic_Spread-OpenAccess_Energy_Blueprint_WGSI_2017.pdf (Accessed Nov 18, 2019).

Ashwal LD, Morgan P, Kelley SA & Percival JA (1987) Heat production in an Archean crustal profile and implications for heat flow and mobilization of heat-producing elements. *Earth and Planetary Science Letters* 85:439-450.

Athens ND & Caers JK (2019) A Monte Carlo-based framework for assessing the value of information and development risk in geothermal exploration. *Applied Energy* 256, 113932.

Audet P & Mareschal J-C (2004) Variations in elastic thickness in the Canadian Shield. *Earth and Planetary Science Letters* 226(1-2):17-31.

Augustin M, Bauer M, Blick C, Eberle S, Freeden W, Gerhards C, Ilyasov M, Kahnt R, Klug M, Möhringer S, Neu T, Nutz H, Ostermann IM & Punzi A (2014) Modeling deep geothermal reservoirs: recent advances and future perspectives. Freeden W, Nashed T & Sonar T (Eds.) Handbook of Geomathematics, Springer, Berlin, pp. 1-74.

Augustine CR (2011) *Updated US geothermal supply characterization and representation for market penetration model input*, NREL/TP-6A20-47459. NREL, Golden. 103 p: https://www.nrel.gov/docs/fy12osti/47459.pdf (Accessed Mar 5, 2021).

Augustine C, Tester JW & Anderson B (2006) A comparison of geothermal with oil and gas well drilling costs. Proceedings, Thirty-First Workshop on Geothermal Reservoir Engineering. (Stanford, CA, US, Jan 30 – Feb 1, 2006).

Bandis SC, Lumsden AC & Barton NR (1983) Fundamentals of rock joint deformation. *International Journal of Rock Mechanics and Mining Sciences & Geomechanical Abstracts* 20(6):249-268.

Banks D (2012) *An Introduction to Thermogeology: Ground Source Heating and Cooling*. Wiley-Blackwell, Oxford, 539 p.

Barbier E (2002) Geothermal energy technology and current status: an overview. *Renewable and Sustainable Energy Reviews* 6:3-65.

Bardoux M, Digonnet S, Donohue L, Girad B, Robillard M, David J, Parent M & Gariépy C (1998) Paleoproterozoic tectonics affecting Archean lower crust of southern Ungava Bay. Wardle RJ & Hall J (Eds.) Eastern Canadian Shield Onshore–Offshore Transect (ECSOOT), University of British Columbia, Vancouver, pp.1-17.

Baroudi HA, Awoyomi A, Patchigolla K, Jonnalagadda K & Anthony EJ (2021) A review of large-scale CO_2 shipping and marine emissions management for carbon capture, utilisation and storage. *Applied Energy* 287, 116510.

Barton N (2013) Shear strength criteria for rock, rock joints, rockfill and rock masses: Problems and some solutions. *Journal of Rock Mechanics and Geotechnical Engineering* 5(4):249-261.

Barton N & Quadros EF (1997) Joint aperture and roughness in the prediction of flow and groutability of rock masses. *International Journal of Rock Mechanics and Mining Sciences* 34(3-4):1-14.

Barton CC & Hsieh PA (1989) Physical and hydrological-flow properties of fractures, Field Trip Guidebook. 28th International Geological Congress. (Washington D.C., US, Jan 1,1989).

Barton N & Choubey V (1977) The shear strength of rock joints in theory and practice. *Rock Mechanics* 10:1-54.

Bauer JF, Krumbholz M, Meier S & Tanner DC (2017) Predictability of properties of a fractured geothermal reservoir: the opportunities and limitations of an outcrop analogue study. *Geothermal Energy* 5, 24.

Beardsmore GR, Rybach L, Blackwell D & Baron C (2010) A protocol for estimating and mapping global EGS potential. *GRC Transactions* 34:301–312.

Beardsmore GR & Cull JP (2001) *Crustal Heat Flow: A Guide to Measurement and Modelling.* Cambridge Press University, Cambridge, 324 p.

Beck AE & Shen PY (1989) On a more rigorous approach to geothermic problems. *Tectonophysics* 164:83-92.

Beck AE (1977) Climatically perturbed temperature gradients and their effect on regional and continental heat-flow means. *Tectonophysics* 41(1-3):17-39.

Beck AE (1976) An improved method of computing the thermal conductivity of fluid-filled sedimentary rocks. *Geophysics* 41(11):133-144.

Beck JV, Blackwell B & St. Clair Jr CR (1985) *Inverse Heat Conduction: Ill-posed problems*. John Wiley & Sons, Inc., New York, 308 p.

Beck JV & Arnold KJ (1977) *Parameter Estimation in engineering and science*. John Wiley & Sons, New York, 367 p.

Beck JV (1970) Nonlinear estimation applied to the nonlinear inverse heat conduction problem. *International Journal of Heat and Mass Transfer* 13:703-716.

Beckers KF & McCabe K (2019) GEOPHIRES V2.0: updated geothermal techno-economic simulation tool. *Geothermal Energy* 7, 5.

Bédard K, Comeau F-A, Raymond J, Gloaguen E, Malo M & Richard M-A (2020) Deep geothermal resource assessment of the St. Lawrence Lowlands sedimentary basin (Québec) based on 3D regional geological modelling. *Geomechanics and Geophysics for Geo-Energy and Geo-Resources* 6, 46.

Bédard K, Comeau F-A, Raymond J, Malo M & Nasr M (2018) Geothermal characterization of the St. Lawrence Lowlands Sedimentary Basin, Québec, Canada. *Natural Resources Research* 27(4):479-502.

Bell JS & Wu P (1997) High horizontal stresses in Hudson Bay, Canada. *Canadian Journal of Earth Sciences* 34:949-957.

Bell M & Laine EP (1985) Erosion of the Laurentide region of North America by glacial and glaciofluvial processes. *Quaternary Research* 23(2):154-174.

Beltrami H, Matharoo GS, Tarasov L, Rath V & Smerdon JE (2014) Numerical studies on the impact of the Last Glacial Cycle on recent borehole temperature profiles: implications for terrestrial energy balance. *Climate of the Past* 10(5):1693-1706.

Beltrami H, Smerdon JE, Matharoo GS & Nickerson N (2011) Impact of maximum borehole depths on inverted temperature histories in borehole paleoclimatology. *Climate of the Past* 7:745-756.

Beltrami H, Ferguson G & Harris RN (2005) Long-term tracking of climate change by underground temperatures. *Geophysical Research Letters* 32, L19707.

Beltrami H, Gosselin C & Mareschal J-C (2003) Ground surface temperatures in Canada: spatial and temporal variability. *Geophysical Research Letters* 30(10), 1499.

Beltrami H (2001) On the relationship between ground temperature histories and meteorological records: a report on the Pomquet station. *Global and Planetary Change* 29(3-4):327-348.

Beltrami H & Taylor AE (1995) Records of climatic change in the Canadian Arctic: towards calibrating oxygen isotope data with geothermal data. *Global and Planetary Change* 11:127-138.

Belzile P, Comeau F-A, Raymond J, Lamarche L & Carreau M (2017) Arctic climate horizontal ground-coupled heat pump. *GRC Transactions* 41:1958-1978.

Bent AL (1994) The 1989 (MS 6.3) Ungava, Quebec, earthquake: a complex intraplate event. *Bulletin of the Seismological Society of America* 84(4):1075-1088.

Bhattacharyya SC & Palit D (2016) Mini-grid based off-grid electrification to enhance electricity access in developing countries: What policies may be required? *Energy Policy* 94:166–178.

Birch AF (1948) The effects of Pleistocene climatic variations upon geothermal gradients. *American Journal of Science* 246(12):729-760.

Bisdom K, Nick HM & Bertotti G (2017) An integrated workflow for stress and flow modelling using outcrop-derived discrete fracture networks. *Computers & Geosciences* 103:21-35.

Bistacchi A, Mittempergher S, Martinelli M & Storti F (2020) On a new robust workflow for the statistical and spatial analysis of fracture data collected with scanlines (or the importance of stationarity). *Solid Earth* 11:2535-2547

Blackwell DD, Negraru PT & Richards MC (2007) Assessment of the Enhanced Geothermal System Resource Base of the United States. *Natural Resources Research* 15:283–308.

Blackwell DD, Steele JL & Brott CA (1980) The terrain effect on terrestrial heat flow. *Journal of Geophysical Research: Solid Earth* 85(B9):4757-4772.

Blázquez CS, Martín AF, Nieto IM, García PC, Pérez LSS & Aguilera DG (2017a) Thermal conductivity map of the Avila region (Spain) based on thermal conductivity measurements of different rock and soil samples. *Geothermics* 65:60-71.

Blázquez CS, Martín AF, Nieto IM & Aguilera DG (2017b) Measuring of thermal conductivities of soils and rocks to be used in the calculation of a geothermal installation. *Energies* 10, 795.

Bodri L & Cermak V (2007) *Borehole Climatology: a new method how to reconstruct climate*. Elsevier Science, Berlin, 352 p.

Bodvarsson GS & Tsang CF (1982) Injection and thermal breakthrough in fractured geothermal reservoirs. *Journal of Geophysical Research: Solid Earth* 87:1031–1048.

Bodvarsson G (1951) Report on the Hengill geothermal area. *Journal of the Engineers' Association of Iceland* 36, 1.

Bolton RS (1973) Management of a geothermal field. Armstead HCH (Ed.) Geothermal Energy—Review and Research and Development, UNESCO, Paris, pp. 175–184.

Bonalumi D (2018) Enhanced Geothermal System with captured CO_2. *Energy Procedia* 148:744-750.

Bottomley DJ (1996) *A Review of Theories on the Origins of Saline Waters and Brines in the Canadian Precambrian Shield*. Atomic Energy Control Board, Ottawa. 32 p: https://inis.iaea.org/collection/NCLCollectionStore/_Public/27/055/27055911.pdf?r=1 (Accessed April 23, 2021).

Bourlon E, Mareschal J-C, Roest WR & Telmat H (2002) Geophysical correlations in the Ungava Bay area. *Canadian Journal of Earth Sciences* 39:625-637.

Brace WF & Kohlstedt DL (1980) Limits on lithospheric stress imposed by laboratory experiments. *Journal of Geophysical Research: Solid Earth* 85(B11):6248-6252.

Breede K, Dzebisashvili K, Liu X & Falcone G (2013) A systematic review of enhanced (or engineered) geothermal systems: past, present and future. *Geothermal Energy* 1, 4.

Bremen LV (2010) Large-scale variability of weather dependent renewable energy sources. Troccoli A (Ed.) Management of Weather and Climate Risk in the Energy Industry, Springer, Dordrecht, pp. 189–206.

Brenna M, Longo M, Yaici W & Abegaz TD (2017) Simulation and optimization of integration of hybrid renewable energy sources and storages for remote communities electrification. IEEE PES ISGT-Europe. (Turin, Italy, Sept 26-29, 2017).

Breuer D (2011) Primordial heat. Gargaud M, Amils R, Quintanilla JC, Cleavesll HJ, Irvine WM, Pinti DL & Viso M (Eds.) Encyclopeia of Astrobiology, Springer, Berlin, pp.1333-1334.

Bristow KL, Kluitenberg GJ & Horton R (1994) Measurements of soil thermal properties with a dual-probe heat-pulse technique. *Soil Science Society of America Journal* 58(5):1288-1294.

Brown DW, Duchane DV, Heiken G, Hriscu VT (2012) *Mining the Earth's Heat: Hot Dry Rock Geothermal Energy*. Springer, Berlin, 669 p.

Brown D (2000) A Hot Dry Rock geothermal energy concept utilizing supercritical CO2 instead of water. Proceedings, 25th Workshop on Geothermal Reservoir Engineering. (Stanford, US, Jan 24-26, 2000).

Bruna P-O, Straubhaar J, Prabhakaran R, Bertotti G, Bisdom K, Mariethoz G & Meda M (2019) A new methodology to train fracture network simulation using multiple-point statistics. *Solid Earth* 10:537-559.

Burbank DW (2002) Rates of erosion and their implications for exhumation. *Mineralogical Magazine* 66(1):25-52.

Burov EB (2011) Rheology and strength of the lithosphere. *Marine and Petroleum Geology* 28(8):1402-1443.

Busby J & Terrington R (2017) Assessment of the resource base for engineered geothermal systems in Great Britain. *Geothermal Energy* 5, 7.

Buyer A, Aichinger S & Schubert W (2020) Applying photogrammetry and semi-automated joint mapping for rock mass characterization. *Engineering Geology* 264, 105332

Byerlee J (1978) Friction of rocks. *Pageoph* 116:615-626.

Caers J (2011) *Modeling Uncertainty in the Earth Sciences.* Wiley-Blackwell, Chichester, 249 p.

Caldwell RL, Baldwin WF, Bargainer JD, Berry JE, Salaita GN & Sloan RW (1963) Gamma-ray spectroscopy in well logging. *Geophysics* 28(4):531-671.

Candy I, Schreve DC, Sherriff J & Tye GJ (2014) Marine Isotope Stage 11: Palaeoclimates, palaeoenvironments and its role as an analogue for current interglacial. *Earth-Science Reviews* 128:18-51.

CanGEA – Canadian Geothermal Energy Association (2021a) *Canadian National Geothermal Database & Provincial resource estimate maps: British Columbia*. https://www.cangea.ca/britishcolumbiageothermal.html (Accessed Feb 25, 2021).

CanGEA – Canadian Geothermal Energy Association (2021b) *Canadian National Geothermal Database & Provincial resource estimate maps: Alberta*. https://www.cangea.ca/albertageothermal.html (Accessed Feb 25, 2021).

CanGEA – Canadian Geothermal Energy Association (2021c) *Canadian National Geothermal Database & Provincial resource estimate maps: Yukon Territory report and maps & Database*. https://www.cangea.ca/ykgeothermal.html (Accessed Feb 25, 2021).

CanGEA – Canadian Geothermal Energy Association (2021d) *Canadian National Geothermal Database & Provincial resource estimate maps: Nunavut Territory*. https://www.cangea.ca/nunavutgeothermal.html (Accessed Feb 25, 2021).

Cao G, Wang B, Xavier H-C, Yang D & Southworth J (2017) A new difference image creation method based on deep neural networks for change detection in remote-sensing images. *International Journal of Remote Sensing* 38(23):7161-7175.

Cardozo N & Allmendinger RW (2013) Spherical projections with OSXStereonet. *Computers & Geoscience* 51:193-205.

Carslaw HS & Jaeger JC (1959) *Conduction of Heat in Solids*. Claredon Press, Oxford, 520 p.

CER – Canada Energy Regulator (2018) *Market Snapshot: Overcoming the challenges of powering Canada's off-grid communities*. https://www.cer-rec.gc.ca/en/data-analysis/energy-markets/market-snapshots/2018/market-snapshot-overcoming-challenges-powering-canadas-off-grid-communities.html (Accessed Feb 22, 2021).

Cermak V (1971) Underground temperature and inferred climatic temperature of the past millennium. *Palaeogeography, Palaeoclimatology, Palaeoecology* 10:1-19.

Chabani A, Mehl C, Cojan I, Alais R & Dominique B (2020) Semi-automated component identification of a complex fracture network using a mixture of von Mises distributions: Application to the Ardeche margin (South-East France). *Computers & Geosciences* 137:104435

Chagnon-Lessard N, Mathieu-Potvin F & Gosselin L (2020) Optimal design of geothermal power plants: A comparison of single-pressure and dual-pressure organic Rankine cycles. *Geothermics* 86, 101787.

Chaminé HI, Afonso MJ, Ramos L & Pinheiro R (2015) Scanline sampling techniques for rock engineering surveys: Insights from intrinsic geologic variability and uncertainty. Lollino G, Giordan D, Thuro K, Carranza-Torres C, Wu F, Marinos P & Delgado C (Eds.) Engineering Geology for Society and Territory – Volume 6, Springer, Cham, pp. 357-361.

Channell JET, Hodell DA, Romero O, Hillaire-Marcel C, Vernal A, Stoner JS, Mazaud A & Röhl U (2012) A 750-kyr detrital-layer stratigraphy for the North Atlantic (IODP Sites U1302-U1303, Orphan Knoll, Labrador Sea). *Earth and Planetary Science Letters* 317-318:218-230.

Chapman DS, Keho TH, Bauer MS & Picard D (1984) Heat flow in the Uinta Basin determined from bottom hole temperature (BHT) data. *Geophysics* 49(4):453-466.

Chen C, Shao H, Naumov D, Kong Y, Tu K & Kolditz O (2019) Numerical investigation on the performance, sustainability, and efficiency of the deep borehole heat exchanger system for building heating. *Geothermal Energy* 7, 18.

Chen M, Feng A, McAlinden R & Soibelman L (2020) Photogrammetric point cloud segmentation and object information extraction for creating virtual environments and simulations. *Journal of Management in Engineering* 36(2), 04019046.

Chen W-P & Molnar P (1983) Focal depths of intracontinental and intraplate earthquakes and their implications for the thermal and mechanical properties of the lithosphere. *Journal of Geophysical Research: Solid Earth* 88(B5):4183-4214.

Chen Z, Narayan SP, Yang Z & Rahman SS (2000) An experimental investigation of hydraulic behaviour of fractures and joints in granitic rock. *International Journal of Rock Mechanics and Mining Sciences* 37(7):1061-1071.

Cherry JE, Knapp C, Trainor S, Ray AJ, Tedesche M & Walker S (2017) Planning for climate change impacts on hydropower in the Far North. *Hydrology and Earth System Sciences* 21:133-151.

Chesnaux R, Allen DM & Jenni S (2009) Regional fracture network permeability using outcrop scale measurements. *Engineering Geology* 108:256-271.

Chiozzi P, Pasquale V & Verdoya M (2003) Heat from radioactive elements in young volcanics by γ-ray spectrometry. *Journal of Volcanology and Geothermal Research* 119(1-4):205-214.

Chmiel Z & Bhattacharyya SC (2015) Analysis of off-grid electricity system at Isle of Eigg (Scotland): Lessons for developing countries. *Renewable Energy* 81:578–588.

Chouinard C & Mareschal J-C (2009) Ground surface temperature history in southern Canada: temperatures at the base of the Laurentide ice sheet and during the Holocene. *Earth and Planetary Science Letters* 227(1-2):280-289.

Chouinard C, Fortier R & Mareschal J-C (2007) Recent climate variations in the subarctic inferred from three borehole temperature profiles in northern Québec, Canada. *Earth and Planetary Science Letters* 263:355-369.

Christensen NI & Fountain DM (1975) Constitution of the lower continental crust based on experimental studies of seismic velocities in granulite. *Geological Society of America Bulletin* 86:227-236.

Clauser C (2006) Geothermal Energy. Heinloth K (Ed.) Energy Technologies, Springer, Berlin, pp. 493-594.

Clauser C & Huenges E (1995) Thermal conductivity of rocks and minerals. Ahrens TJ (Ed.) Rock Physics & Phase Relations: A Handbook of Physical Constants 3, American Geophysical Union, Washington DC, pp. 105-126.

Clauser C (1984) A climatic correction on temperature gradients using surface-temperature series of various periods. *Tectonophysics* 103(1-4):33-46.

Cleveland CJ & Morris C (2014) *Handbook of Energy – Volume II: Chronologies, Top Ten Lists, and Word Clouds*. Elsevier, Amsterdam, 927 p.

Cloetingh S, Van Wees J-D & Wesztergom V (2017) Thermo-mechanical controls on geothermal energy resources: case studies in the Pannonian Basin and other natural laboratories. *Acta Geodaetica et Geophysica* 52:157-160.

Cloetingh S, van Wees JD, Ziegler PA, Lenkey L, Beekman F, Tesauro M, Förster A, Norden B, Kaban M, Hardebol N, Bonté D, Genter A, Guillou-Frottier L, Ter Voorde M, Sokoutis D, Willingshofer E, Cornu T & Worum G (2010) Lithosphere tectonics and thermo-mechanical properties: An integrated modelling approach for Enhanced Geothermal Systems exploration in Europe. *Earth-Science Reviews* 102(3-4):159-206.

Comeau F-A, Séjourné S & Raymond J (2020) *Assessment of geothermal resources in onshore Nova Scotia*. OERA, Halifax. 216 p: https://oera.ca/sites/default/files/2020-12/Assessment%20of%20geothermal%20resources%20in%20onshore%20Nova%20Scotia%20-%20Final%20Report_0.pdf (Accessed Feb 25, 2021).

Comeau F-A, Raymond J, Malo M, Dezayes C & Carreau M (2017) Geothermal potential of northern Québec: a regional assessment. *Transactions Geothermal Resources Council* 41:1076-1094.

Conn AR, Scheinberg K & Vicente LN (2009) *Introduction to derivative-free optimization*. Society for Industrial and Applied Mathematics, Philadelphia, 289 p.

Coretest Systems, Inc (2019) *AP-608 Automated Permeameter-Porosimeter (Porosity)*. http://www.coretest.com/product_detail.php?p_id=115 (Accessed May 15, 2019).

Cornet FH (1987) Results from Le Mayet de Montagne project. *Geothermics* 16(4):355-374.

Corrigan D, Wodicka N, McFarlane C, Lafrance I, van Rooyen D, Bandyayera D & Bilodeau C (2018) Lithotectonic framework of the Core Zone, Southeastern Churchill Province, Canada. *Geoscience Canada* 45(1):1-24.

Corrigan D, Pehrsson S, Wodicka N & de Kemp E (2009) The Palaeoproterozoic Trans-Hudson Orogen: a prototype of modern accretionary processes. Murphy JB, Keppie JD & Hynes AJ (Eds.) Ancient Orogens and Modern Analogues, Geological Society, London, pp. 457-479.

Corrigan D, Hajnal Z, Németh B & Lucas SB (2005) Tectonic framework of a Paleoproterozoic arc-continent to continent-continent collisional zone, Trans-Hudson Orogen, from geological and seismic reflection studies. *Canadian Journal of Earth Sciences* 42(4):421-434.

Crain IK (1969) A simple method of calculating climatic corrections to heat flow measurements. *Canadian Journal of Earth Sciences* 6(3):499-502.

Crain IK (1968) The glacial effect and the significance of continental terrestrial heat flow measurements. *Earth and Planetary Science Letters* 4(1):69-72.

Crowell JC (1982) Continental glaciation through geologic times. National Research Council (Ed.) Climate in Earth History: Studies in Geophysics, The National Academies Press, Washington, pp. 77—82.

Cumming W (2009) Geothermal resource conceptual models using surface exploration data. Proceedings, Thirty-Four Workshop on Geothermal Reservoir Engineering. (Stanford, CA, US, Feb 9 – 11, 2009).

Dahl-Jensen D, Mosegaard K, Gundestrup N, Clow GD, Johnsen SJ, Hansen AW & Balling N (1998) Past temperatures directly from the Greenland Ice Sheet. *Science* 282(5387):268-271.

Dalton AS, Finkelstein SA, Forman SL, Barnett PJ, Pico T & Mitrovica JX (2019) Was the Laurentide Ice Sheet significantly reduced during Marine Isotope Stage 3?. *Geology* 47:111-114.

Darbyshire FA, Bastow ID, Petrescu L, Gilligan A & Thompson DA (2017) A tale of two orogens: Crustal processes in the Proterozoic Trans-Hudson and Grenville Orogens, eastern Canada. *Tectonics* 36:1633-1659.

Davis PM (2017) Dependence of the brittle ductile transition on strain-rate-dependent critical homologous temperature. *Geophysical Journal International* 209(2):1180-1194.

Deb P, Salimzadeh S, Vogler D, Düber S, Clauser C & Settgast RR (2021) Verification of coupled hydraulic fracturing simulators using laboratory-scale experiments. *Rock Mechanics and Rock Engineering* (doi.org/10.1007/s00603-021-02425-y).

Deb P, Düber S, Carducci CGC & Clauser C (2020a) Laboratory-scale hydraulic fracturing dataset for benchmarking of enhanced geothermal system simulation tools. *Scientific Data* 7, 220.

Deb P, Knapp D, Marquart G, Clauser C & Trumpy E (2020) Stochastic workflows for the evaluation of Enahnced Geothermal System (EGS) potential in geothermal greenfields with sparse data: the case study of Acoculco, Mexico. *Geothermics* 88, 101879.

Denis GS & Parker P (2009) Community energy planning in Canada: The role of renewable energy. *Renewable and Sustainable Energy Reviews* 13(8):2088-2095.

Dershowitz WS & Einstein HH (1988) Characterizing rock joint geometry with joint system models. *Rock Mechanics and Rock Engineering* 21:21-51.

Desroches J & Dowell S (2000) Formation Characterization: Well Logs. Economides MJ &. Nolte KG (Eds.) Reservoir Stimulation, Wiley, pp. 114-139.

DESTRESS [2020a] *Pohang, South Korea*. http://www.destress-h2020.eu/en/demonstration-sites/pohang/ (Accessed Feb 26, 2021).

DESTRESS [2020b] *Haute-Sorne, Switzerland*. http://www.destress-h2020.eu/en/demonstration-sites/haute-sorne/ (Accessed Feb 26, 2021).

DESTRESS [2020c] *Bedretto, Switzerland*. http://www.destress-h2020.eu/en/demonstration-sites/bedretto/ (Accessed Feb 26, 2021).

Dieterich JH (1979) Modeling of rock friction 1. Experimental results and constitutive equations. *Journal of Geophysical Research* 84(B5):2161-2168.

Dieterich JH (1978) Time-dependent friction and the mechanics of stick-slip. *Pageoph* 16:790-806.

Dincer I & Zamfirescu C (2014) *Advanced Power Generation Systems*. Elsevier, Oxford, 643 p.

DiPippo R (Ed.) (2016) *Geothermal Power Generation: Developments and Innovation.* Woodhead Publishing, Duxford, 818 p.

Dobson P, Kneafsey TJ, Blankenship D, Valladao C, Morris J, Knox H, Schwering P, White M, Doe T, Roggenthen W, Mattson E, Podgorney R, Johnson T, Ajo-Franklin J & EGS Collab team (2017) An introduction to the EGS Collab project. *GRC Transactions* 41:837-849.

Doran HR, Renaud T, Falcone G, Pan L & Verdin PG (2021) Modelling an unconventional closed-loop deep borehole heat exchanger (DBHE): sensitivity analysis on the Newberry volcanic setting. *Geothermal Energy* 9, 4.

Dubé-Loubert H, Daubois V, Roy M & Allard G (2015) *Géologie des dépôts de surface de la région du lac Saffray (24G)*, Report No.: RP 2014-06. Gouvernement du Québec, Québec. 48 p: http://gq.mines.gouv.qc.ca/documents/examine/RP201406/RP201406.pdf (Accessed Feb 22, 2021).

Dutta A, Karimi IA & Farooq S (2018) Economic Feasibility of Power Generation by Recovering Cold Energy during LNG (Liquefied Natural Gas) Regasification. *ACS Sustainable Chemistry & Engineering* 6:10687–10695.

Drolet J-P, Giroux B & Bouligand C (2017) Estimating the Curie point depth using aeromagnetic data with a fractal model in the Province of Québec, Eastern Canada. 19th EGU General Assembly. (Vienna, Austria, April 8-13, 2017).

Drury MJ (1985) Heat flow and heat generation in the Churchill Province of the Canadian Shield and their paleotectonic significance. *Tectonophysics* 115:25-44.

Drury MJ (1984) Perturbations to Temperature Gradients by Water Flow in Crystalline Rock Formations. *Tectonophysics* 103(1-4):19-32.

Easterbrook DJ (2016) Temperature fluctuations in Greenland and the Arctic. Easterbrook D (Ed.) Evidence-based Climate Science. Data opposing CO2 Emissions as the Primary Source of Global Warming, Elsevier Science, Netherlands, pp. 137-160.

Eavor Technologies Inc. (2021) *Eavor*. https://eavor.com/ (Accessed April 13, 2021).

EBA Engineering Consultants Ltd. (2010) *Geothermal Favourability Map Northwest Territories*, Y22101146. Government of Northwest Territories, Yellowknife. 59 p: https://www.enr.gov.nt.ca/sites/enr/files/reports/geothermal_favorability_report.pdf (Accessed Feb 12, 2021)

ECCC – Environment and Climate Change Canada (2020) *A healthy environment and a healthy economy*. Government of Canada, Ottawa. 79 p: https://www.canada.ca/content/dam/eccc/documents/pdf/climate-change/climate-plan/healthy_environment_healthy_economy_plan.pdf (Accessed March 7, 2021).

ECCC – Environment and Climate Change Canada (2019) *Historical Climate Data*. http://climate.weather.gc.ca/ (Accessed Sept 20, 2019).

Ehlers TA (2005) Crustal thermal processes and the interpretation of thermochronometer data. *Reviews in Mineralogy & Geochemistry* 58:315-350.

Ehlers J & Gibbard P (2011) Quaternary Glaciation. Singh VP, Singh P. & Haritashya UK (Eds.) Encyclopedia of Snow, Ice and Glaciers, Springer, Netherlands, pp. 873-882.

Eidesgaard ÓR, Schovsbo NH, Boldreel L & Ólavsdóttir J (2019) Shallow geothermal energy system in fractured basalt: A case study from Kollafjørður, Faroe Islands, NE-Atlantic Ocean. *Geothermics* 82:296–314.

Emiliani C (1955) Pleistocene temperatures. *The Journal of Geology* 63(6):538-578.

Emirov SN, Beybalaev VD, Gadzhiev GG, Ramazanova AE, Amirova AA & Aliverdiev AA (2017) To the description of the temperature and pressure dependences of the thermal conductivity of sandstone and ceramics. *Journal of Physics: Conf. Series* 891, 012335.

Emmerman R & Lauterjung J (1997) The German continental deep drilling program KTB: Overview and major results. *Journal of Geophysical Research* 102(B8):18179-18201.

England PC & Richardson SW (1980) Erosion and the age dependence of continental heat flow. *Geophysical Journal of the Royal Astronomical Society* 62:421-437.

England PC (1978) The effect of erosion on paleoclimatic and topographic corrections to heat flow. *Earth and Planetary Science Letters* 39:427-434.

Eppelbaum L, Kutasov I & Pilchin A (2014) *Applied Geothermics*. Springer, Heidelberg, 747 p.

Eshelby JD (1957) The determination of the elastic field of an ellipsoidal inclusion, and related problems. *Proceedings of the Royal Society London A* 241:376-396.

Evans KF, Moriya H, Niitsuma H, Jones RH, Phillips WS, Genter A, Sausse J, Jung R & Baria R (2005) Microseismicity and permeability enhancement of hydrogeologic structures during massive fluid injections into granite at 3 km depth at the Soultz HDR site. *Geophysical Journal International* 160:388-412.

Evans K, Cornet F, Hayashi K, Hashida T, Ito T, Matsuki K & Wallroth T (1999) Stress and rock mechanics issues of relevance to HDR/HWR engineered geothermal systems: review of developments during the past 15 years. *Geothermics* 28(4-5):455-474.

Farquharson JI, Kushnir ARL, Wild B & Baud P (2020) Physical property evolution of granite during experimental chemical stimulation. *Geothermal Energy* 8, 14.

Ferguson G (2015) Screening for heat transport by groundwater in closed geothermal systems. *Groundwater* 53(3):503-506.

Ferguson G & Grasby SE (2014) The geothermal potential of the basal clastics of Saskatchewan, Canada. *Hydrogeology Journal* 22(1):143-150.

Ferris DM, Potter G & Ferguson G (2020). Characterization of the hydraulic conductivity of glacial till aquitards. *Hydrogeology Journal* 28:1827-1839.

Figueiredo ERH, Galindo AC, Lins FPL & Moreira JAM (2009) Condutividade térmica em rochas silicáticas cristalinas e sua correlação com a geoquímica de elementos maiores. *Estudos Geológicos* 19(1):55-68.

Figueiredo ERH, Galindo AC, Moreira JAM & Lins FAPL (2008) Condutividade térmica em rochas silicáticas cristalinas, com ênfase a rochas graníticas da província Borborema, NE do Brasil, e sua correlação com parâmetros petrográficos e texturais. *Revista Brasileira de Geofísica* 26(3):293-307.

Fisher JE, Shakoor A & Watts CF (2014) Comparing discontinuity orientation data collected by terrestrial LiDAR and transit compass methods. *Engineering Geology* 181:78-92.

Flint RF (1947) *Glacial geology and the Pleistocene epoch*. John Wiley & Sons, Inc., New York, 616 p.

FOC – Fisheries and Oceans Canada (2020) *7 days tidal predictions*. https://www.waterlevels.gc.ca/eng/station?type=0&date=2019%2F06%2F29&sid=4298&tz=EDT&pres=1 (Accessed Feb 22, 2020).

Fomin S, Jing Z & Hashida T (2004) The effect of thermal, chemical, hydrological, and mechanical factors on water/rock interaction in HDR geothermal systems. Zhang L (Ed) Engineering Properties of Rocks – Volume 2, Elsevier, Berlin, pp. 649-654.

Förster A, Fuchs S, Förster H-J & Norden B (2020) Ambiguity of crustal geotherms: A thermal-conductivity perspective. *Geothermics* 89, 101937.

Fortier R, Allard M, Lemieux JM, Therrien R, Molson J & Fortier D (2011) *Cartographie des depots quaternaires des villages nordiques de Whapmagoostui-Kuujjuarapik, Umijuaq, Salluit, Kuujjuaq,* Report No.: MB 2011-12. Gouvernement du Québec, Québec, 123 p: http://gq.mines.gouv.qc.ca/documents/EXAMINE/MB201112/MB201112.pdf (Accessed Feb 22, 2021).

Franco A & Ponte C (2019) The role of geothermal in the energy transition in the Azores, Portugal. *European Geologist Journal* 47:21–27.

Frankel JI (1996) Residual-minimization least-squares method for inverse heat conduction. *Computers & Mathematics with Applications* 32(4):117-130.

Fraser T, Colpron M & Relf C (2019) Evaluating geothermal potential in Yukon through temperature gradient drilling. *Yukon Exploration and Geology* 2018:75-90.

Frash LP (2014) *Laboratory-scale study of hydraulic fracturing in heterogeneous media for enhanced geothermal systems and general well stimulation*. Doctor of Philosophy (Ph.D.) in Civil and Environmental Engineering (Colorado School of Mines, Golden, US). 155 p. https://mountainscholar.org/handle/11124/17002

Frick S, Van Wees JD, Kaltschmitt M & Schröder G (2010) Economic performance and environmental assessment. Huenges E (Ed.) Geothermal Energy Systems: Exploration, Development, and Utilization, Wiley, Weinheim, pp. 373-421.

Friedman M (1964) Petrographic techniques for the determination of principal stress directions in rocks. Proceedings, International Conference on State of Stress in the Earth's crust.

Fuchs S & Förster A (2014) Well-log based prediction of thermal conductivity of sedimentary successions: a case study from the North German Basin. *Geophysical Journal International* 196(1):291-311.

Furlong KP & Chapman DS (2013) Heat flow, heat generation and the thermal state of the Lithosphere. *Annual Review of the Earth and Planetary Sciences* 41:16:1-16:26.

Gajewski K (2015) Quantitative reconstruction of Holocene temperatures across the Canadian Arctic and Greenland. *Global and Planetary Change* 128:14-23.

Garg SK & Combs J (2015) A reformulation of USGS volumetric “heat in place” resource estimation method. *Geothermics* 55:150–158.

Garnish JD (1985) Hot Dry Rock – A European perspective. *GRC Transactions* 9:329-337.

Gascuel V, Bédard K, Comeau F-A, Raymond J & Malo M (2020) Geothermal resource assessment of remote sedimentary basins with sparse data: lessons learned from Anticosti Island, Canada. *Geothermal energy* 8, 3.

Gascuel V, Comeau F-A, Rivard C & Raymond J (2019) Preliminary modelling of deep geothermal energy use in the Bécancour area (Québec). 1st Canadian Geothermal Students' Days. (Québec City, Canada, Nov 21-22, 2019).

GCan – Government of Canada (2021) *Earthquakes Canada*. https://earthquakescanada.nrcan.gc.ca/stndon/NEDB-BNDS/bulletin-en.php (Accessed April 22, 2021).

GCan – Government of Canada (2020a) *Renewable energy facts*. https://www.nrcan.gc.ca/science-data/data-analysis/energy-data-analysis/energy-facts/renewable-energy-facts/20069 (Accessed Jan 25, 2021).

GCan – Government of Canada (2020b) *Magnetic declination calculator*. https://www.geomag.nrcan.gc.ca/calc/mdcal-en.php (Accessed Jan 25, 2021).

GCan – Government of Canada (2016) *Pan-Canadian Framework on Climate Growth and Climate Change*. Government of Canada, Ottawa. 86 p: http://publications.gc.ca/collections/collection_2017/eccc/En4-294-2016-eng.pdf (Accessed Feb 24, 2021).

Gehringer M (2015) Use of waste heat from geothermal power plants focusing on improving agriculture in developing countries. *GRC Transactions* 39:125–132.

GEMex [2020] *Project description*. http://www.gemex-h2020.eu/index.php?option=com_content&view=article&id=2&Itemid=103&lang=en (Accessed Feb 26, 2021).

Generation Energy (2018) *Canada's Energy Transition: Getting to our energy future, together.* Generation Energy Council, Ottawa. 59 p:

https://www.nrcan.gc.ca/sites/www.nrcan.gc.ca/files/energy/CoucilReport_june27_English_Web.pdf (Accessed Feb 24, 2021).

Genter A, Evans K, Cuenot N, Fritsch D & Sanjuan B (2010) Contribution of the exploration of deep crystalline fractured reservoir of Soultz to the knowledge of enhanced geothermal systems (EGS). *Comptes Rendus Geoscience* 342(7-8):502-516.

Genter A, Castaing C, Dezayes C, Tenzer H, Traineau H & Villemin T (1997) Comparative analysis of direct (core) and indirect (borehole imaging tools) collection of fracture data in the Hot Dry Rock Soultz reservoirs (France). *Journal of Geophysical Research* 102(B7):15419-15431.

GEOENERGY (2020) *Geothermal Country Overview: The Canary Islands*. https://www.geoenergymarketing.com/energy-blog/geothermal-country-overivew-the-canary-islands/ (Accessed Aug 30, 2020).

Ghassemi A (2012) A review of some rock mechanics issues in geothermal reservoir development. *Geotechnical and Geological Engineering* 30:647-664.

Gidley JL, Holditch SA, Nierode DA & Veatch Jr. RW (1989) *Recent Advances in Hydraulic Fracturing.* Society of Petroleum Engineers, Richardson, 461 p.

Gillespie PA, Johnston JD, Loriga MA, McCaffrey KJW, Walsh JJ & Watterson J (1999) Influence of layering on vein systematics in line samples. McCaffrey KJW, Lonergan L & Wilkinson JJ (Eds.) Fractures, Fluid Flow and Mineralization, Geological Society, London, pp. 35-56.

Gilman JR & Ozgen C (2013) *Reservoir Simulation: History Matching and Forecasting*. Society of Petroleum Engineers, Richardson, 129 p.

Gilmour B, Oldfield E, Platis H & Wicks E (2018) *Toward a positive energy future in northern and remote communities*, Summary Report. QUEST, Ottawa. 12 p: https://www.nrcan.gc.ca/sites/www.nrcan.gc.ca/files/emmc/pdf/2018/en/3c-energy-transition-in-northern-and-remote-Communities-workshop-repor-eng.pdf (Accessed Mar 2, 2021).

Giordano N & Raymond J (2019a) Alternative and sustainable heat production for drinking water needs in a subarctic climate (Nunavik, Canada): borehole thermal energy storage to reduce fossil fuel dependency in off-grid communities. *Applied Energy* 252, 113463.

Giordano N, Chicco J, Mandrone G, Verdoya M & Wheeler WH (2019b) Comparing transient and steady-state methods for the thermal conductivity characterization of a borehole heat exchanger field in Bergen, Norway. *Environmental Earth Sciences* 78, 460.

Giordano N, Kanzari I, Miranda MM, Dezayes C & Raymond J (2018) Underground thermal energy storage in subarctic climates: a feasibility study conducted in Kuujjuaq (QC, Canada). IGSHPA. (Stockholm, Sweden, Sept 18-20, 2018).

Giordano N, Kanzari I, Miranda MM, Dezayes C & Raymond J (2017) Shallow geothermal resource assessments for the northern community of Kuujjuaq, Québec, Canada. IGCP636 Annual Meeting 2017. (Santiago de Chile, Chile, Nov 20-24, 2017).

Gischig VS, Giardini D, Amann F, Hertrich M, Krietsch H, Loew S, Maurer H, Villiger L, Wiemer S, Bethmann F, Brixel B, Doetsch J, Doonechaly NG, Driesner T, Dutler N, Evans KF, Jalali M, Jordan D, Kittilä A, Ma X, Meier P, Nejati M, Obermann A, Plenkers K,Saar MO, Shakas A & Valley B (2020) Hydraulic stimulation and fluid circulation experiments in underground laboratories: Stepping up the scale towards engineered geothermal systems. *Geomechanics for Energy and the Environment* 24, 100175.

Glassley WE (2010) *Geothermal energy: Renewable Energy and the Environment*. CRC Press, Boca Raton, 285 p.

Gomes RK, Oliveira LPL, Gonzaga jr. L, Tognoli FMW, Veronez MR & Souza MK (2016) An algorithm for automatic detection and orientation estimation of planar structures in LiDAR-scanned outcrops. *Computers & Geosciences* 90:170-178.

Gonzalez de Vallejo LI & Hijazo T (2008) A new method of estimating the ratio between in situ rock stresses and tectonics based on empirical and probabilistic analyses. *Engineering Geology* 101(3-4):185-194.

Gonzalez de Vallejo LI, Serrano AA, Capote R & de Vicente G (1988) The state of stress in Spain and its assessment by empirical methods. ISRM International Symposium. (Madrid, Spain, Sept 12-16, 1988).

Goodman RE (1976) *Methods of geological engineering in discontinuous rocks*. West Publishing Company, New York, 484 p.

Görgen MA (2016) *Feasibility Study of Renewable Energy Systems for Off-Grid Islands: A Case Study Concerning Cuttyhunk Island*. Master of Science (M.Sc.) (University of Rhode Island). 208 p. https://digitalcommons.uri.edu/cgi/viewcontent.cgi?article=1914&context=theses

Gosnold W, Majorowicz J, Klenner R & Hauck S (2011) Implications of post-glacial warming for Northern Hemisphere heat flow. *GRC Transactions* 35:795-800.

Goulet N (1995) *Étude structurale, stratigraphique et géochronologique de la partie nord de la Fosse du Labrador*, MB 95-36. Gouvernment of Québec, Quebec. 42 p: https://gq.mines.gouv.qc.ca/documents/EXAMINE/MB9536/MB9536.pdf (Accessed Feb 26, 2021)

Graham C & Talay D (2013) *Stochastic Simulation and Monte Carlo Methods: Mathematical Foundations of Stochastic Simulation.* Springer, Berlin, 264 p.

Grant MA & Bixley PF (2011) *Geothermal Reservoir Engineering*. Academic Press, Oxford, 379 p.

Grasby SE, Ansari SM, Bryant R, Calahorrano-DiPatre A, Chen Z, Craven JA, Dettmer J, Gilbert H, Hanneson C, Harris M, Hormozzade F, Liu J, Montezadian D, Muhammad M, Russel JK, Salvage RO, Savard G, Tschirhart V, Unsworth MJ, Vigouroux-Caillibot N, Williams-Jones G & Williamson AR (2020) *Garibaldi Geothermal Energy Project – Mount Meager 2019 – Field Report*, Geoscience BC Report 2020-09. Geoscience BC, Vancouver. 153 p: http://www.geosciencebc.com/i/project_data/GBCReport2020-09/GeoscienceBCReport%202020-09.pdf (Accessed Feb 12, 2021).

Grasby SE, Majorowicz J & McCune G (2013) *Geothermal Energy Potential for Northern Communities*, Report No.: Open File 7350. Geological Survey of Canada, Ottawa. 50 p: http://ftp.geogratis.gc.ca/pub/nrcan_rncan/publications/ess_sst/292/292840/of_7350.pdf (Accessed July 23, 2019).

Grasby SE, Allen DM, Bell S, Chen Z, Ferguson G, Jessop A, Kelman M, Ko M, Majorowicz J, Moore M, Raymond J & Therrien R (2012) *Geothermal Energy Resource Potential of Canada*, Report No.: Open File 6914. Geological Survey of Canada, Ottawa. 322 p: http://ftp.geogratis.gc.ca/pub/nrcan_rncan/publications/ess_sst/291/291488/of_6914.pdf (Accessed July 23, 2019).

Gray J, Boutray B, Hillaire-Marcel C & Lauriol B (1980) Postglacial emergence of the West coast of Ungava Bay, Quebec. *Arctic and Alpine Research* 12(1):19-30.

Green S, McLennan J, Panja P, Kitz K, Allis R & Moore J (2021) Geothermal battery energy storage. *Renewable Energy* 164:777-790.

Gunawan E, Giordano N, Jensson P, Newson J & Raymond J (2020) Alternative heating systems for northern remote communities: techno-economic analysis of ground-coupled heat pumps in Kuujjuaq, Nunavik, Canada. *Renewable Energy* 147(1):1540-1553.

Guo J, Liu S, Zhang P, Wu L, Zhou W & Yu Y (2017) Towards semi-automatic rock mass discontinuity orientation and set analysis from 3Dpoint clouds. *Computers & Geosciences* 103:164-172.

Guo L, Yu Z, Wang C, Li F, Schiettekatte J, Deslauriers J-C & Bai L (2016) Optimal design of battery energy storage system for a wind-diesel off-grid power system in a remote Canadian community. *IET Generation, Transmission & Distribution* 10(3):608-616.

Guo T, Gong F, Wang X, Lin Q, Qu Z & Zhang W (2019) Performance of enhanced geothermal system (EGS) in fractured geothermal reservoirs with CO_2 as working fluid. *Applied Thermal Engineering* 152:215-230.

Gutierrez M & Youn DJ (2015) Effects of fracture distribution length scale on the equivalent continuum elastic compliance of fractured rock masses. *Journal of Rock Mechanics and Geotechnical Engineering* 7(6):626-637.

Haenel R (1982) *The Urach geothermal project, (Swabian Alb,Germany).* Schweizerbart'sche Verslagsbuchhandlung, Germany, 419 p.

Haimson BC & Cornet FH (2003) ISRM suggested methods for rock stress estimation – Part 3: hydraulic fracturing (HF) and/or hydraulic testing of pre-existing fractures (HTPF). *International Journal of Rock Mechanics and Mining Sciences* 40(7-8):1011-1020.

Hall J, Louden KE, Funck T & Deemer S (2002) Geophysical characteristics of the continental crust along the Lithoprobe Eastern Canadian Shield Onshore-Offshore Transect (ECSOOT): a review. *Canadian Journal of Earth Sciences* 39(5):569-587.

Hall J, Wardle RJ, Gower CF, Kerr A, Coflin K, Keen CE & Carroll P (1995) Proterozoic orogens of the northeastern Canadian Shield: new information from the Lithoprobe ECSOOT crustal reflection seismic survey. *Canadian Journal of Earth Sciences* 32(8):1119-1131.

Hammer PTC, Clowes RM, Cook FA, Velden AJ & Vasudevan K (2010) The Lithoprobe trans-continental lithospheric cross sections: imaging the internal structure of the North American continent. *Canadian Journal of Earth Sciences* 47(5):821-857.

Han W, Yan Y & Yan X (2020) Uncertainty and sensitivity analysis of in-situ stress in deep inclined strata. *Geotechnical and Geological Engineering* 38:2699-2712.

Hao Q, Wang L, Oldfield F & Guo Z (2015) Extra-long interglacial in Northern Hemisphere during MISs 15-13 arising from limited extent of Arctic ice sheets in glacial MIS 14. *Scientific Reports* 5, 12103.

Hardebol NJ & Bertotti G (2013) DigiFract: A software and data model implementation for flexible acquisition and processing of fracture data from outcrops. *Computers & Geosciences* 54:326-336.

Häring MO, Schanz U, Ladner F & Dyer BC (2008) Characterisation of the Basel 1 enahnced geothermal system. *Geothermics* 37(5):469-495.

Harlé P, Kushnir ARL, Aichholzer C, Heap MJ, Hehn R, Maurer V, Baud P, Richard A, Genter A & Duringer P (2019) Heat flow density estimates in the Upper Rhine Graben using laboratory measurements of thermal conductivity on sedimentary rocks. *Geothermal Energy* 7, 38.

Harris B (2017) *A CFD study on the extraction of geothermal energy from abandoned oil and gas wells*. Master of Science (M.Sc.) (McMaster University). https://macsphere.mcmaster.ca/bitstream/11375/21455/2/Harris_Brianna_E_2017March_MASc.pdf.

Harris RN & Chapman DS (1998) Geothermics and climate change 1. Analysis of borehole temperatures with emphasis on resolving power. *Journal of Geophysical Research* 103(B4): 7363-7370.

Hartmann A & Rath V (2005a) Uncertainties and shortcomings of ground surface temperature histories derived from inversion of temperature logs. *Journal of Geophysics and Engineering* 2:299-311.

Hartmann A, Rath V & Clauser C (2005b) Thermal conductivity from core and well log data. *International Journal of Rock Mechanics and Mining Sciences* 42(7-8):1042-1055.

Hasegawa HS & Basham PW (1989) Spatial Correlation between Seismicity and Postglacial Rebound in Eastern Canada. Gregersen S & Basham PW (Eds.) Earthquakes at North-Atlantic Passive Margins: Neotectonics and Postglacial Rebound, Kluwer Academic Publishers, Dordrecht, pp 483-500.

Hashida T (2015) Geothermal Energy. Tanaka Y, Norton M & Li YY (Eds.) Topical Themes in Energy and Resources, Springer, Tokyo, pp. 93-111.

Hashizume M (1974) Surface wave study of earthquakes near north-western Hudson Bay, Canada. *Journal of Geophysical Research* 79:5458-5468.

Hasterok D, Gard M & Webb J (2018) On the radiogenic heat production of metamorphic, igneous, and sedimentary rocks. *Geoscience Frontiers* 9(6):1777-1794.

Hasterok D & Webb J (2017) On the radiogenic heat production of igneous rocks. *Geoscience Frontiers* 8:919-940.

Hayashi K, Willis-Richards J, Hopkirk RJ & Niibori Y (1999) Numerical models of HDR geothermal reservoirs – a review of current thinking and progress. *Geothermics* 28(4-5):507-518.

Healy D, Rizzo RE, Cornwell DG, Farrell NJC, Watkins H, Timms NE, Gomez-Riva E & Smith M (2017) FracPaQ: A MATLAB™ toolbox for the quantification of fracture patterns. *Journal of Structural Geology* 95:1-16.

Heidbach O, Rajabi M, Reiter K & Ziegler MO (2019) World Stress Map. Sorkhabi R (Ed.) Encyclopedia of Petroleum Geoscience, Springer, Cham, pp 1-8.

Heim A (1878) *Untersuchungen tiber den Mechanismus der Gebirgsbildung*. Anschluss and die Geologische Monographie der TodiWindgtilen-Gruppe, B. Schwabe, Basel.

Herget G (1993) Rock Stresses and Rock Stress Monitoring in Canada. Hudson JA (Ed) Rock Testing and Site Characterization: Principles, Practice and Projects, Elsevier, Berlin, pp 473-496.

Herget G (1987) Stress assumptions for underground excavations in the Canadian shield. *International Journal of Rock Mechanics & Mining Sciences & Geomechanics Abstracts* 24(1):95-97.

Herget G (1982) High stress occurrences in the Canadian Shield. 23rd US Symposium on Rock Mechanics (USRMS). (Berkeley, US, Aug 25, 1982).

Herget G (1974) Ground stress determinations in Canada. *Rock mechanics* 6:53-64.

Hertzog RC & Plasek RE (1979) Neutron-excited gamma-ray spectrometry for well logging. *IEEE Transactions on Nuclear Science* 26(1):1558-1567.

Hickson C, Raymond J, Maurice D, Tiffani F, Katie H, Marcia K, Miranda M, Poux B, Kathryn F, Grant F, Janis D, Banks J, Unsworth M, Brunskill B, Grasby S, Witter J (2020) Geothermal energy in Canada – Times are “a changing”. *GRC Transactions* 44:819-844.

Hjartarson A & Armannsson H (2010) Geothermal Research in Greenland. Proceedings, World Geothermal Congress. (Bali, Indonesia, April 25–29, 2010).

Hoek E & Brown ET (1980) *Underground Excavation in Rock*. Institute of Mining & Metallurgy, London, 532 p.

Hoffman PF (1988) United plates of America, the birth of a craton: Early Proterozoic assembly and growth of Laurentia. *Annual review of Earth and Planetary Sciences* 16:543-603.

Hofmann H, Babadagli T, Yoon JS, Blöcher G & Zimmermann G (2016) A hybrid discrete/finite element modeling study of complex hydraulic fracture development for enhanced geothermal systems (EGS) in granitic basements. *Geothermics* 64:362-381.

Hofmann H, Weides S, Babadagli T, Zimmermann G, Moeck I, Majorowicz J & Unsworth M (2014) Potential for enhanced geothermal systems in Alberta, Canada. *Energy* 69:578-591.

Hogarth R & Holl H-G (2017) Lessons learned from the Habanero EGS project. *GRC Transactions* 41:865-877

Homuth S & Sass I (2014) Outcrop Analogue vs. Reservoir Data: Characteristics and controlling factors of physical properties of the upper Jurassic geothermal carbonate reservoirs of the Molasse Basin, Germany. Proceedings, Thirty-Eighth Workshop on Geothermal Reservoir Engineering. (Stanford, CA, US, Feb 24 – 26, 2014).

Hopcroft PO, Gallagher K & Pain CC (2009) A Bayesian partition modelling approach to resolve spatial variability in climate records from borehole temperature inversion. *Geophysical Journal International* 178(2):651-666.

Hou X & Roos P (2008) Critical comparison of radiometric and mass spectrometric methods for the determination of radionuclides in environmental, biological and nuclear waste samples. *Analytica Chimica Acta* 608(2):105-139.

Hossain I, Sharip N & Viswanathan KK (2012) Efficiency and resolution of HPGe and NaI(Tl) detectors using gamma-ray spectroscopy. *Scientific Research and Essays* 71:86-89.

Howell JA, Martinius AW & Good TR (2014) The application of outcrop analogues in geological modelling: A review, present status and future outlook. *Geological Society London* 387:1-25.

Hu L, Ghassemi A, Pritchett J & Garg S (2020) Characterization of laboratory-scale hydraulic fracturing for EGS. *Geothermics* 83, 101706.

Huang KK, Hickson CJ, Cotterill D & Champollion Y (2021) Geothermal assessment of target formations using recorded temperature measurements for the Alberta No.1 geothermal project. *Applied Sciences* 11(2), 608.

Huang L, Tang H, Tan Q, Wang D, Wang L, Eldin MAME, Li C & Wu Q (2016) A novel method for correcting scanline-observational bias of discontinuity orientation. *Scientific Reports* 6, 22942.

Huang S, Shen PY & Pollack HN (1996) Deriving century-long trends of surface temperature change from borehole temperatures. *Geophysical Research Letters* 23(3):257-260.

Hubbert MK & Willis DG (1957) Mechanics of hydraulic fracturing. *Transactions of Society of Petroleum Engineers of AIME* 210:153-163

Hubert L, Comeau F-A, Raymond J & Malo M (2019) Évaluation des ressources géothermiques aux Îles-de-la-Madeleine. XIVème Colloque International Franco-Québécois en énergie. (Baie St-Paul, Canada, June 16-20, 2019).

Hudson JA, Cornet FH & Christiansson R (2003) ISRM suggested methods for rock stress estimation – part 1: strategy for rock stress estimation. *International Journal of Rock Mechanics and Mining Sciences* 40:991-998.

Hughes JD (2018) *Canada's Energy Outlook: Current realities and implications for a carbon-constrained future*. CCPA, Vancouver. 180 p: https://ccpabc2018.files.wordpress.com/2018/05/cmp_canadas-energy-outlook-2018_full.pdf (Accessed Feb 24, 2021).

Hussain N (1991) Radon modelling and the heat transfer surface area of the British hot dry rock geothermal reservoir. *Proceedings of the Indian Academy of Sciences – Earth and Planetary Sciences* 100:1-11.

Hydro Québec (2019) *Rate DN*. http://www.hydroquebec.com/residential/customer-space/rates/rate-dn.html (Accessed May 11, 2020).

Hydro Quebec (2002) *Particularites des Reseaux Autonomes,* Hydro-Quebec Distribution. Hydro Quebec, Quebec City. 17 p: http://www.regie-energie.qc.ca/audiences/3492-02/Requete3492/HQD-02-02-1.pdf (Accessed Feb 22, 2021)

Hyman JD, Karra S, Makedonska N, Gable CW, Painter SL & Viswanathan HS (2015) DFNWorks: A discrete fracture network framework for modeling subsurface flow and transport. *Computers & Geosciences* 84:10-19.

Ibrahim H, Younès R, Ilinca A, Ramdenee D, Dimitrova M, Perron J, Adegnon M, Boulay D & Arbez C (2011) Potential of a hybrid wind-diesel-compressed air system for nordic remote Canadian areas. *Energy Procedia* 6:795-804.

IGSHPA – International Ground Source Heat Pump Association [2021] *Geothermal: An overview of Geothermal Ground Source Heat Pumps*. https://igshpa.org/geothermal/ (Accessed Feb 26, 2021).

Imre A, Kustán R & Groniewsky A (2020) Mapping of the Temperature–Entropy Diagrams of van der Waals Fluids. *Energies* 13, 1519.

IRENA—International Renewable Energy Agency (2019) *Off-Grid Renewable Energy Solutions to Expand Electricity Access: An Opportunity Not to Be Missed*. IRENA, Abu Dhabi. 28 p: https://www.irena.org/-/media/Files/IRENA/Agency/Publication/2019/Jan/IRENA_Off-grid_RE_Access_2019.pdf (Accessed Feb 22, 2021).

IRENA–International Renewable Energy Agency (2016) *Off-Grid Renewable Energy in Africa*. https://www.irena.org/-/media/Files/IRENA/Agency/Data-Statistics/Off-grid-renewable-energy-in-Africa.pdf?la=en&hash=0FEC28407B13C1A7AAD58F5AC28E295A4541EEA4 (Accessed Aug 12, 2020).

Islam FMR, Mamun KA & Amanullah MTO (Eds.) (2017) *Smart Energy Grid Design for Island Countries: Challenges and Opportunities.* Springer, Cham, 468 p.

ISRM - International Society for Rock Mechanics Commission on Standardization of Laboratory and Field Tests suggested methods for the quantitative description of discontinuities in rock masses. *International Journal of Rock Mechanics and Mining Sciences & Geomechanics Abstracts* 15:319-368.

Jaeger JC, Cook NGW & Zimmerman RW (2007) *Fundamentals of Rock Mechanics*. Blackwell Publishing, Oxford, 489 p.

Jalali M, Gischig V, Doetsch J, Näf R, Krietsch H, Klepikova M, Amann F & Giardini D (2018) Transmissivity changes and microseismicity induced by small-scale hydraulic fracturing tests in crystalline rock. Geophysical Research Letters 45:2265-2273.

James DT, Connelly JN, Wasteneys HA & Kilfoil GJ (1996) Paleoproterozoic lithotectonic divisions of the southeastern Churchill Province, western Labrador. *Canadian Journal of Earth Sciences* 33:216-230.

Jaume-Santero F, Pickler C, Beltrami H & Mareschal J-C (2016) North American regional climate reconstruction from ground surface temperature histories. *Climate of the Past* 12:2181-2194.

Jaupart C, Mareschal J-C & Iarotsky L (2016) Radiogenic heat production in the continental crust. *Lithos* 262:398-427.

Jaupart C & Mareschal J-C (2014) Constraints on crustal heat production from heat flow data. Rudnick RL (Ed.) Treatise on Geochemistry, Elsevier, Amsterdam, pp. 53-73.

Jaupart C & Mareschal J-C (2011) *Heat Generation and Transport in the Earth*. Cambridge University Press, Cambridge, 490 p.

Jaupart C & Mareschal J-C (2007) Heat flow and thermal structure of the lithosphere. Watts AB (Ed.) Treatise on Geophysics, Elsevier, Amsterdam, pp. 217-251.

Jennings CE, Aber JS, Balco G, Barendregt R, Bierman PR, Rovey CW, Roy M, Thorleifson LH & Mason JA (2013) Mid-Quaternary in North America. Elias S & Mock C (Eds.) Encyclopedia of Quaternary Science, Elsevier Science, Netherlands, pp. 180-186.

Jennings S, Hasterok D & Payne J (2019) A new compositionally based thermal conductivity model for plutonic rocks. *Geophysical Journal International* 219(2):1377-1394.

Jessop A (2008) *Review of National Geothermal Energy Program Phase 2 – Geothermal Potential of the Cordillera*, Report No.: Open File 5906. Geological Survey of Canada, Ottawa. 86 p: http://ftp.geogratis.gc.ca/pub/nrcan_rncan/publications/ess_sst/225/225917/of_5906.pdf (Accessed October 13, 2020)

Jessop AM (1998) Geothermal energy in Canada. *Geoscience Canada* 25(1):33-41.

Jessop AM, MacDonald JK & Spence H (1995) Clean energy from abandoned mines at Springhill, Nova-Scotia. *Energy Sources* 17:93-106.

Jessop AM, Ghomshei MM & Drury MJ (1991a) Geothermal energy in Canada. *Geothermics* 20(5/6):369-385.

Jessop AM & Church BN (1991b) *Geothermal drilling in the Summerland Basin, British Columbia, 1990*, Open File 2348. Geological Survey of Canada, Ottawa. 19 p: http://ftp.geogratis.gc.ca/pub/nrcan_rncan/publications/ess_sst/131/131508/of_2348.pdf (Accessed October 14, 2020).

Jessop AM (1990) *Thermal Geophysics*. Elsevier, Amsterdam, 304 p.

Jessop AM & Vigrass LW (1989) Geothermal measurements in a deep well at Regina, Saskatchewan. *Journal of Volcanology and Geothermal Research* 37(2):151-166.

Jessop AM (1971) The distribution of glacial perturbation of heat flow in Canada. *Canadian Journal of Earth Sciences* 8:162-166.

Jessop AM (1968) Three measurements of heat flow in eastern Canada. *Canadian Journal of Earth Sciences* 5:61-68.

Jing L & Stephansson O (1997) Network topology and homogenization of fractured rocks. Jamtveit B & Yardley BW (Eds.) Fluid Flow and Transport in Rocks – Mechanisms and effects, Chapman & Hall, Netherlands, pp. 191-202.

Jing Y, Jing Z, Willis-Richards J, Hashida T (2014) A simple 3-D thermoelastic model for assessment of the long-term performance of the Hijiori deep geothermal reservoir. *Journal of Volcanology and Geothermal Research* 269:14-22.

Jing Z, Watanabe K, Willis-Richards J & Hashida T (2002) A 3-D water/rock chemical interaction model for prediction of HDR/HWR geothermal reservoir performance. *Geothermics* 31:1-28.

Jing Z, Willis-Richards J, Watanabe K & Hashida T (2000) A three-dimensional stochastic rock mechanics model of engineered geothermal systems in fractured crystalline rock. *Journal of Geophysical Research* 150(10):23663-23679.

Kagel A, Bates D & Gawell KA (2005) *A* Guide *to Geothermal Energy and the Environment.* Geothermal Energy Association, Washington, DC. 88 p: https://www.osti.gov/servlets/purl/897425-q5NDer/ (Accessed Feb 22, 2021).

Kaieda H, Ito H, Kiho K, Suzuki K, Suenaga H & Shin K (2005) Reviewof the Ogachi HDR project in Japan. Proceedings, World Geothermal Congress. (Antalya, Turkey, April 24-29, 2005).

Kana JD, Djongyang N, Raïdandi D, Nouck PN & Dadjé A (2015) A review of geophysical methods for geothermal exploration. *Renewable and Sustainable Energy Reviews* 44:87–95.

Kanase-Patil AB, Saini R & Sharma M (2010) Integrated renewable energy systems for off grid rural electrification of remote area. *Renewable Energy* 35:1342–1349.

Kanzari I (2019) *Évaluation du potentiel des pompes à chaleur géothermique pour la communauté nordique de Kuujjuaq*. Master of Science (M.Sc.) (INRS). 99 p. http://espace.inrs.ca/id/eprint/9063/1/T922.pdf.

Kappelmeyer O & Jung R (1987) HDR experiments at Falkenberg/Bavaria. *Geothermics* 16(4):375-392.

Karanasios K & Parker P (2018) Tracking the transition to renewable electricity in remote indigenous communities in Canada. *Energy Policy* 118:169-181.

Karanasios K & Parker P (2016a) Recent developments in renewable energy in remote aboriginal communities, Yukon, Canada. *Paper in Canadian Economic Development* 16:29-40.

Karanasios K & Parker P (2016b) Recent developments in renewable energy in remote aboriginal communities, NWT, Canada. *Paper in Canadian Economic Development* 16:41-53.

Karanasios K & Parker P (2016c) Recent developments in renewable energy in remote aboriginal communities, Nunavut, Canada. *Paper in Canadian Economic Development* 16:54-64.

Karanasios K & Parker P (2016d) Recent developments in renewable energy in remote aboriginal communities, British Columbia, Canada. *Paper in Canadian Economic Development* 16:65-81.

Karanasios K & Parker P (2016e) Recent developments in renewable energy in remote aboriginal communities, Ontario, Canada. *Paper in Canadian Economic Development* 16:82-97.

Karanasios K & Parker P (2016f) Recent developments in renewable energy in remote aboriginal communities, Québec, Canada. *Paper in Canadian Economic Development* 16:98-108.

Karanasios K & Parker P (2016g) Recent developments in renewable energy in remote aboriginal communities, Newfoundland and Labrador, Canada. *Paper in Canadian Economic Development* 16:109-118.

Kaufman DS, Ager TA, Anderson NJ, Anderson PM, Andrews JT, Bartlein PJ, Brubaker LB, Coats LL, Cwynar LC, Duvall ML, Dyke AS, Edwards ME, Eisner WR,GajewskiK, Geirsdóttir A, Hu FS, Jennings AE, Kaplan MR, Kerwin MW, Lozhkin AV, MacDonald GM, Miller GH, Mock CJ, Oswald WW, Otto-Bliesner BL, Porinchu DF, Rühland K, Smol JP, Steig EJ & Wolfe BB (2004) Holocene thermal maximum in the western Arctic (0-180 ºW). *Quaternary Science Reviews* 23(5-6):529-560.

Kazemi AR, Mahbaz SB, Dehghani-Sanij AR, Dusseault MB & Fraser R (2019) Performance evaluation of an enhanced geothermal system in the Western Canada Sedimentary Basin. *Renewable and Sustainable Energy Reviews* 113, 109278.

Kelkar S, Gabriel GW & Rehfeldt (2016) Lessons learned from the pioneering hot dry rock project at Fenton Hill, USA. *Geothermics* 63:5-14.

Keller A (1998) High resolution, non-destructive measurement and characterization of fracture apertures. *International Journal of Rock Mechanics and Mining Sciences* 35(8):1037-1050.

Keller AA (1997) High resolution cat imaging of fractures in consolidated materials. *International Journal of Rock Mechanics and Mining Sciences* 34(3-4):1-16.

Khan FI, Hawbolt K & Iqbal MT (2005) Life cycle analysis of wind-fuel cell integrated system. *Renewable Energy* 30(2):157-177.

Kinney C, Dehghani-Sanij A, Mahbaz SB, Dusseault MB, Nathwani JA & Fraser RA (2019) Geothermal energy for sustainable food production in Canada's remote northern communities. *Energies* 12(21), 4058.

Kneafsey TJ, Blankenship D, Dobson PF, Morris JP, White MD, Knox HA, Johnson TC, Ajo-Franklin JB, Schwering PC, Fu P, Podgorney R, Huang L, Johnston B, Roggenthen W, Doe T, Ghassemi A, Mattson E, Valladao C & EGS Collab Team (2019) EGS Collab project: Accomplishments and plans. *GRC Transactions* 43:366-367.

Knoblauch TAK & Trutnevyte E (2018) Siting enhanced geothermal systems (EGS): Heat benefits versus induced seismicity risks from an investor and societal perspective. *Energy* 164:1311-1325.

Koelbel T & Genter A (2017) Enhanced Geothermal Systems: The Soultz-sous-Forêts Project. Uyar TS (Ed.) Towards 100% Renewable Energy: Techniques, Costs and Regional Case-Studies, Springer, Cham, pp 243-248.

Kohl T (1999) Transient thermal effects below complex topographies. *Tectonophysics* 306(3-4):311-324.

Koon RK, Marshall S, Morna D, McCallum R & Ashtine M (2020) A review of Caribbean geothermal energy resource potential. *West Indian Journal of Engineering* 42:37–43.

KRG – Kativik Regional Government (2019) *Community Maps*. https://www.krg.ca/en-CA/map/community-maps (Accessed May 11, 2020).

KRG - Kativik Regional Government & Makivik Corporation (2010) *Plan Nunavik*. Avataq Cultural Institute, Québec, 469 p.

Krupa J (2012) Identifying barriers to aboriginal renewable energy deployment in Canada. *Energy Policy* 42:710-714.

Kruszewski M, Hofmann H, Alvarez FG, Bianco C, Haro AJ, Garduño VH, Liotta D, Trumpy E, Brogi A, Wheeler W, Bastesen E, Parisio F & Saenger EH (2021) Integrated stress field estimation and implications for enhanced geothermal system development in Acoculco, Mexico. *Geothermics* 89, 101931.

Kukkonen IT & Clauser C (1994) Simulation of heat transfer at the Kola deep-hole site: implications for advection, heat refraction and paleoclimatic effects. *Geophysical Journal International* 116(2):409-420.

Kumari WGP & Ranjith PG (2019) Sustainable development of enhanced geothermal systems based on geotechnical research – A review. *Earth-Science Reviews* 199, 102955.

Kunkel T, Ghomshei M & Ellis R (2012) Geothermal energy as an indigenous alternative energy source in British Columbia. *Journal of Ecosystems and Management* 13(2):1-16.

Kusznir NJ (1991) The distribution of stress with depth in the lithosphere: thermo-rheological and geodynamic constraints. *Philosophical Transactions of the Royal Society of London. Series A: Physical and Engineering Sciences* 337:95-110.

Kusznir NJ & Park RG (1986) Continental lithosphere strength: the critical role of lower crustal deformation. *Geological Society* 24:79-93.

Kusznir NJ & Park RG (1984a) Intraplate lithosphere deformation and the strength of the lithosphere. *Geophysical Journal International* 79(2):513-538.

Kusznir NJ & Park RG (1984b) The strength of intraplate lithosphere. *Physics of the Earth and Planetary Interiors* 36(3-4):224-235.

Kusznir NJ & Park RG (1982) Intraplate lithosphere strength and heat flow. *Nature* 290:540-542.

Kusznir NJ (1982) Lithosphere response to externally and internally derived stresses: a viscoelastic stress guide with amplification. *Geophysical Journal International* 70(2):399-414.

Lachenbruch AH (1970) Crustal temperature and heat production: Implications of the linear heat-flow relation. *Journal of Geophysical Research* 75(17):3291–3300.

Lacirignola M & Blanc I (2013) Environmental analysis of practical design options for enhanced geothermal systems (EGS) through life-cycle assessment. *Renewable Energy* 50:901-914.

Lafrance I, Charette B & Vanier M-A (2018) *Southeastern Churchill Province, Nunavik, Quebec, Canada: Geological Synthesis*. http://gq.mines.gouv.qc.ca/bulletins-geologiques_en/churchill_en/ (Accessed Feb 26, 2021).

Lafrance I, Simard M & Bandyayera D (2014) *Géologie de la Région du Lac Saffray (SNRC 24F, 24G)*, Report No.: RG 2014-02. Gouvernement du Québec, Québec. 51 p: http://gq.mines.gouv.qc.ca/documents/examine/RG201402/RG201402.pdf (Accessed May 5, 2019).

Lahiri S (2021) Estimating effective permeability using connectivity and branch length distribution of fracture network. *Journal of Structure Geology* 146, 104314

Lam H-L & Jones FW (1985) Geothermal energy potential in the Hinton-Edson area of west-central Alberta. *Canadian Journal of Earth Sciences* 22(3):369-383.

Lamas R, Miranda MM, Pereira AJSC, Neves LJPF, Ferreira N & Rodrigues NV (2017) 3-D distribution of the radioelements in the granitic rocks of northern and central Portugal and geothermal implications. *Journal of Iberian Geology* 43(1):3-12.

Lamontagne M (2008) Earthquakes in eastern Canada: a threat that can be mitigated. Proceedings, 4th Canadian Conference on Geohazards. (Quebec, Canada, May 20-24, 2008).

Lang N & Wolff EW (2011) Interglacial and glacial variability from the last 800 ka in marine, ice and terrestrial archives. *Climate of the Past* 7:361-380.

Lanyon GW, Batchelor AS & Ledingham P (1993) Results from a discrete fracture network model of a hot dry rock system. Proceedings, 18th Workshop on Geothermal Reservoir Engineering. (Stanford, US, Jan 26-28, 1993).

Larssen K, Senger K & Grundvag S-A (2020) Fracture characterization in Upper Permian carbonates in Spitsbergen: A workflow from digital outcrop to geo-model. *Marine and Petroleum Geology* 122, 104703.

Lato M, Kemeny J, Harrap RM & Bevan G (2013) Rock bench: Establishing a common repository and standards for assessing rockmass characteristics using LiDAR and photogrammetry. *Computers & Geosciences* 50:106-114.

Lato MJ, Bevan G & Fergusson M (2012) Gigapixel imaging and photogrammetry: Development of a new long range remote imaging technique. *Remote Sensing* 4(10):3006-3021.

Laughlin AW, Eddy AC, Laney R & Aldrich Jr. MJ (1983) Geology of the Fenton Hill, New Mexico, hot dry rock site. *Journal of Volcanology and Geothermal Research* 15(1-3) :21-41.

Lauriol B (1982) Géomorphologie quaternaire du sud de l'Ungava. *Paleo-Quebec* 15:180 p.

Lea E (2020) *A step towards a lower carbon future: Integrating closed loop geothermal technology in district cooling applications.* Master of Science (M.Sc.) (University of Calgary). 79 p. https://prism.ucalgary.ca/bitstream/handle/1880/112636/capstone_Lea_2020.pdf?sequence=1&isAllowed=y.

Lee CF, Zhang JM & Zhang YX (1996) Evaluation and origin of the ground fissures in Xian, China. *Engineering Geology* 43(1):45-55.

Lee HS & Cho TF (2002) Hydraulic characteristics of rough fractures in linear flow under normal and shear load. *Rock Mechanics and Rock Engineering* 35:299-318.

Lee T-C (1991) On terrain corrections in terrestrial heat flow. *Pure and Applied Geophysics* 135:1-13.

Lee Y & Deming D (1998) Evaluation of thermal conductivity temperature corrections applied in terrestrial heat flow studies. *Journal of Geophysical Research* 103(B2):2447-2454.

Lehtonen A, Cosgrove JW, Hudson JA & Johansson E (2012) An examination of *in situ* rock stress estimation using the Kaiser effect. *Engineering Geology* 124:24-37.

LeMenager A, O'Neill C, Zhang S & Evans M (2018) The effect of temperature-dependent thermal conductivity on the geothermal structure of the Sydney Basin. *Geothermal Energy* 6, 6.

Lepillier B, Bruna P-O, Bruhn D, Bastesen E, Daniildis A, Garcia O, Torabi A & Wheeler W (2020) From outcrop scanlines to discrete fracture networks, an integrative workflow. *Journal of Structural Geology* 133, 103992.

Lepillier B, Daniilidis A, Gholizadeh ND, Bruna P-O, Kummerow J & Bruhn D (2019) A fracture flow permeability and stress dependency simulation applied to multi-reservoirs, multi-production scenarios analysis. *Geothermal Energy* 7, 24.

Lerche I (1991) Temperature dependence of thermal conductivity and its impact on assessments of heat flux. *Pure and Applied Geophysics* 136:191-200.

Lévy F, Jaupart C, Mareschal J-C, Bienfait G & Limare A (2010) Low heat flux and large variations of lithospheric thickness in the Canadian Shield. *Journal of Geophysical Research Solid Earth* 115(B6), 404.

Lewis JF & Jessop AM (1981) Heat flow in the Garibaldi volcanic belt, a possible Canadian geothermal energy resource area. *Canadian Journal of Earth Sciences* 18:366-375.

Lianheng Z, Dongliang H, Jingyu C, Xiang W, Wei L, Zhiheng Z, Dejian L & Shi Z (2020) A practical photogrammetric workflow in the field for the construction of a 3D rock joint surface database. *Engineering Geology* 279, 105878.

Limberger J, Bonte D, Vicente G, Beekman F, Cloetingh S & van Wees JD (2017) A public domain model for 1D temperature and rheology construction in basement-sedimentary geothermal exploration: an application to the Spanish Central System and adjacent basins. *Acta Geodaetica et Geophysica* 52:269-282.

Limberger J, Calcagno P, Manzella A, Trumpy E, Boxem T, Pluymaekers MPD & Van Wees J-D (2014) Assessing the prospective resource base for enhanced geothermal systems in Europe. *Geothermal Energy Science* 2:55–71.

Lindal B (1973) Industrial and other Application of Geothermal Energy. Armstead HCH (Ed.) Geothermal Energy, UNESCO, Paris, pp. 135-148.

Lisiecki LE & Raymo ME (2005) A Pliocene-Pleistocene stack of 57 globally distributed benthic $\delta^{18}O$ records. *Paleoceanography* 20, PA1003.

Liu X, Wei M, Yang L & Wang X (2017) Thermo-economic analysis and optimization selection of ORC system configurations for low temperature binary-cycle geothermal plant. *Applied Thermal Engineering* 125:153–164.

Lovekin D & Heerema D (2019a) *Diesel, renewables, and the future of Canada's remote communities*. https://www.pembina.org/blog/remote-microgrids-intro (Accessed October 13, 2020).

Lovekin D & Heerema D (2019b) *The True Cost of Energy in Remote Communities*. https://www.pembina.org/reports/diesel-cost-backgrounder-2019.pdf (Accessed Feb 24, 2021).

Lu S-M (2018) A global review of enhanced geothermal system (EGS) *Renewable and Sustainable Energy Reviews* 81(2):2902-2921.

Lund JW & Chiasson A (2007) Examples of combined heat and power plants using geothermal energy. Proceedings, European Geothermal Congress. (Unterhaching, Germany, May 30 – June 1, 2007).

MacDonald P, Stedman A & Symons G (1992) The UK geothermal hot dry rock R&D programme. Proceedings, 17th Workshop on Geothermal Reservoir Engineering. (Stanford, US, Jan 29-31, 1992).

Mackay DJC (1998) Introduction to Monte Carlo methods. Jordan MI (Ed.) Learning in Graphical Models, Kluwer Academic Press, Dordrecht, pp. 175–204.

Mah J, Samson C & McKinnon SD (2011) 3D laser imaging for joint orientation analysis. *International Journal of Rock Mechanics and Mining Sciences* 48(6):932-941.

Mahbaz SB, Yaghoubi A, Dehghani-Sanij A, Sarvaramini E, Leonenko Y & Dusseault MB (2021) Well-doublets: A first-order assessment of geothermal sedheat systems. *Applied Sciences* 11(2), 697.

Mahbaz SB, Dehghani-Sanij AR, Dusseault MB & Nathawani JS (2020) Enhanced and integrated geothermal systems for sustainable development of Canada's northern communities. *Sustainable Energy Technologies and Assessments* 37, 100565.

Majorowicz J & Grasby SE (2021) Deep geothermal heating potential for the communities of the Western Canadian Sedimentary Basin. *Energies* 14(3), 706.

Majorowicz JA & Grasby SE (2020) Heat transition for major communities supported by geothermal energy development of the Alberta Basin, Canada. *Geothermics* 88, 101883.

Majorowicz J & Minea V (2015a) Shallow and deep geothermal energy potential in low heat flow/cold climate environment: northern Québec, Canada, case study. *Environmental Earth Sciences* 74:5233-5244.

Majorowicz J & Minea V (2015b) Geothermal Energy Potential in Low Enthalpy Areas as a Future Energy Resource: identifying Feasible Targets, Québec, Canada, Study Case. *Resources* 4(3):524-547.

Majorowicz J & Safanda J (2015c). Effect of postglacial warming seen in high precision temperature log deep into the granites in NE Alberta. *International Journal of Earth Sciences* 104:1563-1571.

Majorowicz J & Moore M (2014a) The feasibility and potential of geothermal heat in the deep Alberta foreland basin—Canada for CO_2 savings. *Renewable Energy* 66:541-549.

Majorowicz J & Grasby SE (2014b) Geothermal Energy for Northern Canada: is it economical? *Natural Resources Research* 23(1):159-173.

Majorowicz J & Minea V (2012a) Geothermal energy potential in the St-Lawrence River area, Québec. *Geothermics* 43:25-36.

Majorowicz J, Gosnold W, Gray Al, Safanda J, Klenner R & Unsworth M (2012b) Implications of post-glacial warming for northern Alberta heat flow-correcting for the underestimate of the geothermal potential. *GRC Transactions* 36, 693-698.

Majorowicz J & Wybraniec S (2011) New terrestrial heat flow map of Europe after regional paleoclimatic correction application. *International Journal of Earth Sciences* 100:881-887.

Majorowicz J & Grasby SE (2010a) Heat flow, depth-temperature variations and stored thermal energy for enhanced geothermal systems in Canada. *Journal of Geophysics and Engineering* 7(3):232-241.

Majorowicz J & Grasby SE (2010b) High potential regions for enhanced geothermal systems in Canada. *Natural Resources Research* 19:177-188.

Majorowicz JA, Skinner WR & Safanda J (2005) Ground surface warming history in Northern Canada inferred from inversions of temperature logs and comparison with other proxy climate reconstructions. *Pure and Applied Geophysics* 162:109-128.

Makivik Corporation (2018) *Rise in the Cost of Gasoline*. https://www.makivik.org/rise-in-the-cost-of-gasoline/ (Accessed July 6, 2020).

Manesh FH, Mazraeh HD & Tabasi SH (2015) Solving Inverse Heat Conduction Problem by Nelder-Mead simplex search method. 8th International Conference of the Iranian Society of Operations Research. (Mashhad, Iran, May 21-22, 2015).

Mansure AJ & Reiter M (1979) A vertical groundwater movement correction for heat flow. *Journal of Geophysical Research: Solid Earth* 84(B7):3490-3496.

Manzocchi T (2002) The connectivity of two-dimensional networks of spatially correlated fractures. *Water Resources Research* 38(9):1162.

Mao R, Feng Z, Liu Z & Zhao Y (2017) Laboratory hydraulic fracturing test on large-scale pre-cracked granite specimens. *Journal of Natural Gas Science and Engineering* 44:278-286

Mareschal J-C & Jaupart C (2013) Radiogenic heat production, thermal regime and evolution of continental crust. *Tectonophysics* 609:524-534.

Mareschal J-C & Jaupart C (2006) Archean thermal regime and stabilization of the cratons. *Archean Geodynamics and Environments* 164:61-73.

Mareschal J-C, Poirier A, Rolandone F, Bienfait G, Gariépy C, Lapointe R & Jaupart C (2000) Low mantle heat flow at the edge of the North American continent, Voisey Bay, Labrador. *Geophysical Research Letters* 27(6):823-826.

Mareschal J-C, Rolandone F & Bienfait G (1999) Heat flow variations in a deep borehole near Sept-Îles, Québec, Canada: paleoclimatic interpretation and implications for regional heat flow estimates. *Geophysical Research Letters* 26(14):2049-2052.

Mareschal J-C & Beltrami H (1992) Evidence for recent warming from perturbed geothermal gradients: examples from eastern Canada. *Climate Dynamics* 6:135-143.

Mareschal J-C, Coletta GD, Clevenot I & Goulet N (1990) Gravity profile and crustal structure across the northern New Québec Orogen. *Geoscience Canada* 17(4):250-255.

Markovaara-Koivisto M & Laine E (2012) MATLAB script for analyzing and visualizing scanline data. *Computers & Geosciences* 40:185-193.

Masoud AA & Koike K (2011) Auto-detection and integration of tectonically significant lineaments from SRTM DEM and remotely-sensed geophysical data. *ISPRS Journal of Photogrammetry and Remote Sensing* 66:818-832.

Massiot C, Townend J, Nicol A & McNamara DD (2017) Statistical methods of fracture characterization using acoustic borehole televiewer log interpretation. *JGR Solid Earth* 122(8):6836-6852.

Mather B, Farrell T & Fullea J (2018) Probabilistic surface heat flow estimates assimilating paleoclimate history: new implications for the thermochemical structure of Ireland. *Journal of Geophysical Research: Solid Earth* 123:10951-10967.

Matos CR, Carneiro JF & Silva PP (2019) Overview of large-scale underground energy storage technologies for integration of renewable energies and criteria for reservoir identification. *Journal of Energy Storage* 21:241-258.

Matsumoto M & Nishimura T (1998) Mersenne twister: A 623-dimensionally equidistributed uniform pseudo-random number generator. *ACM Transactions on Modeling and Computer Simulation* 8:3–30.

Matsunaga I, Niitsuma H & Oikawa Y (2005) Review of the HDR development at Hijiori site, Japan. Proceedings, World Geothermal Congress. (Antalya, Turkey, April 24-29, 2005).

Mattauer M (1973) *Les deformations des matériaux de l'écorce terrestre*. Hermann, Paris, 493 p.

Mazzotti (2007) Geodynamic models for earthquake studies in intraplate North America. Stein S & Mazzotti S (Eds.) Continental Intraplate Earthquake: Science, Hazard, and Policy Issues, Geological Society of America, pp. 17-34

McAliley WA & Li Y (2019) Methods to invert temperature data and heat flow data for thermal conductivity in steady-state conductive regime. *Geosciences* 9, 293.

McCay A, Harley TL, Younger PL, Sanderson DCW & Cresswell AJ (2014) Gamma-ray spectrometry in geothermal exploration: state of the art techniques. *Energies* 7:4757-4780.

McClure MW & Horne RN (2014) An investigation of stimulation mechanisms in Enhanced Geothermal Systems. *International Journal of Rock Mechanics and Mining Sciences* 72:242-260.

McClure M (2012) *Modeling and characterization of hydraulic stimulation and induced seismicity in geothermal and shale gas reservoirs*, Doctor of Philosophy (Ph.D.) (Stanford University, Stanford). 369 pp. https://pangea.stanford.edu/ERE/pdf/pereports/PhD/McClure2012.pdf

McCutchen WR (1982) Some elements of a theory for in-situ stress. *International Journal of Rock Mechanics and Mining Sciences & Geomechanical Abstracts* 19:201-203.

McFarlan A (2018) Techno-economic assessment of pathways for electricity generation in northern remote communities in Canada using methanol and dimethyl ether to replace diesel. *Renewable and Sustainable Energy Reviews* 90:863-876.

McLeod T, Samson C, Labrie M, Shehata K, Mah J, Lai P, Wang L & Elder JH (2013) Using video acquired from an Unmanned Aerial Vehicle (UAV) to measure fracture orientation in an open-pit mine. *Geomatica* 67(3):173-180.

Mehmood A, Yao J, Fan D, Bongole K, Liu J & Zhang X (2019) Potential for heat production by retrofitting abandoned gas wells into geothermal wells. *PLoS ONE* 14(8), e0220128.

Menegoni N, Meisina C, Perotti C & Crozi M (2018) Analysis by UAV digital photogrammetry of folds and related fractures in the Monte Antola Flysch Formation (Ponte Organasco, Italy). *Geosciences* 8(8), 299.

MERN – Énergie et Ressources naturelles Québec (2020a) *Churchill Province*. http://gq.mines.gouv.qc.ca/lexique-stratigraphique/province-de-churchill_en/ (Accessed Feb 26, 2021).

MERN – Énergie et Ressources naturelles Québec (2020b) *Baleine Lithotectonic Domain*. http://gq.mines.gouv.qc.ca/lexique-stratigraphique/province-de-churchill/domaine-lithotectonique-de-baleine_en/ (Accessed Feb 26, 2021).

MERN – Énergie et Ressources naturelles Québec (2020c) *Ungava Complex*. http://gq.mines.gouv.qc.ca/lexique-stratigraphique/province-de-churchill/complexe-ungava_en/ (Accessed Feb 26, 2021).

MERN – Énergie et Ressources naturelles Québec (2020d) *False Suite*. http://gq.mines.gouv.qc.ca/lexique-stratigraphique/province-de-churchill/suite-de-false_en/ (Accessed Feb 26, 2021).

MERN – Énergie et Ressources naturelles Québec (2020e) *Kuujjuaq Pluton*. http://gq.mines.gouv.qc.ca/lexique-stratigraphique/province-de-churchill/pluton-de-kuujjuaq_en/ (Accessed Feb 26, 2021).

MERN – Énergie et Ressources naturelles Québec (2020f) *Aveneau Suite*. http://gq.mines.gouv.qc.ca/lexique-stratigraphique/province-de-churchill/suite-aveneau_en/ (Accessed Feb 26, 2021).

MERN – Énergie et Ressources naturelles Québec (2020g) *Kaslac Complex.* http://gq.mines.gouv.qc.ca/lexique-stratigraphique/province-de-churchill/complexe-de-kaslac_en/ (Accessed Feb 26, 2021).

MERN – Énergie et Ressources naturelles Québec (2020h) *Ralleau Suite.* http://gq.mines.gouv.qc.ca/lexique-stratigraphique/province-de-churchill/suite-de-ralleau_en/ (Accessed Feb 26, 2021).

MERN – Énergie et Ressources naturelles Québec (2020i) *Dancelou Suite.* http://gq.mines.gouv.qc.ca/lexique-stratigraphique/province-de-churchill/suite-de-dancelou_en/ (Accessed Feb 26, 2021).

MERN – Énergie et Ressources naturelles Québec (2020j) *Falcoz Swarm.* http://gq.mines.gouv.qc.ca/lexique-stratigraphique/province-de-churchill/essaim-de-falcoz_en/ (Accessed Feb 26, 2021).

Miao SQ, Li HP & Chen G (2014) Temperature dependence of thermal diffusivity, specific heat capacity, and thermal conductivity for several types of rocks. *Journal of Thermal Analysis and Calorimetry* 115:1057-1063.

Midttome K, Jochmann M, Henne I, Wangen M & Thomas PJ (2015) Is geothermal energy an alternative for Svalbard? Proceedings, 3rd Sustainable Earth Sciences Conference & Exhibition. (Celle, Germany, Oct 13–15, 2015).

Mignan A, Karvounis D, Broccardo M, Wiemer S & Giardini D (2019) Including seismic risk mitigation measures into the Levelized Cost of Electricity in enhanced geothermal systems for optimal siting. *Applied Energy* 238:831-850.

Milker Y, Rachmayani R, Weinkauf MFG, Prange M, Raitzsch M, Schulz M & Kucera M (2013) Global and regional sea surface temperature trends during Marine Isotope Stage 11. *Climate of the Past* 9:2231-2252.

Miller GH, Brigham-Grette J, Alley RB, Anderson L, Bauch HA, Douglas MSV, Edwards ME, Elias SA, Finney BP, Fitzpatrick JJ, Funder SV, Geirsdóttir A, Herbert TD, Hinzman LD, Kaufman DS, MacDonald GM, Plyak L, Robock A, Serreze MC, Smol JP, Spelhagen R, White JWC, Wolfe AP & Wolff EW (2013) Paleoclimate history of the Arctic. Elias S & Mock C (Eds.) Encyclopedia of Quaternary Science, Elsevier, Oxford, pp. III:113-III:125

Minissale A (1991) The Larderello geothermal field: a review. *Earth-Sciences Reviews* 31(2):133-151.

Minnick M, Shewfelt D, Hickson C, Majorowicz J & Rowe T (2018) *Nunavut Geothermal Feasibility Study*, Report No.: Topical Report RSI-2828. Qulliq Energy Corporation, Iqaluit. 42 p: https://www.cangea.ca/nunavutgeothermal.html (Accessed July 23, 2019).

Miranda MM, Marquez MIV, Raymond J & Dezayes C (2021) A numerical approach to infer terrestrial heat flux from shallow temperature profiles in remote northern regions. *Geothermics* 93, 102064.

Miranda MM, Giordano N, Raymond J, Pereira AJSC & Dezayes C (2020a) Thermophysical properties of surficial rocks: a tool to characterize geothermal resources of remote northern regions. *Geothermal Energy* 8, 4.

Miranda MM, Raymond J & Dezayes C (2020b) Uncertainty and risk evaluation of deep geothermal energy source for heat production and electricity generation in remote northern regions. *Energies* 13(6), 4221.

Miranda MM, Giordano N, Kanzari I, Raymond J & Dezayes C (2018a) Temperature-depth profiles measured in the Inuit community of Kuujjuaq, Northern Quebec, Canada. 2nd Northern Research Day. (Montreal, Canada, Jan 24, 2018).

Miranda MM, Dezayes C, Giordano N, Kanzari I, Raymond J & Carvalho J (2018b) Fracture network characterization as input for geothermal energy research: Preliminary data from Kuujjuaq, Northern Québec, Canada. Proceedings, 43rd Workshop on Geothermal Reservoir Engineering. (Stanford, US, Feb 12-14, 2018).

Mitchell EK, Fialko Y & Brown KM (2013) Temperature dependence of frictional healing of Westerly granite: Experimental observations and numerical simulations. *Geochemistry, Geophysics, Geosystems* 14(3):567-582.

Moeck IS (2014) Catalog of geothermal play types based on geologic controls. *Renewable and Sustainable Energy Reviews* 37:867-882.

Mogensen P (1983) Fluid to duct wall heat transfer in duct system heat storages. Proceedings, International Conference on Subsurface Heat Storage in Theory and Practice. (Stockholm, Sweden, June 6-8, 1983).

Moore J, McLennan J, Pankow K, Simmons S, Podgorney R, Wannamaker P, Jones C, Rickard W & Xing P (2020) The Utah Frontier Observatory for Research in Geothermal Energy (FORGE): A Laboratory for Characterizing, Creating and Sustaining Enhanced Geothermal Systems. Proceedings, 45th Workshop on Geothermal Reservoir Engineering. (Stanford, US, Feb 10-12, 2020).

Moore J, McLennan J, Allis R, Pankow K, Simmons S, Podgorney R, Wannamaker P, Bartley J, Jones C & Rickard W (2019) The Utah Frontier Observatory for Research in Geothermal Energy (FORGE): An International Laboratory for Enhanced Geothermal System Technology Development. Proceedings, 44th Workshop on Geothermal Reservoir Engineering. (Stanford, US, Feb 11-13, 2019).

Moorhead J (1989) *Stratigraphy, structure and metamorphism of the Renia basement gneiss body and the adjacent cover succession in the Western hinterland zone of the Northern Labrador Trough, West of Kuujjuaq, Northern Quebec*. Master of Science (M.Sc.) (McGill University). 284 p. https://escholarship.mcgill.ca/concern/theses/1g05fc91n.

Morgan P (2013) Advantages of choosing a sedimentary basin as the site for an EGS field laboratory. *GRC Transactions* 37:179-184.

Morley CK & Nixon CW (2016) Topological characteristics of simple and complex normal fault networks. *Journal of Structural Geology* 84:68-84.

Mouchot J, Genter A, Cuenot N, Scheiber J, Seibel O, Bosia C & Ravier G (2018) First year of operation from EGS geothermal plants in Alsace, France: scaling issues. Proceedings, 43rd Workshop on Geothermal Reservoir Engineering. (Stanford, US, Feb 12-14, 2018).

Muffler P & Cataldi R (1978) Methods for regional assessment of geothermal resources. *Geothermics* 7:53–89.

Mukherjee S (2011) *Applied mineralogy: applications in industry and environment*. Springer, Dordrecht, 562 p.

Murphy H & Dash Z (1985) The shocking behavior of fluid flow in deformable joints. *GRC Transaction*s 9:115-118.

Nagaraju P & Roy S (2014) Effect of water saturation on rock thermal conductivity measurements. *Tectonophysics* 626:137–143.

Nakamura K, Jacob KH & Davies JN (1977) Volcanoes as possible indicators of tectonic stress orientation – Aleutians and Alaska. *Pure and Applied Geophysics* 115:87-112.

Nakatsuka K (1999) Field characterization for HDR/HWR: a review. *Geothermics* 28:519-531.

Nasr M, Raymond J, Malo M & Gloaguen E (2018) Geothermal potential of the St. Lawrence Lowlands sedimentary basin from well log analysis. *Geothermics* 75:68-80.

Nelder JA & Mead R (1965) A simplex method for function minimization. *The Computer Journal* 7(4):308-313.

Nielsen SB & Beck AE (1989) Heat flow density values and paleoclimate determined from stochastic inversion of four temperature-depth profiles from the Superior Province of the Canadian Shield. *Tectonophysics* 164:345-359.

Norbeck JH, McClure MW & Horne RN (2018) Field observations at the Fenton Hill enhanced geothermal system test site support mixed-mechanism stimulation. *Geothermics* 74:135-149.

Norden B, Förster A, Förster H-J & Fuchs S (2020) Temperature and pressure corrections applied to rock thermal conductivity: impact on subsurface temperature prognosis and heat-flow determination in geothermal exploration. *Geothermal Energy* 8, 1.

NRCan – Natural Resources Canada (2021) Emerging Renewable Power Program. https://www.nrcan.gc.ca/climate-change/green-infrastructure-programs/emerging-renewable-power/20502 (Accessed Jul 30, 2021).

NRCan – Natural Resources Canada (2018a) Earthquakes Canada – Canada. https://www.earthquakescanada.ca/index-en.php (Accessed Oct 6, 2020).

NRCan – Natural Resources Canada (2018b) The atlas of Canada—remote communities energy database. https://atlas.gc.ca/rced-bdece/en/index.html (Accessed Jan 19, 2019).

NRCan—Natural Resources Canada (2011) *Status of Remote/Off-Grid Communities in Canada,* M154-71/2013E. Government of Canada, Quebec City. 44 p: https://www.nrcan.gc.ca/sites/www.nrcan.gc.ca/files/canmetenergy/files/pubs/2013-118_en.pdf (Accessed Feb 22, 2021).

Nyberg B, Nixon CW & Sanderson DJ (2018) NetworkGT: A GIS tool for geometric and topological analysis of two-dimensional fracture networks. *Geosphere* 14(4):1-17.

Occhietti S, Parent M, Lajeunesse P, Robert F & Govare E (2011) Late Pleistocene-Early Holocene decay of the Laurentide Ice Sheet in Québec-Labrador. Ehlers J, Gibbard PL & Hughes PD (Eds.) Quaternary glaciations – extent and chronology: a closer look, Elsevier, Oxford, pp. 601-630.

Occhietti S, Govare E, Klassen R, Parent M & Vincent J-S (2004) Late Wisconsinan-Early Holocene deglaciation of Québec-Labrador. Ehlers J & Gibbard PL (Eds.) Quaternary Glaciations – Extent and Chronology, Part II, Elsevier, Oxford, pp. 243-273.

Ojo A, Kao H, Jiang Y, Craymer M & Henton J (2020). Strain accumulation and release rate in Canada: Implications for long-term crustal deformation and earthquake hazards. *Journal of Geophysical Research: Sloid Earth* (pre-print).

Olasolo P, Juárez MC, Morales MP, Olasolo A & Agius MR (2018) Analysis of working fluids applicable in Enhanced Geothermal Systems: Nitrous oxide as an alternative working fluid. *Energy* 157:150-161.

Olasolo P, Juárez MC, Morales MP, D'Amico S & Liarte IA (2016a) Enhanced geothermal systems (EGS): A review. *Renewable and Sustainable Energy Reviews* 56:133-144.

Olasolo P., Juárez MC, Olasolo J, Morales MP & Valdani D (2016b) Economic analysis of Enhanced Geothermal Systems (EGS). A review of software packages for estimating and simulating costs. *Applied Thermal Engineering* 104:647-658.

Ouzzane M, Eslami-Nejad P, Badache M & Aidoun Z (2015) New correlations for the prediction of the undisturbed ground temperature. *Geothermics* 53:379-384.

Özisik MN & Orlande HRB (2017) *Inverse Heat Transfer: fundamentals and applications*. CRC Press, Boca Raton, 349 p.

Özisik MN (1993) *Heat Conduction*. John Wiley & Sons, Inc., New York, 356 p.

Palisade (2019) @*RISK*. https://www.palisade.com/risk/default.asp (Accessed June 18, 2020).

Palit D & Chaurey A (2011) Off-grid rural electrification experiences from South Asia: Status and best practices. *Energy for Sustainable Development* 15:266–276.

Pan S-Y, Gao M, Shah KJ, Zheng J, Pei S-L & Chiang P-C (2019) Establishment of enhanced geothermal energy utilization plans: Barriers and strategies. *Renewable Energy* 132:19-32.

Pan S, Kong Y, Chen C, Pang Z & Wang J (2020) Optimization of the utilization of deep borehole heat exchangers. *Geothermal Energy* 8, 6.

Park HJ & West TR (2002) Sampling bias of discontinuity orientation caused by linear sampling technique. *Engineering Geology* 66(1-2):99-110.

Parker J (1973) The relationship between structure, stress, and moisture. *Engineering and Mining Journal* October:91-95.

Parker R (1999) The Rosemanowes HDR project 1983-1991. *Geothermics* 28(4-5):603-615.

Pasquale V, Verdoya M & Chiozzi P (2014) *Geothermics: Heat Flow in the Lithosphere*. Springer, Cham, 126 p.

Past Interglacials Working Group of PAGES (2016) Interglacials of the last 800,000 years. *Reviews of Geophysics* 54:162-219.

Pater I & Lissauer JJ (2001) *Planetary Sciences*. Cambridge University Press, Cambridge, 558 p.

Peacock DCP, Harris SD & Mauldon M (2003) Use of curved scanlines and boreholes to predict fracture frequencies. *Journal of Structural Geology* 25:109-119.

Pei Q, Ding X, Lu B, Zhang Y, Huang S & Dong Z (2016) An improved method for estimating in situ stress in an elastic rock mass and its engineering application. *Open Geosciences* 8(1):523-537.

Peltier WR (2004) Global glacial isostasy and the surface of the ice-age Earth: The ICE-5G (VM2) model and GRACE. *Annual Review of Earth and Planetary Sciences* 32:111-149.

Peltier WR (2002) Global glacial isostatic adjustament: palaeogeodetic and space-geodetic tests of the ICE-4G (VM2) model. *Journal of Quaternary Science* 17(5-6):491-510.

Percival JA, Bleeker W, Cook FA, Rivers T, Ross G & van Staal C (2004) PanLITHOPROBE Workshop IV: Intra-orogen correlation and comparative orogenic anatomy. *Geoscience Canada* 31(1):23-39

Perreault S & Hynes A (1990) Tectonic evolution of the Kuujjuaq terrane, New Quebec Orogen. *Geoscience Canada* 17:238-240.

Perry HKC, Jaupart C, Mareschal J-C & Bienfait G (2014) Estimating concentrations of heat producing elements in the crust near the Sudbury Neutrino Observatory, Ontario, Canada. *Tectonophysics* 622:135-144.

Perry HKC, Jaupart C, Mareschal J-C & Bienfait G (2006) Crustal heat production in the Superior Province, Canadian Shield, and in North America inferred from heat flow data. *Journal of Geophysical Research: Solid Earth* 111, B04401.

Phaneuf C & Mareschal J-C (2014) Estimating concentrations of heat producing elements in the crust near the Sudbury Neutrino Observatory, Ontario, Canada. *Tectonophysics* 622:135–144.

Pickler C, Beltrami H & Mareschal J-C (2016a) Climate trends in northern Ontario and Québec from borehole temperature profiles. *Climate of the Past* 12:2215-2227.

Pickler C, Beltrami H & Mareschal J-C (2016b) Laurentide Ice Sheet basal temperatures during the last glacial cycle as inferred from borehole data. *Climate of the Past* 12:1-13.

Pine RJ & Batchelor AS (1984) Downward migration of shearing in jointed rock during hydraulic injections. *International Journal of Rock Mechanics and Mining Sciences & Geomechanical Abstracts* 21(5):249-263.

Poirier G, Perreault S & Hynes A (1990) Nature of the eastern boundary of the Labrador Trough near Kuujjuaq, Quebec. Lewry JF & Stauffer MR (Eds.) The Early Proterozoic Trans-Hudson Orogen, Geological Association of Canada, St John's, pp. 397-412.

Poirier GG (1989) *Structure and metamorphism of the Eastern boundary of the Labrador Trough near Kuujjuaq, Quebec, and its tectonic implications*. Master of Science (M.Sc.) (McGill University). 229 p. https://escholarship.mcgill.ca/concern/theses/5h73px09v.

Popek MA & Saffer DM (2011) Heat advection by groundwater flow through a heterogeneous permeability crust: A potential cause of scatter in surface heat flow near Parkfield, California. *Journal of Geophysical Research: Solid Earth* 116(B3), B03404.

Popov Y, Beardsmore G, Clauser C & Roy S (2016) ISRM suggested methods for determining thermal properties of rocks from laboratory tests at atmospheric pressure. *Rock Mechanics and Rock Engineering* 49:4179-4207.

Powell WG, Chapman DS, Balling N & Beck AE (1988) Continental Heat-Flow Density. Haenel R, Rybach L & Stegena L (Eds.) Handbook of Terrestrial Heat-Flow Density Determination with Guidelines and Recommendations of the International Heat Flow Commission, Kluwer Academic Publishers, Dordrecht, pp. 167-223.

Priest SD (2004) Determination of discontinuity size distributions from scanline data. *Rock Mechanics and Rock Engineering* 37:347-368.

Priest SD (1993) *Discontinuity Analysis for Rock Engineering*, Chapman & Hall, Netherlands, 489 p.

Priest SD & Hudson JA (1981) Estimation of discontinuity spacing and trace length using scanline surveys. *International Journal of Rock Mechanics and Mining Sciences & Geomechanical Abstracts* 18(3):183-197.

Pruess K (2008) On production behavior of enhanced geothermal systems with CO_2 as working fluid. *Energy Conversion and Management* 49(6):1446-1454.

Pruess K (2006) Enhanced geothermal systems (EGS) using CO_2 as working fluid—A novel approach for generating renewable energy with simultaneous sequestration of carbon. *Geothermics* 35(4):351-367.

Quitoras MR, Campana PE & Crawford C (2020) Exploring electricity generation alternatives for Canadian Arctic communities using a multi-objective genetic algorithm approach. *Energy Conversion and Management* 2010, 112471.

Rajaobelison M, Raymond J, Malo M & Dezayes C (2020) Classification of geothermal systems in Madagascar. *Geothermal Energy* 8, 22

Ranalli G & Rybach L (2005) Heat flow, heat transfer and lithosphere rheology in geothermal areas: Features and examples. *Journal of Volcanology and Geothermal Research* 148(1-2):3-19.

Ranalli G (1997) Rheology of the lithosphere in space and time. Burg J-P & Ford M (Eds.) Orogeny Through Time, Geological Society Special Publication, London, pp. 19-37.

Ranalli G (1991) Regional variations in lithosphere rheology from heat flow observations. Cermak V & Rybach L (Eds.) Terrestrial Heat Flow and the Lithosphere Structure, Springer, Berlin, pp. 1-22.

Ranalli G & Murphy DC (1987) Rheological stratification of the lithosphere, *Tectonophysics* 132:281-295.

Ranjitkar G, Huang J & Tung T (2006) Application of Micro-Hydropower Technology for Remote Regions. IEEE EIC Climate Change Conference. (Ottawa, Canada, Jan 15, 2006).

Rath V, Rouco JFG & Goosse H (2012) Impact of postglacial warming on borehole reconstructions of last millennium temperatures. *Climate of the Past* 8:1059-1066.

Raymond J, Comeau F-A, Malo M, Blessent D & Sánchez IJL (2017) The Geothermal Open Laboratory: a free space to measure thermal and hydraulic properties of geological materials. IGCP636 Annual Meeting. (Santiago de Chile, Chile, Nov 21, 2017).

Raymond J, Malo M, Tanguay D, Grasby S & Bakhteyar F (2015) Direct utilization of geothermal energy from coast to coast: a review of current applications and research in Canada. Proceedings, World Geothermal Congress. (Melbourne, Australia, April 19-25, 2015).

Reid PW, Bendall BR & McAllister L (2010) Developing large scale, base load EGS power – The Paralana project, South Australia. Proceedings, World Geothermal Congress. (Bali, Indonesia, April 25-29, 2010).

Renssen H, Seppä H, Crosta X, Goose H & Roche DM (2012) Global characterization of the Holocene Thermal Maximum. *Quaternary Science Reviews* 48:7-19.

Richard M-A (2016) *Production d'électricité avec des systèmes géothermiques stimulés au Québec : analyse des résultats d'un outil de simulation*, IREQ-2016-0001. Hydro Québec Institut de recherche, Varennes. 164 p: http://espace.inrs.ca/id/eprint/7688/1/R1747.pdf (Accessed Feb 26, 2021).

Richards HG, Parker RH, Green ASP, Jones RH, Nicholls JDM, Nicol DAC, Randall MM, Richards S, Stewart RC & Willis-Richards J (1994) The performance and characteristics of the experimental hot dry rock geothermal reservoir at Rosemanowes, Cornwall (1985-1988). *Geothermics* 23(2):73-109.

Richards HG, Willis-Richards J & Pye J (1991) A review of geological investigations associated with the UK Hot Dry Rock programme. *Proceedings of the Usher Society* 7:321-326.

Richerol T, Fréchette B, Rochon A & Pienitz R (2016) Holocene climate history of the Nunatsiavut (northern Labrador, Canada) established from pollen and dinoflagellate cyst assemblages covering the past 7000 years. *The Holocene* 26(1):44-60.

Richter A, Ko M & Thompson A (2012) Geothermal Energy Development in Canada – Country Update 2012. *GRC Transactions* 36:757-760.

Ringkjøb H-K, Haugan PM & Nybø A (2020) Transitioning remote Arctic settlements to renewable energy systems—A modelling study of Longyearbyen, Svalbard. *Applied Energy* 258, 114079.

Rolandone F, Jaupart C, Mareschal J-C, Gariépy C, Bienfait G, Carbonne C & Lapointe R (2002) Surface heat flow, crustal temperatures and mantle heat flow in the Proterozoic Trans-Hudson Orogen. Canadian Shield. *Journal of Geophysical Research* 107(B12): ETG7-1-ETG7-19.

Rose P, Sheridan J, McCulloch J, Moore JN, Kovac K, Spielman P, Weidler R & Hickman S (2004) The Coso EGS project – recent developments. *GRC Transactions* 28:227-231.

Roy C (2012) *The great geological domains of Québec*. https://mern.gouv.qc.ca/english/publications/mines/publications/geological-domains-quebec.pdf (Accessed March 5, 2021)

Rubinstein RY & Kroese DP (2008) *Simulation and the Monte Carlo Method.* John Wiley & Sons, Inc., Hoboken, 377 p.

Rud JN, Hørmann M, Hammervold V, Ásmundsson R, Georgiev I, Dyer G, Andersen SB, Jessen JE, Kvorning P & Brødsted MR (2018) *Energy in the West Nordics and the Arctic: Cases Studies*, TemaNord 2018:539. Nordic Council of Ministers, Copenhagen. 82 p: http://norden.diva-portal.org/smash/get/diva2:1250869/FULLTEXT01.pdf (Accessed Feb 22, 2021).

Rummel F, Möhring-Erdmann G & Baumgärtner J (1986) Stress constraints and hyrofracturing stress data for the continental crust. *Pure and Applied Geophysics* 124:875-895.

Rutqvist J, Birkholzer J, Cappa F & Tsang C-F (2007) Estimating maximum sustainable injection pressure during geological sequestration of CO_2 using coupled fluid flow and geomechanical fault-slip analysis. *Energy Conversion and Management* 48(6):1798-1807.

Ruuska T, Vinha J & Kivioja H (2017) Measuring thermal conductivity and specific heat capacity values of inhomogeneous materials with a heat flow meter apparatus. *Journal of Building Engineering* 9:135-141.

Rybach L (2015) Classification of geothermal resources by potential. *Geothermal Energy Science* 3:13–17.

Rybach L & Kohl T (2004) Waste heat problems and solutions in geothermal energy. *Geological Society, London, Special Publications* 236:369–380.

Rybach L (1988) Determination of heat production rate., Hänel R, Rybach L & Stegena L (Eds.) Handbook of Terrestrial Heat Flow and Density Determination, Springer, Dordrecht, pp. 125-142.

Rybach L (1976) Radioactive heat production, a physical property determined by the chemistry of rocks. Strens RGJ (Ed.) The Physics and Chemistry of Minerals and Rocks, Wiley, London, pp. 309-318.

Saadat A, Frick S, Kranz S & Regenspurg S (2010) Energetic use of EGS reservoirs. Huenges E (Ed.) Geothermal Energy Systems: Exploration, Development, and Utilization, Wiley, Potsdam, pp. 303–372.

Saevik PN & Nixon CW (2017) Inclusion of topological measurements into analytic estimates of effective permeability in fractured media. *Water Resources Research* 53:9424-9443.

Salvini R, Mastrorocco G, Seddaiu M, Rossi D & Vanneschi C (2017) The use of an unmanned aerial vehicle for fracture mapping within a marble quarry (Carrara, Italy): photogrammetry and discrete fracture network modelling. *Geomatics, Natural Hazards Risk* 8(1):34-52.

Sanderson DJ & Peacock DCP (2019a) Line sampling of fracture swarms and corridors. Journal of Structural Geology 122:27-37.

Sanderson DJ, Peacock DCP, Nixon CW & Rotevatn A (2019b) Graph theory and the analysis of fracture networks. *Journal of Structural Geology* 125:155-165.

Sanderson DJ & Nixon CW (2015) The use of topology in fracture network characterization. *Journal of Structural Geology* 72:55-66.

Sanner B (2014) Geothermal energy – shallow geothermal: Introduction. Plataforma Portuguesa para a geothermal superficial. (Lisbon, Portugal, Oct 7-8, 2014).

Sanyal SK, Morrow JW, Butler SJ & Robertson-Tait A (2007) Cost of electricity from enhanced geothermal systems. Proceedings, 32nd Workshop on Geothermal Reservoir Engineering. (Stanford, US, Jan 22-24, 2007).

Sanyal SK & Butler SJ (2005) An Analysis of Power Generation Prospects from Enhanced Geothermal Systems. Proceedings, World Geothermal Congress. (Antalya, Turkey, April 24–29, 2005).

Sanyal SK, Butler SJ, Swenson D & Hardeman B (2000) Review of the state-of-the-art of numerical simulation of enhanced geothermal systems. Proceedings, World Geothermal Congress. (Kyushu-Tohoku, Japan, May 28-June 10, 2000).

Sarmiento ZF, Steingrímsson B & Axelsson G (2013) Volumetric Resource Assessment. Proceedings, Short Course V on Conceptual Modelling of Geothermal Systems. (Santa Tecla, El Salvador, Feb 2 – Mar 2, 2013).

Sarmineto ZF & Steingrimsson B (2008) Computer Programme for Resource Assessment and Risk Evaluation Using Monte Carlo Simulation. Proceedings, Short Course on Geothermal Project Management and Development. (Entebbe, Uganda, Nov 20–22, 2008).

Sass I & Götz AE (2012) Geothermal reservoir characterization: a thermofacies concept. *Terra Nova* 24:142-147.

Sass JH, Lachenbrunch AH & Moses Jr. TH (1992) Heat flow from a scientific research well at Cajon Pass, California. *Journal of Geophysical Research* 97(B4):5017-5030.

Sass JH, Lachenbruch AH & Jessop AM (1971) Uniform heat flow in a deep hole in the Canadian Shield and its paleoclimatic implications. *Journal of Geophysical Research* 76:8586-8596.

Sass JH (1965) The thermal conductivity of fifteen feldspar specimens. *Journal of Geophysical Research* 76(14):3391-3401.

Sayab M, Aerden D, Paananen M & Saarela P (2018) Virtual structural analysis of Jokisivu open pit using “structure-from-motion” unmanned aerial vehicles (UAV) photogrammetry: Implications for structurally-controlled gold deposits in Southwest Finland. *Remote Sensing* 10(8):1296.

Schallenberg J (2002) Renewable energies in the Canary Islands: Actual situation and perspectives. Afgan NH & da Graça Carvalho M (Eds.) New and Renewable Technologies for Sustainable Development, Springer, Boston, pp. 233–246.

Schatz JF & Simmons G (1972) Thermal conductivity of earth materials at high temperatures. *Journal of Geophysical Research* 77(35):6966-6983.

Scheidegger AE (1995) Geojoints and geostresses. Rossmanith H-P (Ed.) Proceedings, 2nd International Conference of the Mechanics of Jointed and Faulted Rock, Vienna, pp 3-35.

Scheidegger AE (1982) *Principles of Geodynamics*. Springer, Berlin, 398 p.

Scheidt C, Li L & Caers J (Eds.) (2018) *Quantifying Uncertainty in Subsurface Systems*. AGU and Wiley, Washington, DC, 281 p.

Schindler M, Baumgärtner J, Gandy T, Hauffe P, Hettkamp T, Menzel H, Penzkofer P, Teza D, Tischner T & Wahl G (2010) Successful hydraulic stimulation techniques for electric power production in the Upper Rhine Graben, central Europe. Proceedings, World Geothermal Congress. (Bali, Indonesia, April 25-29, 2010).

Scholz CH & Engelder JT (1976) The role of asperity indentation and ploughing in rock friction – I: Asperity creep and stick-slip. *International Journal of Rock Mechanics and Mining Sciences & Geomechanics Abstracts* 13(5):149-154.

Schön JH (2011) *Physical Properties of Rocks: A Workbook.* Elsevier, Amsterdam, 494 p.

Schulte T, Zimmermann G, Vuataz F, Portier S, Tischner T, Junker R, Jatho R & Huenges E (2010) Enhancing geothermal reservoirs. Huenges E. (Ed.) Geothermal Energy Systems: Exploration, Development, and Utilization, Wiley, Weinheim, pp. 173-243.

Scott DJ & St-Onge MR (1998) Proterozoic assembly of northeast Laurentia revisited: a model based on southward extrapolation of Ungava – Baffin crustal architecture. Warle RJ & Hall J (Eds.) Eastern Canadian Shield Onshore-Offshore Transect (ECSOOT), University of British Columbia, Vancouver, pp:134-147.

Sêco SLR, Pereira AJSC, Duarte LV & Domingos FP (2021) Sources of uncertainty in field gamma-ray spectrometry: Implications for exploration in the Lower-Middle Jurassic sedimentary succession of the Lusitanian Basin (Portugal). *Journal of Geochemical Exploration* (available online), 106799.

Seeburger DA & Zoback MD (1982) The Distribution of Natural Fractures and Joints at Depth in Crystalline Rock. *Journal of Geophysical Research* 87(B7):5517-5534.

Seguin MK & Goulet N (1990) Gravimetric transect of eastern Ungava Bay, northern Torngat Orogen. *Geoscience Canada* 17(4):273-275.

Seifollahi S, Dowd PA & Xu C (2014) An enhanced stochastic optimization in fracture network modelling conditional on seismic events. *Computers and Geotechnics* 61:85-95.

Seipold U (1998) Temperature dependence of thermal transport properties of crystalline rocks – a general law. *Tectonophysics* 291:161-171.

Selosse S, Garabedian S, Ricci O & Maizi N (2018) The renewable energy revolution of reunion island. Renewable and Sustainable Energy Reviews 89:99–105.

SERC (2020) *Paleoclimatology: How can we infer past climates?* https://serc.carleton.edu/microbelife/topics/proxies/paleoclimate.html (Accessed Dec 16, 2020).

Serdjuk M, Dumas P, Angelino L & Tryggvadóttir L (2013) *Geothermal Investment Guide*, Deliverable nº 3.4. GEOELEC. 38 p: http://www.geoelec.eu/wp-content/uploads/2011/09/D3.4.pdf (Accessed Aug 12, 2020)

Shah A, Pandey SN, Vishal V & Saha SK (2019) Modeling of heat transfer in abandoned oil and gas wells. Proceedings, 44th Workshop on Geothermal Reservoir Engineering. (Stanford, US, Feb 11-13, 2019).

Shen PY, Pollack HN & Huang S (1996) Inference of ground surface temperature history from borehole temperature data: a comparison of two inverse methods. *Global and Planetary Change* 14(1-2):49-57.

Shen PY & Beck AE (1992) Paleoclimate change and heat flow density inferred from temperature data in the Superior Province of the Canadian Shield. *Palaeogeography, Palaeoclimatology, Palaeoecology* 98:143-165.

Shen PY & Beck AE (1991) Least squares inversion of borehole temperature measurements in functional space. *Journal of Geophysical Research: Solid Earth* 96(B12):19965-19979.

Shen PY & Beck AE (1983) Determination of surface temperature history from borehole temperature gradients. *Journal of Geophysical Research: Solid Earth* 88(B9):7485-7493.

Sheorey PR, Mohan GM & Sinha A (2001) Influence of elastic constants on the horizontal in situ stress. *International Journal of Rock Mechanics and Mining Sciences* 38(8):1211-1216.

Sheorey PR (1994) A theory for in-situ stresses in isotropic and transversely isotropic rock. *International Journal of Rock Mechanics and Mining Sciences & Geomechanical Abstracts* 31:23-34.

Shi W & Pan L (2019) Optimization Study on Fluids for the Gravity-Driven Organic Power Cycle. *Energies* 12, 732.

Sibson RH (2004) Controls on maximum fluid overpressure defining conditions for mesozonal mineralization. *Journal of Structural Geology* 26(6-7):1127-1136.

Sicking C & Malin P (2019) Fracture seismic: mapping subsurface connectivity. *Geosciecnes* 9(12), 508.

SIGÉOM—Système d'information géominière du Québec. *Carte interactive.* http://sigeom.mines.gouv.qc.ca/signet/classes/I1108_afchCarteIntr (Accessed May 5, 2019).

Simard M, Lafrance I, Hammouche H & Legouix C (2013) *Géologie de la Région de Kuujjuaq et de la Baie d'Ungava (SRNC 24J, 24K)*, Report No.: RG 2013-04. Gouvernement du Québec, Québec. 62 p: http://gq.mines.gouv.qc.ca/documents/EXAMINE/RG201304/RG201304.pdf (Accessed May 5, 2019).

Singhal BBS & Gupta RP (2010) *Applied Hydrogeology of Fractured Rocks*, Springer, Netherlands, 429 p.

Sjöberg J, Christiansson R & Hudson JA (2003) ISRM suggested methods for rock stress estimation – Part 2: overcoring methods. *International Journal of Rock Mechanics and Mining Sciences* 40(7-8):999-1010.

Snow DT (1969) Anisotropic permeability of fractured media. *Water Resources Research* 5:1273-1289.

Somerton WH (1992) *Thermal properties and temperature-relate behavior of rock/fluid systems*. Elsevier, Amsterdam, 262 p.

Somma R, Blessent D, Raymond J, Madelaine C, Cotton L, Natale G, Fedele A, Jurado MJ, Marcia K, Miranda M, Troise C & Wiersberg T Transitioning to renewable energy development: a review of unconventional geothermal resource exploration at Campi Flegrei caldera, Cornubian Batholith, and Williston sedimentary basin. Submitted to *Energies*.

Sousa LMO (2007) Granite fracture index to check suitability of granite outcrops for quarrying. *Engineering Geology* 92(3-4):146-159.

Souther JG & Dellechaie F (1984) Geothermal exploration at Mt. Cayley – A Quaternary volcano in Southwestern British Columbia. *GRC Transactions* 8:463-468.

Souther JG (1976) Geothermal power, the Canadian potential. *Geoscience Canada* 3(1):14-20.

Srinivas KNSSS, Rao MS, Kishore PP, Gopinadh D, Raza H, Arora K & Satyanarayana S (2018) Delineation of fractures through acoustic televiewer log. *Journal of the Geological Society of India* 91:569-574.

St-Onge MR, Scott DJ & Wodicka N (2002) Review of crustal architecture and evolution in the Ungava Peninsula–Baffin Island area: connection to the Lithoprobe ECSOOT transect. *Canadian Journal of Earth Sciences* 39(5):589-610.

Statistics Canada (2019) *Census Profile, 2016 Census*. https://www12.statcan.gc.ca/census-recensement/2016/dp-pd/prof/details/page.cfm?Lang=E&Geo1=POPC&Code1=1466&Geo2=PR&Code2=24&SearchText=Kuujjuaq&SearchType=Begins&SearchPR=01&B1=All&GeoLevel=PR&GeoCode=1466&TABID=1&type=0 (Accessed Oct 6, 2020).

Statistics Canada (2016) *Data products, 2016 Census*. www12.statcan.gc.ca/census-recensement/2016/dp-pd/index-eng.cfm (Accessed May 11, 2020).

Steffen R, Eaton DW & Wu P (2012) Moment tensors, state of stress and their relation to post-glacial rebound in northeastern Canada. *Geophysical Journal International* 189:1741-1752.

Stephansson O & Zang A (2012) ISRM Suggested Methods for Rock Stress Estimation—Part 5: Establishing a model for the in situ stress at a given site. *Rock Mechanics and Rock Engineering* 45:955-969.

Stephen JD, Mabee WE, Pribowo A, Pledger S, Hart R, Tallio S & Bull GQ (2016) Biomass for residential and commercial heating in a remote Canadian aboriginal community. *Renewable Energy* 86:563-575.

Stephens MA (1970) Use of the Kolmogorov–Smirnov, Cramér–von Mises and related statistics without extensive tables. *Journal of the Royal Statistical Society B* 32(1):115-122.

Stober I & Butcher K (2013) *Geothermal Energy: From Theoretical Models to Exploration and Development*. Springer, Berlin, 290 p.

Streit JE & Cox SF (2001) Fluid pressures at hypocenters of moderate to large earthquakes. *Journal of Geophysical Research: Solid Earth* 106(B2):2235-2243.

Sturzenegger M, Stead D & Elmo D (2011) Terrestrial remote sensing-based estimation of mean trace length, trace intensity and block size/shape. *Engineering Geology* 119(3-4):96-111.

Sugden DE (1978) Glacial erosion by the Laurentide Ice Sheet. *Journal of Glaciology* 20(83):367-391.

Sugden DE (1977) Reconstruction of the morphology, dynamics, and thermal characteristics of the Laurentide ice sheet at its maximum. *Arctic and Alpine Research* 9(1):21-47.

Sugden DE (1976) A case against deep erosion of shields by ice sheets. *Geology* 4(10):580-582.

Suman A & White D (2017) Quantifying the variability of paleotemperature fluctuations on heat flow measurements. *Geothermics* 67:102-113).

Sundquist U, Wallroth T & Eliasson T (1988) *The Fjällbacka HDR geothermal energy research project: Reservoir characterization and injection well stimulation*. Geothermal Energy Project, Göteborg, 96 p.

TA Instruments (2019) *FOX50*. https://www.tainstruments.com/fox-50/ (Accessed May 4, 2019).

Taghipour M, Ghafoori M, Lashkaripour GR, Moghadas NH & Molaghab A (2019) Estimation of the current stress field and fault reactivation analysis in the Asmari reservoir, SW Iran. *Petroleum Science* 16:513-526.

Taler J & Duda P (2006) *Solving Direct and Inverse Heat Conduction Problems*. Springer, Berlin, 890 p.

Tavani S, Pignalosa A, Corradetti A, Mercuri M, Smeraglia L, Riccardi U, Seers T, Pavlis T & Billi A (2020) Photogrammetric 3D model via smartphone GNSS sensor: Workflow, error estimate, and best practices. *Remote Sensing* 12, 3616.

Taylor A & Judge A (1979) Permafrost studies in northern Québec. *Géographie physique et Quaternaire* 33(3-4):245-251.

Telmat H, Mareschal J-C & Gariépy C (1999) The gravity field over the Ungava Bay region from satellite altimetry and new land-based data: implications for the geology of the area. *Canadian Journal of Earth Sciences* 36:75-89.

Telmat H (1998) *Crustal Structure and Gravity Field Anomalies in Eastern Canada*. Doctor of Philosophy (Ph.D.) in Mineral Ressources (Université du Québec à Montréal). 150 p. https://constellation.uqac.ca/1046/1/11622103.pdf.

Terzaghi K (1962) Measurement of stresses in rock. *Geotechnique* 12(2):105-124.

Terzaghi K & Richart FE (1952) Stresses in rock about cavities. *Géotechnique* 3(2):57-90.

Tesauro M, Kaban MK & Mooney WD (2015) Variations of the lithospheric strength and elastic thickness in North America. *Geochemistry, Geophysics, Geosystems* 16(7):2197-2220.

Tester JW, Reber TJ, Beckers KF & Lukawski MZ (2016) Deep geothermal energy for district heating: lessons learned from the U.S. and beyond. Wiltshire R (Ed.) Advanced District Heating and Cooling (DHC) System, Elsevier, Cambridge, pp. 75-98.

Tester JW, Anderson BJ, Batchelor AS, Blackwell DD, DiPippo R, Drake EM, Garnish J, Livesay B, Moore MC, Nichols K, Petty S, Toksoz MN, Veatch RW, Baria R, Augustine C, Murphy E, Negraru P, Richards M (2007) Impact of enhanced geothermal systems on US energy supply in the twenty-first century. *Philosophical Transactions of the Royal Society A Mathematical, Physical and Engineering Sciences* 365:1057–1094.

Tester JW, Anderson BJ, Batchelor AS, Blackwell DD, DiPippo R, Drake EM, Garnish J, Livesay B, Moore MC, Nichols K, Petty S, Toksöz MN & Veatch Jr RW (2006) *The Future of Geothermal Energy: Impact of Enhanced Geothermal Systems (EGS) on the United States in the 21st Century*. MIT, Idaho Falls. 372 p: https://energy.mit.edu/wp-content/uploads/2006/11/MITEI-The-Future-of-Geothermal-Energy.pdf (Accessed Feb 22, 2021).

Thomopoulos NT (2013) *Essentials of Monte Carlo Simulation: Statistical Methods for Building Simulation Models.* Springer, New York, 183 p.

Thompson A (2010) Geothermal development in Canada: Country update. Proceedings, World Geothermal Congress. (Bali, Indonesia, April 25-29, 2010).

Thompson S & Duggirala B (2009) The feasibility of renewable energies at an off-grid community in Canada. *Renewable and Sustainable Energy Reviews* 13:2740–2745.

Tillmanns D, Gertig C, Schilling J, Gibelhaus A, Bau U, Lanzerath F & Bardow A (2017) Integrated design of ORC process and working fluid using PC-SAFT and Modelica. *Energy Procedia* 129:97–104.

Tomac I & Sauter M (2018) A review of challenges in the assessment of geomechanical rock performance for deep geothermal reservoir development. *Renewable and Sustainable Energy Reviews* 82(3):3972-3980.

Tomarov GV & Shipkov AA (2017) Modern geothermal power: Binary cycle geothermal power plants. *Thermal Engineering* 64:243–250.

Townend J & Zoback MD (2000) How faulting keeps the crust strong. *Geology* 28(5):399-402.

Trice R (1999) Application of borehole image logs in constructing 3D static models of productive fracture networks in the Apulian Platform, Southern Apennines. Lovell MA, Williamson G &

Harvey PK (Eds.) Borehole imaging: Applications and case histories, The Geological Society London, Bath, pp 155-176.

Trota A, Ferreira P, Gomes L, Cabral J & Kallberg P (2019) Power production estimates from geothermal resources by means of small-size compact Climeon heat power converters: case studies from Portugal (Sete Cidades, Azores and Longroiva Spa, Mainland). *Energies* 14(14), 2838.

UN – United Nations (2020) *Sustainable Development Goals*. https://www.un.org/sustainabledevelopment/energy/ (Accessed Jan 25, 2021).

UNECE—United Nations Economic Commission for Europe (2016). *Specifications for the Application of the United Nations Framework Classification for Fossil Energy and Mineral Reserves and Resources 2009 (UNFC—2009) to Geothermal Energy Resources*. UNECE, Geneva. 28 p: https://unece.org/fileadmin/DAM/energy/se/pdfs/UNFC/unfc2009/UNFC2009_ES39_e.pdf (Accessed Feb 22, 2021).

UNFCCC – United Nations Framework Convention on Climate Change (2021) *The Paris Agreement*. https://unfccc.int/process-and-meetings/the-paris-agreement/the-paris-agreement (Accessed Feb 24, 2021).

Uosif MAM, Issa SAM & El-Salam LMA (2015) Measurement of natural radioactivity in granites and its quartz-bearing gold at El-Fawakhir area (central Eastern Desert), Egypt. *Journal of Radiation Research and Applied Sciences* 8(3):393-398.

USGS – United States Geological Survey (2021) *Earthquakes*. https://www.usgs.gov/natural-hazards/earthquake-hazards/earthquakes (Accessed Apr 9, 2021)

Valera M, Guo Z, Kelly P, Matz S, Cantu VA, Percus AG, Hyman JD, Srinivasan G & Viswanathan HS (2018) Machine learning for graph-based representations of three-dimensional discrete fracture networks. *Computers & Geosciences* 22:695-710.

Vasseur G, Bernard Ph, Van de Meulebrouck J, Kast Y & Jolivet J (1983) Holocene paleotemperatures deduced from geothermal measurements. *Palaeogeography, Palaeoclimatology, Palaeoecology* 43(3-4):237-259.

Vasuki Y, Holden E-J, Kovesi P & Micklethwaite S (2014) Semi-automatic mapping of geological Structures using UAV-based photogrammetric data: An image analysis approach. *Computers & Geosciences* 69:22-32.

Vavrus SJ, He F, Kutzbach JE, Ruddiman WF & Tzedakis PC (2018) Glacial inception in Marine Isotope Stage 19: An orbital analog for a natural Holocene climate. *Scientific Reports* 8, 10213.

Velez Marquez MI, Raymond J, Blessent D & Philippe M (2019) Terrestrial heat flow evaluation from thermal response tests combined with temperature profiling. *Physics and Chemistry of the Earth, Parts A/B/C* 113:22-30.

Velez Marquez MI, Blessent D, Córdoba S, López-Sánchez J, Raymond J & Parra-Palacio E (2018a) Geothermal potential assessment of the Nevado del Ruiz volcano based on rock thermal conductivity measurements and numerical modeling of heat transfer. *Journal of South American Earth Sciences* 81:153–164.

Velez Marquez MI, Raymond J, Blessent D, Philippe M, Simon N, Bour & Lamarche L (2018b) Distributed thermal response tests using a heating cable and fiber optic temperature sensing. *Energies* 11(11), 3059.

Vervaet F & Darbyshire FA (2016) Moho depth and bulk crustal properties in Northern Quebec and Labrador. American Geophysical Union, Fall Meeting. (San Francisco, US, Dec 12-16, 2016), abstract #T11B-2608.

Viau AE, Gajewski K, Sawada MC & Fines P (2006) Millennial-scale temperature variations in North America during the Holocene. *Journal of Geophysical Research* 111, D9102.

Vigrass L, Jessop A & Brunskill B (2007) *Regina Geothermal Project*, Summary of Investigations 1. Saskatchewan Geological Survey, Regina. 21 p: https://publications.saskatchewan.ca/api/v1/products/29447/formats/36428/download (Accessed October 13, 2020).

Vilà M, Fernández M & Jiménez-Munt I (2010) Radiogenic heat production variability of some common lithological groups and its significance to lithospheric thermal modeling. *Tectonophysics* 40:152-164.

Viteri JP, Henao F, Cherni J & Dyner I (2019) Optimizing the insertion of renewable energy in the off-grid regions of Colombia. Journal of Cleaner Production 235:535–548.

Vöge M, Lato MJ & Diederichs MS (2013) Automated rockmass discontinuity mapping from 3-dimensional surface data. *Engineering Geology* 164:155-162.

Vollgger SA & Cruden AR (2016) Mapping folds and fractures in basement and cover rocks using UAV photogrammetry, Cape Liptrap and Cape Paterson, Victoria, Australia. *Journal of Structural Geology* 85:168-187.

Vose D (2008) *Risk Analysis: A Quantitative Guide.* John Wiley & Sons, Ltd, Chichester, 729 p.

Vosteen H-D & Schellschmidt R (2003) Influence of temperature on thermal conductivity, thermal capacity and thermal diffusivity for different types of rock. *Physics and Chemistry of the Earth* 28:499-509.

Walsh W (2013) Geothermal resource assessment of the Clarke Lake Gas Field, Fort Nelson, British Columbia. *Bulletin of Canadian Petroleum Geology* 61(3):241-251.

Walters M & Dobson P (2010) *Demonstration of an Enhanced Geothermal System at the Northwest Geysers geothermal field, California*. https://www.energy.gov/eere/geothermal/downloads/demonstration-enhanced-geothermal-system-northwest-geysers-geothermal-0 (Accessed Feb 26, 2021).

Wang K (1992) Estimation of ground surface temperatures from borehole temperature data. *Journal of Geophysical Research: Solid Earth* 97(B2):2095-2106.

Wang Y, Wang L, Bai Y, Wang Z, Hu J, Hu D, Wang Y & Hu S (2021) Assessment of geothermal resources in the North Jiangsu Basin, East China, using Monte Carlo simulation. *Energies* 14(2), 259.

Wardle RJ, James DT, Scott DJ & Hall J (2002) The southeastern Churchill province: synthesis of a Paleoproterozoic transpressional orogen. *Canadian Journal of Earth Sciences* 39:639-663.

Wardle RJ & van Kranendonk MJ (1996) The Palaeoproterozoic Southeastern Churchill Province of Labrador-Quebec, Canada: orogenic development as a consequence of oblique collision and indentation. *Precambrian Crustal Evolution in the North Atlantic Region*, Brewer TS (Ed.) Geological Society Special Publication 112:137-153.

Wardle RJ, Ryan B & Ermanovics I (1990) The eastern Churchill Province, Torngat and New Québec orogens: An overview. *Geoscience Canada* 17(4):217-222.

Watanabe K & Takahashi H (1995) Fractal geometry characterization of geothermal reservoir fracture networks. *Journal of Geophysical Research* 100(1):521-528.

Watchel A (2010) Energy Today: *Geothermal Energy*. Infobase Publishing, New York, 49 p.

Weides S & Majorowicz J (2014) Implications of spatial variability in heat flow for geothermal resource evaluation in large foreland basins: The case of the Western Canada Sedimentary Basin. *Energies* 7:2573-2594.

Weis TM & Ilinca A (2010) Assessing the potential for a wind power incentive for remote villages in Canada. *Energy Policy* 38(10):5504-5511.

Weis TM, Ilinca A & Pinard JP (2008) Stakeholders' perspectives on barriers to remote wind-diesel power plants in Canada. *Energy Policy* 36(5):1611-1621.

Wendlandt RF (1999) Geothermometry and geobarometry. *Encyclopedia of Geochemistry*, Marshall CP & Fairbridge RW (Eds.), Kluwer Academic Publishers, Dordrecht pp. 305-307.

Westway R & Younger PL (2013) Accounting for paleoclimate and topography: a rigorous approach to correction of the British geothermal dataset. *Geothermics* 48, 31-51.

Weydt LM, Ramírez-Guzmán AA, Pola A, Lepillier B, Kummerow J, Mandrone G, Comina C, Deb P, Norini G, Gonzalez-Partida E, Avellán DR, Marcías JL, Bär K & Sass I (2021) Petrophysical and mechanical rock property database of the Los Humeros and Acoculco geothermal fields (Mexico). *Earth System Science Data* 13:571-598.

Weydt LM, Bär K, Colombero C, Comina C, Deb P, Lepillier B, Mandrone G, Milsch H, Rochelle CA, Vagnoh F & Sass I (2018) Outcrop analogue study to determine reservoir properties of the Los Humeros and Acoculco geothermal fields, Mexico. *Advances in Geosciences* 45:281-287.

White DE & Williams DL (1975) *Assessment of Geothermal Resources of the United States—1975,* Circular 726. USGS, Arlington. 155 p: https://pubs.usgs.gov/circ/1975/0726/report.pdf (Accessed Feb 22, 2021).

White M, Fu P, McClure M, Danko G, Elsworth D, Sonnenthal E, Kelkar S & Podgorney R (2018) A suite of benchmark and challenge problems for enhanced geothermal systems. *Geomechanics and Geophysics for Geo-Energy and Geo-Resources* 4:79-117.

Whitmeyer SJ & Karlstrom KE (2007) Tectonic model for the Proterozoic growth of North America. *Geosphere* 3(4):220-259.

Williams CF (2014) Evaluating the volume method in the assessment of identified geothermal resources. *GRC Transactions* 38:967–974.

Williams CF, Reed MJ & Mariner RH (2008) *A Review of Methods Applied by the U.S. Geological Survey in the Assessment of Identified Geothermal Resources*, Open-File Report 2008–1296. USGS, Reston. 30 p: https://pubs.usgs.gov/of/2008/1296/pdf/of2008-1296.pdf (Accessed Feb 22, 2021).

Williams CF (2007) Updated Methods for Estimating Recovery Factors for Geothermal Resources. Proceedings, 32nd Workshop on Geothermal Reservoir Engineering. (Stanford, US, Jan 22–24, 2007).

Willis-Richards J, Watanabe K & Takahashi H (1996) Progress toward a stochastic rock mechanics model of engineered geothermal systems. *Journal of Geophysical Research* 101(8):17481-17496.

Willis-Richards J & Wallroth T (1995) Approaches to the modelling of hdr reservoirs: A review. *Geothermics* 24(3):307-332.

Willis-Richards J (1995) Assessment of HDR reservoir stimulation and performance using simple stochastic models. *Geothermics* 24(3):385-402.

Witter JB, Trainor-Guitton WJ & Siler DL (2019) Uncertainty and risk evaluation during the exploration stage of geothermal development: a review. *Geothermics* 78:233-242.

World Bank (2016) *Reliable and Affordable Off-Grid Electricity Services for the Poor: Lessons from the World Bank Group Experience.* The World Bank, Washington, DC. 100 p: https://ieg.worldbankgroup.org/sites/default/files/Data/reports/lp_off-grid_electricity_1116.pdf (Accessed Feb 22, 2021).

World Bank (2019) *Off-Grid Innovation Improves Thousands of Lives in Rural Peru*. http://documents1.worldbank.org/curated/en/541211565721769744/pdf/Off-Grid-Innovation-Improves-Thousands-of-Lives-in-Rural-Peru.pdf (Accessed July 29, 2020).

Wu P & Hasegawa HS (1996) Induced stresses and fault potential in eastern Canada due to a realistic load: a preliminary analysis. *Geophysical Journal International* 127:215-229.

Wu Q, Larsen E, Heussen K, Binder H & Douglass P (2017) Remote Off-Grid Solutions for Greenland and Denmark: Using smart-grid technologies to ensure secure, reliable energy for island power systems. IEEE Electrification Magazine 5:64–73.

Wüstefeld P, de Medeiros M, Koehrer B, Sibbing D, Kobbelt L & Hilgers C (2018) Evaluation of a workflow to derive terrestrial light detection and ranging fracture statistics of a tight gas sandstone reservoir analog. *AAPG Bulletin* 102(11):2355-2387.

Xie L, Min K-B & Song Y (2015) Observations of hydraulic stimulations in seven enhanced geothermal system projects. *Renewable Energy* 79:56-65.

Xu C, Dong S, Wang H, Wang Z, Xiong F, Jiang Q, Zeng L, Faulkner L, Tian ZF & Dowd P (2021) Modelling of coupled hydro-thermo-chemical fluid flow through rock fracture networks and its applications. *Geosciences* 11(4), 153.

Xu C & Dowd P (2010) A new computer code for discrete fracture network modelling. *Computers & Geosciences* 36:292-301.

Yan C, Rousse D & Glaus M (2019) Multi-criteria decision analysis ranking alternative heating systems for remote communities in Nunavik. *Journal of Cleaner Production* 208:1488–1497.

Yao J, Zhang X, Sun Z, Huang Z, Liu J, Li Y, Xin Y, Yan X & Liu W (2018) Numerical simulation of the heat extraction in 3D-EGS with thermal-hydraulic-mechanical coupling method based on discrete fractures model. *Geothermics* 74:19-34.

Young KR & Levine A (2018) Using GeoRePORT to report socio-economic potential for geothermal development. *Geothermics* 74:163-171.

Young S & Maloney S (2015) *An Update to the Canadian Shield Stress Database*, NWMO-TR-2015-18. NWMO, Toronto. 33 p: https://www.nwmo.ca/~/media/Site/Reports/2016/08/23/10/52/NWMO_TR_2015_18.ashx?la=en (Accessed Feb 26, 2021)

Yu H, Kim D & Gundersen T (2019) A study of working fluids for Organic Rankine Cycles (ORCs) operating across and below ambient temperature to utilize Liquefied Natural Gas (LNG) cold energy. *Energy* 167:730–739.

Zang A & Stephansson O (2019) Special Issue “Hydraulic fracturing in hard rock”. *Rock Mechanics and Rock Engineering* 52:471-473.

Zeeb C, Gomez-Rivas E, Bons PD & Blum P (2013a) Evaluation of sampling methods for fracture network characterization using outcrops. *AAPG Bulletin* 97(9):1545-1566.

Zeeb C, Gomez-Rivas E, Bons PD, Virgo S & Blum P (2013b) Fracture network evaluation program (FraNEP): A software for analyzing 2D fracture trace-line maps. *Computers & Geosciences* 60:11-22.

Zemach E, Drakos P, Spielman P & Akerley J (2017) *Desert Peak East Enhanced Geothermal Systems (EGS) Project*, DE-FC36-02ID14406. ORMAT, Nevada. 87 p: https://www.osti.gov/servlets/purl/1373310 (Accessed Feb 26, 2021).

Zhang L (2017) *Engineering properties of rocks*. Elsevier, Oxford, 394 p.

Zhang L & Einstein HH (1998) Estimating the Mean Trace Length of Rock Discontinuities. *Rock Mechanics and Rock Engineering* 31(4):217-235.

Zhang S, Yin S & Yuan Y (2015) Estimation of fracture stiffness, in situ stresses, and elastic parameters of naturally fractured geothermal reservoirs. *International Journal of Geomechanics* 15(1).

Zhang Y, Hao S, Yu Z, Fang J, Zhang J & Yu X (2018) Comparison of test methods for shallow layered rock thermal conductivity between in situ distributed thermal response tests and laboratory test based on drilling in northeast China. *Energy & Buildings* 173:634-648.

Zhao Y, Pang Z, Huang Y & Ma Z (2020) An efficient hybrid model for thermal analysis of deep borehole heat exchangers. *Geothermal Energy* 8, 18.

Zhu C, Xu M, Qiu N & Hu S (2017) Comparison of γ-ray spectrometry and ICP-MS methods for measuring radioactive heat-producing elements of rocks: a case study on borehole samples from the Sichuan Basin, China. *Journal of Radioanalytical and Nuclear Chemistry* 314:1527-1537.

Zimmerman RW, Al-Yaarubi A, Pain CC & Grattoni CA (2004) Non-linear regimes of fluid flow in rock fractures. *International Journal of Rock Mechanics and Mining Sciences* 41:163-169.

Zinsalo JM, Lamarche L & Raymond J (2021) Sustainable electricity generation from an Enhanced Geothermal System considering reservoir heterogeneity and water losses with a discrete fractures model. *Applied Thermal Engineering* (in press), 116886.

Zinsalo JM, Lamarche L & Raymond J (2020) Injection strategies in an enhanced geothermal system based on discrete fractures model. *Applied Thermal Engineering* 169, 114812.

Zoback MD (2007) *Reservoir Geomechanics*. Cambridge University Press, Cambridge, 504 p.

Zoback MD & Townend J (2001) Implications of hydrostatic pore pressures and high crustal strength for the deformation of intraplate lithosphere. *Tectonophysics* 336(1-4):19-30.

Zoback MD, Zoback ML, Mount VS, Suppe J, Eaton JP, Healy JH, Oppenheimer D, Reasenberg P, Jones L, Raleigh CB, Wong IG, Scotti O & Wentworth C (1987). New evidence on the state of stress of the San Andreas fault system. *Science* 238(4830):1105-1111.

Zoback ML & Zoback MD (1989) Tectonic stress field of the continental United States. Pakiser LC & Mooney WD (Eds.) Geophysical framework of the continental United States, Geological Society of America, Boulder, pp 523-539.

Zweifel P, Praktiknjo A & Erdmann G (2017) *Energy Economics: Theory and Applications*. Springer, Berlin. 333 p.

9 APPENDIX I – FRACTURE NETWORK CHARACTERIZATION AS INPUT FOR GEOTHERMAL ENERGY RESEARCH: PRELIMINARY DATA FROM KUUJJUAQ, NORTHERN QUEBEC, CANADA

Caractérisation du réseau de fractures comme intrant pour la recherche en énergie géothermique: données préliminaires de Kuujjuaq, Nord du Québec, Canada

Authors:

Mafalda M. Miranda (M.M.M.)

Institut national de la recherche scientifique, Canada

Chrystel Dezayes (C.D.)

Bureau de recherches géologiques et minières, France

Nicolò Giordano (N.G.), Inès Kanzari (I.K.), Jasmin Raymond (J.R.)

Institut national de la recherche scientifique, Canada

Jorge de Carvalho

Geosciences Center of University of Coimbra, Portugal

Conference title:

Proceedings, 43rd Workshop on Geothermal Reservoir Engineering

Stanford University, Stanford, California, February 12-14, 2018

SGP-TR-213

Author's contributions:

Conceptualization, M.M.M., C.D., N.G., I.K., J.R. and J.C.; methodology, M.M.M., N.G. and J.C.; validation, M.M.M.; formal analysis, M.M.M.; investigation, M.M.M.; resources, M.M.M., J.R. and C.D.; data curation, M.M.M.; writing – original draft preparation, M.M.M., J.R., N.G. and C.D.;

writing – review and editing, M.M.M., J.R., N.G. and C.D.; visualization, M.M.M.; supervision, J.R. and C.D.; project administration, J.R.; funding acquisition, J.R.

9.1 Introduction

This research work is part of an on-going project that aims to assess the potential of Nunavik geothermal resources through shallow ground-source heat pumps (GSHP), underground thermal energy storage (UTES), deep enhanced/engineered geothermal systems (EGS) and deep borehole heat exchangers for northern communities of Québec using the Inuit community of Kuujjuaq as case study. If geothermal technologies are proven viable in this village, then it can be possible to replicate the solution to other remote and oof-grid communities to help reduce the fossil fuel consumption and greenhouse gases emissions.

A critical aspect to investigate, especially for EGS development, is the hydraulic connectivity provided by fracture networks. Fractures are present at all scales in the upper crust rocks, from microfractures with dimensions of microns to lineaments of several kilometers (Seeburger et al., 1982). The geometry of the fracture system exerts a profound effect upon the hydro-mechanical properties of rocks (Seeburger et al., 1982, Jing et al., 1997): fractures are the main pathways for water circulation, enabling the storage and movement of fluids or acting as barriers to water flow (Singhal et al., 2010). The study of these discontinuities and the characterization of the fracture network are, thus, key inputs in geothermal systems modelling.

Fracture network modelling is of paramount importance for EGS, where the geothermal reservoir is developed by stimulation (hydraulic, thermal, or chemical) of the existing natural fractures to achieve sufficient permeability to produce adequate fluid flow rates of economic success (e.g., Genter et al., 2010; McClure et al., 2014). In low permeability rocks, the process of hydraulic stimulation is conceptualized as a complex network of newly forming fractures and/or natural fractures that slip and open (McClure, 2012 and references therein) according to the regional stress state. Hydraulic fractures propagate perpendicular to the minimum principal stress (Desroches et al., 2000). Four conceptual models are commonly used for hydraulic stimulation: (1) pure open mode, (2) pure shear stimulation, (3) primary fracturing with shear stimulation leakoff and (4) mixed-mechanism stimulation (McClure, 2012; McClure et al., 2014). Thermal stimulation is carried out by injecting cold water into hot rocks to promote thermal contraction and in this way, create or enhance the fractures close to the borehole. Chemical stimulation removes clogging of pore spaces or enhance fracture permeability close to the borehole by means of acidic treatments (e.g., Schulte et al., 2010). Thus, the results presented in this work are going to be used in numerical models to simulate the behavior of a geothermal reservoir enhanced by hydraulic stimulation.

One key step to characterize the fracture networks is to estimate the number of fractures and their geometrical properties (Seifollahi et al., 2014), which are divided into metric properties and topological properties (Jing et al., 1997). The metric properties include several parameters (e.g., Singhal et al, 2010), the most important being orientation, spacing, aperture and length. These features can vary under certain conditions, like a deformation process (Jing et al., 1997). The topological properties encompass the fractures' connectivity and do not change during continuous deformation processes (Jing et al., 1997).

Several methods are available to acquire the metric properties, including the scanline sampling, the window sampling and the circular scanline and window methods on exposed rock surfaces (Priest, 1993; Zeeb et al., 2013a). The scanline sampling method (e.g., Priest, 1993) was used this work to collect the metrical features of the fractures on outcrops and the topological properties of the system was established by node counting (Sanderson et al., 2015).

9.2 Geological and structural context

The study area is located in the Southeastern Churchill Province (Figure 9.1). This part of the geological province has a tripartite structure caused by the oblique collisions of Nain-Core Zone-Superior cratons. The Torngat Orogen links the Nain and Core zone cratons, the New Québec Orogen connects the Core Zone and Superior cratons (e.g., Wardle et al., 2002). The dominant structural orientation is NNW-SSE characterized by numerous shear zones with several lengths and thrusting structures towards WSW (Simard et al., 2013 and references therein).

The west part of southeastern Churchill Province (SECP) is defined by three main deformation phases (D1 to D3) related to a continuous deformation process connected with New Québec orogeny. Phases D1 and D2 are associated to the compression generated during the collision between Core Zone and Superior and phase D3 is the result of the oblique component of that collision. D1 is responsible for the regional foliation, the NW-SE folds dipping to SW, and the existent thrusting faults. D2 produced the crenulation schistosity and E-W folds. D3 is associated to a late dextral strike-slip movement along the thrust faults and formed NW-SE folds dipping to SE (Simard et al., 2013 and references therein).

The study area within the SECP is in the Core Zone, and more specifically in the Baie aux Feuilles domain. The work was carried out in the Complexe de Kaslac (Areas 3 and 4; Figure 9.1) and Suite de la Baleine (Areas 1 and 2; Figure 9.1) lithological units located within this domain (Simard et al., 2013). The first consists of a complex mixture of intrusive gneiss to mylonitic rocks with composition varying from mafic to felsic. It is divided into four different units according to lithological and textural features: the diorite and quartz-diorite unit, the metagabbro garnet and magnetite-rich unit, the mafic to ultramafic intrusion unit, and the granitoid quartz-rich unit. The second lithological unit (Suite de la Baleine), within the surroundings of Kuujjuaq, is dominantly made of paragneiss. This unit is a set of quartz-feldspathic and pelitic to biotitic gneiss containing minor proportions of marble, calco-silicate rocks, amphibolite, quartzite, ultramafic schist, metaconglomerate and iron formations. The rocks present in the study area are Paleoproterozoic in age. The Baie aux Feuilles domain is characterized by an average orientation of the foliation plan of N338°E-30° and a regional foliation poles with orientation N127°E-16° (Simard et al., 2013).

Five zones were selected to carry out the fracture network modelling (Areas 1 to 5; Figure 9.1). Areas 1 and 4 are located 2 km NE and NW of Kuujjuaq, respectively; area 2 is at 5 km in the SW direction; areas 3 and 5 are located approximately 1 km from the village, in the E and W directions, respectively. Area 1 is located close to the Lac Pingiajjulik fault and areas 3 and 4 in another regional fault intersecting the last one. Lac Pingiajjulik fault is a thrusting fault with dextral movement characterized by mylonitic texture and high recrystallization (Simard et al., 2013 and references therein). No regional fault has been mapped close to areas 2 and 5.

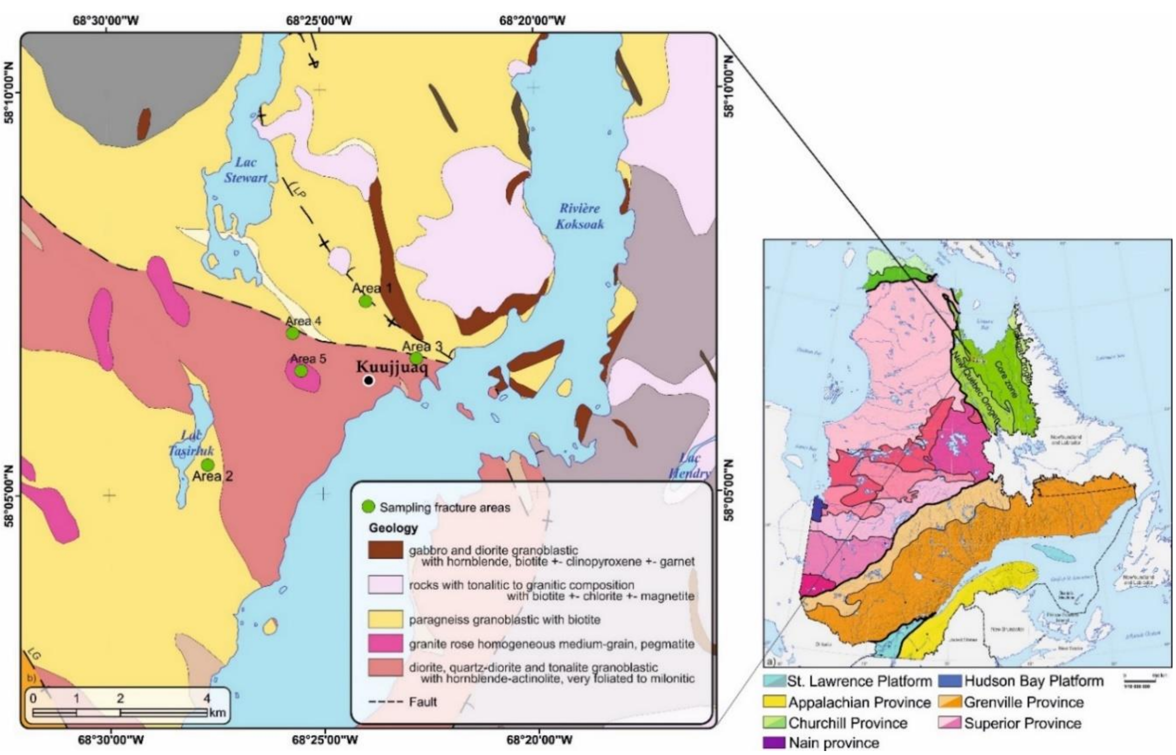

Figure 9.1 **Right, geological setting of the geological provinces in northern Québec – Southeastern Churchill Province. Left, detailed geological map of the studied area with location of the five zones (areas 1 to 5) where the geometrical properties were acquired. *LP* – Lac Pingiajjulik fault, *LG* – Lac Gabriel fault, adapted from Roy (2012).**

9.3 Methods and techniques

The scanline sampling method used in this work is based on data collection by direct observation of fracture characteristics intersecting a scanline on the rock mass surface providing one-dimensional information on fracture networks. Observations were carried out to determine: intersection distance with the scanline, orientation, length, termination and aperture. Others were estimated from the primary observations to calculate the number of sets, spacing and density. This method enables the characterization of metric properties in a quick way, but care must be taken to avoid orientation, truncation, censoring and size biases. In case of occurrence of these sampling biases, corrections need to be applied to avoid under- or over-estimations of the statistical parameters and to avoid prejudice of the fracture network characterization (Zhang et al., 1998). The aperture measurements were performed using a caliper and the value measured is referred to as mechanical aperture. This aperture measured is a maximum value and is bias since the rock surface is exposed to weathering conditions that can lead to erosion of fracture walls. It was also possible to estimate the equivalent secondary (fracture) porosity (φ_{ract}) based on the number of fractures per unit distance (N) and the mean mechanical aperture of the fractures (w_{m}) by the following equation (Singhal et al, 2010)

$$\varphi_{\mathrm{fract}} = N \times w_{\mathrm{m}} \qquad (9.1)$$

The connectivity of the fracture network was evaluated based on Sanderson et al. (2015), considering that a two-dimensional fracture network consists of lines comprising one or more branches that, in turn, have a node at each end. The nodes can be isolated tips (I-nodes), crossing fractures (X-nodes) and abutments or splays (Y-nodes), as shown in Figure 9.2. The proportion of the nodes was then used to characterize the fracture network in terms of connectivity.

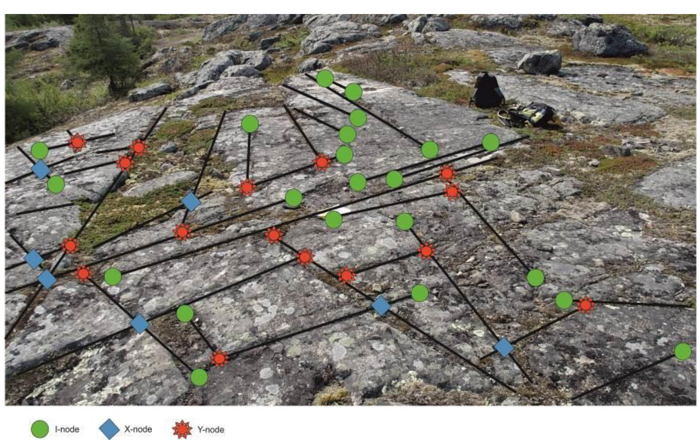

Figure 9.2 Example of node counting carried out during field work.

To count the number of lines (N_L) within a given area, the following relationship was used (Sanderson et al., 2015):

$$N_{\mathrm{L}} = \frac{1}{2}(N_{\mathrm{I}} + N_{\mathrm{Y}}) \quad (9.2)$$

Each branch is characterized by having two nodes and the number of branches (N_B) can be calculated as (Sanderson et al., 2015):

$$N_{\mathrm{B}} = \frac{1}{2}(N_{\mathrm{I}} + 3N_{\mathrm{Y}} + 4N_{\mathrm{X}}) \quad (9.3)$$

The ratio of number of branches to lines is then (Sanderson et al., 2015):

$$\frac{N_{\mathrm{B}}}{N_{\mathrm{L}}} = \frac{N_{\mathrm{I}}+3N_{\mathrm{Y}}+4N_{\mathrm{X}}}{N_{\mathrm{I}}+N_{\mathrm{Y}}} \quad (9.4)$$

For each equation, N_I is the number of I-nodes, N_Y the number of Y-nodes and N_X stands for the number of X-nodes. Thus, it is possible to convert the number of lines to the equivalent number of branches and to understand the connections between each branch and classify the fracture system (Sanderson et al., 2015). The average number of connections per node (C_N) can be calculated by (Saevik et al., 2017):

$$C_{\mathrm{N}} = \frac{N_{\mathrm{I}}+3N_{\mathrm{Y}}+4N_{\mathrm{X}}}{N_{\mathrm{I}}+N_{\mathrm{Y}}+N_{\mathrm{X}}} \quad (9.5)$$

The node counting also provide the average number of connections per line (C_L) and the average number of connections per branch (C_B). These values have been widely used as a measure of connectivity (Sanderson et al., 2015 and references therein). C_L is given by:

$$C_L = 4\frac{N_Y+N_X}{N_I+N_Y} \quad (9.6)$$

and N_B by:

$$C_{\mathrm{B}} = \frac{3N_{\mathrm{Y}}+4N_{\mathrm{X}}}{N_{\mathrm{B}}} \quad (9.7)$$

Beyond the connectivity, the termination index was also evaluated. This provides information about the interconnections between the fractures and allows to classify the persistence of the several fractures present (Priest, 1993; Sousa, 2007). The termination index (T'_i) is calculated with the procedure of ISRM on (1978), based on the number of discontinuity traces that terminate in intact rock (N_I), the number of discontinuities that terminate at another discontinuity (N_A) and number of discontinuities in which termination is obscured (N_O):

$$T'_{\mathrm{i}}(\%) = \frac{100N_{\mathrm{I}}}{N_{\mathrm{I}}+N_{\mathrm{A}}+N_{\mathrm{O}}} \quad (9.8)$$

To calculate the potential fracture transmissivity and permeability and fractured rock mass hydraulic conductivity, the mechanical aperture (w_m) measured by scanline sampling can be transformed to hydraulic aperture w_{hyd} (mm) with the following equation proposed by Lee et al. (1996):

$$w_{\mathrm{hyd}} = \frac{w_{\mathrm{m}}}{JRC^{2.5}} \tag{9.9}$$

where *JRC* is joint roughness coefficient that was assumed equal to 3 for the study area, which is the minimum for natural fractures to account for more realistic conditions (Singhal et al., 2010 and references therein).

The potential fracture transmissivity T^*_{fract} (m^2 s^{-1}) of the studied zones can be calculated using the cubic law by (e.g., Chesnaux et al., 2009):

$$T^*_{\mathrm{fract}} = \frac{w^3_{\mathrm{hyd}}}{12}\frac{\rho g}{\omega} \tag{9.10}$$

where w_h (m) stands for the hydraulic aperture of the fractures, ρ (kg m^{-3}) is the fluid density, g (m s^{-2}) is the gravitational acceleration and ω (kg m^{-1} s^{-1}) is the dynamic fluid viscosity.

The potential fracture permeability κ_{fract} (m^2) can be defined as (e.g., Chesnaux et al., 2009; Singhal et al., 2010):

$$\kappa_{\mathrm{fract}} = \frac{w^2_{\mathrm{hyd}}}{12} \tag{9.11}$$

The fractured rock mass potential hydraulic conductivity K'_{fract} (m s^{-1}) can be calculated by (Singhal et al., 2010):

$$K'_{\mathrm{fract}} = \frac{g w^3_{\mathrm{hyd}}}{12 v S} \tag{9.12}$$

where S (m) is fracture spacing (Figure 9.4c) and v (m^2 s^{-1}) is the coefficient of kinematic viscosity.

9.4 **Results**

9.4.1 Metric properties

The following division in classes was assumed for the statistical analysis of the metric properties of fractures based on alteration and length: master joints, if no alteration is visible and fractures have lengths > 2 m; secondary joints, if no alteration is visible and fractures have lengths < 2 m; altered joints, if alteration is visible; and faults, if the fractures exhibit shearing displacement (mode II – sliding mode of fractures). This division is important as each one of these classes is characterized by intrinsic properties that behave differently when subject to hydraulic stimulation.

Mechanical aperture was classified according to ISRM (1978) as follows: very tight, if aperture < 0.1 mm; tight, if aperture is between 0.1 – 0.25 mm; partly open, if aperture is between 0.25 – 0.50 mm; open, if aperture is between 0.50 – 2.50 mm; moderately wide, if aperture is between 2.50 – 10.0 mm; wide, if aperture > 10.0 mm.

Area 1 is located in paragneiss. Fractures have two equally preferential orientations; NNW-SSE and ENE-WSW (Figure 9.3). The master joints have a length varying from 2.4 to 25 m minimum (Figure 9.4). A possible shear zone was observed to have orientation NW-SE, showing a wide aperture of 49 mm. The master joints show mechanical apertures from close to wide and the secondary joints from close to moderately wide (Figure 9.4). The average spacing between fractures is 1.1 m, with a standard deviation of 0.7 (Table 9.1). The fracture density of this area is 1.03 m^{-1}. Both master and secondary joints are systematic. The fracture sets observed are conjugate and orthogonal, based on the dihedral angle measured from the intersection of sets. In terms of relative timing of joint formation, the ENE-WSW sets are possibly older than the NNW-SSE, since the first show signs of movement in the intersection with the last set. The equivalent fracture (secondary) porosity in this area calculated by Equation (9.1) is on average 7%.

As area 1, area 2 is located in paragneiss and has preferential fracture orientation E-W with scattered fractures along NNE-SSW (Figure 9.3). The master joints have a length varying from 2 to 10 m and mechanical apertures from close to wide (Figure 9.4). The secondary joints have a length in the range of 0.4 to 1 m and mechanical apertures that vary from close to wide (Figure 9.4). The average spacing between fractures in this area is 1.1 m, with a standard deviation of 1.2 (Table 9.1). A fracture density of 1.23 m^{-1} was estimated for this area. Both master and secondary joints are systematic. The fracture sets observed are conjugate, based on the dihedral angle measured from the intersection of sets. The equivalent fracture (secondary) porosity in this area is 6%.

Area 3 is located in diorite, close to the contact (or faulted contact) with paragneiss. Fractures are oriented preferentially to NW-SE, with scattered fractures oriented to NE-SW (Figure 9.3). The master joints have a length varying from 2 to 11 m, the secondary joints have a length in the range of 0.2 to 1.5 m, and the altered joints have a length of 0.3 to 5.2 m (Figure 9.4). The altered joints have schist filling the apertures. All classes have closed apertures (Figure 9.4), which consequently gives an average equivalent fracture (secondary) porosity of 0.1%.

Area 4 is also located in diorite, close to the contact (or faulted contact) with paragneiss. This area shows the same fracture orientations as in area 3, which is a preferential orientation to NW-SE and scattered fractures oriented to NE-SW (Figure 9.3). Most fractures observed were systematic master joints with mechanical apertures varying from close to wide (Figure 9.4). The average spacing between fractures and standard deviation is 0.8 m and 0.6, respectively (Table 9.1). Regarding fracture density, a value of 1.35 m^{-1} was calculated. The fracture sets observed are conjugate and orthogonal, based on the dihedral angle measured from the intersection of sets. In terms of relative timing of joint formation, the NW-SE set is possibly older than the NE-SW, since the first shows signs of movement in the intersection with the last set. The equivalent fracture (secondary) porosity in this area is on average 0.4%.

Area 5 is located in a granite, where the preferential orientation of the fractures is NNW-SSE (Figure 9.3). Most fractures observed were systematic master joints with mechanical apertures varying from close to moderately wide (Figure 9.4). The average spacing between fractures is 0.6 m, with a standard deviation of 0.4 (Table 9.1). The fracture density is 1.88 m^{-1}. The fracture sets observed are conjugate and orthogonal, based on the dihedral angle measured from the intersection of sets. The equivalent fracture (secondary) porosity in this area is on average 0.2%.

The Lac Pingiajjulik fault is an important regional structure present within the study area. This structure is a transpressional fault and its main orientation is NW-SE (Figure 9.3). It can be noted from the same figure that the most prominent system of surface fractures observed in the studied zones are oriented NNW-SSE and NNE-SSW. A thrust fault regime implies minimum principal stress ($\sigma 3$) as the vertical stress (S_v) and the maximum ($\sigma 1$) and intermediate ($\sigma 2$) principal stresses as maximum (S_H) and minimum (S_h) horizontal stresses, respectively. Due to the deformation phase D3, $\sigma 3$ is probably deviated from vertical and correspond to S_h. As the orientation of Lac Pingiajjulik fault and the remaining regional structures is roughly NW-SE, this means that $\sigma 1$ had a NE-SW compressional direction.

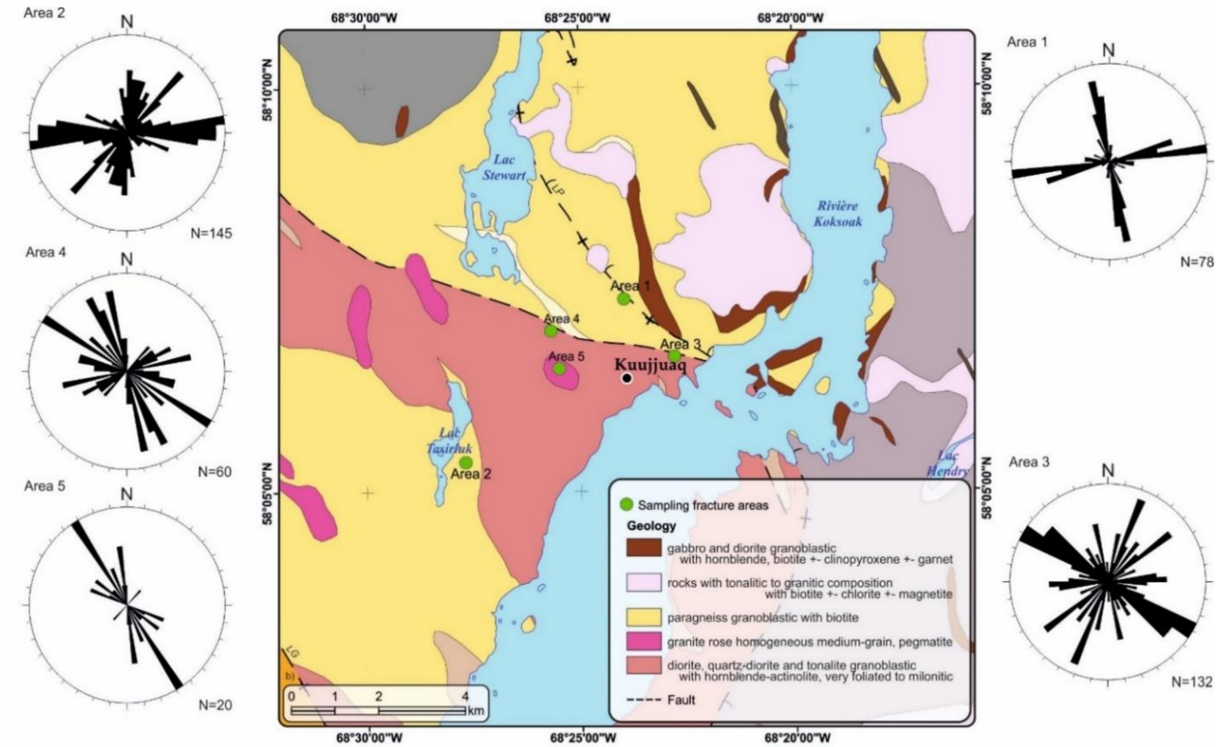

Figure 9.3 Rose diagrams for each examined zone associated with their position in the geological map.

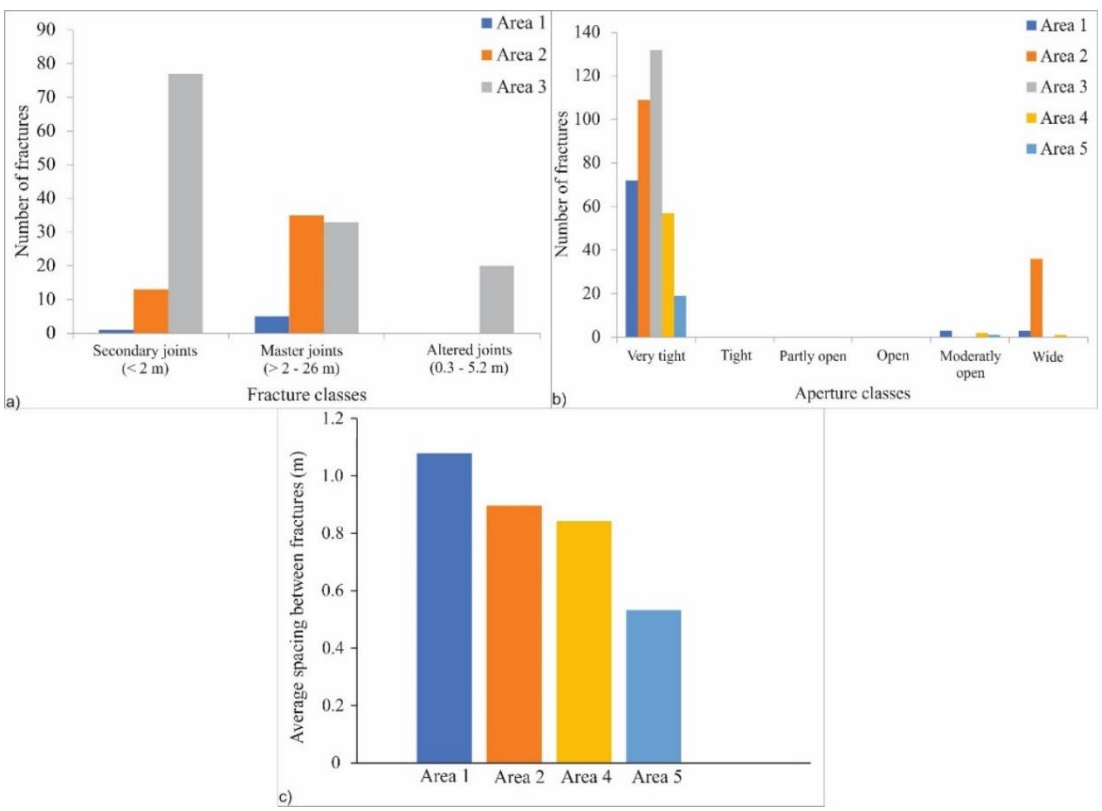

Figure 9.4 Histograms of a) fracture length, b) mechanical aperture and c) average fracture spacing for each area studied.

Table 9.1 **Summary of the results obtained from scanline sampling.**

	Area 1			Area 2			Area 3	Area 4			Area 5		
Orientation	NNW-SSE and ENE-WSW			E-W with scattered fractures NNE-SSW			NW-SE with scattered fractures NE-SW	NW-SE with scattered fractures NE-SW			NNW-SSE		
Length (m)	2 – 25(min)			0.2 – 10			0.2 – 11						
Aperture (mm)	0 – 49.09			0 – 48.85			> 0.1	2.32 – 11.94			4.92		
Spacing (m)	μ^*	σ^*	CV	μ^*	σ^*	CV		μ^*	σ^*	CV	μ^*	σ^*	CV
	1.1	0.7	0.6	1.1	1.2	1.1		0.8	0.6	0.7	0.6	0.4	0.7

μ^* - arithmetic average; σ^* – standard deviation; *CV* – coefficient of variation.

9.4.2 Topological properties

The topological properties analysis was carried out in a sector within area 2, where the node (Figure 9.5a) and termination (Figure 9.5b) counting was performed. The total number of nodes counted is 128, of which 33 are isolated tips (I-nodes), 25 are crossing fractures (X-nodes), and 70 are abutments (Y-nodes). Regarding the terminations, 13 were considered discontinuities that terminates in intact rock material (I-type), 50 terminate in another discontinuity (A-type) and 17 have an obscured termination (O-type). These two parameters indicate that this sector is characterized by a system dominated by abutting fractures terminations, since 55% are Y-nodes and 62.5% are A-type terminations. The isolated fractures correspond to 26% of the system and the cross-cutting fractures 19.5%. Moreover, 21% of the fractures observed show obscured terminations (O-type) and 16% terminates in intact rock (I-type).

Applying Equations (9.2) to (9.7) to the node counting, there is 51.5 lines observed in the sector studied (Equation 9.2) and 171.5 branches (Equation 9.3). The ratio of number of branches to lines is 3.33 (Equation 9.4), while the number of connections per node is 2.68 (Equation 9.5). The number of connections per line for the studied sector is 3.69 (Equation 9.6) and the number of connections per branch is 1.81 (Equation 9.7). The termination index gives a value of 16% (Equation 9.8).

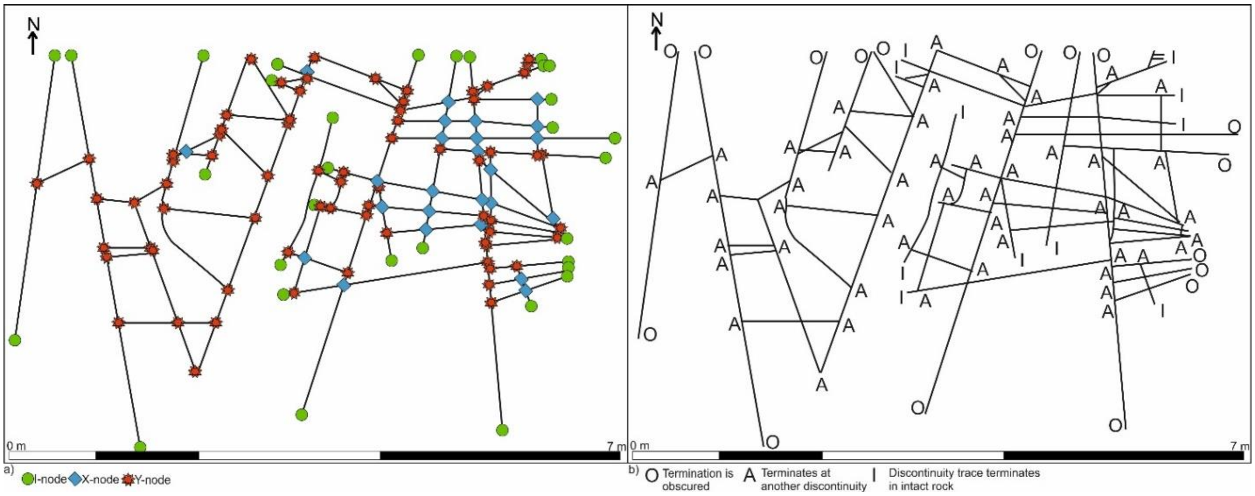

Figure 9.5 a) node counting and b) termination counting in a sector of area 2.

9.4.3 Potential fracture transmissivity and permeability and fractured rock mass potential hydraulic conductivity

The hydraulic apertures calculated by Equation (9.9) are higher than expected in non-weathered fractures as the mechanical apertures were measured in surface rock exposed to weathering conditions, which leads to high values of transmissivity, permeability and hydraulic conductivity.

To calculate the potential average fracture transmissivity (Equation 9.10), pure water was assumed with ρ as 10^3 kg m^{-3}, g as 9.81 m s^{-2} and ω as 10^{-3} kg m^{-1} s^{-1}. For area 1 to 5, the potential average fracture transmissivity is 6.7, 5.6, 2.2×10^{-13}, 7.9×10^{-6} and 3.9×10^{-7} m^2 s^{-1}, respectively (Table 9.2). The potential average fracture permeability (Equation 9.11) for area 1 to 5 is 2.7×10^{-5}, 2.4×10^{-5}, 3.4×10^{-14}, 3.8×10^{-9} and 5.1×10^{-10} m^2, respectively (Table 9.2). To calculate the fractured rock mass potential hydraulic conductivity (Equation 9.12), v was assumed equal to 1.0×10^{-6} m^2 s^{-1}. The hydraulic conductivity of area 1 to 5 is 6.2, 6.2, 2.7×10^{-13}, 9.3×10^{-6} and 2.0×10^{-6} m s^{-1}, respectively (Table 9.2).

Table 9.2 Equivalent fracture porosity (φ_f), potential fracture transmissivity (T_f), potential fracture permeability (k_f) and fractured rock mass potential hydraulic conductivity (K_f)

	Area 1	Area 2	Area 3	Area 4	Area 5
ϕ_{fract} (%)	7	6	0.1	0.4	0.2
T^*_{fract} (m^2 s^{-1})	6.7	5.6	2.2 x10^{-13}	7.9 x10^{-6}	3.9 x10^{-7}
κ_{fract} (m^2)	2.7 x10^{-5}	2.4 x10^{-5}	3.4 x10^{-14}	3.8 x10^{-9}	5.1 x10^{-10}
K'_{fract} (m s^{-1})	6.2	6.2	2.7 x10^{-13}	9.4 x10^{-6}	2.0 x10^{-6}

9.5 Discussion

9.5.1 Fracture network connectivity

In a random continuum percolation model, the fracture system is uniformly clustered with all fractures connected by fracture intersections (X-nodes) and ending as isolated line tips (I-nodes). Y-nodes do not form in these kinds of systems (Manzocchi, 2002 and references therein). On the other hand, in natural fracture systems, the connectivity is achieved through a combination of fracture intersections (X-nodes) and abutments (Y-nodes). Y-nodes are important contributors to the connectivity of natural systems and a system with high proportion of fractures ending as abutments is characterized by fewer I-nodes. The critical density is low in natural fracture systems and the percolation cluster resembles closely to the percolation backbone (Manzocchi, 2002 and references therein). Node counting indicated that the fracture system studied is composed by 55% of Y-nodes, 26% of I-nodes and 19.5% of X-nodes. Generally, natural fracture systems have Y:X node ratios higher than 1 (Manzocchi, 2002), correlating to the system studied that has a ratio of 2.8.

The number of nodes counted can be plotted in a ternary diagram (Figure 9.6). The position on the diagram not only characterizes the nature of the connectivity but also quantifies this connectivity (Barton et al., 1989).

The ratio of number of branches to lines enables to characterize the type of fracture system (Equation 9.4). A fracture system composed by isolated tips has N_B/N_L close to 1 and is disconnected; in turn, a fracture system composed by long, closely-spaced, cross-cutting fractures is dominated by X-nodes and the ratio of number of branches to lines would tend to infinity, meaning a highly connected fracture system. A fracture system with dominating Y-nodes will have a N_B/N_L of 3 (Sanderson et al., 2015). The N_B/N_L in the studied system amounts to 3.33 (Figure 9.6a), meaning a partially connected fracture network.

The average number of connections per node varies from 1 to 4 (C_N; Equation 9.5), in which the maximal value is only attained when all the nodes are X-nodes (Saevik et al., 2017). C_N is 2.68 for the sector studied, highlighting the prevalence of Y-nodes, followed by I- and X-type terminations.

A fracture system becomes connected when the critical connectivity value is higher than 2, while a lower value means an unconnected system and no percolation threshold exist (Manzocchi, 2002). Moreover, if a system has a critical connectivity between 2 and 3.11, it means that it contains fracture orientation populations clustered independently. A uniformly clustered system is characterized by a critical connectivity of 3.11. The critical connectivity for density-clustered systems is higher than 3.11 and the more intense is the clustering the higher this value. Using the number of connections per line to calculate the critical connectivity (C_L; Equation 9.6), the system studied as a value of 3.69 (Figure 9.6b), meaning that it is connected and may be a density-clustered system.

The number of connections per branch can be used to calculate the connectivity of a system (C_B; Equation 9.7) and it gives a value in the range 0 to 2 (Sanderson et al., 2015), in which the maximal value is attained when no fracture terminates as isolated tips. This will be the optimal fracture system, with no dead-ends and isolated branches, with a hydraulic connectivity close to the maximal (Saevik et al., 2017). C_B is 1.81 for the studied sector, indicating that this fracture system has a small number of dead-ends and may have a good hydraulic connectivity (Figure 9.6c).

Each branch, composed by two end-nodes, can be classified as I-I, I-X, I-Y, Y-Y, Y-X, and X-X, or simply as isolated branches (I-I), partly connected branches (I-C), and doubly connected branches (C-C). Partly connected means branches with I-X and I-Y node ends, while doubly connected are branches that end with Y-Y or Y-X nodes (Sanderson et al., 2015 and references therein). The value of C_B observed in the studied sector indicate a high proportion of interconnected branches in doubly connected style (Figure 9.6d).

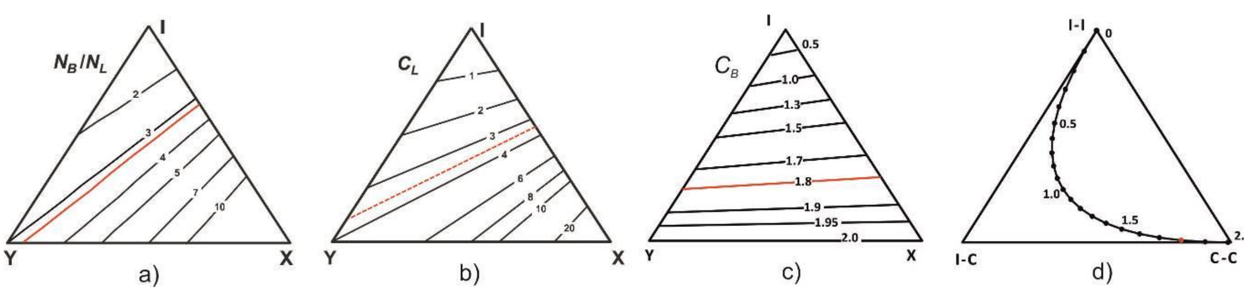

Figure 9.6 **Triangular plots of node proportion with network topology showing a) the ratio of number of branches to lines (N_B/N_L = 3.3), b) the number of connections per line (C_L = 3.7), c) the number of connections per branch (C_B = 1.8) and d) the branch classification plot based on C_B values. Observed values described in this study are highlighted in red, adapted from Sanderson et al. (2015).**

The termination index does not provide complete information about the system connectivity (T'_i; Equation 9.8) but permits to classify the persistence of the joints and understand the susceptibility for rock failure. A large value of the termination index, identified by a large proportion of joints with termination on intact rock, means a rock mass stiffer and stronger than one with a lower index (e.g., Priest, 1993; Sousa, 2007). The sector studied has a T'_i of 16%, showing a rather weak rock mass due to the prevalence of discontinuities that terminate in another discontinuity (A-type; 62.5%).

The high prevalence of fractures that terminate against each other suggest that this system have a high tortuosity, as Y-nodes usually force the fluid to follow a tortuous path through the network, and a lower hydraulic connectivity (Saevik et al., 2017). The potential hydraulic connectivity (*f*) of the system studied can be calculated following the approach described in Saevik et al. (2017):

$$C_H = 2.94 \times C_{\mathrm{f}} - 2.13 \quad (9.13)$$

where C_{f} is the average number of connections per fracture.

This parameter is calculated by (Saevik et al., 2017):

$$C_{\mathrm{f}} = \frac{4N_{\mathrm{X}}+2N_{\mathrm{Y}}}{4N_{\mathrm{X}}+2N_{\mathrm{Y}}+N_{\mathrm{I}}} \quad (9.14)$$

The hydraulic connectivity varies within the range 0.0 to 0.8 and the obtained value for the system studied is 0.46 (Figure 9.7). Besides the high percentage of Y-nodes, the system is not characterized by a high tortuosity.

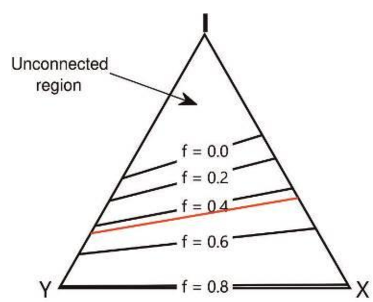

Figure 9.7 **Triangular plot for hydraulic connectivity (C_H). The red line represents the hydraulic connectivity calculated for the fracture network system analyzed, adapted from Saevik et al. (2017).**

9.5.2 Fracture clustering

The coefficient of variation (CV) of fracture separations was used to estimate the fracture clustering. This coefficient is based on the standard deviation of fracture separations divided by the mean separation value. Fractures uniformly clustered with a purely exponential distribution have CV equals to 1. In the case of fractures distribution in a regular pattern, CV is less than 1 and fractures are anticlustered. If CV is higher than 1, it means that fractures have a heterogeneous distribution and they are clustered (e.g., Gillespie et al., 1999; Manzocchi, 2002). A $0 < CV < 1$ can also be related with the randomly oriented and positioned scanline that records fractures from different populations (Manzocchi, 2002) and a fracture system composed by systematic joints in which joint spacing is controlled by bed thickness (Gillespie et al., 1999). Clustered fracture systems with CV > 1 can be density-clustered, for scanlines recording fractures of different populations, or orientation-clustered, for scanlines recording fractures of only one population (Manzocchi, 2002). Spacing between fractures measured from scanline sampling indicates that area 1 is characterized by a CV of 0.62 (Table 9.1), while area 2 by CV of 1.1. The CV calculated for areas 4 and 5 is 0.7.

Areas 1, 4 and 5 have factures with a CV less than 1, meaning that these systems are characterized by anticlustered fractures and the systems have a regular pattern of fractures distribution. The CV values obtained additionally show that the fractures were recorded through a randomly oriented and positioned sample line and orientations from different populations were documented. Area 2, in turn, has fractures with a CV higher than 1, meaning that the fractures are clustered and distributed in a heterogeneous pattern. This area is characterized as a density-clustered system due to the value of critical connectivity of 3.69 (C_L; Figure 9.7b).

9.5.3 Potential fracture transmissivity and permeability and fractured rock mass potential hydraulic conductivity

Areas 1 and 2 are characterized by very high fracture permeability and hydraulic conductivity; area 3 by moderate to low fracture permeability and low fracture hydraulic conductivity; and areas 4 and 5 by high fracture permeability and low fracture hydraulic conductivity (Table 9.2). Permeability and hydraulic conductivity of fractures have a direct proportionality relation, which is seen in most areas except the two-last studied. Referenced values for crystalline rocks in terms of rock mass porosity is 0 to 5% for dense crystalline rocks, 5 to 10% for fractured crystalline rocks and 20 to 40% for weathered crystalline rocks (Singhal et al., 2010 and references therein). The expected range of rock mass permeability and hydraulic conductivity are 1 to 10^{-4} and 10^{-5} to 10^{-9} m s^{-1} for fractured and weathered crystalline rocks, respectively, and 10^{-3} – 10^{-8} and 10^{-8} – 10^{-13} m s^{-1} for massive rocks, respectively (Singhal et al., 2010). The porosities calculated from Equation (9.1) for the 5 areas studied and mentioned in subsection 9.4.1 fall into the fractured crystalline rock mass field for areas 1 and 2, with porosities of 7% and 6% respectively, and the remaining areas into the dense crystalline rocks field.

9.6 **Conclusions**

This paper describes the preliminary results of the fracture network analysis in Kuujjuaq. The main orientations of the natural fractures populations of the studies areas are NNW-SSE and NNE-SSW. The orientation of the maximum principal stress $\sigma 1$ is assumed to be horizontal and the minimum principal stress $\sigma 3$ is still unknown, which can be vertical or horizontal and most likely slightly deviated from vertical. The maximum principal stress $\sigma 1$ was oriented NE-SW during Lac Pingiajjulik fault formation, as this regional fault was formed by compression and it is oriented roughly NW-SE.

The sector studied for topological properties is dominated by abutments (Y-nodes; 55%), followed by fractures ending with isolated tips (I-nodes; 26%) and cross-cutting fractures (X-nodes; 19.5%). The Y:X node ratio is 2.8. The ratio of number of branches to lines (N_B/N_L=3.33), the average number of connections per node (C_N=2.68), the average number of connections per line (C_L=3.69) and the average number of connections per branch (C_B=1.81) all indicates that the system studied is partially connected, with a critical connectivity close to 4. It is also characterized by a high proportion of interconnected branches in doubly connected style. The termination index is 16%. The potential hydraulic connectivity (C_H) is estimated to be 0.46. This system is density-clustered and besides the high proportion of Y-nodes, it is not characterized by a high tortuosity. The data described in this article will be used in discrete fracture network models to evaluate the fluid flow within the medium and to assess the viability of a geothermal reservoir created by hydraulic stimulation.

The equivalent porous media showed very high to low permeability and hydraulic conductivity. These values are dependent on the fracture hydraulic aperture and spacing. Uncertainty is associated with the numerical values obtained since the apertures measured correspond to rock surface exposed to weathering effects that can alter the properties of the fractures. Nevertheless, their qualitative features can be combined with the expected fracture system connectivity to evaluate if the medium show valuable characteristics to be exploited for geothermal purposes.

The orientation of the minimum principal stress is still unknown and further studies are needed to better define this parameter playing a major role in the development of hydraulic fractures. Studies regarding the magnitude of the principal stresses will be performed and the mechanical properties of the rocks (Young’s modulus, bulk modulus, shear modulus, and Poisson’s ratio) will be analyzed, due to their influence on how the system would behave during stimulation. The rock matrix porosity and permeability will be obtained by a combined gas permeameter and porosimeter device to evaluate the bulk hydraulic properties of the medium (Raymond et al., 2017).

The area surrounding the Inuit village of Kuujjuaq appears to have favorable conditions for the exploitation of deep geothermal resources via EGS if the minimum principal stress is oriented in such a way that hydraulic stimulation of natural fractures could be carried out in order to increase the connection of the fracture system. Shallow geothermal applications such as UTES would be feasible in locations where the rock mass hydraulic conductivity is moderate to low, in order to prevent heat losses from the underground storage volume. On the other hand, GSHP systems would benefit of highly permeable media. Numerical simulations are ongoing to evaluate the amount of energy that can be extracted or stored and to define the long-term efficiency and sustainability of these geothermal heat production modes.

10 APPENDIX II – MODAL COMPOSITION, THERMOPHYSICAL PROPERTIES AND RADIOGENIC ELEMENTS

Modal composition analysis was carried out to identify the main mineral phases of the outcropping lithologies. The thin sections were scanned allowing a first-order definition of the percentage mafic/felsic minerals (Figure 10.1).

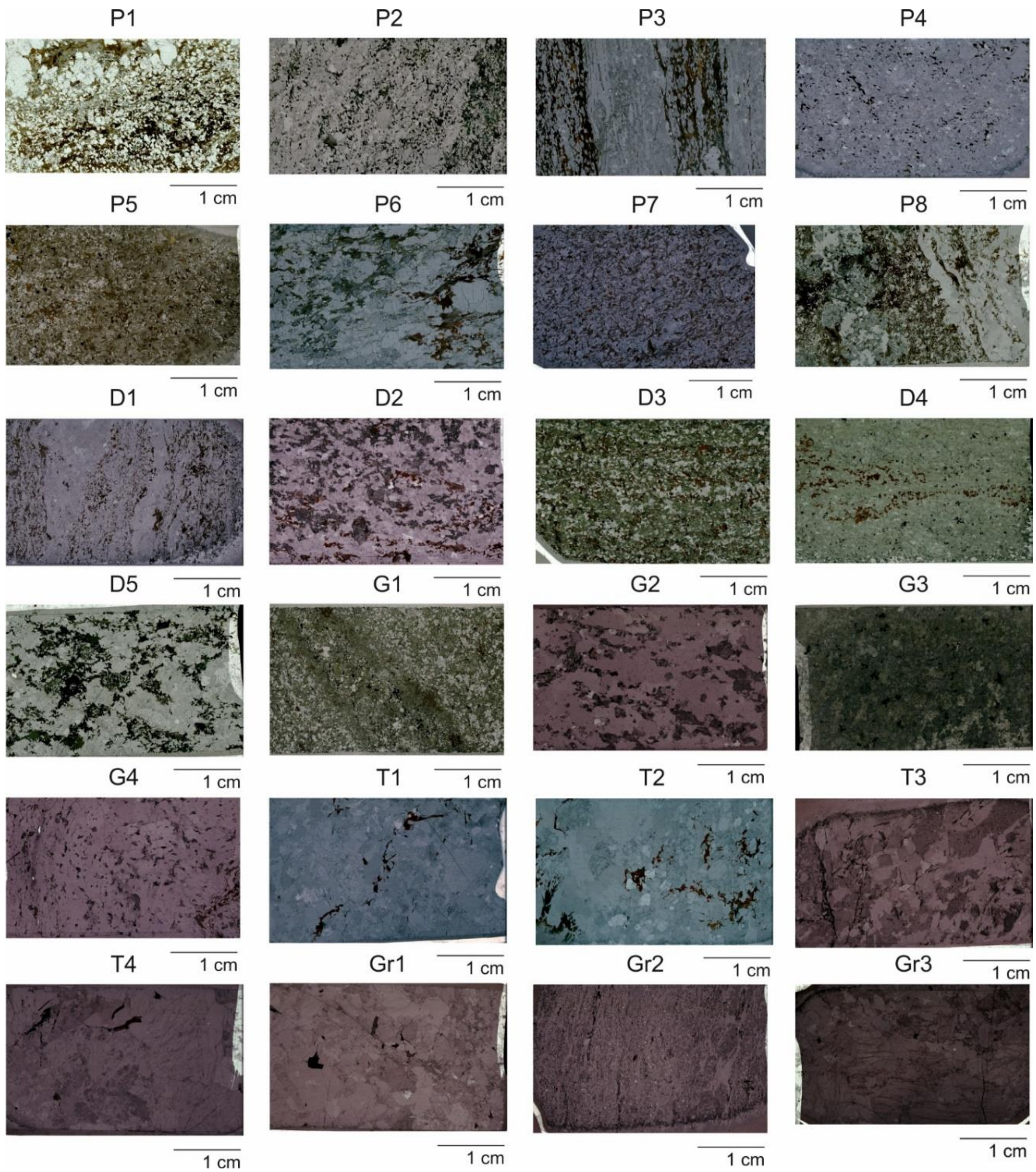

Figure 10.1 High-resolution scanning of the thin sections. P – Paragneiss, D – Diorite, G – Gabbro, T – Tonalite, Gr – Granite.

Posterior microscopic analysis enabled to plot the data in a triangular diagram that allows a first-order classification of the rock samples (Figure 10.2).

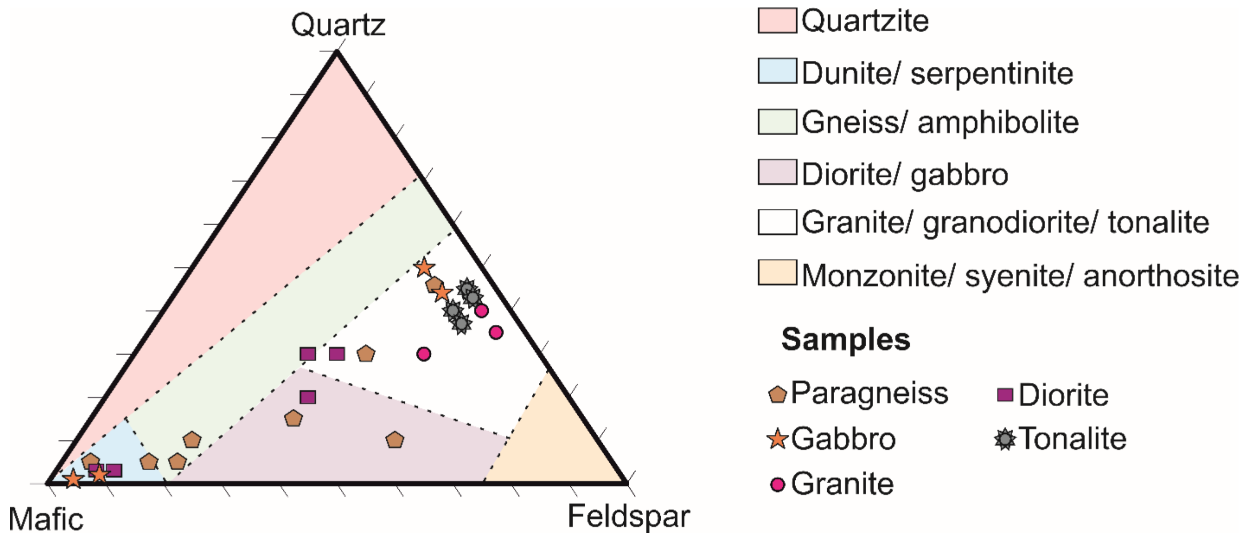

Figure 10.2 Projection of the percentage of the main mineral phases and range for typical rocks.

The relationship between the main mineral phases and thermal conductivity was also evaluated and the results revealed that both quartz and feldspar have a positive correlation with thermal conductivity while the mafic minerals have a negative correlation regardless the rock type (Figure 10.3).

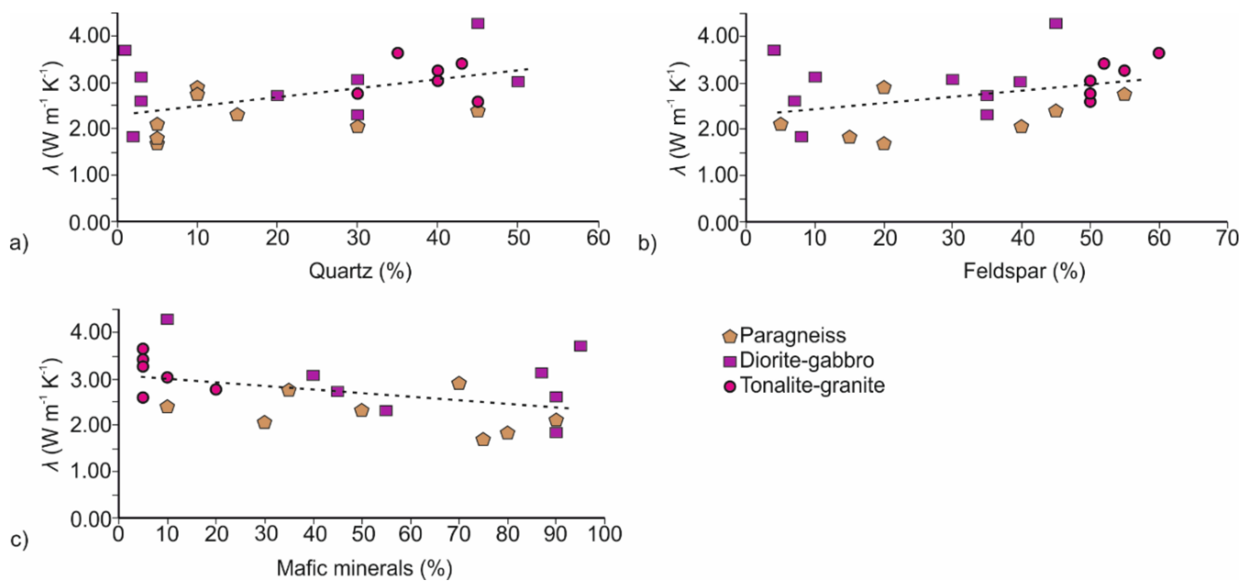

Figure 10.3 Correlation between thermal conductivity and main mineral phases.

The relationship between thermal conductivity and the major geochemical elements revealed a positive correlation with SiO_2 (Pearson coefficient of 47%; Figure 10.4a) and negative correlations with Fe_2O_3 (Pearson coefficient of -46%; Figure 10.4b), Al_2O_3 (Pearson coefficient -

50%; Figure 10.4c) and TiO_2 (Pearson coefficient of -52%; Figure 10.4d). These results agree with Figueiredo et al. (2008) and Figueiredo et al. (2009) and highlight that rocks rich in SiO_2, and thus quartz, tend to have higher thermal conductivity than rocks rich in Fe_2O_3+MgO+CaO+TiO_2, which are geochemical elements present in mafic minerals. In fact, the observed increase of thermal conductivity as a function of quartz is expected given the high thermal conductivity of quartz crystals (7 W m^{-1} K^{-1}; Clauser et al., 1995). Al_2O_3+K_2O+Na_2O are the main geochemical elements of feldspar minerals. The negative correlation observed between Al_2O_3 and thermal conductivity is expected since feldspar minerals are often assumed thermal insulators given their thermal conductivity of 1.5-2.9 W m^{-1} K^{-1} (e.g., Sass, 1965; Clauser et al., 1995). The weak positive correlation inferred between thermal conductivity and feldspar minerals (with a Pearson coefficient of 36%; Figure 10.3) is believed to be caused by the small portion of rock analyzed for modal composition.

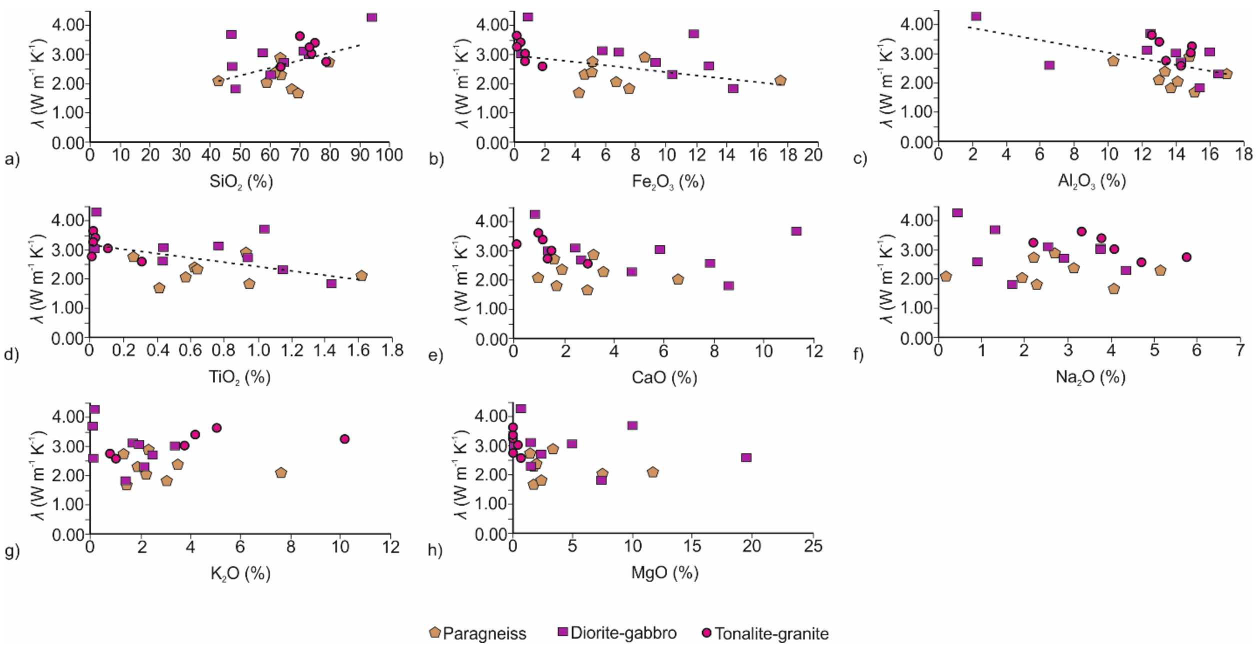

Figure 10.4 Correlation between thermal conductivity and major elements.

A compositional-based thermal conductivity model for plutonic rocks was proposed by Jennings et al. (2019):

$$\lambda = \exp\,(1.72[SiO_2] + 1.018[MgO] - 3.652[Na_2O] - 1.791[K_2O]) \tag{10.1}$$

where λ (W m^{-1} K^{-1}) is thermal conductivity and [*X*] is the concentration of the major elements. This model was here applied to infer the thermal conductivity and evaluate the misfit between the compositional model and laboratory analyzes. It is observed that the compositional model underestimates the thermal conductivity of the rock samples, on average, by 7 to 19% for the diorite, by 2 to 9% for the gabbro, by 8 to 18% for the tonalite and by 15 to 21% for the granite (Table 10.1).

Table 10.1 Thermal conductivity evaluated based on the compositional model and by laboratory methods.

	ID	λ ($W m^{-1} K^{-1}$) Compositional model	GHFM	TCS	Relative difference (%) GHFM	TCS
Diorite	D1 ∥	2.68	3.32	----	-23.62	----
	D1 ⊥		2.12	----	21.08	----
	D2 ∥	2.38	3.42	3.51	-43.45	-47.19
	D2 ⊥		2.72	2.46	-13.92	-3.24
	D3 ∥	3.06	3.98	----	-30.19	----
	D3 ⊥		2.26	----	26.13	----
	D4	2.66	2.60	3.13	2.22	-17.59
	D5 ∥	2.35	2.31	2.50	1.72	-6.67
	D5 ⊥		2.30	----	1.85	----
Gabbro	G1 ∥	2.27	2.07	2.26	8.89	0.76
	G1 ⊥		1.59	----	30.26	----
	G2	4.98	4.28	----	13.98	----
	G3	2.37	3.70	2.57	-56.20	-8.70
	G4	2.88	3.02	3.47	-4.81	-20.26
Tonalite	T1	2.49	2.59	2.87	-4.04	-15.55
	T2 ∥	2.88	3.73	3.69	-29.45	-27.82
	T2 ⊥		2.34	3.69	18.80	-27.95
	T3	2.86	----	----	----	----
	T4	2.94	3.41	2.92	-16.11	0.42
Granite	Gr1	2.71	3.26	----	-20.35	----
	Gr2	3.10	2.76	3.45	10.87	-11.46
	Gr3	2.70	3.64	3.54	-34.95	-31.29

D – diorite, G – gabbro, T – tonalite, Gr – granite. ∥– thermal conductivity evaluated parallel to the foliation, ⊥ – thermal conductivity evaluated perpendicular to the foliation.

The radiogenic elements of the rock samples were analyzed by mass spectrometry (ICP-MS) and gamma-ray spectrometry with a NaI(Tl) detector. For the latter, the energy spectra and the three-window method enabled to identify the energy peak corresponding to ^{40}K, ^{214}Bi (U decay chain) and ^{208}Tl (Th decay chain; Figure 10.5).

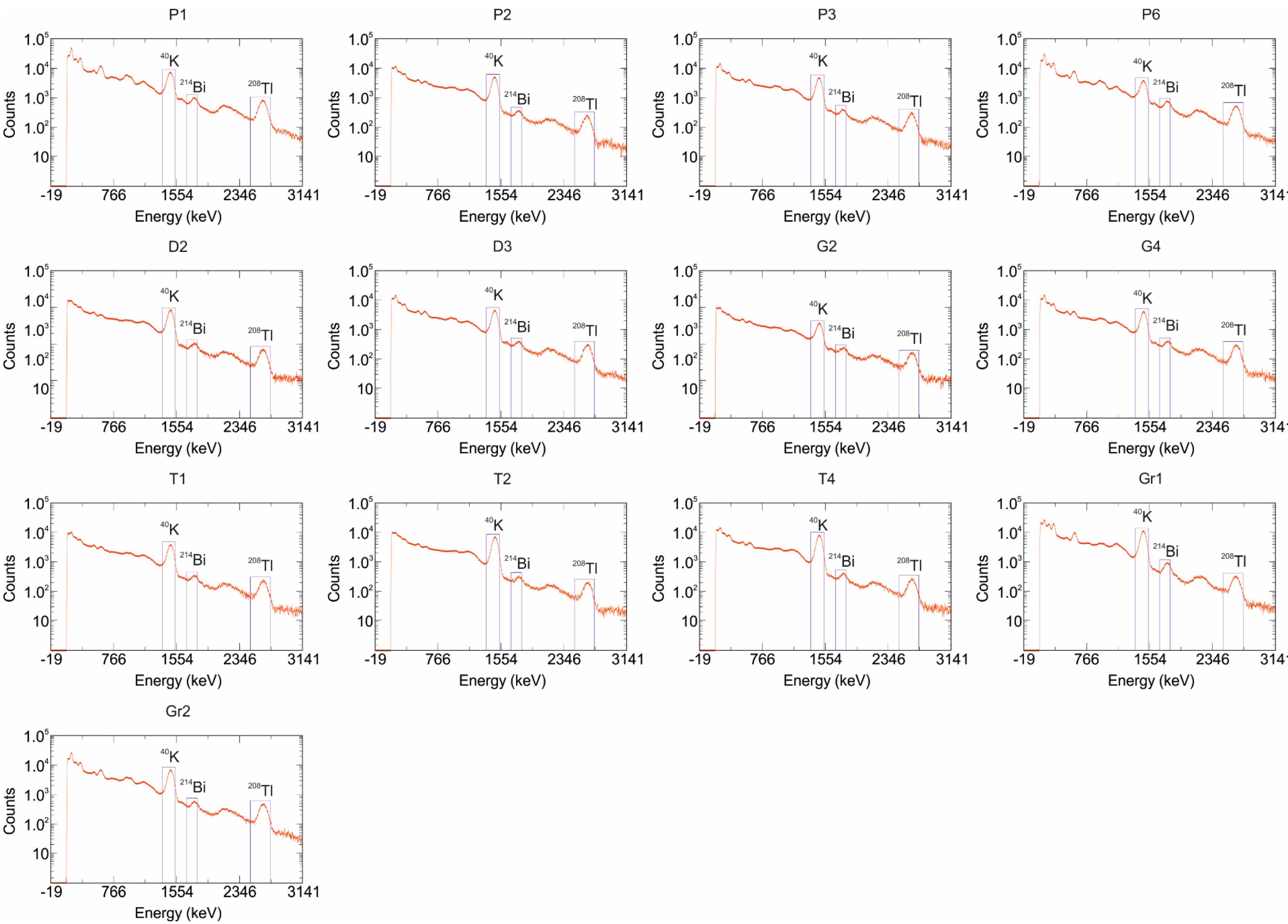

Figure 10.5 **Gamma-ray spectra identifying the radioactive isotopes ^{40}K, ^{214}Bi (U decay chain) and ^{208}Tl (Th decay chain).**

In situ gamma-ray spectrometry profiles using a NaI(Tl) detector were additionally done to compare with laboratory data (Figure 10.6). The results indicate the variability caused by each device, highlighting that biased results can be avoided if several methodologies are used.

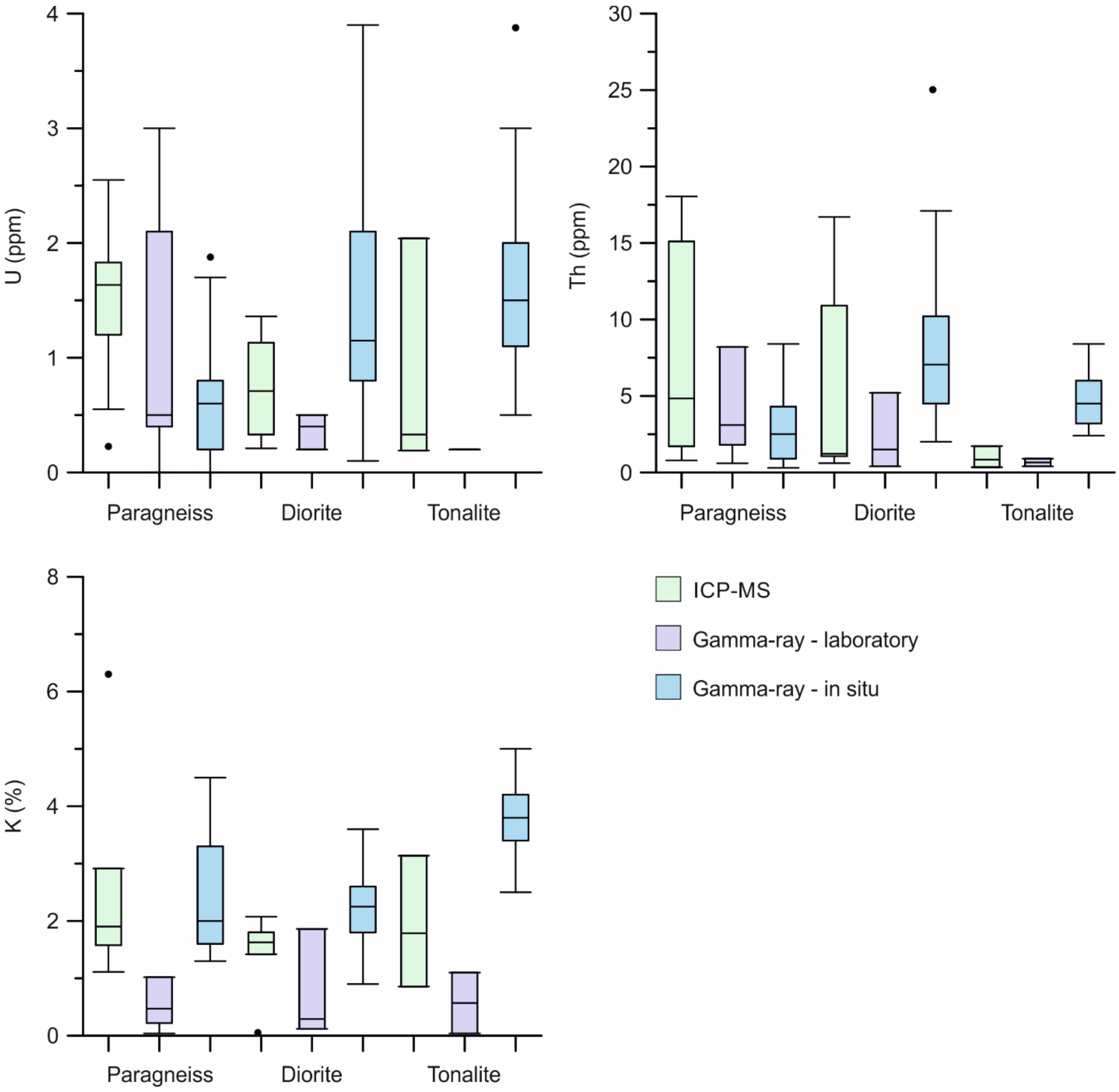

Figure 10.6 Laboratory versus in situ analyzes of the radiogenic elements.

The relationship between radiogenic heat production and major geochemical elements revealed, for the igneous lithologies, a positive correlation with SiO_2 (Figure 10.7a) and negative correlations with Fe_2O_3 (Figure 10.7b), CaO (Figure 10.7c), TiO_2 (Figure 10.7d) and MgO (Figure 10.7d). These results agree with Hasterok et al. (2017) that observed a positive correlation between U and Th and SiO_2 concentration. Both elements tend to increase their concentration with the increase of the latter. Thus, it can be concluded that, for igneous lithologies, radiogenic heat production tends to increase with the increase of felsic minerals and decrease with the increase on mafic minerals.

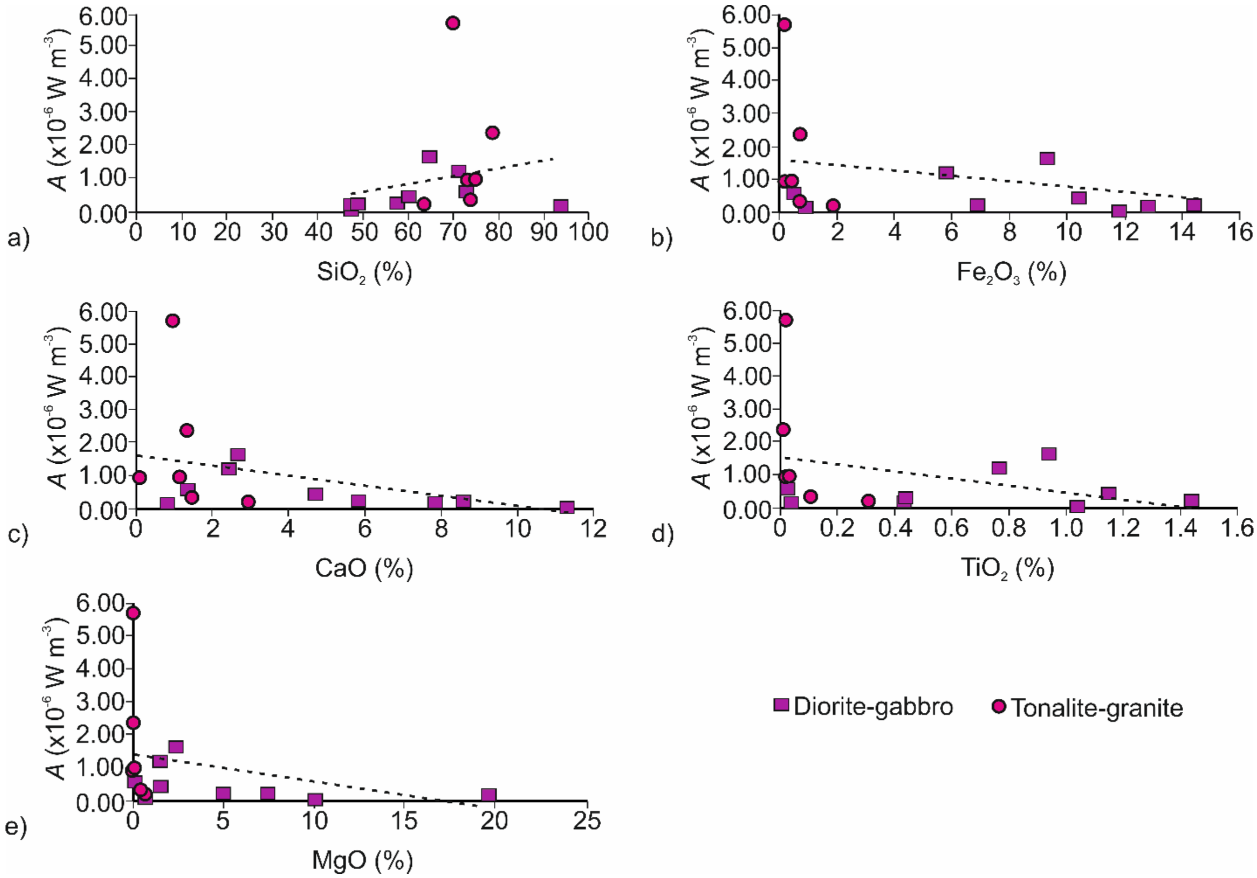

Figure 10.7 Correlation between radiogenic heat production and major elements for the igneous samples.

For metamorphic/metasedimentary rocks, Hasterok et al. (2018) observed that radiogenic heat production is positively correlated with Al_2O_3, FeO and TiO_2 but negatively correlated with CaO. The results of this thesis indicate a negative correlation with Al_2O_3 (Figure 10.8a) and CaO (Figure 10.8d) and positive with Fe_2O_3 (Figure 10.8b) and TiO_2 (Figure 10.8c). Hence, radiogenic heat production of paragneiss rock-type tend to increase as a function of the mafic minerals present.

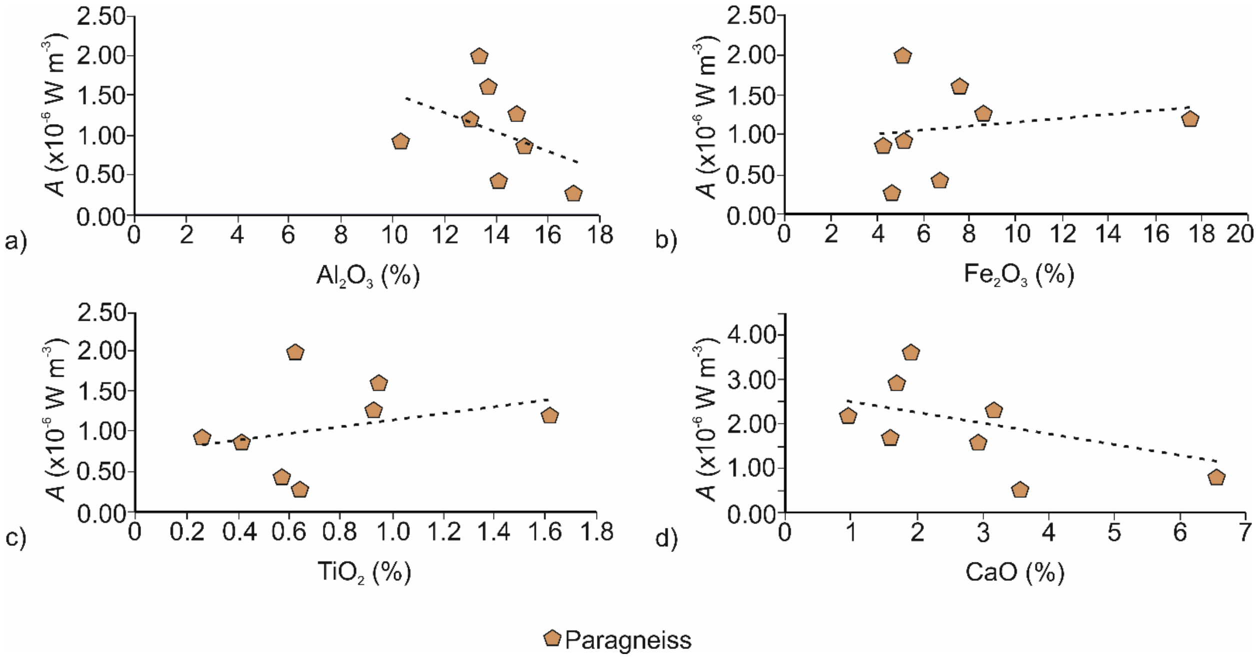

Figure 10.8 **Correlation between radiogenic heat production and major elements for the paragneiss samples.**